

MODELING OF THE PLASMA ETCHING OF POLYSILICON
WITH CHLORO- AND BROMO-TRIFLUOROMETHANE DISCHARGES

Vol 1

by

Kenneth Donald Allen

B.S., University of Massachusetts (1981)
S.M., Massachusetts Institute of Technology (1985)

SUBMITTED IN PARTIAL FULFILLMENT
OF THE REQUIREMENTS OF THE DEGREE OF

DOCTOR OF PHILOSOPHY
IN CHEMICAL ENGINEERING

at the

MASSACHUSETTS INSTITUTE OF TECHNOLOGY
June 1986

© Massachusetts Institute of Technology 1986

Signature of Author _____
Department of Chemical Engineering
May 13, 1986

Certified by _____
Professor Herbert H. Sawin
Thesis Supervisor

Accepted by _____
Professor William M. Deen
Chairman, Departmental Committee on Graduate Students

MASSACHUSETTS INSTITUTE
OF TECHNOLOGY

JUN 03 1986

LIBRARIES

ARCHIVES
Vol 1

MODELING OF THE PLASMA ETCHING OF POLYSILICON
WITH CHLORO- AND BROMO-TRIFLUOROMETHANE DISCHARGES

by

KENNETH DONALD ALLEN

Submitted to the Department of Chemical Engineering
on May 13, 1986 in partial fulfillment of the requirements
for the Degree of Doctor of Philosophy in Chemical Engineering

ABSTRACT

An experimental study of the plasma etching of polysilicon in various halocarbon gases is described. In particular, etching with CF_3Cl (Freon^R 13) is studied extensively. Experimental measures of etching rate, etching directionality, plasma impedance, atomic chlorine concentration, and total positive ion bombardment flux and energy are shown over wide ranges of three process variables: power input, pressure, and gas composition. Considerable experimental work with CF_3Br (Freon 13B1) discharges is also presented - the etching of n^+ -polysilicon, undoped polysilicon, and silicon dioxide are discussed. Etching directionality and uniformity are also examined for this chemical system.

Important plasma properties such as electron concentration are estimated by analysis of the discharge impedance using electrical analog models. Response Surface Methodology (RSM), a statistical design and analysis tool, is used for efficient examination of the above parameter space. RSM is a powerful tool for plasma process development, and is a necessary experimental technique because of the importance of interactions between process variables in determining plasma properties and etching characteristics.

Two primary mechanisms contribute to the etching process: (i) ion-assisted etching, which results in anisotropic profiles, and (ii) chemical etching, which results in isotropic profiles. Assuming the ion-assisted and chemical etching processes to be independent, a two-adjustable parameter model which successfully describes both etching rate and directionality is presented.

As suggested both by previous work and by the present data, the ion-assisted etching rate is assumed proportional to the flux of ions on the surface with energies in excess of a 15 eV threshold. Mean ion energies are described using a simple sheath transport model which incorporates results from the plasma impedance analysis, while ion bombardment energy distributions are modeled empirically.

Chemical etching is presumed to occur via attack of the silicon surface by chlorine atoms. The rate is assumed proportional to the atomic chlorine concentration near the wafer surface. Atomic chlorine concentrations, as measured by laser infrared absorption and corroborated by optical emission actinometry, were modeled by accounting for the rates of Cl^\cdot formation (via electron-impact dissociation of CF_3Cl) and loss in steady-state models. The dominant loss process at pressures lower than 0.5 torr is apparently recombination on the electrode surfaces, although gas-phase recombination may be important at higher pressures. Despite the low pressures used in plasma reactors, diffusion limitations must be considered.

The etching model is also consistent with the observed lack of a loading effect in CF_3Cl discharges, and provides a qualitative explanation for the variations in etching uniformity with conditions.

Thesis Supervisor: Professor Herbert H. Sawin

Title: Associate Professor of Chemical Engineering

Thesis Committee:

Professor R.A. Brown
Professor A.F. Sarofim
Professor J.I. Steinfeld
Professor U.W. Suter

May 13, 1986

Professor Jack P. Ruina
Secretary of the Faculty
Massachusetts Institute of Technology

Dear Professor Ruina:

In accordance with the regulations of the faculty, I submit herewith a thesis entitled "Modeling of the Plasma Etching of Polysilicon with Chloro- and Bromo-trifluoromethane Discharges," in partial fulfillment of the requirements for the degree of Doctor of Philosophy in Chemical Engineering at the Massachusetts Institute of Technology.

Respectfully Submitted,

Kenneth D. Allen

ACKNOWLEDGEMENTS

I would first like to thank my thesis advisor, Herb Sawin, for his interest in this work and for his patience with and support of my project. His insight and experience were often helpful when the inevitable problems struck - particularly his expertise with vacuum systems and computer hardware. My thesis committee was also helpful in guiding this work, by asking the tough questions that needed to be asked.

The success of this work was due in no small part to the contributions of my friends and cellmates Brian Thompson and Bert Richards. Thanks to their efforts, I was fortunate enough to find a mostly functional apparatus when I came aboard. Our continuing discussions of the mysterious world of plasma etching were usually enlightening, while conversations on other topics were always entertaining. Many of the ideas presented in this thesis benefitted greatly from these discussions. Jeff Schwartz and Becca Rossen also kicked in to make the office an interesting place.

The Freon Products Division of E.I. DuPont de Nemours and Co., Inc. provided most of the funding for this work. The contributions of Mike Mocella, Mary Jenkins, Akimichi Yokozeki, and Aaron Owens at DuPont are greatly appreciated. Additional support by the Semiconductor Research Corporation is also acknowledged.

My long stay here at MIT was made more enjoyable by many friends I made along the way: Jorge and Ann Leis, Andreas Kridiotis, Tom McKinnon, Sean Gallagher, Lou Durlifsky, Pat Houghton, Alain Bourhis, Jim Comfort, Craig Vaughn, Howie Rosen, Horacio Valeiras, Miral Kim-E, and all of their spouses and spouses to be. I also thank my older friends for their support: Geoff Jodry, Paul and Lynn Hirt, Bob and Mary Price, Laurel Dallmeyer and Tom Drennan, and many others too numerous to mention.

During my prolonged education, the support of the Allen and Barber families has been very welcome. Dad, Mom, Steve, Debbie, Scott, Bob, Jane, and all the others - I want you to know that I have been working these past five years - I just haven't been getting paid for it.

Finally, and most importantly, I would like to dedicate this thesis to my wife Susan. Through all the early mornings, late nights, lost weekends, and abject poverty, her love and support have been unwavering. Everything she has done to make my life easier and happier is truly appreciated. Thanks, Sue - I couldn't have done it without you.

TABLE OF CONTENTS

Title	1
Abstract	2
Letter	4
Acknowledgements	5
Table of Contents	6
List of Figures	9
List of Tables	17
1 INTRODUCTION	20
1.1 General Background	20
1.1.1 Integrated Circuit Fabrication	20
1.1.2 Dry vs. Wet Etching	22
1.1.3 Plasma Etching Reactor Configurations	25
1.2 Objectives and Scope	28
1.3 Halocarbon Etching of Polysilicon- Previous Work	30
1.3.1 CF_4	30
1.3.2 CF_3Cl	30
1.3.3 CF_3Br	31
2 EXPERIMENTAL	32
2.1 Apparatus	32
2.1.1 Geometry	32
2.1.2 Vacuum System	35
2.1.3 Powered Electrode Assemblies	36
2.2 Plasma Diagnostics	42
2.2.1 Electrical Impedance	42
2.2.2 Laser Interferometry	43
2.2.3 Optical Emission Spectroscopy	47
2.2.4 Mass Spectrometry	51
2.2.5 Langmuir Probe	54
2.2.6 Faraday Cup/Energy Analyzer	55
2.2.7 Laser Infrared Absorption	58
2.2.8 Computer Control	59
2.2.9 Data Analysis	59
2.3 Response Surface Methodology	60
2.3.1 Plasma Process Complexity	61
2.3.2 Response Surface Methodology	65
2.3.3 Experimental Designs	69
2.3.4 Statistical Analysis	74

3	PLASMA IMPEDANCE	89
3.1	Introduction	89
3.2	Experimental Results - Parameter Dependence	90
3.2.1	CF_3Cl	91
3.2.2	CF_3Br	96
3.3	Electrical Analog Models	99
3.3.1	Purely Capacitive Sheaths	99
3.3.2	Resistive Sheaths	117
3.4	Estimates of Plasma Properties	122
3.4.1	Plasma Resistance	122
3.4.2	Sheath Capacitance	129
3.4.3	Electron Concentrations	134
3.4.4	Electric Field/Pressure Ratio	143
3.4.5	Sheath Potential	146
3.4.6	Resistive-Sheath Model Results	153
4	ENERGETIC ION BOMBARDMENT OF SURFACES	154
4.1	Introduction	154
4.2	CF_3Cl Ion Flux Parametric Dependence	156
4.2.1	Introduction	156
4.2.2	Time Dependence	158
4.2.3	Flow Rate Dependence	159
4.2.4	Electrode Spacing Dependence	164
4.2.5	Power Input and Pressure Dependence	164
4.3	CF_3Cl Ion Energy Distributions	171
4.3.1	Data Analysis	171
4.3.2	Parametric Dependence - Experimental Measurements	174
4.3.3	Empirical Model	179
4.4	CF_3Cl Ion Chemistry	190
4.5	CF_3Br Experimental Results	194
4.5.1	Ion Flux	194
4.5.2	Ion Energy	197
4.5.3	Ion Chemistry	197
4.6	Ion Transport through Sheaths	203
4.6.1	Ion Energy	203
4.6.2	Ion Directionality	217
4.7	Ion-Assisted Etching	219

5	ACTIVE ETCHANT CONCENTRATIONS222
5.1	Experimental Measurements222
5.1.1	Laser Infrared Absorption in CF_3Cl222
5.1.2	Argon Optical Emission Actinometry224
5.1.3	Br^{\cdot} Emission from CF_3Br Plasmas232
5.2	Models for Atomic Chlorine Concentration in CF_3Cl236
5.2.1	Electron-Impact Dissociation of CF_3Cl236
5.2.2	Simplistic Steady-State Analyses240
5.2.3	Spatially-Dependent Models249
5.2.4	The Influence of Homogeneous Reactions252
6	POLYSILICON ETCHING263
6.1	Experimental Results263
6.1.1	Etching Rate of n^+ -Polysilicon in CF_3Cl Plasmas264
6.1.2	Etching Directionality in CF_3Cl Plasmas270
6.1.3	Etching Rate of n^+ -Polysilicon in CF_3Br Plasmas277
6.1.4	Etching Directionality in CF_3Br Plasmas281
6.1.5	Etching Uniformity287
6.1.6	Selectivity to Oxide294
6.2	Modeling of CF_3Cl Etching Rate and Directionality295
6.2.1	Model A295
6.2.2	Model B298
6.2.3	Model C301
6.2.4	Model D301
6.2.5	Comparison of Models303
	References319
	Appendix A - Nomenclature342
	Appendix B - Computer Program Listings348
B.1	Program ANALYZE348
B.2	Program RSM383
B.3	Program UNIFORM389
B.4	Program MODEL393
	Appendix C - Equipment Drawings396
C.1	Electrode Assembly C396
C.2	LN_2 Cold Traps405

LIST OF FIGURES

Fig. 1-1: Planar processing schematic 21

Fig. 2-1: Etching reactor schematic 33

Fig. 2-2: Vacuum system schematic 37

Fig. 2-3: Powered electrode schematic 40

Fig. 2-4: Typical current and voltage waveforms, CF₃Br plasma . 44

Fig. 2-5: Typical laser interferometry scan 46

Fig. 2-6: Typical high resolution optical emission scan 48

Fig. 2-7: Typical low resolution optical emission scan 49

Fig. 2-8: Typical QMS ion scan 52

Fig. 2-9: Typical QMS neutral scan 53

Fig. 2-10: Typical Langmuir probe I-V curve 56

Fig. 2-11: Faraday cup assembly schematic 57
(a-b)

Fig. 2-12: Interaction effects between process variables 64
(a-b)

Fig. 2-13: Effect of experimental design
(a-c) on modeling capability 68

Fig. 2-14: (a-b)	Common three-variable experimental designs	71
Fig. 2-15:	Residual plot for quadratic model fit of Box-Behnken design	80
Fig. 2-16:	Contour plot of polysilicon etching rate in CF_3Cl/Ar discharges vs. power input and pressure, quadratic model fitting of Box-Behnken design	83
Fig. 2-17:	Experimental design to support cubic model	85
Fig. 2-18:	Contour plots of polysilicon etching rate in CF_3Cl plasma vs. power input and pressure, cubic model fitting of experimental design, two compositions	87 88
Fig. 3-1:	Dependence of rms voltage on power input and pressure in CF_3Cl plasmas	94
Fig. 3-2:	Dependence of rms current on power input and pressure in CF_3Cl plasmas	95
Fig. 3-3:	Fit of eqn. (3.2.2-1) to rms current data in CF_3Br plasmas - dependence of rms current on power input and pressure	98
Fig. 3-4:	AC electrical analog model for plasma100
Fig. 3-5:	Plasma voltages with rf cycle time104
Fig. 3-6:	Plasma potential at grounded electrode sheath vs. time in rf cycle106
Fig. 3-7:	Comparison of impedance model prediction of V_s with maximum ion energy data in CF_3Cl plasmas110

Fig. 3-8: (a-c)	Contour plots of bulk plasma resistance vs. power density, pressure, and Ar fraction in CF ₃ Cl/Ar plasmas126 -128
Fig. 3-9:	Contour plot of bulk plasma resistance vs. power density and pressure in a CF ₃ Br plasma130
Fig. 3-10: (a-c)	Contour plots of sheath capacitance vs. power density, pressure, and Ar fraction in CF ₃ Cl/Ar plasmas131 -133
Fig. 3-11:	Contour plot of sheath capacitance vs. power density and pressure in a CF ₃ Br plasma135
Fig. 3-12: (a-c)	Contour plots of estimated electron concentration vs. power density, pressure, and Ar fraction in CF ₃ Cl/Ar plasmas136 -138
Fig. 3-13:	Contour plot of estimated electron concentration vs. power density and pressure in CF ₃ Br plasmas . .	.142
Fig. 3-14:	Best fit of eqn. (3.4.3-1) to impedance model estimate of [e ⁻] in CF ₃ Br plasmas144
Fig. 3-15:	Contour plot of bulk plasma electric field to pressure ratio vs. power density and pressure in CF ₃ Cl plasmas145
Fig. 3-16:	Best fit of eqn. (3.4.4-1) to impedance model estimate of E ₀ /P in CF ₃ Br plasmas147
Fig. 3-17: (a-c)	Contour plots of estimated sheath voltage vs. power density, pressure, and Ar fraction in CF ₃ Cl/Ar plasmas148 -150

Fig. 3-18:	Contour plot of estimated sheath voltage vs. power density and pressure in CF_3Br plasmas152
Fig. 4-1:	Ion flux with blank electrode vs. time-averaged ion flux during etching of 1/4 wafer, several plasma conditions in CF_3Cl plasmas157
Fig. 4-2: (a-c)	Ion flux vs. time during etching of 1/4 wafer, three plasma conditions in CF_3Cl plasmas160 -162
Fig. 4-3:	Dependence of ion flux on flow rate in CF_3Cl plasmas163
Fig. 4-4:	Dependence of ion flux on electrode spacing in CF_3Cl plasmas167
Fig. 4-5: (a-c)	Contour plot of ion flux vs. power and pressure, 10% Ar in a CF_3Cl plasma168 -170
Fig. 4-6:	Measured ion current to flag vs. grid retarding potential172
Fig. 4-7:	Ion energy distribution in CF_3Cl plasmas, 0.7 torr .	.176
Fig. 4-8:	Ion energy distribution in CF_3Cl plasma, 0.5 torr .	.177
Fig. 4-9:	Ion energy distribution in CF_3Cl plasma, 0.3 torr .	.178
Fig. 4-10:	Contour plot of mean ion energy vs. power and pressure in CF_3Cl plasmas180
Fig. 4-11:	Empirical model for ion energy distribution183
Fig. 4-12: (a-b)	Empirical ion energy distribution model vs. experiment, worst and typical cases189

Fig. 4-13: (a-c)	QMS ion scans of CF_3Cl plasmas, three conditions193
Fig. 4-14:	Contour plot of ion flux vs. power and pressure in CF_3Br plasmas, 15 sccm flow rate196
Fig. 4-15:	Contour plot of mean ion energy vs. power and pressure in CF_3Br plasmas199
Fig. 4-16:	Ion energy distributions in CF_3Br plasmas200
Fig. 4-17: (a-b)	QMS ion scans of CF_3Br plasmas, two conditions202
Fig. 4-18:	Sheath transport model predictions of mean ion energy in CF_3Cl discharges211
Fig. 4-19:	Sheath transport model predictions of mean ion energy in CF_3Br discharges214
Fig. 5-1:	Atomic chlorine concentration in CF_3Cl plasmas, dependence on power input226
Fig. 5-2:	Atomic chlorine concentration in CF_3Cl plasmas, dependence on pressure227
Fig. 5-3:	Atomic chlorine mole fraction X_{Cl} vs. power density, CF_3Cl plasmas228
Fig. 5-4:	Comparison of $[Cl]$ measurements via LIA with argon actinometry predictions, CF_3Cl plasmas231
Fig. 5-5:	High resolution optical emission scan, CF_3Br plasma233
Fig. 5-6:	Contour plot of $[Ar]I_{Br}/I_{Ar}$ vs. power density and pressure, during polysilicon etching in CF_3Br235

Fig. 5-7:	$\cdot\text{Cl}$ formation rate constant k_F vs. mean electron energy, Maxwellian and Druyvestyn distributions239
Fig. 5-8:	Measured $[\text{Cl}]$ vs. prediction: first-order recombination, reaction-limited model243
Fig. 5-9:	Measured $[\text{Cl}]$ vs. prediction: first-order recombination, diffusion-limited model246
Fig. 5-10:	Measured $[\text{Cl}]$ vs. prediction: second-order recombination, diffusion-limited model251
Fig. 5-11:	Homogeneous reaction model, base case analysis258
Fig. 5-12:	Homogeneous reaction model, effect of $\cdot\text{Cl}$ formation rate259
Fig. 5-13:	Homogeneous reaction model, effect of homogeneous recombination rate260
Fig. 5-14:	Homogeneous reaction model, effect of electrode surface recombination rate261
Fig. 5-15:	Homogeneous reaction model, effect of silicon etching rate262
Fig. 6-1:	Contour plot of polysilicon etching rate vs. power density and pressure, 10% Ar in CF_3Cl plasmas267
Fig. 6-2:	Contour plot of polysilicon etching rate vs. power density and pressure, 20% Ar in CF_3Cl plasmas268
Fig. 6-3:	Contour plot of polysilicon etching rate vs. power density and composition at 0.5 torr, CF_3Cl plasmas269

Fig. 6-4:	Definition of anisotropy coefficient α271
Fig. 6-5:	Contour plot of anisotropy coefficient α for poly etching vs. power density and pressure, 15% Ar in CF ₃ Cl plasmas275
Fig. 6-6:	Polysilicon etching rate vs. total ion flux in CF ₃ Cl/Ar plasmas, influence of ion energy276
Fig. 6-7:	Contour plot of polysilicon etching rate vs. power density and pressure at 10 sccm flow rate, CF ₃ Br plasmas279
Fig. 6-8:	Contour plot of polysilicon etching rate vs. power density and pressure at 20 sccm flow rate, CF ₃ Br plasmas280
Fig. 6-9:	SEM of polysilicon etch in CF ₃ Br, trial BR_18285
Fig. 6-10:	SEM of polysilicon etch in CF ₃ Br, trial BR_19285
Fig. 6-11:	SEM top view of Fig. 6-9286
Fig. 6-12:	Placement of wafer sample on lower electrode288
Fig. 6-13:	Clearing patterns observed in CF ₃ Cl plasmas288
Fig. 6-14:	Dependence of clearing on process conditions289
Fig. 6-15:	Etch uniformity model, geometry and nomenclature .	.292
Fig. 6-16:	Contour plot of polysilicon etching rate vs. power density and pressure, 15% Ar in CF ₃ Cl plasmas306
Fig. 6-17:	Etching rate predictions of model A, contour plot for same range as in Fig. 6-16307

Fig. 6-18:	Anisotropy coefficient predictions of model A vs. experiment309
Fig. 6-19:	Etching rate predictions of model B, contour plot for same range as in Fig. 6-18310
Fig. 6-20:	Anisotropy coefficient predictions of model B vs. experiment311
Fig. 6-21:	Etching rate predictions of model C, contour plot for same range as in Fig. 6-16313
Fig. 6-22:	Anisotropy coefficient predictions of model C vs. experiment314
Fig. 6-23:	Anisotropy coefficient predictions of model C, contour plot for same range as in Fig. 6-16315

LIST OF TABLES

Table 2-1:	Important plasma etching process variables	62
Table 2-2:	Important plasma etching process specifications	62
Table 2-3:	Polysilicon etching rates in CF_3Cl plasmas, data for Box-Behnken experimental design	75
Table 2-4:	Correlation matrix for Box-Behnken design	77
Table 2-5:	Regression coefficients for Box-Behnken design	78
Table 2-6:	Analysis of variance for Box-Behnken design	81
Table 3-1:	Impedance properties of CF_3Cl plasmas at various conditions, blank electrodes	92
Table 3-2:	Impedance properties of CF_3Cl plasmas at various conditions, during polysilicon etching	93
Table 3-3:	Impedance properties of CF_3Br plasmas at various conditions, during polysilicon etching	97
Table 3-4:	Impedance model predictions of plasma properties in CF_3Cl plasmas, various conditions123
Table 3-5:	Impedance model predictions of plasma properties in CF_3Br plasmas, various conditions124
Table 3-6:	Resistive-sheath impedance model predictions of plasma properties in CF_3Br plasmas125
Table 3-7:	Comparison of impedance model predictions of $[e^-]$ in CF_3Cl plasmas vs. Langmuir probe data141

Table 4-1:	Ion fluxes for 37-run experimental design F13A, CF ₃ Cl plasmas165
Table 4-2:	Ion fluxes for additional conditions, CF ₃ Cl plasmas166
Table 4-3:	Mean ion energy at various plasma conditions, CF ₃ Cl plasmas175
Table 4-4:	$\delta(E^*)$ at various CF ₃ Cl plasma conditions181
Table 4-5:	Best fit values of E ₁ and E ₂ for various plasma conditions, CF ₃ Cl plasmas184
Table 4-6:	$\Delta(E^*)$, $\delta(E^*)$, and $\tilde{\Lambda}(E^*)$ for various plasma conditions, CF ₃ Cl plasmas186
Table 4-7:	QMS peak heights for major ions in CF ₃ Cl plasmas, various plasma conditions192
Table 4-8:	Ion fluxes for 35-run experimental design BR, various conditions in CF ₃ Br plasmas195
Table 4-9:	Mean ion energies in CF ₃ Br plasmas198
Table 4-10:	QMS peak heights for major ions in CF ₃ Br plasmas, various plasma conditions201
Table 5-1:	Atomic chlorine concentrations in CF ₃ Cl discharges, as measured by laser infrared absorption (LIA)225
Table 5-2:	Optical emission intensities in CF ₃ Cl discharges, same conditions as in Table 5-1230
Table 5-3:	Optical emission intensities during etching of polysilicon in CF ₃ Br discharges234

Table 5-4:	Reactions important in determining [C1]253
Table 5-5:	Rate constants for homogeneous reaction model257
Table 6-1:	Polysilicon etching rates in CF_3Cl/Ar discharges, experimental design F13A265
Table 6-2:	Polysilicon etching rates in CF_3Cl/Ar discharges, experimental design F13B266
Table 6-3:	Polysilicon etching directionality in CF_3Cl/Ar plasmas, experimental design F13B274
Table 6-4:	Polysilicon etching rate in CF_3Br plasmas, experimental design BR278
Table 6-5:	Polysilicon etching directionality in CF_3Br plasmas, experimental design BR282
Table 6-6:	Parameter dependence of linewidth loss in CF_3Br etching of polysilicon283
Table 6-7:	Regression results for models A-C304

CHAPTER 1 - INTRODUCTION

1.1 GENERAL BACKGROUND

1.1.1 Integrated Circuit Fabrication

Since the invention of the transistor by William Shockley and coworkers in 1950, integrated circuit (IC) technology has become increasingly important to the world economy. Tremendous advances in both device physics and processing technology have allowed rapid increase in device density and computing speed.

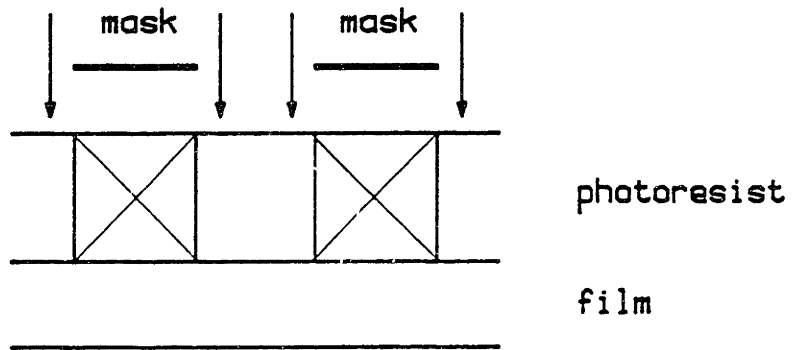
Integrated circuit fabrication relies on planar processing, i.e., electronic devices are produced on a substrate by selectively adding and subtracting material from the surface. The general process for making lines on a substrate is shown schematically in Fig. 1-1. First, a thin layer of material (.1-1 μm thick) is deposited by chemical vapor deposition (CVD). By photolithographic techniques, the desired pattern is transferred to a photoresist mask on the surface of the film. The pattern is replicated in the film by selectively etching away unwanted material.

One common film, polysilicon, is used as a gate metallization material in metal oxide semiconductor (MOS) devices, and as electrical interconnects between devices (Ghandi, 1983). The resistance of polysilicon decreases dramatically as it is doped with either group

Thin Film Deposition (CVD)



Pattern Transfer (Photolithography)



Selective Film Removal (Etching)

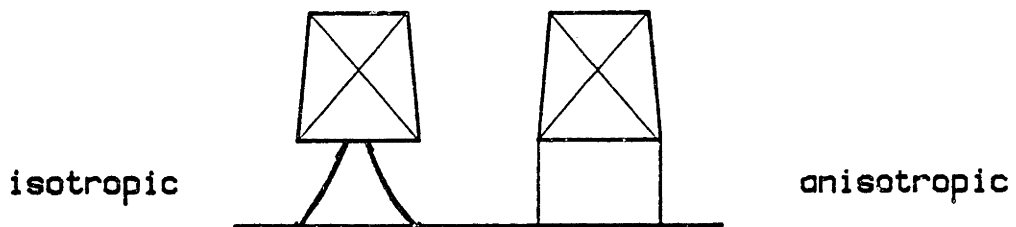


Figure 1-1: Planar processing schematic - CVD, photolithography, and etching.

III (e.g., boron) or group V (e.g., phosphorus) compounds - therefore, most polysilicon used in semiconductor applications is heavily doped (about 1 atomic percent). As is discussed later, doping at this level has dramatic effects on the etching characteristics of the film.

1.1.2 Dry vs. Wet Etching

Until 1980, thin film etching was performed in acid baths by a wet etching technique. The acid solution reacts selectively with the film to remove unwanted regions on the surface. However, wet etching is isotropic, i.e., the etching rate is the same in all directions. Consequently, as a film is etched, the mask is undercut from each side by a distance equal to the mask thickness (see Fig. 1-1). The importance of this undercut depends on the aspect ratio of the line; undercutting is a serious problem when the linewidth/film thickness is less than 5:1 (Mogab and Harshbarger, 1978). As linewidths decreased to 2 microns and below, wet etching became undesirable since a significant fraction of the line was lost during the etching process. Therefore, wet etching is unacceptable for very-large-scale integration (VLSI) technology.

Another technique, plasma etching, can be used for VLSI processing because the vertical etching rate is in many cases much higher than the lateral etching rate, i.e., the etch can be anisotropic. Energetic ion bombardment of the film surface is used to achieve the

directionality of etching. The plasmas used in microelectronic fabrication are more correctly named non-equilibrium glow discharges. Plasma etching is essentially a gas-solid reaction for selective removal of a thin film, however, the energy input to the chemical process is not thermal. Rather, a rapidly-oscillating radio-frequency (rf) voltage is applied across the low-pressure gas. Free electrons in the gas are accelerated by this applied electric field. Because of their low mass, the electrons cannot efficiently exchange energy with the gas molecules. Consequently, the mean electron temperature is much higher than that of the gas and the high-energy electrons initiate flame-type reactions in the gas: ionization, free radical formation, etc. These highly reactive chemical species react with the film to form volatile compounds; in this way the film is etched.

A plasma is a partially ionized gas, with ionized fractions in the range of 10^{-7} to 10^{-6} being common for glow discharges. Because the electrons in the discharge are much more mobile than the heavier positive ions they diffuse to the reactor walls much more rapidly, leaving the plasma net positive. The charge separation results in a potential difference between the plasma and the surfaces in contact with it. This electric field, which points along the macroscopic surface normal, opposes the further loss of electrons and aids the loss of positive ions until the fluxes of the two species equalize and the plasma becomes net neutral. Because the plasma potential can reach hundreds of volts, the positive ions striking the electrode surfaces may have very high energies. Ions, which can only strike the

microscopic features exposed to the plasma (i.e., normal to the electric field), contribute energy to the etching reactions and thereby increase the vertical etching rate. Since ion bombardment of the film sidewalls is not generally important, ion bombardment selectively accelerates etching in the vertical direction while leaving lateral etching unaffected. In this way, directional profiles can be achieved via plasma etching.

Apart from the issue of directionality, plasma processing offers several advantages over wet etching. First, plasma processes are automatable and can be integrated into the fabrication lines of the future (Lam, 1982). Second, plasma processing uses much smaller volumes of dangerous chemicals than does wet etching - the environmental impact of a dry process is therefore less than that of a wet process (Coburn, 1982). Third, plasma etching is compatible with most organic photoresist masks, especially if the wafer is cooled during etching (Parry and Rodde, 1979). This is in contrast to many wet etching processes, which require silicon dioxide masking (Poulsen, 1977) - therefore, wet etching processes may require extra steps in wafer fabrication. Finally, plasma processes are inherently cleaner than wet processes, i.e., wafer contamination can be more strictly controlled.

The disadvantages of plasma processing are the high capital equipment costs, the use of small volumes of highly toxic gases, and most importantly, the complexity of these poorly-understood processes. Plasma etching is an empirical science at best; presently, many processes are developed via hit-or-miss experimentation.

At present, plasma etching accounts for about 20% of all etching steps in VLSI fabrication; in the next five years the fraction is expected to increase to 80% (Strategic Incorporated, 1984). Since most fabrication sequences involve at least 3-5 etching steps, the importance of plasma etching is obvious given the enormous economic potential of VLSI.

1.1.3 Plasma Etching Reactor Configurations

Several etching reactor configurations have been described in the literature - among these are barrel etchers, hexode batch reactors, single-wafer plasma etchers and single-wafer reactive-ion etchers. Although each configuration offers great advantages for a particular purpose, the single-wafer tools are most important for VLSI. In this subsection, the strengths and weaknesses of each configuration are briefly outlined. The interested reader is referred to Chapman (1980) or Coburn (1982) for schematic diagrams and more detailed discussion.

In barrel etchers, a large number of wafers can be processed simultaneously. Therefore, throughput can be very good if etching rates are appropriately high. Generally, high pressures (0.5-1 torr) are used in barrel etcher systems to achieve high etching rates. However, energetic ion bombardment of surfaces in a barrel reactor is generally insignificant, so etching is nearly isotropic. Plasma ashing of photoresist and silicon dioxide mask removal are two important processes well suited to the barrel configuration.

Hexode batch reactors (so named because the powered electrode/wafer support is hexagonal) have been the mainstay of the industry for the past five years. Many wafers can be etched simultaneously in these systems, and good etch directionality can be achieved. However, directionality is obtained at the expense of etching rate because low pressures (~0.1 torr) must be used. Also, process control is difficult because of etching nonuniformities over the large wafer surface area.

Single-wafer tools can be used in two modes: plasma etch (PE) or reactive-ion etch (RIE). In both cases, a parallel-plate electrode assembly is used (Reinberg, 1973). Single-wafer etchers offer several important advantages over batch systems. First, single-wafer tools are physically smaller, which is vital as clean room floor space becomes almost prohibitively expensive. Single-wafer etch processes are easier to control due to better spatial uniformity (Weiss, 1984), which will be more important as wafer sizes increase and the cost per wafer becomes higher. Finally, process development is easier in single-wafer etchers because of the simplified geometry.

In PE, the wafer sits on the grounded electrode, and the system is symmetric (i.e., the electrodes are of equal area). Etch directionality can be controlled by varying system pressure, power input, etc. Generally, PE results in directional but not completely anisotropic etching.

In RIE, the powered electrode is much smaller than the ground electrode. Therefore, most of the voltage is dropped across the plasma sheath of the powered electrode, on which the wafer is placed (Bondur, 1976). Consequently, the wafer is subject to very energetic ion bombardment. As discussed later in this thesis, energetic ion bombardment increases etch directionality. For this reason, RIE has been the preferred mode for VLSI etching (Wang and Maydan, 1983); even deep and narrow trenches can be etched in silicon by this technique. However, energetic ion bombardment also causes device damage (Ephrath, 1982), so a tradeoff between directionality and damage must be made. In the future, etching processes may incorporate some of the advantages of both PE and RIE by operating in intermediate pressure ranges (e.g., 100-200 mtorr).

1.2 OBJECTIVES AND SCOPE

A better understanding of the physical and chemical processes important in plasma etching will provide a more rational basis for process development, optimization, and control. For example, by examining the relationships between externally-controlled variables, internal plasma properties, and etching responses, heuristics to aid in process development can be developed. Weiss (1983b) noted that plasma etching equipment manufacturers need to supply etching processes with their product, and that workable etching process models would be most welcome. Of course, a fully descriptive theoretical model for the etching process would be very helpful. As such a model is not possible given the present state of our knowledge of plasma etching, and may never be possible given the tremendous complexity of these processes, simplified models which indicate process trends with controllable parameters and identify important physical processes would be most useful.

In this thesis, I have taken the following approach to the problem of etch process modeling. A large volume of experimental data, both of etching responses and of important physical plasma properties, was collected for two chemical systems - CF_3Cl and CF_3Br . Etch gases based on multiple halogen chemistries are particularly interesting because of the wide range of etching characteristics which can be obtained by varying process conditions. The importance of chemistry is seen in that fluorine-based chemistries undercut polysilicon films more than do chlorine-based ones (Winkler, 1983).

Experimental design and statistical analysis techniques for rapid identification and quantification of process trends with external variables were developed and used. The relationships between important process responses (e.g., etching rate) and plasma properties (e.g., ion bombardment flux) were then examined using simple models. The importance of energetic ion bombardment on the etching process was examined in detail. The final result is a phenomenological model which accounts for observed trends in etching rate and directionality with varying power input, pressure, and gas composition using a minimum of adjustable parameters. The model, although not fully predictive, provides considerable insight into the important mechanisms of plasma etching.

1.3 HALOCARBON ETCHING OF POLYSILICON - PREVIOUS WORK

1.3.1 CF_4

Most of the studies involving halocarbon etchant gases have centered on CF_4 and its mixtures with O_2 (for polysilicon etching) or H_2 (for silicon dioxide etching). Since such a large body of work, including several modeling attempts, exists for this gas, it will be not be examined here. Several excellent reviews of many aspects of halocarbon etching are available (e.g., Coburn 1982).

1.3.2 CF_3Cl

Few studies of CF_3Cl etching can be found in the literature, although the gas has frequently been used as an additive to fluorocarbon (e.g., CF_4) etching systems to improve etch directionality (Borghesani and Mori, 1983; Adams and Capio, 1981; Mogab and Levinstein, 1980). Because of its high selectivity to silicon dioxide and its relatively small loading effect, CF_3Cl is an industrially interesting etching gas (Mogab and Levinstein, 1980).

Leahy (1981) observed that the etching rate of doped polysilicon in CF_3Cl discharges reaches a maximum with increasing pressure at about 0.4-0.5 torr. He also observed that etching rate increased with power input. As in other chlorine-based discharges, CF_3Cl etching of

polysilicon becomes more rapid with increasing dopant concentration (n-type dopants). The etching rate of p-doped polysilicon was not significantly different than that of undoped polysilicon.

1.3.3 CF_3Br

The literature on CF_3Br etching of polysilicon is even more sparse, although the gas has been used to etch other films. Flamm et al. (1980) reported some observations on polymeric film formation in these plasmas, while Flamm (1981) examined the production of the radical species $\cdot CF_2$ and $\cdot CF_3$ in both CF_3Cl and CF_3Br discharges. Only Matsuo (1980) has reported previously on the etching properties of CF_3Br plasmas, wherein it was seen that the selectivity of CF_3Br for Si:SiO₂ etching is adequate for many applications.

CHAPTER 2 - EXPERIMENTAL

2.1 APPARATUS

The equipment used in this thesis is described in this section, both etching system hardware and diagnostic hardware and software. Equipment designed or built by the author is explained in detail, including equipment drawings. Further details of the apparatus may be found elsewhere (Richards, 1986a), as may the specifics of the microcomputer control system (Thompson, 1986).

2.1.1 Geometry

The etching reactor is a single-wafer tool, see the schematic in Fig. 2-1. It is a symmetric parallel-plate system, i.e., the powered and ground electrodes are of equal diameter (12.7 cm). The upper electrode is powered, the lower grounded; the wafer sits on the grounded electrode. The upper electrode is suspended from the chamber lid on a Mitutoyo model 297-101 micrometer drive; the micrometer allows the electrode spacing to be varied from 0-4 cm. The lower electrode rests on the chamber baseplate. Three powered electrode assemblies were used over the course of this thesis - these designs are discussed in section 2.1.3.

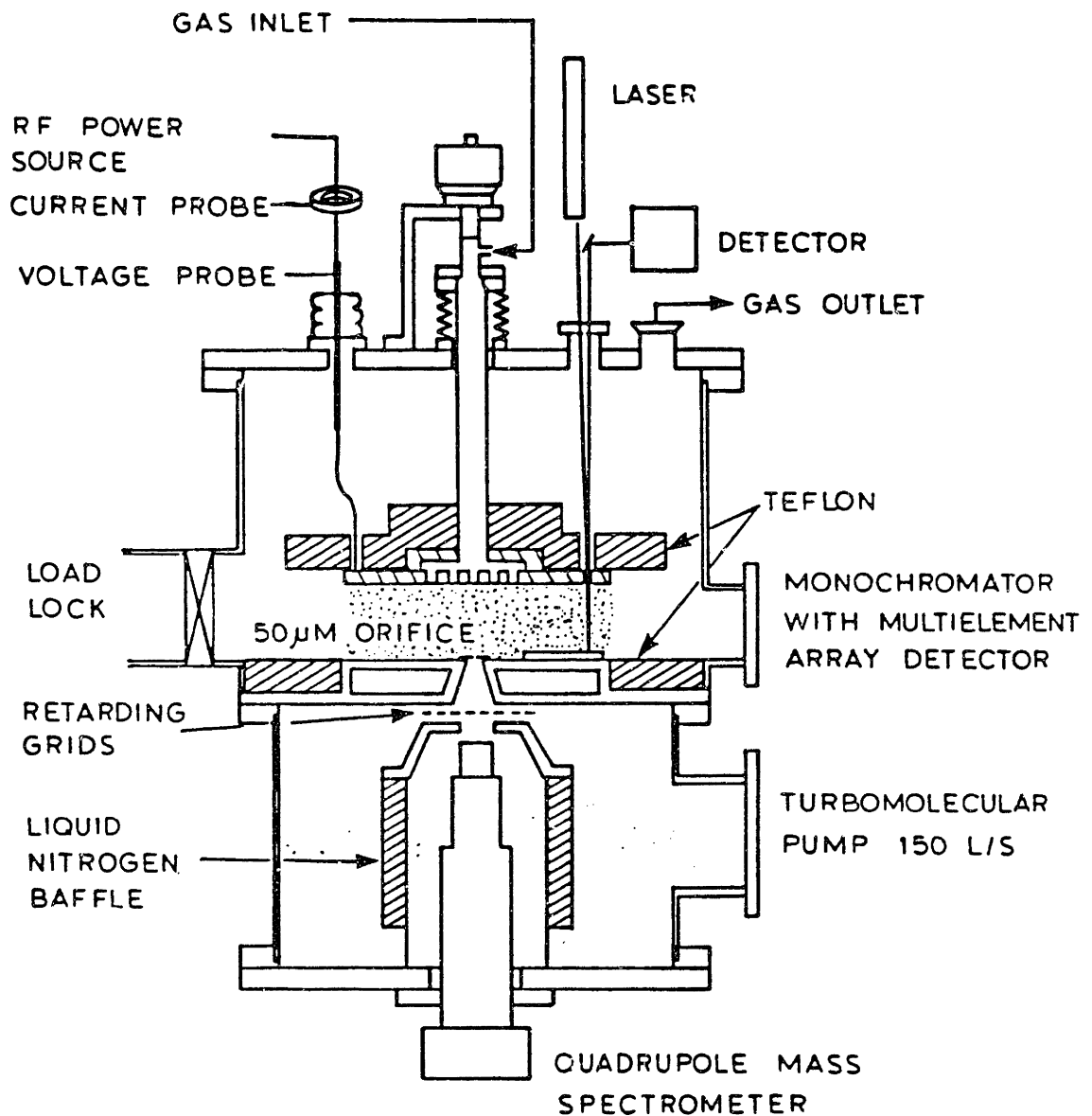


Figure 2-1: Plasma etching reactor apparatus schematic with associated diagnostics.

The main chamber itself is a cylinder 19 cm high by 27 cm in diameter. As shown in Fig. 2-1, Teflon rings extend from both electrodes toward the chamber walls; the lower ring to the wall and the upper ring to within a few cm of the wall. The Teflon rings serve to isolate the plasma from the metal surfaces by dropping the high electric fields through the insulating rings. All metal surfaces inside the etching chamber are stainless steel (304L or 316L).

The lower electrode, to which the wafer sample is clipped, can be removed from the main chamber to the outer chamber through a load-lock gate valve. Since the outer chamber is vented and pumped separately, this system allows the sample to be changed without losing vacuum in the main chamber. Pump-down time due to degassing of the chamber is greatly reduced by this system; turnaround time from sample to sample is less than 5 minutes.

The lower chamber, which houses the mass spectrometer and the Faraday cup, is also constructed of 304L stainless steel. The lower chamber is separated from the upper chamber by a 25-50 μm diameter pinhole aperture in the main chamber baseplate, and is differentially pumped. The small flux of neutrals or ions through the pinhole is effusive, since the diameter is less than the mean free path ($\sim 100 \mu\text{m}$ at 0.3 torr). The mass spectrometer is encased in a liquid nitrogen baffle to minimize background noise.

2.1.2 Vacuum System

The etcher's gas manifold is capable of mixing up to five gases from a selection of ten ports. The feed gases to the chamber are metered with Tylan mass flowmeters; flowmeter ratings are 10 and 50 sccm. The gas feedthrough to the chamber is a hollowed Teflon tube connected to the upper electrode. The gases exit the upper electrode through a showerhead arrangement in the center, flow radially outward between the electrodes, and are pumped out of the chamber at an exit port in the chamber lid. System pressure is measured with an MKS 22-AHS capacitance manometer on the chamber lid. Independent control of pressure and flow rate is achieved with an MKS Baratron 252A exhaust valve controller, which varies the effective pumping speed with a butterfly valve in the exhaust line.

After passing through the exhaust valve controller, gases are pumped through a pair of liquid nitrogen (LN_2) cold traps to remove corrosive/reactive chemical species; each trap consists of a "coldfinger" on which the gases are frozen. The LN_2 level in the traps is maintained by a pair of thermal sensors in conjunction with a solenoid-valve flow system (manufactured by Cryo-Med). The traps are vented to a laminar flow hood when the system is not in use. During this time the chamber is purged with nitrogen, which is pumped through a bypass line containing a molecular sieve trap to prevent backstreaming of pump oil to the chamber. Schematic drawings of the cold trap assembly are shown in Appendix C.2. Upon leaving the cold

trap the gases enter the line to the main pump, an Edwards E2M80 rotary vane pump (80 CFM), and are exhausted to the hood. All gas lines between the chamber and the main pump are at least 3.5 cm in diameter, so gas conductance is adequate. System base pressure is about 10^{-3} torr at low flow rates and leak rates are on the order of .005 sccm.

The lower chamber is differentially pumped by either a Varian ion pump or a 150 liter/sec Leybold-Heraeus turbomolecular pump backed by a roughing pump. Lower chamber background pressure is 10^{-6} torr; an order of magnitude lower pressure is obtained when the mass spectrometer's LN_2 baffle is filled.

The outer chamber is pumped by a roughing pump. Load-lock pressure is measured with a thermocouple gauge, and is generally less than 10 mtorr.

A schematic of the vacuum system is shown in Fig. 2-2.

2.1.3 Powered Electrode Assemblies

Three powered electrode designs evolved during the course of this thesis; these are referred to as electrode assemblies A, B, and C, respectively. Briefly, assembly A is a thin (about 1/8 inch) stainless steel plate of 15 cm diameter. A 17.7 cm diameter by 1 cm thick Teflon sheet rests on top of the powered electrode. The electrical feedthrough to this electrode consists of two Teflon-

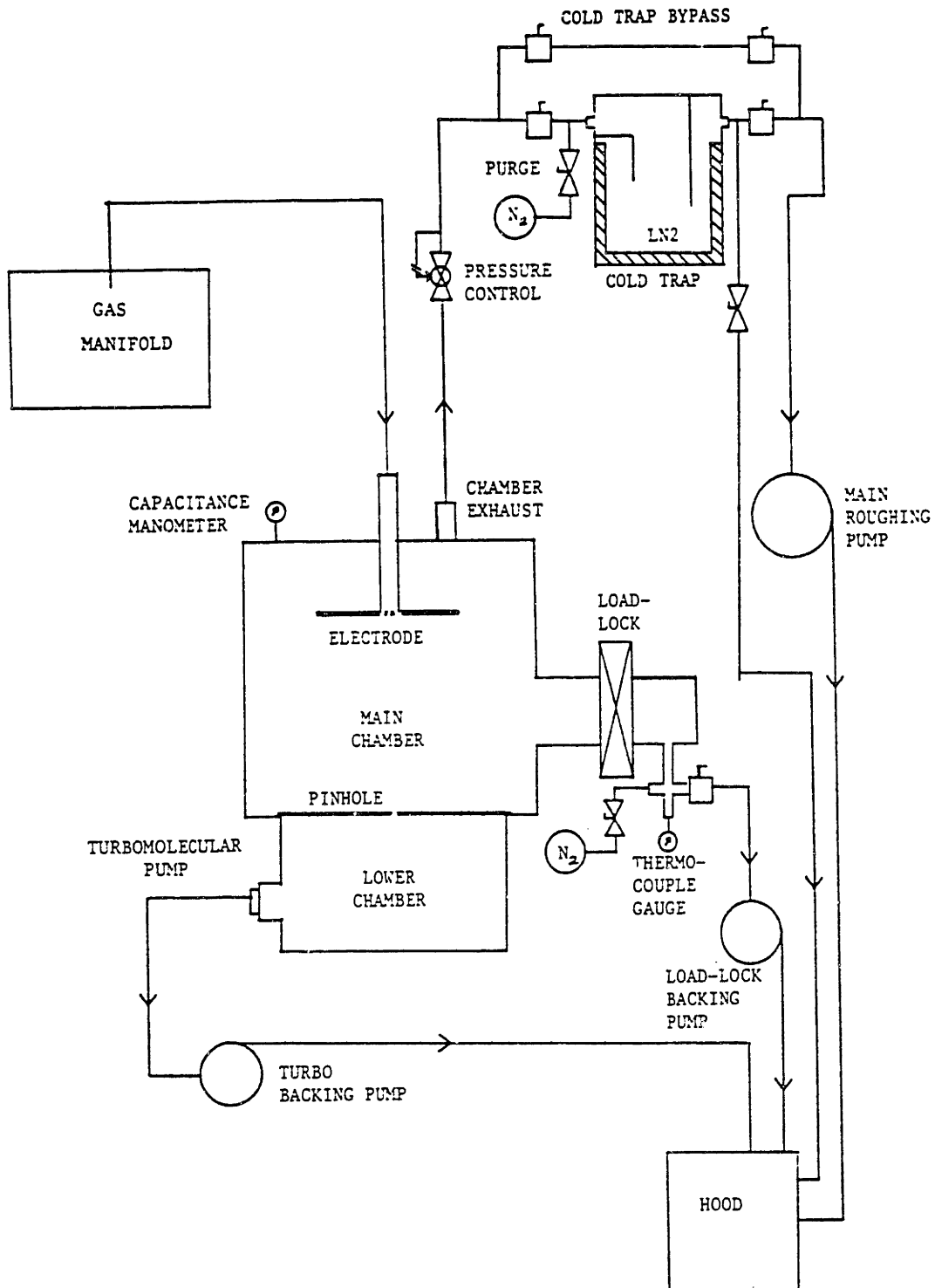


Figure 2-2: Vacuum system schematic.

coated wires inside a flexible Teflon tube. The gas feedthrough is a ground quartz tube; the electrode is connected to the feedthrough by tightening a pair of O-rings onto the tube with a Cajon fitting.

At pressures below 0.4 torr, or at high power densities, a parasitic discharge formed around the electrical feedthrough wire. This presents great problems because the discharge must be contained solely between the electrodes if the impedance measurements are to be interpreted in any meaningful way. Another difficulty with assembly A is the strength of the quartz tube. As the chamber lid is removed from the chamber (a frequent procedure), the upper electrode may strike the chamber walls. Concern over the fragile quartz tube resulted in the design of electrode assembly B.

Electrode assembly B is connected to the chamber lid via a threaded stainless steel tube fit snugly inside a 5 cm diameter Teflon tube. The electrode is 12.7 cm diameter by 1 cm thick, and is cooled by flowing water through its hollow interior. Again, a Teflon sheet rests on the electrode. The electrical feedthrough is again a pair of Teflon-coated wires, but the wires are isolated from the plasma. The wires are fed from the chamber lid to the electrode in a 0.15 cm wide slot milled out of a 2 cm thick Teflon block; the high electric fields around the wires are dropped in the block and a plasma sheath cannot form around the feedthrough. A plasma cannot form in the milled slot because the gap spacing is smaller than the oscillation amplitude of electrons at 13.56 MHz.

However, assembly B does not contain the plasma between the electrodes at low pressures; a parasitic glow forms in the upper chamber (between the powered electrode and the chamber walls). At these pressures, electrical breakdown of the gas is oscillation-limited, i.e., a plasma can only form if the distance travelled by an electron in the electric field is less than the interelectrode spacing (Brown, 1965). Since the distance between the powered electrode and the chamber lid is greater than the interelectrode spacing, the gas breaks down above the electrode before breaking down between the electrodes.

Electrode assembly C circumvents this problem by removing all electric fields, except between the electrodes. The assembly is modeled after a triaxial cable, see Fig. 2-3 and Appendix C.1. The periphery of the electrode itself (the same one used in assembly B) is surrounded by a Teflon ring which also supports the remainder of the assembly. A powered shield of 1/16-inch sheet stainless steel rests on the Teflon support; this shield extends about 7 cm above the electrode, and is covered. A 1-cm thick Teflon sheet rests on the cover of the powered shield; a Teflon pipe (1 cm thick) encircles the sides of the powered shield. Finally, a ground shield (similar to the powered shield) surrounds the assembly. Consequently, all electric fields are dropped through Teflon and no fields are exposed to the gas, except between the powered and grounded electrodes. The electrical feedthrough is also a triaxial cable, fashioned from Teflon-coated wire, Teflon tubing, and silver-coated copper braid.

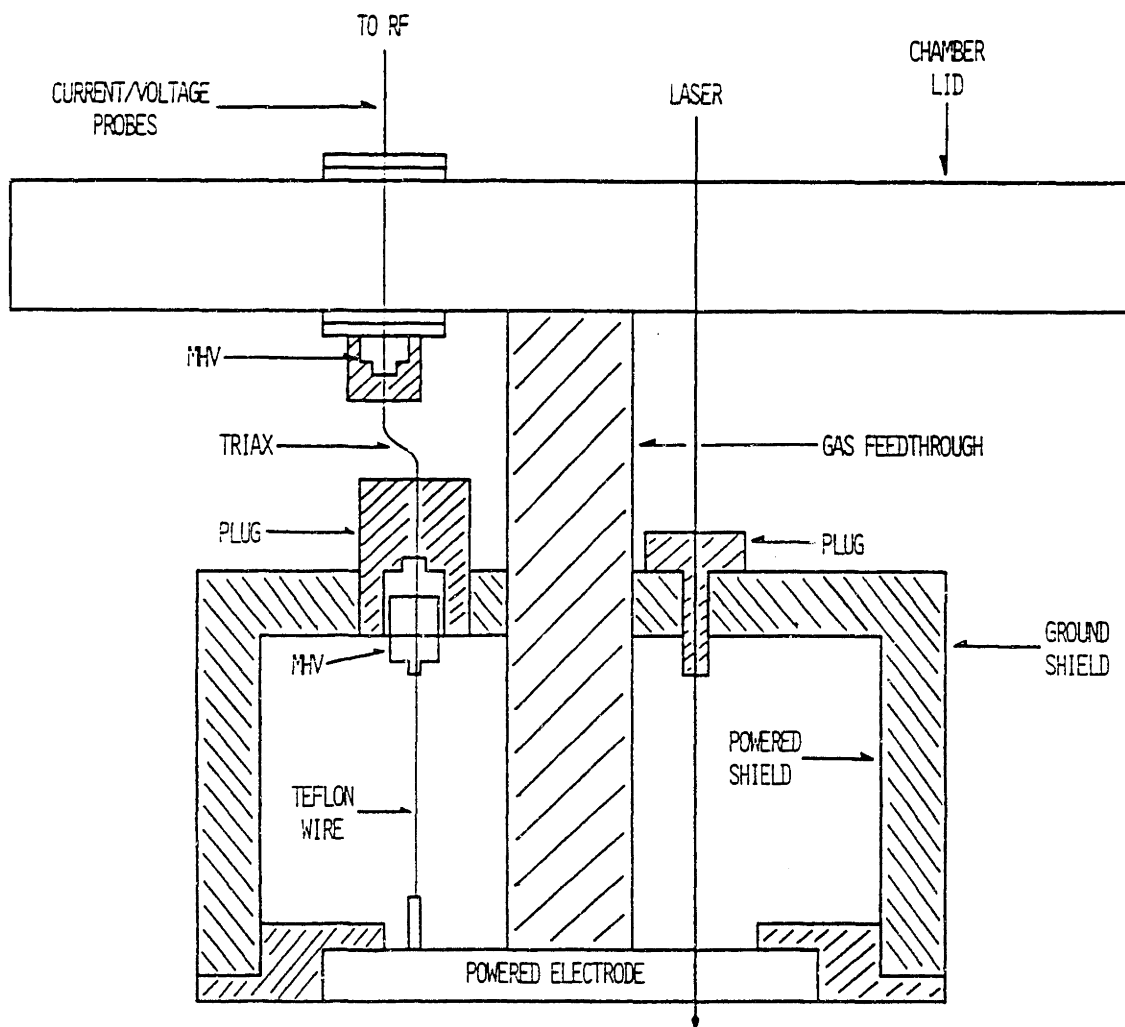


Figure 2-3: Schematic of electrode assembly C, triaxial shielded electrode.

No parasitic discharges are observed using assembly C. Of course, at very low pressures the plasma is not well contained because it expands out between the electrodes toward the chamber walls. In CF_3Br , the minimum operating pressure (defined as the pressure at which plasma containment disappears) is about 0.15 torr using assembly C, as opposed to 0.25 torr using assembly B.

Another important consideration in electrode design is the parasitic impedance of the assembly. Since parasitic impedances must be subtracted out from total measured impedances to get the plasma impedance, they should be minimized. For example, a parasitic capacitance of 30 pF is a significant fraction of the total measured capacitance in electronegative gas plasmas. The parasitic capacitance and feedthrough line inductance of assembly B are about 25 pF and 0.3 μH , respectively (for further discussion see Thompson *et al.*, 1986a or subroutine IMPED of computer program ANALYZE, Appendix B.1). The triaxial design of assembly C reduces the stray capacitance to 5 pF, a significant improvement. The measured line inductance of assembly C is 0.35 μH .

2.2 PLASMA DIAGNOSTICS

In this section, the diagnostic equipment associated with the plasma etching system are described. In addition, special diagnostic and data analysis techniques are detailed where necessary, although further details are presented in other sections of this thesis. Most of the diagnostic equipment is controlled by a microcomputer, which is also used to acquire the data from the diagnostic tools.

2.2.1 Electrical Impedance

The discharge geometry and electrode construction are described in subsections 2.1.1 and 2.1.3, respectively. In this subsection, the power system and impedance measurement equipment are described in more detail.

The applied voltage is supplied by an ENI model 2100L broadband amplifier (100 KHz - 10 MHz), fed by a Hewlett-Packard model 3312A function generator. This apparatus allows variation of the plasma excitation shape and frequency, as well as amplitude modulation of the power input to the plasma. The forward and reflected powers are measured with a Bird model 43 power meter or with an ENI model 2K250 power meter. A π network (capacitor-inductor-capacitor) is used to match the 50 Ω output impedance of the amplifier to the plasma impedance. In general, matching is sufficiently good that less than 1 watt is reflected.

High frequency-response voltage (Tektronix 100 MHz bandwidth, 10M Ω impedance) and current (Ion Physics, 30 MHz bandwidth) probes are located at the vacuum electrical feedthrough to the chamber, between the matching network and the powered electrode. A Tektronix 7603 oscilloscope, with a bandwidth of 70 MHz, acquires the voltage and current waveforms. The waveforms are then processed by a Tektronix 7D20 programmable digitizer and stored for further analysis. Typical current and voltage waveforms are shown in Fig. 2-4. The waveform analysis procedures are presented in Appendix B.1.

2.2.2 Laser Interferometry

The etching rate of the polysilicon is measured in situ by laser interferometry. A Hughes 5 mW He-Ne laser is mounted above the chamber lid. The laser passes through a window in the chamber lid, through a hole in the upper electrode assembly, and is reflected back at the Si/SiO₂ interface of the wafer sample. After passing back through the electrode and the chamber lid, the beam is redirected by a beam splitter and focused onto a photodetector. The photodetector output is sent simultaneously to a chart recorder and to an A/D port on the microprocessor. Laser alignment is accomplished with a series of three X-Y tables.

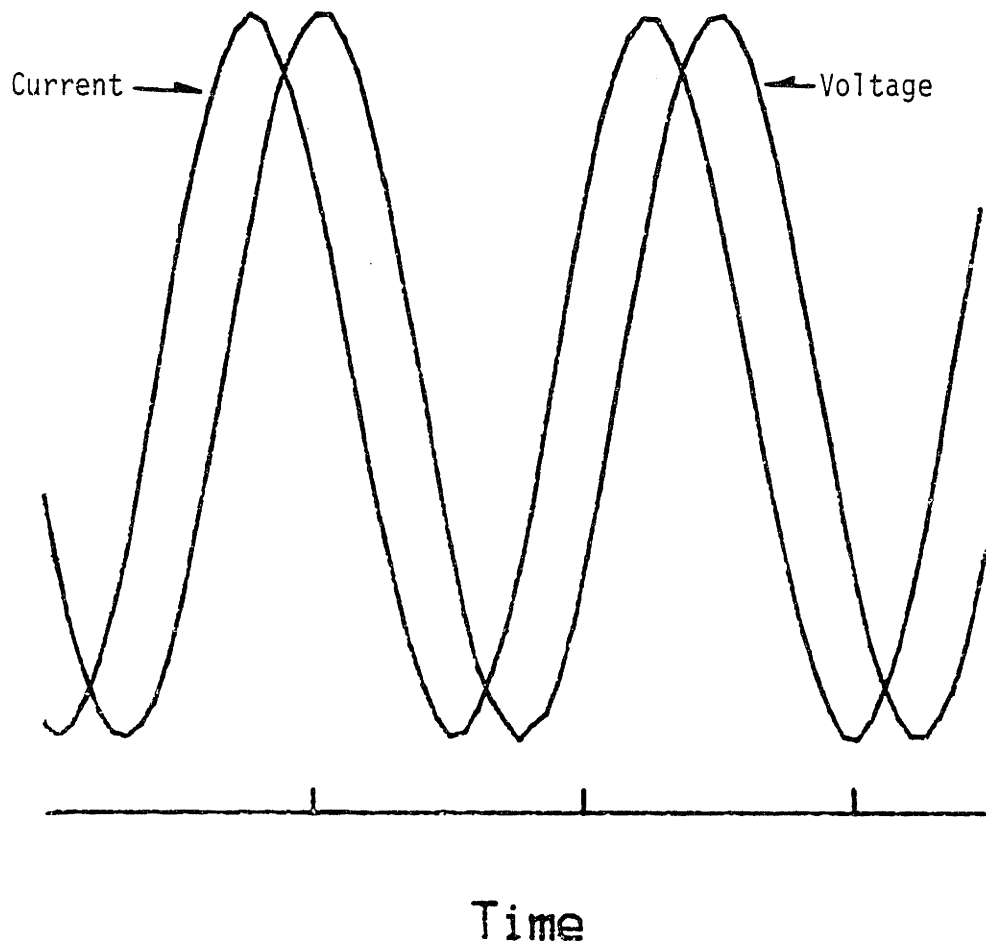


Figure 2-4: Typical current and voltage waveforms in CF_2Br plasma, using electrode assembly C.

The intensity of the reflected beam is dependent on the phase of the laser light as it leaves the wafer surface. As film thickness is varied the reflected intensity varies sinusoidally. The period of the oscillation, in film thickness, is (Marcoux and Foo, 1981)

$$d = (\lambda/2) N , \quad (2.2.2-1)$$

where d is the film thickness between intensity maxima, λ is the wavelength of the laser, and N is the refractive index of the material. In this study, $\lambda=632.8$ nm and $N=3.42$; therefore, the film thickness between intensity peaks is 925 \AA . Fig. 2-5 is a typical laser interferometry scan, showing etch start and endpoint.

The effects of surface topography on laser interference patterns have been examined previously (Heimann, 1985; Roland et al., 1985). Sternheim et al. (1983) developed an algorithm by which the optimum placement of the laser on a patterned wafer could be determined. Interference effects are also useful for determining absolute thicknesses of some films by colorimetry (Pliskin and Conrad, 1964).

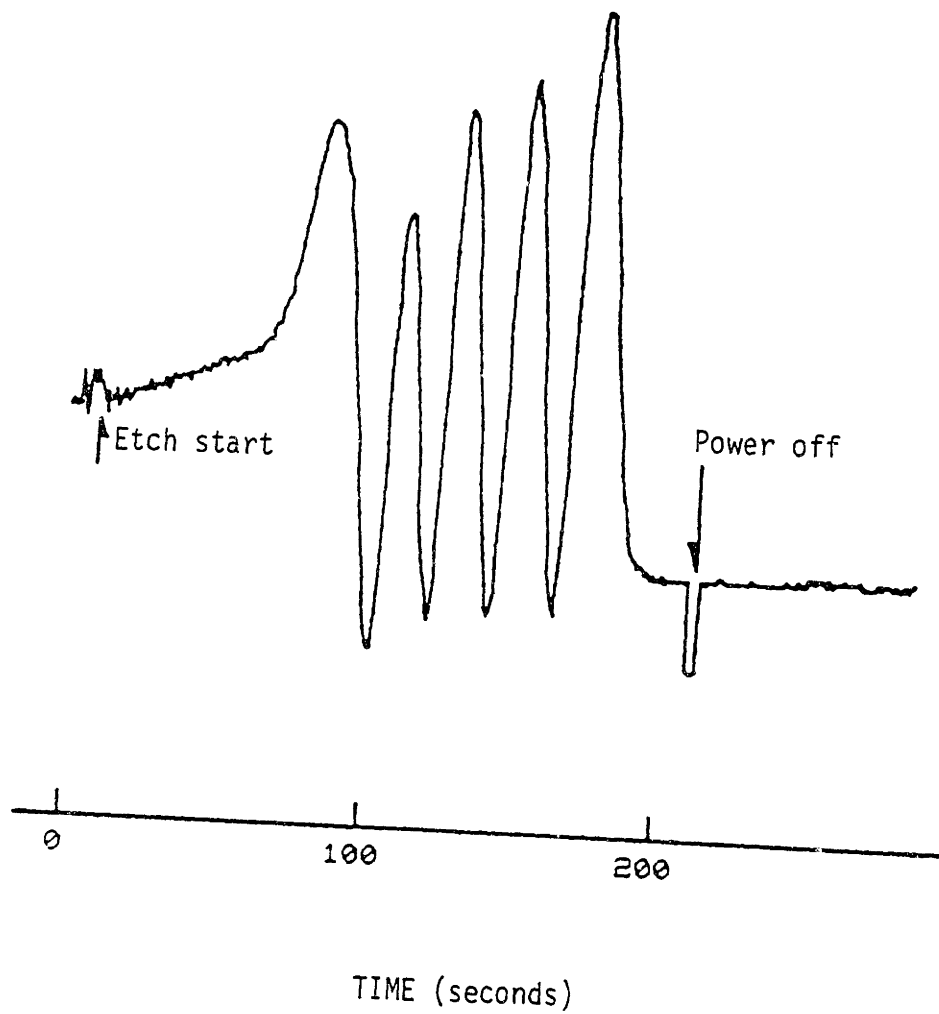


Figure 2-5: Typical laser interferometry scan for doped polysilicon etch in CF_3Cl plasma. Etch start and full clearing are noted.

2.2.3 Optical Emission Spectroscopy

Perhaps the most commonly employed endpoint detection technique (Weiss, 1983), optical emission spectroscopy is a very useful tool for monitoring known species in a plasma because of its simplicity and ease of installation (Harshbarger et al., 1977). Visible optical emission data are obtained with a Jarrell-Ash Monospec monochromator and a Tracor-Northern TN-6100 multielement array detector. The monochromator is equipped with three gratings, which allows both low resolution (200-800 nm) and high resolution (20 nm range) scans. High and low resolution scans are shown in Figs. 2-6 and 2-7, for a CF₃Cl plasma. The outboard microcomputer controls the monochromator and receives and stores the emission data.

Optical emission from a plasma occurs as electronically-excited species in the discharge (created by collision with energetic electrons) relax to lower energy states by emitting photons. The energy (and hence, wavelength) of this transition is indicative of the particular species involved. Because discrete energy states are involved, optical emission spectroscopy is generally limited to small molecules; large molecules emit a diffuse continuum rather than discrete peaks. The intensity of emission from a given species X at a characteristic wavelength is a function of the species concentration, the electron concentration and energy distribution, and the excitation cross section of that species. Atomic fluorine and chlorine are

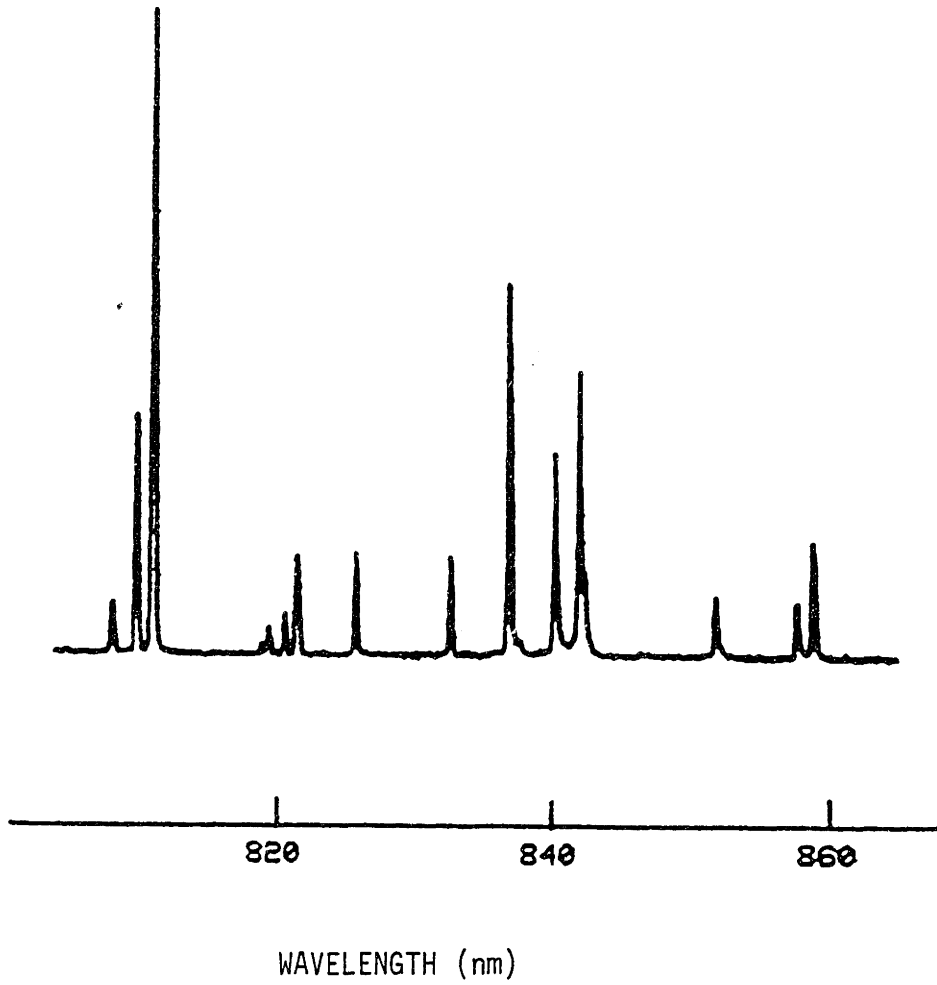


Figure 2-6: High resolution optical emission scan of $\text{CF}_3\text{Cl}/\text{Ar}$ plasmas. Several atomic chlorine and argon lines are shown.

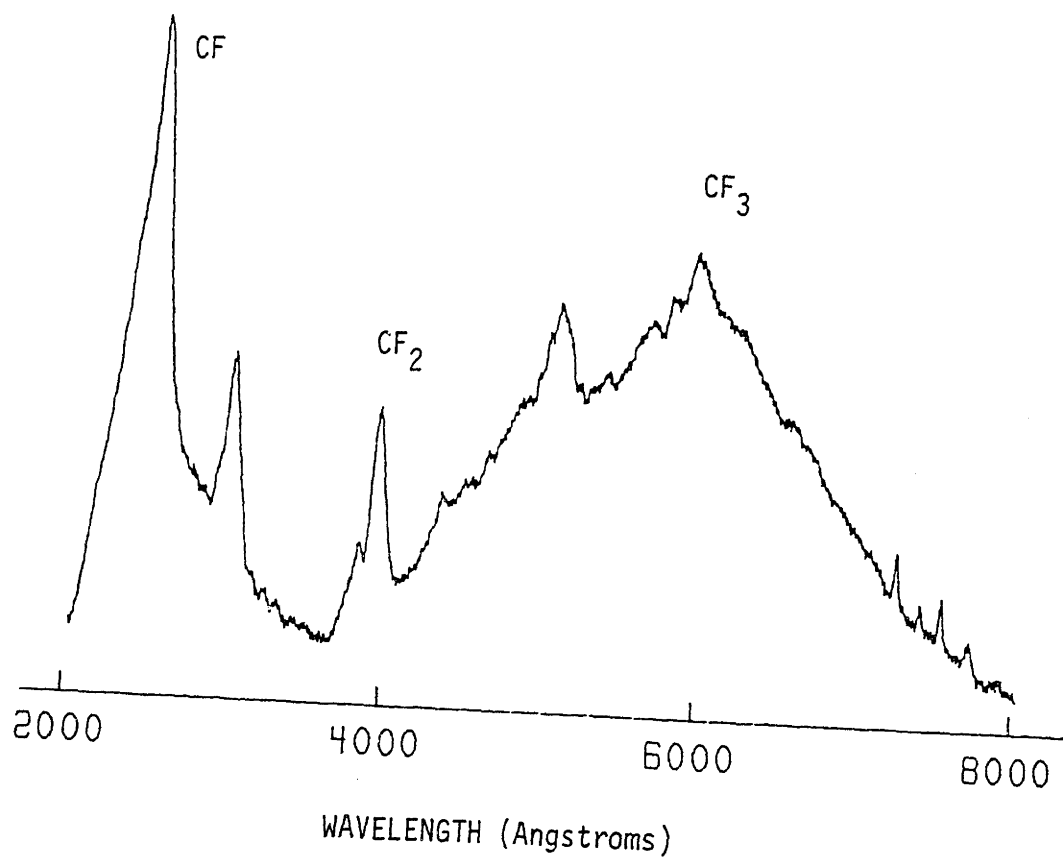


Figure 2-7: Low resolution optical emission scan of CF,Cl/Ar plasma. Tentative assignments of each major continuum are shown.

commonly studied by optical emission, although atomic silicon (Bulat et al., 1982), CF_2 radicals (Millard and Kay, 1982; Trung et al., 1977), (Washida et al., 1983; Suto and Lee, 1983; Suto and Washida, 1983a; Suto and Washida, 1983b; Suto et al., 1983), and many others have also been studied.

Optical emission spectroscopy cannot, in general, be used to determine absolute species concentrations. However, addition of a small amount of an inert gas with similar excitation cross-section to species X allows evaluation of relative changes in [X] with varying plasma conditions. By this technique (optical emission actinometry) the effects of electron concentration and energy are removed by taking the ratio of the emission intensity from species X to that of the actinometer. The technique was first developed by Coburn and Chen (1980), and has been used in many more recent studies (d'Agostino et al., 1981a and 1981b; d'Agostino et al., 1984; Donnelly et al., 1985). The benefits and pitfalls of optical emission actinometry are described in more detail elsewhere (Richards et al., 1986).

2.2.4 Mass Spectrometry

Mass spectrometry is a very useful technique for identifying species present in a glow discharge (Höfler, 1984). For example, many species characteristic of sheath ion-molecule reactions have been seen in plasmas (Vasile and Smolinsky, 1973). However, quantitative analysis to yield species fluxes to the surface is not straightforward. For example, cracking patterns of radical species formed in a plasma are unknown; the measured peak height ratios cannot be converted to relative fluxes. The sensitivity of mass spectrometer gain to the energy state of the species is also a problem.

The Leybold-Heraeus Q200 quadrupole mass spectrometer (QMS) is located in the differentially-pumped lower chamber, directly below the 50 μm pinhole orifice. The flux through the pinhole is representative of the flux upon the electrode surface because the mean free path of the ions or neutrals (about 100 μm at 0.3 torr) is greater than the pinhole diameter; therefore, flow through the pinhole is effusive.

The QMS can be used to observe two types of species - ions and neutrals. When in neutral mode, neutral species are ionized by a 70 eV ionizing cage. When observing ions, the ionizer is turned off and the QMS is biased so as to be at a slightly negative potential (about 10 V below ground). Example ion and neutral scans in CF_3Cl plasmas are shown in Figs. 2-8 and 2-9, respectively.

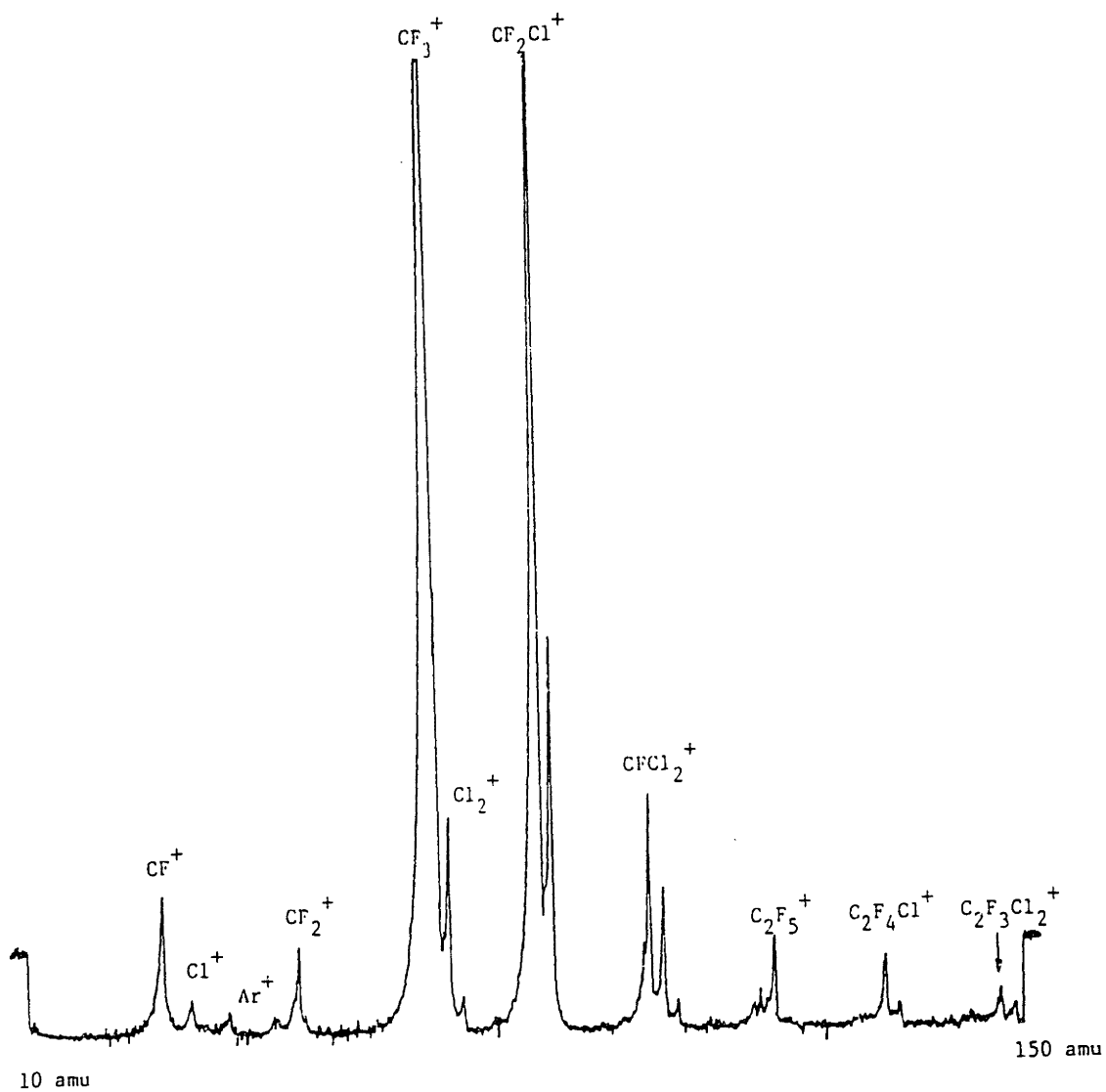


Figure 2-8: Sample QMS ion scan of CF_2Cl plasma.

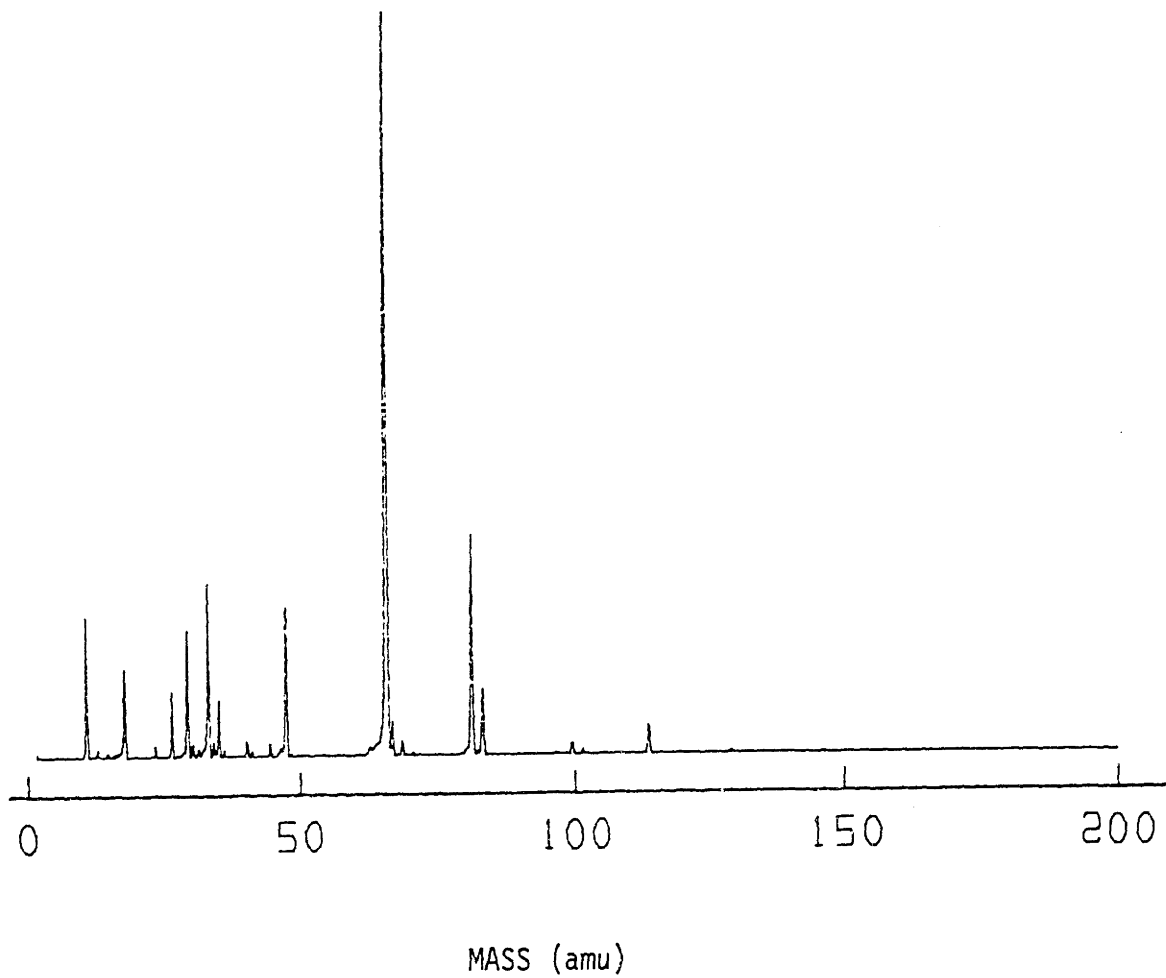


Figure 2-9: Sample QMS neutral scan of CF_2Cl plasma.

In the present study, the mass spectrometer was used primarily in the ion mode because the corrections (e.g., cracking patterns) which must be made to the raw data are less vital than in the neutral case. Relative peak heights are reported, with no attempt at correction for ion energy distribution.

2.2.5 Langmuir Probe

Electrostatic (Langmuir) probes are the simplest of the few diagnostic tools available for investigation of plasma electrical properties. In addition, the theoretical analysis of the measurements required for plasma property estimation is fairly well developed (e.g., Cherrington, 1982; Laframboise, 1966; Chen, 1965). A considerable volume of data exists for inert sputtering discharges such as argon, but relatively little information is available regarding chemical systems pertinent to plasma etching.

A Langmuir probe is a thin wire inserted into the plasma. By varying the applied potential to the probe and measuring the resulting current from the plasma (i.e., determining the I-V curve), much information about the plasma electrical properties can be obtained: electron and positive ion densities, floating and plasma potentials, and mean electron energy.

Limited probe data are available for rf plasmas (Kushner, 1982; Norstrom, 1979; Steinbrüchel, 1983), although a wealth of information exists for dc sputtering discharges. A major problem encountered in the rf system is the coupling of the rf voltage with the probe; to obtain accurate and noise-free measurements the probe must have a very high impedance at the plasma excitation frequency and a low impedance to dc current. This problem is solved by inserting a series of inductors in the probe circuit (Surendra, 1985; Surendra et al., 1986). The I-V curves are obtained by applying a triangle-wave voltage to the probe, amplifying the current with a Keithley 427 current amp, and averaging over many cycles with an EG&G PAR 4203 signal averager. A sample I-V curve is shown in Fig. 2-10.

2.2.6 Faraday Cup/Energy Analyzer

A schematic of the Faraday cup assembly is shown in Fig. 2-11. The assembly consists of a pair of 97%-transmission tungsten-mesh grids and a collection plate. By biasing the upper grid to -90V, positive ions are focused into the assembly. The potential on the lower grid is controlled externally via the microcomputer. The current to the collection plate is amplified by a Keithley 427 current amp and recorded by the outboard microcomputer.

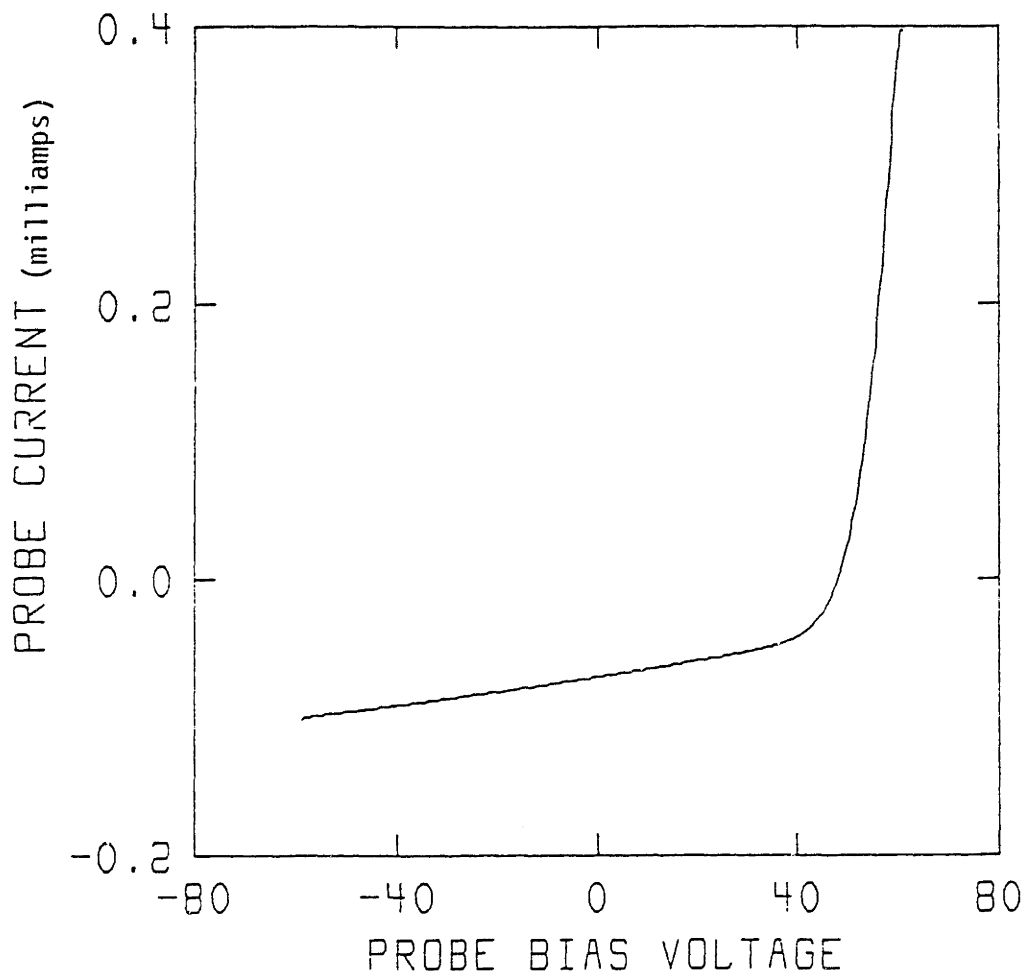
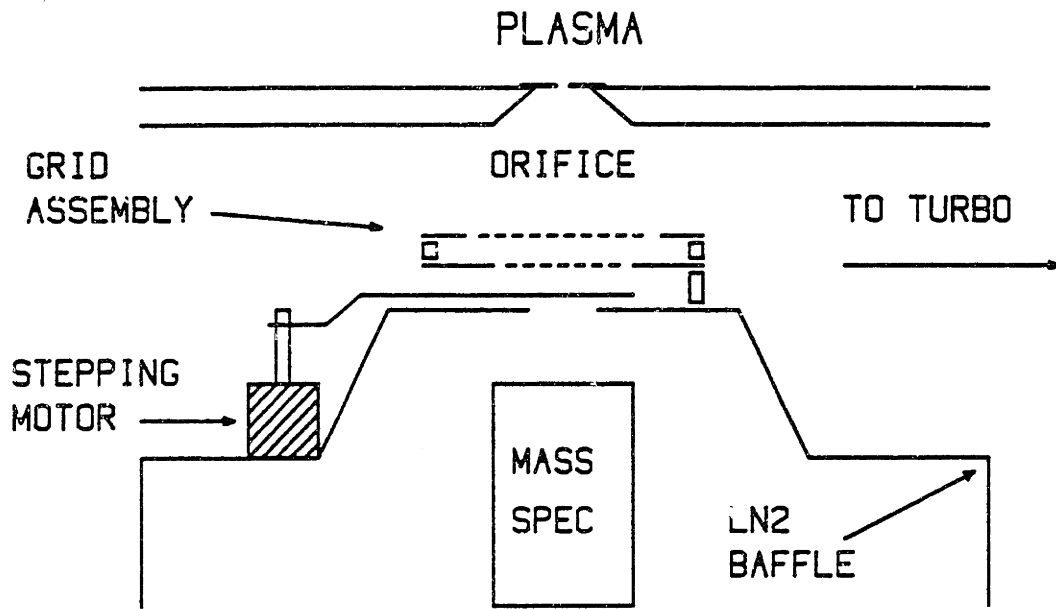
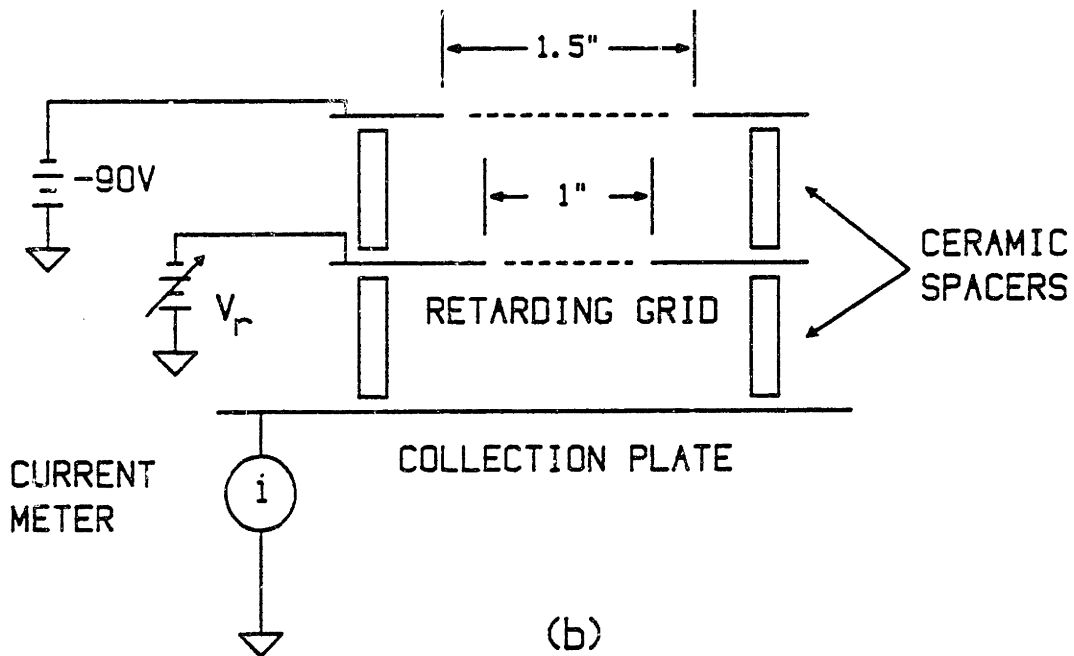


Figure 2-10: Sample Langmuir probe I-V curve in CF₃Cl plasma.



(a)



(b)

Figure 2-11: Faraday cup assembly: (a) overall schematic, (b) expanded view of grids.

By biasing the lower grid and the collection plate to -45 V, any ions which enter the assembly are collected and observed as a current. If the lower grid is biased positively ions with energy less than the grid bias potential are repelled by the grid, and are not collected by the plate. In this way the ion energy distribution is obtained, as discussed in chapter 4. Many subtleties of ion flux and ion energy measurement by this technique are discussed in Thompson et al. (1986a).

2.2.7 Laser Infrared Absorption

Laser infrared absorption of atomic chlorine was first demonstrated by Wormhoudt et al. (1983), and was recently used to measure [Cl] in Cl₂ plasmas (Wormhoudt et al., 1986). A diode laser is tuned to a known absorption frequency of the atomic chlorine. The beam is then directed through the plasma; the intensity lost by absorption in the plasma is related to the atomic chlorine density by Beer's law.

In this thesis, laser infrared absorption atomic chlorine measurements in CF₃Cl plasmas were compared with optical emission actinometry results and with kinetic discharge models (chapter 5).

2.2.8 Computer Control

Much of the analytical equipment on this apparatus is controlled by an Intel 8088-based outboard minicomputer. Further details on the computer design can be found elsewhere (Thompson, 1986). The outboard computer also serves as a storage facility for the data acquired by the analytical equipment. Operation of this computer is performed by software written and compiled on a Labtech microcomputer and transferred to the outboard; listings of the data acquisition routine FORTRAN code can be found elsewhere (Thompson, 1986). Before an etching run, the user selects from among the various diagnostics the set of data to be acquired during the run. Laser interferometry, mass spectrometry, and optical emission data are displayed on a graphics terminal as acquired - therefore, the user has the option of changing scales, etc., during an etching run.

After the etch is complete all data (including waveforms from the oscilloscope, ion fluxes, and ion energy data) are transferred to the departmental minicomputer, a Data General MV/4000. Data analyses are performed on this minicomputer. Both raw and analyzed data are transferred to magnetic tape for permanent storage.

2.2.9 Data Analysis

All computer programs used in the data analysis are presented in Appendix B.1. The function of each routine is specified, and sample input and output files are included where appropriate.

2.3 RESPONSE SURFACE METHODOLOGY

The goals of this thesis are threefold: to fully characterize the plasma etching process in one chemical system via extensive experimental measurements, to understand variations in the observed etching responses with respect to changing process conditions, and to relate the external plasma conditions (power input, pressure, etc.) to physically-important internal plasma properties (e.g., electron density) so that a physical model for etching can be developed. Unfortunately, a very large set of experimental data is necessary if these goals are to be met. Conventional experimental techniques are very inefficient; therefore, a statistical experimentation technique, Response Surface Methodology (RSM), was applied in this thesis.

Response Surface Methodology is an efficient and effective way of modeling plasma processes. Using this technique, plasma etching processes can be modeled quantitatively, permitting both rapid and efficient process development. RSM is often used in the chemical process industry (CPI) for the optimization of complex chemical processes. This statistical approach is not commonly used in the microelectronics industry; however, it offers significant savings in both time and expense for the testing and optimization of microelectronic fabrication processes. A mathematical process model permits an engineer to manipulate and to optimize a process in a short period of time, with a minimum of experimentation.

A statistical approach is warranted because the present understanding of plasma etching processes for microelectronic fabrication is such that kinetic modeling is infeasible. Plasma etching is a complex process in which many chemical reactions occur simultaneously, e.g., electron-impact, gas-gas, and gas-surface reactions. A large set of potentially significant plasma reactions could be posed and the creation, transport, and loss of species can be mathematically represented by either a continuum approach (Edelson and Flamm, 1985) or by Monte Carlo simulation (Kushner, 1982a). However, the rate coefficients and/or cross-sections for most of the reactions are unknown and the physics and chemistry of the etching process are not well understood. Since it is presently not possible to model plasma processes from a fundamental approach, parametric modeling techniques are both necessary and appropriate.

2.3.1 Plasma Process Complexity

In plasma process development the effect of a large number of process variables (factors) must be considered. Even if a particular etching tool and the etching gases are predetermined, a typical list would include many variables (Table 2-1). Process specifications which must be considered to optimize the total process are listed in Table 2-2. Histories of similar systems or stock 'recipes' may be used as a starting point; however, the complexity of plasma

Table 2-1
Process Variables (factors)

Gas mixture
Gas flow rate
Pressure
Power
Electrode spacing
Electrode temperature
Electrode material
Total wafer area (loading)
Previous processing steps

Table 2-2
Etching Specifications (responses)

Etching rate
Edge profile
Selectivity
Loss of critical dimension
Uniformity

processes makes their development and optimization an onerous task unless a structured strategy is implemented. To use RSM most effectively the number of parameters to be examined must be reduced to those which are most significant. Those variables which have little effect should be fixed at some convenient level. Important and unimportant variables are identified using screening designs. A physical understanding of the process can suggest which parameters are important; however, a priori decisions about the significance of variables are difficult.

A further complication of this multi-dimensional problem is that process variables may interact, i.e., the setting of one variable influences the response of the system to another variable. For example, the etching rate typically increases with power; however, the rate of increase depends on pressure, feed gas composition, electrode temperature, total wafer area, etc. Therefore, to optimize this process, the settings of all parameters must be considered simultaneously.

Traditionally, processes are developed by varying one factor at a time while holding all other factors at some constant level. While this approach does not require a statistical design, it is expensive and can yield incomplete, and often misleading, results. Traditional experimentation requires testing at many levels of a given factor, does not account for experimental error, and ignores interactions among the independent variables. Fig. 2-12a demonstrates a potential interaction effect, in which a decrease in the response Y is observed

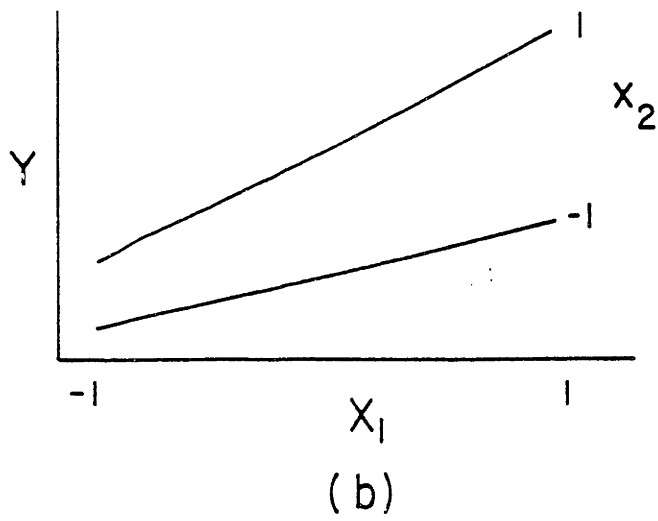
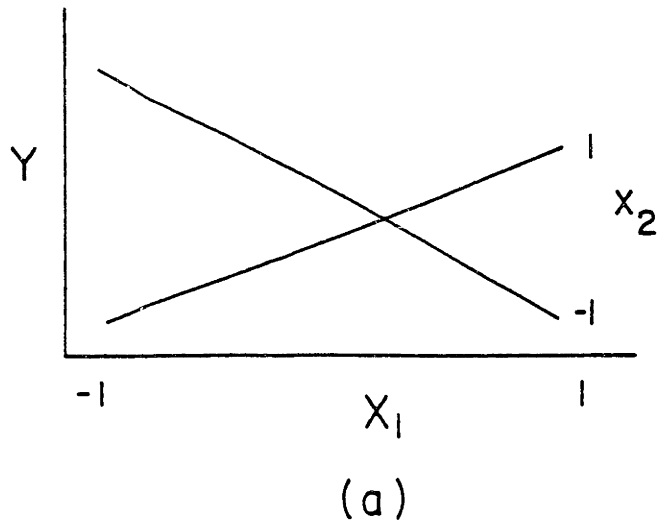


Figure 2-12: Interaction effects between variables (a) strong interaction and (b) typical interaction.

as process variable X_1 increases with X_2 set at a low level, but an increase in Y is observed if X_2 is set at a high level. A more common interaction, in which the slope of the response to X_1 varies with the setting of X_2 , is shown in Figure 2-12b.

Given interaction between process variables, the complexity of the process becomes too great to allow efficient optimization without a model. It is highly desirable to construct a mathematical model which quantitatively represents process responses as a function of process variables, as such a model will permit identification of the best process settings for a given set of etching requirements. A quantitative model is also useful in process control; it can suggest the direction in which process settings should be varied to adjust for a minor change in the process specifications or process conditions. The limits of the parameter changes which can be tolerated while maintaining process specifications can also be determined using a process model.

2.3.2 Response Surface Methodology

RSM is a statistical technique by which experimental strategy and analysis of data are combined efficiently to generate a parametric model which represents the process responses. RSM can be applied to any process in which the response can be measured in a continuous fashion and in which the process settings can be independently

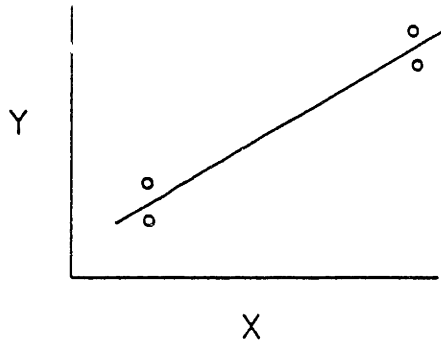
manipulated. The number of required experiments is minimized by experimental design, i.e., careful selection of process settings. Once the response has been modeled, graphical representations of the response surfaces (e.g., contour plots) can be generated for use in process optimization. Contour plots allow rapid visualization of the change in a process response with respect to a process variable.

In most chemical processes, including plasma processing, the response of the process to variations of the process settings has a continuous and smooth functionality. For example, the etching rate often increases approximately linearly with increasing power, while the selectivity between films (e.g., Si over SiO₂) declines in a continuous fashion. Some process conditions lead to instabilities which can produce abrupt changes; however, such process conditions are typically avoided because of their uncontrollable nature. Therefore, polynomial functions can be used to model the response, with the process variable settings as terms in the expansion.

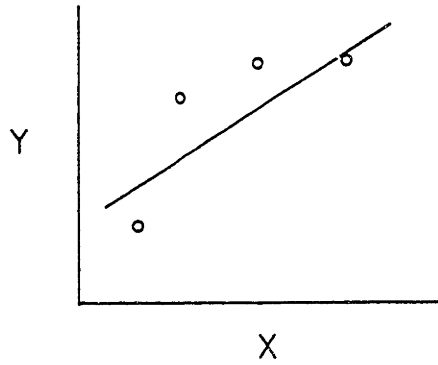
RSM is only applicable to responses that can be represented as continuous functions. For example, etching rate, selectivity, and anisotropy can be represented as continuous functions. Discrete effects such as etching-induced electrical defects can be converted to continuous functions by some scaling procedure, e.g. the percentage of defective die per wafer. By modeling several responses simultaneously, the tradeoffs in etch quality with varying process conditions can be examined.

Experimental error effects on the model predictions are assessed using statistical analysis. Experimental error is estimated by repeating experimental runs and calculating the standard deviation of the replicate differences. The lack-of-fit of a parametric model is estimated by performing more trials than are necessary to specify the coefficients of the model, and thereafter calculating the standard deviation of the differences between the model and the experimental data.

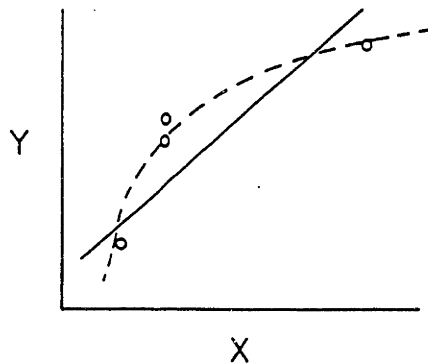
Consider the characterization (by a linear model) of a function Y of one variable X . If four experimental trials are to be performed, the selection of the trial conditions influences the information which can be gained. If two process conditions are selected, and each is replicated, a linear model is represented by a line between the average of the observations at each condition (Figure 2-13a). The difference between the replicates indicates the magnitude of the experimental error, and is therefore an estimate of the confidence in the model predictions. However, the correctness of the linear model cannot be assessed. With four equally-spaced (in X) trials a least squares regression can be performed to obtain a linear model, as well as the standard deviation between model and data (Fig. 2-13b). However, the experimental error cannot be determined since no replicates are included. In this case, the lack-of-fit error cannot be separated from the experimental error. By choosing two extreme conditions and a replicated intermediate condition, both the experimental error and the fit of the model can be estimated (Fig.



(a)



(b)



(c)

Figure 2-13: Impact of experimental design on modeling: (a) two levels with each replicated, (b) four levels with no replicates, and (c) three levels with middle level repeated.

2-13c). The lack-of-fit error indicates whether the functionality of the model is sufficient to represent the process. In Fig. 2-13c, the presence of curvature is indicated since the lack of fit is significantly greater than the experimental error. Therefore, a quadratic model, as shown by the dashed line, better represents the data. The experimental designs described in the following subsection incorporate these concepts in a statistically efficient manner for more complex models. The distribution of experimental points in the parameter space is selected to generate models which represent the process with uniform precision over the entire parameter space of interest.

2.3.3 Experimental Designs

In general, a design should be chosen that will support at least a full quadratic model. Quadratic models include linear, two-factor interaction, and quadratic terms to describe curvature. The general form of the full quadratic model is

$$Y = b_0 + \sum_{i=1}^f b_i X_i + \sum_{i=1}^f \sum_{j=1}^{i-1} b_{ij} X_i X_j + \sum_{i=1}^f b_{ii} X_i^2, \quad (2.3.3-1)$$

where Y is the process response, the X_i are the process variables, f is the number of factors, and the b 's are the constants in the fit. This model requires testing at least three levels of X_i ; ideally, the levels should be equally spaced on some scale (e.g., linear, log, square root) consistent with the expected dependence of Y on X .

Response surface designs were developed by G.E.P. Box and coworkers. These designs are fractional factorial designs requiring three or more levels (settings) of each process variable (factor). The number of trials in a full factorial design is k^f , where k is the number of levels and f is the number of factors. A full two-level, three-factorial design would consist of experimental measurement points at each corner of a cube in parameter space (8 trials), while a full three-level design would have additional trials at the center of each edge and the center of the cube (27 trials). A fractional factorial design is a selected subset of the full design.

Common three-variable designs are illustrated in Figure 2-14: a) the Box-Behnken Design with 15 trials, and b) the Face-Centered Cube (FCC) Design with 17 trials. The factor level codings of -1, 0, and +1 designate the lower, middle, and upper level of the variables, respectively. These designs replicate the center point to aid in error prediction and have at least five degrees of freedom to estimate quality of model fit. Used together without center point replication, the combination produces the full three-level factorial design of 27 trials. The designs are easily extended to cases involving more factors (DuPont, 1978; Box et al., 1978; Cochran and Cox, 1957).

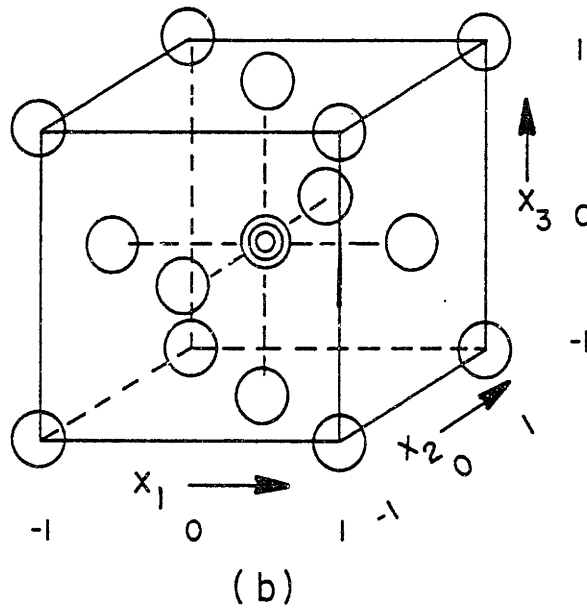
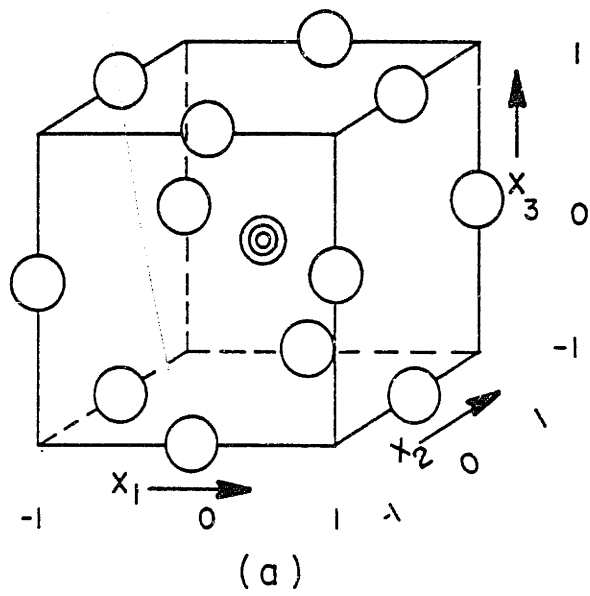


Figure 2-14: Common three-variable experimental designs: (a) Box-Behnken design with 15 trials, and (b) Face-centered cube design with 17 trials.

A third type of design, the central composite rotatable design, tests five levels per factor. It is a variation of the FCC design with the trials at the centers of the faces pushed outward a distance of $2^{f/4}$, thereby sampling at positions equally spaced from the center. The central composite designs generally require fewer trials than do the Box-Behnken or FCC designs for large numbers of factors, but have the disadvantage of covering the primary region of interest (-1 to +1) less well.

If there are more than six independent variables under consideration, screening designs should be used as a first step in the analysis to determine which variables which are most significant. Once the important variables have been identified, the less significant variables can be fixed at convenient levels. Designs such as the Plackett-Burman (Plackett and Burman, 1946) and small fractional factorial designs (DuPont, 1978; Box et al., 1978) can be used to determine the significance of a large number of independent variables with only a few trials, typically 16 runs for 7 to 8 variables and 20 runs for as many as 14 variables. The response surface design used would be based on the significant variables only.

Several other factors must be considered while designing an experiment. The factor levels should span as broad a range as possible, for two reasons. First, the empirical model fit to the data cannot be used for prediction outside of the region explored experimentally - for example, a quadratic model will revert to an elliptical shape, giving nonsensical results. Only a physically-

correct theoretical model can be used for extrapolation; however, these are usually difficult and costly to develop. Second, the difference observed in the response when going from the low to the high factor level must be greater than the experimental error, otherwise the significance of a factor cannot be evaluated.

The number of experimental trials in the design must exceed the number of coefficients in the model; if the number of trials and coefficients are equal, the fit will have no degrees of freedom for error estimation and a 'perfect', but usually erroneous, representation of the data will be obtained. In fact, the empirical model will give accurate predictions at the data points but will not necessarily provide the correct interpolation to other conditions within the parameter space of the design.

In addition, replication of data points allows comparison of the lack-of-model-fit to the experimental error. A full quadratic model for f process variables contains a constant term, f linear terms, $f(f-1)/2$ interaction terms, and f quadratic terms. Thus, with three factors, 10 coefficients must be determined. The full quadratic model is:

$$\begin{aligned}
 Y = & b_0 + b_1X_1 + b_2X_2 + b_3X_3 + b_{12}X_1X_2 + b_{13}X_1X_3 + b_{23}X_2X_3 \\
 & + b_{11}X_1^2 + b_{22}X_2^2 + b_{33}X_3^2 .
 \end{aligned}
 \tag{2.3.3-2}$$

The number of levels of each factor must be adequate to support the model under consideration. A minimum of two levels is needed for a linear model, three levels for a quadratic model, and four for a cubic model.

2.3.4 Statistical Analysis

The data generated by the response surface design are analyzed using Least Squares Regression (LSR) Analysis, which determines the model coefficients by minimizing the residual variance. Computer LSR analysis programs are readily available from many sources; a simple example written for this thesis is shown in Appendix B.2. The inputs and the more important outputs of one such program (property of DuPont) are illustrated (Tables 2-3 to 2-6 and Figs. 2-15 and 2-16) for a LSR of a 15-run, 3-factor Box-Behnken design with 3 extra replicates fitted to a quadratic model. The response (etching rate of P-doped polysilicon in a $\text{CF}_3\text{Cl}/\text{Ar}$ plasma) was measured as a function of pressure, power, and argon dilution. The results of a more complete design are discussed later.

If in an experimental design, two factors are varied in some related fashion, these factors are said to be correlated and their independent effects on the response cannot be separated. For example, if power input and pressure are tested only at conditions where their ratio is constant, they are perfectly correlated and the effect of

Table 2-3
 Box-Behnken Design (including replicates) for Polysilicon Etching
 in CF₃Cl Plasmas.

RUN #	POWER DENSITY (W/cm ²)	PRESSURE (torr)	CF ₃ Cl FRACTION	ETCHING RATE (μm/min)
1	0.315	0.6	0.865	0.088
2	0.315	0.6	0.865	0.081
3	0.315	0.6	0.865	0.081
4	0.315	0.6	0.865	0.094
5	0.315	0.6	0.865	0.104
6	0.087	0.3	0.865	0.039
7	0.715	0.3	0.865	0.100
8	0.715	0.9	0.865	0.356
9	0.315	0.3	0.738	0.052
10	0.715	0.6	0.738	0.217
11	0.315	0.9	0.738	0.062
12	0.087	0.6	0.738	0.045
13	0.315	0.3	0.956	0.110
14	0.087	0.6	0.956	0.042
15	0.315	0.9	0.956	0.045
16	0.715	0.6	0.956	0.392
17	0.087	0.9	0.865	0.042

varying either power or pressure alone cannot be determined. The correlation matrix (Table 2-4) shows the degree of linear correlation among all combinations of the model terms and the responses. A correlation coefficient of ± 1.0 indicates a perfect positive or negative relationship. A coefficient of 0 indicates that the terms are independent, which is desirable. Correlation among the terms of the model can occur when small experimental designs and higher order terms are used, and commonly occurs in undesigned experiments. If the correlation is high, the model coefficients from a least squares regression analysis are not interpretable. With significant correlation among the model terms to be fitted, ridge or biased regression (Hoerl and Kennard, 1970) must be used to stabilize the values of the coefficients such that they are meaningful.

The variables are standardized by the transformation $x_i = (x_i - \bar{X}_i) / S_i$ for each X_i . Here, \bar{X}_i is the average value of X_i for the experimental design, and S_i is the standard deviation of X_i . Standardized variables x_i have an average value of 0 and a standard deviation of 1. Since all variables are now on the same basis, this scaling allows direct interpretation of the relative importance of model terms via the magnitude of the coefficients. The utility of this scaling is demonstrated in Table 2-5, in which the standardized power input has the largest coefficient of the model terms. Power input is therefore the dominant factor in the etching of polysilicon with CF_3Cl , while argon fraction is less important.

Table 2-4
Correlation Matrix for Terms in Box-Behnken Design.

X_1	1.00										
X_2	0.00	1.00									
X_3	0.00	0.00	1.00								
X_1X_2	0.00	0.01	0.00	1.00							
X_1X_3	0.01	0.00	0.01	0.00	1.00						
X_2X_3	0.00	-0.01	0.00	-0.02	0.00	1.00					
X_1^2	-0.54	0.00	-0.01	0.00	0.00	0.00	1.00				
X_2^2	0.01	0.00	-0.01	0.00	0.02	0.00	0.05	1.00			
X_3^2	0.01	0.00	-0.35	0.00	0.00	0.00	0.05	0.05	1.00		
Y	0.80	0.17	0.17	0.34	0.20	-0.06	0.61	-0.13	0.01	1.00	
	X_1	X_2	X_3	X_1X_2	X_1X_3	X_2X_3	X_1^2	X_2^2	X_3^2	Y	

X_1 =Power Density
 X_2 =Pressure
 X_3 =CF₃Cl Fraction
Y=Etching Rate

Table 2-5
Least Squares Regression Output for Box-Behnken Design.

Term	Standardized Regression Coefficient	F-Ratio
X_1	0.0708	30.5*
X_2	0.0176	2.7
X_3	0.0204	3.2*
X_1X_2	0.0365	11.5*
X_1X_3	0.0225	4.3
X_2X_3	-0.0069	0.4
X_1^2	0.0253	4.4
X_2^2	-0.0160	2.3
X_3^2	0.0068	0.4
CONSTANT	0.0996	

*Significant at 95% level of confidence or greater; the critical F value in this case is 5.6.

The analysis typically includes the decremental F-ratio, which is a measure of the statistical significance of each term. The F-ratio compares the variation in the response accounted for by each term in the model (the decremental sum of squares) to the residual error (the variation between the model and the data). Significance levels for the F value are given in tabular form in most statistical texts (e.g., Larsen and Marx, 1981). Statistical significance is obtained when the decremental F-ratio for a model term is greater than or equal to the tabulated F-value with 1 and $n-p-1$ degrees of freedom, where p is the number of terms in the model (excluding the constant term) and n is the number of experimental data points. The experimenter chooses the confidence level, typically 0.90, 0.95, or 0.99.

A residual plot for the etching model is shown in Fig. 2-15. The residual is the difference between each observed value of the response, Y_i , and the value predicted by the model, \hat{Y}_i . When plotted against Y_i or \hat{Y}_i , the residuals should be randomly distributed around zero. Other patterns indicate model inadequacy, e.g. a transformation of the response may be needed, or additional terms in the model may be required.

From the analysis of variance (Table 2-6), the sources of the statistical variance in the response can be determined. The adjusted R^2 is defined as $1.0 - (\text{residual mean square})/(\text{total mean square})$ and is the fraction of the variation in the data accounted for by the model. A perfect fit would have an adjusted R^2 value of 1.0. The value of 0.81 from Table 2-6 suggests that the data is reasonably well

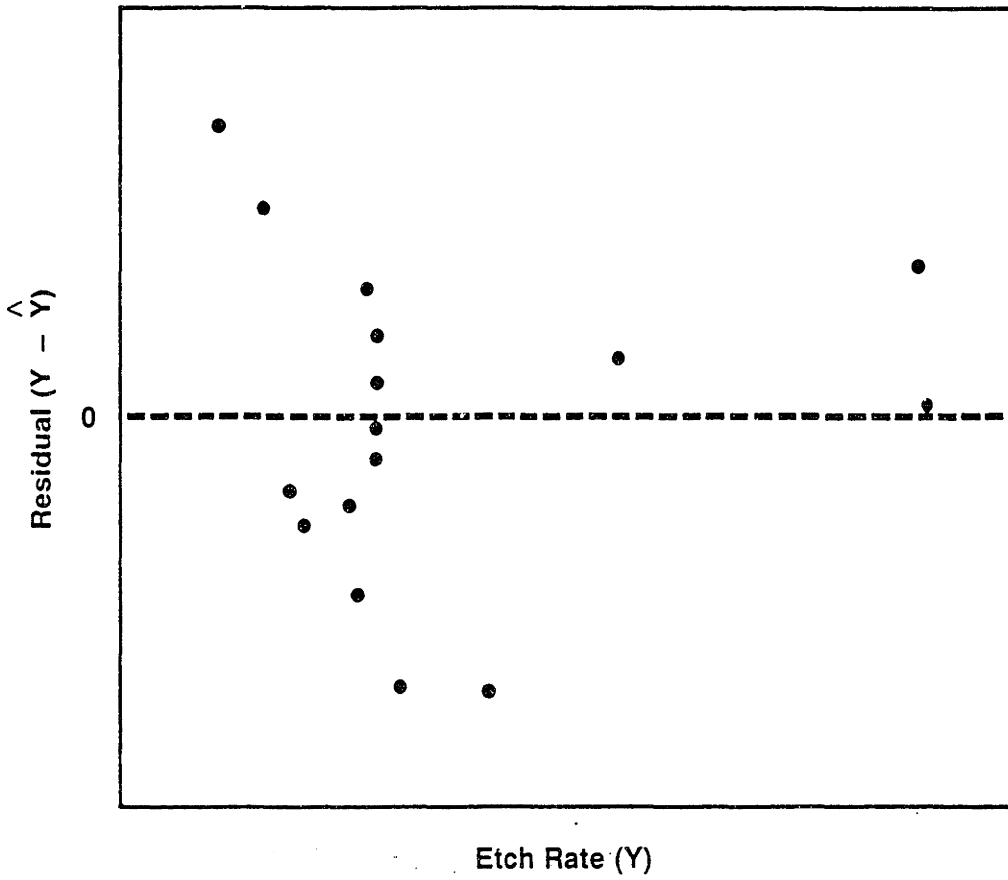


Figure 2-15: Residual plot for quadratic model fit of the Box-Behnken design data (Table 2-3).

Table 2-6
Analysis of Variance Results for Box-Behnken Design.

LEAST SQUARES REGRESSION ANALYSIS

SOURCE	SUM OF SQUARES	DEGREES OF FREEDOM	MEAN SQUARE	F-RATIO
Regression	0.16911	9	0.01879	10.1*
Residual	0.01297	7	0.00185	
Total	0.18208	16	0.11380	

Adjusted $R^2 = 0.84$

LACK-OF-FIT ANALYSIS OF VARIANCE

SOURCE	SUM OF SQUARES	DEGREES OF FREEDOM	MEAN SQUARE	F-RATIO
Residual	0.01297	7	0.001853	44.5*
Lack-of-fit	0.01259	3	0.004197	
Replicate				
Error	0.00038	4	0.000094	

*Significant at the 95% level of confidence or greater.

represented. If the design includes replication, the residual mean square can be split into its lack-of-fit and replicate components. The very large F value of 77.02, which is the ratio of the lack-of-fit to the replicate error residuals, indicates that the residual is primarily caused by lack-of-fit rather than experimental error. This suggests that despite its reasonable representation of the data, the model functionality could be improved, perhaps by including additional terms such as third-order interactions. Transformation of the response by fitting the \log_{10} of the etching rate was found to significantly improve both the fit and the randomness of the residual pattern.

Once the data has been analyzed by RSM, it must be presented in a convenient form. Contour plots are useful for finding combinations of process variable levels that optimize a response. The generation of contour plots for a number of responses permits the trade-offs between process responses to be examined and optimized; contour plots also show the sensitivity of the response to a change in the level of a process variable. For example, Fig. 2-16 is a contour plot of the etching rate as a function of power and pressure. Note that the etching rate changes more rapidly with power at high pressure than at low pressure, which is indicative of an interaction between power and pressure.

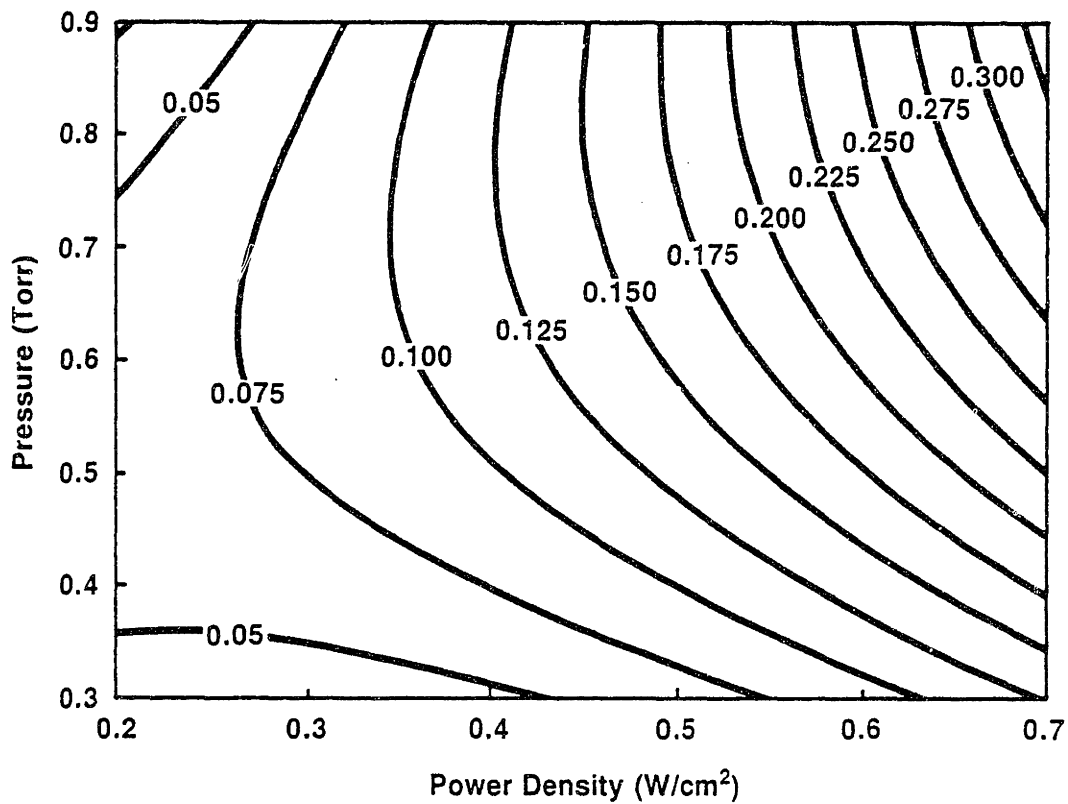


Figure 2-16: Contour plot of doped polysilicon etching rate ($\mu\text{m}/\text{min}$) in $\text{CF}_3\text{Cl}/\text{Ar}$ discharges generated from quadratic model fit of Box-Behnken design data. Variables are power density (watts/cm²) and pressure (torr).

Several important results were pointed out by this simple experimental design. From this study and from the previous work of Leahy (1981), it is known that in the CF_3Cl system the etching rate has complicated curvature, and exhibits an inflection as a function of pressure. Because of this complexity, it was suspected that cubic terms would be needed in the model to fit the response. In addition, it was suspected from kinetic theory that the functionality of the response to power, pressure, and composition might be very complex, and that third-order interaction terms might be significant.

Therefore, an experimental design was developed (Fig. 2-17) which would support a cubic model. A cubic model requires at least four levels of experimental sampling. The independent variables were coded to a range of ± 2 for power densities between 0.05 and 1.0 W/cm^2 , total pressures between 0.2 and 1.0 torr, and Ar concentrations between 5 and 50%. This design has seven levels, more than sufficient to characterize the process as a function of all first, second, and third-order terms with low correlation among most terms. Unlike quadratic models and designs, cubic designs are not standard and must be formulated to satisfy the statistical principles already described. Also, caution must be exercised in the fitting of a cubic model to ensure that the model represents real process trends rather than random experimental error.

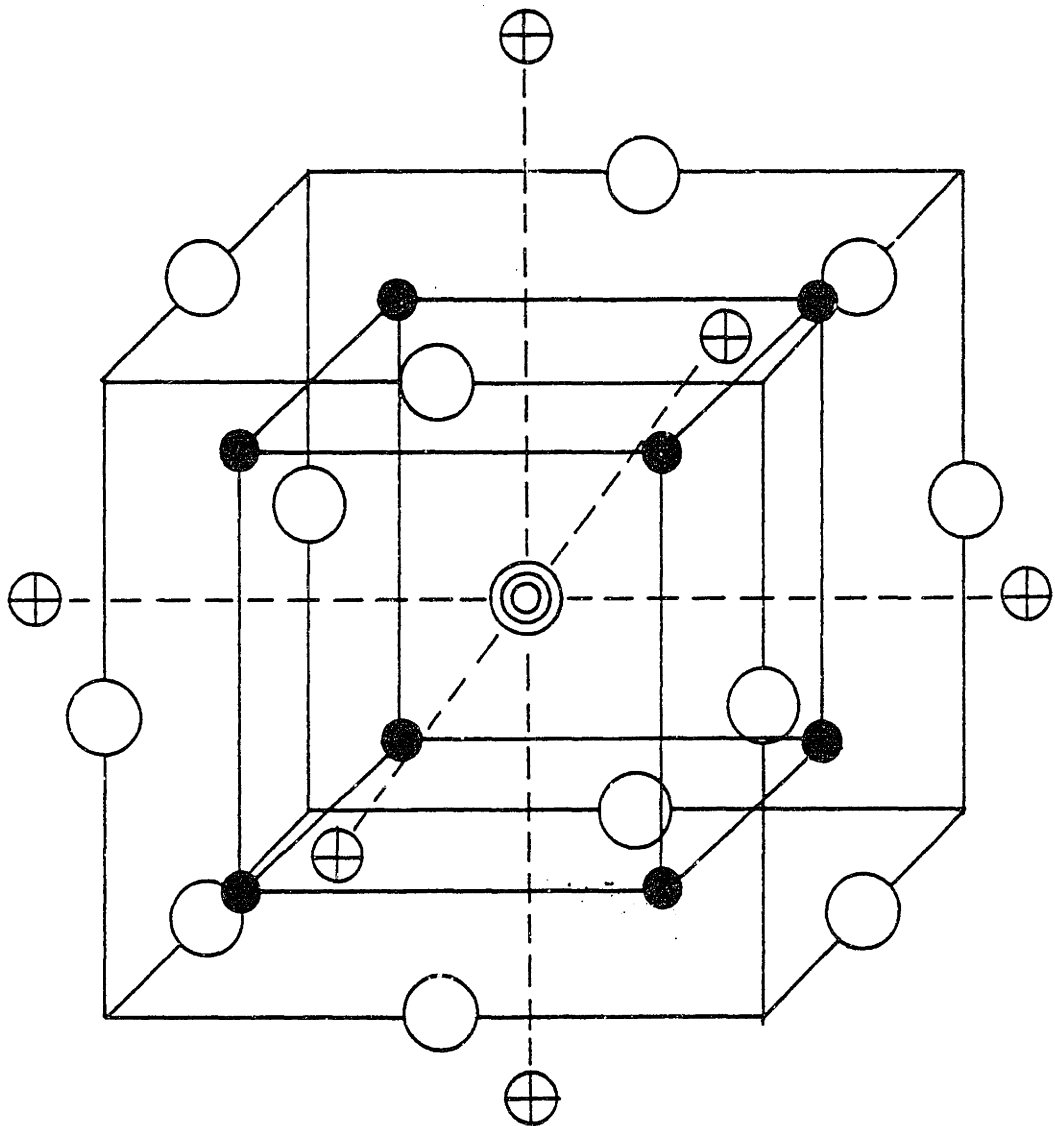


Figure 2-17: Three-variable cubic model experimental design.

Shown in Fig. 2-18 are contour plots of the etching rate generated using a cubic model via ridge regression. The quality of the fit was excellent, with the adjusted R^2 being 0.97, i.e. the model predicts 97% of the variation in the etching rate. Recall that the adjusted R^2 for the quadratic model was only 0.81. Since the adjusted R^2 is based upon the number of degrees of freedom, it is independent of the number of points in the data set and the number of fitted terms. If a more restricted region of parameter space were to be modeled, the complexity of the curvature would be reduced and a quadratic model should better represent the data.

The utility of RSM in modeling other response variables, including selectivity and directionality, has been demonstrated by Bergeron and Duncan (1982). They successfully optimized the etching of polysilicon in C_2F_5Cl/O_2 discharges for gas ratio, electrode temperature, power, and pressure to give the desired etching profile with sufficient selectivity with respect to both the photoresist and the underlying oxide. Bergendahl et al. (1982) used the concept of a desirability function for mathematical process optimization of plasma etching.

In conclusion, RSM is an excellent tool for process development. The experimental work required for complete and accurate characterization of a complex response in a multivariable system is greatly reduced by the experimental design. Unlike traditional experimentation techniques (one variable at a time), RSM allows for interactions between process variables. This feature is especially important in plasma processing.

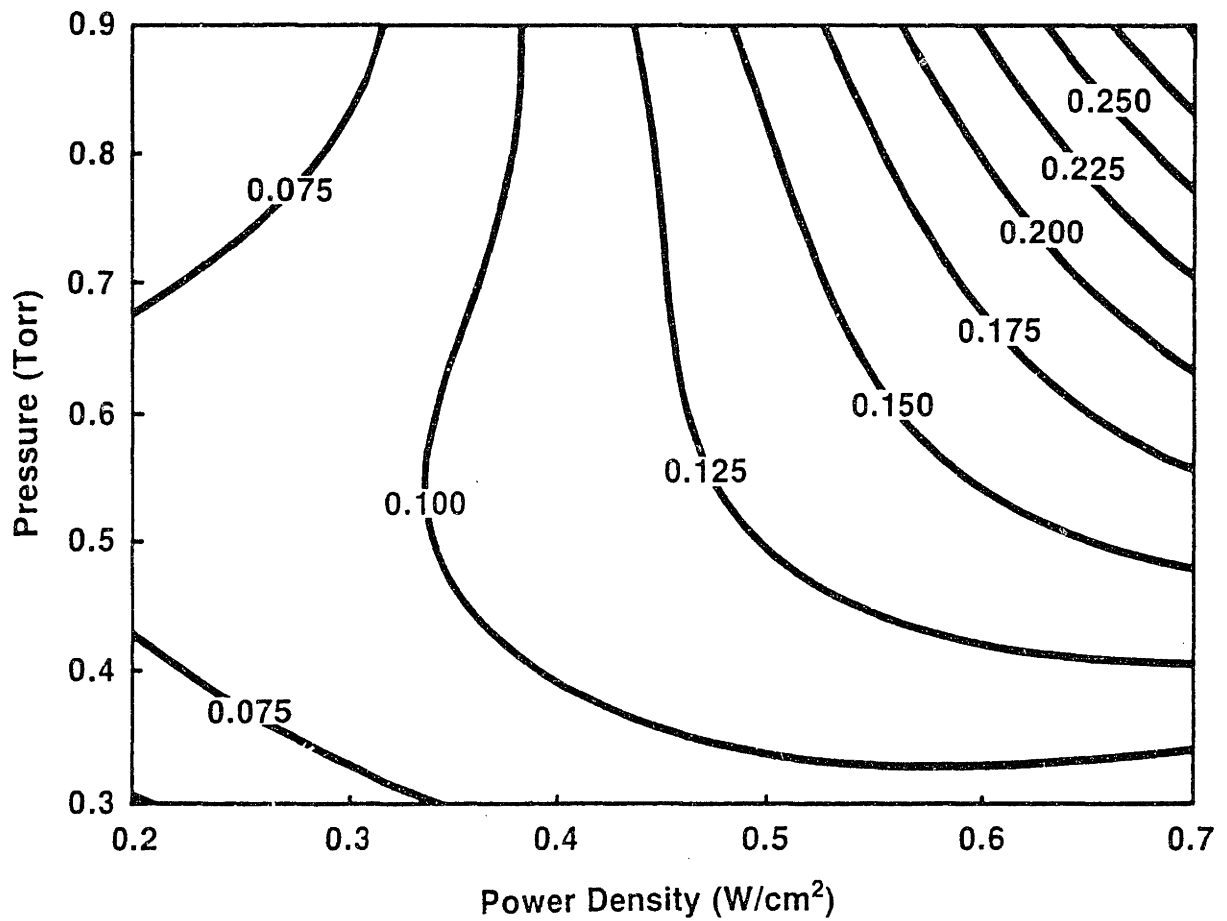


Figure 2-18a: Contour plots of doped polysilicon etching rate ($\mu m/min$) in CF_3Cl discharges using cubic-model fit to experimental design (Fig. 2-17), vs. power density (watts/ cm^2) and pressure (torr) for 20% Ar in CF_3Cl .

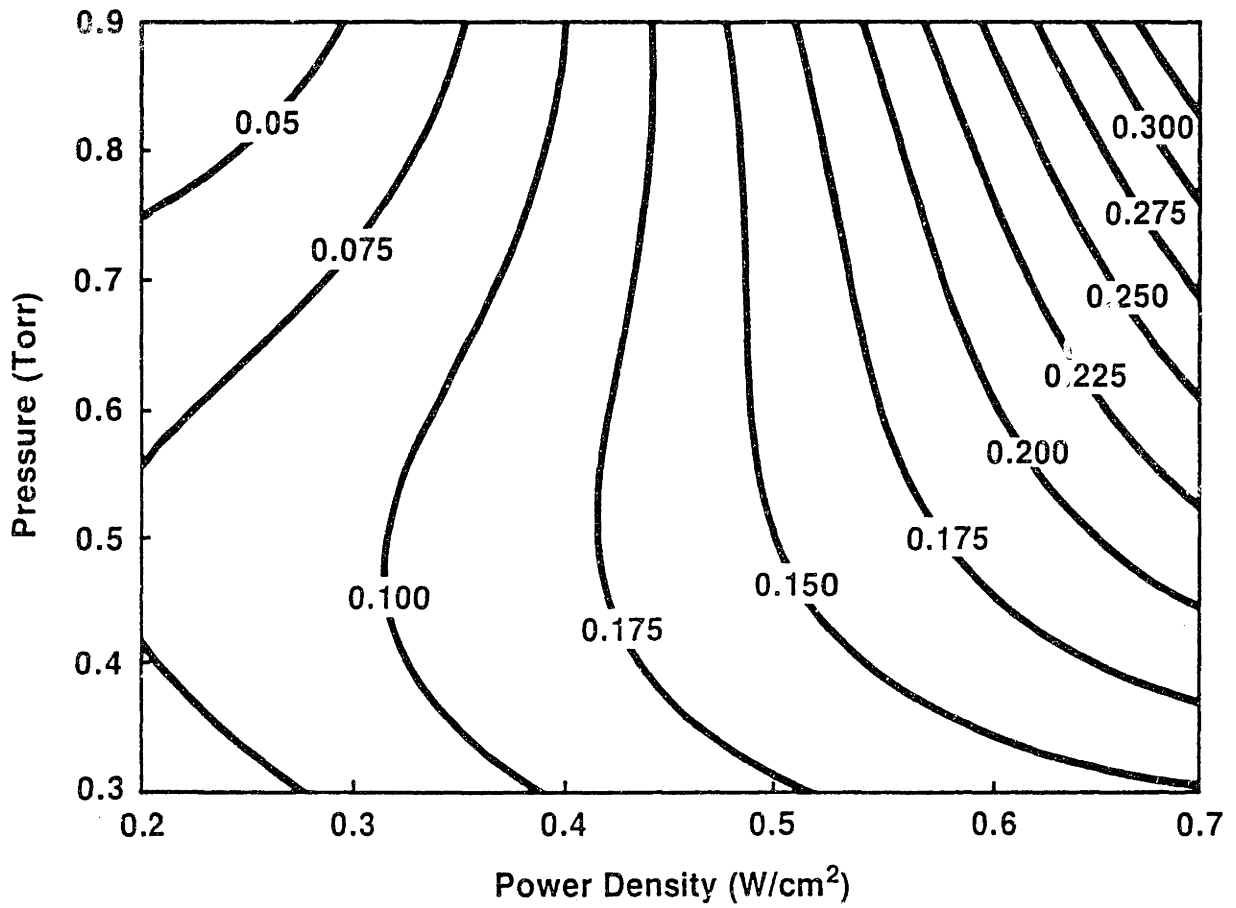


Figure 2-18b: Contour plot of doped polysilicon etching rate ($\mu\text{m}/\text{min}$) in CF_3Cl discharges using cubic-model fit to experimental design (Fig. 2-17), vs. power density and pressure for 10% Ar in CF_3Cl .

CHAPTER 3 - PLASMA IMPEDANCE

3.1 INTRODUCTION

A plasma is an electrical entity; current flows between the two electrodes in response to the applied voltage. The relationship between the current and voltage waveforms is determined by the electrical impedance of the plasma, which may include both resistive and reactive components depending on the particular system involved. Since current is carried by charged particles (i.e., electrons and ions), the plasma impedance is a useful measure of electrical properties. In this chapter techniques for measuring and interpreting the plasma impedance are presented; some discussion of the importance of stray reactor impedances is included. Experimental data for the CF_3Cl and CF_2Br systems are presented. The impedance results are related to internal plasma properties such as plasma density via circuit analogies which are used to model plasma physics.

Circuit analogies of radio-frequency glow discharges have been investigated previously (Keller and Pennebaker, 1979). The measured discharge impedance determines the values of the components in the electrical analog. In turn, circuit models have been used to predict plasma properties (van Roosmalen, 1983). In section 3.3 the assumptions implicit in the circuit analogies are discussed in detail; the strengths and weaknesses of the circuit analogy approach are outlined.

3.2 EXPERIMENTAL RESULTS - PARAMETER DEPENDENCE

Previous investigators have measured the impedance of CF_4 , C_2F_5Cl , and BCl_3 (Mathur and Huang, 1984), Ar (Logan et al., 1969), and BCl_3 plasmas (Mlynko and Hess, 1985). The experimental impedance results are in the form of applied voltages across the electrodes and the corresponding currents and phase shifts between the voltage and current waveforms. In addition, the DC bias on the powered electrode was measured, as this offset provides some information about the physical structure of the discharge.

The applied voltage is a sinusoid, and in most cases the second and higher-order harmonics of the current waveform are insignificant (as determined by Fourier analysis). Therefore, a sinusoidal approximation of the waveforms is appropriate; the two waveforms are adequately described using only root mean square (rms) amplitudes and the phase shift between the voltage and current waveforms.

As discussed in subsection 2.2.1 the measured rms current $|I|$, voltage $|V|$, and phase shift θ are corrected for parasitic losses in the electrical feedthrough; the corrected values are representative of the actual conditions at the powered electrode. The importance of minimizing stray impedances so that measured phase angles are far from 90° was demonstrated by van Roosmalen et al. (1985). Power input to the plasma is calculated by digitally multiplying the current and voltage waveforms measured by the oscilloscope over an entire rf cycle. Note that if the waveforms are purely sinusoidal, net power input to the plasma is given by the product

$$W = |I||V|\cos(\theta)/2 . \quad (3.2.0-1)$$

3.2.1 CF_3Cl

Variations in rms voltage and current of a $\text{CF}_3\text{Cl}/\text{Ar}$ plasma, along with phase shifts between the waveforms, are listed in Tables 3-1 and 3-2 for blank electrodes and for polysilicon etching, respectively. The dependence of $|V|$ on power input and pressure (P) is shown in Fig. 3-1, while the response of $|I|$ to changes in these variables is seen in Fig. 3-2.

In general, increasing pressure results in increasing $|V|$, decreasing $|I|$, and decreasing θ ; each of these responses is consistent with the plasma impedance becoming more resistive. As power input is increased, $|V|$ and $|I|$ both rise; the phase shift increases slightly. Addition of argon diluent (lowering the CF_3Cl mole fraction γ) decreases $|V|$, increases $|I|$, and increases θ .

Note that the impedance properties are not significantly changed by the presence of a polysilicon wafer. This is reasonable since, as shown in chapter 6, the etching reaction does not consume an appreciable fraction of the CF_3Cl gas.

Table 3-1
 Impedance Measurements in CF₃Cl/Ar plasmas during etching
 of P-doped polysilicon, various conditions.
 Flow rate of 6 sccm, blank electrodes (assembly A),
 excitation frequency of 13.56 MHz.

RUN ID	W (Watts)	P (Torr)	γ	V (Volts)	I (Amps)	θ (Deg.)
F13A_9	36.9	0.2	0.81	186.4	0.87	62.7
F13A_2	17.1	0.8	0.89	148.2	0.24	17.9
F13A_22	83.0	0.9	0.81	206.9	0.99	24.2
F13A_10	36.0	1.0	0.81	208.5	0.38	23.2
F13A_24	64.2	0.3	0.81	245.3	1.40	68.0
F13A_37	35.0	0.6	0.81	142.2	0.62	37.4
F13A_12	89.2	0.6	0.81	222.6	1.70	61.9
F13A_15	33.2	0.4	0.81	160.1	0.90	62.5
F13A_21	11.8	0.9	0.81	134.1	0.18	12.0
F13A_1	17.2	0.4	0.89	108.9	0.45	45.5
F13A_29	36.1	0.9	0.94	196.8	0.40	23.6
F13A_36	35.3	0.6	0.82	143.1	0.62	37.1
F13A_3	59.1	0.4	0.89	206.4	1.32	64.2
F13A_30	39.1	0.9	0.68	175.3	0.51	28.8
F13A_23	11.3	0.3	0.82	105.1	0.38	56.0
F13A_18	68.7	0.6	0.81	159.2	1.14	40.8
F13A_28	12.1	0.6	0.93	108.8	0.23	16.0
F13A_11	4.4	0.6	0.82	95.1	0.11	35.1
F13A_35	34.2	0.6	0.81	141.7	0.60	36.6
F13A_20	33.7	0.6	0.73	133.1	0.67	40.9
F13A_4	64.1	0.8	0.89	187.8	0.83	34.5
F13A_26	94.8	0.6	0.93	169.9	1.46	40.2
F13A_31	30.8	0.3	0.68	191.0	0.88	68.4
F13A_7	61.3	0.4	0.73	237.8	0.97	57.8
F13A_13	33.5	0.6	0.97	153.0	0.53	34.4
F13A_34	36.8	0.6	0.82	140.9	0.64	35.3
F13A_5	16.6	0.4	0.73	117.0	0.50	55.6
F13A_27	13.2	0.6	0.68	101.3	0.30	29.2
F13A_16	32.7	0.8	0.82	170.3	0.44	28.5
F13A_6	20.4	0.8	0.73	142.4	0.31	21.8
F13A_33	33.0	0.6	0.81	138.6	0.59	36.9
F13A_25	86.9	0.6	0.68	213.1	1.59	59.1
F13A_19	33.2	0.6	0.89	147.3	0.57	37.3
F13A_17	19.9	0.6	0.82	120.3	0.39	32.6
F13A_14	34.8	0.6	0.63	132.3	0.71	42.4
F13A_8	74.9	0.8	0.72	173.1	1.09	37.8
F13A_32	35.4	0.3	0.94	176.5	0.93	64.3

Table 3-2
 Impedance Measurements in CF₄/Ar plasmas
 during etching of heavily P-doped polysilicon,
 various conditions in a 22-run experimental design.
 Flow rate of 6 sccm, excitation frequency of 13.56 MHz.

RUN ID	W (Watts)	P (Torr)	γ	$ V $ (Volts)	$ I $ (Amps)	θ (Deg.)
F13B_1	60.4	0.8	0.87	204.3	0.65	24.5
F13B_2	18.1	0.8	0.86	156.5	0.25	20.8
F13B_3	52.5	0.4	0.87	146.6	0.98	42.9
F13B_4	20.9	0.4	0.86	113.5	0.48	39.4
F13B_5	39.4	0.8	0.79	180.9	0.49	26.6
F13B_6	38.8	0.8	0.92	193.9	0.44	24.7
F13B_7	29.6	0.4	0.79	124.5	0.67	44.9
F13B_8	34.8	0.4	0.92	129.1	0.68	37.6
F13B_9	68.9	0.6	0.79	167.9	0.96	31.5
F13B_10	67.0	0.6	0.92	180.9	0.84	28.7
F13B_11	20.6	0.6	0.79	125.7	0.37	28.5
F13B_12	23.5	0.6	0.92	137.8	0.38	25.6
F13B_13	33.1	0.6	0.86	153.1	0.49	28.4
F13B_14	29.9	0.6	0.86	147.1	0.46	28.5
F13B_15	38.6	0.6	0.87	156.2	0.57	28.9
F13B_16	37.8	0.4	0.86	133.3	0.76	41.3
F13B_17	30.0	0.4	0.87	124.9	0.63	39.9
F13B_18	34.3	0.4	0.87	128.2	0.70	40.5
F13B_19	21.7	0.2	0.86	171.3	0.69	68.4
F13B_20	32.6	0.2	0.82	194.2	0.89	67.8
F13B_21	34.0	0.2	0.79	190.8	0.86	65.6
F13B_22	62.7	0.2	0.87	227.6	1.26	64.1

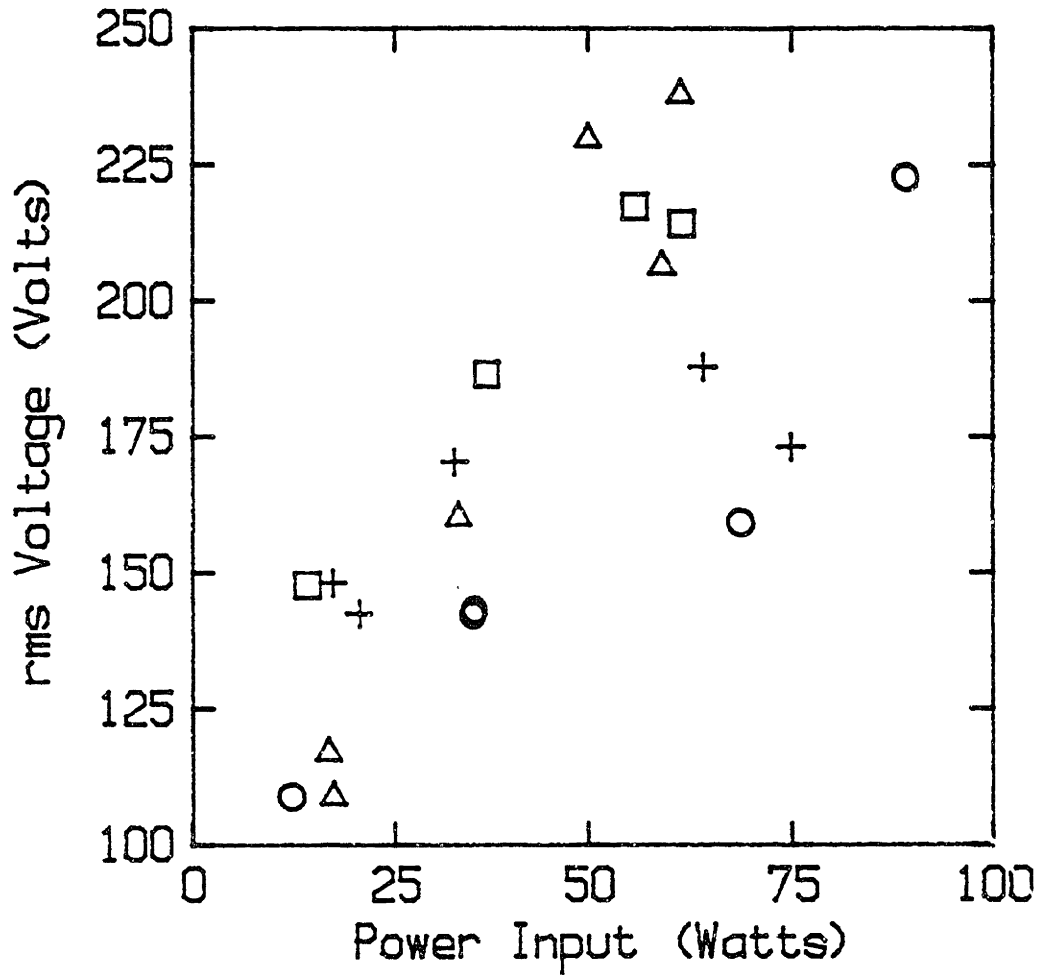


Figure 3-1: Dependence of rms voltage $|V|$ (volts) on power input (watts) in CF_3Cl/Ar discharges. Symbols: \square = 0.3 torr, Δ = 0.4 torr, \circ = 0.6 torr, $+$ = 0.9 torr.

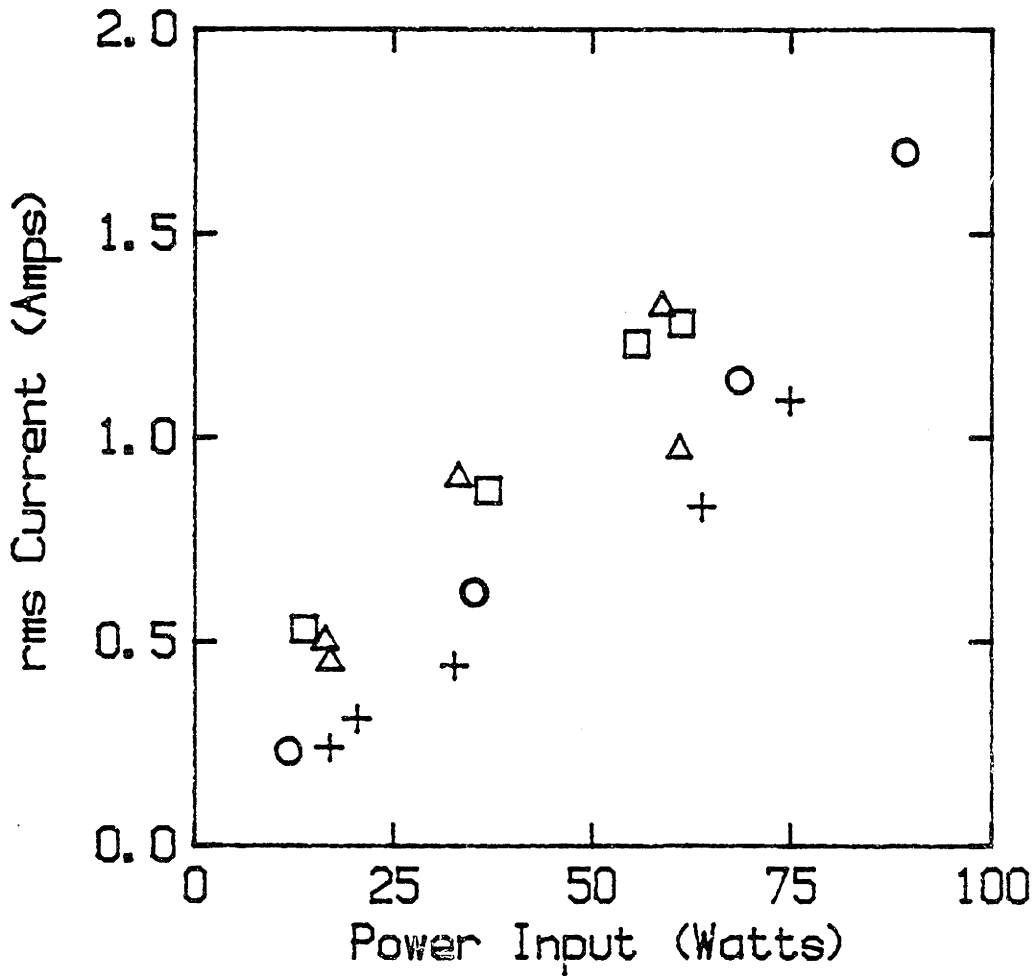


Figure 3-2: Dependence of rms current $|I|$ (amps) on power input (watts) in CF₃Cl/Ar discharges. Symbols: \square = 0.3 torr, Δ = 0.4 torr, \circ = 0.6 torr, $+$ = 0.9 torr.

3.2.2 CF_3Br

In CF_3Br plasmas, the impedance is a much simpler function of the plasma conditions. Impedance results for a 35-run experimental design are listed in Table 3-3; the measurements were taken during etching of a polysilicon sample.

The rms voltage $|V|$ is nearly independent of the power input while the current is proportional to power; note also that θ increases very slightly with increasing power input. Voltage increases with increasing pressure, while current and phase shift decline. Flow rate (Q) has very little effect on the plasma electrical properties.

A two-parameter fit of the measured current to a simple function of the process variables P and \dot{W} yields

$$|I| = k\dot{W}/P^n, \quad (3.2.2-1)$$

where $k=1.01 \pm 0.03$ and $n=0.78 \pm 0.03$. In eqn. (3.2.2-1), $|I|$ is expressed in amps, \dot{W} in watts/cm², and P in torr. In Fig. 3-3 the predictions of eqn. (3.2.2-1) are plotted vs. experiment for the 35 conditions listed in Table 3-3. The two data points which are significantly off the line of perfect fit are at low pressure and high power, where the discharge is not well contained between the electrodes. Due the loss of containment, the structure of the discharge is different than in the other experiments. Plasma containment is discussed further in subsection 3.3.1.

Table 3-3
 Impedance Measurements in CF₃Br plasmas
 during etching of heavily P-doped polysilicon,
 various conditions in a 35-run experimental design.
 Excitation frequency of 13.56 MHz, electrode assembly B.

RUN ID	W (Watts)	P (Torr)	Q (sccm)	V (Volts)	I (Amps)	θ (Deg.)
BR_1	54.2	0.5	15.3	160.8	0.75	25.8
BR_2	53.8	0.5	15.1	158.5	0.76	26.3
BR_3	50.6	0.5	15.4	160.5	0.70	24.3
BR_4	70.0	0.625	15.3	189.8	0.80	23.1
BR_5	71.8	0.375	15.3	150.1	1.23	38.8
BR_6	32.3	0.625	15.2	186.9	0.37	20.5
BR_7	30.6	0.375	15.1	126.4	0.55	28.6
BR_8	73.9	0.5	20.4	167.0	1.01	28.6
BR_9	72.7	0.5	10.0	165.2	1.00	28.0
BR_10	31.8	0.5	20.6	155.1	0.44	22.2
BR_11	30.5	0.5	10.3	153.5	0.43	22.7
BR_12	51.0	0.625	20.2	193.4	0.56	20.9
BR_13	51.8	0.625	10.0	190.3	0.58	21.2
BR_14	50.3	0.375	20.4	137.2	0.89	34.2
BR_15	47.9	0.375	10.0	133.3	0.87	34.1
BR_16	86.9	0.75	26.9	217.3	0.86	22.0
BR_17	99.7	0.75	4.7	224.0	0.96	21.7
BR_18	89.4	0.25	26.9	245.4	1.75	65.3
BR_19	89.1	0.25	4.6	226.1	1.81	64.2
BR_20	13.4	0.75	25.8	213.8	0.14	26.5
BR_21	12.9	0.75	4.7	231.4	0.13	28.5
BR_22	11.6	0.25	26.9	94.6	0.34	42.8
BR_23	12.7	0.25	4.8	95.8	0.34	37.7
BR_24	80.1	0.5	15.2	168.3	1.09	28.8
BR_25	22.0	0.5	15.1	156.1	0.30	22.4
BR_26	51.3	0.692	15.2	209.0	0.52	19.7
BR_27	51.2	0.312	15.4	138.1	1.03	43.9
BR_28	52.0	0.5	23.1	159.1	0.73	25.9
BR_29	50.8	0.5	7.4	165.8	0.67	23.9
BR_30	79.0	0.5	15.2	168.4	1.07	28.6
BR_31	22.0	0.5	15.1	152.4	0.31	22.4
BR_32	50.3	0.692	15.1	208.1	0.52	20.5
BR_33	51.0	0.312	15.1	136.9	1.06	45.4
BR_34	51.5	0.5	23.1	158.7	0.72	25.9
BR_35	52.0	0.5	7.5	156.4	0.74	25.6

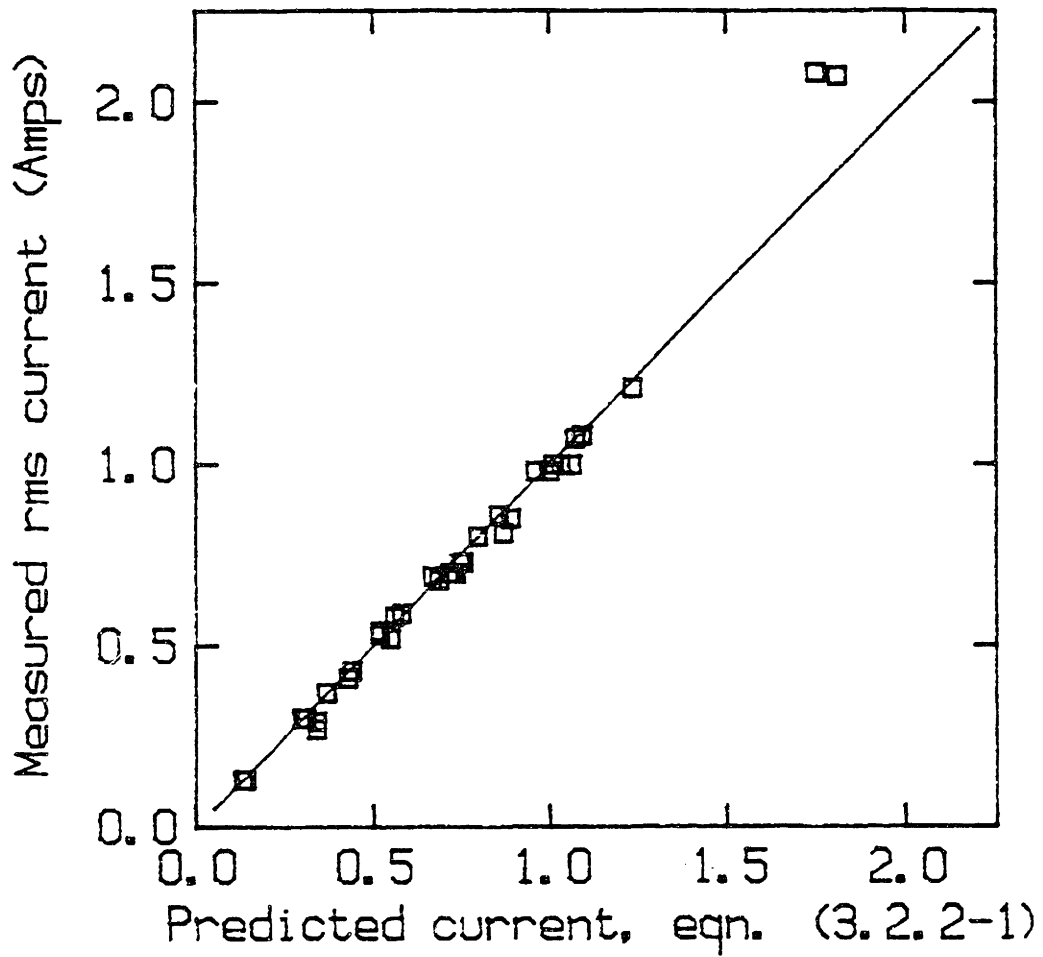


Figure 3-3: RMS currents in CF_3Br discharges - comparison of eqn. (3.2.2-1) with experimental data.

3.3 ELECTRICAL ANALOG MODELS

3.3.1 Purely Capacitive Sheaths

In this subsection I derive expressions for bulk plasma resistance, sheath capacitance, potential drop across the sheaths, bulk electric field, and electron density, using a simple electrical model of an rf discharge. Each of these quantities varies with temporal position in the rf cycle. However, since calculation of electrical properties on nanosecond time scales involves the solution of a very stiff set of coupled differential equations, we examine only time-averaged plasma properties here.

The ac electrical analog model consists of a resistor and two capacitors in series, see Fig. 3-4. In this model, the resistive component of the impedance is attributed solely to the bulk plasma, while the reactive component arises from the sheaths; consequently, the bulk of the plasma is modeled as a resistance R_b and each sheath is represented by a capacitance C_s . In reality, a small portion of the total capacitance (~ 5 pF) can be attributed to the capacitance between the electrodes, which is inversely proportional to the electrode spacing. This correction is important for highly electronegative gases (e.g., CFC_1 , or SF_6) where bulk-resistive impedance is comparable to capacitive impedance, i.e., at very high or very low pressures. Current is carried primarily by electrons since the excitation frequency (13.56 MHz in this study) is greater than the ion plasma frequency (~ 3 MHz), so ions do not respond to the ac field.

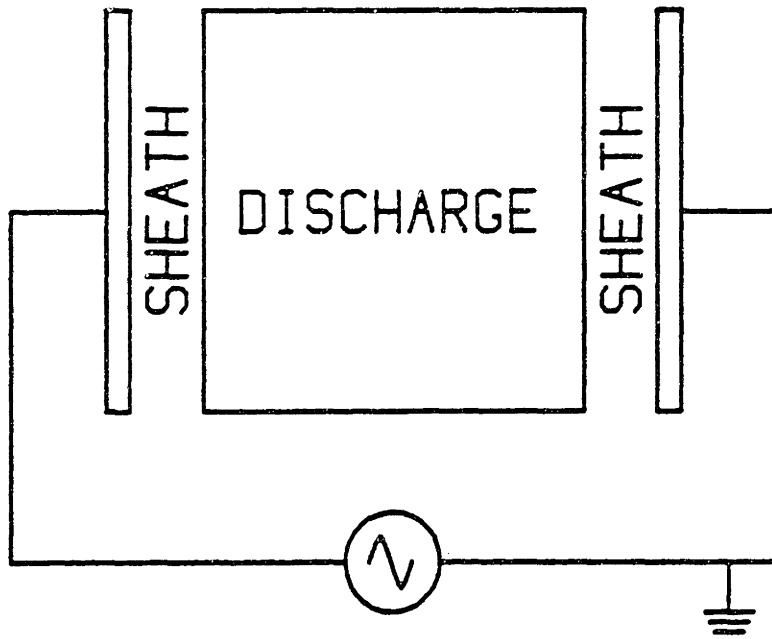
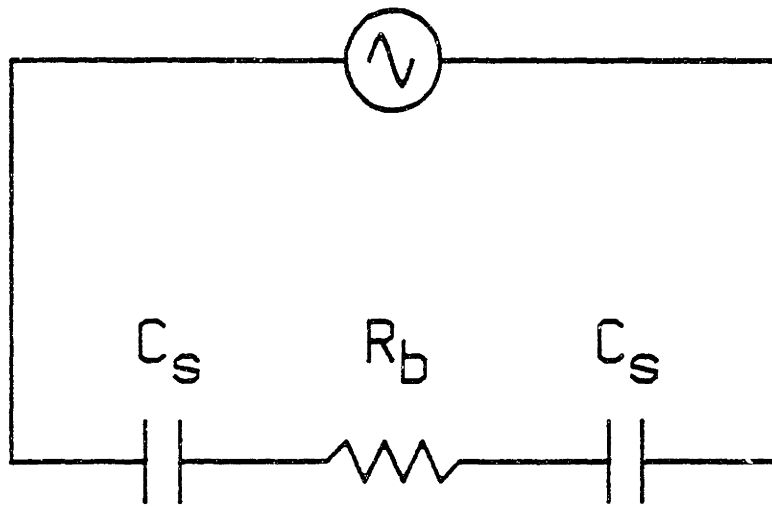


Figure 3-4: Electrical analog model for 13.56 MHz glow discharge.

No inductive component is included in the model since the electron-neutral collision frequency is much greater than the excitation frequency; therefore, electrons do not store directed energy over a power cycle. Higher harmonics (second and above) of the current waveform are only 0.1% of the fundamental, indicating that the electrical impedance of the discharge is nearly linear.

Physically, R_b represents the resistance to the passage of electron current through the plasma, i.e., we assume that electron transport is mobility-limited. More specifically, we assume that both the electron and ion concentrations are spatially uniform across the bulk plasma, and that the electrons move in response to the time-averaged applied rf electric fields. The current through the sheath is primarily displacement current because the high sheath electric fields repel electrons, causing a low electron density in the sheath. Therefore, the sheaths are modeled as capacitors.

The assumption of a purely capacitive sheath is not valid if significant power is dissipated in the sheath; in this case some resistive component must be added to the model (Köhler et al., 1985). Sheath power dissipation (the product of total positive ion current and sheath voltage) accounts for less than 20% of the total power dissipation over most of the experimental range investigated here, and is lumped into the bulk resistance. The accuracy of the impedance model depends on the validity of this assumption; however, errors caused by small sheath power losses should not affect the qualitative prediction of trends. Sheath power dissipation becomes important in the high power, high pressure regime, where the total positive ion current is significant compared to the discharge current. Further

refinements of such impedance models must allow for sheath resistance as well as the effects of excitation frequency on ion transport and sheath thickness. The effects of sheath ionization on plasma impedance have also been examined (Pennebaker, 1979).

The voltage and current waveforms (corrected for the stray impedances) are used with standard impedance analysis techniques (e.g., Senturia and Wedlock, 1975) to determine the time-averaged values of both R_b and C_s ,

$$R_b = \frac{|V|}{|I|} \cos\theta \quad \text{and} \quad C_s = \frac{2|I|}{\omega|V| \sin\theta} . \quad (3.3.1-1)$$

Here, $|V|$ is the rf voltage amplitude at the powered electrode, $|I|$ is the rf current amplitude, ω is the angular excitation frequency, and θ is the phase angle between the waveforms. As seen in section 3.2, phase angles varied between 25 and 65 degrees. Consequently, the phase angle experimental error of about 2.5 degrees is unimportant.

In reality, the magnitude of C_s oscillates with time during the rf cycle. The sheath width, and hence the capacitance, varies as electrons are sequentially displaced toward and away from either electrode by the rf electric fields. The periodic displacement induces a net space charge in the sheath which alters the effective sheath capacitance. The increase of the effective capacitance at one electrode should be approximately balanced by a decrease in the sheath capacitance at the opposing electrode. Therefore, the use of a fixed C_s in the impedance model gives an analogous circuit response and the derived values of C_s are the time-averaged values.

Plasma voltage distributions for high ($\phi=0$) and low ($\phi=\pi$) applied voltages to the powered electrode are shown in Fig. 3-5. Bruce (1981b) presented a similar diagram, but did not allow for the finite potential difference across the bulk plasma observed in the CF_3Cl discharge. Note that although most of the voltage is dropped in the sheaths, 20-40% of the voltage drop occurs across the bulk. The temporal variations in sheath thickness discussed above and pointed out by Bruce are not included in Fig. 3-5 since the impedance model predicts only time-averaged properties. Although the model is only an ac representation of the plasma, the requirement that the plasma potential always be positive with respect to either electrode allows evaluation of both the minimum and time-averaged sheath potentials.

First, we examine sheath potentials for the simpler case of a dc discharge. In a dc discharge, the potential difference between the plasma and a floating electrode is given by the Bohm sheath criterion (Chapman, 1980),

$$V_p - V_f = (kT_e/2q) \ln(m_i/2.3m_e) , \quad (3.3.1-2)$$

where V_p is the plasma potential, V_f is the surface floating potential, T_e is the electron temperature, m_e and m_i are the electron and ion masses, q is the electronic charge, and k is Boltzmann's constant. The magnitude of the potential difference, assuming an average electron energy of 3-5 eV (as measured with a Langmuir probe) and an ion mass of about 70 amu (CF_3^+), is 15-25 volts.

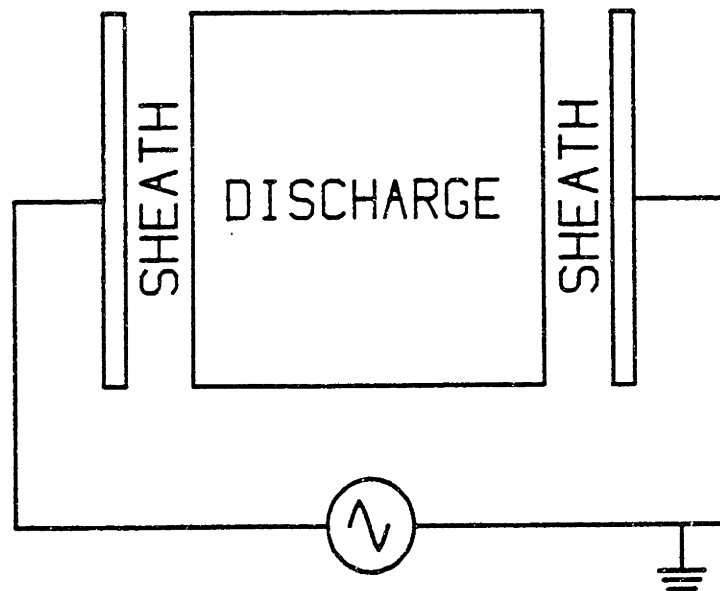
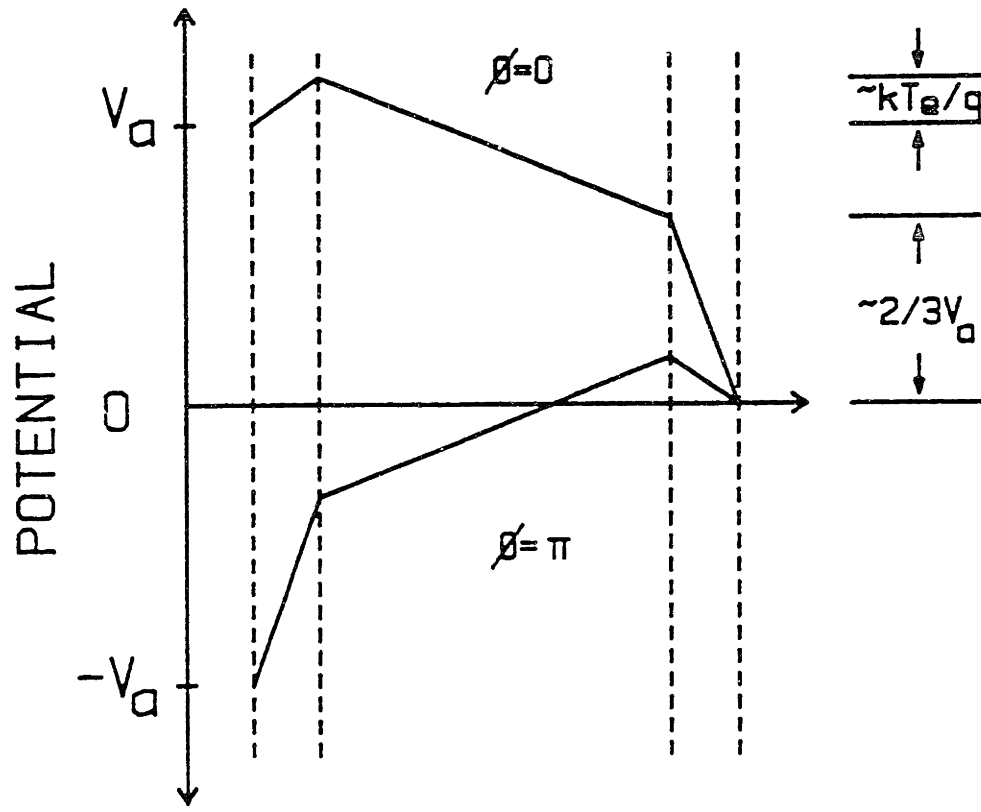


Figure 3-5: Plasma voltage distributions at two phases of the applied rf voltage.

In a rf discharge, the minimum dc potential difference between plasma and electrode is considerably smaller than in a dc discharge. Charge neutrality requires that the time-averaged ion and electron fluxes be equal. Positive ion current flows throughout the cycle since the electrode potential is on average more negative than the plasma, and because the ions respond slowly with respect to the rf electric field for frequencies above 3 MHz. However, an appreciable electron current flows only when the sheath potential approaches a few kT_e/q , allowing the higher energy electrons to penetrate the sheath and strike the electrode. Since the fraction of the rf cycle during which the electron flux occurs is very small, the minimum sheath potential barrier must be smaller than that of the dc plasma floating potential barrier to allow a large periodic electron flux, and therefore, a net neutral flux to the surface. Assuming a Maxwellian electron energy distribution, the electron flux depends exponentially on the ratio of the retarding sheath potential to the electron energy. Therefore, an electron current sufficient to balance the ion current can be obtained only if the minimum sheath potential barrier, symbolized here by $V_{p,min}$, is on the order of kT_e/q (about 3-5 volts).

The limits of the sheath voltage oscillation are most clearly seen in Fig. 3-5 as the potentials at the grounded electrode sheath for $\phi=0$ and $\phi=\pi$, respectively. Effective applied ac potential refers to the portion of the rf voltage not dissipated in the bulk plasma, i.e., the amplitude of the effective applied potential $|V|_{eff}$ is the voltage dropped across one of the capacitors in the impedance model. Fig. 3-6 shows the plasma potential at the sheath of the grounded electrode, assuming that a third of the applied voltage is dropped across the

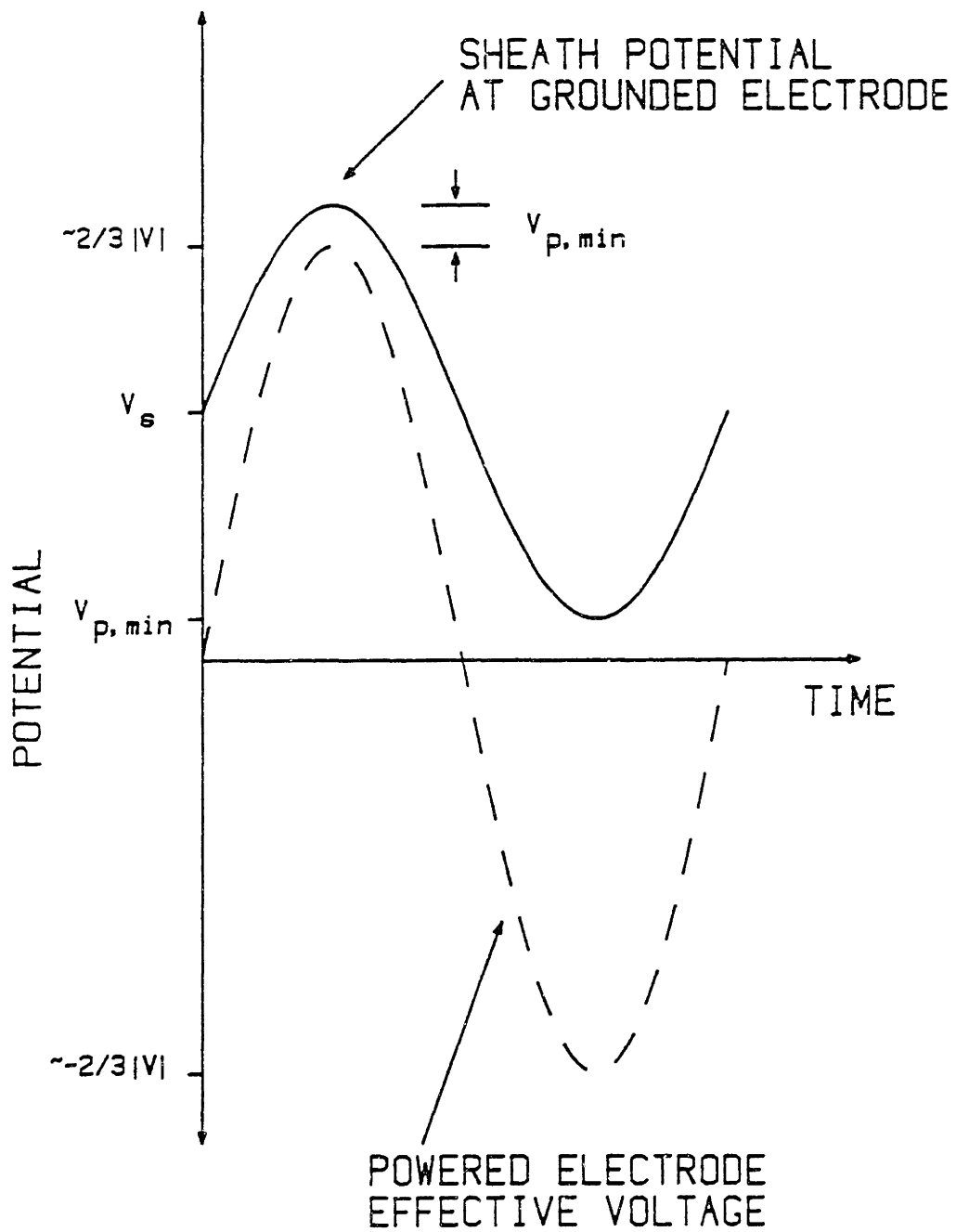


Figure 3-6: Sheath potential at the grounded electrode as a function of the rf cycle time.

bulk plasma. Plasma potentials of low pressure plasmas, which have a much more capacitive impedance, have been treated similarly and are discussed in detail elsewhere (Köhler et al., 1985).

The plasma sheath can also be modeled as a system of diode, resistor, and capacitor in parallel (Köhler et al., 1985); therefore, the sheath potential is obtained by rectifying the effective applied potential. If the frequency response of the rectifying circuit is much faster than the rf, half-wave rectification will occur (Bruce, 1981b) and the time-averaged sheath potential V_s is

$$V_s \approx 2 |V|_{\text{eff}}/\pi + V_{p,\text{min}} . \quad (3.3.1-3)$$

Eqn. (3.3.1-3) applies for low excitation frequencies (e.g., 100 KHz) where the electrons respond so rapidly to the electric field that the rectifying resistance is due solely to the ions; i.e., the electron concentration in the sheath is in a pseudo-steady state with respect to the applied field.

At high excitation frequencies the ions cannot respond to the rf field, so any rectification must be due to the motion of the electrons. A correct description of this situation requires a complex dynamical model of the charged particles in the plasma, and is beyond the scope of the present work, although preliminary calculations indicate that the electron response time is slightly less than the half-cycle time at 13.56 MHz (Thompson et al., 1986b). Later in this section, we show that the electrons require about one-quarter of the

rf cycle time to move a distance comparable to the sheath thickness. Therefore, the pseudo-steady-state approximation is beginning to fail at 13.56 MHz. Because the pseudo-steady-state assumption is no longer valid, the sheath potential does not behave as in the 100 KHz case; in fact, the slower electron response damps the rectification response. This causes the sheath potential to approach a sinusoid in time; therefore, at 13.56 MHz we assume that the plasma potential oscillates sinusoidally. For a sinusoidal sheath potential the time-averaged potential is the midpoint between the maximum effective applied ac potential and $V_{p,min}$, i.e.,

$$V_s \approx |V|_{eff} + V_{p,min} \quad (3.3.1-4)$$

In terms of the impedance model,

$$V_s = \frac{|I|}{\omega C_s} + V_{p,min} \quad (3.3.1-5)$$

The sheath voltages estimated from the impedance model are supported by ion energy experiments, the details of which are presented in chapter 4. If the sheath transit time is much less than the rf cycle time, the most energetic ions striking the electrode should have energies near the maximum sheath potential. However, at high frequencies (e.g., 13.56 MHz) the maximum ion energy should

approach the time-averaged sheath potential since sheath transit encompasses several rf cycles. In Fig. 3-7 the maximum observed ion energy is plotted against the predicted sheath voltage for a wide range of process conditions. A line with unity slope and with $V_{p,min} = 5$ volts, representing the prediction of eqn. (3.3.1-5), is shown for comparison of the model and the data. The shaded data points in the lower left corner of Fig. 3-7 were taken at high pressures (0.7-0.8 torr), where virtually no ions pass through the sheath without suffering collisions. In these cases, the maximum observed ion energy may be considerably less than the actual sheath voltage.

Note that a lower dc offset would better represent the data of Fig. 3-7. In the previous discussion of $V_{p,min}$ it was implicitly assumed that the electrons respond instantaneously to the applied electric field. In reality, the transit time for electrons to cross the sheath is of the same order as the cycle time (74 ns at 13.56 MHz). This time lag is due to the mobility-limited motion of electrons across the sheath, and results in a lowering of the $V_{p,min}$ at which the necessary flux of electrons is achieved. The lower $V_{p,min}$ (approximately zero volts) results in better agreement between theory and experiment.

If the sheath thickness is much less than the electrode spacing d , the root mean square (rms) electric field to pressure ratio in the bulk plasma, E_b/P , is

$$E_b/P = R_b |I| / \sqrt{2} Pd . \quad (3.3.1-6)$$

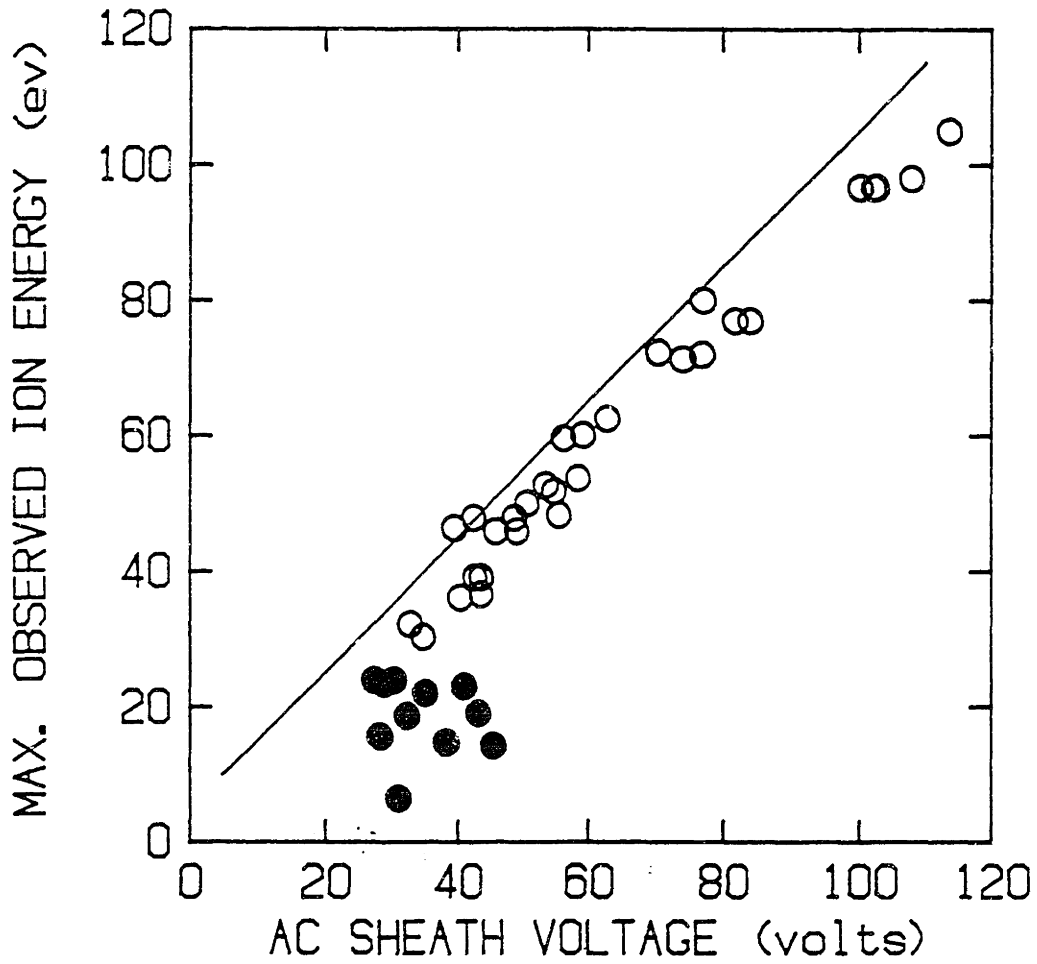


Figure 3-7: Comparison of impedance model prediction of V_s with measured maximum ion energy $E_{+,max}$.

We are interested in estimating E_0/P because it is the plasma property which controls the electron energy distribution. The rms electric field incorporates the assumption that the electron concentration is uniform throughout the plasma bulk, i.e., space-charge effects within the bulk plasma are neglected. Typical rms electric fields predicted by the model were between 20 and 50 V/cm (see subsection 3.4.4)

To predict the electron density correctly from the measured plasma impedance, one must account for the variation in electron concentration with time and position. This calculation would include field-induced electron motion, electron diffusion due to concentration gradients, space-charge effects caused by electron displacement with respect to positive ions, creation of electrons by ionization, and electron losses by attachment with plasma neutrals and by collision with electrode surfaces. Using such a model the electron concentration could be determined given the measured rf current and voltage waveforms. However, solving the resulting model is very difficult, although simplified cases have been examined (Kushner, 1983; Graves and Jensen, 1986; Thompson and Sawin, 1986; Thompson et al., 1986c). Since the kinetic data necessary for such a model are not available for CF_3Cl , we resort to a greatly simplified electron transport model. This simplified model should allow identification of the major trends in electron density with varying process conditions.

To estimate the electron density from the resistance of the circuit analog, assume that the electron and ion densities are spatially uniform, and that the electrons oscillate with the applied rf field. Power is dissipated by inelastic electron-neutral

collisions as the electrons move back and forth in the plasma bulk at a velocity determined by their mobility and the electric field strength. The ions are assumed to be uniformly distributed throughout the bulk plasma, their positions fixed with time. Since the 13.56 MHz excitation frequency is greater than the ion plasma frequency (~3 MHz), the assumption that the ions do not move in response to the rf field is quite good. To estimate the electron density, consider the current flow through the bulk plasma by electron mobility. Since electrons are the primary charge carrier, the rms electron flux j_e is related to the discharge current by

$$j_e = |I|/\sqrt{2} \text{ qA} , \quad (3.3.1-7)$$

where A is the electrode area. For mobility-limited electron motion, the electron density $[e^-]$ is related to the flux by

$$j_e = [e^-]q\mu_e E_p , \quad (3.3.1-8)$$

where μ_e is the electron mobility. Eqn. (3.3.1-8) expresses the flux of electrons in an electric field across a plane normal to the field. The electric field is the rms voltage across the bulk plasma divided by the inter-electrode distance, leaving

$$[e^-] = d/qAR_0\mu_e . \quad (3.3.1-9)$$

Electron mobility in CF_3Cl was estimated from drift velocity data for CF_4 (Naidu and Prasad, 1972) and CF_2Cl_2 (Naidu and Prasad, 1969). The product of electron mobility and pressure is assumed constant at $20 \text{ m}^2\text{-torr/V-s}$ over the entire pressure range.

As mentioned previously, the uniform electron density model does not explicitly consider certain significant effects such as space charge. In response to the rf electric field the highly mobile electrons are displaced relative to the fixed positive ions. Electric fields are induced at both sheaths by the resulting net separation of charge. These electric fields oppose the flux of electrons to the electrodes, thereby lowering the velocity of the electrons, and in turn the discharge current, for a given electron density.

We consider the importance of these space-charge effects by examining the motion of electrons in the rf electric field. Neglecting electron diffusion by assuming a uniform spatial density of electrons, the space charge is dependent only on the distance travelled by the electrons as they move during a half cycle (recall that the positive ions are too massive to respond to the rf field). The maximum distance the electrons can be displaced during a half-cycle is equal to the sheath thickness; otherwise, they would be captured by collision with the electrodes. The validity of the electron density model is determined by both the magnitude of this space-charge-induced electric field and the amplitude of the electrons' spatial displacement in response to the applied rf potential.

The displacement of the electrons is estimated as follows. The electron velocity is determined by the mobility and the electric field strength,

$$dx/dt = -\mu_e E_0 \sin(\omega t) , \quad (3.3.1-10)$$

where x and t are distance and time, respectively. The electric field is assumed to be sinusoidal in time, with amplitude E_0 and angular frequency ω . The maximum displacement L from the average position is the distance travelled in first quadrant of the rf cycle,

$$L = \int_0^{\pi/2\omega} \mu_e E_0 \sin(\omega t) dt = \sqrt{2} \mu_e E_0 / 2\pi f . \quad (3.3.1-11)$$

At 13.56 MHz and 0.5 torr a typical field of 30 V/cm gives a maximum displacement of approximately 2 mm; therefore, the time-averaged sheath thickness must be 2 mm or greater. As discussed later, sheath thicknesses obtained from the impedance model are approximately 1 mm, indicating that electron motion is restricted by the space charge and/or other sheath fields.

The electric field caused by the uniform displacement of the electrons with respect to the ions can be calculated by integrating Poisson's equation over the displacement distance. Assuming a positive ion and electron concentration of $2 \times 10^9 \text{ cm}^{-3}$, the potential difference induced by a 2 mm displacement is 70 V. The existence of a 70 V potential opposing the flux of electrons to the electrode would reduce the maximum displacement to less than 2 mm. If the electron and positive ion concentrations are not spatially uniform across the electrode gap (e.g., a cosine distribution), the space-charge field

caused by the displacement is distributed across a wider region of the plasma. The potential barrier opposing electron flow to the electrodes, which is confined to the sheath-bulk interface in the uniform electron density model, will be less abrupt in the case of a spatially-variant electron concentration or if electron diffusion is considered.

Because space-charge effects within the bulk plasma are neglected in the uniform density model, the estimated electron concentrations may be somewhat low. The velocity of the electrons is less than predicted from mobility considerations due to the opposing space-charge electric field. Therefore, to carry the measured current a greater number of electrons must traverse a shorter distance.

The space-charge effects are reactive and therefore are incorporated into the circuit analog's sheath capacitance. As discussed before, the major fraction of the rf power is dissipated in the bulk plasma via electron-neutral collisions. Therefore, the plasma resistance should still be related to the electron density, and it is expected that the model will predict the general trends of the electron density with process conditions.

The impedance model as described here is only applicable when the plasma is well confined between the electrodes, i.e., the plasma has a known constant volume. Upon loss of containment two factors preclude use of this model: (i) the area of the grounded electrode is no longer known because the plasma contacts the chamber walls, and (ii) the motion of electrons in the electric fields is no longer limited to one spatial dimension. In this apparatus, CF_3Cl plasmas are well confined for pressures greater than about 0.25 torr; no change in plasma volume

was observed by optical emission in the range 0.25-1 torr. In addition, measured dc bias voltages on the powered electrode were small and positive (~5 V), indicating that the effective electrodes are of approximately equal area. At pressures lower than 0.2 torr the plasma fills the etching chamber and contacts the chamber walls. In this case the dc bias is negative and relatively large (less than -50 V) compared to the peak applied voltage (~150 V), as would be expected for the case of unequal electrode areas (Koenig and Maissel, 1970). The sharp transition between well-contained and poorly-contained plasma behavior is observed visually as well as through the sign and magnitude of the dc bias voltage. The impedance results presented here were obtained under constant plasma volume conditions. Insertion of a Teflon ring at the perimeter of the electrodes to confine the discharge resulted in no significant changes in plasma properties for pressures greater than 0.25 torr, where the plasma was well-confined in the absence of the ring.

In conclusion, the desired simplicity of the electrical analog model necessitates the use of many assumptions; however, the results obtained can be quite useful in understanding the physics responsible for observed trends in etching. The assumptions made in the impedance model are fairly good for the processing conditions examined in this thesis, as discussed above. Detailed balance equations for charged particles can be written; however, the complexity of the problem makes it difficult to pose as well as to solve, although work is being done in this area. The utility of a simple algebraic plasma model in describing the etching process must be acknowledged, given the present status of more sophisticated modeling efforts.

3.3.2 Resistive Sheaths

The impedance model described in the previous subsection does not allow for power dissipation in the glow discharge sheaths via energetic ion bombardment of the surfaces. It has been suggested by several authors that this problem might be solved by adding a parallel resistance to the capacitor which represents the plasma sheath. In this way, positive ion current can dissipate power through the resistor. The insight added by this evolution of the previous model is discussed in this section, along with some possible pitfalls. The voltage-current relationships of this circuit analogy are used to derive expressions for the bulk resistance R_b , sheath capacitance C_s , and sheath resistance R_s . A small set of the predictions of this model for CF_3Br plasmas are presented in subsection 3.4.6.

The resistive sheath model electrical analog consists of a series of three parallel-resistor-capacitor circuits. The bulk resistance has the same physical meaning as in the simpler impedance model. Since the parallel-plate electrode assembly has some capacitance (about 5 pF), a bulk capacitor is included. In the sheaths, most of the current is carried capacitively as in the previous model, but positive ion current to the electrode is represented by a parallel sheath resistance. The current through the resistor is specified by the measured ion current, so a diode (to reflect electrons from the sheath) is not needed in the circuit analogy.

The physical inconsistency of this analog is that the heavy ions are essentially immobile during the time scale of an rf cycle. The sheath thickness oscillates because the electrons respond rapidly to the field; i.e., the sheath boundary is determined by the position of the electrons rather than that of the ions. Nevertheless, some useful information is gained from this analogy, although the results are similar to those of the simpler model.

Combining the two sheaths into one and writing the total impedance of the plasma, Z_p ,

$$Z_p = \frac{R_b/j\omega C_b}{R_b + 1/j\omega C_b} + \frac{2R_s/j\omega C_s}{R_s + 1/j\omega C_s} . \quad (3.3.2-1)$$

This expression is equated with the general form of an impedance,

$$Z_p = |V|/|I| (\cos\theta - j \sin\theta) . \quad (3.3.2-2)$$

Using the current-divider relationship between the sheath resistor (ion current) and capacitor (displacement current),

$$i_R^2 + i_C^2 = |I|^2, \quad (3.3.2-3)$$

where

$$i_R = A\Gamma_+ . \quad (3.3.2-4)$$

In the preceding equations, i_R is the current through the sheath resistor (the product of the electrode area A and the positive ion current density Γ_+) and i_C is the displacement current through the sheath capacitor.

Now define two simplifying expressions,

$$X^2 = i_R^2 / (|I|^2 - i_R^2) , \quad (3.3.2-5)$$

and

$$Y = |V| / |I| (\cos\theta - X\sin\theta) . \quad (3.3.2-6)$$

Equations (3.3.2-1) through (3.3.2-6) are now solved simultaneously. First, since C_b is a parallel-plate capacitance we write,

$$C_b = \epsilon_0 A / d . \quad (3.3.2-7)$$

R_b is determined by matching the real portions of equations (3.3.2-1) and (3.3.2-2),

$$R_b = \frac{2Y}{1 + \sqrt{1 - 4[(\omega C_b Y)^2 + \omega X Y C_b]}} \quad (3.3.2-8)$$

The sheath capacitance C_s is determined by matching the imaginary portions of equations (3.3.2-1) and (3.3.2-2),

$$2/\omega C_s = (X^2 + 1) \left[\frac{|V|}{|I|} \sin\theta - \frac{\omega C_b}{(1/R_b)^2 + (\omega C_b)^2} \right] \quad (3.3.2-9)$$

Finally, R_s is obtained by manipulation of equations (3.3.2-1), (3.3.2-8) and (3.3.2-9),

$$R_s = 1/\omega C_s X \quad (3.3.2-10)$$

The restriction that the resistance be real requires that,

$$(\omega C_b Y)^2 + \omega C_b X Y < 1/4 \quad (3.3.2-11)$$

Equation (3.3.2-11) corresponds to the physical requirement that the positive ion current cannot be greater than the total discharge current.

Unfortunately, there are several physical inconsistencies in the resistive-sheath model. Most importantly, the sheath width is not constant with time - the sheath expands and contracts with the rf electric field. Since the electrons respond much more quickly to the field than do the ions, the sheath properties are determined almost solely by the electrons. In the resistive sheath model, the ion flux through the sheath is used to determine the sheath resistance. In reality, the sheath resistance is a complex function of both electron and ion properties.

3.4 ESTIMATES OF PLASMA PROPERTIES

Plasma impedance model predictions (subsection 3.3.1) for CF_3Cl and CF_3Br plasmas are presented in Tables 3-4 and 3-5, respectively. Plasma resistance, sheath capacitance, bulk plasma electric field to pressure ratio, electron density, and sheath voltage are tabulated. These results are discussed in the remainder of this section.

The predictions of the resistive-sheath model for CF_3Br plasmas are shown in Table 3-6 and discussed in subsection 3.4.6.

3.4.1 Plasma Resistance

The resistance R_b of a $\text{CF}_3\text{Cl}/\text{Ar}$ plasma, as determined from eqn. (3.3.1-1), varied from 80 to 600 Ω over the following plasma conditions representative of the center of experimental design F13A: power density of 0.2-0.6 W/cm^2 , pressure of 0.2-0.8 torr, 5-30% Ar in CF_3Cl . Plasma resistance increases with increasing pressure, apparently because of the lowered electron mobility in the denser gas. Increasing power input results in a lower resistance, as does increasing the argon fraction; these effects are both attributable to increased electron density and mobility.

Contour plots of R_b with power density and pressure are shown in Figs. 3-8a and 3-8b, for CF_3Cl mole fraction $\gamma=0.9$ and 0.8, respectively. The lines of constant R_b were generated from the RSM fit of the experimental design data sets. The dependence of R_b on power density and composition ($P=0.5$ torr) is shown as Fig. 3-8c.

Table 3-4
 Impedance Model Estimates in CF₃Cl/Ar plasmas,
 various conditions in a 37-run experimental design.
 Flow rate of 6 sccm, blank electrodes (assembly A),
 excitation frequency of 13.56 MHz.

RUN ID	R _b (Ω)	C _s (pF)	E _b /P (V/cm-torr)	[e ⁻] (x10 ⁻⁹ cm ⁻³)	V _s (Volts)
F13B_1	287	180	82.1	1.40	42.3
F13B_2	591	104	64.7	0.70	27.8
F13B_3	110	231	95.0	1.82	49.8
F13B_4	183	156	77.3	1.09	36.0
F13B_5	332	139	71.5	1.23	40.6
F13B_6	400	126	77.9	1.02	40.5
F13B_7	131	178	77.9	1.54	43.9
F13B_8	150	199	90.3	1.33	39.4
F13B_9	149	248	84.4	2.03	43.8
F13B_10	188	219	93.6	1.61	43.4
F13B_11	296	144	65.1	1.02	30.0
F13B_12	328	145	73.2	0.91	29.8
F13B_13	274	152	79.3	1.09	36.4
F13B_14	280	155	76.2	1.09	35.0
F13B_15	242	171	80.6	1.23	37.8
F13B_16	133	202	88.4	1.51	44.0
F13B_17	153	184	84.7	1.30	40.0
F13B_18	138	195	86.1	1.44	41.6
F13B_19	92	101	111.3	1.09	79.7
F13B_20	83	112	129.9	1.19	89.9
F13B_21	92	115	139.5	1.09	86.8
F13B_22	79	145	175.6	1.26	102.4

Table 3-5
 Impedance Model Estimates in CF₃Br plasmas
 during etching of heavily P-doped polysilicon,
 various conditions in a 35-run experimental design.
 Excitation frequency of 13.56 MHz, electrode assembly B.

RUN ID	R _b (Ω)	C _s (pF)	E _b /P (V/cm-torr)	[e ⁻] (x10 ⁻⁹ cm ⁻³)	V _s (Volts)
BR_1	193	239	102.4	1.29	35.0
BR_2	188	242	100.5	1.33	35.1
BR_3	211	238	103.5	1.18	33.0
BR_4	218	244	98.8	1.43	37.3
BR_5	119	226	110.3	1.64	25.5
BR_6	474	128	98.9	0.66	32.8
BR_7	202	206	104.7	0.93	30.2
BR_8	146	287	103.8	1.72	39.9
BR_9	146	293	103.2	1.71	38.7
BR_10	325	173	101.6	0.77	29.3
BR_11	329	169	100.1	0.76	29.7
BR_12	320	188	102.2	0.98	34.6
BR_13	304	192	100.3	1.03	34.4
BR_14	128	260	107.0	1.47	38.6
BR_15	127	263	104.0	1.48	37.4
BR_16	234	239	95.0	1.60	40.7
BR_17	217	271	98.1	1.73	41.4
BR_18	59	179	144.9	2.13	111.5
BR_19	54	202	139.3	2.30	101.7
BR_20	1367	33	90.2	0.27	47.7
BR_21	1600	26	95.9	0.23	55.2
BR_22	207	119	98.3	0.60	32.1
BR_23	225	131	107.1	0.56	29.3
BR_24	136	304	104.3	1.84	40.5
BR_25	474	116	102.1	0.53	29.8
BR_26	381	172	101.0	0.91	35.3
BR_27	97	245	112.9	1.61	47.9
BR_28	197	237	101.2	1.27	34.8
BR_29	226	230	107.2	1.11	33.5
BR_30	139	302	104.6	1.80	40.3
BR_31	451	122	99.6	0.55	29.0
BR_32	378	160	99.6	0.92	36.4
BR_33	90	246	108.9	1.73	48.8
BR_34	198	236	101.0	1.26	34.6
BR_35	191	244	99.7	1.31	33.8

Table 3-6
 Comparison of Plasma Impedance Estimates in CF₃Br Plasmas,
 Using Capacitive Sheath and Resistive Sheath Models.

RUN ID	Capacitive Model	Resistive Model
BR_1	$R_b = 193 \Omega$ $C_s = 239 \text{ pF}$ $E_b/P = 102 \text{ V/cm-torr}$ $[e^-] = 1.3 \times 10^9 \text{ cm}^{-3}$	$R_b = 149 \Omega$ $C_s = 210 \text{ pF}$ $R_s = 97 \Omega$ $E_b/P = 108 \text{ V/cm-torr}$ $[e^-] = 1.6 \times 10^9 \text{ cm}^{-3}$
BR_4	$R_b = 218 \Omega$ $C_s = 244 \text{ pF}$ $E_b/P = 99 \text{ V/cm-torr}$ $[e^-] = 1.4 \times 10^9 \text{ cm}^{-3}$	$R_b = 157 \Omega$ $C_s = 176 \text{ pF}$ $R_s = 83 \Omega$ $E_b/P = 107 \text{ V/cm-torr}$ $[e^-] = 1.9 \times 10^9 \text{ cm}^{-3}$
BR_5	$R_b = 119 \Omega$ $C_s = 226 \text{ pF}$ $E_b/P = 110 \text{ V/cm-torr}$ $[e^-] = 1.6 \times 10^9 \text{ cm}^{-3}$	$R_b = 70 \Omega$ $C_s = 276 \text{ pF}$ $R_s = 83 \Omega$ $E_b/P = 115 \text{ V/cm-torr}$ $[e^-] = 2.6 \times 10^9 \text{ cm}^{-3}$
BR_6	$R_b = 474 \Omega$ $C_s = 128 \text{ pF}$ $E_b/P = 99 \text{ V/cm-torr}$ $[e^-] = 0.6 \times 10^9 \text{ cm}^{-3}$	$R_b = 332 \Omega$ $C_s = 72 \text{ pF}$ $R_s = 120 \Omega$ $E_b/P = 122 \text{ V/cm-torr}$ $[e^-] = 0.8 \times 10^9 \text{ cm}^{-3}$
BR_7	$R_b = 202 \Omega$ $C_s = 206 \text{ pF}$ $E_b/P = 105 \text{ V/cm-torr}$ $[e^-] = 0.9 \times 10^9 \text{ cm}^{-3}$	$R_b = 158 \Omega$ $C_s = 191 \text{ pF}$ $R_s = 127 \Omega$ $E_b/P = 111 \text{ V/cm-torr}$ $[e^-] = 1.1 \times 10^9 \text{ cm}^{-3}$

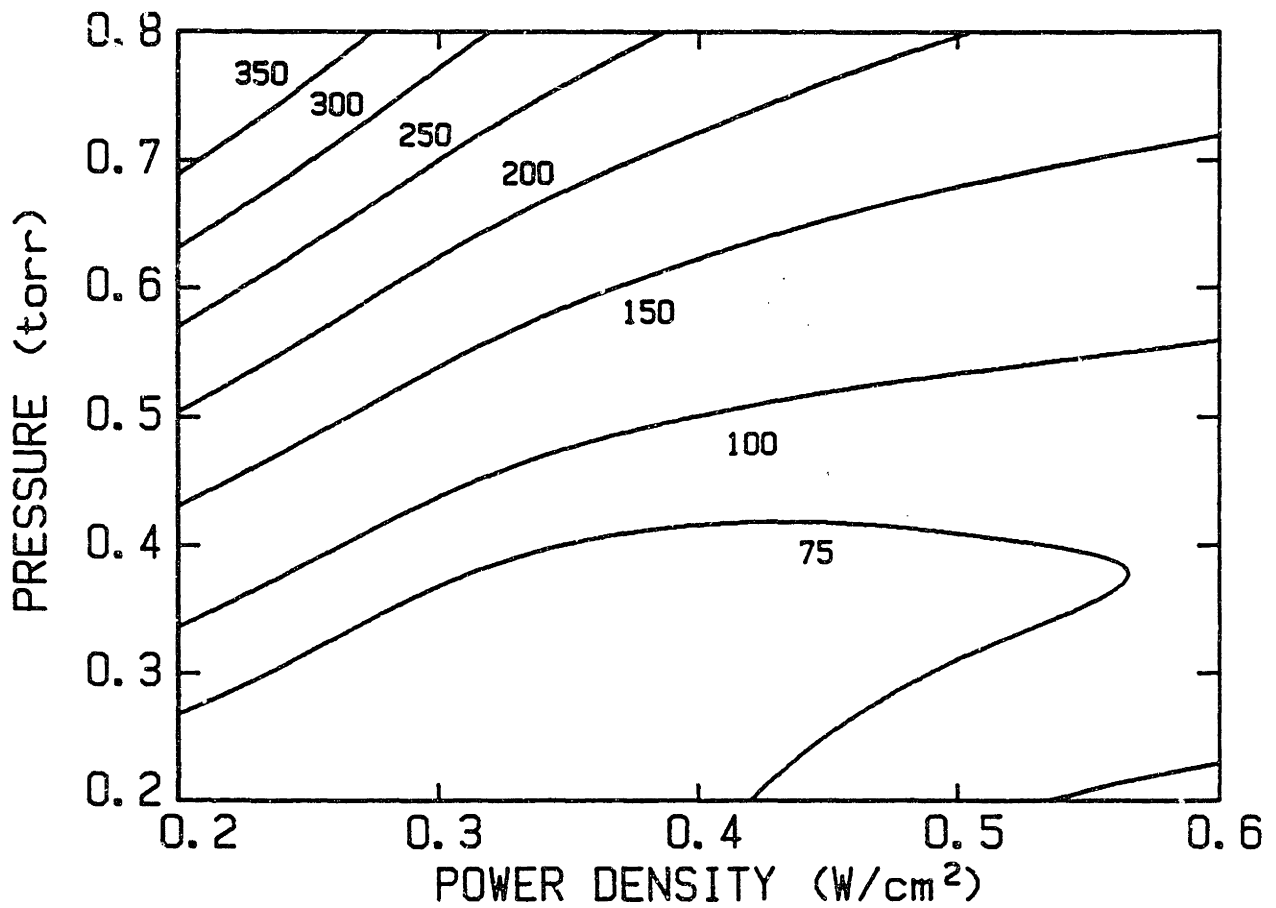


Figure 3-8a: Contour plot of CF_2Cl discharge bulk plasma resistance R_b (ohms) vs. power density (watts/ cm^2) and pressure (torr), $\gamma = 0.9$.

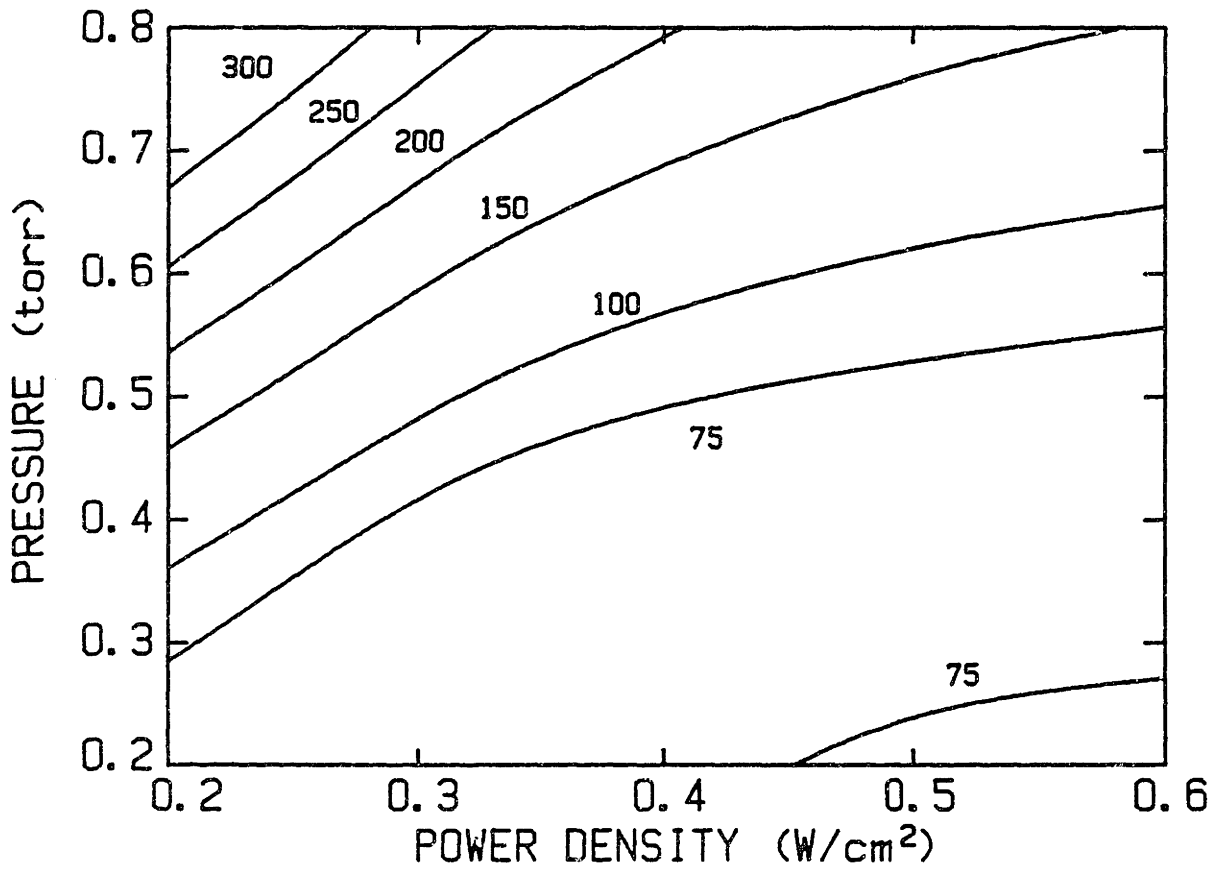


Figure 3-8b: Contour plot of CF_3Cl discharge bulk plasma resistance R_b (ohms) vs. power density (watts/ cm^2) and pressure (torr), $\gamma = 0.8$.

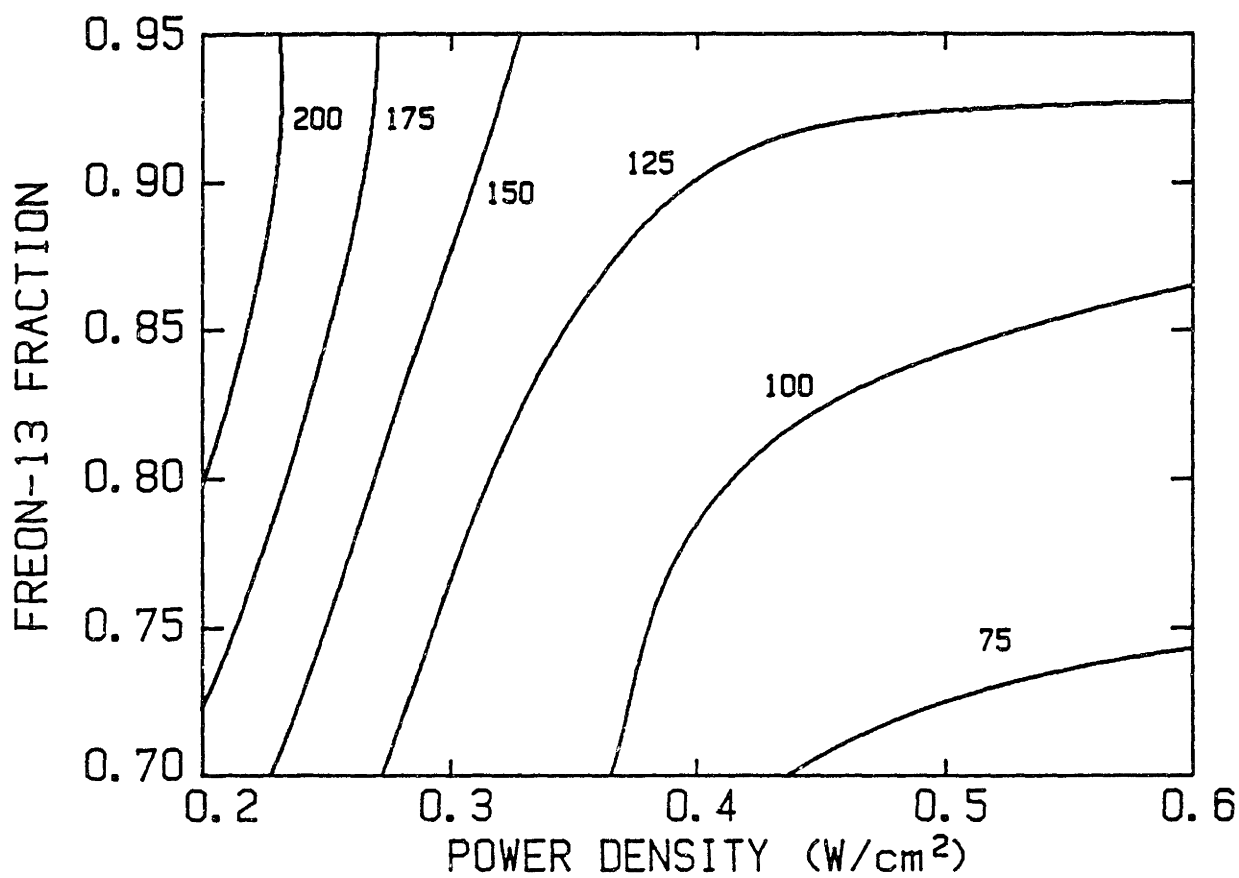


Figure 3-8c: Contour plot of CF_3Cl discharge bulk plasma resistance R_b (ohms) vs. power density (watts/cm²) and composition, $P=0.5$ torr.

The response of R_b to power input and pressure in a CF_3Br plasma is shown in Fig. 3-9. The resistance of a CF_3Br plasma is generally higher than that of CF_3Cl , although the general trends with plasma conditions are similar. The simple dependence of R_b on power input and pressure can be written using eqns. (3.2.2-1) and (3.3.1-1),

$$R_b = k(2A) P^n / \dot{W} , \quad (3.4.1-1)$$

where $k=1.06 \pm .05$ and $n=1.64 \pm .03$ by least-squares regression. In equation (3.4.1-1) all variables are expressed in units listed in Appendix A.

3.4.2 Sheath Capacitance

The sheath capacitance of a CF_3Cl plasma, using eqn. (3.3.1-1), shows a maximum with pressure at about 0.6 torr and increases monotonically with power density. The range of calculated capacitances is 100-250 pF, corresponding to sheath thicknesses between 1 and 0.4 mm, in qualitative agreement with visual observation of the discharge. Therefore, at high pressure and low power the plasma impedance is primarily resistive, while at low pressure and high power the reactive impedance dominates. Contour plots of C_s are shown in Figs. 3-10a to 3-10c.

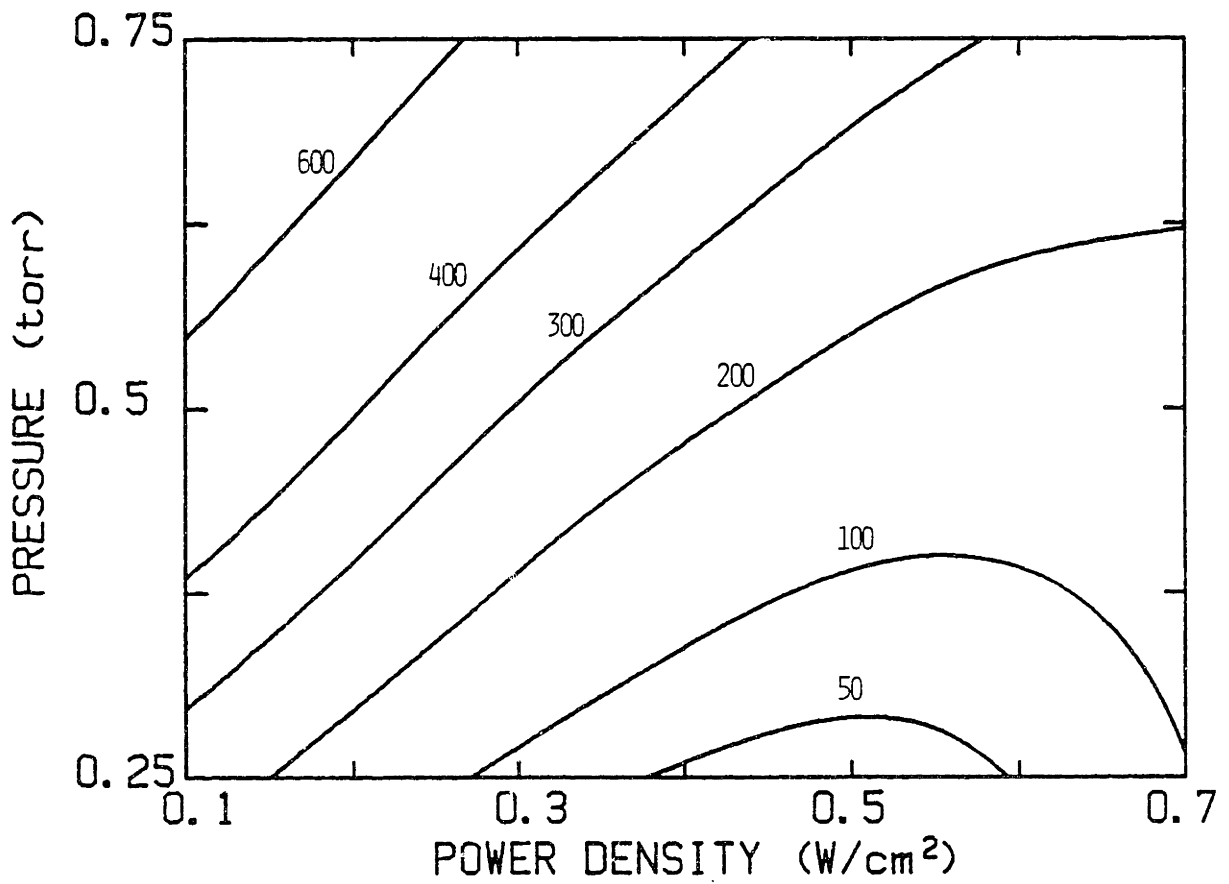


Figure 3-9: Contour plot of CF_3Br discharge bulk plasma resistance R_b (ohms) vs. power density (watts/ cm^2) and pressure (torr).

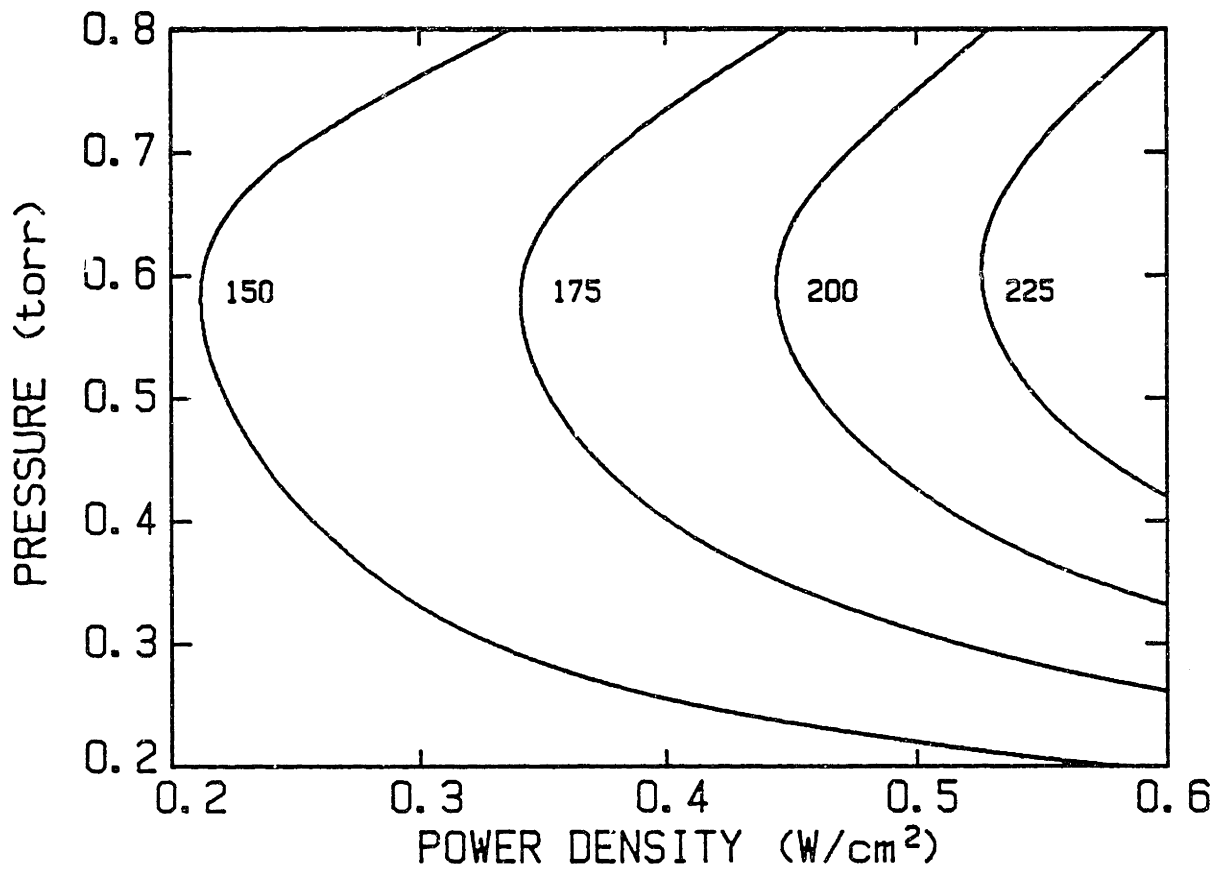


Figure 3-10a: Contour plot of CF₃Cl/Ar discharge sheath capacitance C_s (pF) vs. power density (watts/cm²) and pressure (torr), $\gamma=0.9$.

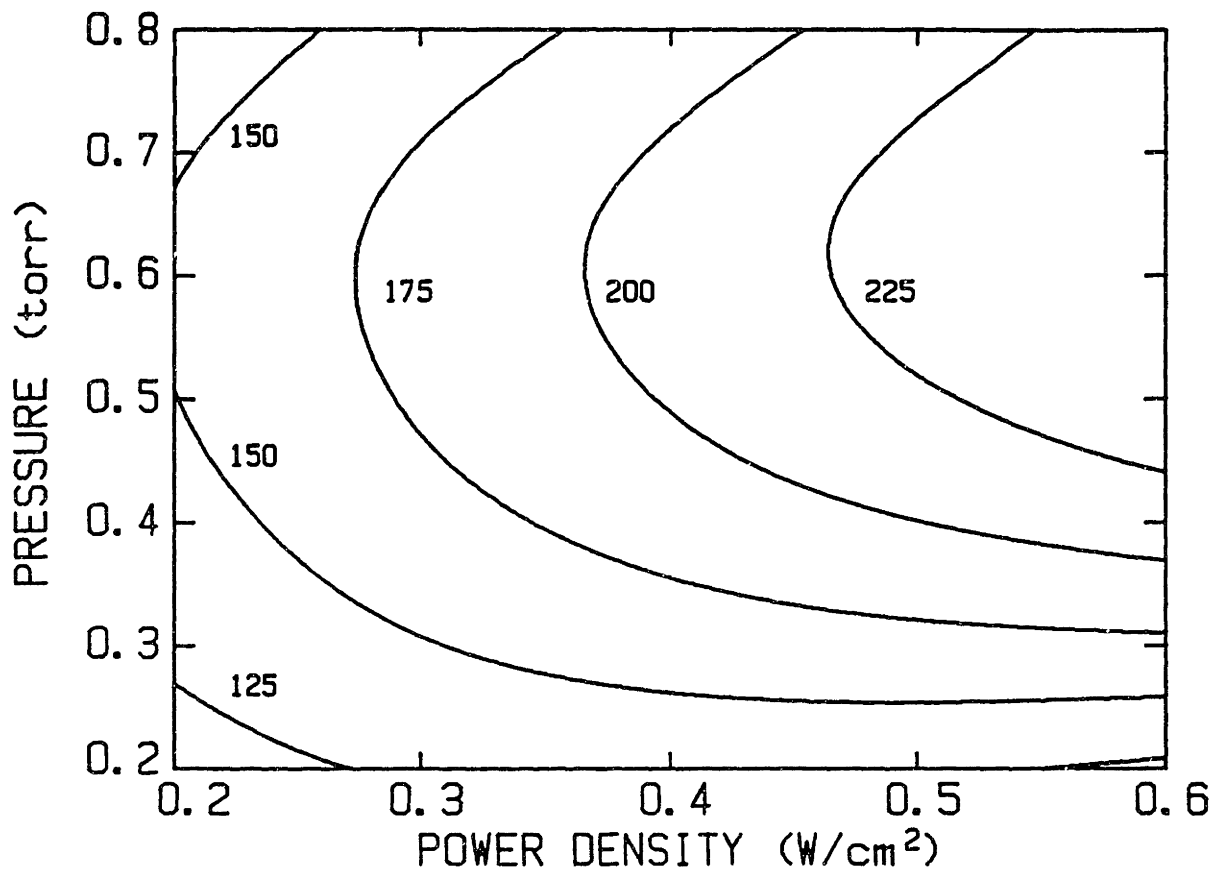


Figure 3-10b: Contour plot of CF_3Cl/Ar discharge sheath capacitance C_s (pF) vs. power density (watts/cm²) and pressure (torr), $\gamma=0.8$.

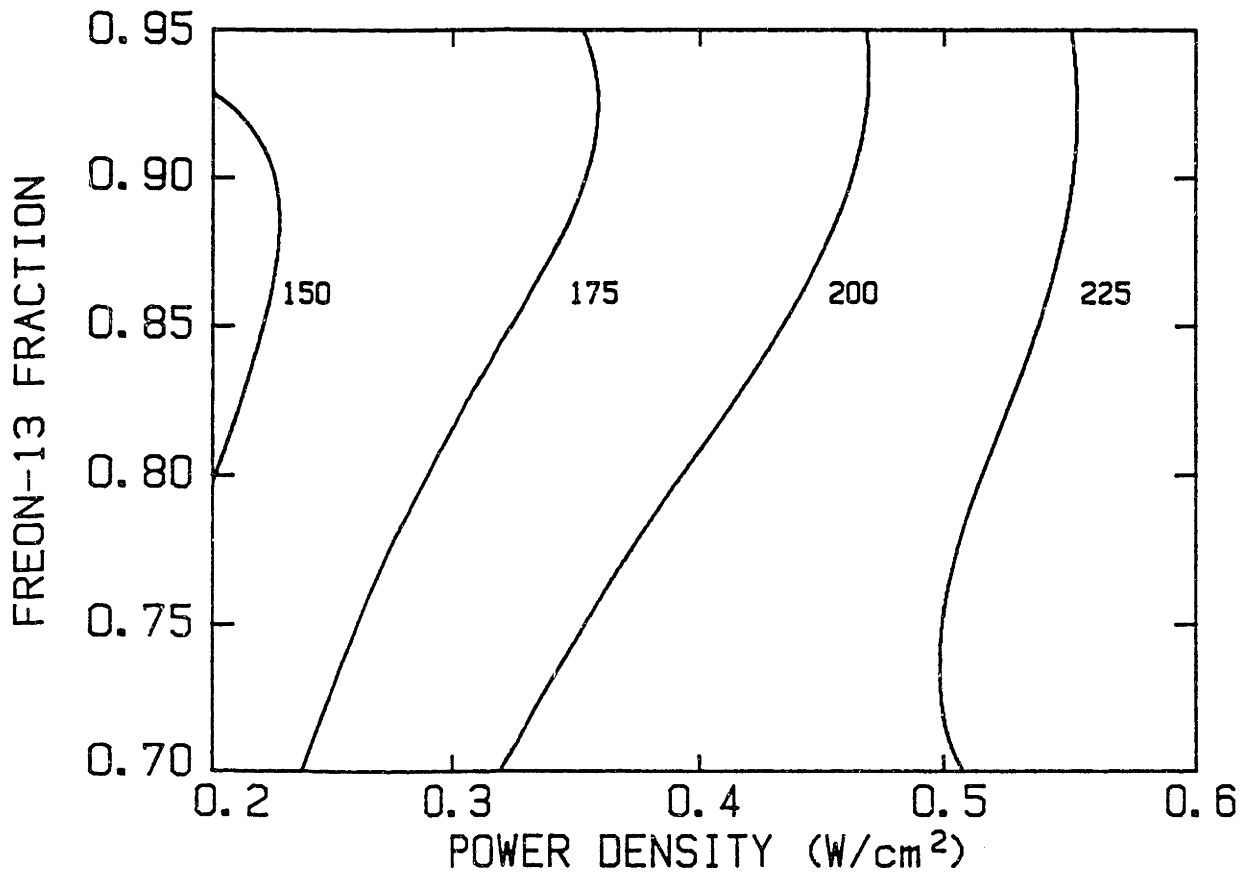


Figure 3-10c: Contour plot of $\text{CF}_3\text{Cl}/\text{Ar}$ discharge sheath capacitance C_s (pF) vs. power density (watts/cm²) and pressure (torr), $\gamma=0.9$.

CF₃Br plasmas exhibit similar dependence of C_s on power input, but the maximum with pressure is not observed. The sheath capacitance in CF₃Br covers a wide range, from 25 to 300 pF. A contour plot (with \dot{W} and P) of the CF₃Br results is shown as Fig. 3-11.

3.4.3 Electron Concentrations

Electron density contours (in CF₃Cl) for $\gamma=0.8$ and $\gamma=0.9$ are shown in Figs. 3-12a and 3-12b, respectively. Fig. 3-12c depicts the effects of γ and \dot{W} on the electron density. The adjusted R² value of the fit was 0.87, less than for other responses but still adequate for representation of the electron density behavior with power, pressure, and composition. Electron density increases approximately linearly with power input, suggesting that mean electron energy remains relatively constant with power. This observation is made because the product of electron density and energy should scale with power input if electron processes are primarily responsible for power dissipation in the plasma. Langmuir probe experiments confirm the weak dependence of mean electron energy on process conditions (see Table 3-7).

There is a maximum in electron density with pressure at about 0.5 torr. One possible explanation for this behavior is the competition between attachment and mobility/diffusion processes as the dominant electron loss mechanism in the discharge. At higher pressures formation of negative ions via electron attachment is likely to be important, while electron loss by collision with the electrodes and by radial diffusion out of the plasma may be more important at lower

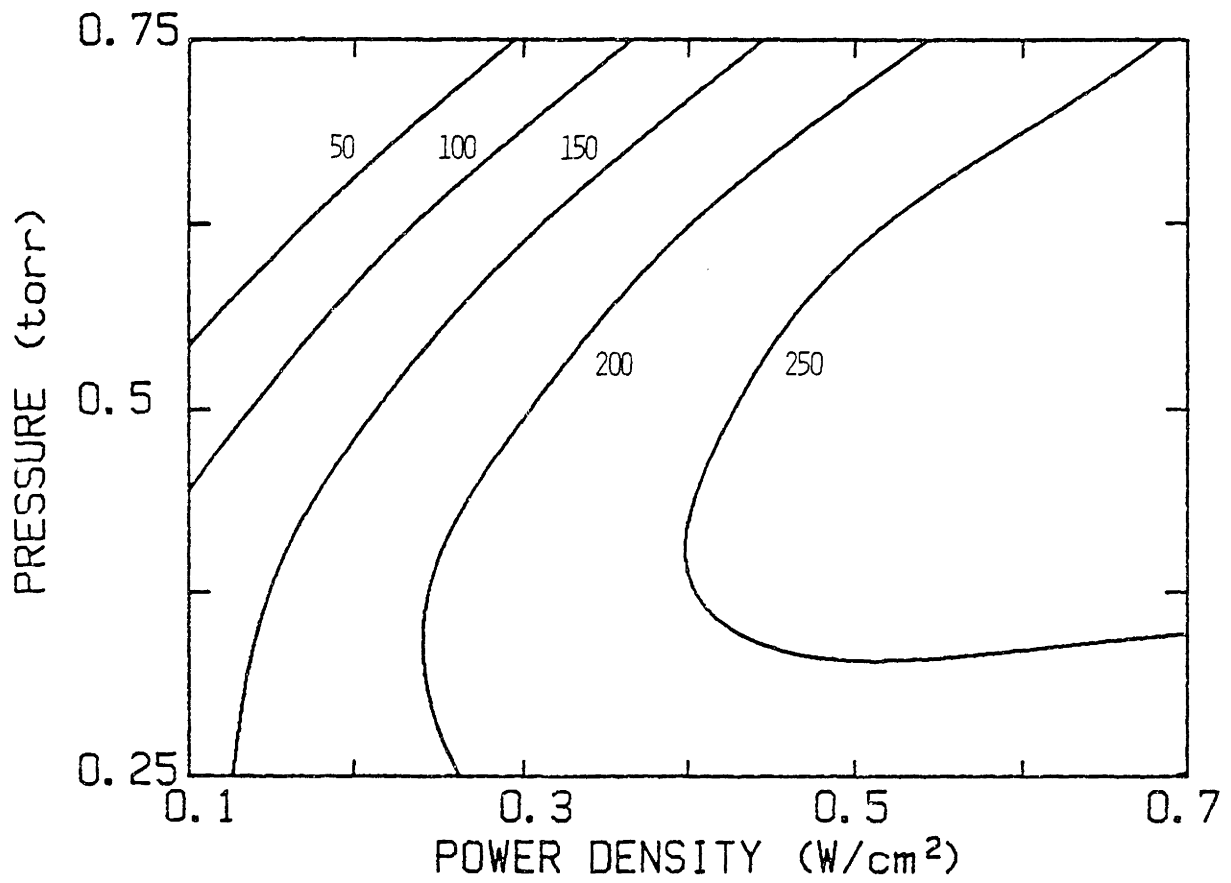


Figure 3-11: Contour plot of sheath capacitance C_s in CF_3Br discharges (pF) vs. power density (watts/ cm^2) and pressure (torr).

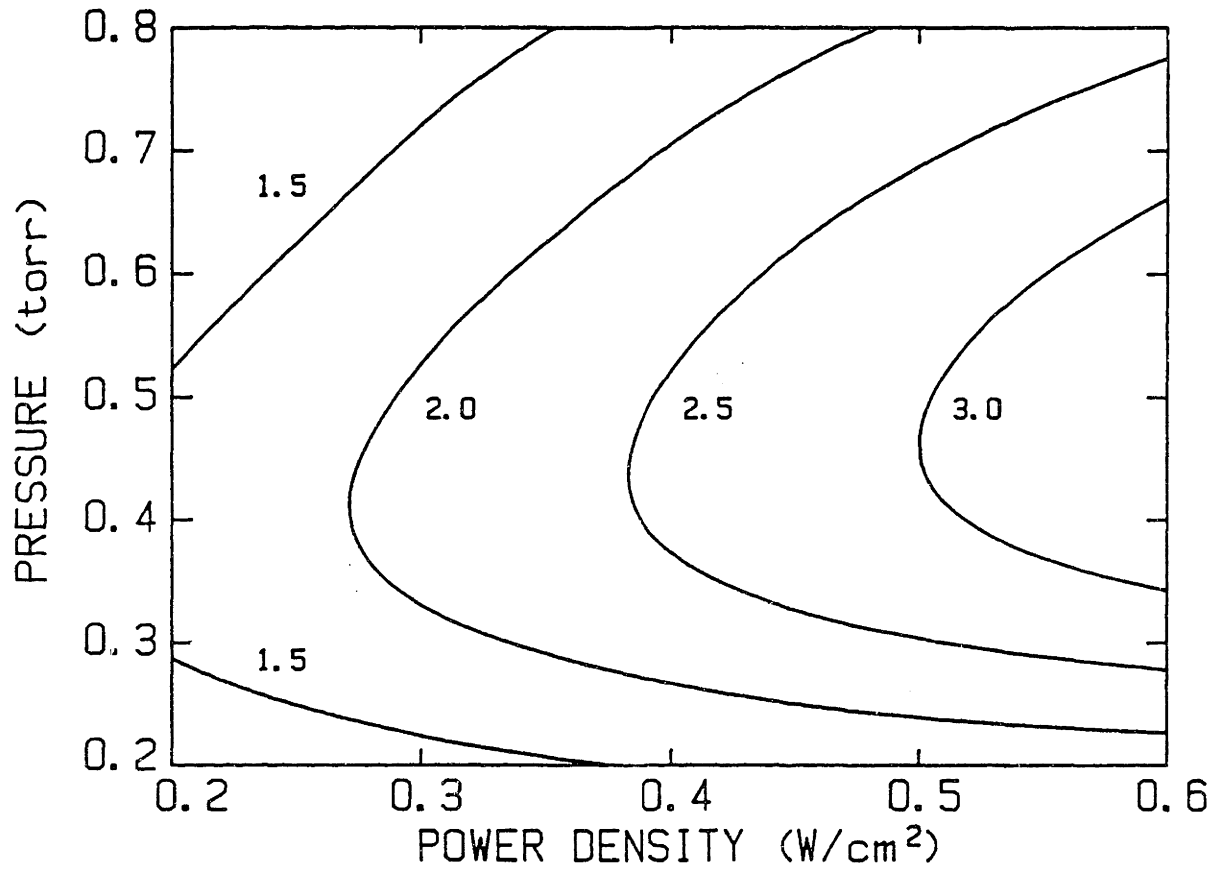


Figure 3-12a: Contour plot of impedance model predictions of electron concentration $[e^-] \times 10^{-9} \text{ cm}^{-3}$ in $\text{CF}_3\text{Cl}/\text{Ar}$ discharges, vs. power density (watts/cm²) and pressure (torr), $\gamma=0.9$.

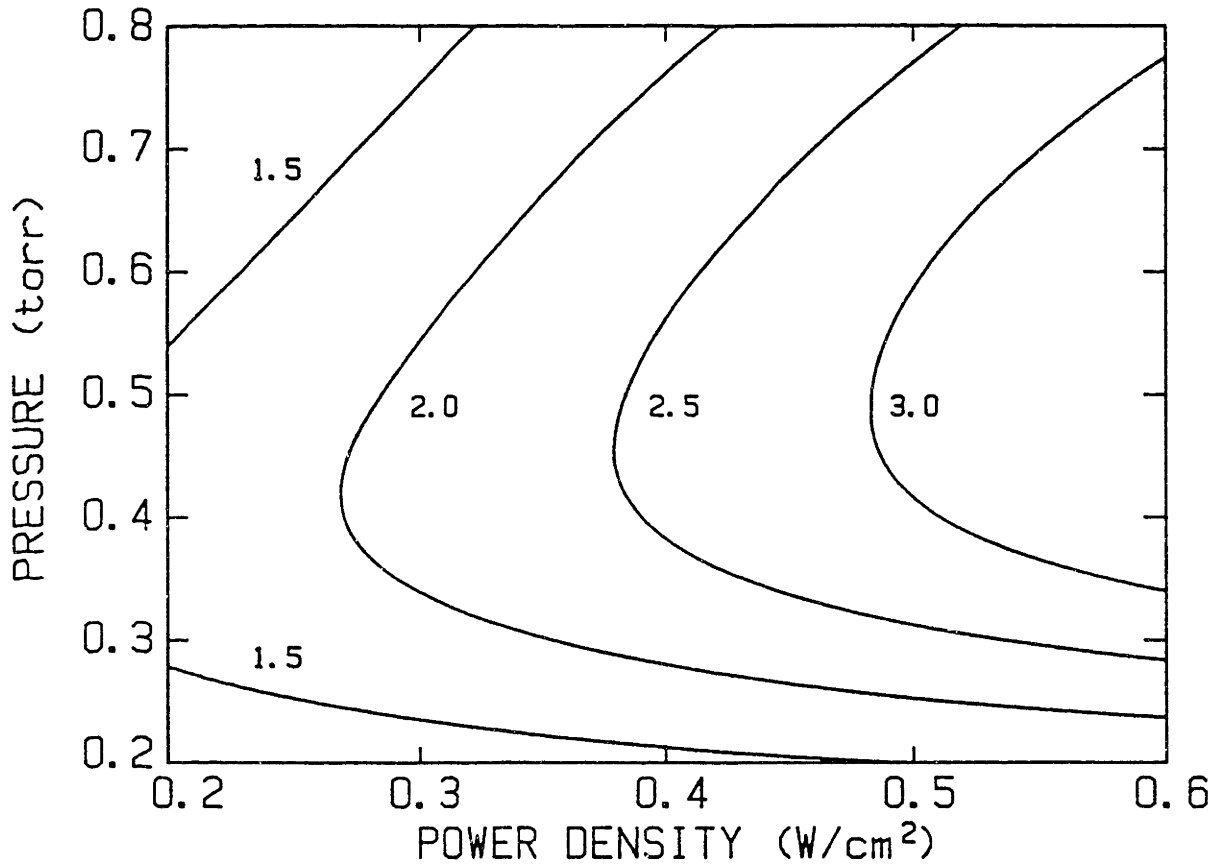


Figure 3-12b: Contour plot of impedance model predictions of electron concentration $[e^-] \times 10^{-9} \text{ cm}^{-3}$ in $\text{CF}_3\text{Cl}/\text{Ar}$ discharges, vs. power density (watts/cm²) and pressure (torr), $\gamma=0.8$.

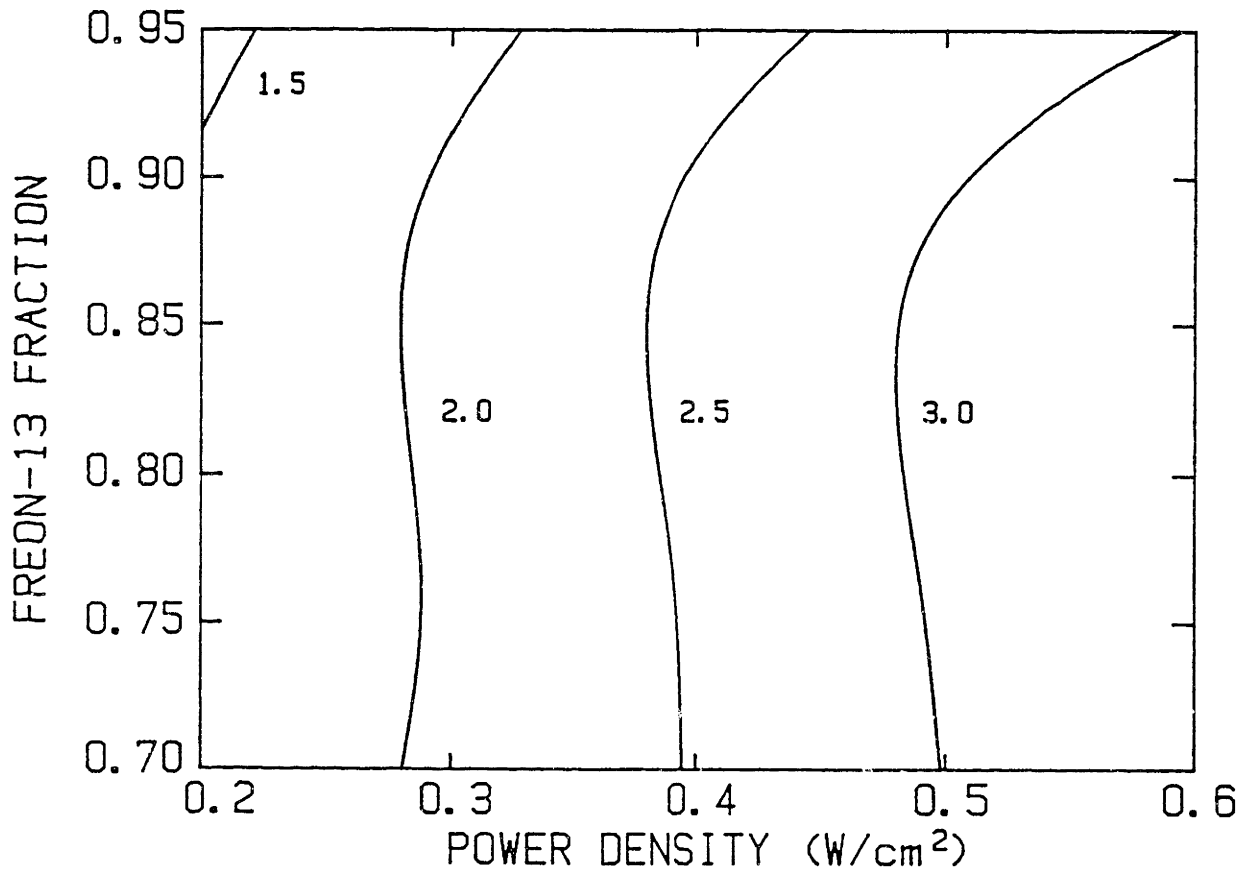


Figure 3-12c: Contour plot of impedance model predictions of electron concentration $[e^-] \times 10^{-9} \text{ cm}^{-3}$ in $\text{CF}_3\text{Cl}/\text{Ar}$ discharges, vs. power density (watts/cm²) and composition, $P=0.5$ torr.

pressures. Electron density increases slightly with decreasing γ , presumably because most of the low-energy inelastic processes available to CF_3Cl cannot occur in argon. Consequently, less energy (per electron) is dissipated by electron-argon processes than by electron- CF_3Cl processes. To maintain constant power input to the plasma the electron density must then increase with argon dilution.

Calculated electron densities are 10^9 to 10^{10} cm^{-3} , in good agreement with recent Langmuir probe results (Surendra, 1985; Surendra et al., 1986) as discussed later in this subsection. Based on the probe results and on simple ion density calculations, the values of $[e^-]$ presented here may be somewhat low. Because the density is calculated assuming that all resistive losses occur in the bulk plasma, resistive losses in the sheaths also cause a low prediction of electron density; this effect will be most pronounced at the higher pressures where high ion fluxes are observed. Addition of resistive sheaths to the model (subsection 3.3.2) brings the electron density predictions slightly closer to the expected values.

Direct comparison of the impedance model predictions of electron density with Langmuir probe experimental results is not straightforward. The probe results are only valid for pressures at which the assumption of collisionless ion transport across the probe sheath is valid, i.e., below about 0.3 torr in CF_3Cl (Laframboise, 1966; Schultz and Brown, 1955; Cherrington, 1982). However, for electrode assemblies A and B the impedance model is not completely valid at pressures below 0.2-0.25 torr due to loss of plasma containment. Consequently, there is a limited range of conditions over which comparisons between theory and experiment can be made. In

addition, the probe is used to measure positive ion concentrations rather than electron concentrations. If the concentration of negative ions is significant the electron density would be appreciably lower than the positive ion density. Since CF_3Cl is not a very electronegative gas, electron attachment cross sections for CF_3Cl are quite small (Illenberger et al., 1979) - therefore, negative ion concentrations should be low in CF_3Cl . Attachment cross sections are on the order of 10^{-16} cm^2 for CF_2Cl_2 (Pejcev et al., 1979), a much more electronegative gas.

Probe experimental data (Surendra et al., 1986) and impedance model predictions for CF_3Cl plasmas are shown in Table 3-7; electron densities vary from 3×10^9 to 10^{10} cm^{-3} , while electron energies are relatively constant at about 4 eV. The Langmuir probe electron density and electron energy results are very reproducible; variations in repeat runs were about 5%. Note that electron density increases sublinearly with both power input and gas pressure (up to 0.3 torr). At the few plasma conditions where both the probe measurements and the impedance model predictions are expected to be reliable, the agreement is very good; the model predictions are within 10-20% of the measured values.

A contour of electron density in CF_3Br plasmas is shown as Fig. 3-13. Electron density increases with power and decreases with pressure. Combining equations (3.2.2-1), (3.3.1-1), and (3.3.1-9) we note that $[e^-]$ is a very simple function of power density \dot{W} and P . Upon regression of the resulting expression,

Table 3-7
Langmuir Probe Measurements in CF₃Cl Plasmas (Surendra et al., 1986),
and Comparison with Impedance Model Estimates.

PRESSURE (torr)	POWER METER READING (Watts)	[e ⁻] FROM MEASUREMENT (cm ⁻³)	[e ⁻] FROM IMPEDANCE (cm ⁻³)	ELECTRON ENERGY (eV)
0.1	25	3.7x10 ⁹	NV	3.9
	50	5.0x10 ⁹	NV	3.5
	75	6.3x10 ⁹	NV	3.6
	100	7.9x10 ⁹	NV	3.7
0.15	25	4.8x10 ⁹	NV	3.8
	50	6.0x10 ⁹	NV	3.7
	75	7.2x10 ⁹	NV	3.9
	100	8.0x10 ⁹	NV	3.5
0.2	25	6.0x10 ⁹	NV	3.9
	50	7.5x10 ⁹	NV	3.9
	75	8.4x10 ⁹	NV	3.8
0.25	12	3.8x10 ⁹	4.9x10 ⁹	4.2
	25	6.7x10 ⁹	6.8x10 ⁹	4.2
	50	9.0x10 ⁹	8.1x10 ⁹	4.1
	75	1.0x10 ¹⁰	NV	3.9
	100	1.1x10 ¹⁰	NV	3.9
0.3	12	3.8x10 ⁹	4.8x10 ⁹	4.1
	25	6.3x10 ⁹	6.6x10 ⁹	4.0

NV = impedance model not valid.

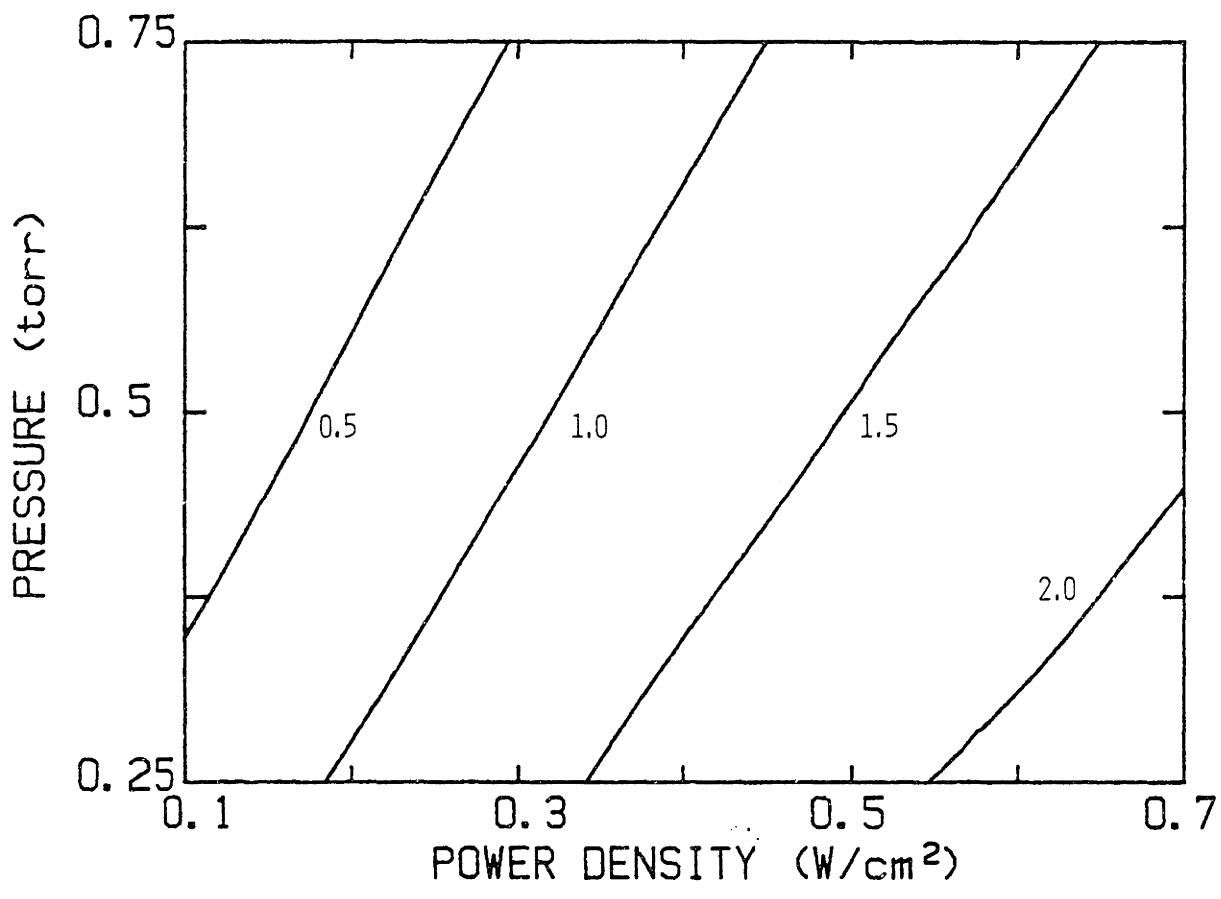


Figure 3-13: Contour plot of impedance model prediction of electron concentration $[e^-] \times 10^{-9} \text{ cm}^{-3}$ in CF_3Br discharges, vs. power density (watts/cm²) and pressure (torr).

$$[e^-] = k (d/qA\mu_e) \dot{W}/P^n, \quad (3.4.3-1)$$

with $k=2.07 \pm 0.11$ and $n=0.50 \pm 0.07$, where $[e^-]$ is in units of 10^9 cm^{-3} and all other terms are as listed in Appendix A. The predictions of eqn. (3.4.3-1) are plotted against "experiment" (i.e., the impedance model prediction) in Fig. 3-14. Again, only the high power, low pressure points are significantly in error.

3.4.4 Electric Field/Pressure Ratio

In general, the bulk plasma electric field to pressure ratio E_b/P increases with power input and decreases with pressure. Argon dilution has a relatively minor effect; E_b/P decreases slightly as argon is added to the discharge. In CF_3Cl plasmas E_b/P varies from 30 to 200 volts/cm-torr over the plasma conditions examined. Contours of constant E_b/P are shown in Fig. 3-15.

In CF_3Br discharges E_b/P does not vary with conditions as widely as in CF_3Cl ; a value of 100 V/cm-torr is a good estimate for most operating conditions examined in experimental design BR (see Table 3-5). Previous expressions from this section can be combined to give the general form of E_b/P 's dependence on power and pressure,

$$E_b/P = k (\sqrt{2} A/d) P^{\bar{n}}, \quad (3.4.4-1)$$

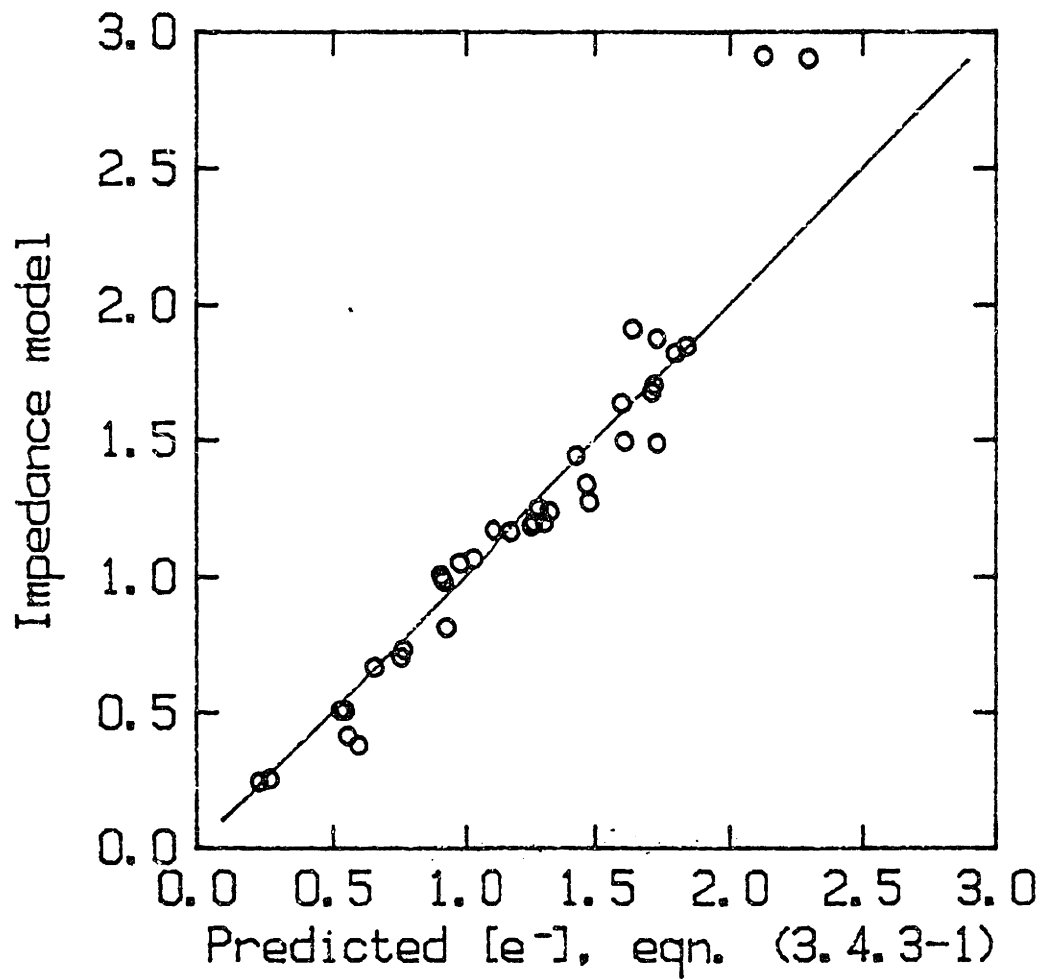


Figure 3-14: Impedance model estimate of $[e^-]$ in CF_3Br discharges vs. prediction of eqn. (3.4.3-1).

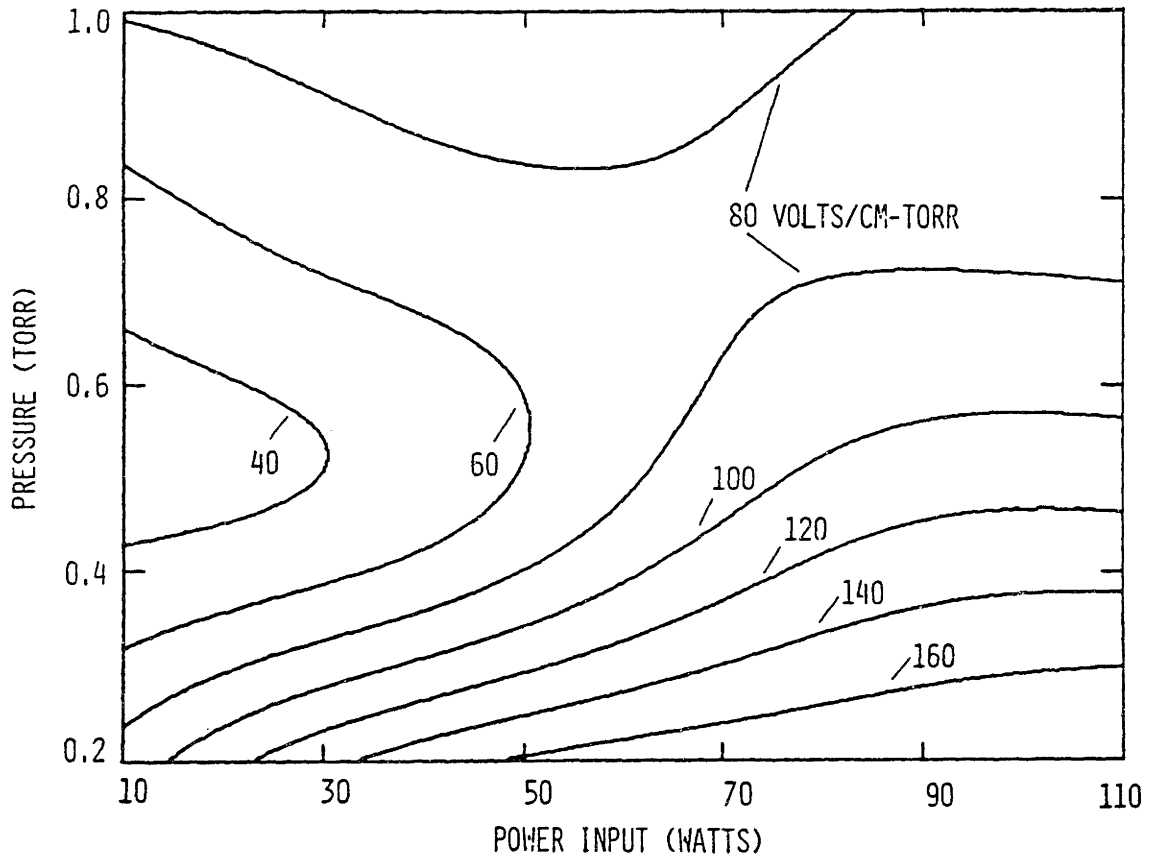


Figure 3-15: Contour plot of bulk electric field to pressure ratio E_0/P (V/cm-torr) in 85% CF_3Cl /15% Ar discharges, vs. power input (watts) and pressure (torr).

where $k = 1.02 \pm 0.02$ and $n = -0.17 \pm 0.03$ by least squares regression, and E_b/P is in units of V/cm-torr. Consequently, E_b/P is essentially constant with plasma conditions in a CF_3Br discharge. It is therefore expected that mean electron energy, which depends on E_b/P , is also insensitive to plasma conditions. A plot of predicted vs. "measured" E_b/P is given as Fig. 3-16.

3.4.5 Sheath Potential

Sheath voltage contours for CF_3Cl plasmas are shown in Figs. 3-17a through 3-17c. The adjusted R^2 of this RSM fit is 0.82. Sheath voltages of 20-100 volts are calculated for the range of conditions studied. Since sheath voltage is coupled with the sheath capacitance, the trends in V_s follow those in C_s . The sheath voltage increases with power, decreases with pressure, and slightly increases with argon dilution. Peak voltage across the discharge varies only from 100 to 250 volts, so V_s does not scale with $|V|$, as is often assumed in lower pressure discharges. The lack of correlation between $|V|$ and mean ion bombardment energy should also be pointed out, as ion energies are important in determining etching characteristics. The dependence of ion bombardment energies on process conditions will be treated in the subsequent chapter, and has also been investigated in SF_6 discharges (Thompson et al., 1986a).

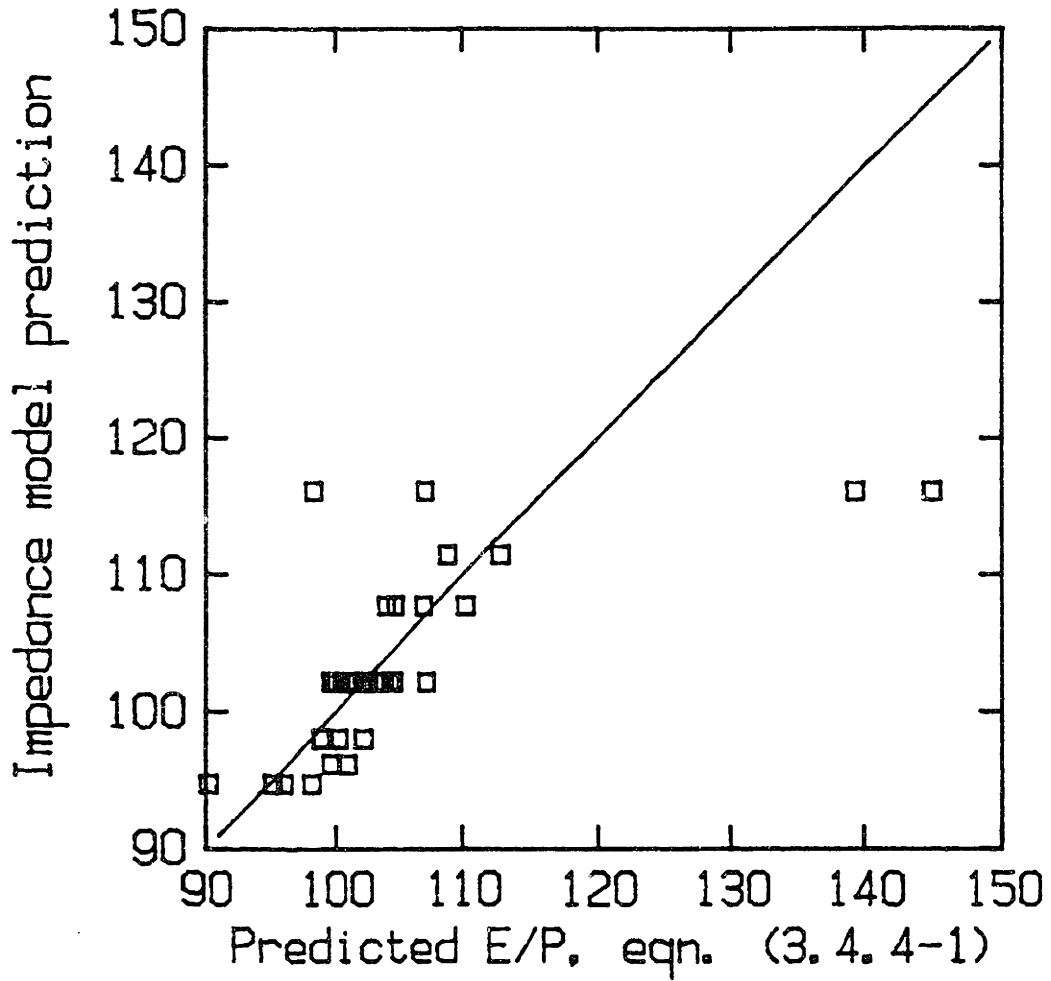


Figure 3-16: Impedance model estimate of E_0/P (V/cm-torr) vs. prediction of eqn. (3.4.4-1).

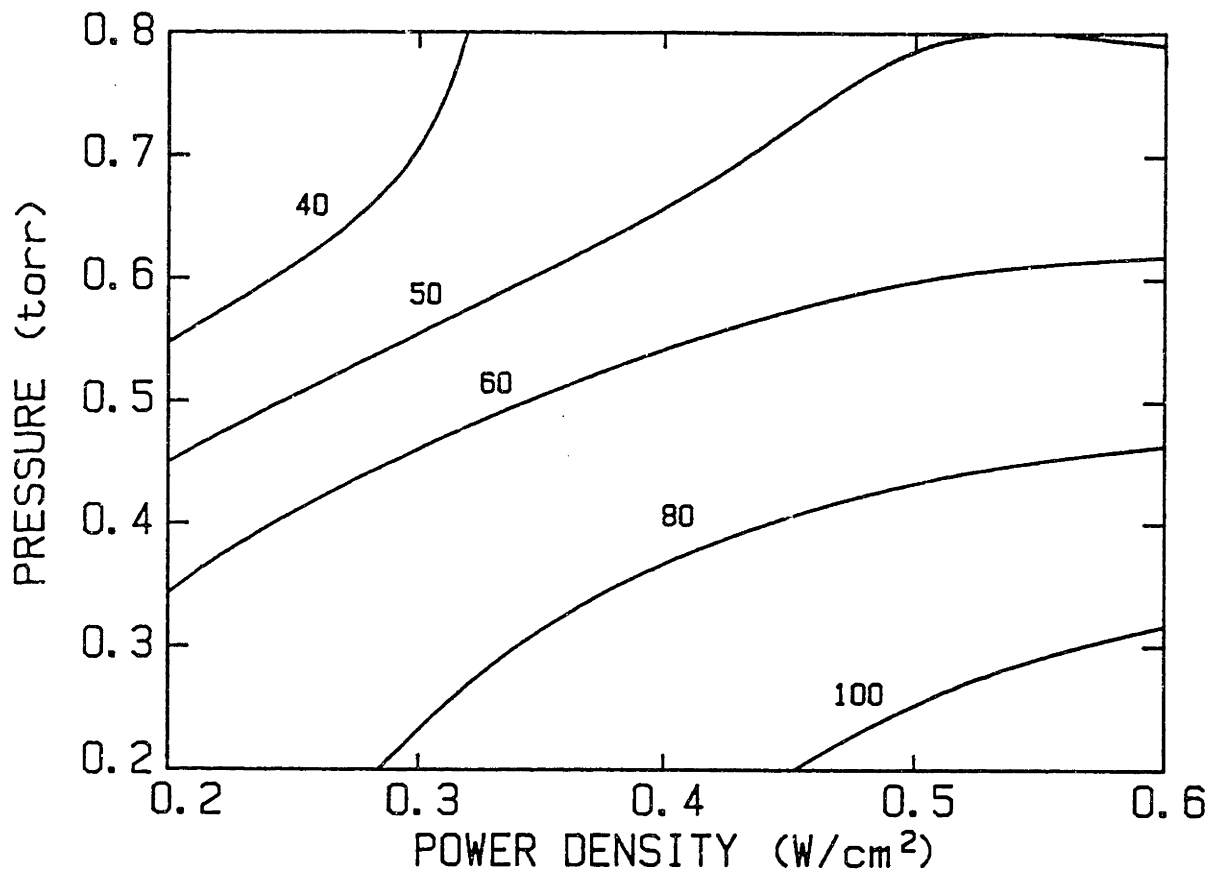


Figure 3-17a: Contour plot of impedance model estimate of sheath potential V_s (volts) in CF_3Cl/Ar discharges, vs. power density (watts/cm²) and pressure (torr), $\gamma=0.9$.

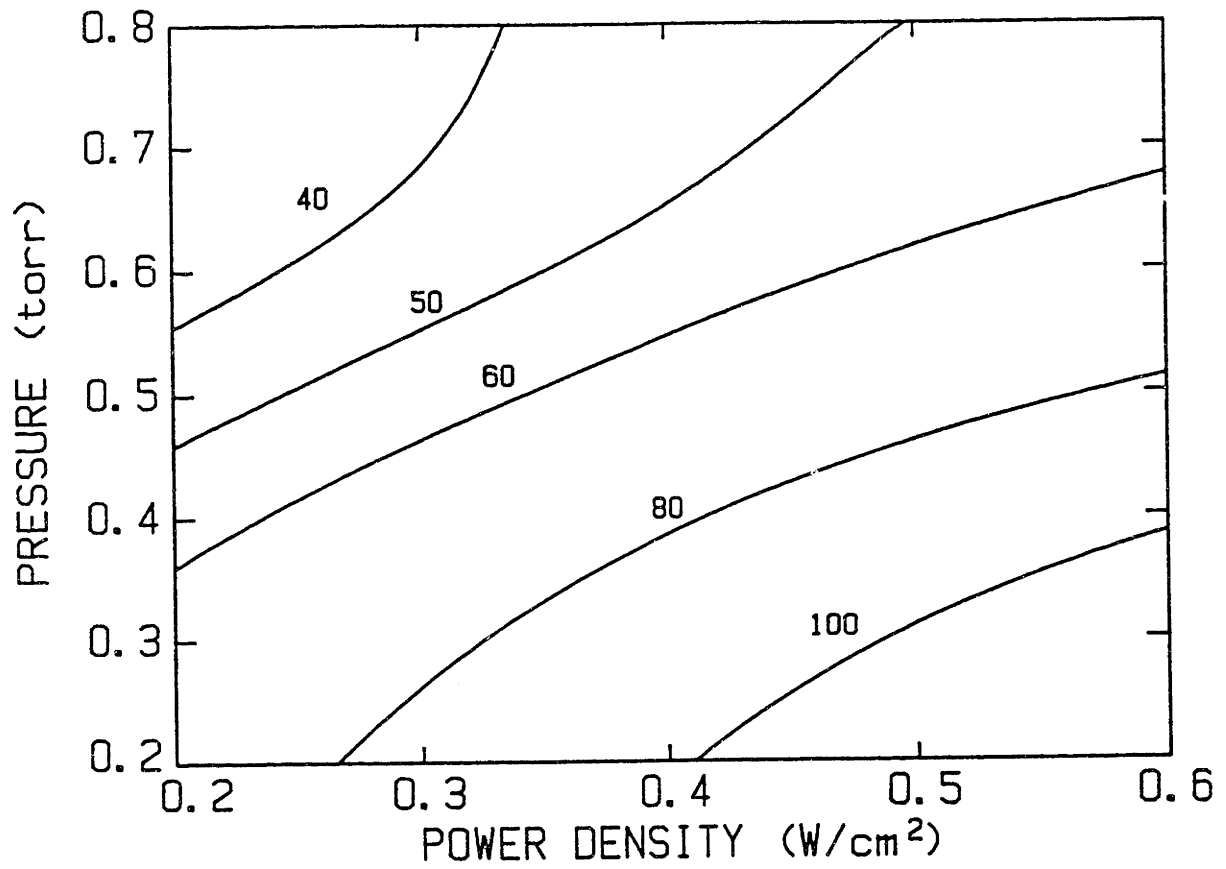


Figure 3-17b: Contour plot of impedance model estimate of sheath potential V_s (volts) in $\text{CF}_3\text{Cl}/\text{Ar}$ discharges, vs. power density (watts/cm^2) and pressure (torr), $\gamma=0.8$.

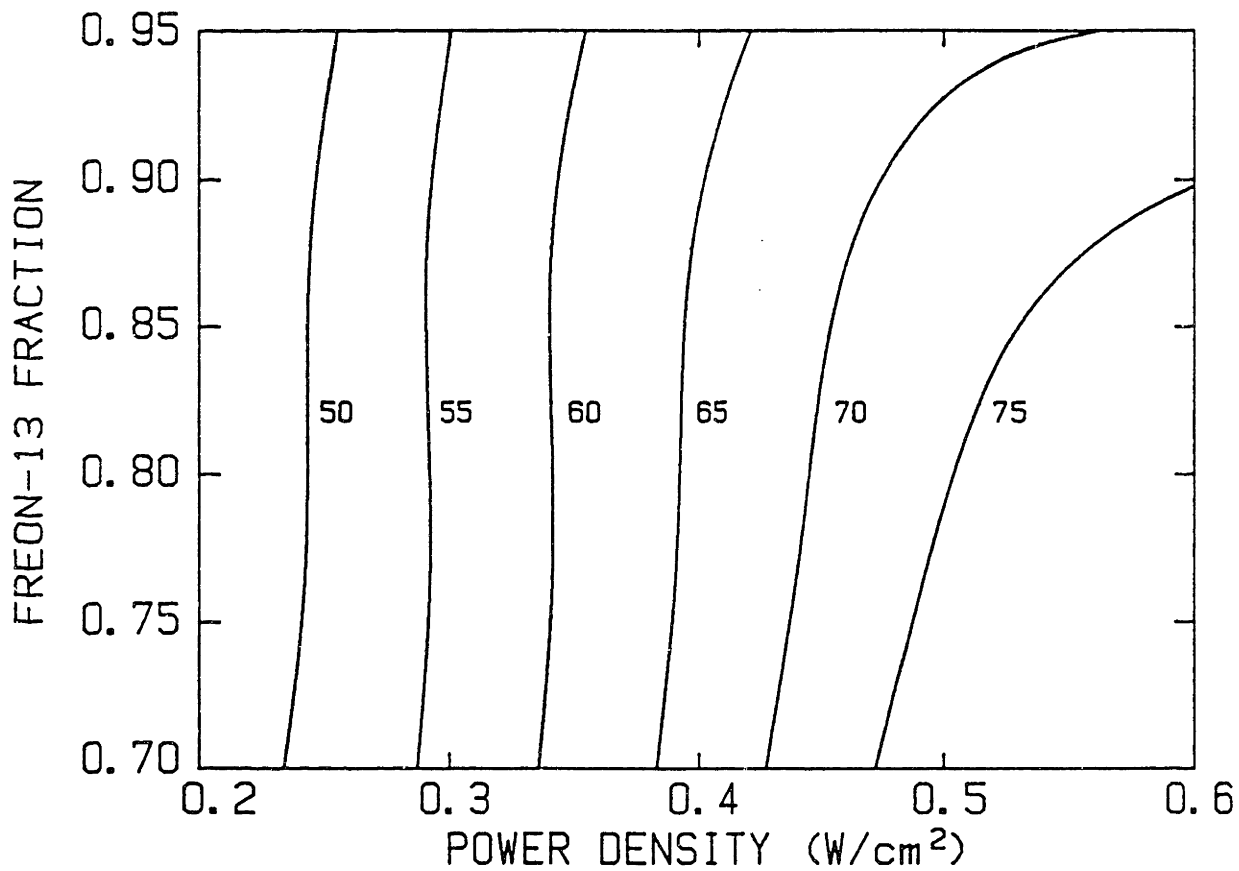


Figure 3-17c: Contour plot of impedance model estimate of sheath potential V_s (volts) in CF_3Cl/Ar discharges, vs. power density (watts/cm²) and composition, $P=0.5$ torr.

Sheath voltages in CF_3Br plasmas increase with increasing power input and decrease with increasing pressure; Fig. 3-18 is a contour plot demonstrating these trends. Since $V_s = |I|/\omega C_s$, a simple expression for V_s is unavailable. However, the sheath electric field to pressure ratio E_s/P can be written as

$$E_s/P = V_s/Pd . \quad (3.4.5-1)$$

Therefore, using eqn. (3.4.1-1),

$$E_s/P = k (\epsilon_0 A/\omega) \dot{W}/P^{1.78} , \quad (3.4.5-2)$$

where k is given as $1.06 \pm .05$ in section 3.4.1. In section 4.4 it is shown that the mean ion bombardment energy of the electrodes is proportional to E_s/P . Consequently, the mean ion bombardment energy in CF_3Br discharges can be estimated easily, given the plasma conditions (power input and pressure).

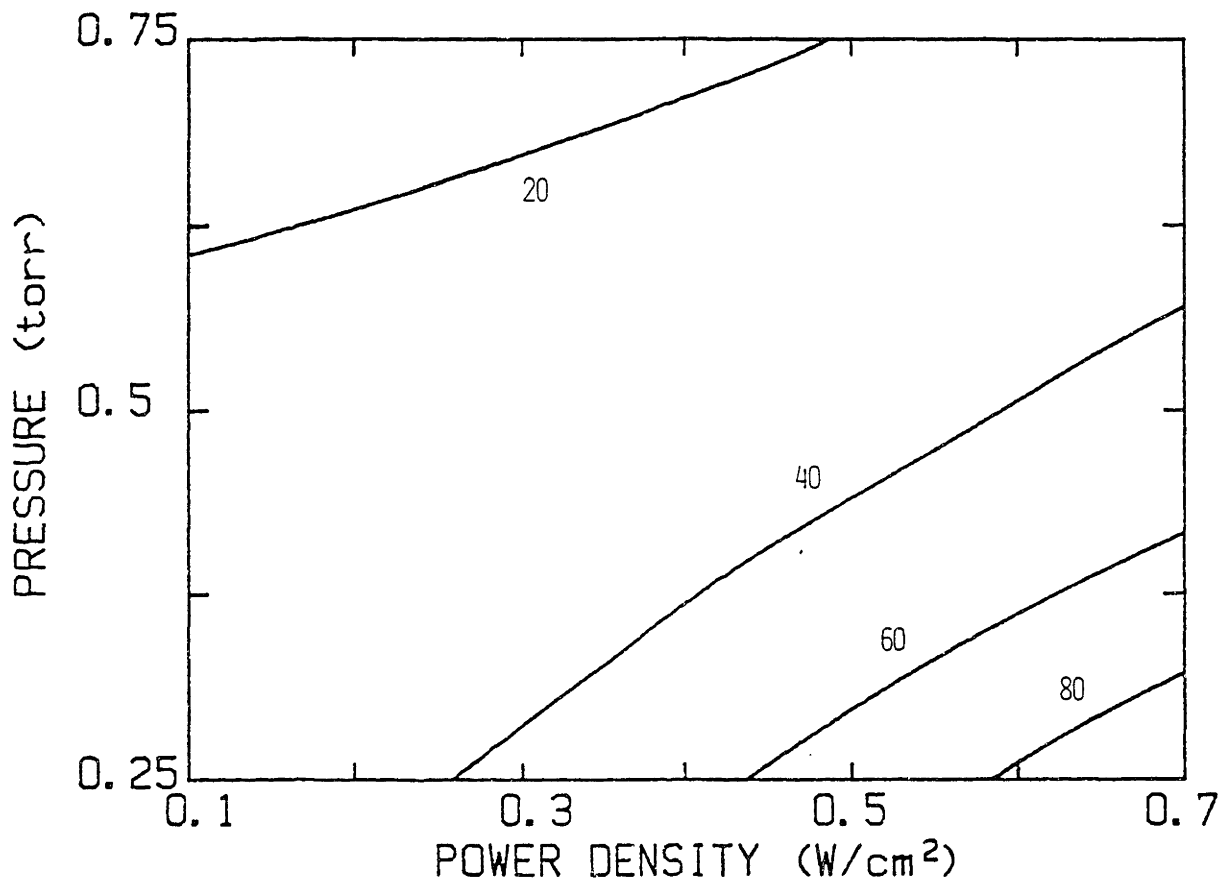


Figure 3-18: Contour plot of impedance model estimate of sheath potential V_s (volts) in CF₃Br discharges, vs. power density (watts/cm²) and pressure (torr).

3.4.6 Resistive-Sheath Model Results

The trends in estimated plasma properties predicted by the resistive-sheath model are very similar to those calculated using the capacitive-sheath analog (see Table 3-6). In the resistive sheath model, bulk resistance is about 25% lower, sheath capacitance is generally lowered, electron density increases by about 30%, and electric field to pressure ratio is not significantly changed. Calculated sheath resistances are 75-150 Ω .

CHAPTER 4 - ENERGETIC ION BOMBARDMENT OF SURFACES

4.1 INTRODUCTION

In this chapter the ion bombardment of the silicon surface during etching is examined. Experimental measurements of ion bombardment flux, energy, and chemical composition are presented. It is also shown that ion energy can be predicted using the plasma impedance results and a simple elastic collision model for ion transport through the plasma sheath. The results obtained are crucial to the formulation of kinetic models of etching rate and directionality, to be discussed in Chapter 6.

To obtain the essential characteristics of thin film plasma etching in VLSI fabrication, the effects of ion bombardment must be controlled. Ion bombardment influences directionality, selectivity over increasingly thin gate oxides, uniformity across the wafer (or set of wafers), surface damage, etc. Each of these etching characteristics is dependent on both the total ion flux and the ion energy distribution, as well as the neutral chemistry. Etching directionality results from ion-assisted etching or the sputtering of etch-inhibiting species from the film surface. However, selectivity generally decreases with increased ion bombardment flux and energy. In the limit of high ion energies, selectivity becomes unacceptably low as physical sputtering becomes dominant. For ion-driven processes

the importance of chemical reactant transport and depletion are reduced, and uniformities may therefore be improved. However, energetic ion bombardment can induce crystallographic defects and other damage in a thin layer at the device surface, which can result in interface traps and reduced carrier lifetimes (Ephrath and DiMaria, 1981; Harper et al., 1982; Pang, 1984; Wei, 1985).

In a rf discharge, positive ions are accelerated toward the electrodes by plasma sheaths formed at both electrodes. The sheaths are caused by the initially larger electron flux (to the electrodes) relative to the ion flux, which induces the depletion of electrons from the bulk plasma. This electron loss creates an electric field in the sheath, which retards the time-averaged electron flux until it equals the positive ion flux. Ions formed in the bulk plasma by electron-impact processes drift to the sheath region by diffusion, and with the aid of weak dc electric fields in the bulk. The large (~1000 V/cm) sheath field accelerates the ions toward the electrode, causing energetic ion bombardment of the surface. In the sheath, the ions lose energy and directionality by elastic and inelastic collisions with neutral gas particles. The balance between the sheath potential drop and the energy lost by collisions in the sheath determines the energy of the ions striking the surface.

4.2 CF₃Cl ION FLUX PARAMETRIC DEPENDENCE - EXPERIMENTAL MEASUREMENTS

4.2.1 Introduction

Few previous studies (if any) have provided measurements of the total positive ion flux to a surface immersed in a plasma at conditions important to plasma etching processes. For a CF₃Cl plasma, the dependence of total positive ion flux on process parameters such as power, pressure, inert gas dilution, flow rate, and electrode spacing is presented in this section. The Faraday cup apparatus for measuring the ion flux incident on the surface was described in detail in section 2.6.

Several clarifications regarding ion bombardment fluxes are necessary, beyond the issues of accuracy discussed in section 2.6. First, the ion flux is dependent on the nature of the surfaces in contact with the plasma. For example, at identical process parameters (power, pressure, composition, flow rate), the ion flux observed during etching of a photoresist-masked, n⁺-type polysilicon sample (1/4 of a 4 inch wafer) is larger than that observed for blank stainless steel electrodes. However, as seen in Fig. 4-1, the ion fluxes for the two cases were simply related; the ion flux during etching is 20-25% higher than for the blank electrodes. In light of this observation, it is likely that the ion flux is also dependent on the wafer surface area.

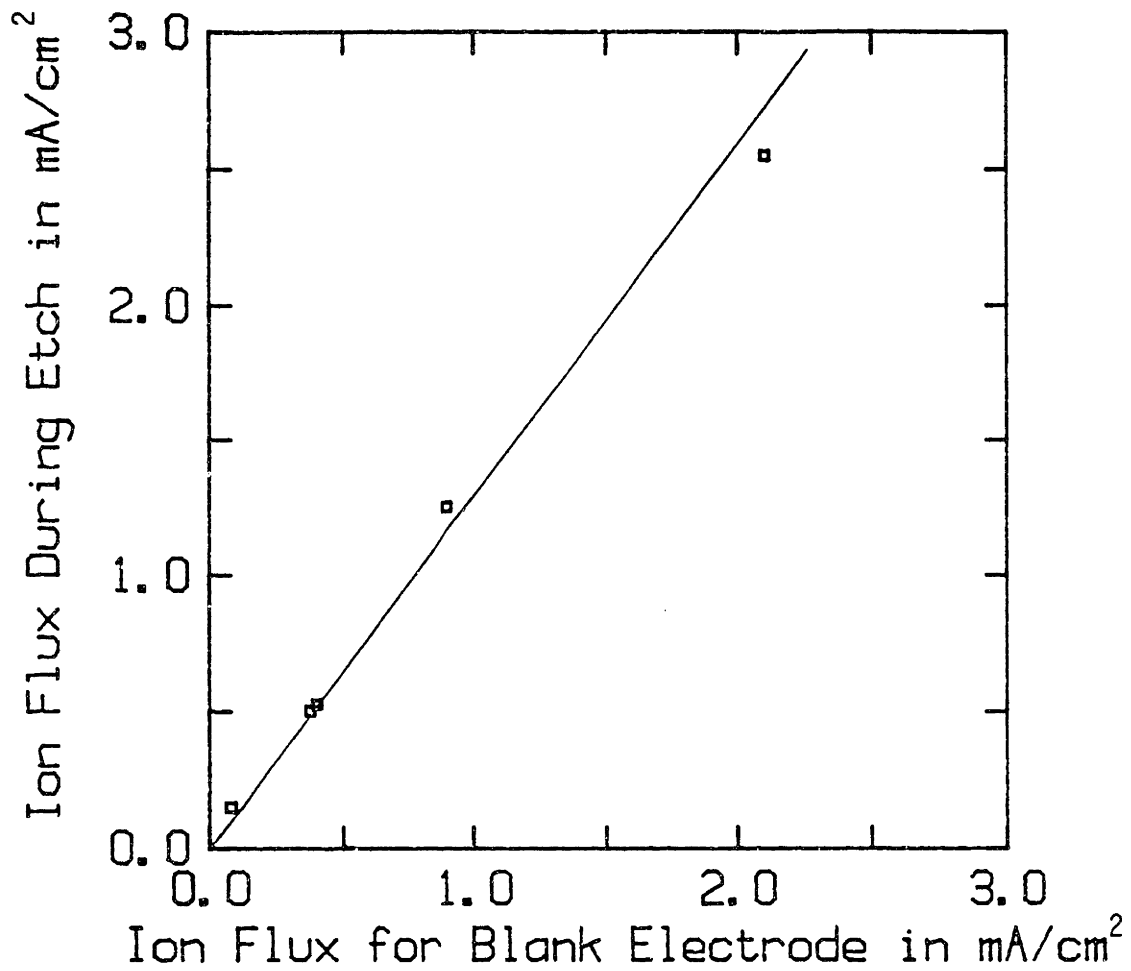


Figure 4-1: Total positive ion flux (mA/cm²) during CF₂Cl etching of doped polysilicon vs. ion flux on blank electrodes, identical plasma conditions.

4.2.2 Time Dependence

It is also noted that the ion flux is not time-invariant, irregardless of the surfaces present in the reactor. With blank electrodes, the ion flux increases slowly with time after plasma ignition. After several minutes, the ion flux stabilizes at about 10% higher than its initial value. One possible explanation for this behavior is the heating of the electrodes by the plasma until a steady-state temperature is achieved. As the electrodes heat, radical species on the surface (e.g., CF_x) may be more rapidly desorbed, and the net radical concentration of the discharge may increase. Since radicals have significantly lower ionization potentials than do stable species (Watanabe et al., 1960; Lias, 1978; Franklin et al., 1969), electron-impact ionization of the radicals species may account for a significant fraction of the ion flux at higher electrode temperatures (50-100 °C). A similar explanation is based on the buildup of a polymeric film on the electrodes via free-radical reactions. As the polymeric film becomes thicker with time, the sticking probability of radicals on the surface would become lower. Consequently, the plasma radical concentration would increase and radical ionization processes could become important. Yet another possibility is the introduction of radicals to the plasma by ion sputtering of the growing polymeric film. Since the sputtering rate would be dependent on the ion flux, this process is self-sustaining.

The temporal variation of ion flux is more significant during etching of a sample. Three distinct patterns of ion flux vs. time were observed, depending reproducibly on process conditions. The three patterns, along with typical process conditions, are shown as Fig. 4-2. In pattern (a) the flux increases slowly throughout the etch. In pattern (b) the ion flux increases rapidly to a maximum about 20% into the etch and decays to about half the peak value. Lastly, in pattern (c) the ion flux rises quickly to a maximum, decays slowly, and then drops significantly as the wafer begins to clear.

Due to these complexities ion fluxes reported here are generally for blank electrodes, unless otherwise stated. The electrode assembly used is also specified, as the geometry of the system had some effect on ion fluxes. When ion-bombardment fluxes measured during polysilicon etching are given, the cited value is time-averaged over the entire etch, including any overetch.

4.2.3 Flow Rate Dependence

Positive ion flux is dependent on flow rate. The effect of flow rate on ion flux at two process conditions is shown in Fig. 4-3. At 0.4 torr and 0.2 W/cm², ion flux decreases monotonically with flow rate over the given range. However, at 0.8 torr and 0.6 W/cm² there is a slight maximum in ion flux with flow rate at about 15 sccm.

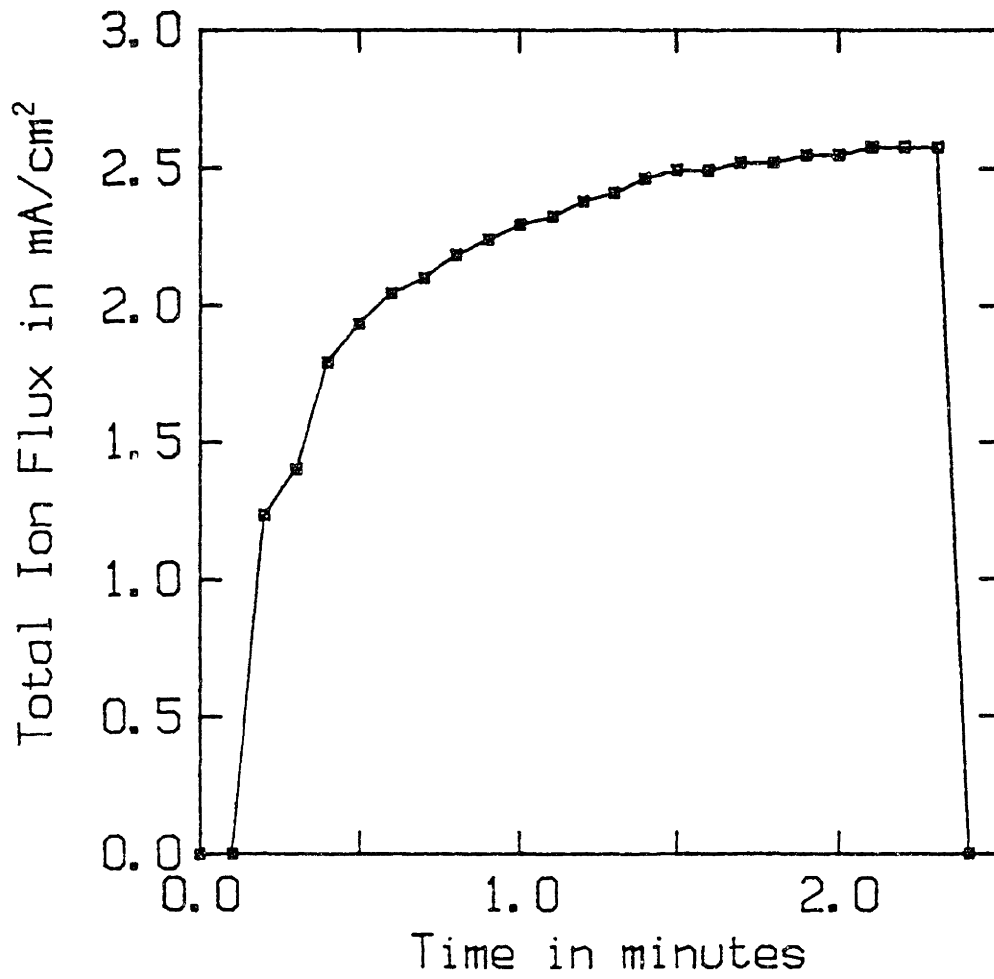


Figure 4-2a: Temporal variation of total positive ion flux (mA/cm²) during CF₃Cl etching of doped polysilicon, pattern A.

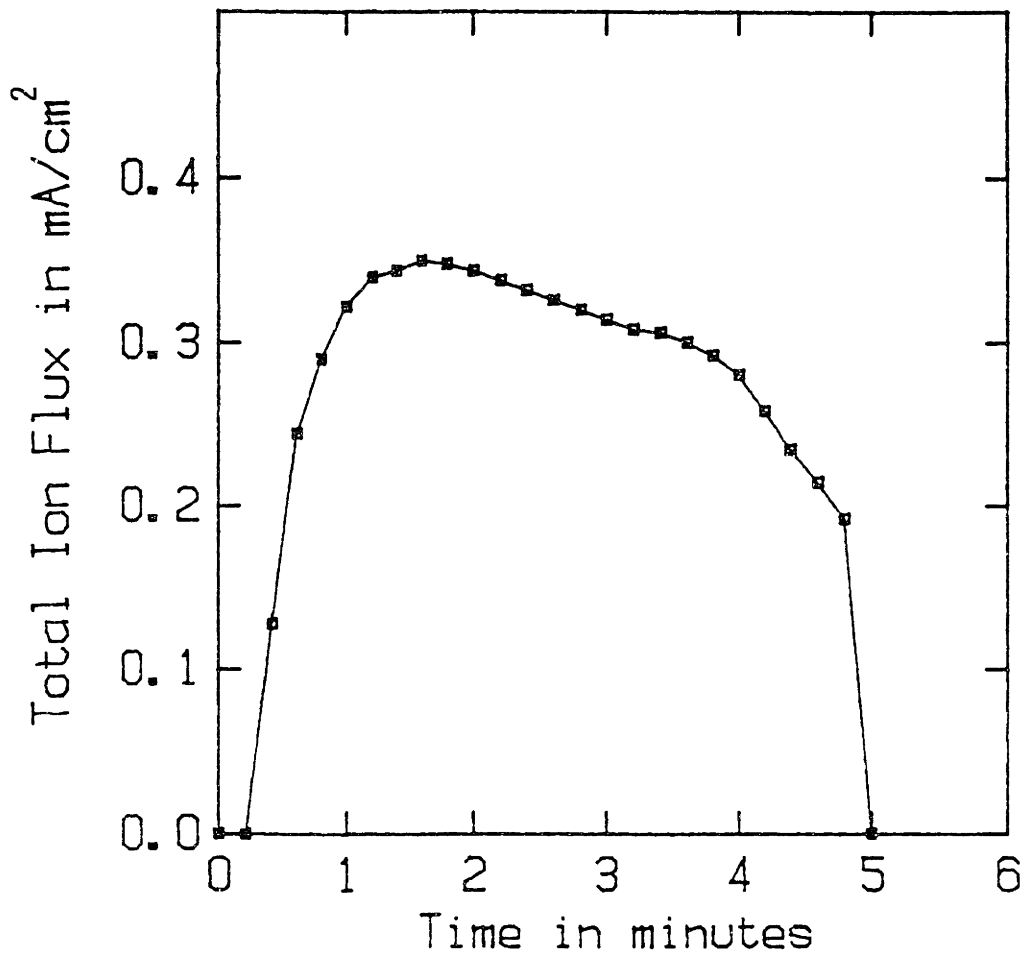


Figure 4-2b: Temporal variation of total positive ion flux (mA/cm²) during CF₂Cl etching of doped polysilicon, pattern B.

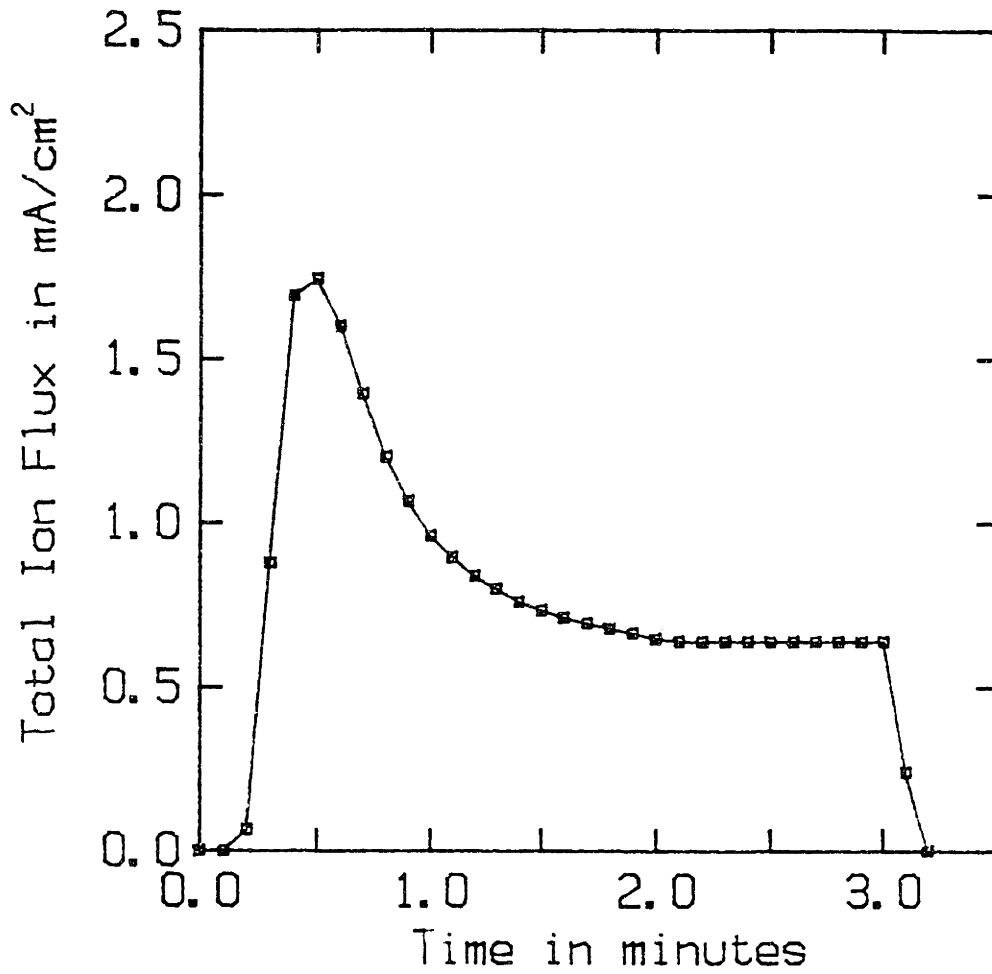


Figure 4-2c: Temporal variation of total positive ion flux (mA/cm²) during CF₃Cl etching of doped polysilicon, pattern C.

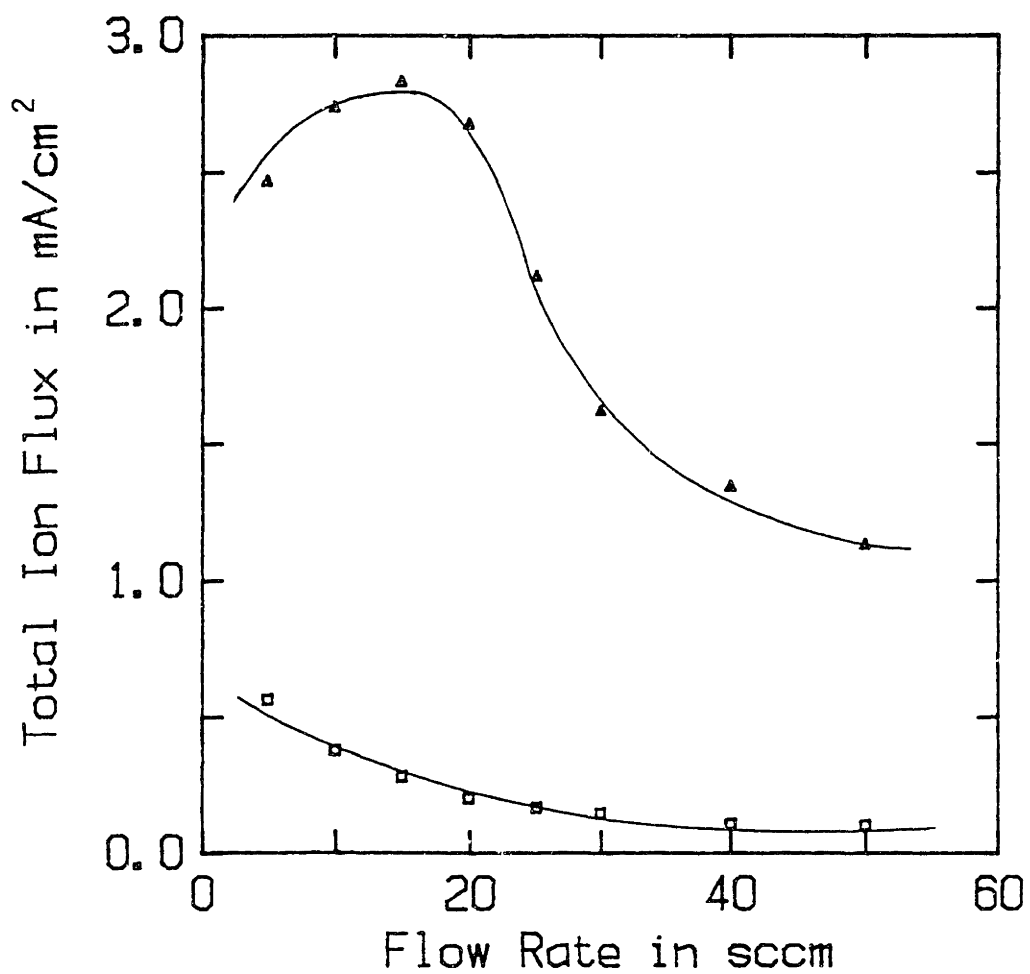


Figure 4-3: Effect of flow rate (sccm) on total positive ion flux (mA/cm²) in CF₃Cl discharges at two process conditions: □ = 0.4 torr and 0.2 watts/cm², Δ = 0.8 torr and 0.6 watts/cm².

These observations suggest that sequential reactions or gas-phase loading effects may be important in determining ion fluxes. These effects are not solely due to changes in the discharge electrical properties, which remain relatively constant with flow rate.

4.2.4 Electrode Spacing Dependence

The effect of electrode spacing is seen in Fig. 4-4. Generally, ion flux decreases with increasing electrode spacing. Note that the plasma properties vary significantly with electrode spacing due to the changing length of the current path through the discharge.

4.2.5 Power Input and Pressure Dependence

The effects of power input, pressure, and gas composition on total positive ion flux are shown in Tables 4-1 and 4-2 for a 37-run experimental design and an additional set of conditions, respectively. The results are also displayed as contour plots, see Figs. 4-5a through 4-5c. Note that the interaction between power and pressure is significant, i.e., the effect of power is more pronounced at high pressure than at low pressure. In general, ion flux increases with power input, increases with system pressure, and slightly decreases with argon dilution.

Table 4-1

Measured total positive ion fluxes in CF_3Cl discharges, for 37-run experimental design. Blank electrodes (assembly A), 50 μm pinhole diameter. $d=2$ cm, $Q=6$ sccm, $\omega=13.56$ MHz.

RUN #	POWER INPUT (Watts)	PRESSURE (torr)	CF_3Cl FRACTION	TOTAL ION FLUX (mA/cm ²)
F13A_9	36.9	0.2	0.81	0.08
F13A_2	17.1	0.8	0.89	0.29
F13A_22	83.0	0.9	0.81	2.52
F13A_10	36.0	1.0	0.81	0.73
F13A_24	64.2	0.3	0.81	0.27
F13A_37	35.0	0.6	0.81	0.89
F13A_12	89.2	0.6	0.81	1.62
F13A_15	33.2	0.4	0.81	0.38
F13A_21	11.8	0.9	0.81	0.15
F13A_1	17.2	0.4	0.89	0.18
F13A_29	36.1	0.9	0.94	0.74
F13A_36	35.3	0.6	0.82	0.92
F13A_3	59.1	0.4	0.89	0.69
F13A_30	39.1	0.9	0.68	0.92
F13A_23	11.3	0.3	0.82	0.08
F13A_18	68.7	0.6	0.81	1.48
F13A_28	12.1	0.6	0.94	0.14
F13A_11	4.4	0.6	0.82	0.03
F13A_35	34.2	0.6	0.81	0.90
F13A_20	33.7	0.6	0.73	0.67
F13A_4	64.1	0.8	0.89	2.28
F13A_26	94.8	0.6	0.93	1.86
F13A_31	30.8	0.3	0.68	0.16
F13A_7	61.3	0.4	0.73	0.50
F13A_13	33.5	0.6	0.97	0.87
F13A_34	36.8	0.6	0.82	0.90
F13A_5	16.6	0.4	0.73	0.17
F13A_27	13.2	0.6	0.68	0.14
F13A_16	32.7	0.8	0.82	0.79
F13A_6	20.4	0.8	0.73	0.38
F13A_33	33.0	0.6	0.81	0.86
F13A_25	86.9	0.6	0.68	1.47
F13A_19	33.2	0.6	0.89	0.98
F13A_17	19.9	0.6	0.82	0.32
F13A_14	34.8	0.6	0.63	0.51
F13A_8	74.9	0.8	0.72	1.75
F13A_32	35.4	0.3	0.94	0.27

Table 4-2
 Measured total positive ion flux in CF₃Cl discharges
 for additional plasma conditions, see Table 4-1 for details.

RUN #	POWER INPUT (Watts)	PRESSURE (torr)	CF ₃ Cl FRACTION	TOTAL ION FLUX (mA/cm ²)
F13A_38	34.0	0.9	0.68	0.90
F13A_39	18.7	0.6	0.89	0.27
F13A_40	68.2	0.6	0.82	1.50
F13A_41	13.6	0.6	0.82	0.15
F13A_42	19.2	0.8	0.82	0.34
F13A_43	39.3	0.9	0.82	0.86
F13A_44	2.5	1.0	0.82	0.07
F13A_45	9.9	1.0	0.82	0.16
F13A_46	95.2	0.8	0.82	2.55
F13A_47	106.1	0.9	0.82	3.05
F13A_48	65.3	1.0	0.82	1.55
F13A_49	91.5	1.0	0.82	2.82
F13A_50	51.4	0.3	0.82	0.30
F13A_51	50.0	0.4	0.82	0.53
F13A_52	70.5	0.4	0.82	0.60
F13A_53	70.2	0.8	0.82	2.21
F13A_54	47.9	0.8	0.82	1.28
F13A_55	6.8	0.8	0.82	0.10
F13A_56	9.0	0.8	0.73	0.12
F13A_57	18.9	0.8	0.73	0.34
F13A_58	65.3	0.8	0.73	1.80
F13A_59	16.4	0.9	0.73	0.32
F13A_60	14.0	0.2	0.73	0.07
F13A_61	55.8	0.2	0.73	0.12
F13A_62	13.8	0.2	0.89	0.07
F13A_63	61.5	0.2	0.89	0.11
F13A_64	35.3	0.6	0.89	0.98
F13A_65	10.4	0.8	0.89	0.12
F13A_66	17.4	0.8	0.89	0.30
F13A_67	68.8	0.8	0.89	2.31
F13A_68	16.7	0.9	0.89	0.28
F13A_69	37.6	0.9	0.93	0.86
F13A_70	34.5	0.6	0.97	1.00

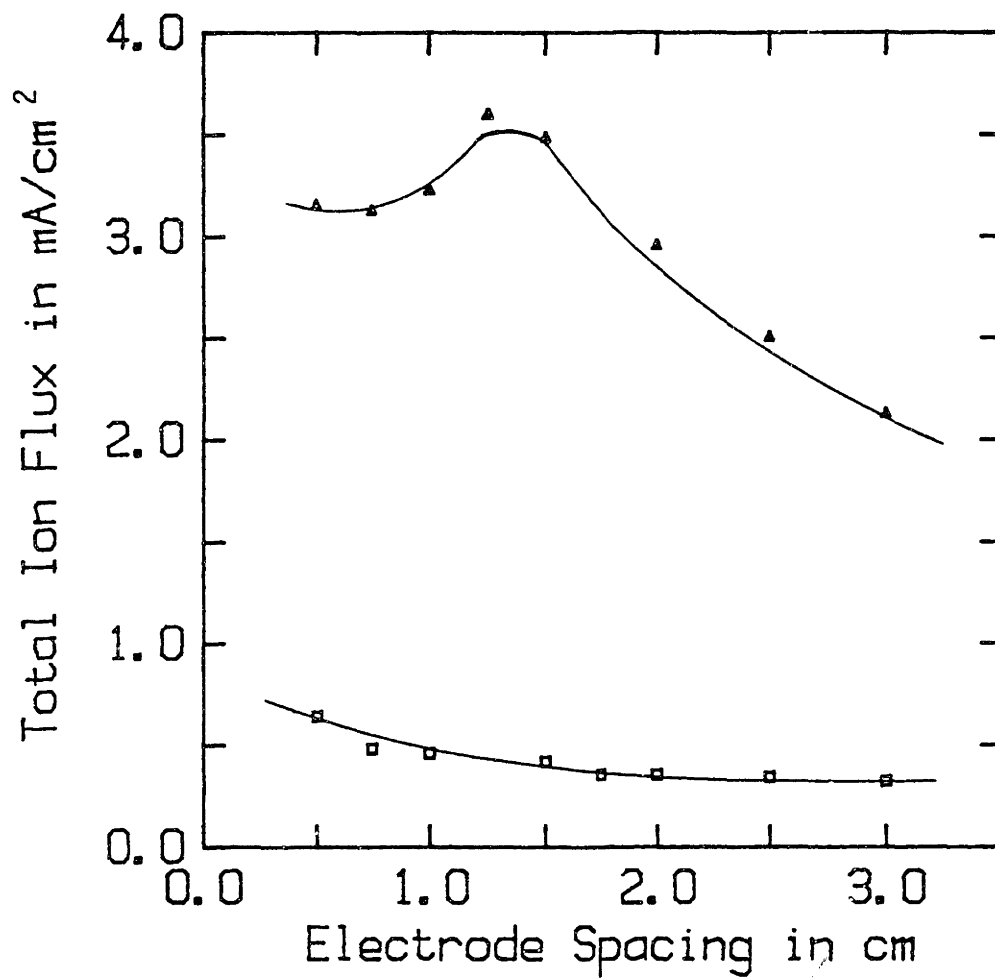


Figure 4-4: Effect of electrode spacing (cm) on total positive ion flux (mA/cm²) in CF₃Cl discharges at two process conditions: □ = 0.4 torr and 0.2 watts/cm², Δ = 0.8 torr and 0.6 watts/cm².

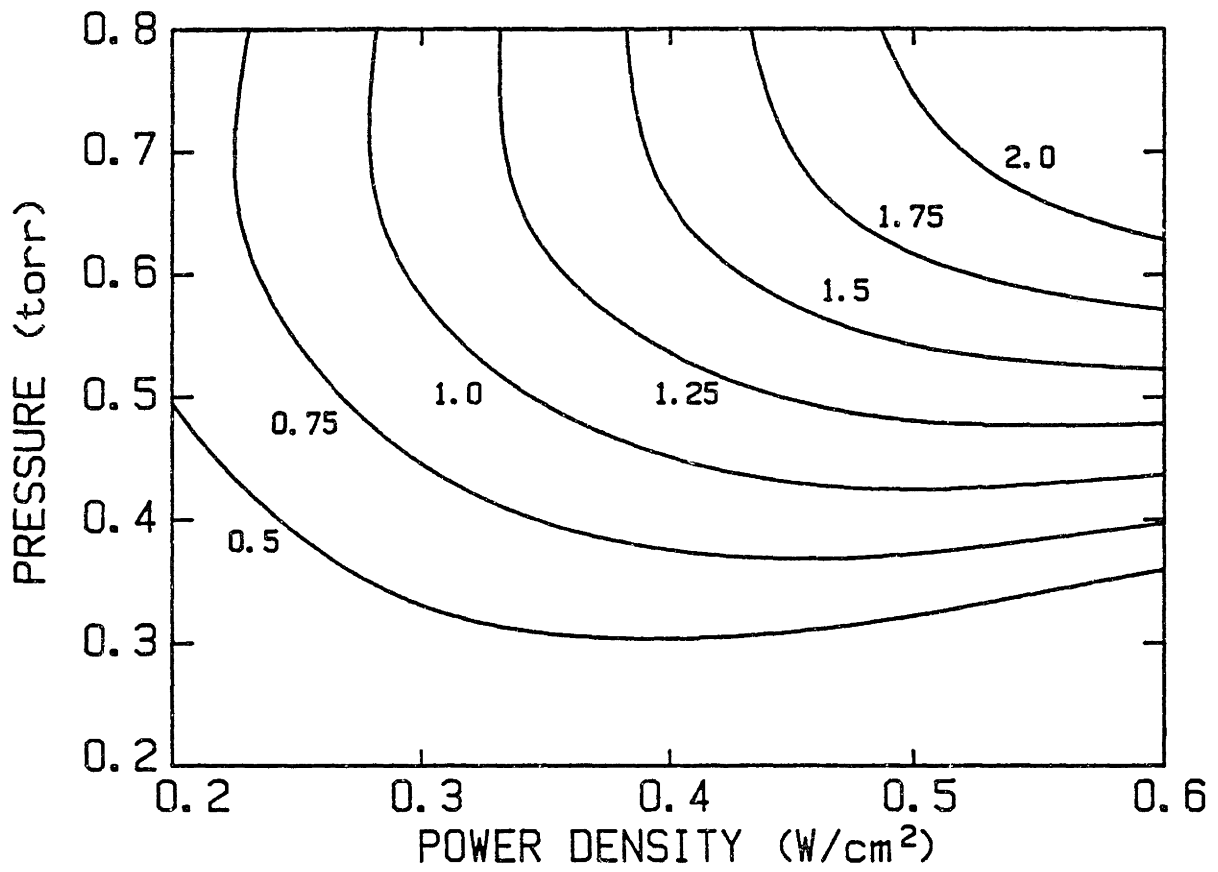


Figure 4-5a: Contour plot of total positive ion flux (mA/cm^2) in $\text{CF}_3\text{Cl}/\text{Ar}$ discharges, vs. power density (watts/cm^2) and pressure (torr), $\gamma=0.9$.

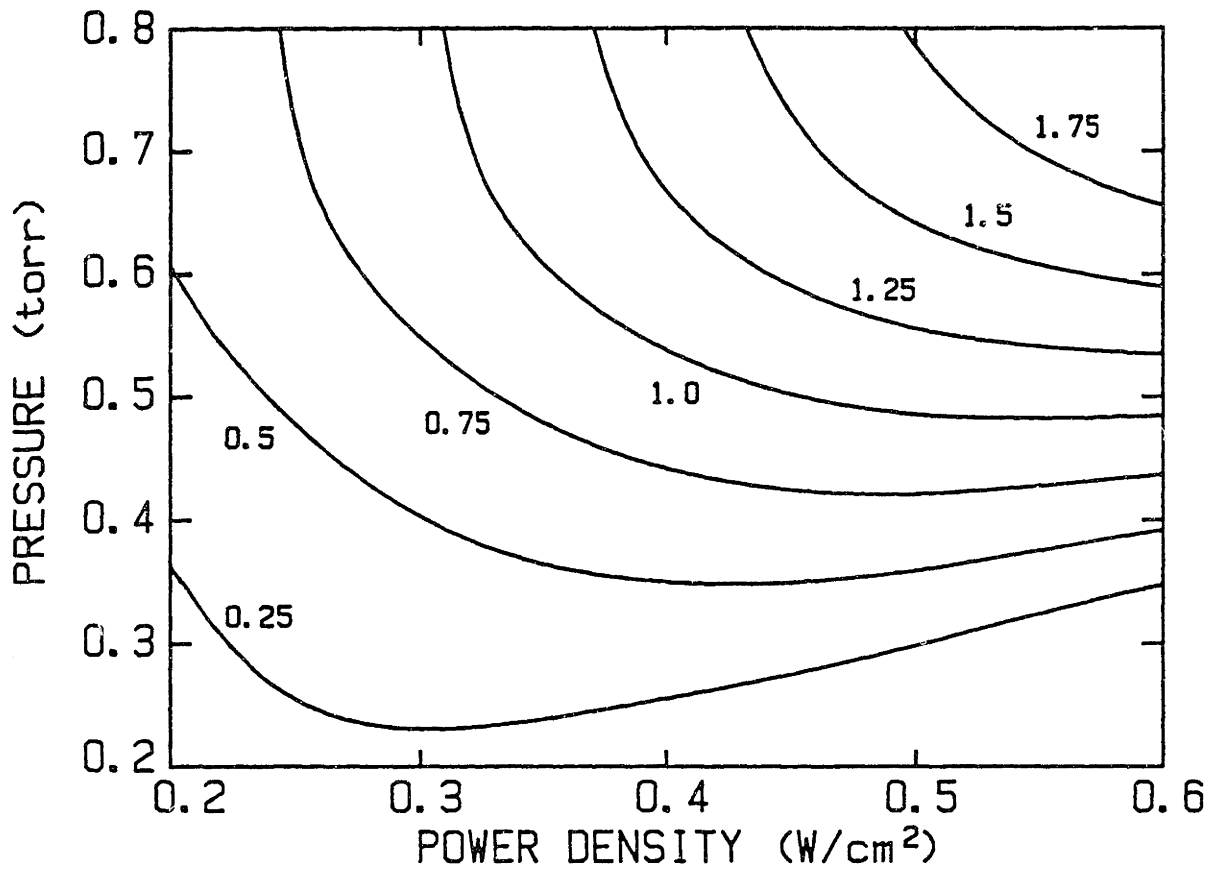


Figure 4-5b: Contour plot of total positive ion flux (mA/cm^2) in $\text{CF}_2\text{Cl/Ar}$ discharges, vs. power density (watts/cm^2) and pressure (torr), $\gamma=0.8$.

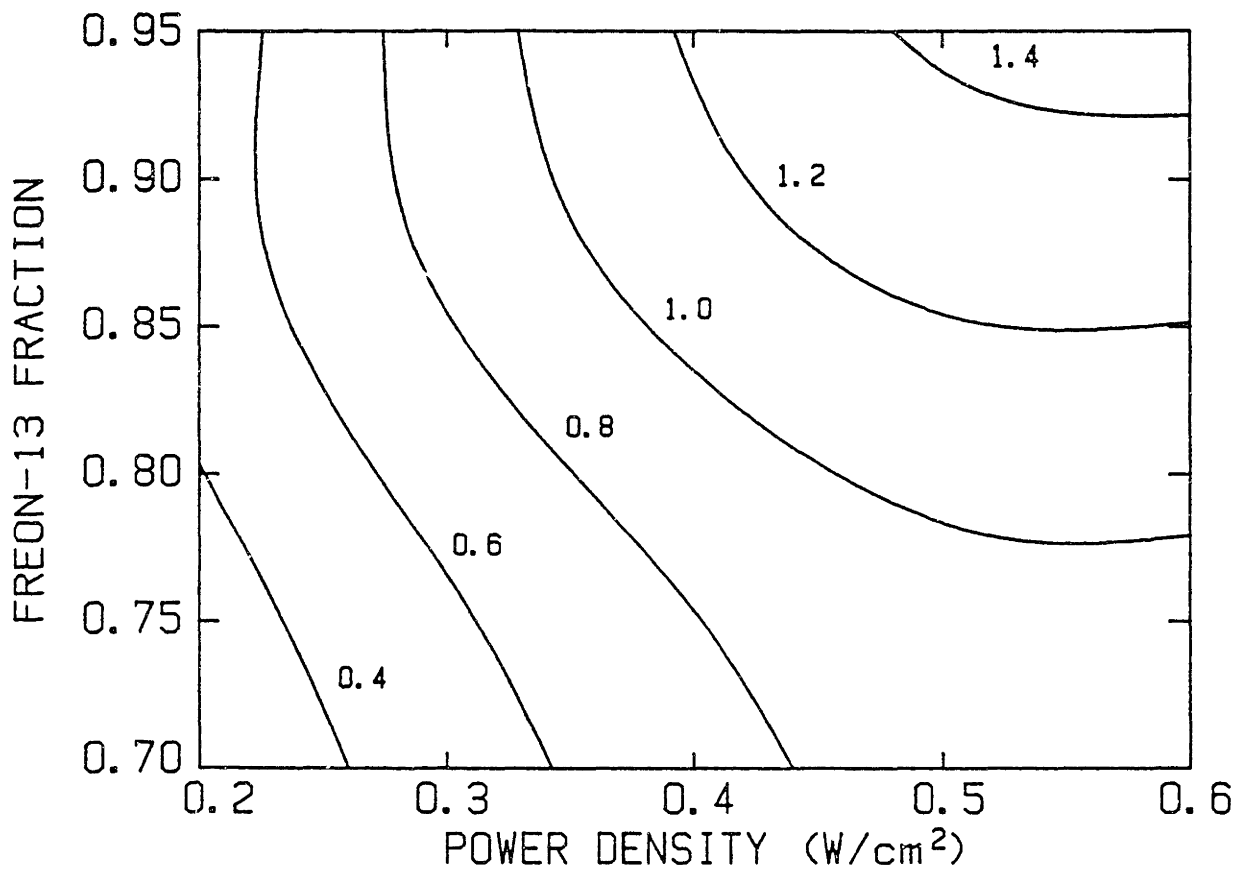


Figure 4-5c: Contour plot of total positive ion flux (mA/cm²) in CF₃Cl/Ar discharges, vs. power density (watts/cm²) and composition, P=0.5 torr.

4.3 CF₃Cl ION ENERGY DISTRIBUTIONS

4.3.1 Data Analysis

The addition (to the surface) of ion-bombardment energy from the plasma depends not only on the flux of ions, but also on the distribution of ion energies striking the surface. In section 4.3.2 the results of ion energy distribution experiments are presented. Given the measured mean ion energy, the ion energy distributions in CF₃Cl discharges are well described by the empirical model derived in section 4.3.3. Later (section 4.6), the mean ion energy is related to the plasma impedance properties, the final result being that the ion bombardment energy distribution can be predicted given only the discharge current, which can be measured external to the plasma reactor.

The ion energy distribution, $f(E_+)$, is defined as the derivative of the ion flux with respect to the ion energy. Experimentally, the dependence of measured flag current (see section 2.6) on the retarding grid bias potential is measured. A sample plot of the flag current Γ_+ vs. retarding potential V_r is shown in Fig. 4-6. Mathematically,

$$f(E_+) = (1/\bar{\Gamma}_+) d[\Gamma_+(qV_r)]/d[qV_r] , \quad (4.3.1-1)$$

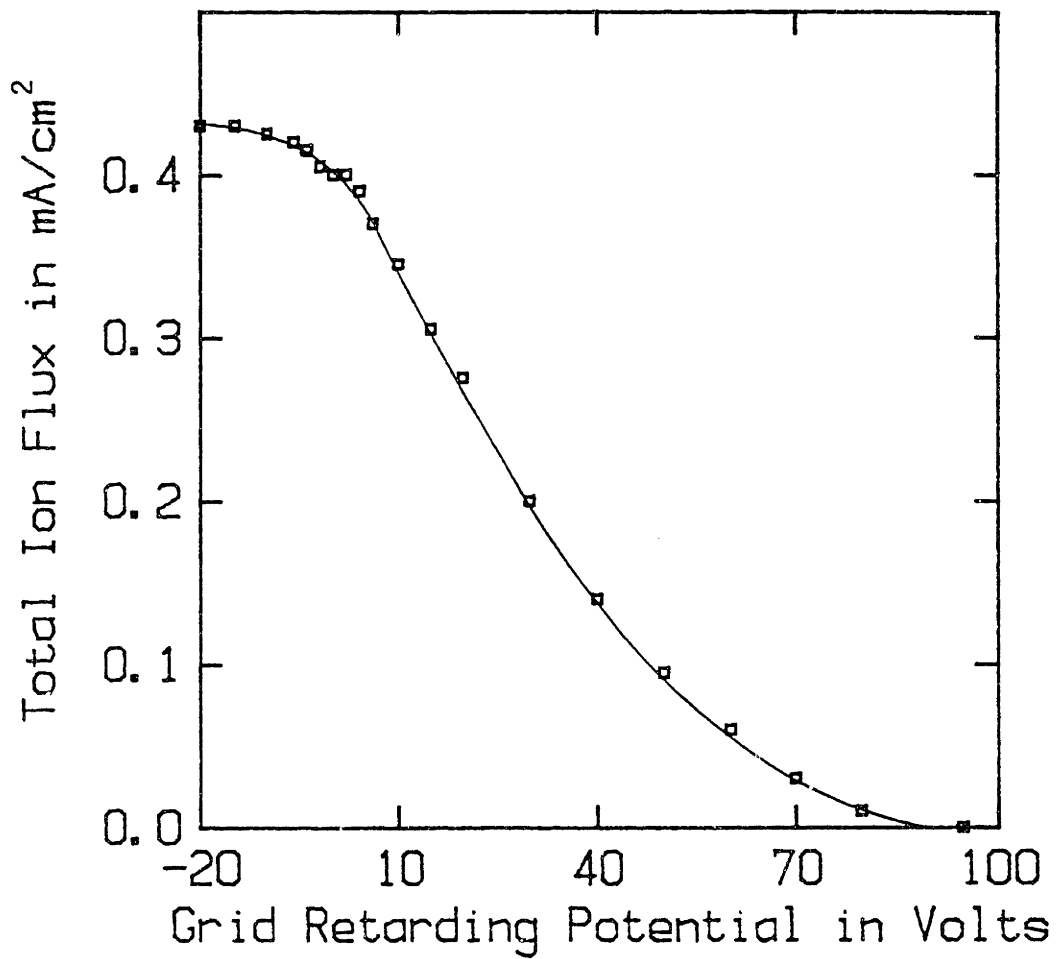


Figure 4-6: Measured positive ion flux (mA/cm²) to collection flag vs. lower grid retarding potential V_r (volts).

where $f(E_+)$ has been converted to a probability density function by normalization with the saturation ion flux, that is,

$$\int_0^{\infty} f(E_+) dE_+ = 1 . \quad (4.3.1-2)$$

Note that the ion energy E_+ corresponds to the retarding potential qV_r . The exact differentials were approximated by finite differences using ion flux data at discrete values (0.5 V spacing) of V_r , although wider spacings are shown in Fig. 4-6. The mean ion energy, \bar{E}_+ , is defined by

$$\bar{E}_+ = \int_0^{\infty} E_+ f(E_+) dE_+ . \quad (4.3.1-3)$$

It is seen in Chapter 6 that the mean energy alone is insufficient to describe the effects of ion bombardment on an etching film. Only ions with energy in excess of some threshold energy contribute to the etching process. The experimentally-measured fraction of ions with energy greater than or equal to a given energy E^* is given the symbol $\delta(E^*)$, and defined by

$$\delta(E^*) = \int_{E^*}^{\infty} f(E_+) dE_+ , \quad (4.3.1-4)$$

$$= \Gamma_+(qV_r=E^*) / \dot{\Gamma}_+ . \quad (4.3.1-5)$$

4.3.2 Parametric Dependence - Experimental Measurements

The ion energy distributions (IEDs) are most sensitive to power input and, in particular, system pressure. Ion energies were seen to be relatively insensitive to gas dilution for $\gamma=0.7-1.0$, and to flow rate Q for $Q=5-30$ sccm. The IEDs are not well fit by commonly-used forms such as the Boltzmann distribution.

The effects of power and pressure on mean ion energy are shown in Table 4-3. The effect of pressure on ion energy is clearly demonstrated in Figs. 4-7 to 4-9, in which $f(E_+)$ is shown for constant power input (0.4 W/cm^2), excitation frequency (13.56 MHz), electrode spacing (2 cm), and composition (10% argon in CF_3Cl) at 0.7, 0.5, and 0.3 torr, respectively. Note that the energy distributions shift to higher energies as pressure is decreased; $\langle E_+ \rangle$, \bar{E}_+ , $E_{+, \text{max}}$, and V_s all increase with decreasing pressure. The modes of the distributions (the peaks) occur at relatively low energies (around 10 eV), even at low pressure where the maximum ion energy is about 100 eV. The mean and median energies are within a few eV, so either may be used as a figure of merit.

Table 4-3

Measured mean ion bombardment energy in $\text{CF}_3\text{Cl}/\text{Ar}$ plasmas.
 $d=2$ cm, blank electrodes (assembly B), $Q=10$ sccm, $\omega=13.56$ MHz.

POWER (Watts)	PRESSURE (torr)	CF_3Cl FRACTION	MEAN ENERGY (eV)
32.6	0.8	0.87	2.57
15.4	0.8	0.87	2.53
30.2	0.4	0.87	20.19
16.6	0.4	0.87	11.61
35.9	0.8	0.78	6.85
36.3	0.8	0.92	3.72
27.4	0.4	0.78	22.59
31.2	0.4	0.92	20.63
58.7	0.6	0.78	16.44
57.0	0.6	0.92	13.56
23.4	0.6	0.78	8.81
20.9	0.6	0.92	6.30
28.2	0.6	0.87	8.25
30.4	0.4	0.87	21.66
22.1	0.2	0.87	27.01
28.2	0.2	0.92	28.60
27.3	0.2	0.78	28.72
55.6	0.2	0.87	34.78
13.0	0.7	0.78	5.01
55.7	0.7	0.78	11.83
13.7	0.7	0.85	4.52
30.0	0.7	0.85	5.47
55.5	0.7	0.85	11.89
74.8	0.7	0.85	15.75
55.1	0.7	0.92	11.52
52.9	0.5	0.78	27.86
14.7	0.5	0.78	8.49
27.5	0.5	0.85	14.60
52.6	0.5	0.85	21.78
71.3	0.5	0.85	31.17
52.1	0.5	0.92	18.51
14.1	0.3	0.78	20.11
50.7	0.3	0.78	37.43
14.9	0.3	0.85	19.67
26.3	0.3	0.85	29.66
53.3	0.3	0.85	37.85
67.8	0.3	0.85	41.47
14.6	0.3	0.92	18.57
50.9	0.3	0.92	39.26

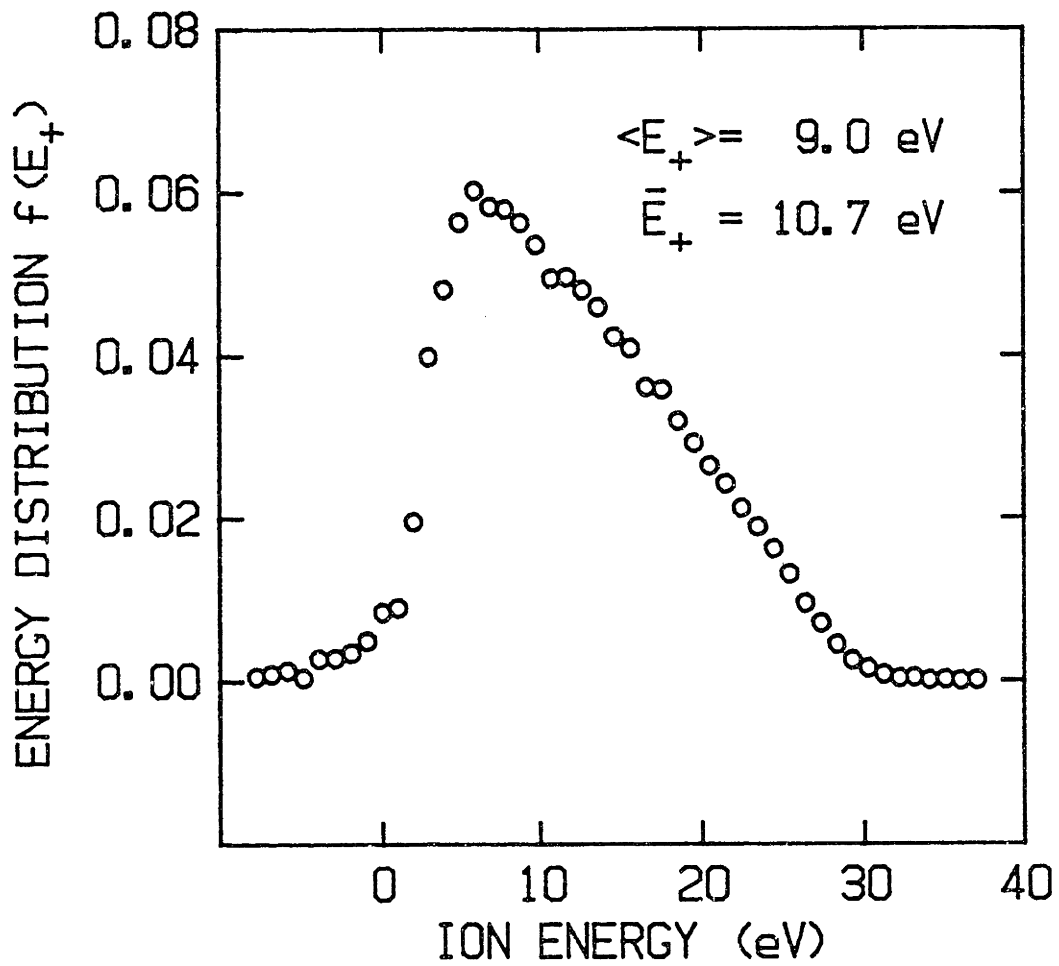


Figure 4-7: Ion energy distribution (IED) in CF_3Cl discharge at 0.7 torr pressure - other plasma conditions given in text.

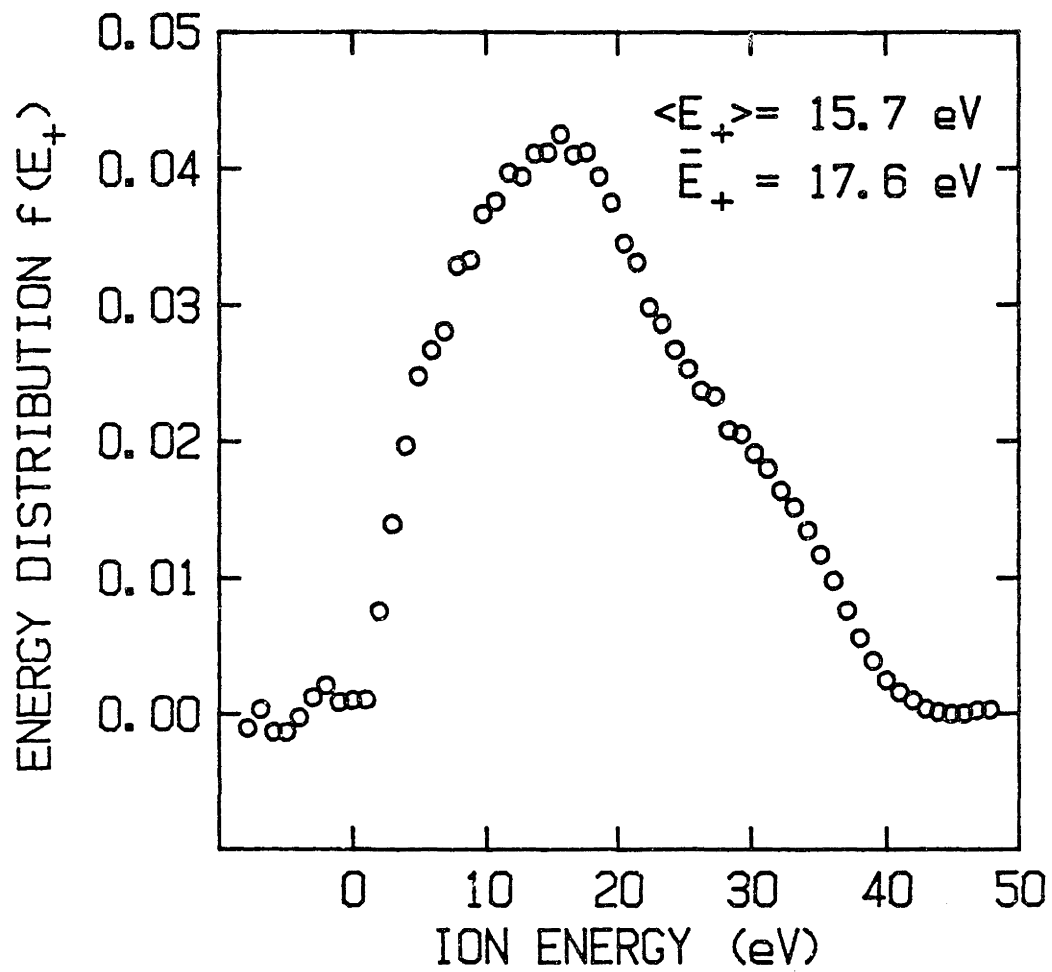


Figure 4-8: Ion energy distribution (IED) in CF_3Cl discharge at 0.5 torr pressure - other plasma conditions given in text.

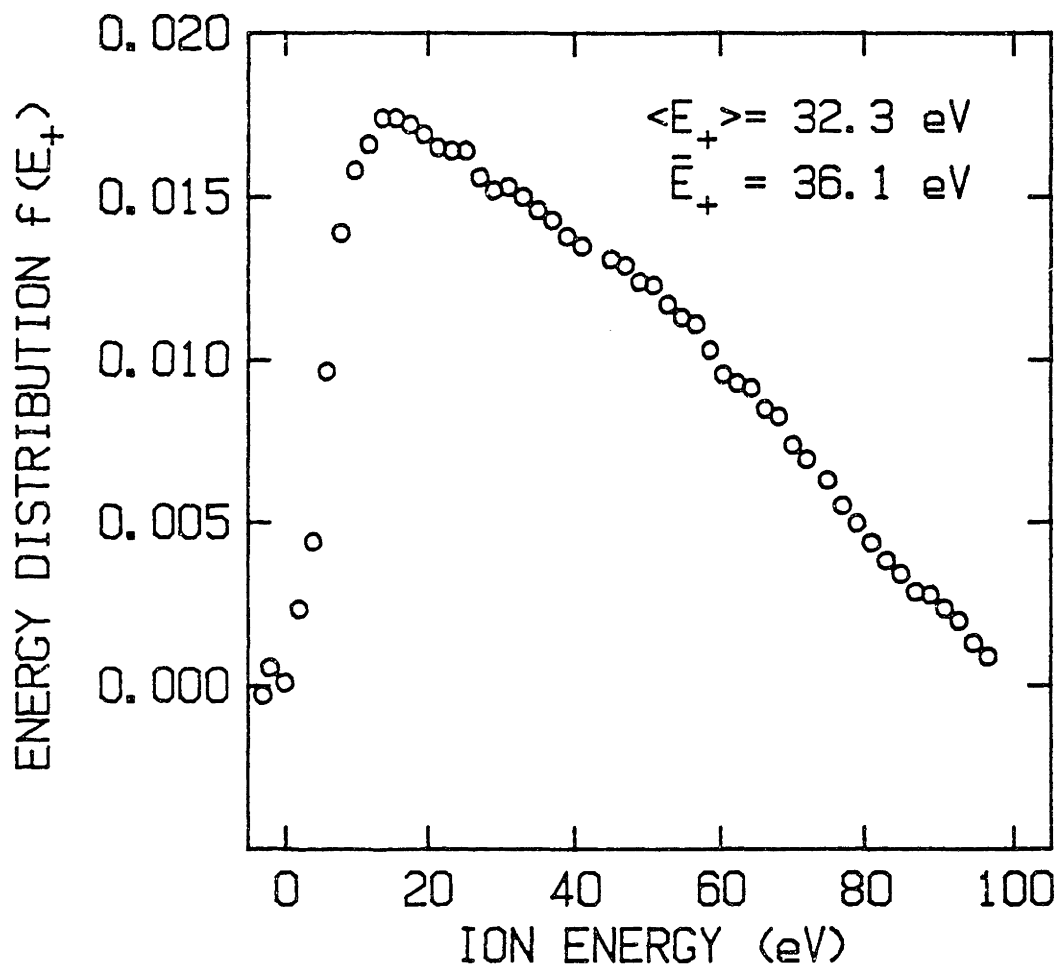


Figure 4-9: Ion energy distribution (IED) in CF_3Cl discharge at 0.3 torr pressure - other plasma conditions given in text.

The mean ion energy was determined using blank electrodes (no wafer present) for a wide range of plasma conditions (0.1-0.8 W/cm² input power density, 0.2-0.9 torr pressure, 0-30% argon in CF₃Cl), and the data was analyzed using RSM. Mean ion energies varied from 2 to 40 eV, with typical values of approximately 10 eV for much of the experimental range. Fig. 4-10 is a contour plot of \bar{E}_+ with power density \dot{W} and pressure P for a CF₃Cl mole fraction γ of 0.85. The quality of the RSM quadratic model fit was excellent, the adjusted R² being 0.94, so the experimental data are well represented by the contours. As described previously, mean ion energies decrease with increasing pressure while increasing slightly with increasing argon fraction. \bar{E}_+ increases rapidly with power input.

Table 4-4 shows the variation of $\delta(E^*)$ with process conditions ($E^*=10, 15, \text{ and } 20 \text{ eV}$). Note that the trends in $\delta(E^*)$ are similar to those in \bar{E}_+ ; $\delta(E^*)$ increases with power input, decreases with pressure, and increases slightly with argon dilution of CF₃Cl.

4.3.3 Empirical Model

Although the mean ion energy provides a qualitative prediction of the effects of energetic ion bombardment on the etching process, quantitative analysis requires knowledge of the ion bombardment energy distribution. The contribution of ion bombardment to the ion-assisted

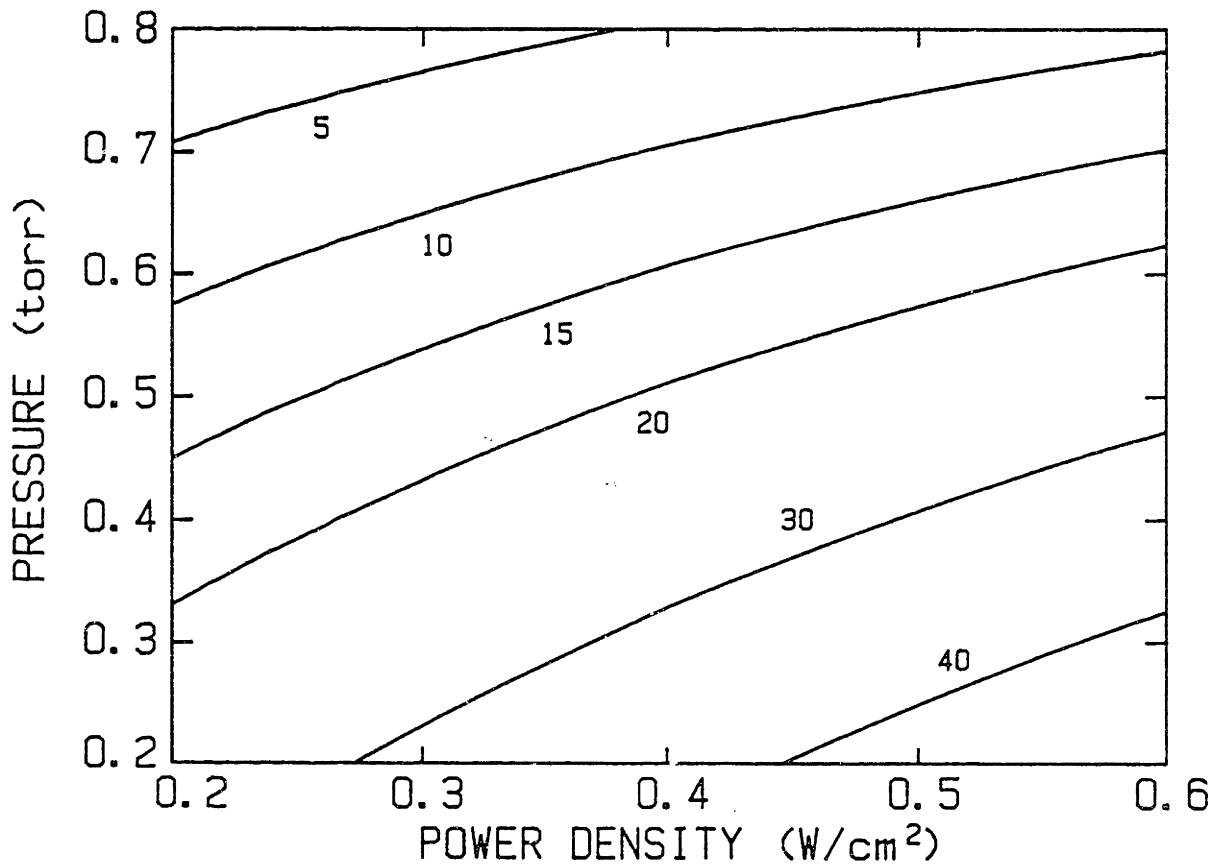


Figure 4-10: Contour plot of measured mean ion bombardment energy (eV) in CF_2Cl discharges, vs. power density (watts/cm^2) and pressure (torr).

Table 4-4

Measured ion fraction with above-threshold energy in $\text{CF}_3\text{Cl}/\text{Ar}$ plasmas.
 $d=2$ cm, blank electrodes (assembly B), $Q=10$ sccm, $\omega=13.56$ MHz.

POWER (Watts)	PRESSURE (torr)	CF_3Cl FRACTION	$\delta(10 \text{ eV})$	$\delta(20 \text{ eV})$
32.6	0.8	0.87	0.001	0.000
15.4	0.8	0.87	0.000	0.000
30.2	0.4	0.87	0.757	0.473
16.6	0.4	0.87	0.529	0.141
35.9	0.8	0.78	0.207	0.000
36.3	0.8	0.92	0.003	0.000
27.4	0.4	0.78	0.770	0.514
31.2	0.4	0.92	0.763	0.474
58.7	0.6	0.78	0.747	0.310
57.0	0.6	0.92	0.622	0.192
23.4	0.6	0.78	0.374	0.014
20.9	0.6	0.92	0.160	0.000
28.2	0.6	0.87	0.314	0.004
30.4	0.4	0.87	0.794	0.511
22.1	0.2	0.87	0.814	0.589
28.2	0.2	0.92	0.824	0.617
27.3	0.2	0.78	0.831	0.623
55.6	0.2	0.87	0.875	0.716
13.0	0.7	0.78	0.065	0.000
55.7	0.7	0.78	0.564	0.154
13.7	0.7	0.85	0.018	0.000
30.0	0.7	0.85	0.086	0.000
55.5	0.7	0.85	0.584	0.172
74.8	0.7	0.85	0.729	0.336
13.9	0.7	0.92	0.009	0.000
55.1	0.7	0.92	0.543	0.143
52.9	0.5	0.78	0.850	0.623
14.7	0.5	0.78	0.422	0.040
14.6	0.5	0.85	0.388	0.012
27.5	0.5	0.85	0.704	0.221
52.6	0.5	0.85	0.828	0.525
71.3	0.5	0.85	0.877	0.695
52.1	0.5	0.92	0.778	0.385
14.1	0.3	0.78	0.737	0.439
50.7	0.3	0.78	0.901	0.728
14.9	0.3	0.85	0.734	0.432
26.3	0.3	0.85	0.840	0.630
53.3	0.3	0.85	0.882	0.720
67.8	0.3	0.85	0.900	0.753
14.6	0.3	0.92	0.716	0.402
50.9	0.3	0.92	0.918	0.740

etching rate is likely a function of ion energy, although the form of this dependence is not known. The empirical expression given below adequately represents the energy distribution of a CF_3Cl/Ar plasma in terms of the mean ion energy, which will be modeled in section 4.6.

Examination of Figs. 4-7 to 4-9 reveals that the ion energy distribution is reproduced quite well by two intersecting lines, one for the low energy region and one for the higher energy tail. This "triangular" approximation of $f(E_+)$ is especially good at the lower pressures where a significant fraction of the ions have energies of 20 eV or above. Unfortunately, at higher pressures (≥ 0.7 torr) $f(E_+)$ tails off exponentially rather than linearly. However, since the fraction of ions with high energies is small at high pressures the contribution of ion-assisted etching is relatively unimportant, and the errors in the ion energy distribution are acceptable.

The triangular approximation of the ion energy distribution is derived as follows. The model vertices are written in $\{E_+, f(E_+)\}$ coordinates as $\{0,0\}$, $\{E_1, F_1\}$, and $\{E_2, 0\}$, see Fig. 4-11. E_1 and E_2 are constants representing the energy at the peak of the distribution and the maximum ion energy, respectively. The constant F_1 is chosen such that the area of the triangle is unity, making the model a probability distribution,

$$F_1 = 2/E_2 . \quad (4.3.3-1)$$

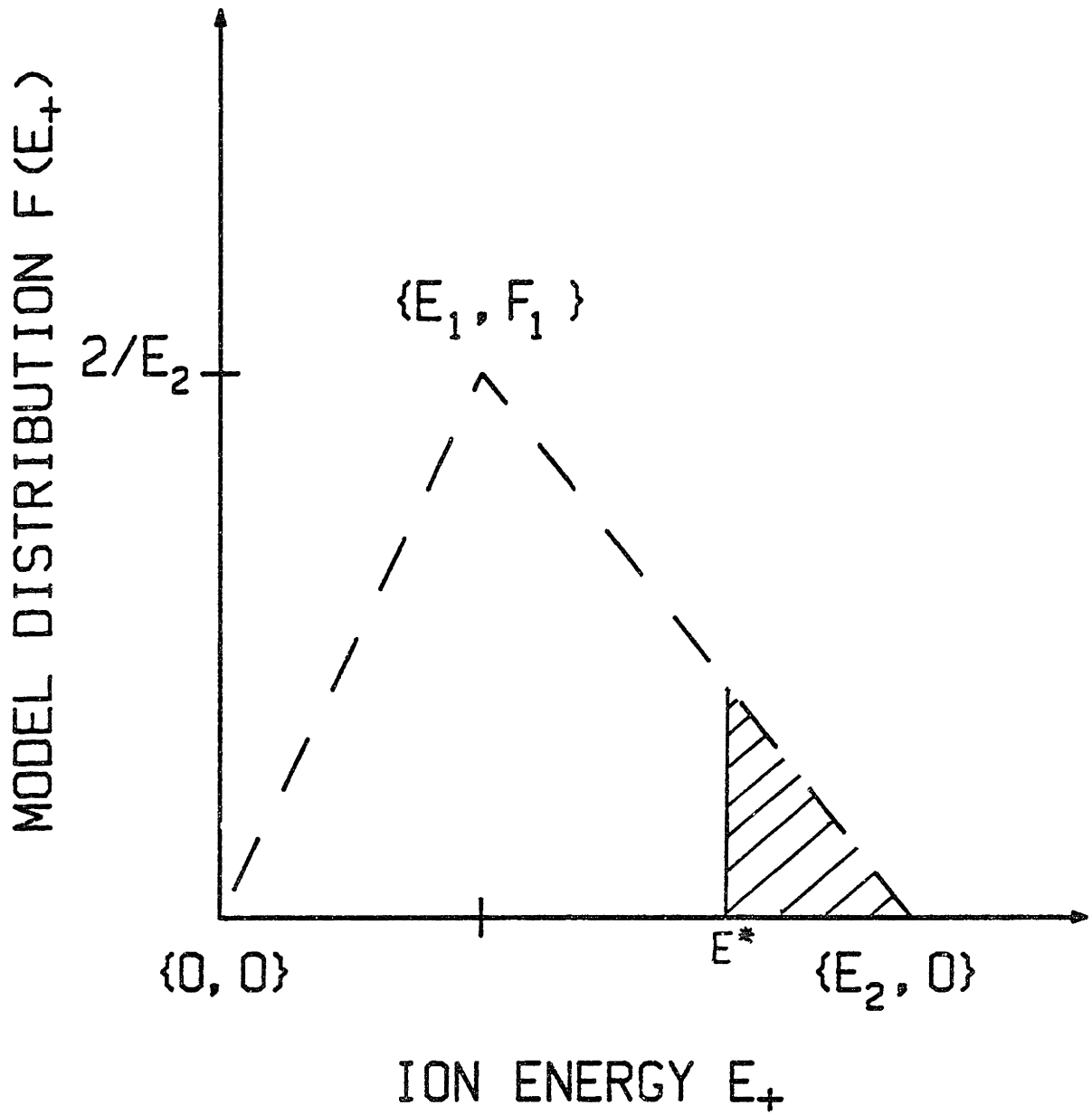


Figure 4-11: Triangular approximation model of measured ion energy distributions in CF_3Cl discharges.

The model distribution function, $F(E_+)$, is then expressed,

$$\begin{aligned}
 F(E_+) &= 2E_+/E_1E_2, & 0 \leq E_+ \leq E_1, \\
 &2(1-E_+/E_2)/(E_2-E_1), & E_1 \leq E_+ \leq E_2.
 \end{aligned}
 \tag{4.3.3-2}$$

Upon determining the best fit of $F(E_+)$ to the data for a range of plasma conditions (see Table 4-5), we find that the following rules of thumb provide good estimates of E_1 and E_2 :

$$\begin{aligned}
 E_1 &\sim (P/P_0)\bar{E}_+, \\
 E_2 &\sim (8/3)\bar{E}_+ \sim 2.67\bar{E}_+.
 \end{aligned}
 \tag{4.3.3-3}$$

In general, these estimates for E_1 and E_2 predict the peak of the distribution within about 3 eV and the maximum ion energy within about 5 eV. The triangle model is then explicit in the mean ion energy,

$$\begin{aligned}
 F(E_+) &= 0.75(P_0/P)E_+/\bar{E}_+^2, & 0 \leq E_+ \leq (P/P_0)\bar{E}_+, \\
 &\frac{(1-0.75E_+/\bar{E}_+)}{(2.67-P/P_0)\bar{E}_+} & (P/P_0)\bar{E}_+ \leq E_+ \leq 2.67\bar{E}_+.
 \end{aligned}
 \tag{4.3.3-4}$$

Table 4-5

Best fit values of E_1 and E_2 to measured ion energy distribution at various process conditions for CF_3Cl/Ar discharges. $d=2$ cm, blank electrodes (assembly B), $Q=10$ sccm, $\omega=13.56$ MHz.

POWER INPUT (Watts)	PRESSURE (torr)	CF_3Cl FRACTION	E_1	E_2
13.0	0.7	0.78	3.0	12.6
55.7	0.7	0.78	8.0	30.3
13.7	0.7	0.85	3.0	10.9
30.0	0.7	0.85	4.0	14.0
55.5	0.7	0.85	7.0	30.1
74.8	0.7	0.85	8.1	39.9
13.9	0.7	0.92	2.6	10.1
55.1	0.7	0.92	6.7	31.3
52.9	0.5	0.78	17.1	66.2
14.7	0.5	0.78	5.8	26.5
14.6	0.5	0.85	6.5	23.2
27.5	0.5	0.85	11.5	34.3
52.6	0.5	0.85	16.5	59.0
71.3	0.5	0.85	21.9	77.2
52.1	0.5	0.92	14.2	41.2
14.1	0.3	0.78	7.7	55.8
50.7	0.3	0.78	7.7	98.3
14.9	0.3	0.85	14.4	51.0
26.3	0.3	0.85	9.8	74.7
53.3	0.3	0.85	7.8	102.0
67.8	0.3	0.85	14.5	110.4
14.6	0.3	0.92	8.8	50.2
50.9	0.3	0.92	14.2	103.7

The model prediction for fractional ion flux above a threshold energy E^* , $\Delta(E^*)$, is simply the area under the triangle between $E_+ = E^*$ and $E_+ = E_2$ (the shaded area in Fig. 4-11). We define the scaled variables $\rho = P/P_0$ and $\xi = E^*/\bar{E}_+$ and write,

$$\Delta(E^*) = \frac{(1 - 0.375\xi)^2}{(1 - 0.375\rho)}, \quad \rho < \xi < 2.67,$$

$$= 1 - 0.375\xi^2/\rho, \quad 0 \leq \xi \leq \rho. \quad (4.3.3-5)$$

It is shown in section 4.6 that $\bar{E}_+ = K_E |I|/\omega P$. This expression may be used with eqns. (4.3.3-4) and (4.3.3-5) to write the ion energy distribution solely in terms of impedance properties. The ion energy distribution model using the impedance result is given the symbol $\tilde{F}(|I|/\omega P)$, and allows estimation of the ion energies using only the measured discharge current. The fractional ion flux using the impedance result rather than the experimental data is given the symbol $\tilde{\Delta}(E^*)$. $\tilde{\Delta}(E^*)$ is obtained by using $\tilde{\xi} = E^* \omega P / K_E |I|$, the threshold energy divided by the impedance model prediction of \bar{E}_+ , in place of ξ in eqn. (4.3.3-5). Table 4-6 contains values of $\tilde{\Delta}(E^*)$, $\Delta(E^*)$, and the measured $\delta(E^*)$ for various plasma conditions at $E^* = 15$ eV. Note that $\Delta(E^*)$ is within 5-10% of the measured $\delta(E^*)$, and that $\tilde{\Delta}(E^*)$ is in general within 10-15% of $\delta(E^*)$.

Table 4-6
 Measured ion fraction with above 15 eV energy
 compared with triangle model approximation
 at various process conditions for CF₃Cl/Ar plasmas.
 d=2 cm, blank electrodes (assembly B), Q=10 sccm, ω=13.56 MHz.

POWER (Watts)	PRESSURE (torr)	CF ₃ Cl FRACTION	δ(15 eV)	Δ(15 eV)
13.0	0.7	0.78	0.001	0.000
55.7	0.7	0.78	0.322	0.373
13.7	0.7	0.85	0.000	0.000
30.0	0.7	0.85	0.000	0.000
55.5	0.7	0.85	0.349	0.378
74.8	0.7	0.85	0.513	0.560
13.9	0.7	0.92	0.000	0.000
55.1	0.7	0.92	0.313	0.356
52.9	0.5	0.78	0.742	0.783
14.7	0.5	0.78	0.149	0.140
14.6	0.5	0.85	0.120	0.108
27.5	0.5	0.85	0.452	0.465
52.3	0.5	0.85	0.682	0.677
71.3	0.5	0.85	0.791	0.826
52.1	0.5	0.92	0.583	0.596
14.1	0.3	0.78	0.579	0.584
50.7	0.3	0.78	0.814	0.799
14.9	0.3	0.85	0.576	0.574
26.3	0.3	0.85	0.733	0.740
53.3	0.3	0.85	0.800	0.804
67.8	0.3	0.85	0.831	0.836
14.6	0.3	0.92	0.550	0.547
50.9	0.3	0.92	0.834	0.818

$\tilde{F}(|I|/\omega P)$ is compared with experiment in Fig. 4-12 for the same plasma conditions specified in Figs. 4-8 and 4-9, respectively. The impedance/sheath transport model's ability to represent the ion energy distribution is good in that Fig. 4-12a is the poorest fit of the model to the data for the conditions examined. Fig. 4-12b is more typical of the results obtained.

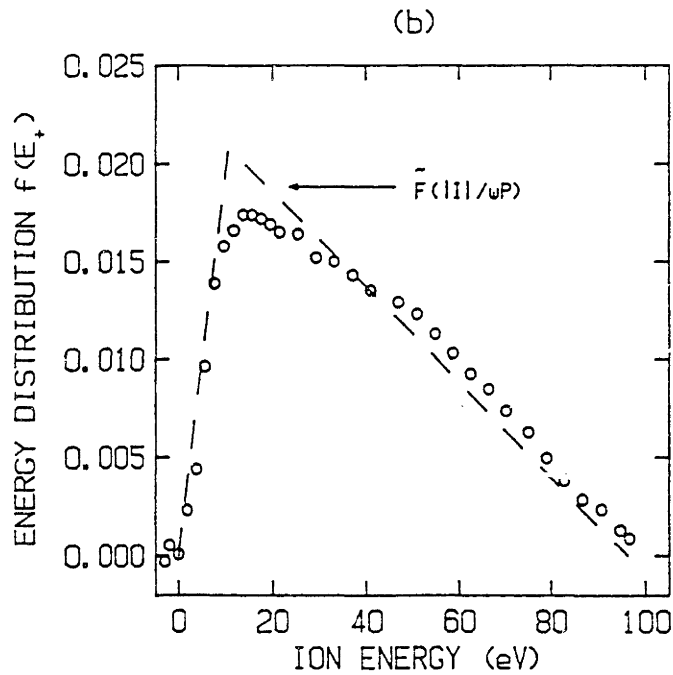
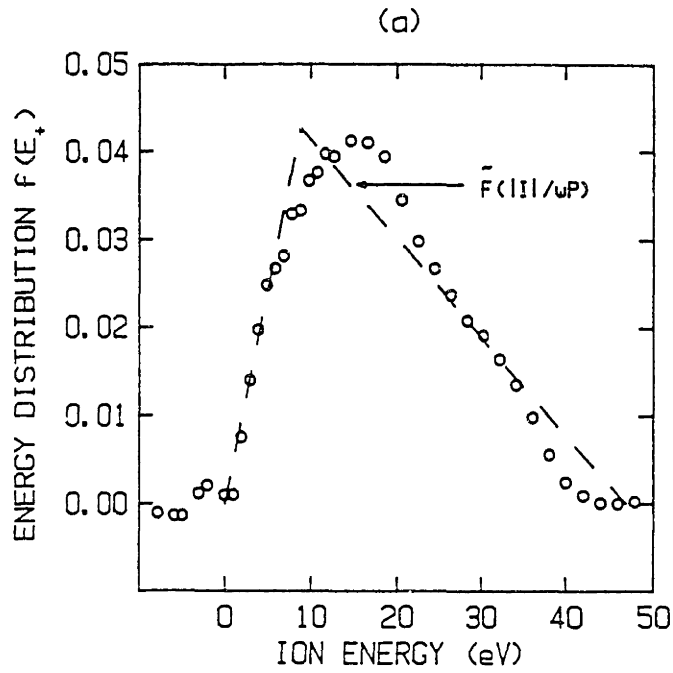


Figure 4-12: Comparison of triangle model estimate $\tilde{F}(|I|/\omega P)$ with measured ion energy distribution at two plasma conditions: (a) poorest fit observed, corresponding to data of Fig. 4-8 (0.5 torr), (b) typical fit, corresponding to data of Fig. 4-9 (0.3 torr).

4.4 CF₃Cl ION CHEMISTRY

To properly quantify the fluxes of the various ionic species, an energy analyzer must be used in conjunction with the mass spectrometer. Since the gain of the QMS is dependent on the energy of the ion being measured, some bias in the measurements occurs due to the variation of ion energy with ion mass and plasma conditions. In this study an energy analyzer was not used, so quantitative analysis of the ion species distribution is difficult. However, the general trends with process conditions were observed, and are presented below.

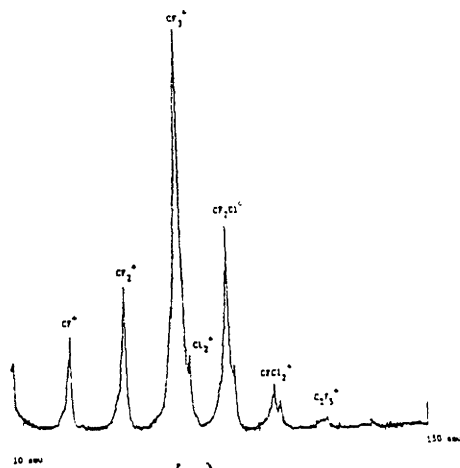
The ion species distribution of a CF₃Cl/Ar plasma is very complex. Many species can be seen by varying the plasma conditions. For example, each of the following species has been observed with the mass spectrometer: CF⁺, Cl⁺, Ar⁺, CF₂⁺, CF₃⁺, CF₂Cl⁺, CF₃Cl⁺, C₂F₅⁺, C₂F₄Cl⁺, and SiCl₃⁺. Some heavier ions were observed but could not be identified due to the peak broadening caused by the distribution in ion energies.

Except at very low E/P (low power and high pressure), CF₃⁺ is the dominant ion. Another important ion is CF₂Cl⁺. In general, lighter ions are important at high E/P, while heavier ions are seen at low E/P. The variations in some important ions during single crystal silicon etching are listed in Table 4-7. In Fig. 4-13a through 4-13c, QMS scans using blank electrodes at high, low, and intermediate E/P are shown.

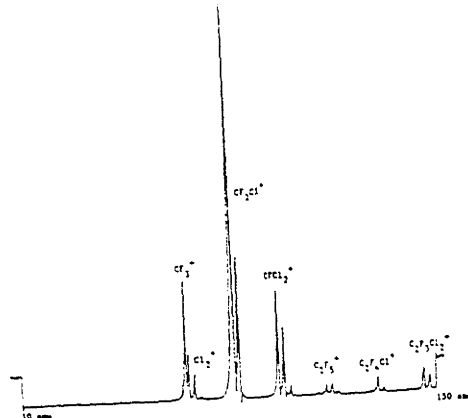
In general, CF^+ and CF_2^+ are seen at low pressures, and become more important relative to CF_3^+ at higher powers. CF_3^+ is the dominant ion except at low pressures and high power, where CF_2Cl^+ is the most intense peak. The trends in Cl^+ and Cl_2^+ follow those in CF_3^+ . The ion flux of the parent species, CF_3Cl^+ , is only appreciable at very low E/P. The recombinant ions $C_2F_5^+$ and $C_2F_4Cl^+$ are most important at higher pressures, and follow the trends of CF_3^+ with power.

Table 4-7
 Mass Spectrometer Peaks Heights (normalized to CF_3^+)
 with varying plasma conditions
 for important ions in a CF_3Cl/Ar discharge.
 $d=2$ cm (assembly B), $Q=6$ sccm, $\omega=13.56$ MHz.
 Full 4" single crystal silicon wafer present, unmasked.

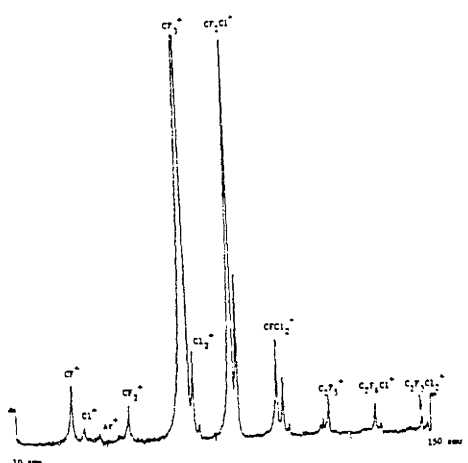
PRESS, POWER (torr), (W)	RELATIVE PEAK INTENSITIES						
	CF^+	CF_2^+	CF_3^+	Cl_2^+	CF_2Cl^+	CF_3Cl^+	$C_2F_5^+$
0.3, 10	0	.42	1	.10	1.25	.19	0
30	.53	.76	1	.08	.55	.08	0
50	.77	.68	1	.08	.53	.08	0
70	.91	.66	1	.08	.53	.11	.03
90	.99	.66	1	.08	.55	.11	.03
110	1.02	.65	1	.07	.53	.11	.04
0.6, 10	0	0	1	0	2.45	0	0
30	0	0	1	.08	1.20	.30	.06
50	.05	.07	1	.09	.86	.23	.07
70	.05	.08	1	.09	.84	.23	.08
90	.06	.12	1	.10	.82	.24	.08
110	.06	.20	1	.10	.84	.28	.08
0.9, 10	0	0	1	.10	5.45	0	0
30	0	0	1	.10	1.48	.18	0
50	.04	.02	1	.10	.95	.14	.04
70	.04	.02	1	.08	.85	.16	.04
90	.05	.03	1	.08	.69	.12	.05
110	.07	.05	1	.07	.69	.12	.05



(a)



(b)



(c)

Fig. 4-13: QMS ion scans in CF_3Cl discharges: (a) high power and low pressure, (b) low power and high pressure, and (c) intermediate power and pressure.

4.5 CF₃Br EXPERIMENTAL RESULTS

The experimental data presented in this section consist primarily of a single 35-run experimental design with power, pressure, and flow rate as the independent variables. Gas composition was 95% CF₃Br, with 5% Ar added as an actinometer. Ion flux and species distribution results were averaged with time over the etching of one-fourth of a 4-inch wafer (heavily P-doped polysilicon with a photoresist mask). Ion energies were determined using blank electrodes. In all cases the electrode spacing was 2 cm (using electrode assembly B) and the excitation frequency 13.56 MHz.

4.5.1 Ion Flux

The ion flux data is presented as Table 4-8. Note that the general trends are similar to those of CF₃Cl; ion flux increases about linearly with power, increases sublinearly with pressure, and decreases slightly with increasing flow rate. The effects of power and pressure are clearly demonstrated in Fig. 4-14.

Table 4-8
 Measured Total Positive Ion Flux During CF₃Br Etching
 of P-doped polysilicon wafer. d=2 cm, ω=13.56 MHz.

RUN ID	POWER INPUT (Watts)	PRESSURE (Torr)	FLOW RATE (Sccm)	TOTAL ION FLUX (mA/cm ²)
BR_1	54.2	0.5	15.3	1.21
BR_2	53.8	0.5	15.1	1.14
BR_3	50.6	0.5	15.4	1.11
BR_4	70.0	0.625	15.3	1.64
BR_5	71.8	0.375	15.3	1.31
BR_6	32.3	0.625	15.2	0.98
BR_7	30.6	0.375	15.1	0.77
BR_8	73.9	0.5	20.4	1.60
BR_9	72.7	0.5	10.3	1.45
BR_10	31.8	0.5	20.6	0.87
BR_11	30.5	0.5	10.3	0.95
BR_12	51.0	0.625	20.2	1.48
BR_13	51.8	0.625	10.0	1.49
BR_14	50.3	0.375	20.4	0.87
BR_15	47.9	0.375	10.0	1.04
BR_16	86.9	0.75	26.9	1.96
BR_17	99.7	0.75	4.7	2.54
BR_18	89.4	0.25	26.9	0.87
BR_19	89.1	0.25	4.6	1.05
BR_20	13.4	0.75	25.8	0.28
BR_21	12.9	0.75	4.7	0.35
BR_22	11.6	0.25	26.9	0.18
BR_23	12.7	0.25	4.8	0.29
BR_24	80.1	0.5	15.2	1.72
BR_25	22.0	0.5	15.1	0.74
BR_26	51.3	0.692	15.2	1.45
BR_27	51.2	0.312	15.4	0.77
BR_28	52.0	0.5	23.1	1.19
BR_29	50.8	0.5	7.4	1.40
BR_30	79.0	0.5	15.2	1.68
BR_31	22.0	0.5	15.1	0.72
BR_32	50.3	0.692	15.1	1.60
BR_33	51.0	0.312	15.2	0.82
BR_34	51.5	0.5	23.1	1.19
BR_35	52.0	0.5	7.5	1.04

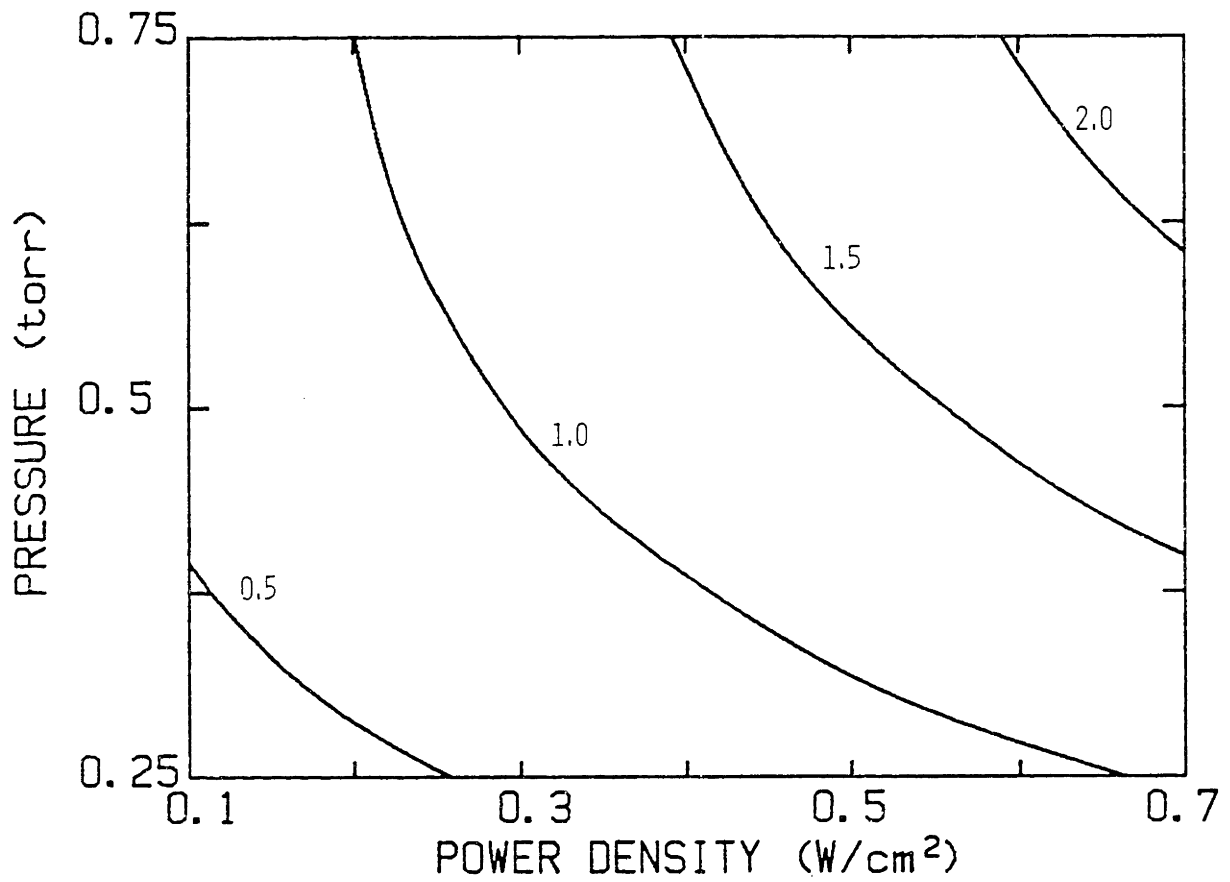


Figure 4-14: Contour plot of total positive ion flux (mA/cm²) in CF₃Br discharges during doped polysilicon etching, vs. power density (watts/cm²) and pressure (torr), Q=15 sccm.

4.5.2 Ion Energy

The variations in mean ion energy with process conditions are seen in Table 4-9. For clarity, a contour plot is presented as Fig. 4-15. Note that mean ion energy is independent of flow rate, increases linearly with power, and decreases with the square of pressure.

The ion energy distributions are narrower than in CF_3Cl , i.e., the maximum observed ion energy is only twice the mean energy. Typical CF_3Br ion energy distributions are shown in Fig. 4-16.

4.5.3 Ion Chemistry

Relative QMS peak heights for the major ionic species observed in CF_3Br plasmas are listed in Table 4-10, while QMS scans for selected plasma conditions are shown in Fig. 4-17. Note that CF_3^+ is always the predominant ion over the experimental range, while CF_2Br^+ and Br_2^+ are also major ions. In addition, CF^+ , CF_2^+ , Br^+ , C_2F_4^+ , CF_3Br^+ , and C_2F_4^+ are observed. Another minor peak at about 190 amu could be either CFBr_2^+ or SiBr_2^+ ; calibration of the mass spec made this identification difficult.

Table 4-9
 Measured Mean Ion Energies in CF₃Br Discharges.
 d=2 cm, blank electrodes, $\omega=13.56$ MHz.

RUN ID	POWER INPUT (Watts)	PRESSURE (Torr)	FLOW RATE (Sccm)	MEAN ION ENERGY (eV)
BR_1	54.2	0.5	15.3	6.2
BR_2	53.8	0.5	15.1	5.4
BR_3	50.6	0.5	15.4	5.2
BR_4	70.0	0.625	15.3	4.5
BR_5	71.8	0.375	15.3	18.5
BR_6	32.3	0.625	15.2	2.1
BR_7	30.6	0.375	15.1	8.9
BR_8	73.9	0.5	20.4	7.9
BR_9	72.7	0.5	10.3	8.1
BR_10	31.8	0.5	20.6	4.1
BR_11	30.5	0.5	10.3	4.3
BR_12	51.0	0.625	20.2	3.1
BR_13	51.8	0.625	10.0	3.0
BR_14	50.3	0.375	20.4	18.3
BR_15	47.9	0.375	10.0	13.4
BR_16	86.9	0.75	26.9	3.4
BR_17	99.7	0.75	4.7	4.2
BR_18	89.4	0.25	26.9	48.7
BR_19	89.1	0.25	4.6	49.8
BR_20	13.4	0.75	25.8	0.1
BR_21	12.9	0.75	4.7	0.3
BR_22	11.6	0.25	26.9	10.6
BR_23	12.7	0.25	4.8	9.2
BR_24	80.1	0.5	15.2	9.3
BR_25	22.0	0.5	15.1	2.9
BR_26	51.3	0.692	15.2	2.2
BR_27	51.2	0.312	15.4	21.0
BR_28	52.0	0.5	23.1	5.8
BR_29	50.8	0.5	7.4	5.8
BR_30	79.0	0.5	15.2	9.4
BR_31	22.0	0.5	15.1	2.8
BR_32	50.3	0.692	15.1	2.2
BR_33	51.0	0.312	15.2	21.2
BR_34	51.5	0.5	23.1	6.0
BR_35	52.0	0.5	7.5	6.0

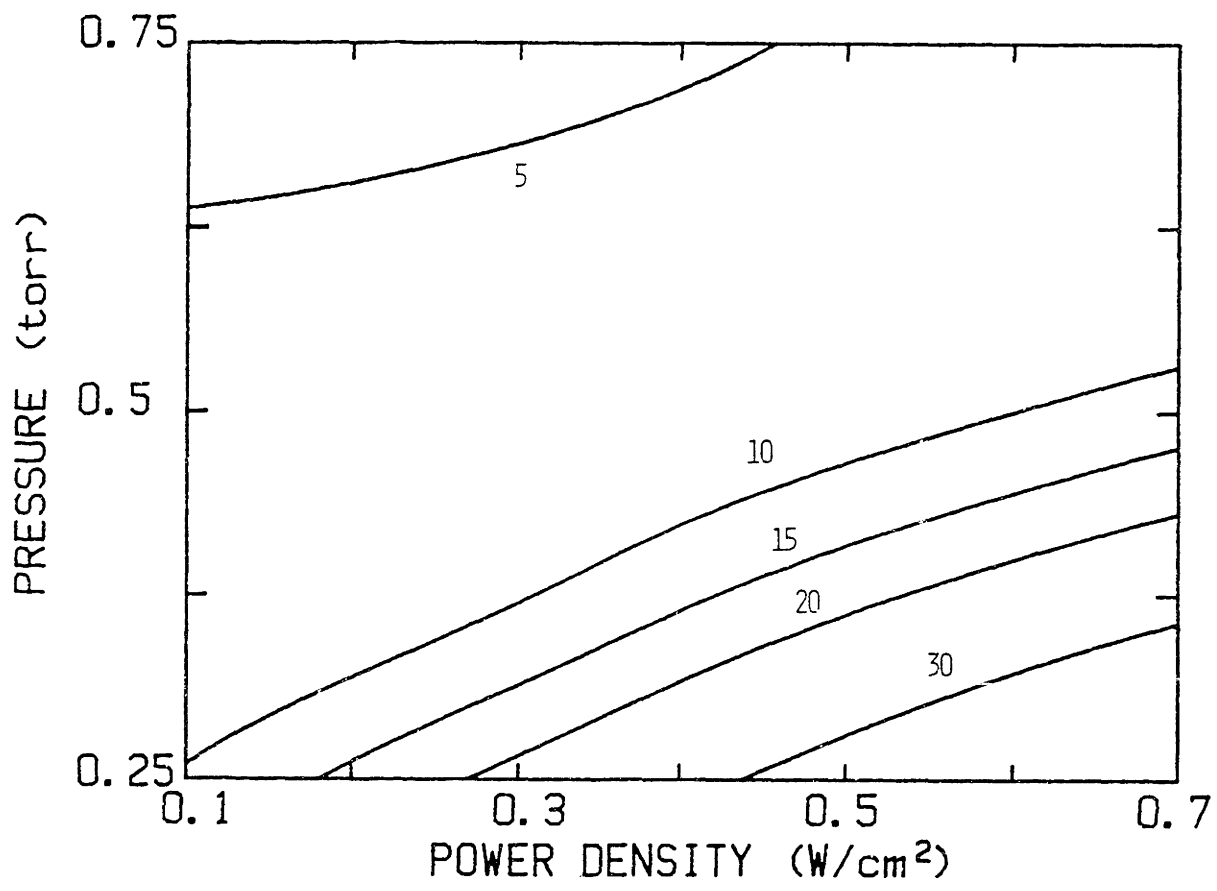
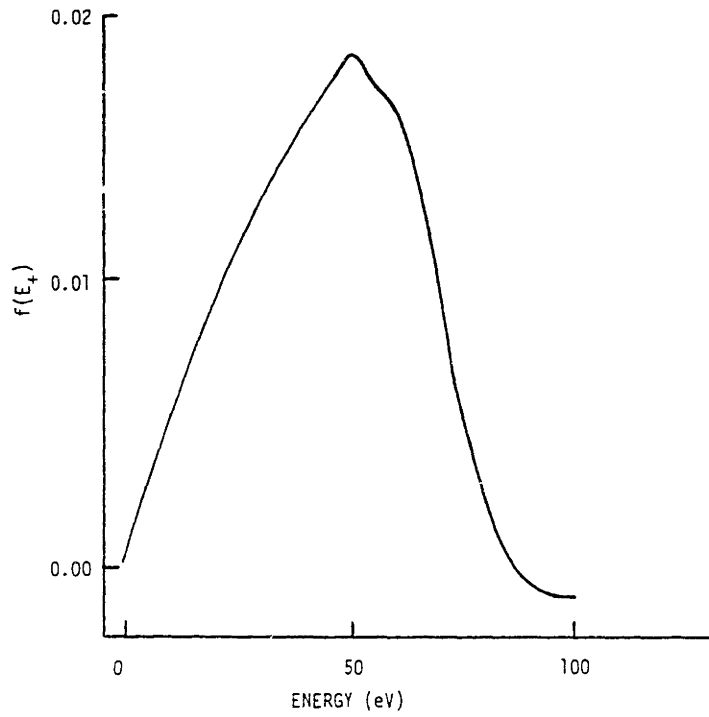
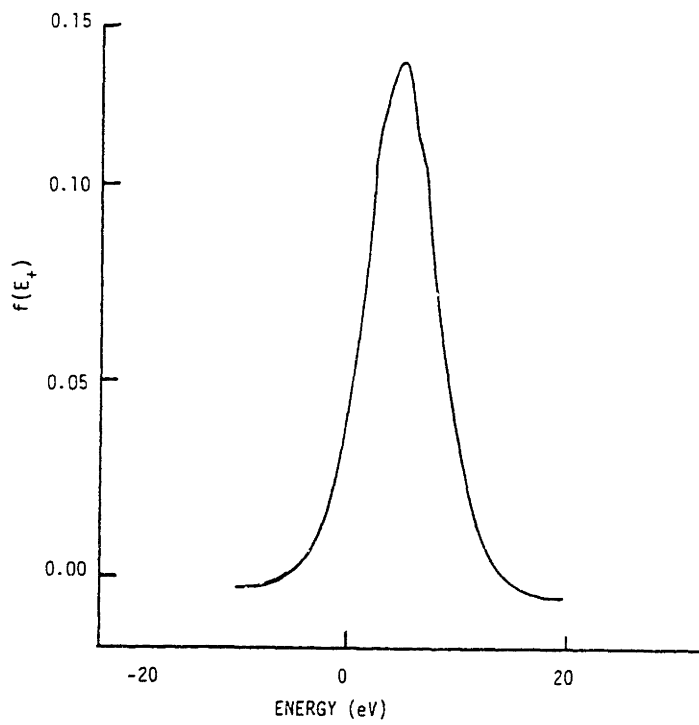


Figure 4-15: Contour plot of measured mean ion energy in CF_3Br discharges (eV), vs. power density (watts/cm²) and pressure (torr).



(a)

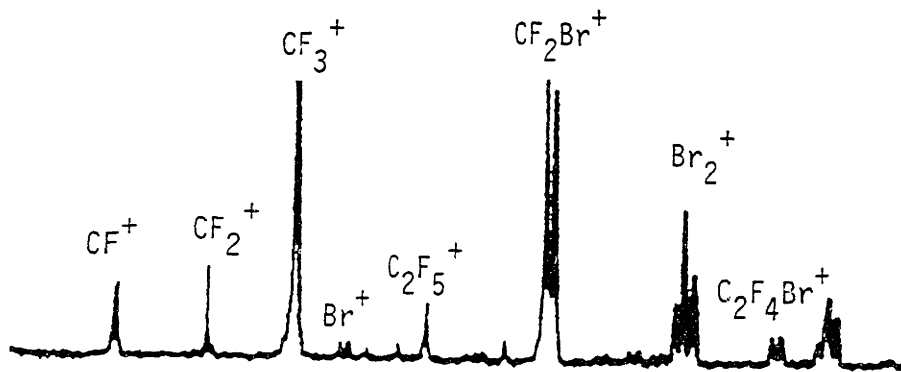


(b)

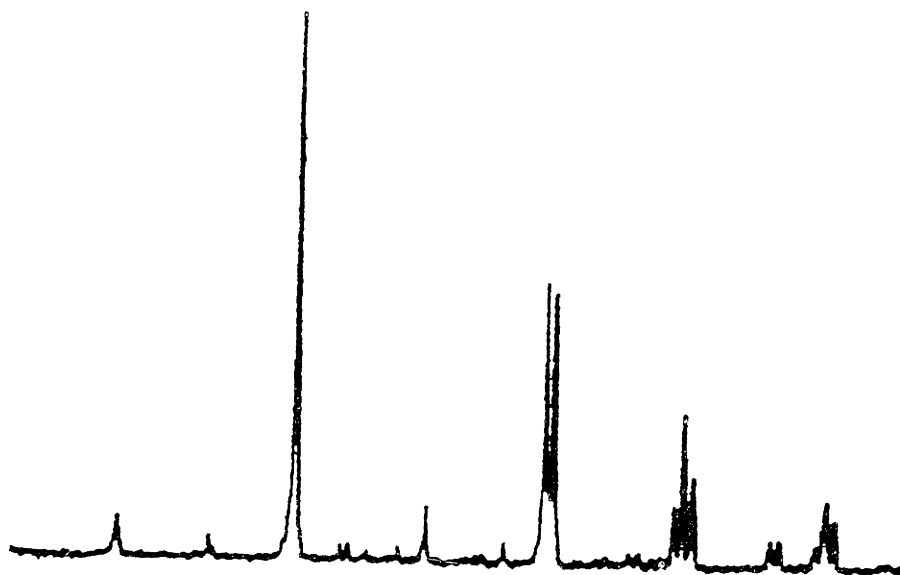
Figure 4-16: Typical measured ion energy distributions in CF_3Br discharges: (a) high E/P , (b) low E/P .

Table 4-10
 Peak Heights (relative to CF_3^+) of Important Ions During CF_3Br Etching
 of P-doped polysilicon, photoresist mask. $d=2$ cm, $\omega=13.56$ MHz.
 Conditions for Run IDs are given in Table 4-9.

RUN ID	RELATIVE PEAK HEIGHTS								
	CF^+	CF_2^+	CF_3^+	C_2F_4^+	C_2F_5^+	CF_2Br^+	CF_3Br^+	Br_2^+	$\text{C}_2\text{F}_4\text{Br}^+$
BR_1	.05	.05	1	.09	.04	.61	.04	.18	.07
BR_2	.05	.04	1	.09	.05	.69	.04	.21	.08
BR_3	.05	.04	1	.11	.05	.78	.04	.23	.08
BR_4	.06	.03	1	.11	.04	.67	.04	.19	.07
BR_5	.07	.10	1	.07	.04	.31	.04	.18	.04
BR_6	.05	.03	1	.13	.04	.95	.05	.19	.10
BR_7	.04	.06	1	.07	.04	.73	.04	.17	.09
BR_8	.05	.04	1	.09	.04	.68	.04	.20	.06
BR_9	.06	.05	1	.12	.04	.52	.04	.30	.06
BR_10	.04	.05	1	.10	.04	.88	.05	.17	.08
BR_11	.05	.04	1	.13	.05	.89	.05	.24	.11
BR_12	.05	.03	1	.10	.04	.80	.04	.15	.09
BR_13	.07	.05	1	.12	.05	.63	.05	.23	.09
BR_14	.04	.06	1	.08	.04	.60	.04	.19	.05
BR_15	.05	.06	1	.08	.04	.51	.04	.25	.06
BR_16	.07	.05	1	.10	.05	.64	.06	.17	.08
BR_17	.09	.06	1	.11	.05	.50	.04	.28	.06
BR_18	.22	.22	1	.04	.03	.25	.05	.12	.02
BR_19	.29	.23	1	.07	.05	.24	.04	.23	.03
BR_20	.13	.15	1	.19	.15	5.28	.21	.34	.58
BR_21	.11	.11	1	.17	.12	3.37	.16	.47	.60
BR_22	.03	.08	1	.03	.03	.76	.05	.06	.06
BR_23	.04	.07	1	.12	.05	.68	.05	.33	.10
BR_24	.06	.05	1	.10	.04	.52	.04	.23	.05
BR_25	.05	.05	1	.10	.05	.97	.06	.16	.12
BR_26	.05	.03	1	.11	.04	.68	.04	.21	.08
BR_27	.05	.10	1	.08	.03	.38	.04	.20	.03
BR_28	.05	.03	1	.09	.04	.80	.04	.16	.07
BR_29	.07	.06	1	.10	.04	.54	.05	.25	.09
BR_30	.06	.06	1	.10	.04	.46	.04	.23	.05
BR_31	.05	.04	1	.11	.04	1.07	.06	.18	.12
BR_32	.06	.03	1	.11	.04	.78	.04	.19	.10
BR_33	.07	.13	1	.06	.04	.34	.04	.15	.04
BR_34	.05	.03	1	.09	.03	.78	.04	.15	.07
BR_35	.06	.05	1	.12	.06	.62	.05	.31	.09



(a)



(b)

Figure 4-17: QMS ion scans in CF_3Br discharges: (a) high E/P, (b) low E/P.

4.6 ION TRANSPORT THROUGH SHEATHS

4.6.1 Mean Ion Energy

In this section a simple sheath transport model is derived, to be used in conjunction with the plasma impedance model to predict mean ion energies. The mean energy is shown to be proportional to the sheath electric field to pressure ratio, E_s/P , where E_s is expressed as the quotient of the time-averaged sheath potential and the sheath thickness. In addition, the proportionality constant obtained by fitting the model to the data gives a physically reasonable estimate of the ion-neutral elastic-scattering cross section.

Previous workers have presented more elegant treatments of ion motion at both low and high (>2 V/cm-torr) electric field to pressure ratios, but were concerned only with the fully-developed energy distribution in dc fields. Wannier (1951, 1953) utilized a recursive method to obtain analytical solutions of the Boltzmann equation for certain special cases, such as equal ion and neutral masses. More recently, Skullerud (1973) employed a Monte Carlo technique to investigate the effects of ion-neutral mass ratio and scattering behavior on ion transport. It was found that the ion drift velocity is proportional to the ratio of the electric field to the collision frequency in the low field limit, and the ion drift energy is

proportional to (electric field)/(collision frequency) in the high field limit. In each of these treatments, the time between ion-neutral collisions was assumed to be constant.

In the sheath of a glow discharge, several complications make such rigorous approaches less tenable. First, the electric field is not time-invariant; the sheath field oscillates at the plasma excitation frequency. Excitation frequency effects on maximum ion energy have been investigated for a low pressure Cl_2 discharge (Bruce, 1981b). At low frequencies (<1 MHz) and low pressures ion transport across the sheath occurs in a fraction of a power cycle (in the absence of scattering collisions), and the maximum ion energy is approximately equal to the peak applied voltage. Maximum ion energies are considerably lower at high (>3 MHz) frequency, where the sheath transit encompasses several rf power cycles. Another complication is the effect of space charge on the sheath electric fields. The ion and electron densities are not constant with distance from the electrode, causing the electric field to vary with position.

In the following derivation of the mean ion bombardment energy, we neglect charge exchange or ion-molecule reactions in the sheath, as well as the aforementioned effects of ac excitation and space-charge perturbation of the electric field. Symmetric charge-exchange cross sections are about the same size as elastic scattering cross sections for simple ions (Cramer, 1957; 1958; 1959), and asymmetric charge-exchange cross sections are much smaller. Also, symmetric collisions will be rare in these plasmas, as discussed later.

In addition, no allowance for ion composition changes with plasma conditions is made. The major ions in a $\text{CF}_3\text{Cl}/\text{Ar}$ discharge are generally CF_3^+ and CF_2Cl^+ , as observed by mass spectrometry in this and other studies (d'Agostino *et al.*, 1982), although many other ions are present. I also assume that ions diffuse to the sheath/bulk plasma interface with kinetic energy thermalized to the temperature of the neutrals. In 13.56 MHz plasma etching discharges, the excitation frequency is higher than the ionic plasma frequency ($\sim 3\text{MHz}$), so ions do not respond to the ac fields. Since dc electric fields in the plasma bulk are small, ions gain little energy between collisions with neutrals, and the assumption of thermalization is reasonable. Finally, only elastic ion-neutral collisions are accounted for, between which a constant mean free path is assumed.

Given these assumptions we now model ion transport through the sheath. Ions entering the sheath are accelerated toward the electrode by the high electric field. At high excitation frequency (13.56 MHz in this case), where sheath transit occurs over several rf cycles, ions which traverse the sheath without suffering collisions have energy $E_+ \approx qV_s$. Those undergoing collisions have energies lower than qV_s , the energy determined by the number and nature of the collision events. In an elastic collision, the maximum energy transferred from an incident ion of mass m_+ to a target neutral of mass m_0 (which is essentially motionless relative to the fast ion) is (Chapman, 1980)

$$\Delta E/E_+ = \frac{4m_+m_0}{(m_+ + m_0)^2} \cos^2 \beta_i , \quad (4.6.1-1)$$

where ΔE is the energy transferred, E_+ refers to the energy of the incident ion prior to collision, and β_i is the angle between the line of centers at collision and the incident ion velocity vector. Hard-sphere collision scattering is isotropic with respect to the center of mass. However, the ion (and therefore the center of mass) is directed toward the electrode by the electric field, so the angular distribution of the scattering is directed along the field. The average angle between the electric field and the ion velocity vector after collision is given the symbol β_f . For m_+/m_0 between 0.5 and 1.0, β_f varies between $\pi/4$ and $\pi/6$ (Wannier, 1953). Consequently, the velocity component of the ion normal to the field is about half of the field-directed velocity, meaning that a considerable fraction of the ion's kinetic energy is randomized in direction. In subsequent calculations, β_f is assumed to be $\pi/6$.

Collisions involving either argon neutrals or argon ions may be neglected without significant error. Collisions with argon neutrals are unimportant because the argon mole fractions are low and argon is smaller in cross-section than CF_3Cl , causing scattering events of ions with argon neutrals in the sheaths to be much less frequent than collisions with CF_3Cl . Argon ions are ignored because few Ar^+ ions bombard the surface; since the ionization potential of argon is much higher than that of CF_3Cl , argon is not appreciably ionized in the

sheath by asymmetric charge exchange with energetic ions. Also, little Ar^+ is created in the discharge by electron-impact processes; experimentally, very little Ar^+ is seen by mass spectrometry. To be completely correct we must establish appropriately weighted averages for ion mass, neutral mass, and scattering cross section. The simple weighting process used here includes only the CF_3Cl mole fraction γ in the neutral gas number density expression. Because argon concentrations were low this had no effect on the model's ability to represent the data. Therefore, argon dilution effects are not considered. However, for greater Ar concentrations I expect that composition would become important.

Since CF_3^+ and CF_2Cl^+ are the primary ions, I assume that the masses of the incident ion and the target neutral are approximately equal. Consequently, the average energy loss during an elastic collision is $\Delta E/E_+ = 0.5$; i.e., the post-collision ion has, on average, about one-half of its pre-collision energy. Although the mass ratio m_+/m_0 does influence the energy transfer, the effect is not large for ratios of order unity. For example, if $m_+/m_0 = 1/3$ (corresponding to, for example, a $\text{CF}^+/\text{CF}_3\text{Cl}$ collision) the average fractional ion energy loss is 0.375, assuming elastic hard-sphere scattering.

Consider the flight of an ion through a sheath of thickness d_s in which the sheath electric field is $E_s = V_s/d_s$. Assume that the ion travels exactly one mean free path λ_+ between collisions, of which $\lambda_+ \cos\beta_f$ is directed along the electric-field line normal to the electrode surface; this correction factor allows for the two-

dimensional nature of the ion motion. Define λ_E as this field-directed component of the mean free path. After travelling a distance λ_E along the field, the ion suffers an elastic collision and transfers half its energy to a neutral. This sequence is repeated as the ion is accelerated by the field and loses energy upon collision, until the ion strikes the electrode. The mean ion energy following j such collisions is

$$\bar{E}_+ = (1-0.5^j) q\lambda_+V_s/d_s \cos\beta_f , \quad (4.6.1-2)$$

which converges rapidly to the steady-state result, where the energy loss per collision balances the energy gained from the field between scattering events,

$$\bar{E}_+ = q\lambda_+V_s/d_s \cos\beta_f , \quad (4.6.1-3)$$

$$= q\lambda_E V_s/d_s = qV_s/\eta . \quad (4.6.1-4)$$

The number of collisions in the sheath, η , is defined by the ratio of sheath thickness d_s to the field-directed mean free path λ_E , and varied from about 2 to 25 over the range of conditions examined. The rapid convergence is demonstrated in that eqns. (4.6.1-2) and (4.6.1-3) compare within 12% for $j \geq 3$. The rate of convergence is relatively insensitive to the energy loss per collision; using as an example the mass ratio $m_+/m_0=1/3$, only 5 collisions are required to converge within 6%. Note that the entire range of possible elastic collision events (e.g., varying collision angle) has not been considered in this argument. The average ion energies calculated should not be significantly affected by this. However, the model cannot account for the distribution of ion energies due to the heterogeneity of the series of scattering events.

The sheath thickness is determined from the impedance model (through the sheath capacitance) by assuming that the sheath is a parallel-plate capacitor bounded by the electrode and the bulk plasma,

$$d_s = \epsilon A / C_s , \quad (4.6.1-5)$$

where A is the electrode area, C_s is the sheath capacitance, and ϵ is the permittivity of free space. The mean free path is expressed as

$$\lambda_+ = 1/N\sigma_+ = P_0/N_0P\sigma_+ , \quad (4.6.1-6)$$

where N is the neutral gas number density, σ_+ is the ion-neutral collision cross-section, and N_0 is the gas number density at pressure P_0 (arbitrarily chosen as 1 torr) and temperature 350 K (often assumed to be typical of glow discharges). Combining equations (4.6.1-3) through (4.6.1-6) yields

$$\bar{E}_+ = \left[\frac{qP_0 \cos \beta_f}{\epsilon AN_0 \sigma_+} \right] \frac{V_s C_s}{P} . \quad (4.6.1-7)$$

Equation (4.6.1-7) can be expressed solely in terms of externally-measurable plasma variables since the product $V_s C_s$ is simply related to the discharge current $|I|$ and the angular excitation frequency ω (see section 3.3.2),

$$\bar{E}_+ = K_E |I| / \omega P . \quad (4.6.1-8)$$

The predictive power of the model is illustrated in Fig. 4-18, in which experimentally determined \bar{E}_+ for CF_3Cl/Ar discharges are plotted against the quantity $|I|/\omega P$. The Fig. 4-18 data span a wide range of pressures (0.2-0.8 torr), power densities (0.1-0.8 W/cm^2),

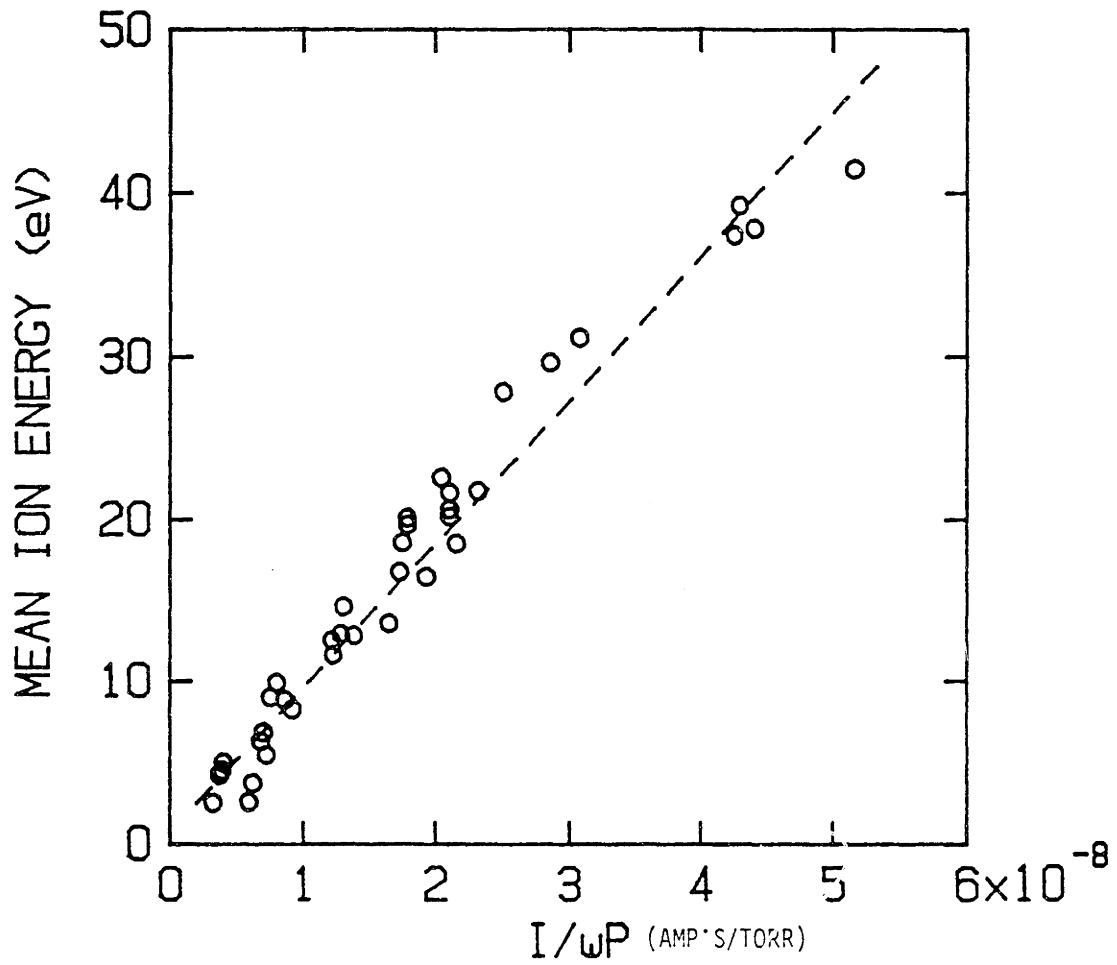


Figure 4-18: Sheath transport model prediction ($I/\omega P$) vs. measured mean ion energy (eV) in CF_3Cl discharges.

compositions (5-30% Ar in CF_3Cl), and electrode spacings (1.5-3.0 cm), as presented in Table 4-3. The data are well described (correlation coefficient of 0.96) by the line of slope 8.8×10^8 torr-volt and intercept zero, corresponding to a collision cross-section of about 3×10^{-15} cm^2 . The standard error between the model and the data is only 2 eV. Assuming hard-sphere ion-neutral interactions, and using an estimated Lennard-Jones diameter of 4.7 Å as an approximation of the diameters of both CF_3Cl and the ions (Reid et al., 1977), a collision cross-section σ_+ of 7×10^{-15} cm^2 is obtained, corresponding to a K_E of about 4×10^8 torr-volt. Since the CF_3^+ ion is smaller than CF_3Cl and the effective cross-section of high energy ion-molecule collisions is less than the Lennard-Jones potential would predict, the actual collision cross section should be smaller. For example, typical σ_+ are on the order of 5×10^{-15} cm^2 (McDaniel and Mason, 1973), in good agreement with the experimental result. Of course, a higher plasma temperature would result in a lower neutral density, and consequently increase the elastic-scattering cross section required for the same observed K_E . In fact, gas rotational temperatures of 400-600K have been measured in CF_3Cl discharges (Richards, 1986). Using 500 K as the temperature gives a cross section of 4.5×10^{-15} cm^2 .

At pressures less than 0.2 torr the model predictions are about 20% higher than the experimental result. One plausible explanation is that the sheath voltage predicted by the impedance model is too high. The plasma potential will decrease at lower pressures due to the expansion, and observed loss of containment, of the discharge with

the increased electron mobility. The entire chamber serves as the effective ground electrode and most of the applied voltage is dropped across the sheath of the smaller powered electrode (Koenig and Maissel, 1970). Also, the expected number of collisions in these low pressure sheaths is on the order of 1-2; the assumptions leading to eqn. (4.6.1-9) are not valid in this case.

The results of the sheath transport model analysis for CF_3Br discharges are shown in Fig. 4-19. Note that although the data is fairly well described by the model the mean error of the model is larger than in the CF_3Cl case. One possible explanation is the tremendous variation in mean ion mass with plasma conditions for CF_3Br plasmas (see section 4.5). It should also be noted that the mean number of sheath ion-neutral collisions in CF_3Br plasmas was lower than in CF_3Cl plasmas. Therefore, at low pressures, the ion energy distribution is not expected to be fully developed.

A similar approach to modeling ion energies was examined previously (Zarowin, 1984). The improvements offered by the present model are threefold. First, the sheath electric field is determined from the sheath voltage and capacitance, both of which are obtained by impedance analysis. In the previous work the sheath electric field was assumed proportional to the square root of the power input, implying both that the bulk plasma is field-free and also that the discharge current and voltage each vary as the square root of power. Neither assumption is borne out by observation (the voltage remains relatively constant as the power input is increased in a CF_3Cl plasma,

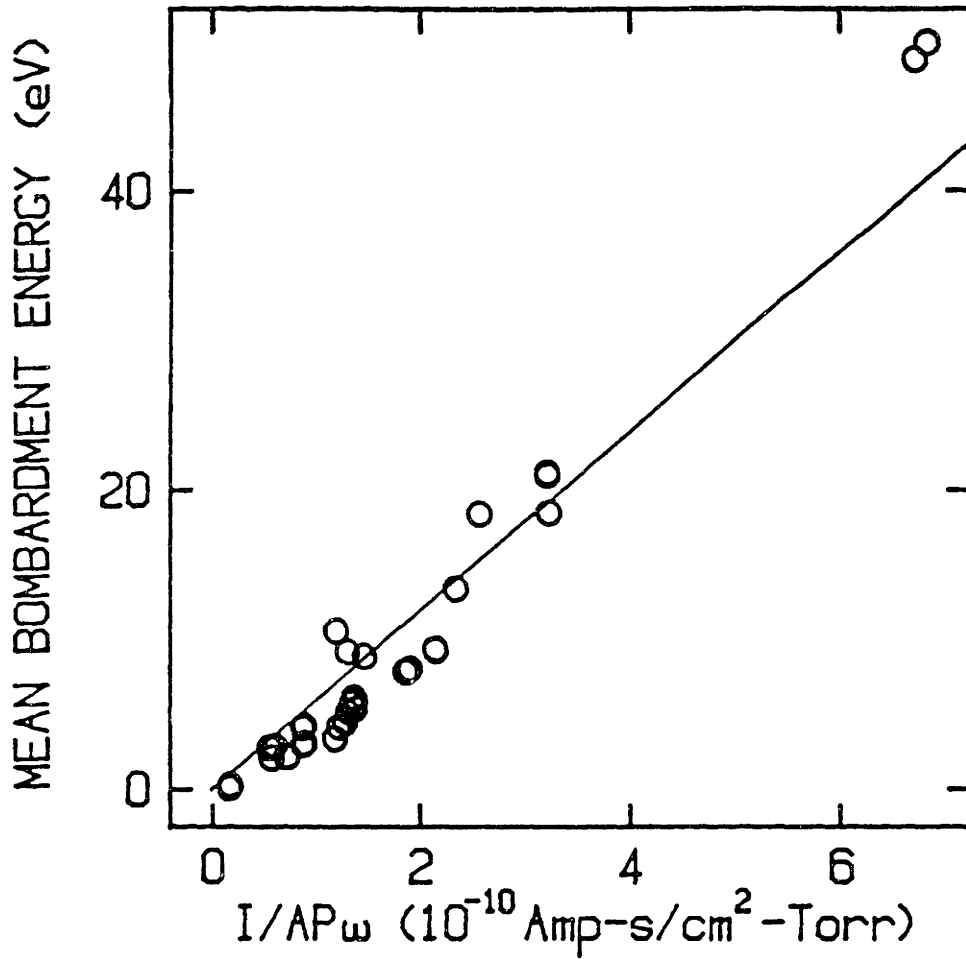


Figure 4-19: Sheath transport model prediction ($|I|/\omega P$) vs. measured mean ion bombardment energy (eV) in CF_3Br discharges.

and the impedance model predicts a significant voltage drop across the bulk). Another practical concern is that the actual power input to the plasma may be significantly (20%) less than the power measured with the power meter, since some power may be dissipated in the matching network. The present model also predicts the effect of frequency on ion energy, at least for high frequencies (Thompson et al., 1986a). Also, gas composition effects are accounted for by the discharge current, and this model can be used to describe ion energies in many gases. An electronegative gas presents a higher resistance, and therefore a lower current flows in CF_3Cl (for a given applied voltage) than, for example, in argon. In addition, the present model offers a reasonable prediction of the proportionality constant between the ion energy and the sheath electric field to pressure ratio.

In conclusion, the impedance/sheath transport model provides a reliable estimate of both mean ion energy and ion energy distribution in CF_3Cl and CF_3Br discharges. This method is also successful in modeling ion bombardment energies in SF_6 discharges (Thompson et al., 1986a). Extension of the technique to other symmetric plasma reactors is expected to yield good results. It is possible that asymmetric systems may also be treated, although the impedance model must be modified to account for the voltage distribution dependence on electrode area ratio. The asymmetric electrode case has not been examined here because the voltage distribution between electrodes of unequal area is not well established; the dependence of sheath

potential on electrode area has been reported as first order (Coburn and Kay, 1972) as well as fourth order (Koenig and Maissel, 1970). In addition, the uniform electron density assumption must be removed in the asymmetric case because the plasma potential will be a strong function of position in the asymmetric system.

The model is not valid at low excitation frequencies ($\ll 3$ MHz), where the impedance model fails because of the significant coupling of the positive ions with the rf field. Also, the large sheath potentials observed at low frequencies, combined with the relatively long rf cycle times, allow ions to traverse the sheath in a fraction of a cycle. The resulting ion bombardment energies may be quite different than those observed in the high frequency case described here. In addition, the sheath transport model cannot be applied to reactive ion etching (RIE) systems, in which ions suffer few collisions in the sheath due to the very low pressures used.

4.6.2 Ion Directionality

Another potentially important ion property is the directionality of an ion striking the surface, i.e., the angle between the ion velocity vector and the electric field vector. For collisionless sheaths in which the electric field points along the macroscopic surface normal (and ignoring the small Coulombic interactions between ions at low density), every ion will strike the surface along the surface normal. However, ion-neutral interactions influence the directionality of the ions by transferring field-directed energy to the transverse direction (i.e., parallel to the macroscopic surface).

The effect of ion-neutral interactions on the ion directionality depends, of course, on the type of interaction. For example, if a charge-exchange event occurs the new ion will have only its random thermal velocity as a transverse component. Although Zarowin (1984) addressed the problem of ion directionality under elastic scattering conditions, he did not correctly account for energy coupling between the field-directed and transverse-field directions by elastic scattering. However, Zarowin's model is reasonable if only charge-exchange interactions are allowed; the ion directionality can then be studied through his definition of an "ion energy ellipsoid", the shape of which is determined by the relative velocities in the field and transverse directions. Under this assumption the mean angle between ion velocity and electric field decreases with increasing E_s/P (i.e.,

the field-directed velocity and transverse velocity are independent). Ion energy and ion angle distributions for charge-exchange collisions in rf plasma sheaths have been modeled by Monte Carlo techniques (Kushner, 1986; Fisher et al., 1986).

Should an elastic collision occur, a fraction (dependent on the scattering angle) of the field-directed energy will couple into the transverse direction. In this case the mean ion angle is independent of E_s/P because the distribution of energy between the field-directed and transverse directions is determined only by the scattering angle (Wannier, 1953); this angle is about 25° for equal masses of ions and neutrals. Monte Carlo simulations have substantiated the theoretical work of Wannier (Skullerud, 1973), and suggest that a steady-state ion angle distribution is reached within 3-5 elastic collisions (Fisher et al., 1986).

4.7 ION-ASSISTED ETCHING

As noted previously, energetic ion bombardment greatly enhances the rate of plasma etching processes. Some of the basic studies from which this conclusion was drawn are discussed in this section. The dependence of ion-assisted etching on ion flux, energy, and surface coverage is also examined. A brief discussion of the mechanisms responsible for the enhancement is given.

Perhaps the most elegant demonstration of energetic ion bombardment effects on etching was performed in a UHV system by Coburn and Winters (1979b). In this experiment the etching rate of silicon was studied for three cases: (i) exposure to a beam of neutral gas (e.g., XeF_2), (ii) exposure to a beam of argon ions (Ar^+) and (iii) simultaneous exposure to both neutral and ion beams. The etching rate under simultaneous bombardment of ions and neutrals is much higher than the sum of the neutral (case i) and ion (case ii) etching rates. A synergy between the ion and neutral etching mechanisms is clearly present; the effect of the ion bombardment is chemical in nature, not purely physical.

The silicon surface must be at least partially covered with active etchant species in order for etching to occur. Experimentally, the etching rate under ion bombardment increases with etchant background pressure (Mayer et al., 1981). Also, Coburn and Winters (1979b) observed a slow decay of the etching rate as active etchant surface coverage decreased.

The observed etch yields (i.e., the number of silicon atoms released per incident ion) provide further evidence that the enhancement is not purely physical. Etch yields of up to 25 atoms/ion were measured for coincident XeF_2/Ar^+ bombardment (Gerlach-Meyer et al., 1981). For molecular chlorine etching of silicon, etch yields from 2 (Gerlach-Meyer et al., 1981) to 4 (Krueger and Ruoff, 1985) have been reported.

In contrast, sputtering yields of inert ions are as low as 0.01 at low (<100 eV) ion energies. Sputtering, a purely physical process, occurs by momentum transfer from the incident ion to surface atoms. Clearly, sputtering alone cannot account for the ion enhancement. Modulated beam studies of Si etching are not consistent with the sputtering mechanism; a surface time delay is observed (McNevin and Becker, 1985; Rossen and Sawin, 1986).

Reactive ions such as F^+ and CF_x^+ give etch yields of about 0.1 atoms/ion (Miyake et al., 1982), presumably by supplying reactant to the surface as they dissociate on impact (Coburn et al., 1977). The importance of the ion chemistry has also been demonstrated by Mayer et al. (1981) and by Mayer and Barker (1982), wherein the reactive-ion etch yields increased in the order $\text{Ar}^+ < \text{CF}_2^+ < \text{CF}_3^+$.

The mechanism of ion-enhanced etching is not completely understood, although several models have been proposed (e.g., Gerlach-Meyer, 1981; McNevin and Becker, 1985). Among the possible explanations for ion enhancement are local surface heating, lowering of the etching reaction activation energy via the breaking of near-surface bonds, and increased desorption of reactive intermediates.

The ion-enhanced etching rate is seen to be linear in the ion flux (Mayer and Barker, 1982; McNevin and Becker, 1984), at least at low ion energies on clean surfaces. The etching rate decreased with increasing flux, presumably due to the decreased surface coverage caused by more rapid desorption of the etchant species. The surface coverage and ion-assisted etching rate in a UHV system have been modeled for the chlorine etching of silicon (Barker et al., 1983).

The ion-enhanced etching yield also increases with ion energy (Us, 1985) above a certain threshold energy. Recent experimental results (Rossen and Sawin, 1986) indicate that below 200 eV, etch yield of silicon with Cl_2/Ar^+ increases sublinearly with ion energy.

CHAPTER 5 -ACTIVE ETCHANT CONCENTRATIONS

In this chapter the measurement of active etchant concentrations in etching plasmas is discussed. In CF_3Cl and CF_3Br discharges, $\cdot Cl$ and $\cdot Br$ are the active etchant species, respectively (Mogab and Levinstein, 1980). A correct description of the surface chemistry must also involve radical species such as $\cdot F$ and $\cdot CF_3$, which are known to adsorb on silicon (Winters, 1978). The relative concentrations of both $\cdot Cl$ and $\cdot Br$ may be monitored by optical emission actinometry, which was found to be accurate by calibration with atomic chlorine concentrations determined by infrared laser absorption.

Several models for the production and loss of atomic chlorine in CF_3Cl discharges are presented. Using literature values for kinetic rate constants where available (and estimating rate constants where unavailable), these models provide good quantitative prediction of atomic chlorine concentrations.

5.1 EXPERIMENTAL MEASUREMENTS

5.1.1 Laser Infrared Absorption in CF_3Cl

Diode laser infrared absorption (LIA) is a useful in situ technique for measuring absolute concentrations of atomic species in glow discharges. The application of LIA to atomic chlorine detection

has been demonstrated previously (Wormhoudt et al., 1983; Wormhoudt et al., 1986; Richards, 1986) - the details of the spectroscopic measurements and the calibration procedures are presented in these publications. The equipment used in these previous studies was also used in the present work.

The laser is tuned to the 882.36 cm^{-1} infrared transition between the $^2P_{3/2}$ and $^2P_{1/2}$ spin orbit levels of ^35Cl . The laser beam is passed through the plasma at about the midpoint between the electrodes, using an interelectrode spacing of 3 cm. A White cell is used to reflect the beam such that it passes through the plasma 20 times before exiting to the photodetector. The intensity of the beam is attenuated by absorption; the attenuation is related to the concentration of ground-state atomic chlorine via Beer's law. Etalon fringes caused by self-interference of the laser beam are subtracted from the absorption signal.

The ground-state concentration is converted to a total concentration, $[\text{Cl}]$, by assuming Boltzmann population of states at the gas temperature. The temperature was determined by analyzing the rotational band structure of a small amount of N_2 added to the CF_3Cl plasma (Porter and Harshbarger, 1979; Oshima, 1978). The rotational temperature of N_2 in a CF_3Cl plasma is between 400 and 600 K, increasing with power input (Richards, 1986). The plasma temperature was assumed constant at 500 K for the $[\text{Cl}]$ calculations; only a 5% error in $[\text{Cl}]$ results from this assumption.

LIA experiments were performed with blank electrodes (assembly B). ^35Cl concentrations of $3 \times 10^{13} \text{ cm}^{-3}$ to $3 \times 10^{14} \text{ cm}^{-3}$ were observed; the results are presented in Table 5-1. The atomic chlorine concentration

[Cl] in a CF_3Cl discharge is linearly dependent on both power input and pressure, as seen in Figs. 5-1 and 5-2, respectively. Because of the linear dependence of [Cl] on pressure, the atomic chlorine mole fraction is nearly independent of pressure, see Fig. 5-3.

Atomic chlorine concentrations in CF_3Cl discharges decrease with decreasing plasma excitation frequency, decrease with inert gas dilution, and decrease with increasing flow rate.

Most surprisingly, the atomic chlorine concentration increases during etching; i.e., [Cl] is higher when a 4-inch wafer is being etched than when two blank electrodes are exposed to the plasma. As discussed in detail later in this chapter, this is presumably due to the more rapid loss of atomic chlorine by recombination on the electrode surfaces than by the etching reaction.

5.1.2 Argon Optical Emission Actinometry

A more commonly used technique for monitoring concentrations of reactive species in plasma etching discharges is optical emission actinometry. By introducing a small amount of an inert gas such as argon, the relative emission intensities from 1Cl and from Ar are compared. Assuming that Ar and 1Cl have similar excitation cross sections, the emission intensity ratio I_{Cl}/I_{Ar} is proportional to $[Cl]/[Ar]$. Since argon is an inert, [Ar] is known from the flow rates, pressure, and gas temperature. Therefore, [Cl] is known within a proportionality constant which is a function of electron energy distribution, electron density, and excitation cross section.

Table 5-1
Atomic Chlorine Concentrations in CF₃Cl Discharges,
as Measured by Laser Infrared Absorption Spectroscopy.
d=3 cm, blank electrodes (assembly B).

RUN ID	POWER INPUT (watts)	PRESSURE (torr)	FREQUENCY (MHz)	FLOW RATE (sccm)	X _{Ar}	[Cl] (cm ⁻³)
FIR_1	19.3	0.2	13.56	6	.07	3.5x10 ¹³
FIR_2	37.2	0.2	"	"	"	5.2x10 ¹³
FIR_3	55.6	0.2	"	"	"	7.0x10 ¹³
FIR_4	72.2	0.2	"	"	"	7.8x10 ¹³
FIR_5	19.3	0.4	"	"	"	8.7x10 ¹³
FIR_6	38.5	0.4	"	"	"	1.1x10 ¹⁴
FIR_7	57.3	0.4	"	"	"	1.2x10 ¹⁴
FIR_8	75.3	0.4	"	"	"	1.4x10 ¹⁴
FIR_9	21.4	0.6	"	"	"	1.3x10 ¹⁴
FIR_10	39.7	0.6	"	"	"	1.6x10 ¹⁴
FIR_11	60.1	0.6	"	"	"	1.8x10 ¹⁴
FIR_12	77.1	0.6	"	"	"	2.0x10 ¹⁴
FIR_13	20.5	0.8	"	"	"	1.8x10 ¹⁴
FIR_14	39.8	0.8	"	"	"	2.1x10 ¹⁴
FIR_15	60.6	0.8	"	"	"	2.3x10 ¹⁴
FIR_16	80.8	0.8	"	"	"	2.5x10 ¹⁴
FIR_17	38.1	0.5	13.56	"	"	1.5x10 ¹⁴
FIR_18	37.9	"	10	"	"	1.2x10 ¹⁴
FIR_19	41.3	"	5	"	"	9.2x10 ¹³
FIR_20	49.8	"	2	"	"	6.5x10 ¹³
FIR_21	36.3	0.5	13.56	"	.15	1.3x10 ¹⁴
FIR_22	32.4	"	"	"	.25	1.1x10 ¹⁴
FIR_23	38.0	0.5	13.56	12	.07	1.2x10 ¹⁴
FIR_24	38.9	0.5	13.56	12*	.07	1.5x10 ¹⁴

*Full wafer present, n⁺-polysilicon

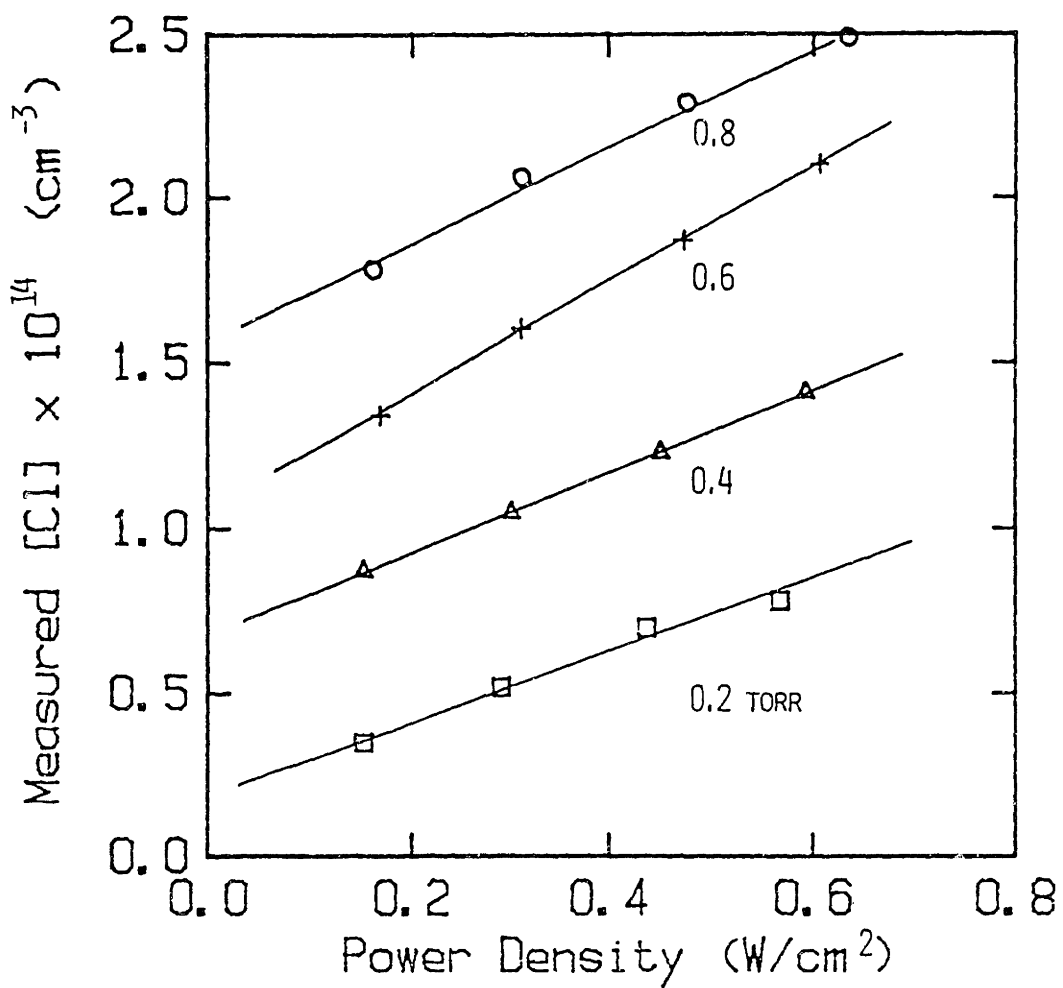


Figure 5-1: Dependence of atomic chlorine concentration $[Cl]$ (cm^{-3}) in CF_2Cl discharges on power density (watts/cm^2), several pressures.

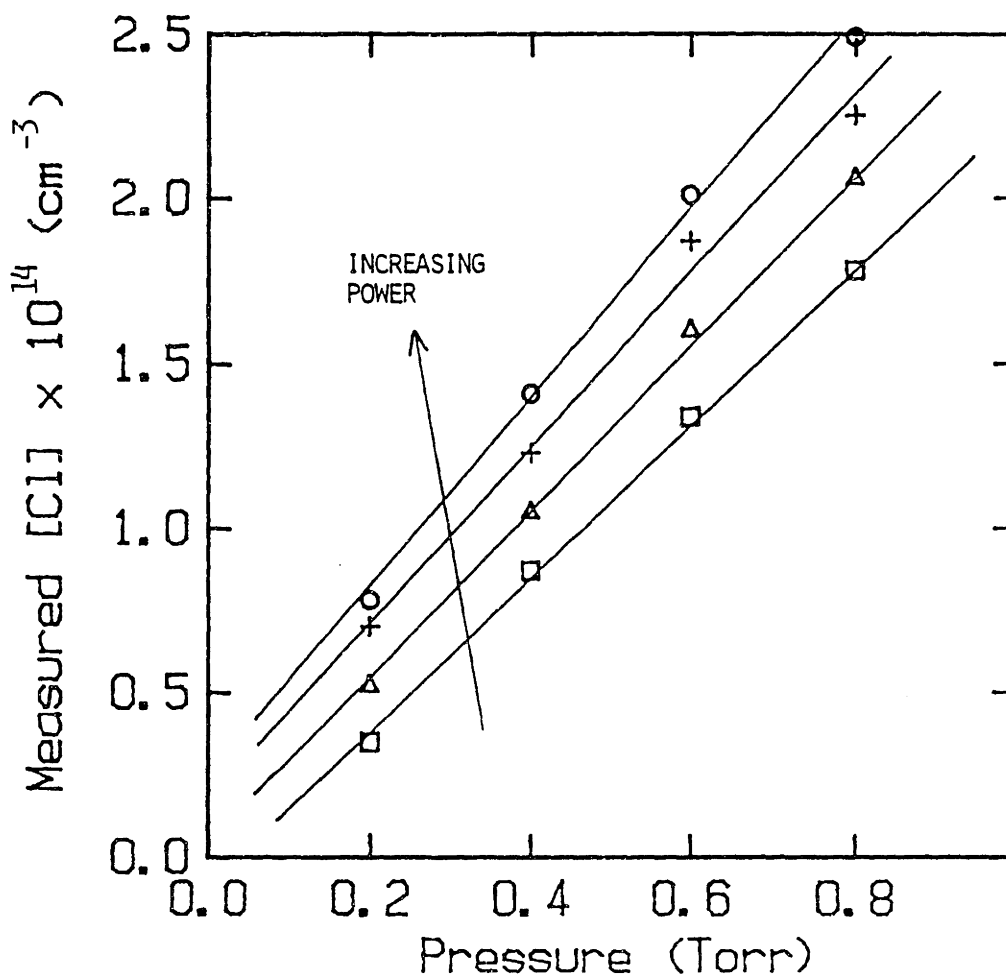


Figure 5-2: Dependence of atomic chlorine concentration [Cl] (cm^{-3}) in CF_3Cl discharges on pressure (torr), several powers.

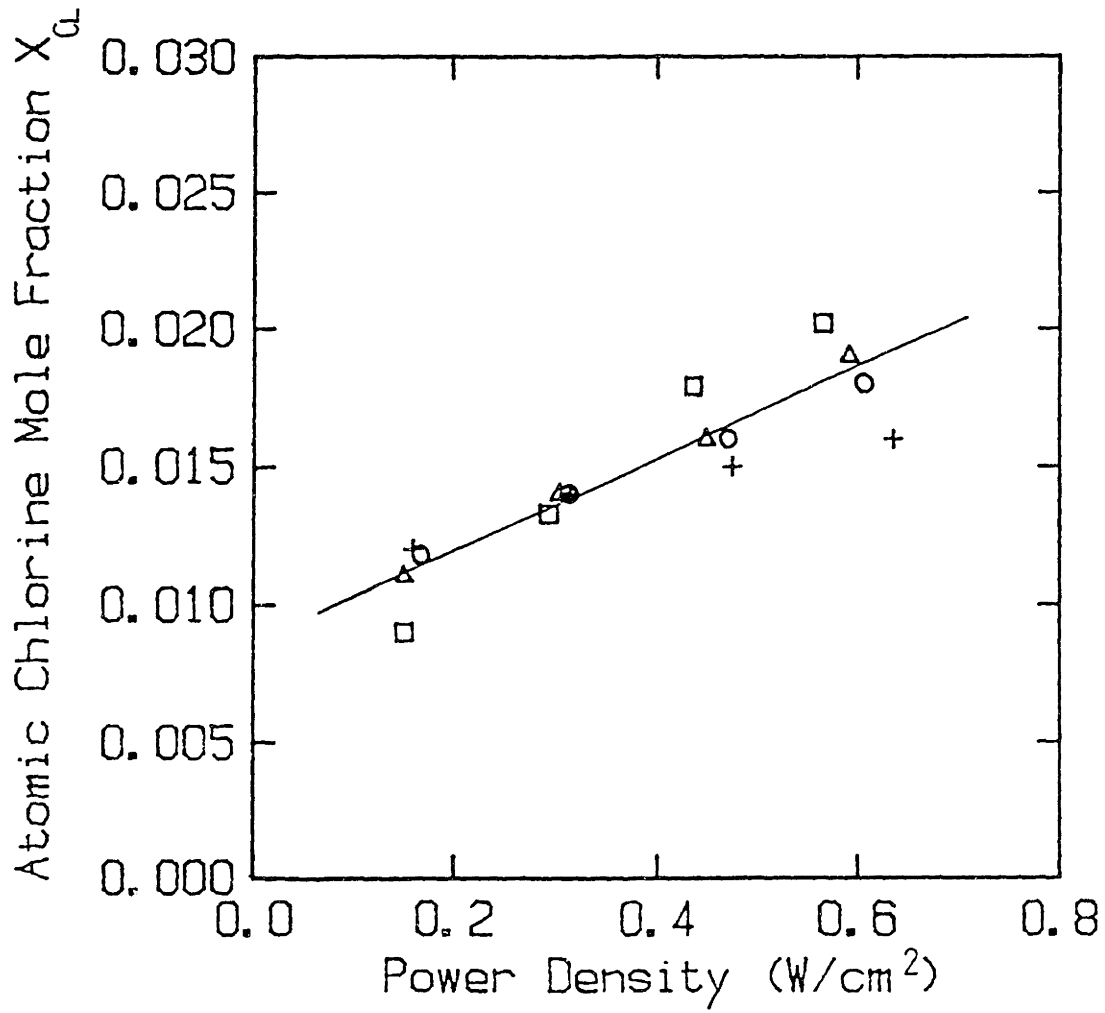


Figure 5-3: Dependence of atomic chlorine mole fraction X_{Cl} in CF_2Cl discharges on power density ($watts/cm^2$), several pressures.

Actinometry is only valid when photoemission from both ^1Cl and Ar occurs only from excited states created by single-event electron-impact excitation of ground-state species. If excited states of either species are formed by other processes, actinometry will give erroneous predictions, as in the case of Cl_2 discharges (Richards et al., 1986).

The emission lines chosen for this study were the 837.6 nm line of atomic chlorine (which results from the decay of an excited state with threshold energy 10.4 eV) and the 842.5 nm line of argon (which results from a 13.1 eV excitation). Other combinations of lines were also examined; the peak intensity ratio was independent of the choice of line. This suggests that either the excitation cross sections of ^1Cl and Ar are similar or that the electron energy distribution does not vary significantly with plasma conditions.

The actinometry data shown in Table 5-2 were taken during the LIA experiments of Table 5-1. The actinometric ratio $[\text{Ar}](I_{\text{Cl}}/I_{\text{Ar}})$ is plotted against the LIA measurements in Fig. 5-4; power input, pressure, gas composition, and flow rate were varied over this set of experiments. The relationship is linear with a zero intercept; as discussed in detail elsewhere (Richards et al., 1986), both of these requirements must be met if actinometry is to provide accurate prediction of concentration variations with process conditions. Consequently, it appears that actinometry is a valid technique for CF_3Cl discharges.

Table 5-2
Actinometric Ratio for Atomic Chlorine Concentration Measurements,
Experimental set FIR.

RUN ID	Intensity Ratio I_{Cl}/I_{Ar}	Actinometric Ratio $PX_{Ar}I_{Cl}/I_{Ar}$
FIR_1	1.80	0.028
FIR_2	1.83	0.029
FIR_3	1.94	0.030
FIR_4	1.97	0.030
FIR_5	1.34	0.041
FIR_6	1.78	0.057
FIR_7	2.28	0.073
FIR_8	2.46	0.079
FIR_9	1.36	0.065
FIR_10	1.77	0.084
FIR_11	2.22	0.107
FIR_12	2.45	0.116
FIR_13	1.23	0.078
FIR_14	1.53	0.097
FIR_15	1.86	0.118
FIR_16	2.18	0.138
FIR_17	1.82	0.064
FIR_18	1.64	0.057
FIR_19	1.30	0.046
FIR_20	1.18	0.041
FIR_21	0.54	0.041
FIR_22	0.23	0.028
FIR_23	1.77	0.062
FIR_24	2.16	0.076

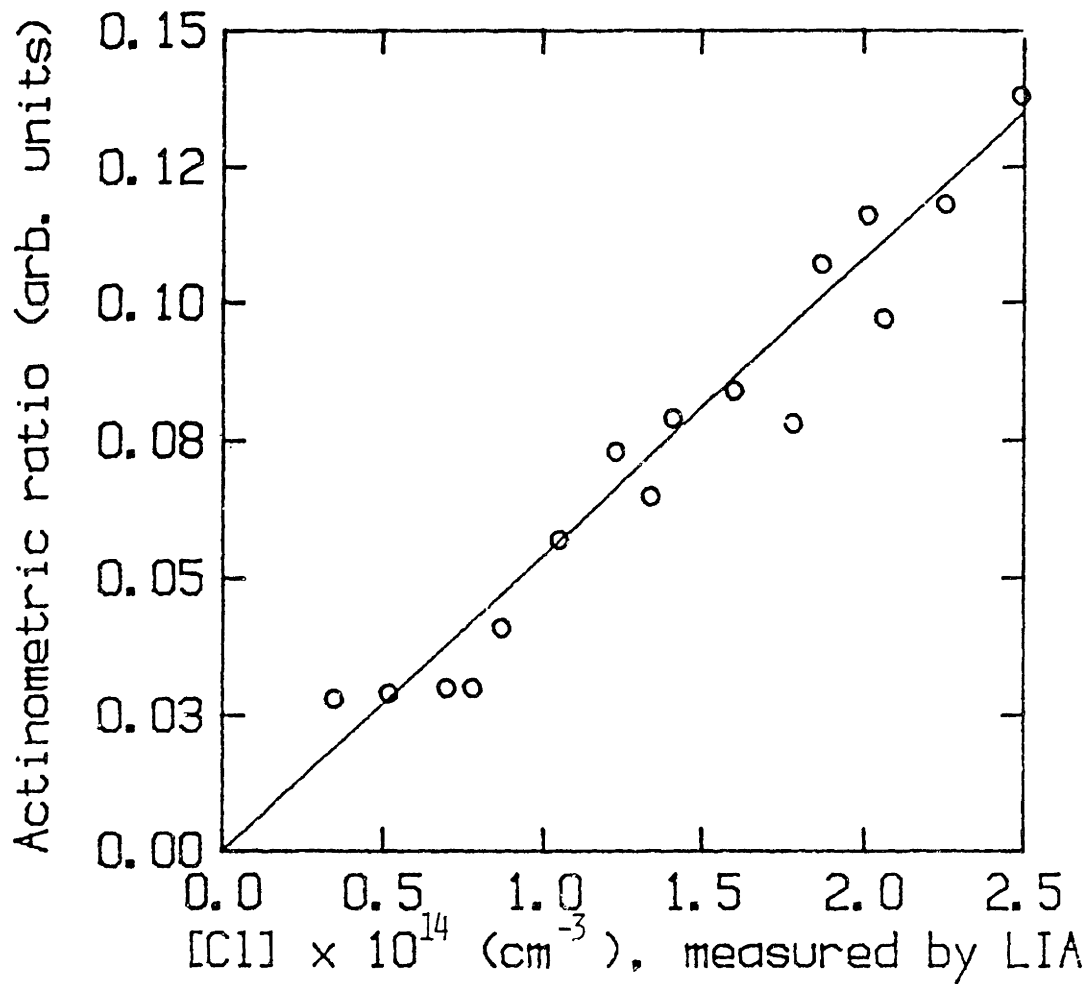


Figure 5-4: Actinometric ratio $[\text{Ar}]I_{\text{Cl}}/I_{\text{Ar}}$ vs. measured atomic chlorine concentration $[\text{Cl}]$ (cm^{-3}) in CF_3Cl discharges.

There are several possible explanations for the scatter in the data of Fig. 5-4: (i) variations in absorption path length due to plasma expansion may influence the LIA density results, (ii) the emission intensity measurements contain some noise, and (iii) the optical emission results are not spatially resolved, so axial concentration gradients will be detected only by LIA - actinometry gives only a spatial-average intensity.

5.1.3 $\cdot\text{Br}$ Emission from CF_3Br Plasmas

Due to its success in the CF_3Cl system, optical emission actinometry was also used for the CF_3Br system. A high resolution optical emission scan of a CF_3Br plasma is shown in Fig. 5-5; the peaks used for actinometry are identified in the figure. The 793.9 nm $\cdot\text{Br}$ line has an excitation threshold of 10.97 eV, while the 763.5 nm Ar line has a 13.17 eV threshold. Assuming that excited-state atomic bromine is formed only by electron-impact with ground-state $\cdot\text{Br}$ (as in CF_3Cl), the proximity of these thresholds suggests that actinometry should be valid in the CF_3Br system.

Optical emission data for experimental design BR are presented in Table 5-3. Fig. 5-6 is a contour plot of the actinometric ratio $[\text{Ar}](I_{\text{Br}}/I_{\text{Ar}})$ as a function of power density and pressure. The actinometric ratio increases very slightly with increasing power input, increases slightly with flow rate, and increases linearly with pressure. Therefore, the $\cdot\text{Br}$ mole fraction X_{Br} is nearly constant over the range of plasma conditions studied here.

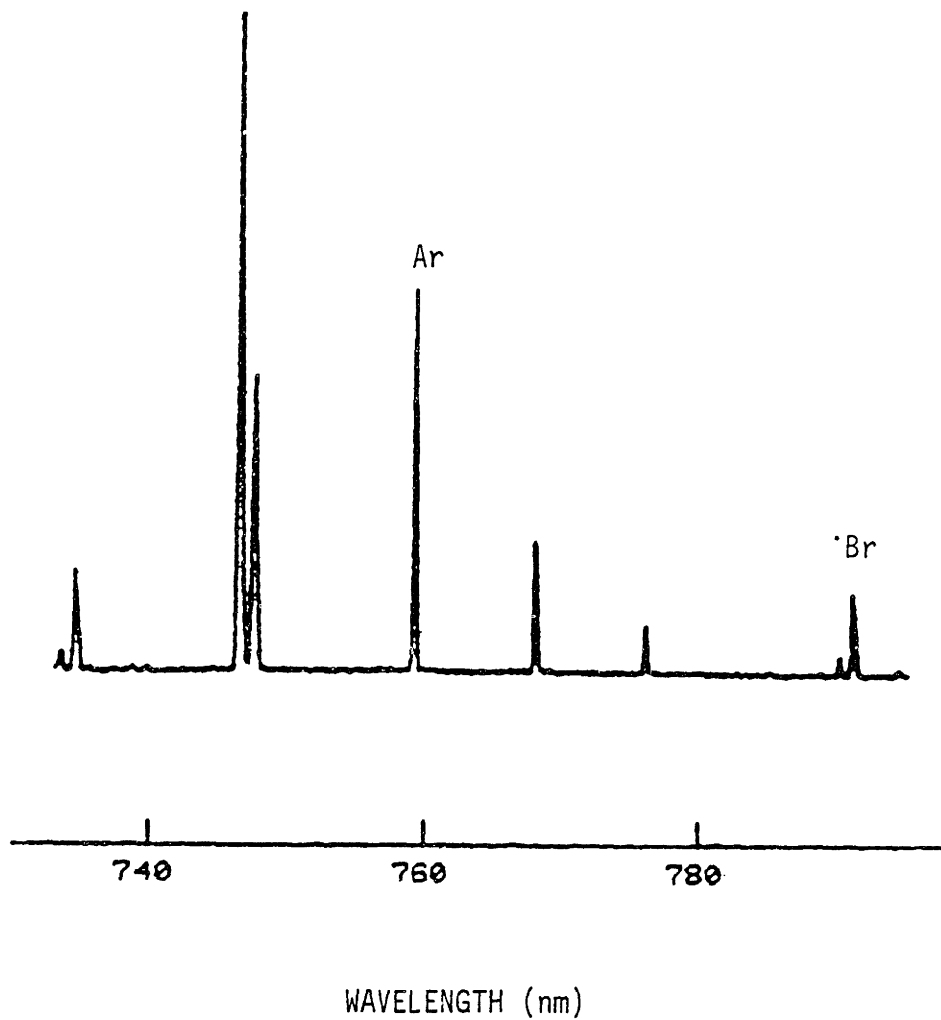


Figure 5-5: High resolution optical emission scan of CF_3Br discharge. Peaks used for actinometry are identified.

Table 5-3
Actinometric Ratio during CF₄Br Etching of Polysilicon,
Experimental Design BR.

RUN ID	Actinometric Ratio $PX_{Ar} I_{Br} / I_{Ar}$
BR_1	8.40×10^{-3}
BR_2	7.85×10^{-3}
BR_3	7.01×10^{-3}
BR_4	9.90×10^{-3}
BR_5	6.15×10^{-3}
BR_6	8.76×10^{-3}
BR_7	6.09×10^{-3}
BR_8	7.94×10^{-3}
BR_9	7.81×10^{-3}
BR_10	7.36×10^{-3}
BR_11	6.94×10^{-3}
BR_12	1.01×10^{-2}
BR_13	1.01×10^{-2}
BR_14	5.45×10^{-3}
BR_15	5.89×10^{-3}
BR_16	2.28×10^{-2}
BR_17	1.10×10^{-2}
BR_18	7.36×10^{-3}
BR_19	3.56×10^{-3}
BR_20	9.50×10^{-3}
BR_21	8.40×10^{-3}
BR_22	7.11×10^{-3}
BR_23	2.93×10^{-3}
BR_24	7.77×10^{-3}
BR_25	7.55×10^{-3}
BR_26	9.96×10^{-3}
BR_27	4.49×10^{-3}
BR_28	7.68×10^{-3}
BR_29	7.69×10^{-3}
BR_30	7.56×10^{-3}
BR_31	7.26×10^{-3}
BR_32	1.10×10^{-2}
BR_33	4.88×10^{-3}
BR_34	7.59×10^{-3}
BR_35	7.62×10^{-3}

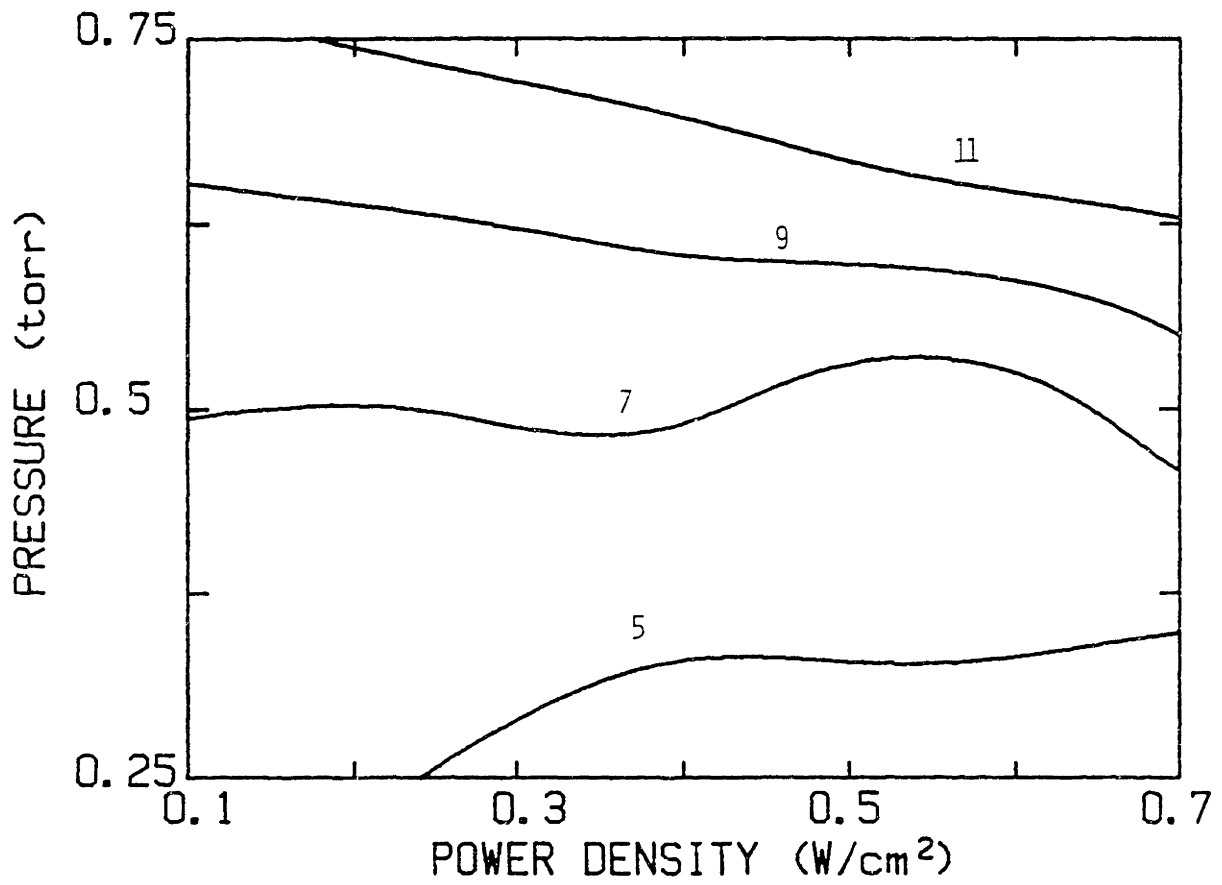


Figure 5-6: Contour plot of actinometric ratio $[Ar]I_{Pr}/I_{Ar}$ in CF_3Br discharges, vs. power density (watts/cm²) and pressure (torr), $Q=15$ sccm.

5.2 MODELS FOR ATOMIC CHLORINE CONCENTRATION IN CF_3Cl

One of the primary goals of this work is to identify the major reaction channels which account for the plasma chemistry responsible for etching. Although large reaction sets for plasma processes have been proposed (e.g., Edelson and Flamm, 1985; Plumb and Ryan, 1986), there is insufficient kinetic information available to justify such an endeavor at this point. Consequently, a simpler approach was taken in this thesis. Atomic chlorine concentration profiles can be modeled by writing mass balances for the production and loss of important species in the discharge. In this chapter several such models are derived - these models provide reasonable quantitative prediction of $[Cl]$.

5.2.1 Electron-Impact Dissociation of CF_3Cl

The unique plasma chemistry of a glow discharge is a result of electron-molecule interactions. In particular, the dissociation of CF_3Cl via electron impact is an important channel for $\cdot Cl$ production. Atomic chlorine could conceivably be liberated from the parent molecule by a number of mechanisms: direct dissociation to $\cdot CF_3$ and $\cdot Cl$, dissociation to $\cdot CF_2Cl$ followed by further dissociation to $\cdot CF_2$ and $\cdot Cl$, ionization to form CF_3^+ and $\cdot Cl$, dissociative attachment to give CF_3^- and Cl^- , etc. However, the first of these should have the highest rate for two reasons: (i) the C-Cl bond is weaker than the C-F bond, so two-step dissociation through $\cdot CF_2Cl$ is unlikely, (ii) positive and negative ion densities are only 10^9 cm^{-3} , so ionization and attachment processes are slow.

The rate of CF_3Cl dissociation upon electron impact is not available in the literature. However, the homolog CF_4 has been studied extensively (e.g., Winters and Inokuti, 1982) - dissociation cross sections are available as functions of electron energy. By integrating over an electron energy distribution, a total dissociation cross section can be obtained. This constant is termed the formation rate constant here, since $\cdot\text{Cl}$ is formed by this reaction.

The formation rate constant k_F is written as (Bell, 1974)

$$k_F = \int_0^{\infty} (\varepsilon/2m_e)^{1/2} f(\varepsilon) \sigma_D(\varepsilon) d\varepsilon , \quad (5.2.1-1)$$

where ε is the electron energy, m_e is the electron mass, $f(\varepsilon)$ is the electron energy distribution, and $\sigma_D(\varepsilon)$ is the dissociation cross section. Adapting the data of Winters and Inokuti to a mathematical form, σ_D is written

$$\sigma_D = 0 \quad \text{for } \varepsilon < 12.5 \text{ eV} ,$$

$$\sigma_D = 1.4 \times 10^{-17} (\varepsilon - 12.5) \quad \text{for } \varepsilon \geq 12.5 \text{ eV} , \quad (5.2.1-2)$$

where ε is expressed in eV and σ_D is expressed in cm^2 .

The electron energy distribution is not known, however, it has been suggested that $f(\epsilon)$ is between Maxwellian and Druyvestyn (Bisschops and de Hoog, 1985) in the range of E_p/P of interest. Given a mean energy $\langle \epsilon \rangle$ and the distribution, eqns. (5.2.1-1) and (5.2.1-2) are used to calculate the rate constant,

$$k_{F,D} = \frac{3.2 \times 10^{-7}}{\langle \epsilon \rangle} \int_{12.5}^{\infty} \epsilon(\epsilon - 12.5) \exp[-0.55\epsilon^2 / \langle \epsilon \rangle^2] d\epsilon, \quad (5.2.1-3)$$

for a Druyvestyn distribution and

$$k_{F,M} = \frac{6.4 \times 10^{-7}}{\langle \epsilon \rangle} \int_{12.5}^{\infty} \epsilon(\epsilon - 12.5) \exp[-1.5\epsilon / \langle \epsilon \rangle] d\epsilon \quad (5.2.1-4)$$

for a Maxwellian distribution. The rate constants of eqns. (5.2.1-3) and (5.2.1-4) have units of cm^3/s . Numerical integration of these equations gives the rate constants shown in Fig. 5-7. The large difference between the two curves occurs because the Druyvestyn distribution drops off much more quickly in the high-energy tail than does the Maxwellian distribution. Recall that for mean electron energies of about 5 eV, most of the electrons have energy below the 12.5 eV threshold for CF_4 dissociation.

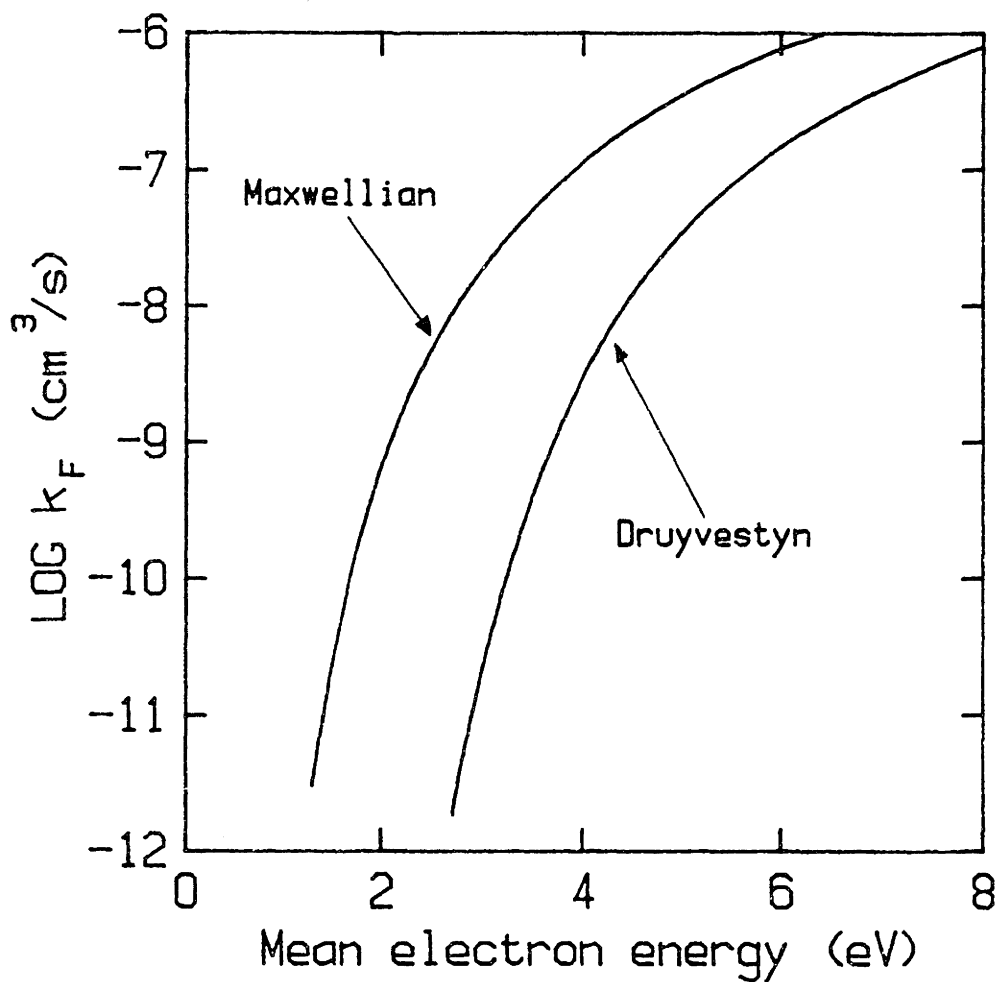


Figure 5-7: CF_3Cl electron-impact dissociation rate constant k_F (cm^3/s) calculated for both Maxwellian and Druyvestyn electron energy distributions, mean electron energy $\langle e \rangle = 4$ eV.

At $\langle \epsilon \rangle = 4$ eV, the mean energy measured in the Langmuir probe experiments of Surendra *et al.* (1986), the rate constants obtained by this method are $k_{F,D} = 2.9 \times 10^{-9}$ cm³/s and $k_{F,M} = 1.1 \times 10^{-7}$ cm³/s. If the dissociation threshold of CF₃Cl is used as the lower bound in eqns. (5.2.1-3) and (5.2.1-4), the calculated values are $k_{F,D} = 6.5 \times 10^{-9}$ cm³/s and $k_{F,M} = 1.5 \times 10^{-7}$ cm³/s.

The rate constant obtained using the Born-Bethe approximation is $k_F = 6 \times 10^{-10}$ cm⁻³ (Yokozeki, 1984). However, this approximation is only valid for energies well above the threshold. In CF₄ dissociation, the electron energy must be about 500 eV before measured dissociation rates reach the Bethe asymptote (Winters and Inokuti, 1982). The Born-Bethe approximation is useful as an independent estimate of the lower bound for k_F .

5.2.2 Simplistic Steady-State Analyses

Atomic chlorine concentrations are estimated by assuming that $\cdot\text{Cl}$ is formed by direct electron-impact dissociation of the CF₃Cl parent molecule and lost by first-order processes. It is also assumed that CF₃Cl is not appreciably dissociated by the plasma (as supported by the low values of X_{Cl} presented in section 5.1), that the reactor is well mixed, and that little $\cdot\text{Cl}$ is lost by flow out of the reactor. The contention that CF₃Cl is not appreciably consumed is also supported by noting that only 0.5 sccm of CF₃Cl is required to supply enough chlorine to produce SiCl₄ at a polysilicon etching rate of 1000 Å/min. Also, the neutral composition of the plasma as detected by

mass spectrometry is indistinguishable from the CF_3Cl cracking pattern with the exception of very small signals attributable to species formed by recombination processes (e.g., Cl_2 and $\text{C}_2\text{F}_x\text{Cl}_y$).

Incorporating these assumptions, a transient mass balance on atomic chlorine yields,

$$d[\text{Cl}]/dt = k_F[e^-][\text{CF}_3\text{Cl}] - k_L[\text{Cl}] \quad (5.2.2-1)$$

where k_F and k_L are total rate constants for etchant formation and loss, respectively. Note that the CF_3Cl concentration could also be expressed in terms of its input partial pressure $P\gamma/RT$, where R is the gas constant and T is the plasma neutral temperature. The implicit assumptions here are that temperature is constant and that CF_3Cl is not significantly depleted by decomposition reactions. The first and second terms on the right side of eqn. (5.2.2-1) are the rates of etchant production (dependent on both the electron and parent concentrations, second order overall) and loss. As k_F is assumed to be a constant, the model does not allow for electron temperature effects on the dissociation rate. Electron temperature estimation requires detailed information about the electric fields in the discharge, as well as basic data regarding electron mobility in CF_3Cl . Since electron temperatures in CF_3Cl discharges are fairly independent of plasma conditions (Table 3-7), the assumption of constant k_F is appropriate.

The form of the loss expression depends on the particular discharge: temperature, reactor geometry, film being etched, electrode material, etc. In this model the loss is assumed to be first order in reactant concentration, consistent with consumption by polysilicon etching, by surface recombination, or by a combination of these loss processes. Solving eqn. (5.2.2-1) at steady-state, the atomic chlorine concentration is

$$[Cl] = (k_F/RTk_L) [e^-]P\gamma . \quad (5.2.2-2)$$

The predictions of eqn. (5.2.2-2) are compared with the LIA data in Fig. 5-8. The fit is unsatisfying - the scatter of the data with respect to the model is quite large.

In a second kinetic model it is postulated not only that the primary loss mechanism for atomic chlorine is recombination at the electrode surfaces, but that the loss rate is governed by the diffusion of atomic chlorine to the electrodes. The implications of this assumption are clear if $[Cl]$ is assumed to vary only in the axial direction z between the electrodes, i.e., the system is one-dimensional. Assume that $\cdot Cl$ is created in the bulk, that the loss rate at the upper electrode is rapid with respect to transport by diffusion, and that the lower electrode covered by the wafer is essentially inert (i.e., recombination on the electrode surfaces is much faster than etching). Because the upper electrode is a sink for $\cdot Cl$, a concentration gradient exists between the bulk and the surface. The flux to the surface, and hence the $\cdot Cl$ loss rate, is approximately

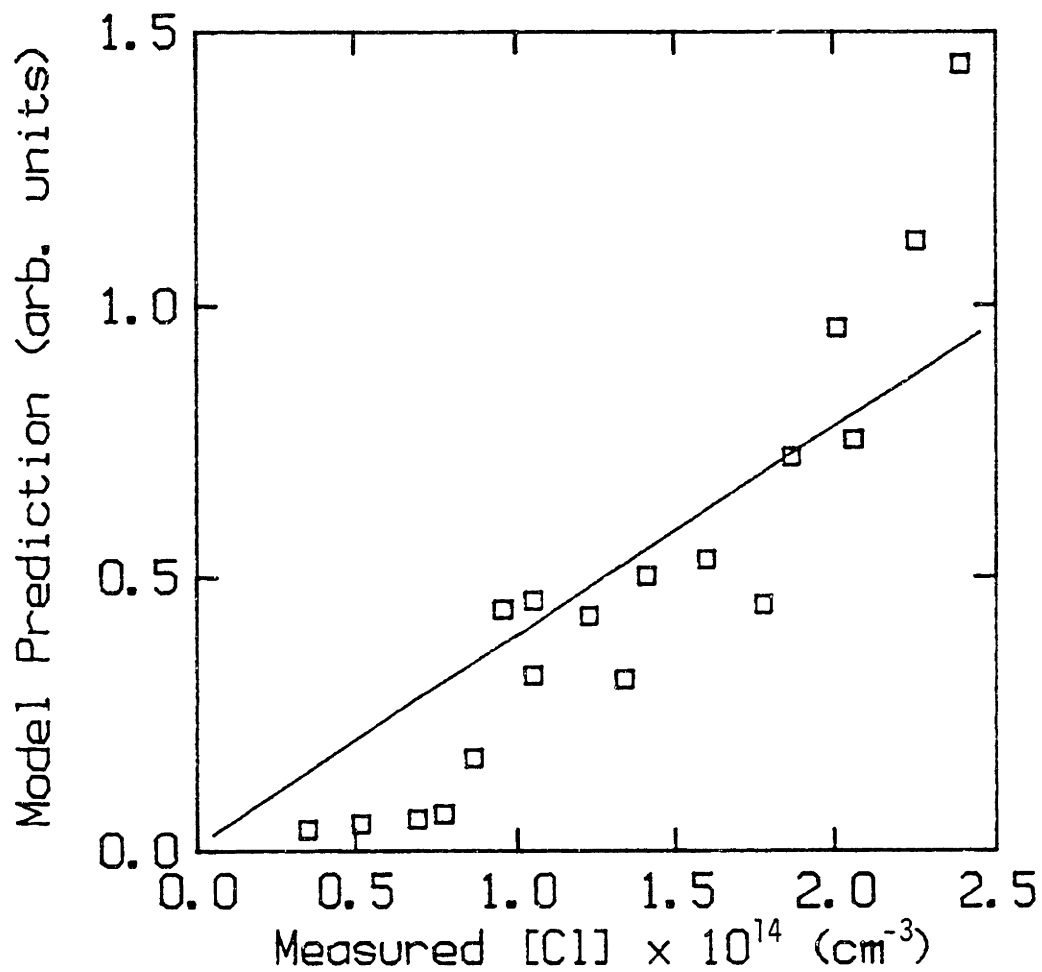


Figure 5-8: Eqn. (5.2.2-2) model prediction of atomic chlorine concentration [Cl] (cm⁻³) vs. experimental measurement. Model assumptions: second-order formation, first-order surface loss of atomic chlorine.

$$N_{Cl} \sim -D \Delta[Cl]/\Delta z \sim D[Cl]/d , \quad (5.2.2-3)$$

where N_{Cl} is the flux, D is the mass diffusivity of Cl in CF_3Cl , and d is the electrode spacing.

Note that eqn. (5.2.2-3) is not strictly correct; it is assumed in the derivation of the flux expression that atomic chlorine is generated only in one plane of the discharge, and that the concentration gradient is constant with z . In reality, chlorine production is a function of both position and time. In addition, recombination on the wafer surface has been ignored. However, eqn. (5.2.2-3) provides the proper functionality and an order of magnitude estimate of the atomic chlorine loss rate.

The transient mass balance on atomic chlorine (per unit volume) is then

$$\begin{aligned} d[Cl]/dt &\sim k_F[e^-][CF_3Cl] - D[Cl]A/Vd , \\ &\sim k_F[e^-]P\gamma/RT - D[Cl]/d^2 , \end{aligned} \quad (5.2.2-4)$$

where the loss rate is set equal to the diffusive flux to the upper electrode. In eqn. (5.2.2-4), A is the total electrode surface area and V is the effective reactor volume (the volume contained between the electrodes). The surface area to volume ratio of the cylindrical reactor gives the square dependence of the loss term on electrode spacing.

Diffusivity in gases is inversely proportional to pressure (Hirschfelder et al., 1964),

$$D = D_0 P_0 / P . \quad (5.2.2-5)$$

Combining the previous two equations, steady-state solution of eqn. (5.2.2-4) yields

$$[Cl] = k' [e^-] P^2 \gamma . \quad (5.2.2-6)$$

where k' is a lumped constant. In Fig. 5-9, the predictions of eqn. (5.2.2-6) are compared with experiment. Although the fit is better than for the reaction-limited model, the results are not convincing.

There is considerable evidence to support the assertion that recombination at the electrodes is the dominant $\cdot Cl$ loss process. Loss by gas flow out of the effective reactor should not be important because the residence time (~ 1 sec) is much longer than the relaxation time for both the diffusion to the electrodes (1-10 msec) and the expected characteristic times for radical recombination. Diffusive losses from the sides of the reactor will be most important at large electrode spacings, short reactor residence times, and slow recombination rates, where there is a high probability that molecules can pass out of the reactor without being consumed. We cannot

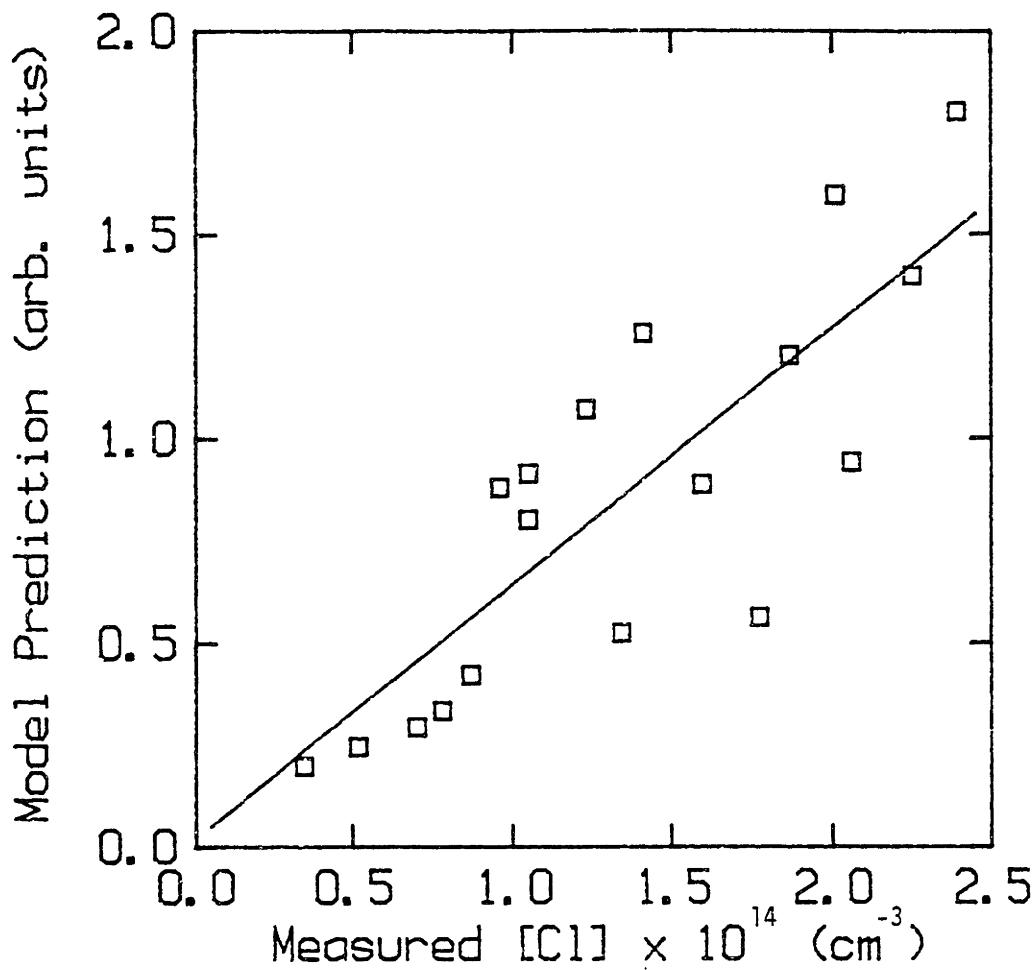


Figure 5-9: Eqn. (5.2.2-6) model prediction of atomic chlorine concentration [Cl] (cm⁻³) vs. experimental measurement. Model assumptions: second-order formation, diffusion-limited surface loss of atomic chlorine.

discount the possibility that this loss process is important without knowing the surface recombination rates. However, the dependence of the loss rate on pressure, for a fixed flow rate, is the same as for diffusion-limited surface recombination; only the length scale is changed.

Several observations indicate that $\cdot\text{Cl}$ consumption by the etching reaction is not rapid relative to recombination at the electrodes. First, Mogab and Levinstein (1980) noted that there is no loading effect in CF_3Cl . If $\cdot\text{Cl}$ were consumed rapidly by etching $[\text{Cl}]$ would decline with increasing silicon surface area, resulting in a lower etching rate. Second, recall that in this study the etching rate increased significantly upon decreasing the powered electrode area, despite the minimal change in discharge impedance. The decrease in electrode surface area available for recombination may account for the increased etching rate. Finally, the LIA studies indicate that the atomic chlorine concentration in CF_3Cl discharges is significantly higher during etching of a full 4" polysilicon wafer than with blank electrodes (the wafer removed). Therefore, it is concluded that $\cdot\text{Cl}$ loss on stainless steel is faster than on polysilicon.

The relative importance of diffusion and surface recombination in determining the atomic chlorine loss rate is seen by comparing the respective rates, i.e., the limiting step will have a lower reaction velocity. Per unit total surface area, the recombination reaction rate is $S\bar{c}[\text{Cl}]/4$, where S is the recombination probability per surface collision and \bar{c} is the mean thermal speed of a chlorine atom at the plasma temperature. The diffusion rate is $D[\text{Cl}]/d$. Solving for the reaction probability at which the two rates are equal, we obtain

$S=4D/d\bar{c}$. At 0.5 torr, an electrode spacing of 2 cm, and a plasma neutral temperature of 500 K, the critical surface recombination probability is $S\sim 0.02$. That is, if $S\gg 0.02$ the atomic chlorine loss process is diffusion-limited. Conversely, if $S\ll 0.02$ the loss process is limited by the surface reaction. The reaction probability of $\cdot\text{Cl}$ on stainless steel is not available, however, the recombination probability of atomic oxygen on quartz (a relatively inert surface) is about 0.0002 (Greaves and Linnett, 1959). I would expect the recombination of atomic chlorine on the more catalytically active metal surfaces to be faster. However, without knowledge of the recombination rate, the rate-limiting step cannot be determined from these experiments.

Experimental evidence for diffusion limitations is also given by observations of wafer clearing patterns (section 6.1.5). At low powers and high pressures, etching is primarily chemical, as evidenced by its isotropic nature. Diffusion limitations should be most important here. The wafers clear from the sample center toward its periphery under these conditions. That is, the etching rate at the sample edges, near the electrode surface, is very slow compared to the rate in the center. Small stainless steel clips which hold the sample to the electrode also cause reduced etching rates in the neighboring area. This behavior suggests that a significant $\cdot\text{Cl}$ concentration gradient exists between the electrode and the sample center, ostensibly caused by rapid recombination on the stainless steel. At lower pressures where diffusion limitations are less important, the clearing patterns are markedly different, and the difference in etching rate between the sample center and the edge is reduced.

5.2.3 Spatially-Dependent Models

Given the body of evidence supporting electrode recombination of $\cdot\text{Cl}$ as the dominant loss mechanism, another model is proposed. The third simple model includes diffusion, but the surface recombination reaction is assumed to be second-order in atomic chlorine. The functionality of this model would be similar if atomic chlorine recombines with other surface radical species (e.g., $\cdot\text{CF}_2$) with similar concentrations. A differential mass balance on $\cdot\text{Cl}$ yields the governing differential equation for the blank electrode case,

$$D \frac{d^2[\text{Cl}]}{dz^2} + k_F[e^-][\text{CF}_2\text{Cl}] = 0, \quad (5.2.3-1)$$

with boundary conditions (i) at $z=\pm d/2$ (the electrodes), $d[\text{Cl}]/dz = k_R[\text{Cl}]^2/D$, and (ii) at $z=0$ (the centerline), $d[\text{Cl}]/dz=0$ by symmetry. The second-order surface recombination rate constant is k_R . Solving eqn. (5.2.3-1) using the specified boundary conditions gives,

$$[\text{Cl}] = k_F(d^2/4-z^2)[e^-]P^2\gamma/2RTD_0P_0 + (k_F d [e^-] P \gamma / 2RT k_R)^{0.5}, \quad (5.2.3-2)$$

Model predictions at $z=0$ are compared with the LIA data in Fig. 5-10, for a two-parameter fit (k_F and k_R). As shown, this model describes the data quite well over a range of plasma conditions. The best-fit values of k_F and k_R are $(2.35 \pm 0.9) \times 10^{-10}$ cm³/s and $(3.1 \pm 1.7) \times 10^{-12}$ cm⁴/s. The surface concentration of [Cl] is,

$$[Cl]_s = (k_F d [e^-] P \gamma / 2RT k_R)^{0.5} . \quad (5.2.3-3)$$

Note that k_F agrees well with the values calculated in subsection 5.2.1. Also, the value of k_R gives a reaction probability $S \sim 0.02$ for atomic chlorine recombination, suggesting that both diffusion and reaction are important in determining [Cl]. Comparing the two terms in eqn. (5.2.3-2) leads to the same conclusion - both diffusion and reaction are important. Of course, diffusion is more limiting at higher pressures while reaction is more important at lower pressures.

A similar derivation assuming first-order recombination provides the following expression for [Cl] at the centerline,

$$[Cl] = k_F (d/k_R + Pd^2/2D_0 P_0) [e^-] P \gamma / RT . \quad (5.2.3-4)$$

However, the fit of the experimental data to eqn. (5.2.3-4) is much poorer than for eqn. (5.2.3-2). Therefore, the first-order recombination model is not discussed further.

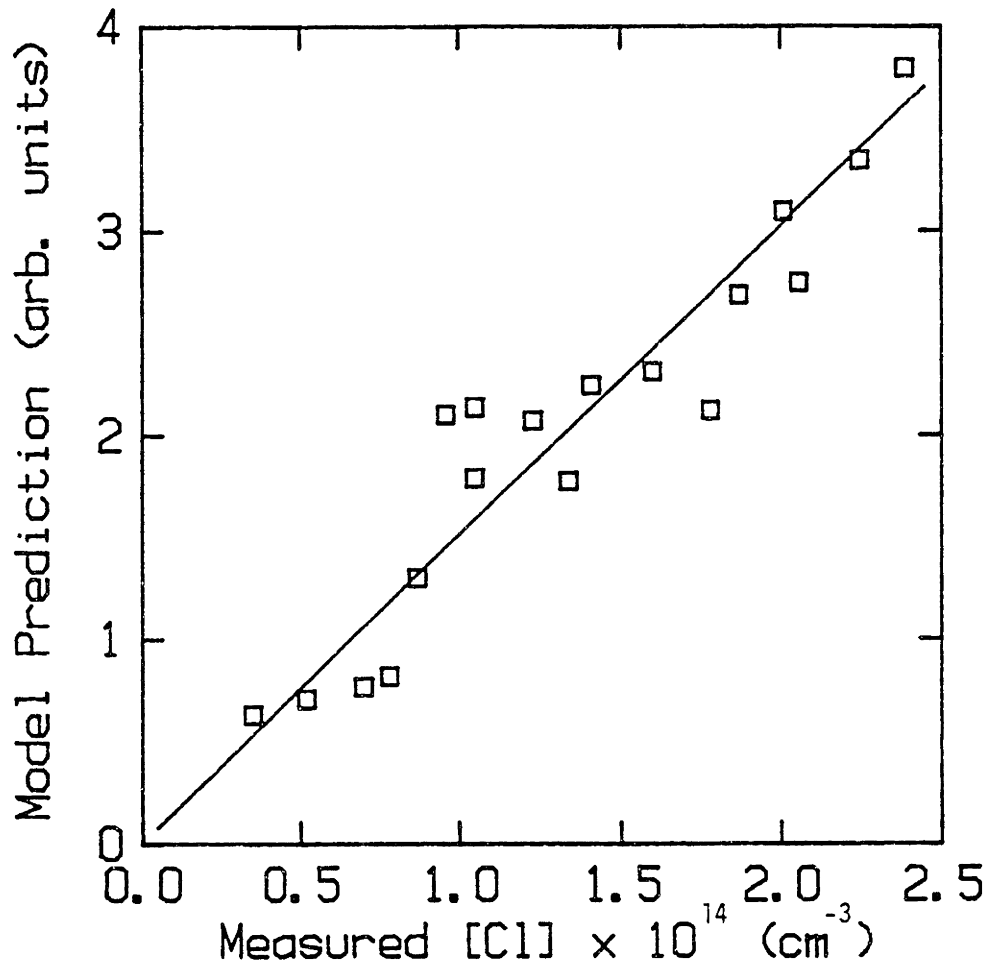


Figure 5-10: Eqn. (5.2.3-2) prediction of atomic chlorine concentration [Cl] (cm⁻³) vs. experimental measurement. Model assumptions: second-order formation, second-order recombination at the electrodes.

5.2.4 The Influence of Homogeneous Reactions

It has been assumed in previous sections that all loss processes for atomic chlorine are heterogeneous gas-surface reactions. However, at certain conditions, e.g., large electrode spacing or high pressure, gas-phase recombination reactions may be important. In this subsection a single-species model for [Cl] is presented, and the results used as a first order estimate of the relative importance of atomic chlorine loss by homogeneous and heterogeneous reactions, respectively. A somewhat more complex model involving several plasma species is then presented.

Although the chlorine-chlorine reaction is a three-body one,



and is therefore slow at low pressures, reactions with larger radicals such as $\cdot\text{CF}_2$ and $\cdot\text{CF}_3$ can occur. To properly model [Cl] as a function of position, both homogeneous and heterogeneous reactions involving all important plasma species must be considered. As a simple model of the reaction network, a small set of species could be chosen: CF_3Cl , e^- , $\cdot\text{Cl}$, $\cdot\text{CF}_2$, $\cdot\text{CF}_3$, and $\cdot\text{F}$. A reaction set involving these species is given as Table 5-4; rate constants are also presented.

Table 5-4
Reaction Set for Calculation of [Cl]

REACTION	RATE CONSTANT
$\text{CF}_3\text{Cl} + \text{e}^- \longrightarrow \text{CF}_3 + \text{Cl}$	$3 \times 10^{-9} \text{ cm}^3/\text{s}$
$\text{CF}_3 + \text{e}^- \longrightarrow \text{CF}_2 + \text{F} + \text{e}^-$	$4 \times 10^{-9} \text{ ''}$
$\text{CF}_3 + \text{F} \longrightarrow \text{CF}_4$	$1 \times 10^{-11} \text{ ''}$
$\text{CF}_3 + \text{Cl} \longrightarrow \text{CF}_3\text{Cl}$	$6 \times 10^{-12} \text{ ''}$
$\text{CF}_2 + \text{F} \longrightarrow \text{CF}_3$	$4 \times 10^{-13} \text{ ''}$
$\text{CF}_2 + \text{Cl} \longrightarrow \text{CF}_2\text{Cl}$	$4 \times 10^{-13} \text{ ''}$
$\text{CF}_2 + \text{CF}_2 \longrightarrow \text{C}_2\text{F}_4$	$4 \times 10^{-13} \text{ ''}$
$\text{CF}_3 + \text{CF}_3 \longrightarrow \text{C}_2\text{F}_6$	$5 \times 10^{-12} \text{ ''}$

As a first approximation, the atomic chlorine concentration is equal to $[\cdot\text{CF}_2] + [\cdot\text{CF}_3]$. The rationale for this assumption is that both $\cdot\text{Cl}$ and $\cdot\text{CF}_x$ are formed by electron-impact dissociation. Also, the rates of $\text{CF}_x\text{-CF}_x$ recombination reactions are not very different from those of $\cdot\text{Cl}$ recombination processes. Assuming that $\cdot\text{Cl}$ recombines only with CF_x species, a material balance on $[\text{Cl}]$ yields,

$$D \frac{\partial^2 [\text{Cl}]}{\partial z^2} + k_F [e^-] [\text{CF}_3\text{Cl}] - k_H [\text{Cl}]^2 \sim 0, \quad (5.2.3-2)$$

where k_H is the homogeneous recombination reaction rate constant. Now define the dimensionless variables

$$\theta \equiv [\text{Cl}] / [\text{CF}_3\text{Cl}]_0, \quad \text{and} \quad \xi \equiv z/d, \quad (5.2.3-3)$$

and the dimensionless groups

$$F \equiv k_F d^2 [e^-] / D, \quad \text{and} \quad L \equiv k_H d^2 [\text{CF}_3\text{Cl}]_0 / D, \quad (5.2.3-4)$$

where $[\text{CF}_3\text{Cl}]_0$ is the input concentration of the parent molecule. Assuming that CF_3Cl is not significantly dissociated in the plasma and that the electron density is spatially uniform,

$$\partial^2 \theta / \partial \xi^2 - L\theta^2 + F = 0 . \quad (5.2.3-5)$$

For the blank electrode case the boundary conditions are

$$\begin{aligned} \partial \theta / \partial \xi &= 0 && \text{at } \xi=0 , \\ \partial \theta / \partial \xi &= S\theta^2 && \text{at } \xi=\pm 1/2 , \end{aligned} \quad (5.2.3-6)$$

where $S = k_R d [CF_3Cl]_0 / D$. The dimensionless concentration θ is therefore a unique function of F, L , and S .

If a wafer is present on the lower electrode, the etching reaction must also be considered. In this case, the boundary conditions become

$$\begin{aligned} \partial \theta / \partial \xi &= E\theta && \text{at } \xi=-1/2 , \\ \partial \theta / \partial \xi &= S\theta^2 && \text{at } \xi=+1/2 , \end{aligned} \quad (5.2.3-7)$$

where E is defined as $k_E d / D$.

The differential equation was solved using finite difference techniques in combination with a shooting method. A concentration of [Cl] at the walls was estimated, and updated given the comparison of the diffusive and reactive fluxes to the opposing wall. Convergence was assumed when the net formation and loss rates agreed within 0.1%.

In Table 5-5, the rate constants used for the base case analysis of the etching system are listed and justified. The plasma conditions chosen for this simple study correspond to those used in the laser absorption experiments: 0.6 torr total pressure, power input such that $[e^-] \sim 2 \times 10^9 \text{ cm}^{-3}$, and a 3 cm electrode spacing. At these conditions, the experimentally measured [Cl] is about $2 \times 10^{14} \text{ cm}^{-3}$ at the center of the discharge, and the plasma temperature is about 500 K. The base case results are shown in Fig. 5-11. Note the steep gradient in [Cl] as the upper electrode is approached, and that the etching reaction does not consume much atomic chlorine.

Given these rate constants, about 65% of the atomic chlorine loss is due to homogeneous recombination with $\cdot\text{CF}_x$ radicals. In reality, the homogeneous loss is probably less important because $[\text{CF}_x]$ is lower than assumed here. Since the $\text{CF}_x\text{-CF}_x$ recombination reactions have been ignored, the estimate of $[\text{CF}_x]$ is too high. The remainder of the loss is due to recombination on the upper electrode. The chemical etching rate of the silicon surface is calculated to be 200 Å/min, which is a factor of 2-3 lower than observed experimentally.

The sensitivity of the model to the rate constants is examined in Figs. 5-12 to 5-15. In each of these calculations, one rate constant was varied by a factor of two from its base value. The model predictions of [Cl] are most sensitive to k_F and k_H .

Table 5-5
Rate Constants for Base Case Analysis of Eqn. (5.2.3-5)

$$k_F = 4 \times 10^{-9} \text{ cm}^3/\text{s}$$

Justification: Calculated assuming a Druyvestyn electron energy distribution with mean energy of 4 eV, using CF_4 dissociation cross-section (Winters and Inokuti, 1982).

$$k_R = 6 \times 10^{-12} \text{ cm}^3/\text{s}$$

Justification: At $[\text{Cl}] \sim 10^{14} \text{ cm}^{-3}$ and $T=500 \text{ K}$, assume a reaction probability of $S \sim 0.05$ for $\cdot\text{Cl}$ on surface.

$$k_E = 25 \text{ cm/s}$$

Justification: Assume a reaction probability of $S \sim 0.002$, in light of etching rate data. For $\cdot\text{F}$ reaction with Si (100), $k_E \sim 50 \text{ cm/s}$.

$$k_H = 1 \times 10^{-12} \text{ cm}^3/\text{s}$$

Justification: Rate constant data for $\text{CF}_x + \text{Cl}$ (Kuznetsova and Maslov, 1979).

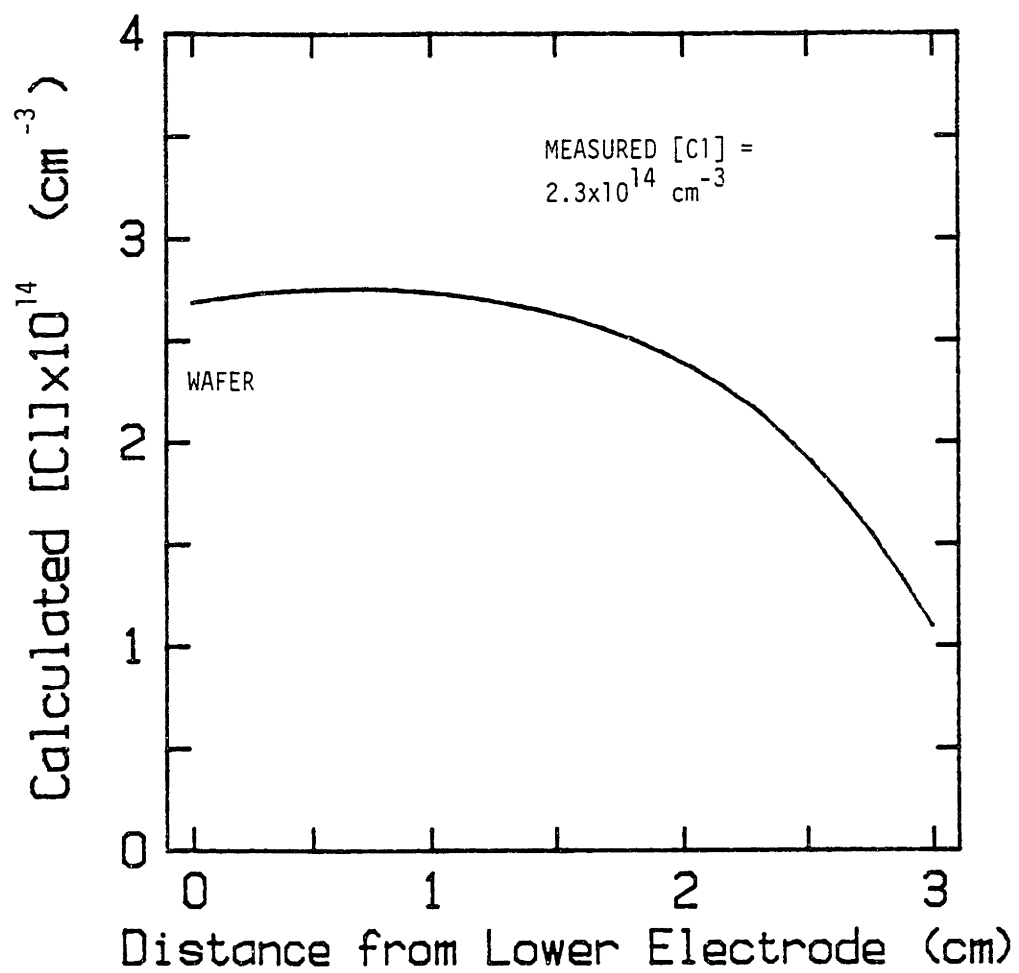


Figure 5-11: Base case analysis of atomic chlorine concentration profiles (cm^{-3}), including homogeneous reactions.

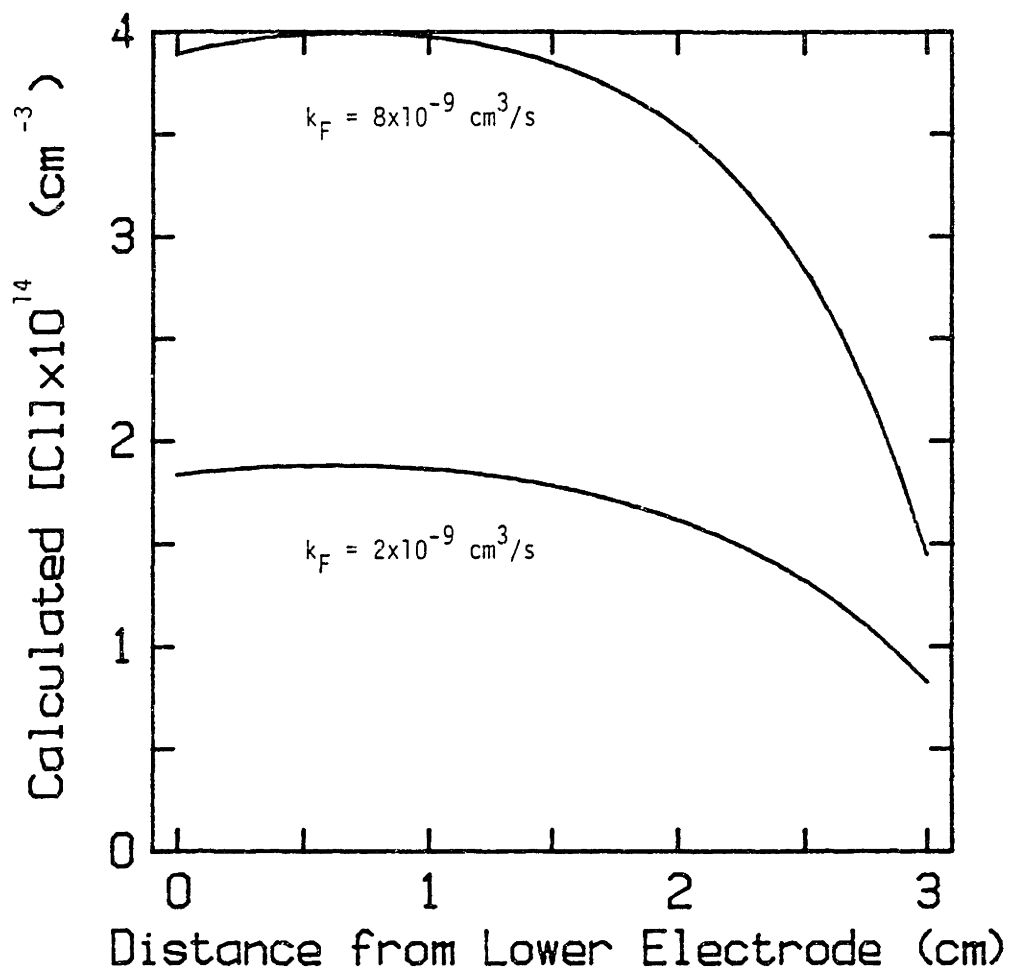


Figure 5-12: Effect of CF_3Cl dissociation rate constant k_F on predicted $[Cl]$ (cm^{-3}).

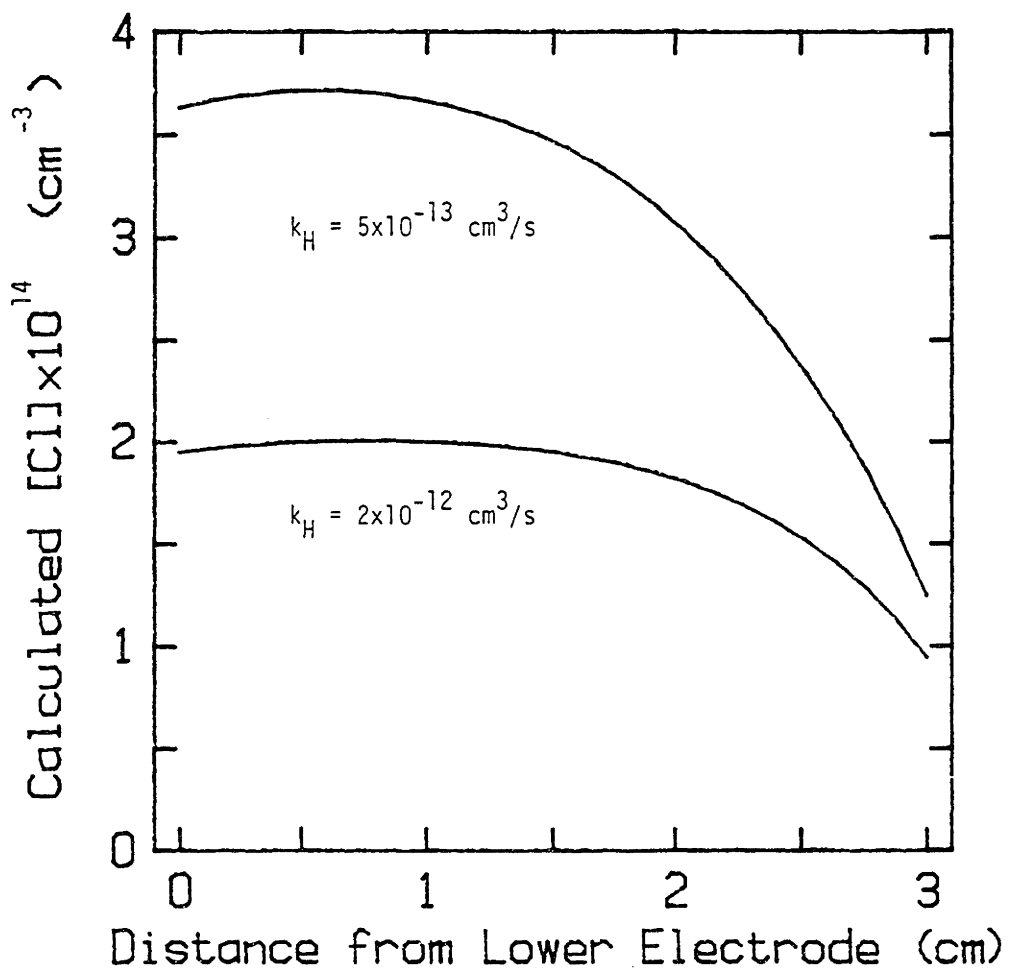


Figure 5-13: Effect of homogeneous recombination rate constant k_H on predicted $[Cl]$ (cm^{-3}).

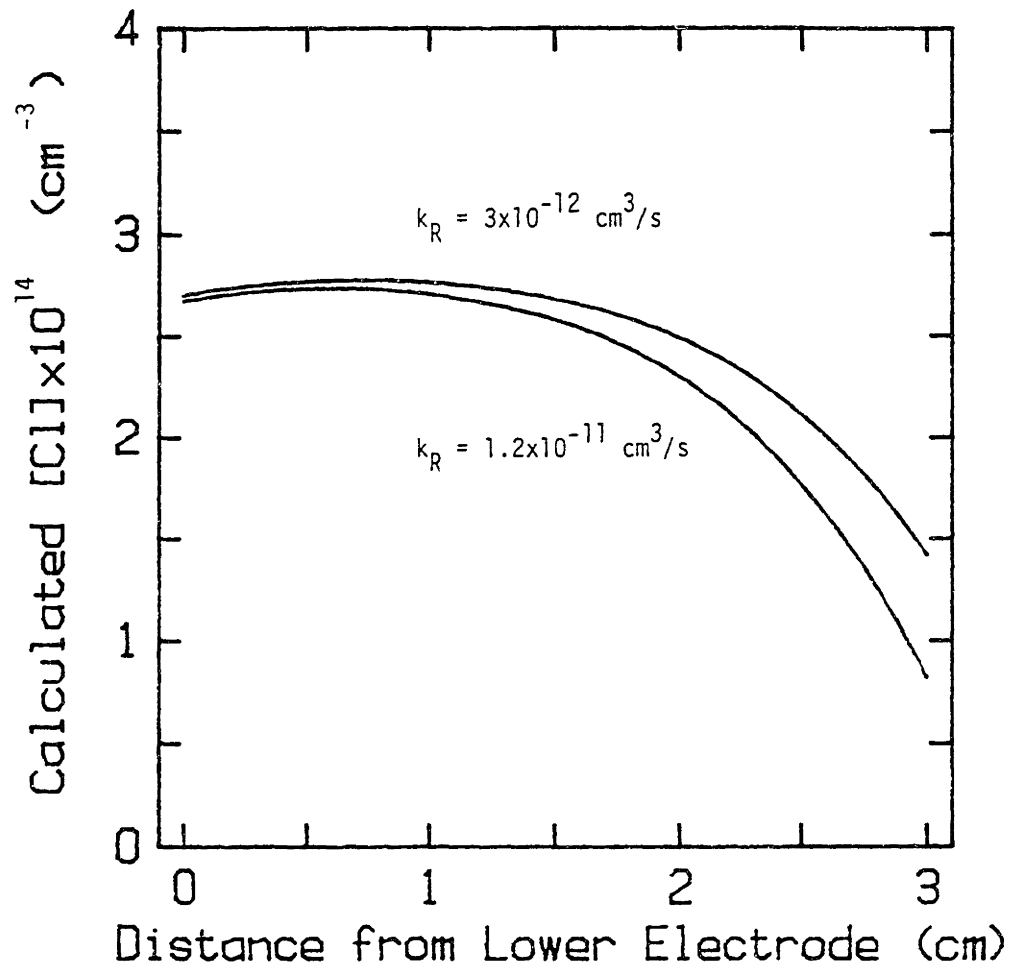


Figure 5-14: Effect of surface recombination rate constant k_R on predicted $[Cl]$ (cm^{-3}).

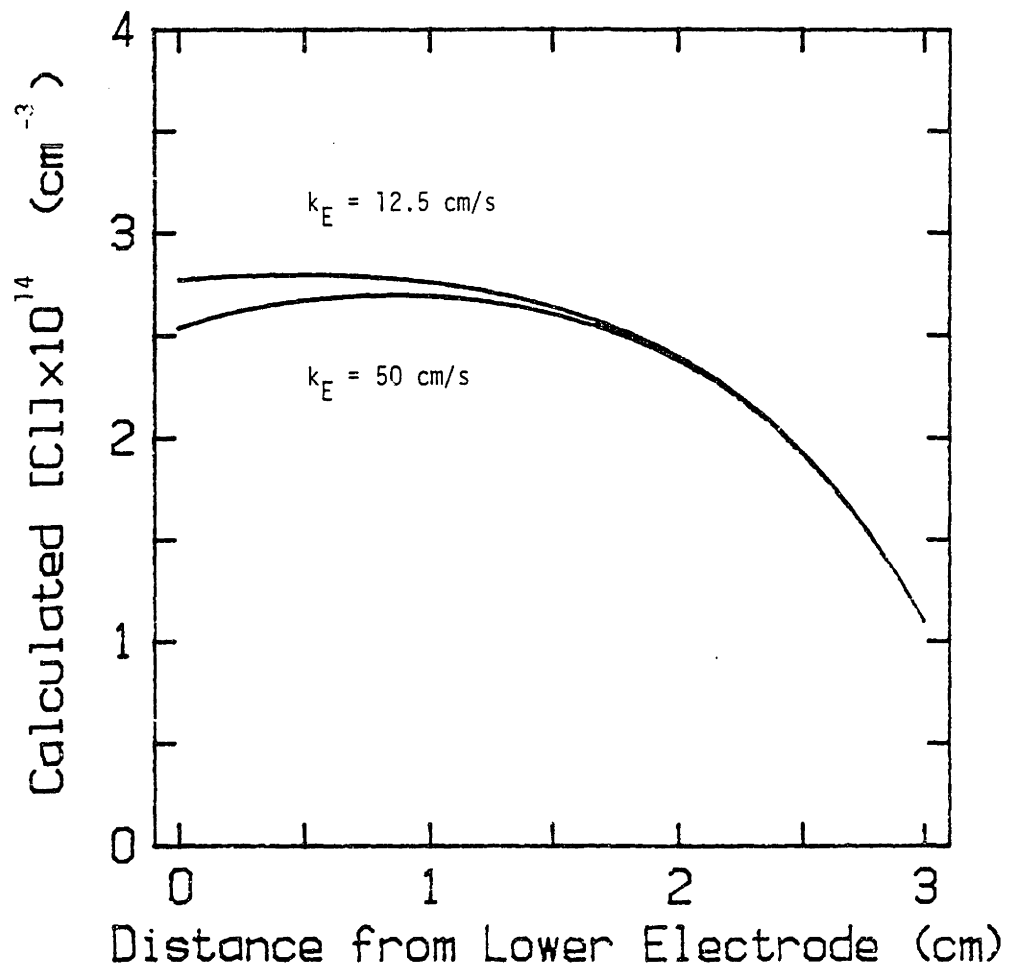


Figure 5-15: Effect of etching rate constant k_E on predicted $[Cl]$ (cm^{-3}).

CHAPTER 6 - POLYSILICON ETCHING

The etching characteristics of polysilicon in CF_3Cl and CF_3Br plasmas are examined in this chapter. Experimental measurements of etching rate, directionality, uniformity, and selectivity are presented. The results of the previous three chapters are combined to generate a series of simple phenomenological models for etching in CF_3Cl discharges. These simple models demonstrate varying success in explaining the observed trends in etching responses with process conditions. These models also prove useful in understanding the important physical processes in this chemical system.

6.1 EXPERIMENTAL RESULTS

In this section, experimental etching results in both CF_3Cl and CF_3Br discharges are presented. Unless otherwise stated, the wafer samples used were one-quarter sections of four-inch wafers in which the $0.4\ \mu\text{m}$ thick film was n^+ -type (phosphorus-doped, $18\ \Omega/\text{sq.}$) CVD polysilicon over a $9300\ \text{\AA}$ thermal oxide substrate. The $1.25\ \mu\text{m}$ thick Kodak 820 photoresist pattern consisted of $2.25\ \mu\text{m}$ wide lines on a 3-5 μm pitch. Etching rate was measured in situ via laser interferometry and each sample was overetched either 10 or 20%, as determined by laser endpoint.

Directionality results were obtained with a scanning electron microscope (SEM). Samples were prepared by cutting a small section where the laser spot on the wafer was used to measure etching rate. An SEM micrograph of the sample was taken at an angle slightly off

parallel with the substrate surface and normal to the cut edge of the sample, i.e., the poly/resist lines appeared end-on. No mask erosion occurred at most plasma conditions, since the interference patterns from photoresist exposure were still evident in the SEM micrographs after etching (also, the resist linewidth did not decrease upon etching). Mask undercut at the poly/resist interface was determined by measuring the poly linewidth and subtracting from the resist linewidth. At most process conditions poly linewidth loss at the poly/oxide interface was very small.

6.1.1 Etching Rate of n^+ -Poly in CF_3Cl Plasmas

As demonstrated previously (Leahy, 1981), the dependence of polysilicon etching rate on power input, pressure, and composition is very complex in CF_3Cl plasmas. In Tables 6-1 and 6-2, etching rate data for CF_3Cl etching of polysilicon are presented for two separate experimental designs. The etching rate results are also shown as contour plots in Figs. 6-1 (vs. power density and pressure at 10% Ar dilution), 6-2 (vs. power density and pressure at 20% dilution), and 6-3 (vs. power density and composition at 0.5 torr). Note the wide range of etching rates - rates as low as 200 Å/min and as high as 4000 Å/min were measured. Also note that the etching rates are different from those of section 2.3, where etching rate was used as an example in the description of RSM. Electrode assembly A was used in the preceding study, while assembly B was used for the data presented in this section. The differences in electrode geometry resulted in a 20% difference in observed etching rates at similar conditions.

Table 6-1
 n^+ -Polysilicon Etching Rate in CF_3Cl Discharges,
 Experimental Design F13B.

RUN ID	Etching Rate ($\text{\AA}/\text{min}$)
F13B_1	2180
F13B_2	265
F13B_3	1630
F13B_4	990
F13B_5	570
F13B_6	440
F13B_7	1010
F13B_8	1220
F13B_9	2485
F13B_10	3280
F13B_11	475
F13B_12	715
F13B_13	810
F13B_14	725
F13B_15	960
F13B_16	1190
F13B_17	1010
F13B_18	1200
F13B_19	460
F13B_20	570
F13B_21	460
F13B_22	650

Table 6-2
 n^+ -Polysilicon Etching Rate in CF_3Cl Discharges,
 Experimental Design F13A.

RUN ID	Etching Rate (Å/min)
F13A_1	875
F13A_2	390
F13A_3	520
F13A_4	360
F13A_5	1000
F13A_6	810
F13A_7	2590
F13A_8	3560
F13A_9	360
F13A_10	940
F13A_11	810
F13A_12	420
F13A_13	745
F13A_14	2200
F13A_15	1910
F13A_16	290
F13A_17	390
F13A_18	1910
F13A_19	615
F13A_20	1845
F13A_21	1295
F13A_22	485
F13A_23	650
F13A_24	1360
F13A_25	520
F13A_26	2170
F13A_27	615
F13A_28	455
F13A_29	1100
F13A_30	420
F13A_31	455
F13A_32	3920
F13A_33	1265
F13A_34	550
F13A_35	1035

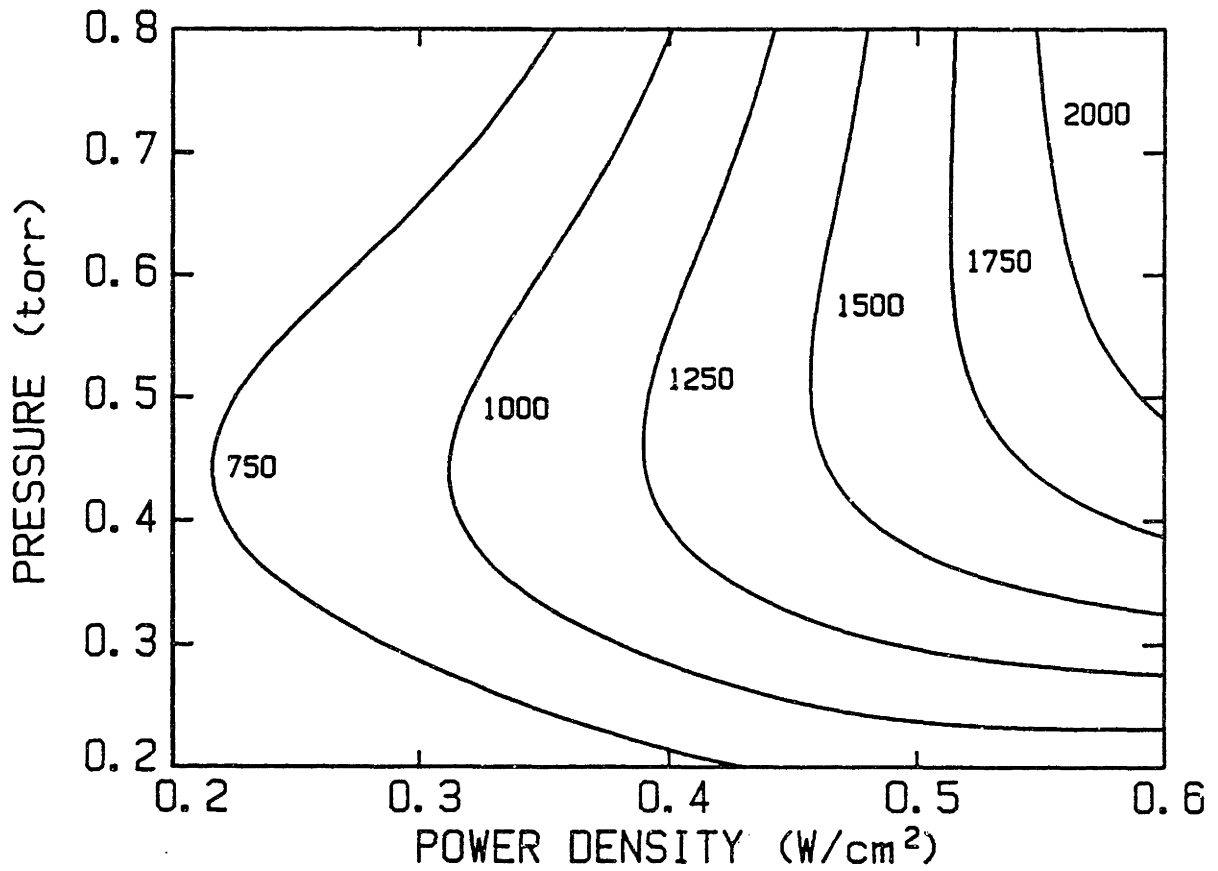


Figure 6-1: Contour plot of doped polysilicon etching rate ($\text{\AA}/\text{min}$) in $\text{CF}_3\text{Cl}/\text{Ar}$ discharges, vs. power density (watts/cm^2) and pressure (torr), $\gamma=0.9$.

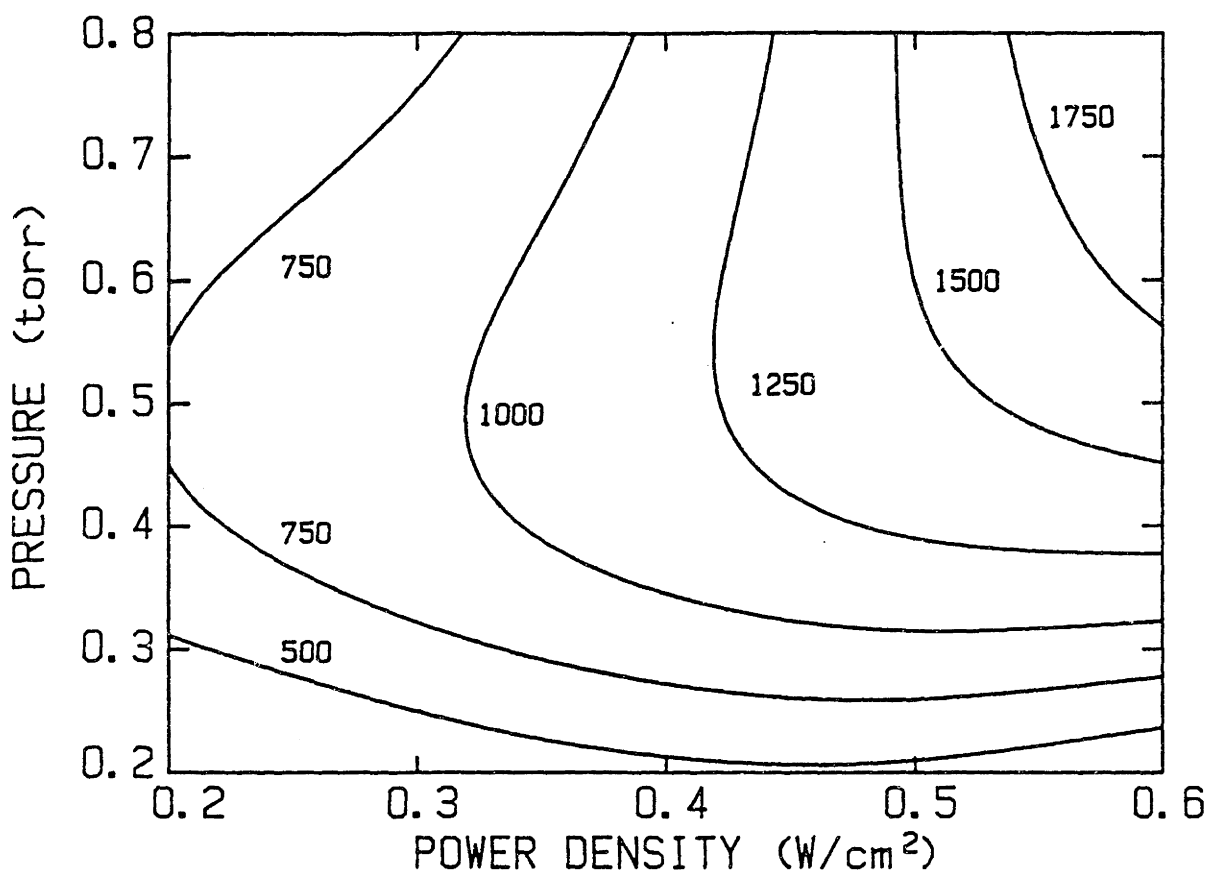


Figure 6-2: Contour plot of doped polysilicon etching rate (Å/min) in CF₃Cl/Ar discharges, vs. power density (watts/cm²) and pressure (torr), $\gamma=0.8$.

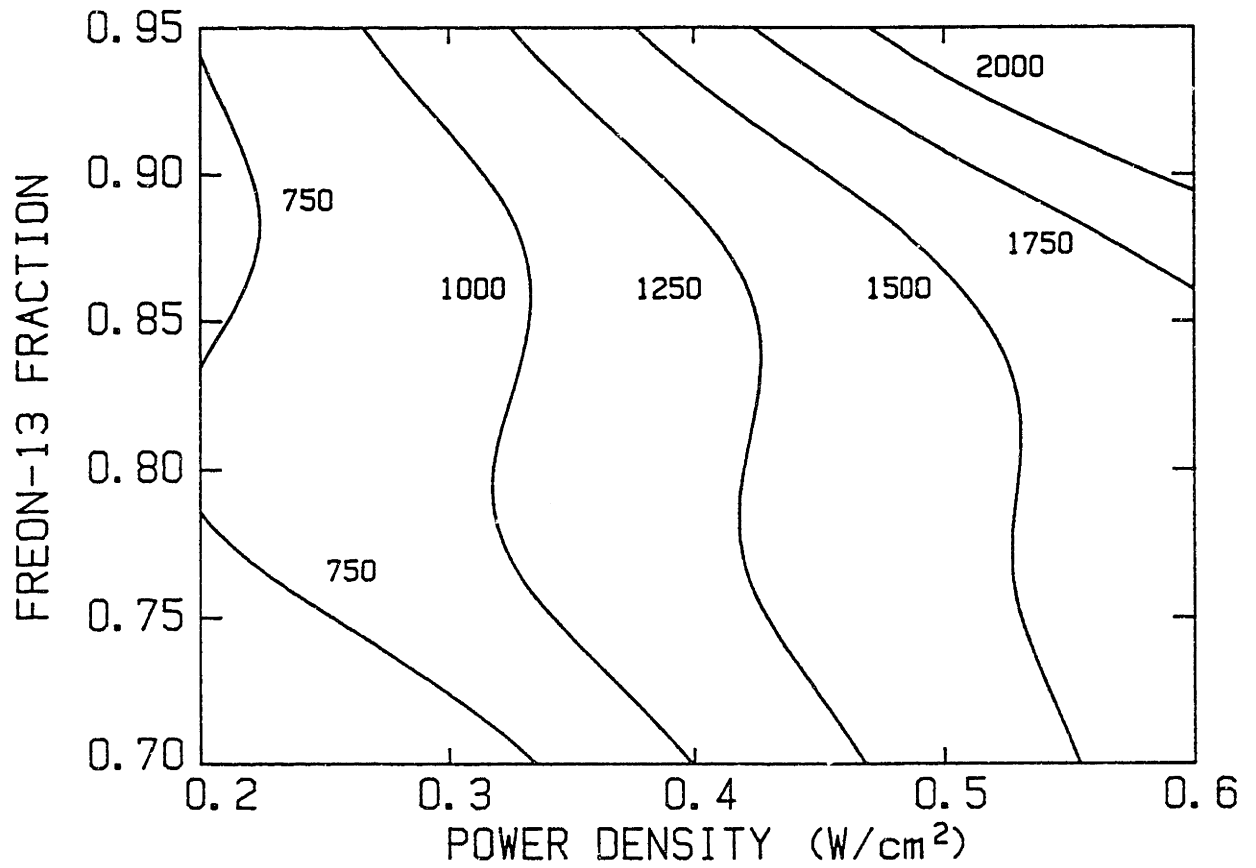


Figure 6-3: Contour plot of doped polysilicon etching rate (Å/min) in CF₃Cl/Ar discharges, vs. power density (watts/cm²) and composition, P=0.5 torr.

Not surprisingly, etching rate increases with increasing power input. The importance of the interaction between power and pressure is obvious; note that the etching rate increases more rapidly with power at higher pressures. At constant power input, etching rate exhibits a maximum with pressure; at $\dot{W} \sim 0.4 \text{ W/cm}^2$ the maximum occurs at about 0.5 torr. As power is increased the pressure at which peak etching rate occurs increases, and the maximum becomes less pronounced (i.e., flatter). Increasing the CF_3Cl mole fraction γ increases the etching rate at low pressures but decreases it at high pressures.

6.1.2 Etching Directionality in CF_3Cl Plasmas

As is well known, the importance of ion bombardment contributions to the etching process is reflected in the etching profiles. Ion-dominated etching will yield anisotropic profiles, while purely chemical etching will result in isotropic profiles. In this subsection the relationship between etching mechanism and directionality is discussed.

A quantitative measure of directionality is required for evaluation of external process variable effects on the resulting profiles. The anisotropy coefficient α is defined as the ratio of the etched lateral distance (mask undercut) U to the etched vertical distance T , see Fig. 6-4. Thus, α varies between 0 (completely vertical etching) and 1 (isotropic etching). The anisotropy coefficient can be greater than 1 if the sample is overetched; therefore α_0 , the anisotropy coefficient at zero overetch, provides a more consistent measure of directionality.

$$\alpha = U/T$$

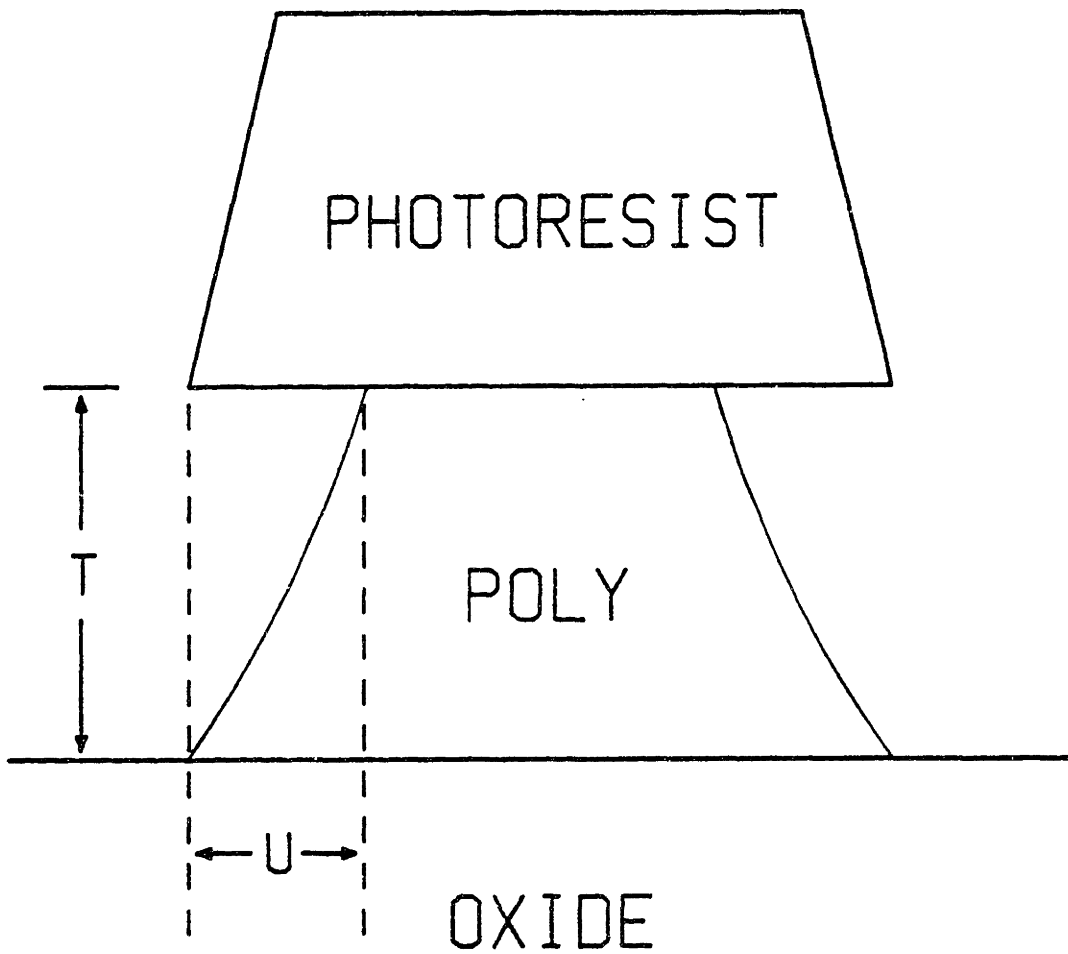


Figure 6-4: Definition of the anisotropy coefficient α .

The anisotropy coefficient is determined by the relative rates of the (directional) ion-assisted and (isotropic) chemical etching. Assuming the two mechanisms to be independent,

$$a = \tau R_0 / (R_0 + R_+) = \tau R_0 / R . \quad (6.1.2-1)$$

In eqn. (6.1.2-1), R is the total etching rate, R_0 is the etching rate attributable to purely chemical processes, R_+ is the etching rate resulting from ion-assisted etching processes, and τ is the fractional overetch, defined as the ratio of the actual etching time to the time required to etch the film to the substrate (in this study $\tau = 1.2$ since each sample was overetched by about 20%). The anisotropy coefficient at zero overetch is simply $a_0 = a/\tau$ provided that the chemical etching rate does not accelerate as the film clears, i.e., loading effects are not important. An extensive study of the acceleration of undercut upon overetch was not undertaken, however, several etches at 10% overetch yielded undercut rates not significantly different from the 20% overetch cases. In addition, no loading effect is seen for CF_2Cl , as discussed later. Therefore, it is assumed that R_0 is independent of τ .

a_0 was determined from SEM micrograph measurements of the undercut and the film thickness,

$$a_0 = U/T\tau . \quad (6.1.2-2)$$

Directionality data for experimental design F13B are shown in Table 6-3. Fig. 6-5 is a contour plot of α_0 with power density \dot{W} and pressure P as independent variables, for CF_3Cl mole fraction $\gamma=0.85$. The adjusted R^2 of the quadratic model RSM fit is 0.85, which implies that the data are fairly well represented. The deviations between the RSM model and the data are primarily caused by random experimental errors, as discussed later. Significant anisotropy ($\alpha_0 \leq 0.5$) is only obtained at pressures below 0.6 torr and at high power densities. The directionality increases with decreasing pressure, with increasing power input, and with decreasing CF_3Cl mole fraction. These results are in general agreement with the findings of previous investigators for other chemical systems (Zarowin, 1983).

Comparison of directionality (Fig. 6-5) with ion bombardment energy (see Fig. 4-10) reveals that directional etching ($\alpha_0 \leq 0.5$) occurs when mean ion energies are above about 15 eV. If $\bar{E}_+ < 15$ eV the etching is primarily isotropic in nature, and is assumed to be purely chemical. The contribution of energetic ion bombardment to etching must be included if the model is to predict etching profiles as well as etching rates, particularly at the lower pressures. The importance of ion bombardment is demonstrated by Fig. 6-6, in which the etching rate R is plotted against total ion flux $\dot{\Gamma}_+$ (as measured during etching). The etching rate scales linearly with ion flux for mean ion energies greater than 10 eV, as represented by the filled circles. Directional etching was observed for these conditions. Presumably, either ion-assisted etching is the dominant mechanism here or the rates of chemical and ion-assisted etching are well correlated. The data at lower \bar{E}_+ (represented by the squares) are scattered

Table 6-3
 n^+ -Polysilicon Etching Directionality in CF_3Cl Discharges,
 Experimental Design F13B.

RUN ID	ANISOTROPY COEFFICIENT, α
F13B_1	0.5
F13B_2	0.9
F13B_3	0.4
F13B_4	0.55
F13B_5	1.15
F13B_6	1.7
F13B_7	0.4
F13B_8	0.75
F13B_9	0.4
F13B_10	0.75
F13B_11	1.2
F13B_12	0.7
F13B_13	1.1
F13B_14	0.9
F13B_15	1.2
F13B_16	0.75
F13B_17	0.8
F13B_18	0.65
F13B_19	0.35
F13B_20	0.35
F13B_21	0.3
F13B_22	0.3

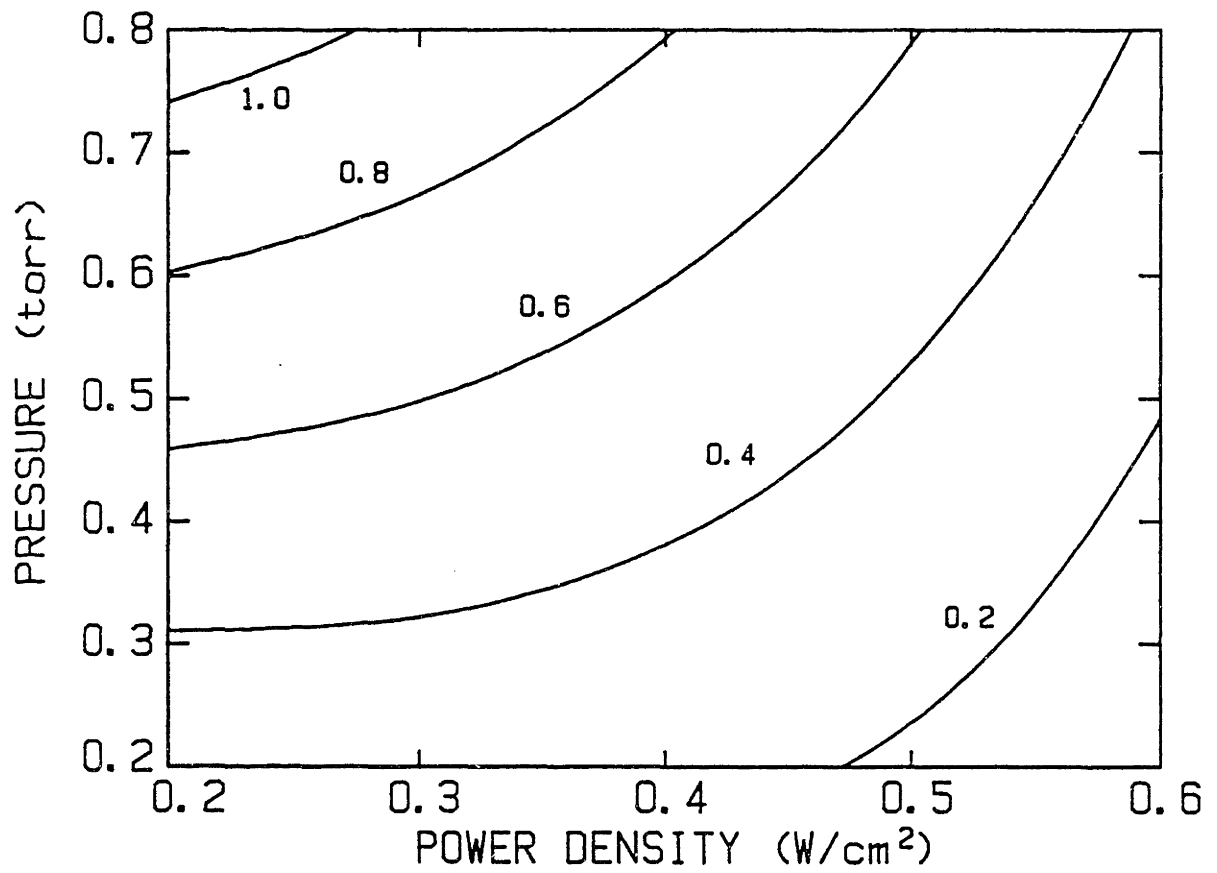


Figure 6-5: Contour plot of measured anisotropy coefficient α_0 in $\text{CF}_3\text{Cl}/\text{Ar}$ discharges, vs. power density (watts/cm^2) and pressure (torr), $\gamma=0.85$.

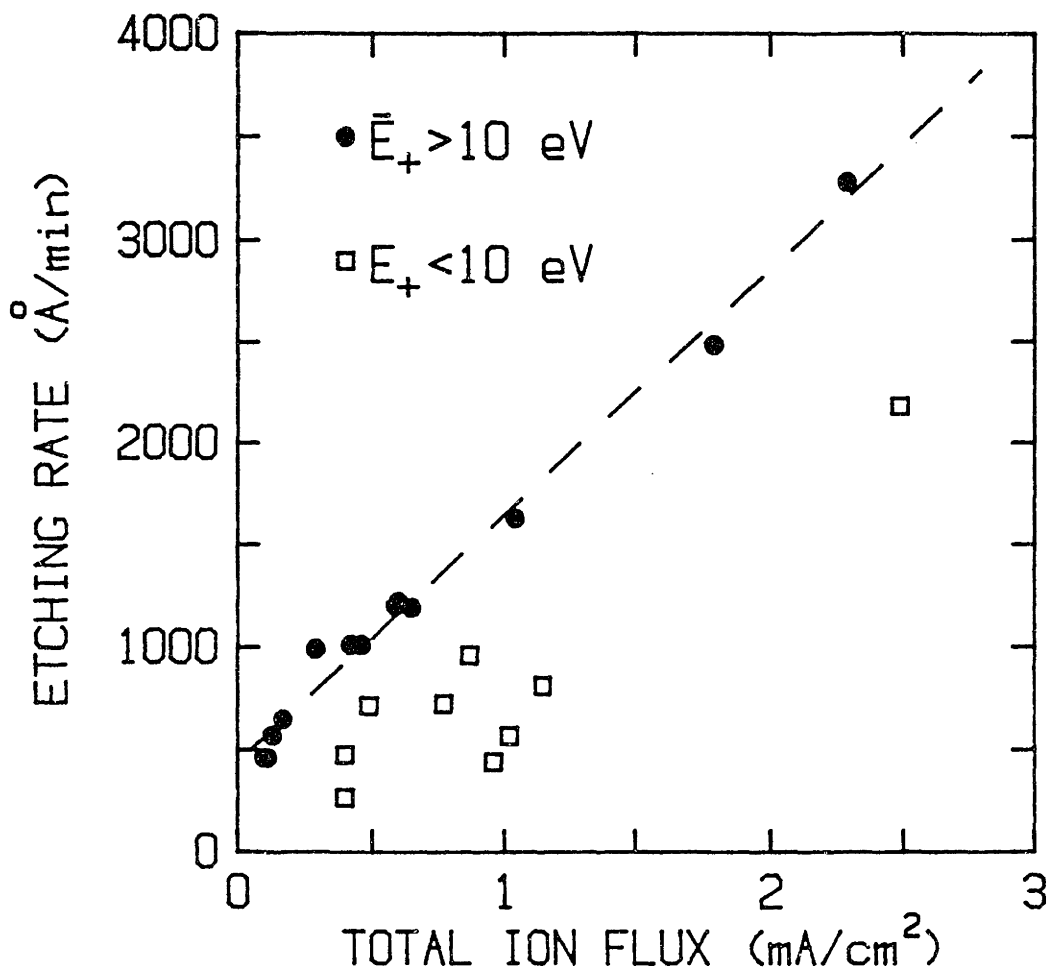


Figure 6-6: Doped polysilicon etching rate (Å/min) in $\text{CF}_2\text{Cl}/\text{Ar}$ discharges vs. total positive ion flux (mA/cm²). Symbols: ● = $\bar{E}_+ \geq 10 \text{ eV}$, □ = $\bar{E}_+ < 10 \text{ eV}$.

because of the reduced importance of ion-assisted relative to chemical processes; nearly isotropic etching was observed in these runs. Note also that the data at low \bar{E}_+ falls significantly below the data at $\bar{E}_+ \geq 10$ eV, highlighting the importance of energetic ion bombardment in increasing the etching rate.

6.1.3 Etching Rate of n^+ -Poly in CF_3Br Plasmas

The etching rate data for experimental design BR are presented in Table 6-4 (see chapters 3 and 4 for further information on these experiments). The three process variables examined in this study were power, pressure, and flow rate. Note that etching rates in CF_3Br plasmas are considerably higher than in CF_3Cl . Also, the dependence of etching rate on power input and pressure is much simpler in the CF_3Br system - the only significant terms in the quadratic model RSM fit of etching rate are, in order of decreasing importance: power density, pressure, (power density)x(flow rate), and (power density)². This simple quadratic RSM model has an adjusted R^2 of 0.92, more than sufficient for representation of the data.

Etching rate contours in CF_3Br are shown in Figs. 6-7 to 6-8; etching rate increases rapidly with power density but flattens out at high power densities, and increases with pressure (particularly at higher power densities). Flow rate has little effect on etching rate except at high pressures and high powers, where at low flow rates the high etching rates (~ 0.5 $\mu\text{m}/\text{min}$) may result in significant depletion of etchant species from the gas. The lack of a loading effect in CF_3Br has been noted previously (Mogab and Levinstein, 1980).

Table 6-4
 n^+ -Polysilicon Etching Rate in CF_3Br Discharges,
 Experimental Design BR.

RUN ID	ETCHING RATE ($\text{\AA}/\text{min}$)
BR_1	3275
BR_2	2935
BR_3	2560
BR_4	3700
BR_5	2890
BR_6	2270
BR_7	1975
BR_8	3385
BR_9	3025
BR_10	1770
BR_11	1900
BR_12	3630
BR_13	3440
BR_14	2170
BR_15	2195
BR_16	5550
BR_17	4870
BR_18	1975
BR_19	2750
BR_20	915
BR_21	860
BR_22	800
BR_23	595
BR_24	3565
BR_25	1865
BR_26	3500
BR_27	1625
BR_28	2735
BR_29	2940
BR_30	3300
BR_31	1430
BR_32	4160
BR_33	2295
BR_34	2660
BR_35	2560

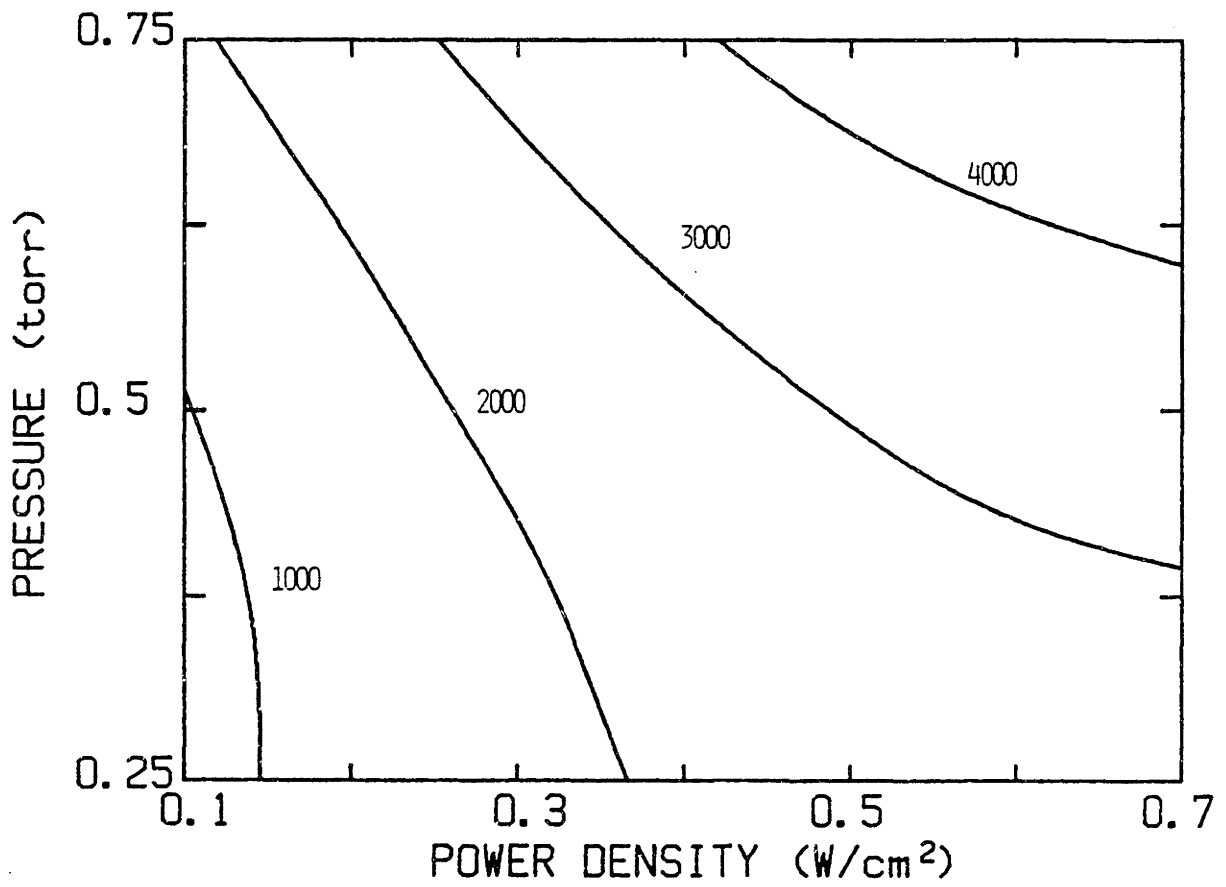


Figure 6-7: Contour plot of doped polysilicon etching rate ($\text{\AA}/\text{min}$) in CF_2Br discharges, vs. power density (watts/cm^2) and pressure (torr), $Q=10$ sccm.

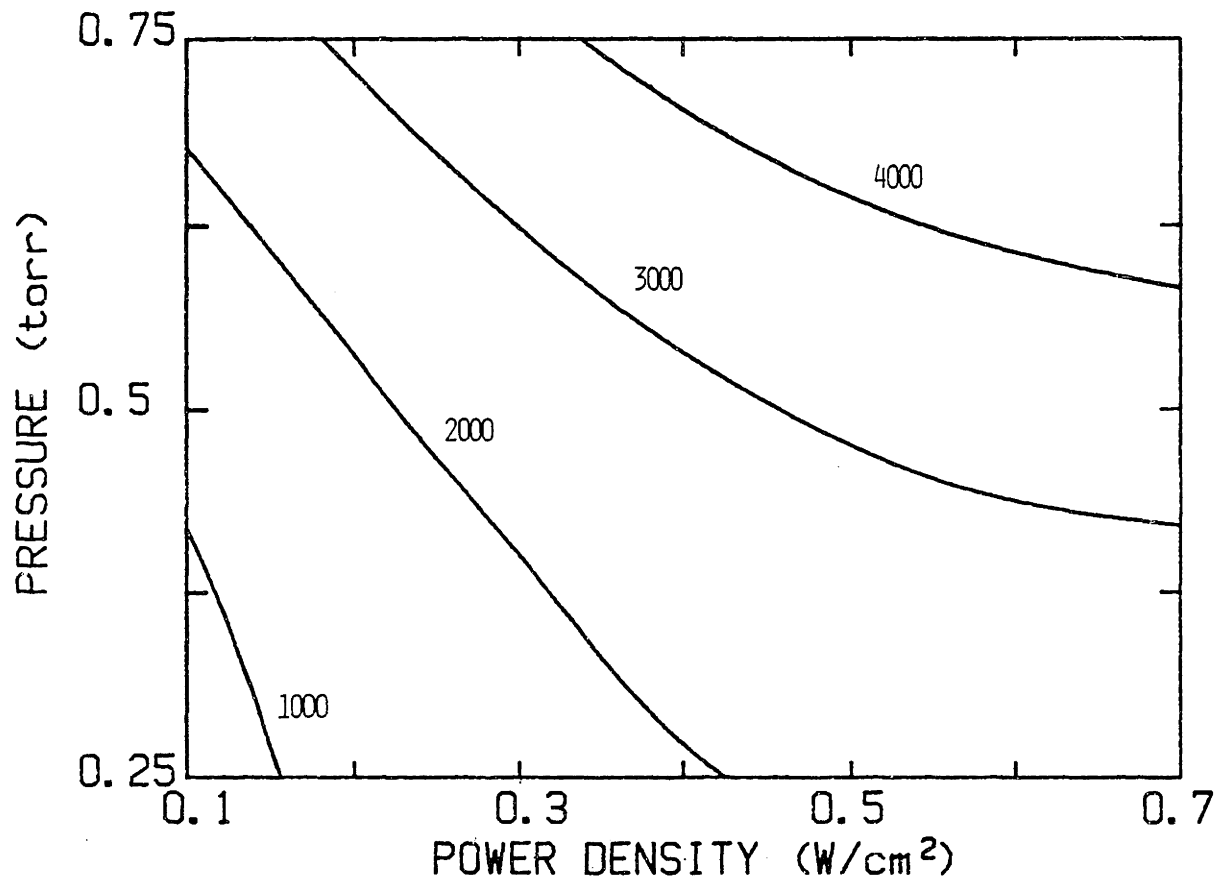


Figure 6-8: Contour plot of doped polysilicon etching rate ($\text{\AA}/\text{min}$) in CF_3Br discharges, vs. power density (watts/cm^2) and pressure (torr), $Q=20$ sccm.

The etching rate of undoped polysilicon in CF_3Br plasmas was also studied (Mocella et al., 1986b). The trends in etching rate with process conditions are similar to those of doped polysilicon, although undoped polysilicon etching rates are lower. Undoped polysilicon etching is seemingly an ion-dominated process.

6.1.4 Etching Directionality in CF_3Br Plasmas

In general, etching in CF_3Br plasmas is more directional than in CF_3Cl plasmas. In addition, the etch directionality is less dependent on process conditions in CF_3Br . The directionality results for experimental design BR, presented as net linewidth loss, are shown in Table 6-5. Linewidth loss is calculated from an SEM micrograph by subtracting the mean polysilicon line width (the average of the widths at the poly/oxide and poly/resist interfaces) from the initial (before etching) photoresist linewidth. A perfectly anisotropic etch gives zero linewidth loss if the mask is not etched by the plasma, while a perfectly isotropic etch will give a large linewidth loss. The linewidth results are organized for easy visualization in Table 6-6.

In the CF_3Br system, generalizations about the effects of process conditions on directionality are not easily made. While decreasing pressure results in a more directional etch, the influence of power is minor over most of the experimental range. Flow rate does not affect directionality, except at low pressures.

Table 6-5
 n^+ -Polysilicon Etching Directionality in CF_3Br Discharges,
 Experimental Design BR, Expressed as Linewidth Loss.

RUN ID	LINEWIDTH LOSS (μm)
BR_1	0.26
BR_2	0.25
BR_3	0.24
BR_4	0.32
BR_5	0.20
BR_6	0.25
BR_7	0.23
BR_8	POOR SEM
BR_9	0.39
BR_10	0.32
BR_11	0.28
BR_12	0.27
BR_13	0.42
BR_14	0.25
BR_15	0.24
BR_16	0.19
BR_17	0.66
BR_18	-0.22
BR_19	-0.32
BR_20	0.30
BR_21	0.32
BR_22	0.14
BR_23	0.26
BR_24	0.21
BR_25	0.19
BR_26	0.40
BR_27	0.16

Note: SEMs were not taken for BR_28 to BR_35, which were repeats of BR_20 to BR_27.

Table 6-6
 Linewidth Loss (μm) for CF_3Br Etching of n^+ -Polysilicon,
 Arranged by Process Conditions.

POWER DENSITY (W/cm^2)	PRESSURE (torr)						
	0.1	0.2	0.3	0.5	0.7	0.8	0.9
0.25	0.26						-0.32
	0.14						-0.22
0.312				0.16			
0.375			0.23	0.24	0.20		
				0.25			
0.5		0.19	0.28	0.25	0.39		0.21
			0.32		BAD		
0.625			0.25	0.42	0.32		
				0.27			
0.692				0.40			
0.75	0.32						0.66
	0.30						0.19

Very interesting results were obtained at 0.25 torr, especially at high power densities. Sample SEMs at this pressure are presented in Figs. 6-9 (low flow rate) and 6-10 (high flow rate). In Fig. 6-10, slight retrograde etching is observed - that is, the undercut at the poly/oxide interface is slightly more than at the poly/resist interface. Retrograde etching can result from redeposition of etched material on the sidewalls of the etched feature - this theory is supported by the slight increase, after etching, of the poly linewidth at the poly/resist interface. Another possible explanation is local depletion of active etchant by the resist, which would result in a lower undercut rate at the top of the feature than at the bottom.

At lower flow rates the increase in linewidth upon etching is more dramatic, see Fig. 6-9. Note also the unetched regions ("grass"), which probably result from contamination of the wafer surface by SiO_2 , or possibly by metals. The density of these structures decreases near the poly lines (see Fig. 6-11, a top view of Fig. 6-9), which suggests that either a microloading effect or an interaction with the photoresist is responsible.

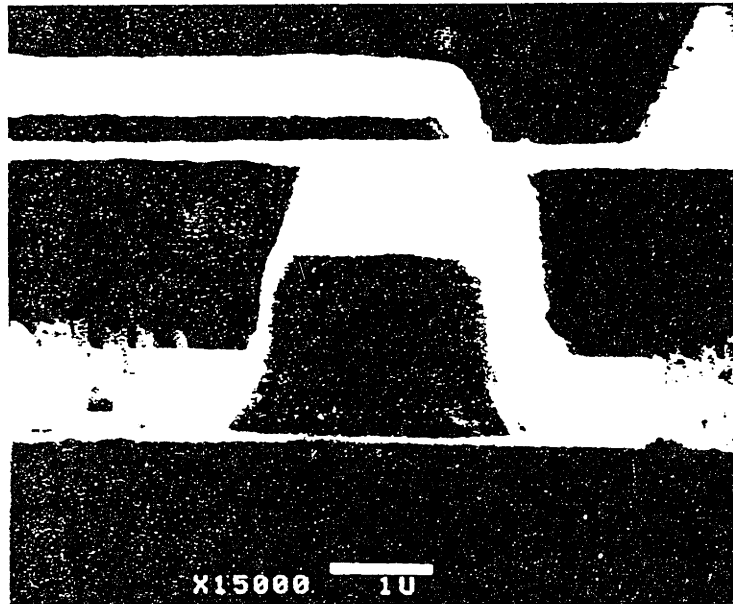
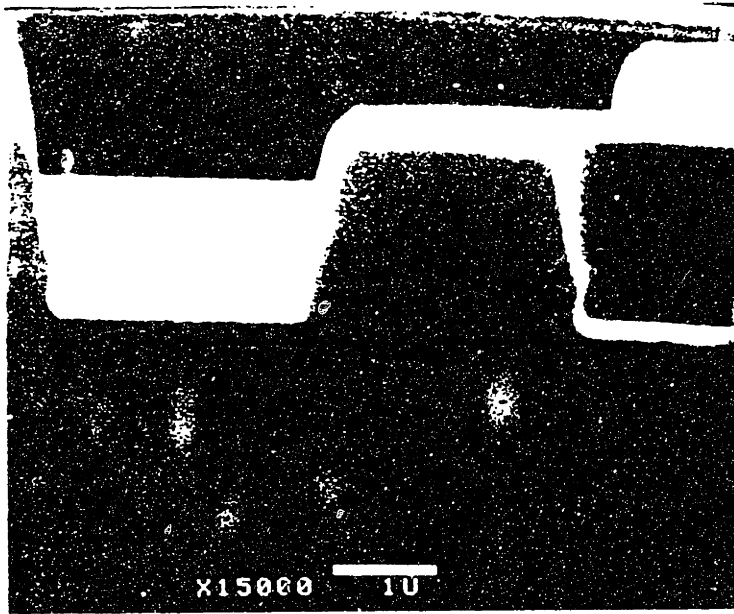


Figure 6-9: SEM micrograph of doped polysilicon etching in CF_3Br discharge, $Q=5$ sccm. (top)

Figure 6-10: SEM micrograph of doped polysilicon etching in CF_3Br discharge, $Q=25$ sccm. (bottom)

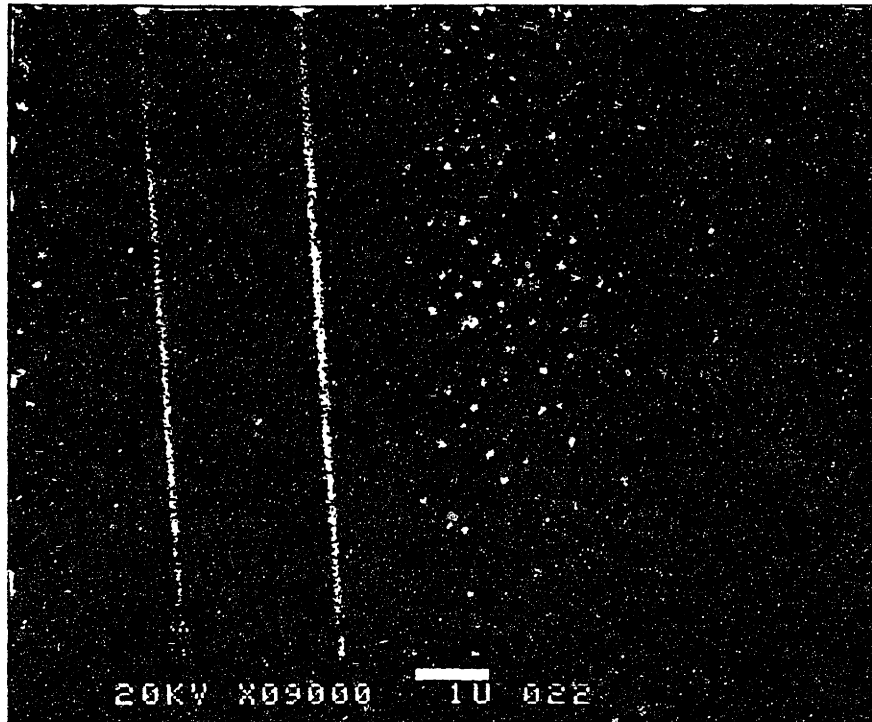


Figure 6-11: SEM micrograph, top view of Figure 6-9.

6.1.5 Etching Uniformity

The uniformity of etching rate across the wafer sample is determined by observing the interference patterns on an etched sample. For example, a perfectly spatially-uniform etching rate results in a totally cleared sample at zero overetch. No regions of unetched poly remain on the surface, as would be evidenced by cloudy areas in the case of very thin films or by colored interference rings for thicker films (Pliskin and Conrad, 1964). Etching in CF_3Cl plasmas is not uniform in this reactor over the range of conditions studied (Mocella *et al.*, 1985), particularly at high pressures. At some conditions, the etching rate varied by as much as 50% over the wafer surface. As discussed in section 6.2, the influence of diffusion and rapid etchant (Cl) loss at the stainless steel electrodes accounts for the observed nonuniformities. Etching in CF_3Br plasmas is considerably more uniform; the etching rate at the wafer periphery is within about 10% of that at the wafer center for pressures less than 0.5 torr.

The most complete examination of etching uniformity was performed on the CF_3Cl system. With quarter sections of 4-inch wafers placed on the lower electrode (Fig. 6-12), three types of clearing patterns are observed: (A) fastest at the center of the wafer, (B) fastest at the outer edge of the wafer, and (C) fastest at the inner edge of the wafer. These patterns are shown schematically in Fig. 6-13.

The occurrence of these patterns is not random; rather, the patterns appear in repeatable, well-defined regions of the process parameter space (Fig. 6-14). For example, B-type etching is dominant at low pressures, where the plasma has a tendency to expand beyond the

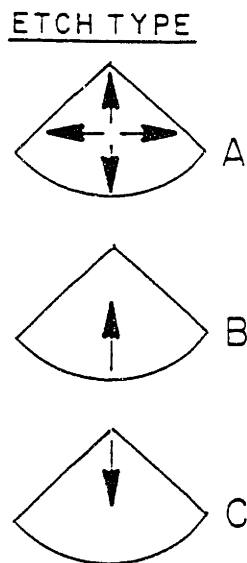
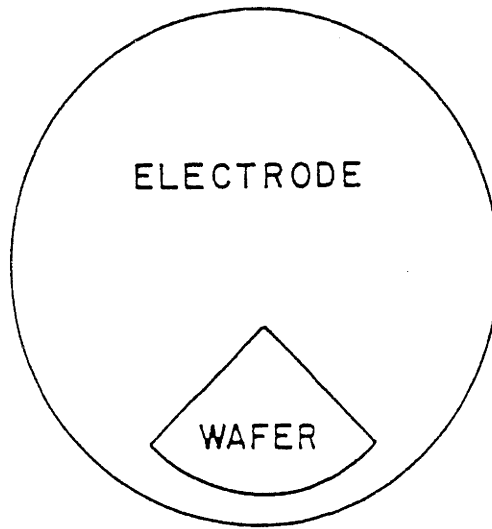


Figure 6-12: Wafer placement on lower electrode.
(top)

Figure 6-13: Observed clearing patterns of doped polysilicon in CF_3Cl discharges.
(bottom)

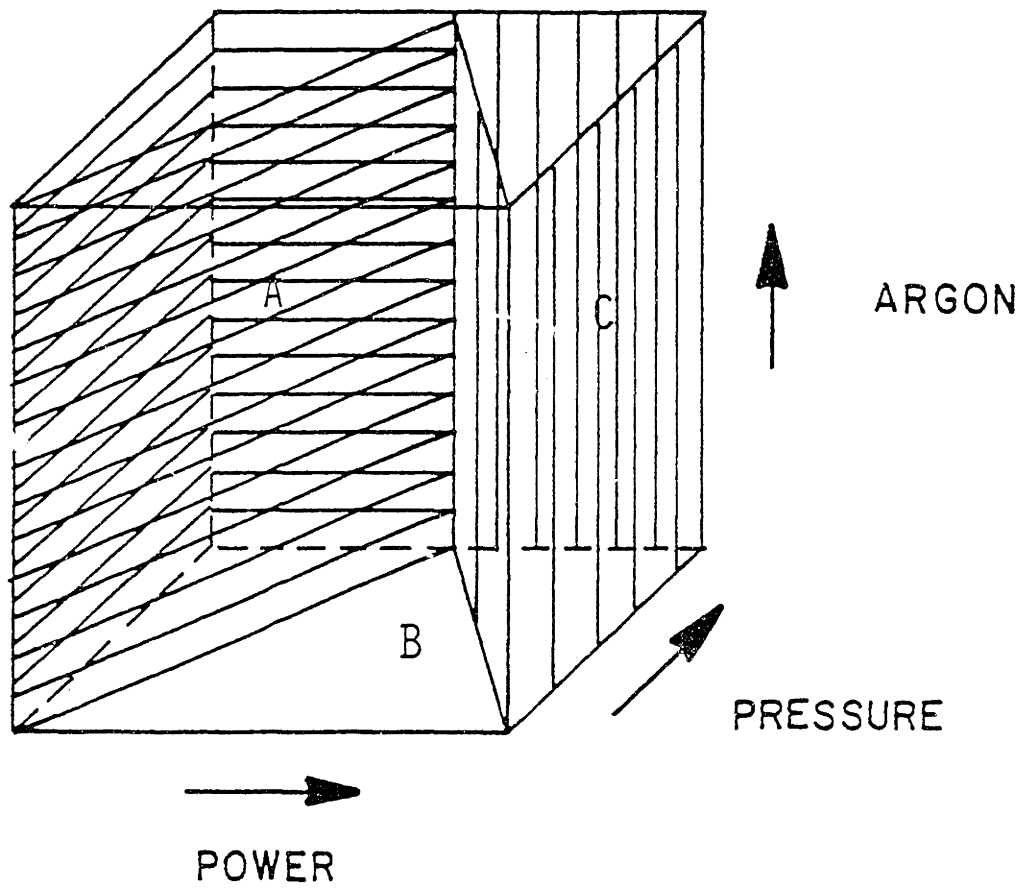


Figure 6-14: Process conditions corresponding to clearing patterns shown in Figure 6-13.

electrodes. Atomic chlorine recombination on the Teflon rings should be considerably slower than on the electrode surfaces, so $\cdot\text{Cl}$ concentrations may be higher at the outer edge of the electrode than in the center. The A-type etching, which occurs primarily at high pressures where diffusive mixing of the plasma is low, is probably due to loss of $\cdot\text{Cl}$ on the electrodes surrounding the sample. Finally, C-type etching occurs at high etching rates (power and pressure both high). The drop in etching rate with radial flow outward over the sample could be explained by depletion of the reactant gas by reaction with the surfaces.

The region of best etching uniformity occurs at the plane intersecting the B and C regions. This is not unreasonable, since the physical processes responsible for edge-in and center-out etching would be expected to balance here.

A reactor model which incorporates most of the physical processes important in etching is quite easily written. The parallel-plate geometry used in this work is well suited to cylindrical coordinates (it is assumed that plasma and etching properties are constant with respect to the θ direction). Recall that the showerhead gas feedthrough is confined to a 1-inch diameter around the center of the upper electrode. In this simple model it is assumed that the gas enters the reactor through a thin cylinder (of radius R_1) connecting the electrodes at their centers; the gas then flows radially outward with a velocity independent of axial position. Obviously, the fluid mechanics are not treated properly in this model. However, the fluid mechanics are expected to have little effect on the etching characteristics.

The geometry and nomenclature are clarified in Fig. 6-15. The radial velocity V_r is assumed independent of the axial distance z , so the radial velocity is a simple function of radius r ,

$$V_r = Q/2\pi dr , \quad (6.1.5-1)$$

where Q is the flow rate and d is the interelectrode spacing. Eqn. (6.1.5-1) is a consequence of incompressible flow - total radial flow rate must be constant with radius. A complete solution of the fluid mechanics in a slightly different geometry was given recently by Dalvie et al. (1986). The flow streamlines calculated in that study are consistent with those assumed here.

Assume that chemical etching is determined by the concentration of atomic chlorine. Of course, ion bombardment is also important, especially at plasma conditions of industrial interest. However, ion bombardment fluxes cannot be predicted at present. In any case, a constant etching rate due to ion bombardment could easily be added to the model. The equation of continuity for atomic chlorine is then,

$$(Q/2\pi d) \frac{\partial C_A}{\partial r} = D \frac{\partial}{\partial r} \left[r \frac{\partial C_A}{\partial r} \right] + D r \left[\frac{\partial^2 C_A}{\partial z^2} \right] + r R_A(z, r) , \quad (6.1.5-2)$$

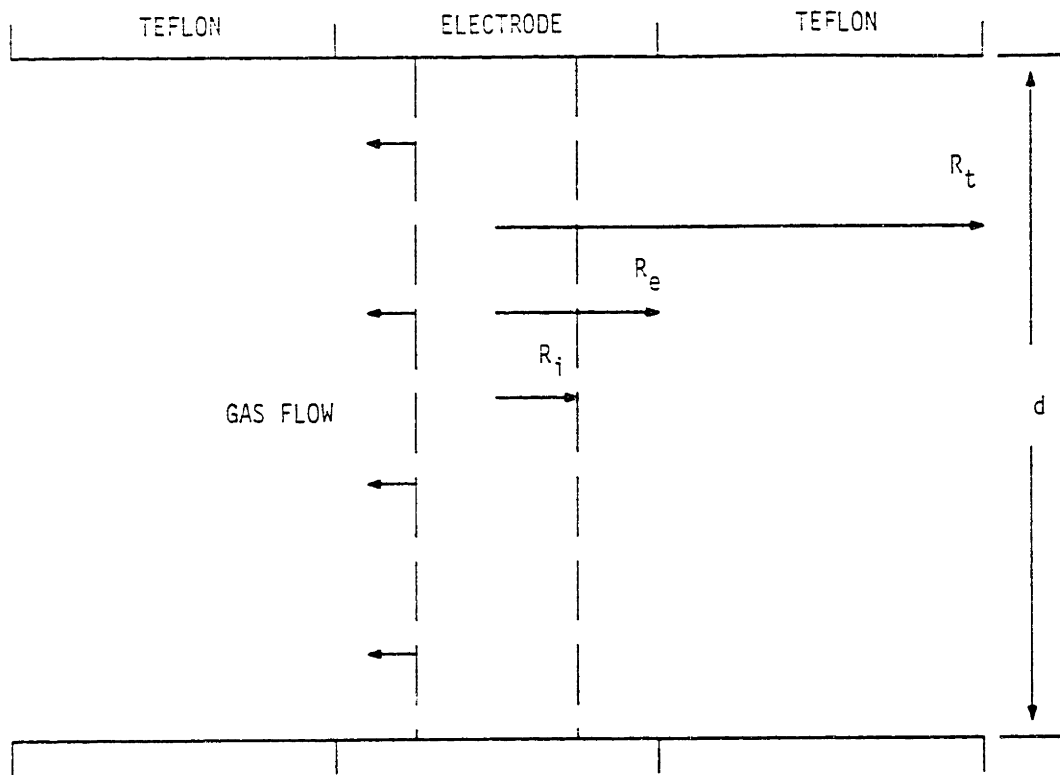


Figure 6-15: Geometry and nomenclature of etching uniformity model.

where C_A is the concentration of atomic chlorine, D is the diffusivity of atomic chlorine, and R_A is the net formation rate of atomic chlorine from all reactions in the plasma.

The boundary conditions (BC's) for r are $C_A=0$ or $\partial C_A/\partial r=0$ at $r=R_i$ and $\partial C_A/\partial r=0$ at R_T , the outer edge of the Teflon ring. The former BC reflects the input conditions of the gas, while the latter requires that no atomic chlorine is lost by flow or diffusion out of the reactor. The boundary conditions in z are more complex - they consist of flux matching conditions at the walls, i.e., the diffusive flux is equated to a reaction loss rate on the surface. Note that three different types of surfaces must be considered: electrode (stainless steel), wafer (silicon), and shielding (Teflon). Loss on the electrodes and shielding is presumed to be via recombination, and loss on the silicon is via the etching reaction to form SiCl_4 .

After writing eqn. (6.1.5-2) in dimensionless form, a FORTRAN routine utilizing finite difference techniques was written to solve the resulting equation (see Appendix B.3 for the listing of the code). Because of the large number of parameters necessary in such a model (e.g., surface reaction rates), detailed calculations are not presented here, but the model results do account for two of the observed clearing patterns (patterns A and C). Clearing pattern B is more difficult to model because it cannot be described by a two-dimensional model. As mentioned previously, the effect can be explained by discharge expansion at low pressures. However, the discharge structure is not well enough understood to allow mathematical modeling.

The different clearing patterns are also described by the model of Dalvie et al. (1986) for CF_4 etching, although recombination on the electrodes (an important sink for atomic species) was not considered in that study.

6.1.6 Selectivity to Oxide

A very brief set of experiments was performed to estimate the selectivity of n^+ -polysilicon to oxide in CF_3Cl and CF_3Br discharges. After completely etching the 4100 Å poly film, the etching rate of the underlying oxide was also measured by laser interferometry. In CF_3Cl discharges, measured selectivities ($\text{Si}:\text{SiO}_2$) were about 12:1 at 0.3 torr. In CF_3Br discharges, selectivities of about 8:1 were obtained at 0.25 torr. These values are lower than reported previously, where selectivities of 30:1 and 15:1 were observed in CF_3Cl and CF_3Br , respectively (Mogab and Levinstein, 1980). The lower selectivity in the present study may be an artifact of the large oxide area exposed to the plasma.

A more complete study of selectivity in low pressure CF_3Br etching was also performed (Mocella et al., 1986b). In general, selectivity decreases as ion bombardment energy increases, i.e., with decreasing pressure, increasing power, and decreasing electrode spacing.

6.2 MODELING OF CF_3Cl ETCHING RATE AND DIRECTIONALITY

Four etching models (A-D) are described below. In each model, the chemical and ion-assisted etching are formulated as independent processes, i.e., these models neglect any interaction between chemical and ion-assisted etching. All plasma property data used for comparison with the model were taken simultaneously during the experimental runs. Steady-state models for $[Cl]$, as discussed in chapter 5, are used for clarity and simplicity.

6.2.1 Model A

Polysilicon etching is influenced by relatively low energy (<30 eV) ion bombardment. For example, recent work suggests that ion-assisted etching is important for ion energies above 20 eV (Us, 1985; Us et al., 1986). Polymer film formation has been postulated to be an important effect in halocarbon discharges; anisotropy may be achieved by sidewall passivation in the absence of ion bombardment (Millard, 1974). The influence of low-energy ion bombardment is not surprising given that carbon-carbon, silicon-silicon, and carbon-halogen bond energies are only 5 eV (Weast, 1975). Sputter cleaning and ion-assisted etching processes are expected for ions with kinetic energy greater than the bond strength. Therefore, a threshold energy for ion-assisted etching of 10-20 eV is assumed. As seen in Fig. 6-6 and as observed in UHV surface science studies (e.g., McNevin and Becker, 1985), there is evidence that ion-assisted etching rates are

proportional to ion flux at high ion energies. Therefore, the ion-assisted etching rate R_{+A} is modeled as proportional to the flux of ions with energies greater than threshold energy,

$$R_{+A} = k_{+A} \dot{\Gamma}_+ \tilde{\Delta}(E^*) . \quad (6.2.1-1)$$

The total ion flux $\dot{\Gamma}_+$ is measured, while the fraction of ions with energy greater than threshold, $\tilde{\Delta}(E^*)$, is predicted using the plasma impedance and sheath transport models. The ion-assisted rate coefficient for model A is k_{+A} .

It is assumed that the surface is saturated with the neutral etchant species, and consequently that the etch product yield per incident ion is independent of the neutral flux to the surface. At the ion to neutral flux ratios observed in this study, coverage should be near unity (Barker et al., 1983). The threshold energy is arbitrarily set to be 15 eV in light of this evidence. The kinetic model was relatively insensitive to the choice of E^* in the range 10-20 eV, although the quality of etching rate representation was slightly improved at lower E^* . Conversely, the anisotropy representation was slightly better at higher E^* .

If etching is a pseudo-steady-state process, the rate of chlorine addition to the surface by adsorption must equal the rate of loss via desorption and etching. For a sticking coefficient independent of etching rate, the addition rate is proportional to the flux of $\cdot\text{Cl}$, and therefore to $[\text{Cl}]$. Recall that by solving eqn. (5.2.2-2) at steady-state, the atomic chlorine concentration was given as

$$[Cl] = (k_F/k_L) [e^-]P\gamma . \quad (6.2.1-2)$$

We now relate the etching rate to [Cl]. It has been suggested that the chemical etching surface reaction proceeds by a series of first-order addition steps (Coburn et al., 1977; Flamm and Donnelly, 1981), one of which will be rate-limiting. Consequently, for reasonably high surface coverages the chemical etching rate is linearly related to [Cl] through the etching rate constant k_E (Flamm et al., 1981), i.e.,

$$\begin{aligned} R_{oA} &= k_E [Cl], \\ &= (k_E k_F/k_L) [e^-]P\gamma , \\ &= k_{oA} [e^-]P\gamma , \end{aligned} \quad (6.2.1-3)$$

where k_{oA} is a lumped rate coefficient for model A. If the dominant loss process for atomic chlorine is the etching process itself ($k_L \sim k_E$), eqn. (6.2.1-3) shows that the etching rate is proportional to the atomic chlorine production rate. If other loss processes such as surface recombination are important ($k_L > k_E$), lower etching rates will be obtained for the same atomic chlorine production rate.

The total etching rate is then assumed to be the sum of the chemical and ion-assisted rates,

$$R_A = k_{oA}[e^-]P\gamma + k_{+A}\dot{P}_+\tilde{\Delta}(E^*) , \quad (6.2.1-4)$$

where it is assumed that the ion-assisted etching does not significantly deplete the surface of atomic chlorine. Therefore, the anisotropy coefficient for model A is expressed as

$$\alpha_A = \frac{\tau}{1 + \frac{k_{+A}\dot{P}_+\tilde{\Delta}(E^*)}{k_{oA}[e^-]P\gamma}} . \quad (6.2.1-5)$$

The etching rate and anisotropy models require two fitted parameters and a specified threshold energy E^* . These parameters have physical significance to the anisotropic and chemical etching rates, and allow prediction of the etching rate and anisotropy given the measured total ion flux and discharge impedance.

6.2.2 Model B

The previous model does not account for increased etching yield as a function of ion energy above the threshold. The higher energy ions should contribute more energy to the surface than do lower energy ions, and therefore may induce more surface reactions. Surface studies of the silicon-chlorine system suggest that the etch yield is linearly dependent on the ion bombardment energy, although recent

results in UHV experiments (Rossen and Sawin, 1986) suggest a square root dependence. Note that ion bombardment energies in these surface studies are generally much higher than those obtained in symmetric plasma reactors, and that the ratio of neutral flux to ion flux in the surface studies may not be similar to that of an etching process. Nonetheless, the importance of ion energy is demonstrated by these experiments. Furthermore, the silicon surface exposed to the Cl flux during plasma etching is not a clean one - a polymeric film is likely adsorbed on the surface.

The energy dependence of etch yield, $g(E_+)$, can be combined with the ion energy distribution to predict the energy-dependent ion-assisted etching rate R_{+B} ,

$$R_{+B} = k_{+B} \dot{\Gamma}_+ \int_{E^*}^{E_{+,max}} f(E_+) g(E_+) dE_+ , \quad (6.2.2-1)$$

where k_{+B} is the ion-assisted rate constant for model B, $E_{+,max}$ is the maximum energy of ions striking the surface, and $f(E_+)$ is the ion energy distribution function. Assuming a linear dependence of the etch yield on the incident ion energy (above the threshold energy), and using the triangular approximation to the energy distribution, eqn. (6.2.2-1) yields

$$R_{+B} = \frac{k_{+B} \dot{I}_+ \bar{E}_+}{(2.67 - \rho)} [2.37 - \tilde{\xi}^2 + \tilde{\xi}^3] , \text{ if } \rho < \tilde{\xi} < 2.67 . \quad (6.2.2-2a)$$

Or,

$$R_{+B} = \frac{k_{+B} \dot{I}_+ \bar{E}_+}{(2.67 - \rho)} [2.37 - \rho^2/3 + (0.25 + 0.67/\rho)\tilde{\xi}^3] , \text{ if } 0 \leq \tilde{\xi} \leq \rho . \quad (6.2.2-2b)$$

In eqn. (6.2.2-2), \bar{E}_+ is the mean ion energy, ρ is a dimensionless pressure, and $\tilde{\xi}$ is the ratio of the E^* to \bar{E}_+ . The two forms of eqn. (6.2.2-2) are necessary to represent the two possible cases: (a) the threshold energy E^* less than the energy at the peak in the distribution ($\rho \bar{E}_+$), and (b) the threshold greater than the peak.

The chemical etching rate is identical to that of model A, so the overall etching rate is

$$R_B = k_{oB} [e^-] P\gamma + R_{+B} . \quad (6.2.2-3)$$

The anisotropy coefficient α_B is obtained by combining eqns. (6.1.2-1), (6.2.2-2), and (6.2.2-3).

6.2.3 Model C

The third kinetic model incorporates the same ion-assisted etching rate as model A, however, the expression for [Cl] differs considerably. Given the evidence that diffusion limitations may be important, the [Cl] predictions of eqn. (5.2.2-5) are used here. The resulting prediction for etching rate is

$$R_C = k_{oC} [e^-] P^2 \gamma + k_{+C} \dot{I}_+ \tilde{\Delta}(E^*) . \quad (6.2.3-1)$$

The model C prediction of anisotropy coefficient is found by combining eqns. (6.2.3-1) and (6.1.2-1).

6.2.4 Model D

In this model, the atomic chlorine concentration is presumed to be determined by diffusion-limited second-order recombination at the electrodes, see eqn. (5.2.2-7); recall that this model gives good agreement with absolute measurements of [Cl] via LIA. The ion-assisted etch yield varies with the square root of ion energy, as suggested by the recent results of Rossen and Sawin (1986).

The ion-assisted etching rate is determined by integrating the product of the etch yield function, $g(E_+) = k_{+D}(E_+ - E^*)^{0.5}$, and the ion energy distribution given by eqn. (4.3.3-4). There are two expressions for the result, depending on the relative position of the mean ion energy \bar{E}_+ and the threshold energy E^* .

For $E^* > (P/P_0)\bar{E}_+$,

$$R_{+D} = \int_{E^*}^{8\bar{E}_+/3} k_{+D} \dot{\bar{I}}_+ (E_+ - E^*)^{0.5} \frac{2(1 - 3E_+/8\bar{E}_+)}{(8/3 - P/P_0)\bar{E}_+} dE_+ . \quad (6.2.4-1)$$

$$= \frac{k_{+D} (4/15 - \xi/10) (8\bar{E}_+/3 - E^*)^{1.5}}{(8/3 - \rho)\bar{E}_+} . \quad (6.2.4-2)$$

For $E^* \leq (P/P_0)\bar{E}_+$,

$$R_{+D} = \frac{2k_{+D} \dot{\bar{I}}_+}{(8/3 - \rho)} \left[(4/15 - 0.1\xi) (8\bar{E}_+/3 - E^*)^{1.5} + (0.15\rho + 0.1\xi - 2/3) (\rho\bar{E}_+ - E^*)^{1.5} \right] . \quad (6.2.4-3)$$

The total etching rate for model D is

$$R_D = k_{0D} ([e^-]P^2\gamma)^{0.5} + R_{+D} . \quad (6.2.4-4)$$

The anisotropy coefficient α_D is found by combining eqns. (6.2.4-4) and (6.1.2-1).

6.2.5 Comparison of Model Results

For each model the rate constants k_0 and k_+ were determined by linear regression, for both etching rate and anisotropy data. The etching rate model contains two adjustable parameters, while the anisotropy model contains only their ratio, $K_a = k_+/k_0$. Using the anisotropy data, the best value of K_a was first determined. Next, the combination of k_0 and k_+ which best fit the etching rate data was found and the ratio $K_R = k_+/k_0$ was calculated. The parameter ratio was then fixed intermediate between K_a and K_R , and the magnitudes of the parameters were chosen to best represent the etching rate. K_a and K_R agreed well for models A and C, while there was considerable disagreement for models B and D. Consequently, models B and D cannot simultaneously describe both etching rate and directionality. In all regressions, the relative error between the model and the data was minimized. The regression results for models A-C are summarized in Table 6-7; the k_+ and k_0 values listed are the "best fit" parameters determined by the procedure described above. Model C provided the best representation of both etching rate and directionality. Model D results were intermediate to those of models A and C, and are therefore not shown.

Using RSM, contour plots were generated from the experimental data and from the model predictions at the same conditions. In each case, the adjusted R^2 was ~ 0.90 , so the contours represent the data well. However, there is some error caused by the relatively small number of experiments, particularly in the anisotropy fits. This error should be considered when comparing the models with the data.

Table 6-7
Regression Results for Etching Models

	Model A	Model B	Model C
K_a	3.9×10^9	1.5×10^8	3.1×10^9
K_R	3.4×10^9	6.7×10^7	2.7×10^9
k_o	5.1×10^{-6}	5.5×10^{-7}	7.9×10^{-7}
k_+	1.9×10^3	4.5×10^1	2.3×10^3
Mean relative error in R	0.19	0.24	0.13
Mean relative error in α	0.40	0.35	0.26

Units:

k_{oA}, k_{oB}	$\text{cm}^3\text{-}\dot{\text{A}}/\text{torr-min}$
k_{oC}	$\text{cm}^3\text{-}\dot{\text{A}}/\text{torr}^2\text{-min}$
k_{+A}, k_{+C}	$\text{cm}^2\text{-}\dot{\text{A}}/\text{mA-min}$
k_{+B}	$\text{cm}^2\text{-}\dot{\text{A}}/\text{mA-eV-min}$

Etching rates were quite reproducible; the experimental error as estimated from the replicate runs is about 10%. However, measured anisotropy coefficients differed by as much as 0.3 for repeated experiments. The large relative errors in anisotropy are attributed to the nonuniformity of the etching rate over the sample surface, since distinct clearing patterns are observed for varying plasma conditions. Particularly in cases where chemical etching is dominant, nonuniform etching magnifies the effects of errors in overetch time (endpoint determination was done manually, by observing the laser interferometry signal) and position of the SEM sample on the etched wafer. In some cases it was also difficult to determine the undercut from the SEM micrographs.

Fig. 6-16 is a contour plot of the etching rate experimental data (design F13B) for the following range of conditions: power density 0.2-0.6 W/cm², pressure 0.2-0.8 torr, and 0.85 CF₃Cl mole fraction. The etching rate varies from about 300 to 3500 Å/min over this parameter space. To facilitate comparison, contour plots for the model predictions cover the same ranges of power and pressure. The etching rate generally decreases slightly with increased argon addition, but the more significant trends with power and pressure are unchanged by the argon dilution.

The etching rate predictions of model A (energy-independent ion-assisted etching rate) are shown in Fig. 6-17. Note that all general trends in the data are reproduced, and that the predicted etching rates are within about 500 Å/min of the data over the entire experimental range. However, the model tends to underpredict the

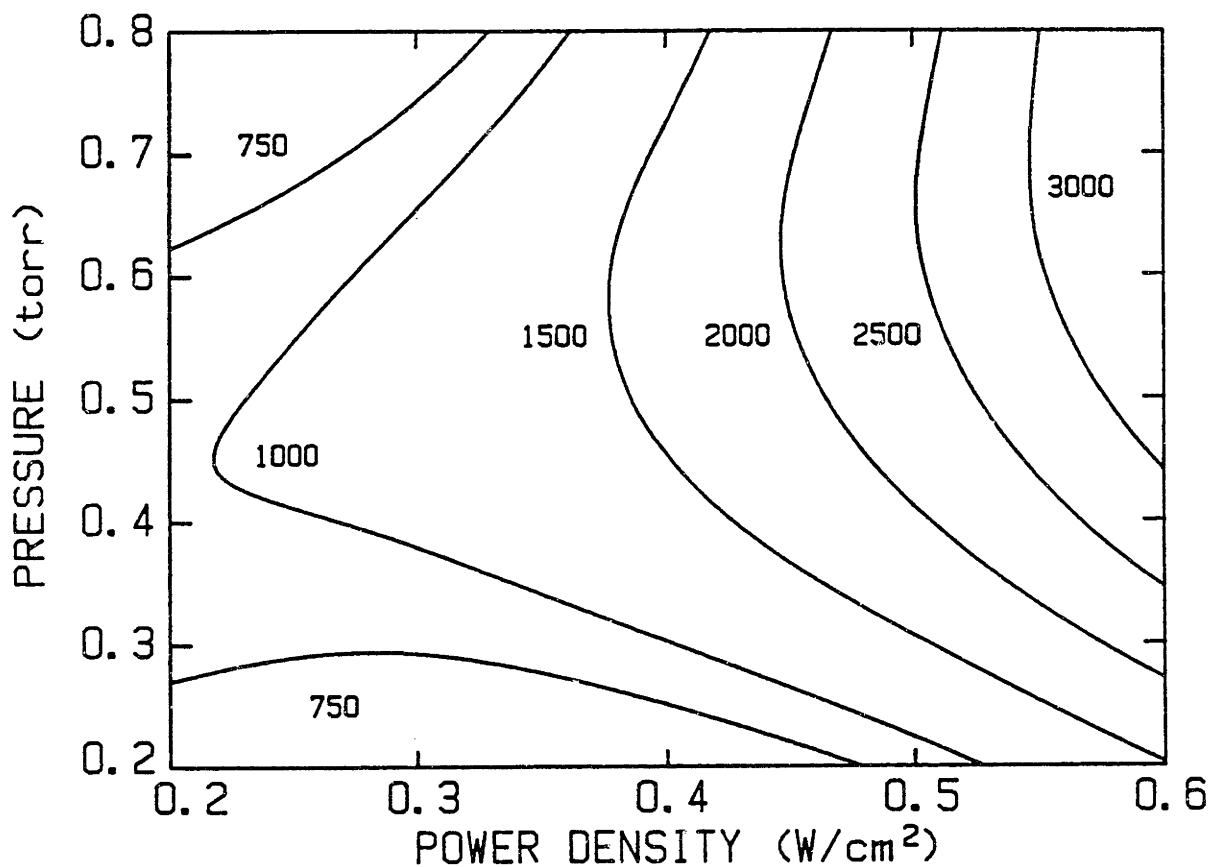


Figure 6-16: Contour plot of doped polysilicon etching rate ($\text{\AA}/\text{min}$) in $\text{CF}_3\text{Cl}/\text{Ar}$ discharges, vs. power density (watts/cm^2) and pressure (torr), $\gamma=0.85$. RSM fit of experimental data.

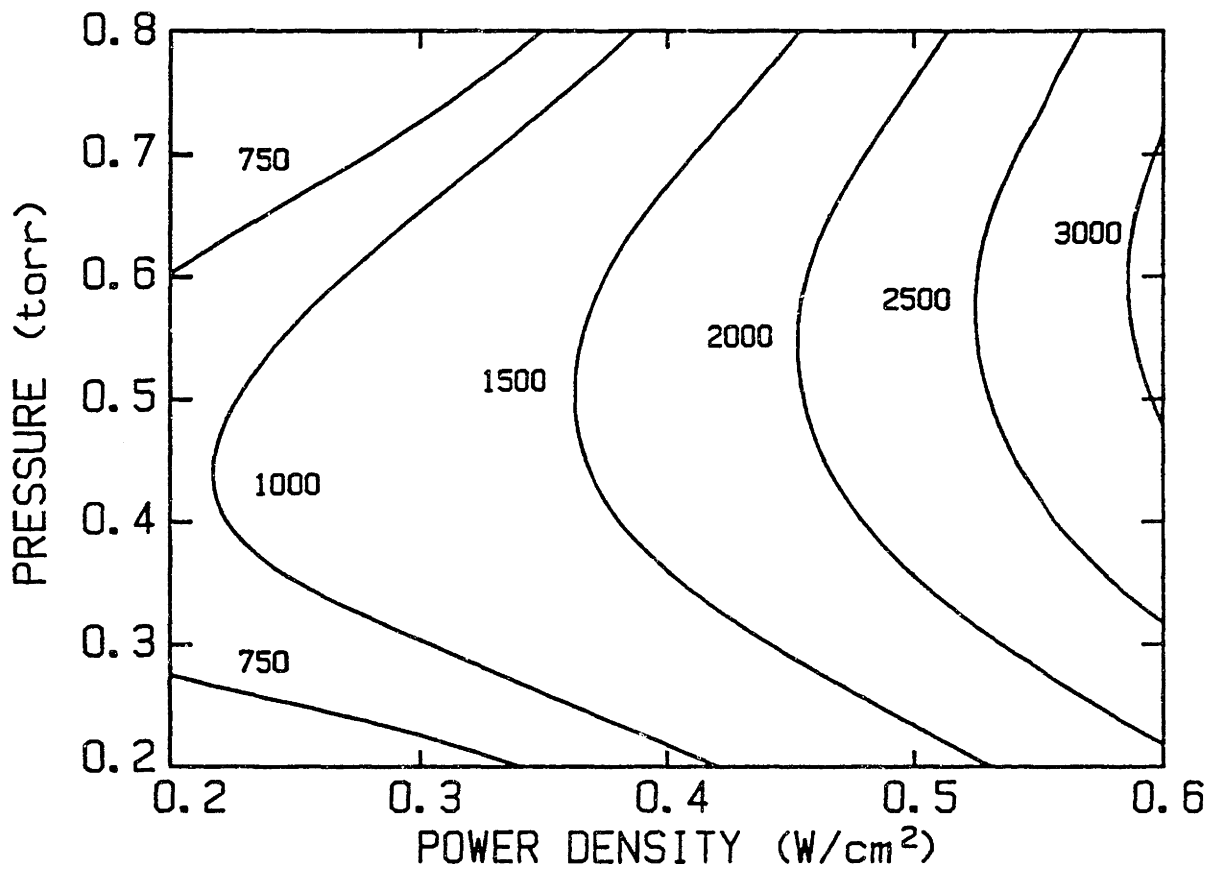


Figure 6-17: Contour plot of model A prediction of etching rate ($\text{\AA}/\text{min}$) in $\text{CF}_2\text{Cl}/\text{Ar}$ discharges, same process conditions as in Figure 6-16.

etching rate at high pressures and overpredict at low pressures. The predicted increase in etching rate with power density at high pressure is not as rapid as observed experimentally.

The anisotropy predictions of model A are less satisfying. The model prediction of α_0 is plotted against experiment in Fig. 6-18. At low pressures, the predicted α_0 is about 0.8, while the experimental result is 0.3. At high pressures, the model predicts more directional etching than is observed. The errors in anisotropy and etching rate indicate that the predicted chemical etching rate is too low at high pressures and too high at low pressures. The large random errors in the predicted anisotropy resulted in a poor RSM fit, so a contour plot of the model predictions is not shown.

Etching rates predicted by model B (energy-dependent ion contribution) are shown in Fig. 6-19. It is obvious that agreement between model and data is poor, as reflected in the higher mean error given in Table 6-7. The model severely underpredicts the increase of etching rate with power density, especially at moderate to high pressures. However, the qualitative shape of the model prediction with increasing pressure more closely mirrors the data than does model A. The linear dependence of etch yield on ion energy has increased the ion-assisted contribution at low pressure, but greatly reduced it for high pressures. Consequently, anisotropy representation is slightly improved over model A, see Fig. 6-20. Note that at the very low pressures etching is again more directional than predicted.

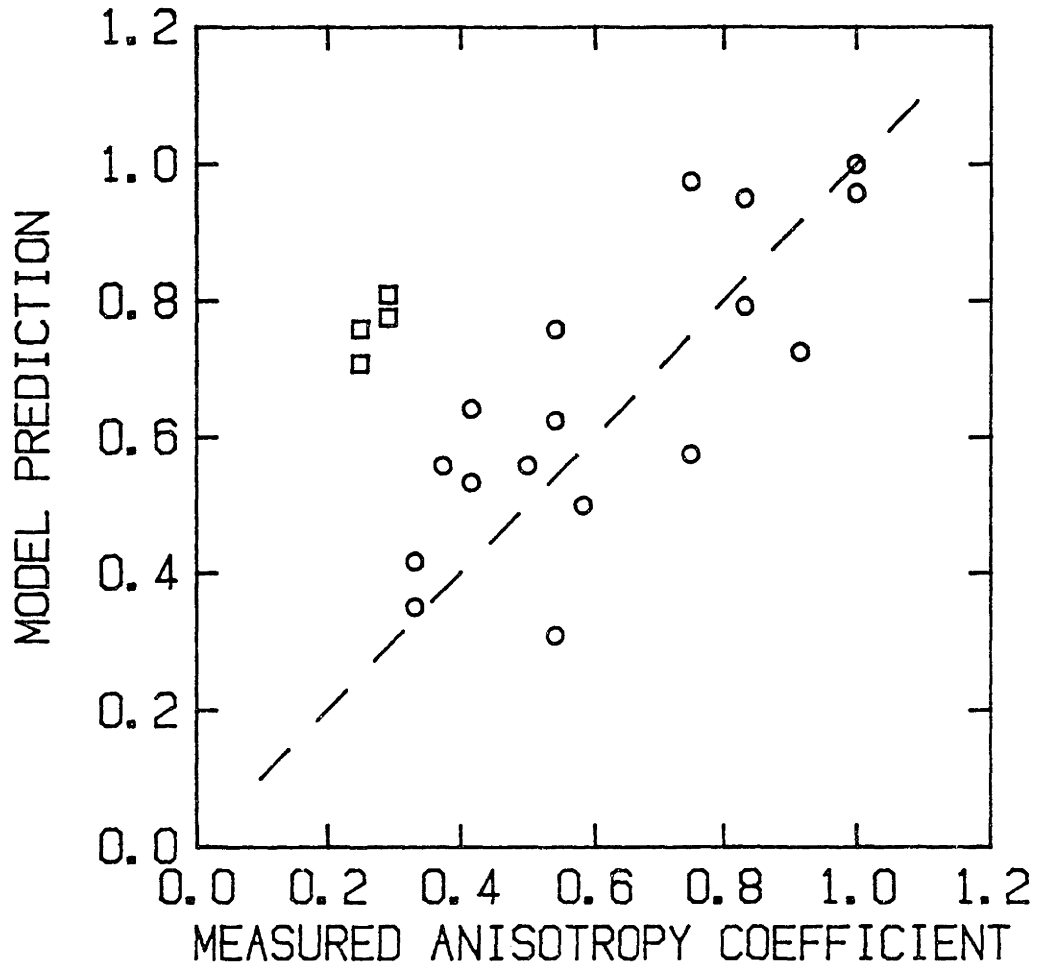


Figure 6-18: Model A prediction of anisotropy coefficient a_0 vs. experimental measure, various process conditions.

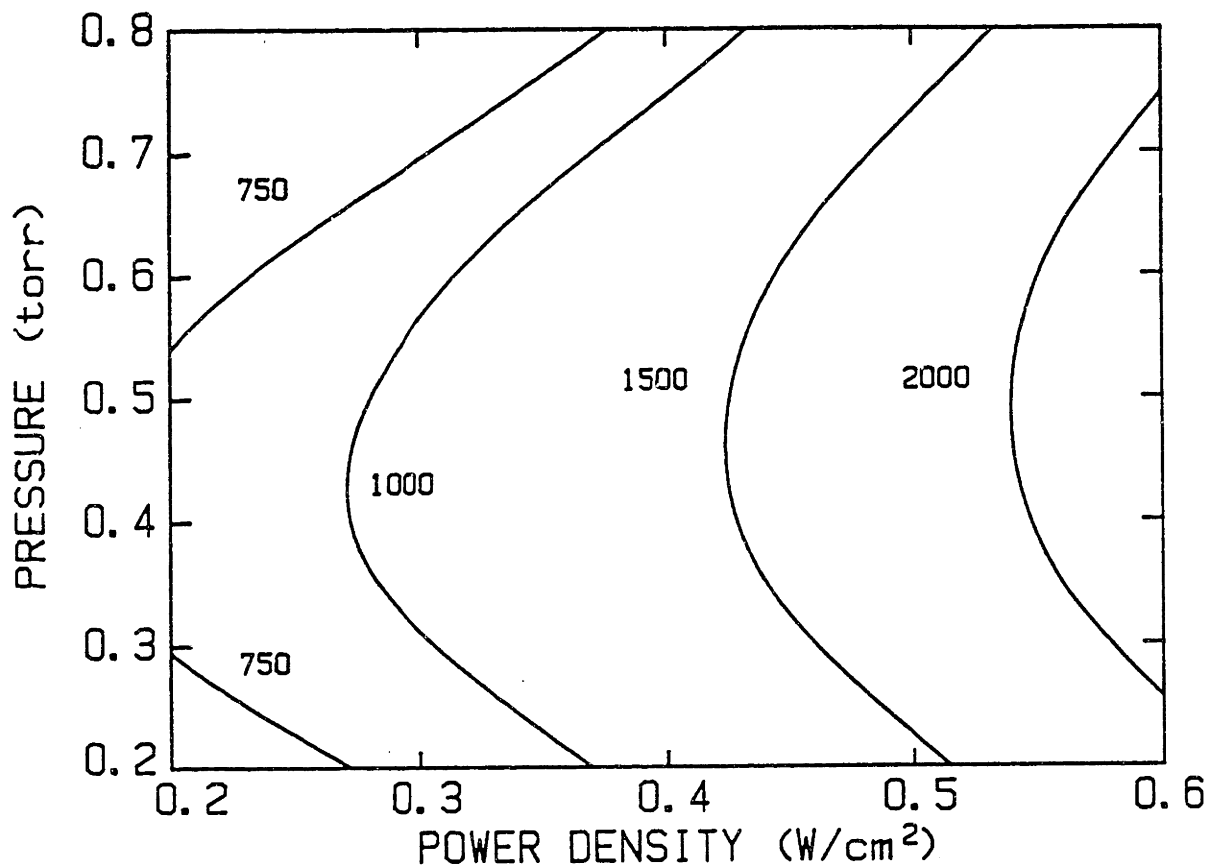


Figure 6-19: Contour plot of model B prediction of polysilicon etching rate ($\text{\AA}/\text{min}$) in CF_2Cl discharges, same process conditions as in Figure 6-16.

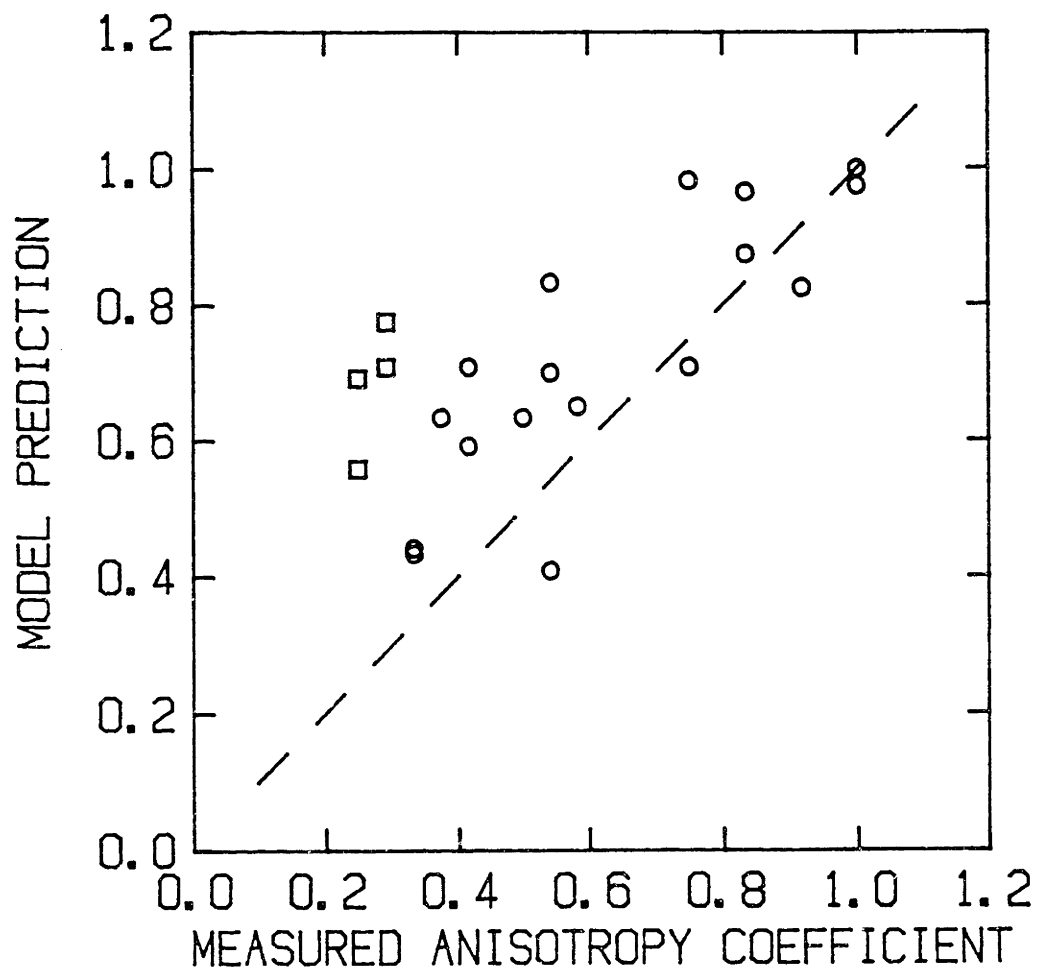


Figure 6-20: Model B prediction of anisotropy coefficient α_0 vs. experimental measure, various process conditions.

The model C (diffusion-limited recombination) results are excellent, as seen in Fig. 6-21. Model and experimental etching rates agree within 250 Å/min over the entire range; in addition, the model contours closely follow the data. Since experimental and RSM fitting errors are at least 10%, the model prediction and data are indistinguishable.

Model C also predicts the etching directionality quite well, see Fig. 6-22. Predicted anisotropy coefficients were generally within 10% of the measured value, with the most notable exception of the 0.2 torr data. At 0.2 torr, the model predictions were $\alpha_C=0.4-0.5$, still higher than measured experimentally, but much improved over the predictions of models A and B. The contours of Fig. 6-23 are somewhat poorer than the individual predictions at the experimental conditions because of the influence of the low pressure points on the RSM fit.

The model D results are not shown as contour plots here, since for both etching rate and anisotropy the results were intermediate between those of model A and model C. Given the unknown nature of the surface properties and the ion-surface properties, it is difficult to distinguish between models C and D; i.e., the differences in quality of fit may be due to random error.

Some interpretation of the fitted parameter values is possible. The energy-independent ion-assisted etching rate constants k_{+A} and k_{+C} are both about $2 \times 10^3 \text{ cm}^2\text{-Å}/\text{mA-min}$, which corresponds to an etching yield of about one silicon atom per incident ion. This etching yield compares favorably with literature values of 2-3 atoms/ion for 1 keV reactive ion bombardment of chlorine-dosed silicon surfaces (Krueger and Ruoff, 1985; Gerlach-Meyer et al., 1981).

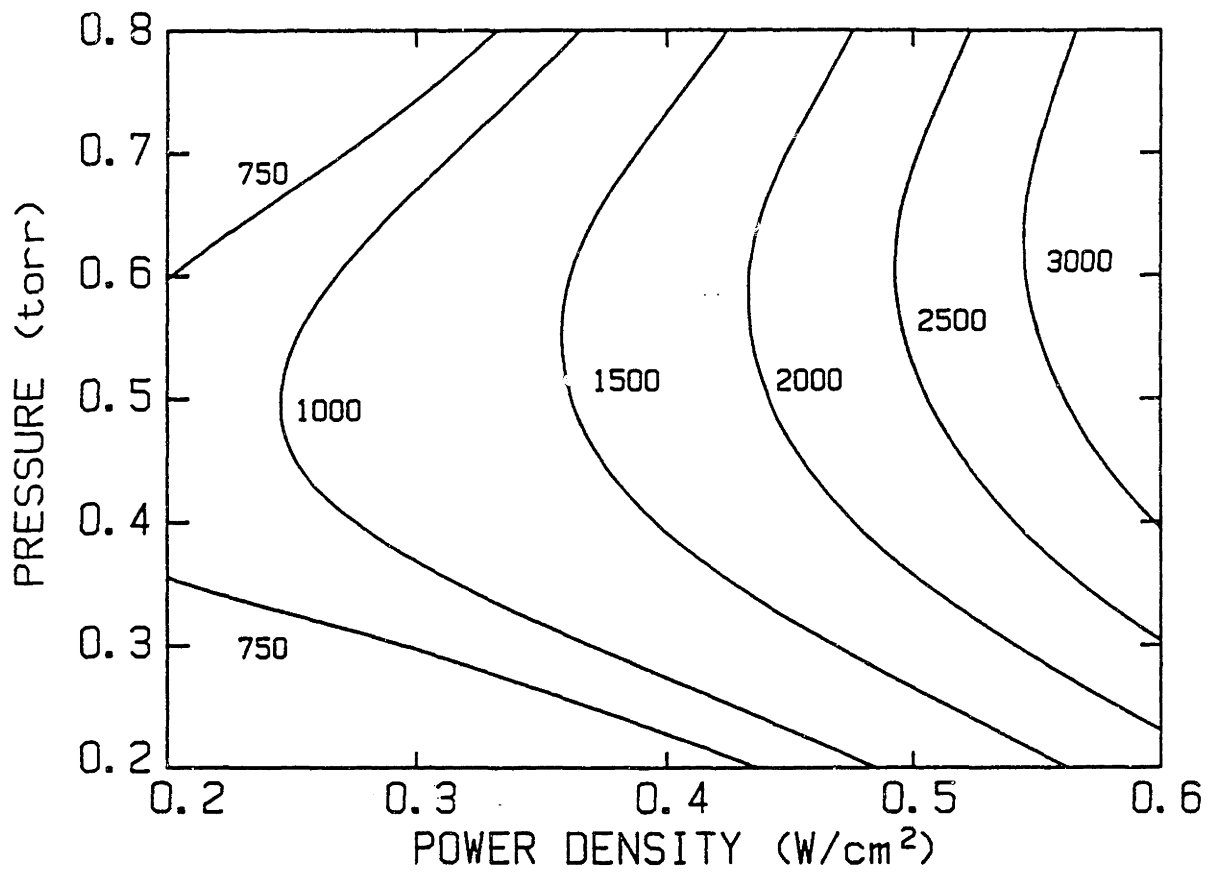


Figure 6-21: Contour plot of model C prediction of polysilicon etching rate ($\text{\AA}/\text{min}$) in $\text{CF}_3\text{Cl}/\text{Ar}$ discharges, same process conditions as in Figure 6-16.

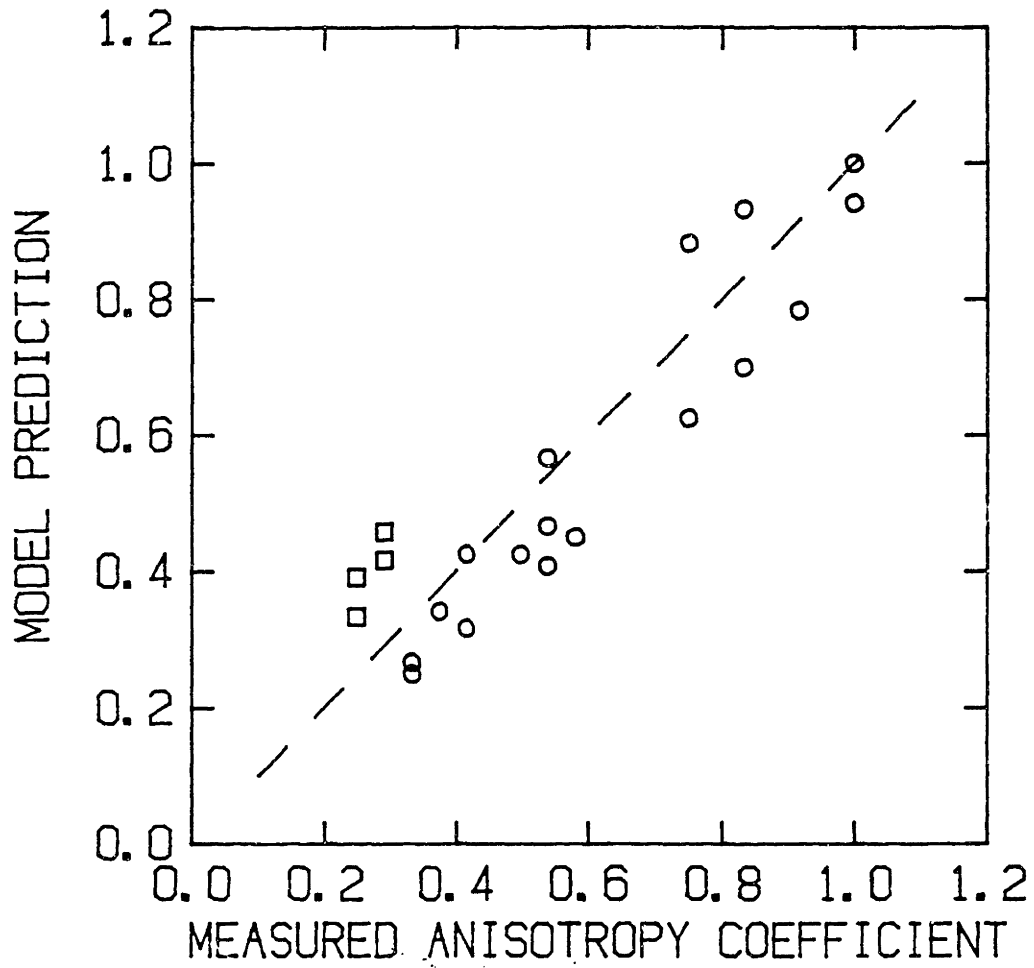


Figure 6-22: Model C prediction of anisotropy coefficient a_0 vs. experimental measure, various process conditions.

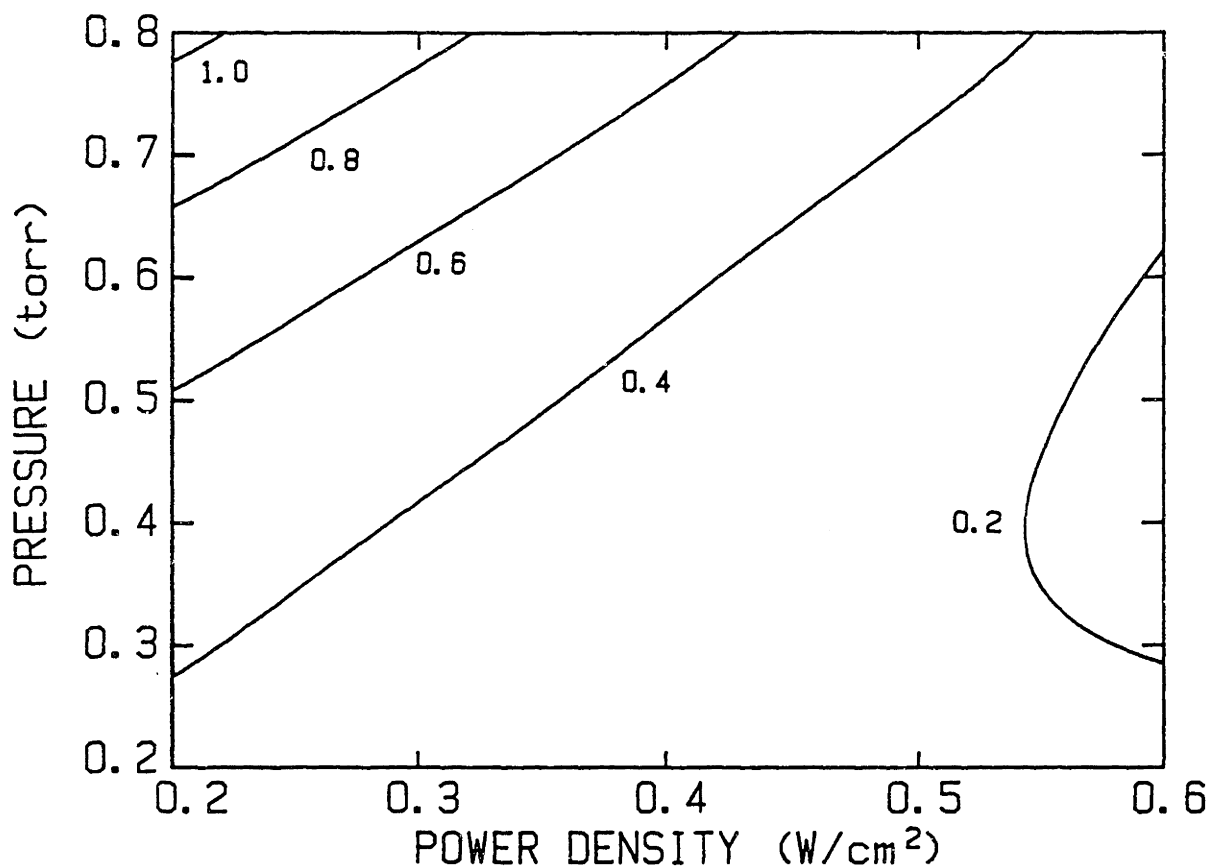


Figure 6-23: Contour plot of model C prediction of polysilicon anisotropy coefficient α_0 in $\text{CF}_3\text{Cl}/\text{Ar}$ discharges, vs. power density (watts/cm^2) and pressure (torr), $\gamma=0.85$. Compare with experimental data of Figure 6-5.

The lower etching yield obtained in the present study may be due to polymer coverage of the silicon surface, which is present in chlorofluorocarbon plasmas but is absent in UHV studies. The ion bombardment contribution is not purely physical in nature because the yield is much larger than silicon sputtering yields for 100 eV ion bombardment, which are about 0.01 atom per ion (Henschke and Derby, 1963; Laegreid and Wehner, 1961; Coburn et al., 1977).

The chemical etching parameters are more difficult to interpret because they contain several rate constants; also, the models do not properly account for species concentration gradients in the reactor. However, the value of k_e obtained using eqns. (5.2.2-4) and (6.2.1-3) along with $k_F \sim 5 \times 10^{-9}$ cm³/s is about 1×10^{-21} cm⁴/s, which corresponds to a surface reaction probability of about 8×10^{-4} . This result agrees fairly well with the etching rate of silicon (100) in atomic fluorine given elsewhere (Flamm et al., 1981), $k_E \sim 3 \times 10^{-22}$ cm⁴/s, although one might expect the atomic chlorine etching rate to be somewhat lower than that of atomic fluorine. The higher rate constant obtained in this study results partially from the higher intrinsic etching rate of doped polysilicon relative to that of single crystal silicon. Also, the atomic chlorine concentrations predicted by the models may be somewhat low, causing a too-high prediction of k_E .

The anisotropy data at 0.2 torr are poorly described by all models; the predicted profiles are more isotropic than the data. There are several possible explanations for the discrepancy. I observed a "microsensitvity" effect (Mogab and Levinstein, 1980) in the etching at low pressures; here, etching is slower in the immediate vicinity of the photoresist lines than on a clear polysilicon surface.

This effect, the opposite of the common loading effect, may be linked with the minor resist degradation observed at 0.2 torr; resist removed from the mask by sputtering or by chemical processes may be redeposited on the polysilicon surface near the mask. Presumably, the increased resist degradation at 0.2 torr is caused by the combination of high ion energy and high surface temperature (~ 50 °C) reached in these experiments. Note that the etching rate at 0.2 torr is on the order of 400 Å/min so the etching time required is long (approximately 10 minutes). Since the low pressure decreases heat transfer from the wafer to the electrode, the sample is expected to be hotter than in the higher pressure runs. The photoresist etching rate was not measured in this work, however, there is strong evidence that chlorinated plasmas can attack photoresist. The resist may act as a source for chlorocarbon species which form a thin passivating film on the sidewalls. This effect may account for the anisotropy observed in SF₆/CFC1₂ (Freon^R 11) discharges as compared with pure SF₆ (Meith and Barker, 1983; Mocella et al., 1986a).

The poor prediction of anisotropy at 0.2 torr may also be attributable to inaccuracies of the impedance model. At 0.2 torr, the discharge is not well confined. Consequently, electron densities predicted by the impedance model could be artificially high due to increased plasma volume, causing a larger contribution to the chemical etching rate in the kinetic model. Lowering the electron densities of these errant points would not only improve the anisotropy prediction to within experimental error of the measured values, but would improve the etching rate predictions as well.

The simplicity of the models is not meant to imply that the chemical processes responsible for etching are well understood, but rather that such a complex system requires cautious evaluation. We have chosen the simplest model possible to describe each important phenomenon in the etching process. Obvious omissions are surface passivation by polymerization reactions, the contributions of the plasma chemistry to etchant loss, the synergy of chemical and ion-assisted surface processes (i.e., the effect of surface coverage and reactant depletion on ion-assisted etching yield), and surface reaction temperature effects. In addition, the primary etchant species may not be produced by direct electron-impact dissociation of the parent gas. The impedance model predictions may be in error at high pressures where significant power dissipation in the sheaths occurs, and at low pressures where loss of containment changes the plasma volume.

The most important shortcoming of these models is the lack of synergy between the neutrals and the ions. It has been shown that the surface coverage of silicon by chlorine influences the yield of etching product per incident ion (Coburn et al., 1977). Surface coverage is also a function of ion flux, due to bombardment-induced desorption. In CF_3Cl plasma etching, the neutral to ion flux ratio, and in turn the surface coverage, may vary considerably with plasma conditions. The rapid increase in etching rate with power at high pressure may be due in part to high fractional chlorine coverages, while the lesser influence of power input at low pressure may result from low fractional chlorine coverage.

REFERENCES

- Adams, A.C., and C.D. Capiro, "Edge Profiles in the Plasma Etching of Polycrystalline Silicon", *J. Electrochem. Soc.* **128**, 366 (1981).
- Ajello, J.M., W.T. Huntress, Jr., and P. Rayermann, "A Photoionization Mass Spectrometer Study of CFCl_3 , CF_2Cl_2 , and CF_3Cl ", *J. Chem. Phys.* **64**, 4746 (1976).
- Allen, K.D., and H.H. Sawin, "The Plasma Etching of Polysilicon with $\text{CF}_3\text{Cl}/\text{Ar}$ Discharges II. Modeling of Ion Bombardment Energy Distributions", *J. Electrochem. Soc.*, to be published (1986).
- Allen, K.D., H.H. Sawin, M.T. Mocella, and M.W. Jenkins, "The Plasma Etching of Polysilicon with $\text{CF}_3\text{Cl}/\text{Ar}$ Discharges I. Parametric Modeling and Impedance Analysis", *J. Electrochem. Soc.*, to be published (1986a).
- Allen, K.D., H.H. Sawin, and A. Yokozeiki, "The Plasma Etching of Polysilicon with $\text{CF}_3\text{Cl}/\text{Ar}$ Discharges III. Modeling of Etching Rate and Directionality", *J. Electrochem. Soc.*, to be published (1986b).
- Allen, K.D., A.D. Richards, B.E. Thompson, and H.H. Sawin, "The Plasma Etching of Polysilicon with $\text{CF}_3\text{Cl}/\text{Ar}$ Discharges IV. Measurement and Modeling of Atomic Chlorine Concentration", in preparation (1986c).
- Aston, G., and P.J. Wilbur, "Ion Extraction from a Plasma", *J. Appl. Phys.* **52**, 2614 (1981).
- Anciello, O., "Ion Interaction with Solids: Surface Texturing, some Bulk Effects, and their Possible Applications", *J. Vac. Sci. Technol.* **19**, 841 (1981).
- Barker, R.A., T.M. Mayer, and W.C. Pearson, "Surface Studies of and a Mass Balance Model for Ar^+ Ion-Assisted Cl_2 Etching", *J. Vac. Sci. Technol. B* **1**, 37 (1983).
- Barish, E.L., D.J. Vitkavage, and T.M. Mayer, "Sputtering of Chlorinated Silicon Surfaces Studied by Secondary Ion Mass Spectrometry and Ion Scattering Spectroscopy", *J. Appl. Phys.* **57**, 1336 (1985).
- Basco, N., and F.G.M. Hathorn, "The Electronic Absorption Spectrum of the Trifluoromethyl Radical", *Chem. Phys. Lett.* **8**(3), 291 (1971).

Bell, A.T., "Fundamentals of Plasma Chemistry", in Techniques and Applications of Plasma Chemistry (H.R. Hollahan and A.T. Bell, eds.), Wiley, New York, 1974, pp. 1.

Benson, S.W., Thermochemical Kinetics: Methods for the Estimation of Thermochemical Data and Rate Parameters, 2nd ed., Wiley-Interscience, New York, 1976.

Bergendahl, A.S., S.F. Bergeron, and B.F. Duncan, "Optimization of Plasma Processing for Silicon-Gate FET Manufacturing Applications", IBM J. Res. Develop. 26(5), 580 (1982).

Bergeron, S.F., and B.F. Duncan, "Controlled Anisotropic Etching of Polysilicon", Solid State Technol. 25(8), 98 (1982).

Bernacki, S.E., and B.B. Kosicki, "Controlled Film Formation during CCl_4 Plasma Etching", J. Electrochem. Soc. 131, 1926 (1984).

Bezmelnitsin, V.N., B.B. Chaivanov, V.A. Legasov, and A.A. Vasiliev, "Kinetics of Three-Body Homogeneous Recombination of Fluorine Atoms at 77 K", React. Kinet. Catal. Lett. (Russian) 24, 287 (1984).

Bohn, P.W., and R.C. Manz, "A Multiresponse Factorial Study of Reactor Parameters in Plasma-Enhanced CVD Growth of Amorphous Silicon Nitride", J. Electrochem. Soc. 132, 1981 (1985).

Bisschops, T.J., and F.J. de Hoog, "On the Plasmaphysics of Plasma Etching", Pure Appl. Chem. 57, 1311 (1985).

Bondur, J.A., "Dry Process Technology (Reactive Ion Etching)", J. Vac. Sci. Technol. 13, 1023 (1976).

Borghesani, A.F., and F. Mori, "Undercut in a CF_4 -Based High-Pressure Poly-Si Etch", Japan. J. Appl. Phys. 22, 712 (1983).

Bower, D.H., "Planar Plasma Etching of Polysilicon using CCl_4 and NF_3 ", J. Electrochem. Soc. 129, 795 (1982).

Box, G.E.P., W.G. Hunter, and J.S. Hunter, Statistics for Experimenters: An Introduction to Design, Data Analysis, and Model Building, Wiley-Interscience, New York, 1983.

Boyd, R.K., and G. Burns, "Halogen Recombination-Dissociation Reactions. Current Status", J. Phys. Chem. 83, 88 (1979).

Bozzelli, J.W., and M. Kaufmann, "Kinetics and Mechanism of Reactions of Atomic Fluorine with CF_3I and CCl_3Br ", J. Phys. Chem. 77, 1748 (1973).

Bozzelli, J.W., C.E. Kolb, and M. Kaufmann, "Reaction Between Atomic Fluorine and CF_3Br : Evidence for a Pseudotrihalogen Radical Intermediate", *J. Chem. Phys.* **59**, 3669 (1973).

Brandt, W.W., and T. Honda, "Mass Spectrometric Transient Study of DC Plasma Etching of Si in CF_4 and CF_4/O_2 Mixtures", *J. Appl. Phys.* **57**, 119 (1985).

Brandt, W.W., and J.J. Wagner, "Kinetic Studies of SF_6 Plasmas During Etching of Si", *Plasma Chem. and Plasma Process.* **3**, 329 (1983).

Brandt, W.W., J.J. Wagner, and T. Honda, "Studies on Product Layers Formed During Etching of Si in a SF_6 Plasma", *J. Appl. Phys.* **56**, 1195 (1984).

Brown, H.L., "Plasma Etcher Capital Equipment Design Trends", *Solid State Technol.* **26**(4), 239 (1983).

Brown, S.C., Introduction to Electrical Discharges in Gases, John Wiley and Sons, New York (1965).

Bruce, R.H., "Anisotropy Control in Dry Etching", *Solid State Technol.* **24**(10), 64 (1981a).

Bruce, R.H., "Ion Response to Plasma Excitation Frequency", *J. Appl. Phys.* **52**, 7064 (1981b).

Bruce, R.H., and A.R. Reinberg, "Effect of Etching Discharge Frequency", in Proceedings of the Second Symposium on Dry Processing, The Electrochemical Society, Pennington, NJ, 1980, pp. 131.

Bruce, R.H., and A.R. Reinberg, "Profile Control with DC Bias in Plasma Etching", *J. Electrochem. Soc.* **129**, 393 (1982).

Broydo, S., "Important Considerations in Selecting Anisotropic Plasma Etching Equipment", *Solid State Technol.* **26**(4), 159 (1983).

Bulat, E.S., G.F. Doyle, and B. Gelernt, "Optical Emission and Pressure Correlations During Plasma Etching", *Semiconductor International* **5**(11), 113 (1982).

Butkovskaya, N.I., Larichev, M.N., Leipunskii, I.O., Morozov, I.I., and Talroze, V.L., "Mass-Spectrometric Study of the Recombination of Atomic Fluorine with Trifluoromethyl and Difluoromethylene Biradical", *Kinet. Katal.* **21**(2), 343 (1980).

Butler, H., and G.S. Kino, "Plasma Sheath Formation by Radio Frequency Fields", *Phys. Fluids* **6**, 1346 (1963).

- Cantin, A., and R.R.J. Gagne, "The Proper Use of Electrostatic Probes in Electrodeless RF Plasmas", IEEE Trans. AP-16, 279 (1968).
- Cappelli, A.L., R.A. Gottscho, and T.A. Miller, "Doppler-Broadened Line Shapes of Atomic Hydrogen in a Parallel-Plate Radio Frequency Discharge", Plasma Chem. Plasma Process. 5(4), 317 (1985).
- Cartier, S., and R. Bosch, "Wide Range Langmuir Probe Sweep Circuit", Rev. Sci. Instrum. 54, 1789 (1983).
- Chang, P.C., and S. Hsia, "Selective Plasma Etching of Polysilicon", Solid State Technol. 27(8), 225 (1984).
- Chapman, B.N., Glow Discharge Processes, Wiley-Interscience, New York, 1980.
- Chen, C.J., "Temperature Effect on Langmuir Probe Measurement", J. Appl. Phys. 35, 1130 (1964).
- Chen, F.F., "Electric Probes", in Plasma Diagnostic Techniques (R.H. Huddlestone and S.L. Leonard, eds.), Academic Press, New York, 1965.
- Cherrington, B.E., "The Use of Electrostatic Probes for Plasma Diagnostics -- A Review", Plasma Chem. Plasma Process. 2, 113 (1982).
- Chuang, T.J., "Electron Spectroscopy Study of Silicon Surfaces Exposed to XeF₂ and the Chemisorption of SiF₄ on Silicon", J. Appl. Phys. 51, 2614 (1980).
- Chow, T.P., and G.M. Fanelli, "Reactive Ion Etching of Silicon and Silicides in SF₆ or NF₃/CCl₄ or HCl Mixtures", J. Electrochem. Soc. 132, 1969 (1985).
- Clements, R.M., "Plasma Diagnostics with Electric Probes", J. Vac. Sci. Technol. 15, 193 (1978).
- Coburn, J.W., "Plasma-Assisted Etching", Plasma Chem. Plasma Process. 2, 1 (1982).
- Coburn, J.W., and M. Chen, "Optical Emission Spectroscopy of Reactive Plasmas: A Method for Correlating Emission Intensities to Reactive Particle Density", J. Appl. Phys. 51, 3134 (1980).
- Coburn, J.W., and M. Chen, "Dependence of F Atom Density on Pressure and Flow Rate in CF₄ Glow Discharges as Determined by Emission Spectroscopy", J. Vac. Sci. Technol. 18, 353 (1981).
- Coburn, J.W., and E. Kay, "Pressure Considerations Associated with Ion Sampling from Glow Discharges", J. Vac. Sci. Technol. 8, 738 (1971).

Coburn, J.W., and E. Kay, "Positive-Ion Bombardment of Substrates in rf Diode Glow Discharge Sputtering", *J. Appl. Phys.* **43**, 4965 (1972).

Coburn, J.W., and E. Kay, "Some Chemical Aspects of the Fluorocarbon Plasma Etching of Silicon and its Compounds", *IBM J. Res. Develop.* **23**(1), 33 (1979).

Coburn, J.W., and H.F. Winters, "Plasma Etching- A Discussion of Mechanisms", *J. Vac. Sci. Technol.* **16**, 391 (1979a).

Coburn, J.W., and H.F. Winters, "Ion- and Electron-Assisted Gas-Surface Chemistry - An Important Effect in Plasma Etching", *J. Appl. Phys.* **50**, 3189 (1979b).

Coburn, J.W., H.F. Winters, and T.J. Chuang, "Ion-Surface Interactions in Plasma Etching", *J. Appl. Phys.* **48**, 3532 (1977).

Cochran, W.G., and G.M. Cox, Experimental Designs, John Wiley, New York (1957).

Collie, M.J., ed., Etching Compositions and Processes, Noyes Data Corporation, Park Ridge, NJ, 1982.

Cramer, W.H., "Elastic and Inelastic Scattering of Low-Velocity He⁺ Ions in Helium", *J. Chem. Phys.* **26**, 1272 (1957).

Cramer, W.H., "Elastic and Inelastic Scattering of Low-Velocity Ions: He⁺ in Ne, Ne⁺ in He, and Ne⁺ in Ne", *J. Chem. Phys.* **28**, 688 (1958).

Cramer, W.H., "Elastic and Inelastic Scattering of Low-Velocity Ions: Ne⁺ in A, A⁺ in Ne, and A⁺ in A", *J. Chem. Phys.* **30**, 641 (1959).

Curran, R.K., "Positive and Negative Ion Formation in CCl₂F", *J. Chem. Phys.* **34**, 2007 (1961).

Dalvie, M., K.F. Jensen, and D.B. Graves, "Modelling of Reactors for Plasma Processing I. Silicon Etching by CF₄ in a Radial Flow Reactor", *Chem. Engin. Science, Proc. Ninth Intern. Symp. Chem. Reactor Engin.*, to be published (1986).

d'Agostino, R., "Summary Abstract: Mechanisms of Polymerization in Discharges of Fluorocarbons", *J. Vac. Sci. Technol. A* **3**, 2627 (1985a).

d'Agostino, R., P. Capezzuto, G. Bruno, and F. Cramarossa, "Mechanism of Etching, Polymerization and Deposition in rf (radio frequency) Discharges", *Pure Appl. Chem.* **57**, 1287 (1985b).

d'Agostino, R., V. Colaprico, and F. Cramarossa, "The Use of 'Actinometer' Gases in Optical Diagnostics of Plasma Etching Mixtures: SF₆-O₂", *Plasma Chem. and Plasma Process.* **1**, 365 (1981a).

d'Agostino, F. Cramarossa, and S. De Benedictis, "Diagnostics and Decomposition Mechanism in Radio-Frequency Discharges of Fluorocarbons Utilized for Plasma Etching or Polymerization", *Plasma Chem. and Plasma Process.* **2**(3), 213 (1982).

d'Agostino, R., F. Cramarossa, S. De Benedictis, and G. Ferraro, "Spectroscopic Diagnostics of CF_4-O_2 Plasmas During Si and SiO_2 Etching Processes", *J. Appl. Phys.* **52**, 1259 (1981b).

d'Agostino, R., F. Cramarossa, S. De Benedictis, and F. Fracassi, "Optical Emission Spectroscopy and Actinometry in CCl_4 Plasmas During Si and SiO_2 Etching Processes", *J. Appl. Phys.* **52**, 1259 (1981c).

Davis, W.D., and T.A. Vanderslice, "Ion Energies at the Cathode of a Glow Discharge", *Phys. Rev.* **131**, 219 (1963).

Degenkolb, E., K.O. Park, J.B. Shorter, and M. Tabasky, "Highly Selective Dry Etching of Polysilicon using Chlorinated Gas Mixtures for VLSI Applications", *J. Electrochem. Soc.* **132**, 2027 (1985).

Dibeler, V.H., R.M. Reese, and F.L. Mohler, "Ionization and Dissociation of Trifluoromethyl Halides by Electron Impact", *J. Res. Nat. Bur. Stds.* **57**, 113 (1956).

Donnelly, V.M., and D.L. Flamm, "Studies of Chemiluminescence Accompanying Fluorine Atom Etching of Silicon", *J. Appl. Phys.* **51**, 5273 (1980).

Donnelly, V.M., and D.L. Flamm, "Anisotropic Etching in Chlorine-Containing Plasmas", *Solid State Technol.* **24**(4), 161 (1981).

Donnelly, V.M., D.L. Flamm, and R.H. Bruce, "Effects of Frequency on Optical Emission, Electrical, Ion, and Etching Characteristics of a Radio Frequency Chlorine Plasma", *J. Appl. Phys.* **58**, 2135 (1985).

Donnelly, V.M., D.L. Flamm, and G. Collins, "Laser Diagnostics of Plasma Etching: Measurement of Cl_2^+ in a Chlorine Discharge", *J. Vac. Sci. Technol.* **21**, 817 (1982).

Doucet, J., P. Sauvageau, and C. Sandorfy, "Vacuum Ultraviolet and Photoelectron Spectra of Fluoro-Chloro Derivatives of Methane", *J. Chem. Phys.* **58**, 3708 (1973).

Dreyfus, R.W., J.M. Jasinski, R.E. Walkup, and G.S. Selwyn, "Optical Diagnostics of Low Pressure Plasmas", *Pure Appl. Chem.* **57**, 1265 (1985).

E.I. Dupont de Nemours and Co., Inc., "Strategy of Experimentation" course notebook, Applied Technology, Wilmington, DE (1978).

Easley, M.A., "Probe Technique for the Measurement of Electron Temperature", J. Appl. Phys. 22, 590 (1951).

Edelson, D., and D.L. Flamm, "Computer Simulation of a CF₄ Plasma Etching Silicon", J. Appl. Phys. 56, 1522 (1984).

Egerton, E.J., A. Nef, W. Milliken, W. Cook, and D. Baril, "Positive Wafer Temperature Control to Increase Dry Etch Throughput and Yield", Solid State Technol. 25(8), 84 (1982).

Enomoto, T., "Loading Effect and Temperature Dependence of Etch Rate of Silicon Materials in CF₄ Plasma", Solid State Technol. 23(4), 117 (1980).

Ephrath, L.M., "Dry Etching for VLSI- A Review", J. Electrochem. Soc. 129, 62C (1982).

Ephrath, L.M., and D.J. DiMaria, "Review of RIE-Induced Radiation Damage in Silicon Dioxide", Solid State Technol. 24(4), 182 (1981).

Ephrath, L.M., D.J. DiMaria, and F.L. Pesavento, "Parameter Dependence of RIE-Induced Radiation Damage in Silicon Dioxide", J. Electrochem. Soc. 128, 2415 (1981).

Eser, E., and R.E. Oglivie, "Measurement of Plasma Discharge Characteristics for Sputtering Applications", J. Vac. Sci. Technol. 15, 199 (1978).

Eser, E., R.E. Oglivie, and K.A. Taylor, "Plasma Characterization in Sputtering Processes Using the Langmuir Probe Techniques", Thin Solid Films 68, 381 (1980).

Farrow, L.A., "Infrared Laser Spectroscopy of BCl₃ in an rf Discharge", J. Chem. Phys. 82, 3625 (1985).

Field, D., A.J. Hydes, and D.F. Klemperer, "Spatially Resolved Optical Emission Spectroscopy of Plasma Etching Systems", Vacuum 34, 347 (1984).

Field, D., A.J. Hydes, and D.F. Klemperer, "Spectroscopic Studies of Fluorescent Emission in Plasma Etching of Si and SiO₂ and the Mechanism of Gas-Surface Interactions", Vacuum 34, 563 (1984).

Finlayson, B.A., Nonlinear Analysis in Chemical Engineering, McGraw-Hill Inc., New York, 1980.

Fisher, D.A., B.E. Thompson, and H.H. Sawin, "Monte Carlo Modeling of Ion Transport through rf Glow Discharge Sheaths", Materials Research Society Spring Meeting, Palo Alto, CA (1986).

Flamm, D.L., "Mechanisms of Radical Production in Radiofrequency Discharges of CF_3Cl , CF_3Br , and Certain Other Plasma Etchants: Spectrum of a Transient Species", *J. Appl. Phys.* **51**, 5688 (1981).

Flamm, D.L., P.L. Cowan, and J.A. Golovchenko, "Etching and Film Formation in CF_3Br Plasmas: Some Qualitative Observations and their General Implications", *J. Vac. Sci. Technol.* **17**, 1341 (1980).

Flamm, D.L., V.M. Donnelly, and J.A. Mucha, "The Reaction of Fluorine Atoms with Silicon", *J. Appl. Phys.* **52**, 3633 (1981).

Flamm, D.L., V.M. Donnelly, and D.E. Ibbotson, "Basic Chemistry and Mechanisms of Plasma Etching", *J. Vac. Sci. Technol. B* **1**, 23 (1983).

Franklin, J.L., J.G. Dillard, H.M. Rosenstock, J.T. Herron, K. Draxl, and F.H. Field, "Ionization Potentials, Appearance Potentials, and Heats of Formation of Gaseous Positive Ions", National Bureau of Standards #NSRDS-NBS 26 (1969).

Gerlach-Meyer, U., "Ion Enhanced Gas-Surface Reactions: A Kinetic Model for the Etching Mechanism", *Surface Science* **103**, 524 (1981).

Gerlach-Meyer, U., J.W. Coburn, and E. Kay, "Ion-Enhanced Gas-Surface Chemistry: The Influence of the Mass of the Incident Ion", *Surface Science* **103**, 177 (1981).

Ghandi, S.K., VLSI Fabrication Principles: Silicon and Gallium Arsenide, Wiley-Interscience, New York, 1983.

Gottscho, R.A., "Time Resolved Diagnostics of RF Plasmas: A Fluid Model for Ion Concentrations in the Sheath", in Plasma Synthesis and Etching of Electronic Materials (R.P. Chang and B. Abeles, eds.), *Mat. Res. Soc. Symp. Proc.* **38** (1985), Materials Research Society, Pittsburgh, pp. 55.

Gottscho, R.A., R.H. Burton, D.L. Flamm, V.M. Donnelly, and G.P. Davis, "Ion Dynamics of rf Plasmas and Plasma Sheaths: A Time-Resolved Spectroscopic Study", *J. Appl. Phys.* **55**, 2707 (1984).

Gottscho, R.A., G.P. Davis, and R.H. Burton, "Spatially Resolved Laser-Induced Fluorescence and Optical Emission Spectroscopy of Carbon Tetrachloride Glow Discharges", *Plasma Chem. Plasma Process.* **3**(2), 193 (1983).

Gottscho, R.A., and T.A. Miller, "Optical Techniques in Plasma Diagnostics", *Pure Appl. Chem.* **56**(2), 189 (1984).

Graves, D.B., and K.F. Jensen, "Modelling Gas Discharge Chemical Reactors", presented at the annual meeting of the AIChE, San Francisco (November 1984).

Graves, D.B., and K.F. Jensen, "A Continuum Model of DC and RF Discharges", IEEE Trans. Plasma Science PS-14, 78 (1986).

Greaves, J.C., and J.W. Linnett, "Recombination of Atoms on Surfaces. Part 6 - Recombination of Oxygen Atoms on Silica From 20 °C to 600 °C", Trans. Faraday Soc. 55, 1355 (1959).

Harshbarger, W.R., R.A. Porter, T.A. Miller, and P. Norton, "A Study of the Optical Emission from an rf Plasma During Semiconductor Etching", Appl. Spectroscopy. 31(3), 201 (1977).

Heimann, P.A., "Optical Etch-Rate Monitoring Using Active Device Areas: Lateral Interference Effects", J. Electrochem. Soc. 132, 2003 (1985).

Henschke, E.B., and S.E. Derby, "Full-Plane Threshold Energies for Cathode Sputtering of Metals with Ar⁺ Ions", J. Appl. Phys. 34, 2458 (1963).

Hiraoka, H., and L.W. Welsh Jr., "Negative Fluorine Ions in Plasma Etching", in Plasma Processing (R.G. Frieser and C.J. Mogab, eds.), Electrochemical Society Proceedings Volume 81-1, The Electrochemical Society, Pennington, NJ, 1981, pp. 59.

Hirschfelder, J.O., C.F. Curtiss, and R.B. Bird, Molecular Theory of Gases and Liquids, John Wiley and Sons, New York (1964).

Hoerl, A.E., and R.W. Kennard, "Ridge Regression: Biased Estimation for Nonorthogonal Problems", Technometrics 12, 55 (1970).

Höfler, K., "Methods of Plasma Characterization", Balzers technical report #BG 800 184 PA (1984).

Honda, T., and W.W. Brandt, "Mass Spectrometric Transient Study of DC Plasma Etching of Si in NF₃ and NF₃/O₂ Mixtures", J. Electrochem. Soc. 131, 2667 (1984).

Horwath, R.S., and C.B. Zarowin, "Flow Effects in Silicon Plasma Etching with Chlorine Containing Gases", Proceedings of the 2nd Symposium on Dry Processing (1980), The Electrochemical Society, Pennington, NJ, 1980.

Hsu, D.S.Y., M.E. Umstead, and M.C. Lin, "Kinetics and Mechanisms of Reactions of CF, CHF, and CF₂ Radicals", in Fluorine-Containing Free Radicals. Kinetics and Dynamics of Reaction (J.W. Root, ed.), ACS Symposium Series 66, American Chemical Society, Washington, 1978.

Illenberger, E., H.-U. Scheunemann, and H. Baumgärtel, "Negative Ion Formation in CF₂Cl₂, CF₂Cl, and CFC1, Following Low-Energy (0-10 eV) Impact with Near Monoenergetic Electrons", Chem. Phys. 37, 21 (1979).

Jenkins, M.W., M.T. Mocella, K.D. Allen, and H.H. Sawin, "The Modeling of Plasma Etching Processes Using Response Surface Methodology", *Solid State Technol.*, **29**(4), 175 (1986).

Jones, R.K., "Absolute Total Cross Sections for the Scattering of Low Energy Electrons by CCl_4 , CCl_3F , CCl_2F_2 , CClF_3 , and CF_4 ", *J. Chem. Phys.* **84**, 813 (1986).

Kaufmann, M., "Some Novel Diagnostic Techniques for Plasma Chemistry", *Pure Appl. Chem.* **48**, 155 (1976).

Kawata, H., K. Murata, and K. Nagami, "The Dependence of Silicon Etching on an Applied DC Potential in CF_4+O_2 Plasmas", *J. Electrochem. Soc.* **132**, 206 (1985).

Kawata, H., T. Shibano, K. Murata, and K. Nagami, "The Relation Between Etch Rate and Optical Emission Intensity in Plasma Etching", *J. Electrochem. Soc.* **129**, 1325 (1982).

Kay, E., J. Coburn, and A. Dilks, "Plasma Chemistry of Fluorocarbons as Related to Plasma Etching and Plasma Polymerization", in *Plasma Chemistry III, Topics in Current Chemistry 94* (S. Veprek and M. Venugopalan, eds.), Springer-Verlag, New York, 1980.

Keller, J.H., and W.B. Pennebaker, "Electrical Properties of RF Sputtering Systems", *IBM J. Res. Develop* **23**(1), 3 (1979).

Kinsey, J.L., "Laser-Induced Fluorescence", *Ann. Rev. Phys. Chem.* **28**, 349 (1977).

Kimizuka, M., and K. Hirata, "Pattern Profile Control of Polysilicon Plasma Etching", *J. Vac. Sci. Technol. B* **3**, 16 (1985).

Kline, L.E., "Electron and Chemical Kinetics in the Low Pressure rf Discharge Etching of Silicon in SF_6 ", *IEEE Trans. Plasma Science* **PS-14**, 145 (1986).

Koenig, H.R., and L.I. Maissel, "Application of RF Discharges to Sputtering", *IBM J. Res. Develop.* **14**(3), 168 (1970).

Köhler, K., J.W. Coburn, D.E. Horne, E. Kay, and J.H. Keller, "Plasma Potentials of 13.56 MHz rf Argon Glow Discharges in a Planar System", *J. Appl. Phys.* **57**, 59 (1984).

Korman, C.S., "Polysilicon Etching and Profile Control in a CCl_4-O_2 Plasma", *J. Vac. Sci. Technol.* **20**, 476 (1982).

Krueger, E.E., and A.L. Ruoff, "Angular Dependence of Etching Yield of Single Crystal Si in Cl_2 Reactive Ion Beam Etching", *J. Vac. Sci. Technol. B* **3**, 1650 (1985).

Kurepa, M.V., D.S. Babic, and D.S. Belic, "Attachment Rate Coefficients of Halogen Molecules (F_2 , Cl_2 , Br_2 , I_2) for Mean Electron Energies 10^{-2} to 10^2 eV", Chem. Phys. 59, 125 (1981).

Kurepa, M.V., and D.S. Belic, "Dissociative Attachment of Electrons to Chlorine Molecule", Chem. Phys. Lett. 49, 608 (1977).

Kurepa, M.V., and D.S. Belic, "Electron-Chlorine Molecule Total Ionization and Electron Attachment Cross Sections", J. Phys. B: Atom. Molec. Phys. 11, 3719 (1978).

Kushner, M.J., "A Kinetic Study of the Plasma-Etching Process I. A Model for the Etching of Si and SiO_2 in C_nF_m/H_2 and C_nF_m/O_2 Plasmas", J. Appl. Phys. 53, 2923 (1982).

Kushner, M.J., "A Kinetic Study of the Plasma-Etching Process II. Probe Measurements of Electron Properties in a rf Plasma-Etching Reactor", J. Appl. Phys. 53, 2939 (1982).

Kushner, M.J., "Monte-Carlo Simulation of Electron Properties in rf Parallel Plate Capacitively Coupled Discharges", J. Appl. Phys. 54, 4958 (1983).

Kushner, M.J., "Floating Sheath Potentials in Non-Maxwellian Plasmas", IEEE Trans. Plasma Sci. 13, 6 (1985).

Kushner, M.J., "Distribution of Ion Energies Incident on Electrodes in Capacitively Coupled rf Discharges", J. Appl. Phys. 58(11), 4024 (1985).

Kupriyanovskaya, A.P., and V.I. Svetsov, "Effect of Oxygen and Helium Additions on the Dissociation of Chlorine Molecules in a Glow Discharge", Zhurnal Fizicheskoi Khimii 58, 2031 (1984).

Kuznetsova, S.V., and A.I. Maslov, "Studies of the Reactions of the Radical CF_3 with Atomic and Molecular Chlorine", Khim. Vys. Energ. 13(5), 448 (1979).

Laegrid, N., and G.K. Wehner, "Sputtering Yields of Metals for Ar^+ and Ne^+ Ions with Energies from 50 to 600 eV", J. Appl. Phys. 32, 365 (1961).

Laframboise, J., "Theory of Cylindrical and Spherical Langmuir Probes in a Collisionless Plasma at Rest", Adv. Appl. Mech. Supplement 3, Volume II (1966), Rarified Gas Dynamics, pp. 22.

Lam, D.K., "Advances in VLSI Plasma Etching", Solid State Technol. 25(4), 215 (1982).

- Larsen, R.J., and M.L. Marx, An Introduction to Mathematical Statistics and its Applications, Prentice-Hall, Englewood Cliffs, NJ (1981).
- Leahy, M.F., "Directional Plasma Etching of Polysilicon in a CF_3Cl Discharge", in Extended Abstracts of the Electrochemical Society Fall Meeting, Volume 81-2, Abstract #271 (1981), pp. 660.
- Leahy, M.F., and D.J. Tanguay, "Silicon Etch Rate as a Function of Dopant Concentration in a CF_3Cl Plasma", in Proceedings of the Fourth Symposium on Plasma Processing (G.S. Mathad, G.C. Schwartz, and G. Smolinsky, eds.), The Electrochemical Society, Pennington, NJ, 1983, pp. 235.
- Lechaton, J.S., and J.L. Maner, "A Model for the Etching of Silicon in a Cl_2/Ar Plasma", in Plasma Processing, Proceedings of the Symposium on Plasma Etching and Deposition (R.G. Frieser and C.J. Mogab, eds.), The Electrochemical Society Volume 81-1, The Electrochemical Society, Pennington, NJ, 1981, pp. 75.
- Lee, Y.H., and M-M Chen, "Silicon Etching Mechanism and Anisotropy in CF_4+O_2 Plasma", *J. Appl. Phys.* **54**, 5966 (1983).
- Lias, S.G., "Ion-Molecule Reactions Involving Fluorine-Containing Organic Compounds", in Fluorine-Containing Free Radicals: Kinetics and Dynamics of Reactions (J.W. Root, ed.), ACS Symposium Series 66, American Chemical Society, Washington, 1978, pp. 152.
- Lias, S.G., and P. Ausloos, "Ion-Molecule Reactions Involving Halomethyl Ions; Heats of Formation of Halomethyl Ions", *Intern. J. Mass Spectrom. Ion Phys.* **23**, 273 (1977).
- Lindinger, W., "Basic Ion Reactions and Kinetics in Plasmas", *Pure Appl. Chem.* **57**, 1223 (1985).
- Logan, J.S., N.M. Mazza, and P.D. Davidse, "Electrical Characterization of Radio-Frequency Sputtering Gas Discharge", *J. Vac. Sci. Technol.* **6**, 120 (1969).
- Lowke, J.J., and D.K. Davies, "Properties of Electric Discharges Sustained by a Uniform Source of Ionization", *J. Appl. Phys.* **48**, 4991 (1977).
- Marcoux, P.J., and P.D. Foo, "Methods of End Point Detection for Plasma Etching", *Solid State Technol.* **24**(4), 115 (1981).
- Mathur, B.P., and J.C. Huang, "Plasma Impedance for Commonly Used Etch Gases", in Electrochemical Society Extended Abstracts 84-2, Proceedings of the 1984 Fall Meeting (New Orleans), The Electrochemical Society, Pennington, NJ, 1984, pp. 520.

Matsuo, S., "Selective Etching of Si Relative to SiO₂ Without Undercutting by CBrF₃ Plasma", Appl. Phys. Lett. 36, 768 (1980).

Mauer, J.L., J.S. Logan, L.B. Zielinski, and G.C. Schwartz, "Mechanism of Silicon Etching by a CF₄ Plasma", J. Vac. Sci. Technol. 15, 1734 (1978).

Mayer, T.M., and R.A. Barker, "Simulation of Plasma-Assisted Etching Processes by Ion-Beam Techniques", J. Vac. Sci. Technol. 21, 757 (1982).

Mayer, T.M., R.A. Barker, and L.J. Whitman, "Investigation of Plasma Etching Mechanisms using Beams of Reactive Gas Ions", J. Vac. Sci. Technol. 18, 349 (1981).

McCorkle, D.L., A.A. Christouloulides, and L.G. Christophorou, "Electron Attachment to Halocarbons of Interest in Gaseous Dielectrics", in Gaseous Dielectrics IV (L.G. Christophorou and M.D. Pace, eds.), Proc. 4th Intern. Symp. Gaseous Dielectrics, Pergamon Press, New York, 1984, pp. 12.

McDaniel, E.W., and E.A. Mason, The Mobility and Diffusion of Ions in Gases, John Wiley and Sons, New York (1973).

McNevin, S.C., and G.E. Becker, "CF₄/Silicon Surface Reactions: Evidence for Parallel Etching Mechanisms from Modulated Ion Beam Studies", J. Vac. Sci. Technol. B 2, 27 (1984).

McNevin, S.C., and G.E. Becker, "Investigation of Kinetic Mechanism for the Ion-Assisted Etching of Si in Cl₂", J. Vac. Sci. Technol. B 3, 485 (1985).

Mieth, M., and A. Barker, "Anisotropic Plasma Etching of Polysilicon using SF₆ and CFCl₃", J. Vac. Sci. Technol. A 1, 629 (1983).

Millard, M.M., and E. Kay, "Difluorocarbene Emission Spectra from Fluorocarbon Plasmas and its Relationship to Fluorocarbon Polymer Formation", J. Electrochem. Soc. 129, 160 (1982).

Miyake, K., S. Tachi, K. Yagi, and T. Tokuyama, "Chemical Sputtering Yields of Silicon Resulting from F⁺, CF_n⁺ (n=1,2,3) Ion Bombardment", J. Appl. Phys. 53, 3214 (1982).

Mlynko, W.E., and D.W. Hess, "Electrical Characterization of rf Glow Discharges using an Operating Impedance Bridge", J. Vac. Sci. Technol. A 3, 499 (1985).

Mocella, M.T., H.H. Sawin, and K.D. Allen, "Polysilicon Etching by FREON 13B1 (CF₃Br) Plasmas: Process Trends and Sensitivities", Twelfth Annual Tegal Plasma Seminar Proceedings, Tegal Corporation, Novato, CA (1986a)

Mocella, M.T., B.E. Thompson, and H.H. Sawin, "Directional Plasma Etching of Polysilicon in SF₆/CFCl₃ Discharges", Materials Research Society Spring meeting, Palo Alto, CA (1986b).

Modica, A.P., and S.J. Sillers, "Experimental and Theoretical Kinetics of High-Temperature Fluorocarbon Chemistry", J. Chem. Phys. **48**, 3283 (1968).

Mogab, C.J., "The Loading Effect in Plasma Etching", J. Electrochem. Soc. **124**, 1262 (1977).

Mogab, C.J., and W.R. Harshbarger, "Plasma Processes Set to Etch Finer Lines with Less Undercutting", Electronics **51**(18), 117 (1978).

Mogab, C.J., and H.L. Levinstein, "Anisotropic Plasma Etching of Polysilicon", J. Vac. Sci. Technol. **17**, 721 (1980).

Mucha, J.A., V.M. Donnelly, D.L. Flamm, and L.M. Webb, "Chemiluminescence and the Reaction of Molecular Fluorine with Silicon", J. Phys. Chem. **85**, 3529 (1981).

Mullins, C., "Single Wafer Plasma Etching 2. SiO₂: Etching Mechanisms and Characteristics", Solid State Technol. **25**(8), 88 (1982).

Naidu, M.S., and A.N. Prasad, "Diffusion and Drift of Electrons in Dichlorodifluoromethane", Brit. J. Appl. Phys. (J. Phys. D) **2**, 1431 (1969).

Naidu, M.S., and A.N. Prasad, "Mobility, Diffusion, and Attachment of Electrons in Perfluoroalkanes", J. Phys. D: Appl. Phys. **5**, 983 (1972).

Nishizawa, J., and N. Hayasaka, "In-situ Observation in Silicon Plasma Etching", in Plasma Processing (R.G. Frieser and C.J. Mogab, eds.), Electrochemical Society Proceedings Volume 81-1, The Electrochemical Society, Pennington, NJ, 1981.

Nisimura, T., E. Wani, T. Tsukada, R. Fox, and M. Nagasaka, "Summary Abstract: Loading Effect Curve and Etching Reaction", J. Vac. Sci. Technol. A **1**, 638 (1983).

Norstrom, H., "Langmuir Probe Studies of the Glow Discharge in an RF Sputtering System at Various Frequencies", Vacuum **29**, 443 (1979).

Novak, J.P., and M.F. Frechette, "Calculation of Transport Properties of N₂, SF₆, CCl₂F₂, and c-C₄F₈ and their Respective Mixtures", in Gaseous Dielectrics IV (L.G. Christophorou and M.D. Pace, eds.), Proc. 4th Intern. Symp. Gaseous Dielectrics, Pergamon Press, New York, 1984, pp. 34.

- Olson, R.E., J.R. Peterson, and J. Moseley, "Ion-Ion Recombination Total Cross Sections- Atomic Species", J. Chem. Phys. **53**, 3391 (1970).
- Oshima, M., "Determination of Plasma Gas Temperature During Reactive Sputter Etching", Japan. J. Appl. Phys. **17**, 1157 (1978).
- Pang, S.W., "Dry Etching Induced Damage in Si and GaAs", Solid State Technol. **27**(4), 249 (1984).
- Paraszczak, J., and M. Hatzakis, "Comparison of CF_4/O_2 and CF_2Cl_2/O_2 Plasmas used for the Reactive Ion Etching of Single Crystal Silicon", J. Vac. Sci. Technol. **19**, 1412 (1981).
- Parry, P.D., and A.F. Rodde, "Anisotropic Plasma Etching of Semiconductor Materials", Solid State Technol. **22**(4), 125 (1979).
- Peart, B., R. Forrest, and K.T. Dolder, "Measurements of Detachment from F^- by Electron Impact and Tests of Classical Scaling for Electron Impact Detachment Cross Sections", J. Phys. B: Atom. Molec. Phys. **12**(3), L115 (1979).
- Pejcev, V.M., M.V. Kurepa, and I.M. Cadez, "Total Ionization and Electron Impact Cross sections of CCl_2F_2 by Electron Impact", Chem. Phys. Lett. **63**, 301 (1979).
- Pennebaker, W.B., "Influence of Scattering and Ionization on RF Impedance in Glow Discharge Sheaths", IBM J. Res. Develop. **23**, 16 (1979).
- Peyerimhoff, S.D., and R.J. Buenker, "Potential Curves for Dissociative Electron Attachment of $CFCl_3$ ", Chem. Phys. Lett. **65**, 434 (1979).
- Plackett, R.L., and J.P. Burman, "The Design of Optimum Multifactorial Experiments", Biometrika **33**, 305 (1946).
- Pliskin, W.A., and E.E. Conrad, "Nondestructive Determination of Thickness and Refractive Index of Transparent Films", IBM Journal (January 1964), pp. 43.
- Plumb, I.C., and K.R. Ryan, "Gas-Phase Reactions of CF_3 and CF_2 with Atomic and Molecular Fluorine: Their Significance in Plasma Etching", Plasma Chem. Plasma Process. **6**(1), 11 (1986a).
- Plumb, I.C., and K.R. Ryan, "A Model Which Describes Processes Occurring in CF_4/O_2 Plasmas for Conditions Relevant to Plasma Etching", to be published in Plasma Chem. and Plasma Process. (1986b).
- Porter, R.A., and W.R. Harshbarger, "Gas Rotational Temperature in an RF Plasma", J. Electrochem. Soc. **126**, 460 (1979).

- Poulsen, R.G., "Plasma Etching in Integrated Circuit Manufacture- A Review", *J. Vac. Sci. Technol.* **14**, 266 (1977).
- Preston, H.J.T., and J.J. Kaufman, "MS X_α Calculations on the Chlorofluoromethanes", *Chem. Phys. Lett.* **50**, 157 (1977).
- Rapp, D., and D.D. Briglia, "Total Cross Sections for Ionization and Attachment in Gases by Electron Impact. I. Positive Ionization", *J. Chem. Phys.* **43**, 1464 (1965).
- Rapp, D., and D.D. Briglia, "Total Cross Sections for Ionization and Attachment in Gases by Electron Impact. II. Negative-Ion Formation", *J. Chem. Phys.* **43**, 1480 (1965).
- Rapp, D., P. Englander-Golden, and D.D. Briglia, "Cross Sections for Dissociative Ionization of Molecules by Electron Impact", *J. Chem. Phys.* **42**, 4081 (1965).
- Reid, R.C., J.M. Prausnitz, and T.K. Sherwood, The Properties of Gases and Liquids, 3rd ed., McGraw-Hill, New York (1977).
- Reinberg, A.R., U.S. Patent #3,757,733 (1973).
- Reynolds, J.L., A.R. Neureuther, and W.G. Oldham, "Simulation of Dry Etched Line Edge Profiles", *J. Vac. Sci. Technol.* **16**, 1772 (1980).
- Richards, A.D., PhD thesis, Department of Chemical Engineering, Massachusetts Institute of Technology, Cambridge, MA (1986a).
- Richards, A.D., unpublished data (1986b).
- Richards, A.D., B.E. Thompson, K.D. Allen, and H.H. Sawin, "Atomic Chlorine Concentration Measurements in a Plasma Etching Reactor I. A Comparison of Infrared Absorption and Optical Emission Actinometry", in preparation (1986).
- Rodgers, A.S., "Thermochemistry of Fluorocarbon Radicals", in Fluorine-Containing Free Radicals. Kinetics and Dynamics of Reaction (J.W. Root, ed.), ACS Symposium Series 66, American Chemical Society, Washington, 1978.
- Rogoff, G.L., J.M. Kramer, and R.B. Piejak, "A Model for the Bulk Plasma in an RF Chlorine Discharge", *IEEE Trans. Plasma Science* **PS-14**, 103 (1986).
- Roland, J.P., P.J. Marcoux, G.W. Ray, and G.H. Rankin, "Endpoint Detection in Plasma Etching", *J. Vac. Sci. Technol.* **A 3**, 631 (1985).

Ryan, K.R., and I.C. Plumb, "Gas-Phase Reactions of CF_3 and CF_2 with Hydrogen Atoms: Their Significance in Plasma Processing", *Plasma Chem. Plasma Process.* 4(3), 141 (1984).

Ryan, K.R., and I.C. Plumb, "A Model for the Etching of Si in CF_4 Plasmas. Comparison with Experimental Measurements", to be published in *Plasma Chem. Plasma Process.* (1986).

Sanders, F.H.M., J. Dieleman, H.J.B. Peters, and J.A.M. Sanders, "Selective Isotropic Dry Etching of Si_3N_4 over SiO_2 ", *J. Electrochem. Soc.* 129, 2559 (1982).

Sanders, F.H.M., A.W. Kolfschoten, J. Dielman, R.A. Haring, A. Haring, and A.E. de Vries, "Ion-Assisted Etching of Silicon by Molecular Chlorine", *J. Vac. Sci. Technol.* 2, 487 (1984).

Sawin, H.H., "A Review of Plasma Processing Fundamentals", *Solid State Technol.* 27(4), 211 (1985).

Sawin, H.H., K.D. Allen, M.W. Jenkins, and M.T. Mocella, "Parametric Modeling of Plasma Etching Processes", *Eleventh Annual Tegal Plasma Seminar Proceedings*, Tegal Corporation, Novato, CA (1985), pp. 17.

Sawin, H.H., A.D. Richards, and B.E. Thompson, "Plasma-Assisted Processing. The Etching of Polysilicon in a Diatomic Chlorine Discharge", in Integrated Circuits: Chemical and Physical Processing (P. Stroeve, ed.), ACS Symposium Series 290, American Chemical Society, Washington, 1985.

Schultz, G.J., and S.C. Brown, "Microwave study of Positive Ion Collection by Probes", *Phys. Rev.* 98, 1642 (1955).

Schwartz, G.C., and P.M. Schaible, "Reactive Ion Etching of Silicon: Temperature Effects", in Plasma Processing, Proceedings of the Symposium on Plasma Etching and Deposition (R.G. Frieser and C.J. Mogab, eds.), The Electrochemical Society Volume 81-1, The Electrochemical Society, Pennington, NJ, 1981, pp. 133.

Schwartz, G.C., and P.M. Schaible, "The Effects of Arsenic Doping in Reactive Ion Etching of Silicon in Chlorinated Plasmas", *J. Electrochem. Soc.* 130, 1898 (1983).

Senturia, S.D., and B.D. Wedlock, Electronic Circuits and Applications, John Wiley and Sons, New York, 1975.

Sherman, C., "A Unified Treatment of the Langmuir Probe and Diode Equations", *J. Appl. Phys.* 52, 6567 (1981).

Skullerud, H.R., "Monte-Carlo Investigation of the Motion of Gaseous Ions in Electrostatic Fields", J. Phys. B: Atom. Molec. Phys. 6, 728 (1973).

Spencer, J.E., D.E. Carter, and G.G. Barna, "Characterization of Plasma Processes with Statistically Designed Experiments", Abstract #385 in Extended Abstracts of the Electrochemical Society Volume 84-2, Proceedings of the 1984 Fall Meeting (New Orleans), The Electrochemical Society, Pennington, NJ, 1984, pp. 548.

Spencer, J.E., D.E. Carter, and G.G. Barna, "Rational Optimization of Plasma Etch Processes with the Simplex Algorithm", Abstract #386 in Extended Abstracts of the Electrochemical Society Volume 84-2, Proceedings of the 1984 Fall Meeting (New Orleans), The Electrochemical Society, Pennington, NJ, 1984, pp. 549.

Spyrou, S.M., I. Saners, and L.G. Christophorou, "Electron Attachment to the Perfluoroalkanes $n\text{-C}_N\text{F}_{2N+2}$ ($N=1,6$) and $i\text{-C}_4\text{F}_{10}$ ", J. Chem. Phys. 78, 7200 (1983).

Steinbruchel, Ch., "Langmuir Probe Measurements on CHF_3 and CF_4 Plasmas: The Role of Ions in the Reactive Sputter Etching of SiO_2 and Si", J. Electrochem. Soc. 130, 648 (1983).

Steinbruchel, Ch., H.W. Lehmann, and K. Frick, "Mechanism of Dry Etching of Silicon Dioxide", J. Electrochem. Soc. 132, 180 (1985).

Sternheim, M., W. van Gelder, and A.W. Hartman, "A Laser Interferometer System to Monitor Dry Etching of Patterned Silicon", J. Electrochem. Soc. 130, 655 (1983).

Stevie, F.A., and M.J. Vasile, "Electron Impact Ionization Cross Sections of F_2 and Cl_2 ", J. Chem. Phys. 74, 5106 (1981).

Strategic Incorporated, "Strategic Issues in VLSI Circuit Fabrication Technologies 1984-1994 Volume I. VLSI Wafer Etching: Issues, Equipment, Market and Industry. User Implications", (Michael Killen, pub.), Cupertino, CA (1984).

Su, C.W., and R.E. Kiel, "Continuum Theory of Electrostatic Probes", J. Appl. Phys. 37, 4907 (1966).

Sugano, T. (H-g Kim, translator), Applications of Plasma Processes to VLSI Technology, Wiley-Interscience, New York, 1983.

Surendra, M., B.S. Thesis, Department of Chemical Engineering, Massachusetts Institute of Technology, Cambridge, MA (1985).

Surendra, M., and H.H. Sawin, "A High Impedance Langmuir Probe", in preparation (1986).

Surendra, M., H.H. Sawin, and K.D. Allen, "Langmuir Probe Measurements in CF_3Cl Discharges", in preparation (1986).

Suto, M., and L.C. Lee, "Emission Spectra of CF_3 Radicals V. Photodissociation of CF_3H , CF_3Cl , and CF_3Br by Vacuum Ultraviolet", *J. Chem. Phys.* **79**, 1127 (1983).

Suto, M., and N. Washida, "Emission Spectra of CF_3 Radicals I. UV and Visible Emission Spectra of CF_3 Observed in the VUV Photolysis and the Metastable Argon Atom Reaction of CF_3H ", *J. Chem. Phys.* **78**, 1007 (1983a).

Suto, M., and N. Washida, "Emission Spectra of CF_3 Radicals II. Analysis of the UV Emission Spectrum of CF_3 Radicals", *J. Chem. Phys.* **78**, 1012 (1983b).

Suto, M., N. Washida, H. Akimoto, and M. Nakamura, "Emission Spectra of CF_3 Radicals III. Spectra and Quenching of CF_3 Emission Bands Produced in the VUV Photolyses of CF_3Cl and CF_3Br ", *J. Chem. Phys.* **78**, 1019 (1983).

Suzuki, K., K. Ninpmiya, S. Nishimatsu, J.W. Thoman Jr., and J.I. Steinfeld, "Analytical Investigation of Plasma and Electrode Potentials in a Diode Type RF Discharge", to be published.

Sze, S.M., ed., VLSI Technology, McGraw-Hill Inc., New York, 1983.

Tedder, J.M., and J.C. Walton, "Kinetics and Mechanism of the Addition of Fluorine-Containing Radicals to Olefins", in Fluorine-Containing Free Radicals. Kinetics and Dynamics of Reaction (J.W. Root, ed.), ACS Symposium Series 66, American Chemical Society, Washington, 1978.

Thompson, B.E., PhD Thesis, Department of Chemical Engineering, Massachusetts Institute of Technology, Cambridge, MA (1986).

Thompson, B.E., K.D. Allen, A.D. Richards, and H.H. Sawin, "Ion Bombardment Energy Distributions in Radio-frequency Glow-Discharge Systems", *J. Appl. Phys.* **59**(6), 1890 (1986a).

Thompson, B.E., A.D. Richards, H.H. Sawin, and A.J. Owens, unpublished results (1986b).

Thompson, B.E., and H.H. Sawin, "Comparison of Measured and Calculated SF_6 Breakdown in rf Electric Fields", *J. Appl. Phys.*, to be published (1986a).

Thompson, B.E., and H.H. Sawin, "Polysilicon Etching in SF_6 rf Discharges: Characteristics and Diagnostic Measurements", *J. Electrochem. Soc.*, to be published (1986b).

Thompson, B.E., H.H. Sawin, and A.J. Owens, "Continuum Model of Charged Particle Transport: rf Breakdown and Discharges of SF₆", Materials Research Society Spring meeting, Palo Alto, CA (1986c).

Trajmar, S., "Electron-Atom (Molecule) Collision Processes", Science **208**, 247 (1980).

Trajmar, S., "Cross Sections for Electron-Molecule Collision Processes", in Gaseous Dielectrics IV (L.G. Christophorou and M.D. Pace, eds.), Proc. 4th Intern. Symp. Gaseous Dielectrics, Pergamon Press, New York, 1984, pp. 1.

Truesdale, E.A. and G. Smolinsky, "The Effect of Added Hydrogen on the rf Discharge Chemistry of CF₄, CF₃H, and C₂F₆", J. Appl. Phys. **50**, 6594 (1979).

Trung, Q.-T., G. Durocher, P. Sauvageau, and C. Sandorfy, "The Emission of the CF₂ Radical in a Microwave Discharge", Chem. Phys. Lett. **47**(3), 404 (1977).

Tu, Y.-Y., T.J. Chuang, and H.F. Winters, "Chemical Sputtering Yield of Fluorinated Silicon", Phys. Rev. B **23**, 823 (1981).

Turban, G., "Basic Phenomena in Reactive Low Pressure Plasmas used for Deposition and Etching- Current Status", Pure and Appl. Chem. **56**, 215 (1984).

Us, N.C., "Ion Bombardment in Plasma Processing of Electronic Materials", M.S. Thesis, Department of Materials Science and Engineering, Massachusetts Institute of Technology, 1985.

Us, N.C., R.W. Sadowski, and J.W. Coburn, "Quartz Crystal Microbalance Simulation of the Directionality of Si Etching in CF₄ Glow Discharges", Plasma Chem. Plasma Process. **6**(1), 1 (1986).

van Roosmalen, A.J., "Plasma Parameter Estimation from rf Impedance Measurements in a Dry Etching System", Appl. Phys. Lett. **42**, 416 (1983).

van Roosmalen, A.J., W.G.M. van den Hoek, and H. Kalter, "Electrical Properties of Planar rf Discharges for Dry Etching", J. Appl. Phys. **58**, 653 (1985).

van Veldhuizen, E.M., Th. Bisschops, E.J.W. van Vliembergen, and J.H.M.C. van Wolput, "Absolute Densities of Reaction Products from Plasma Etching of Quartz", J. Vac. Sci. Technol. A **3**, 2205 (1985).

Vasile, M.J., "A Comparative Study of the Radio Frequency Discharge in Gas Mixtures of Helium with Fluorine, Oxygen, Nitrogen, and Argon", J. Appl. Phys. **51**, 2503 (1980).

Vasile, M.J., and Smolinsky, G., "Mass-Spectrometric Ion Sampling from Reactive Plasmas I. Apparatus for Argon and Reactive Discharges", Intern. J. Mass Spectrom. Ion Phys. **12**, 133 (1976).

Verhaart, G.J., W.J. van der Hart and H.H. Brongersma, "Low Energy Electron Impact on Chlorofluoromethanes and CF_4 : Resonances, Dissociative Attachment, and Excitation", Chem. Phys. **34**, 161 (1978).

Verhaart, G.J., H.A. van Sprang, and H.H. Brongersma, "Electron Chemistry. Chemical Reactions in CCl_4 , $CFCl_3$, and CF_2Cl_2 Induced by Low-Energy Electrons", Chem. Phys. **51**, 381 (1980).

Vossen, J.L., and W. Kern, eds., Thin Film Processes, Academic Press Inc., New York, 1978.

Wagner, J.J., and S. Veprek, "Chemical Relaxation Study of the Heterogeneous Silicon-Hydrogen System Under Plasma Conditions", Plasma Chem. Plasma Process. **3**(2), 219 (1983).

Wang, D.N.K., and D. Maydan, "Reactive Ion Etching Eases Restrictions on Materials and Feature Sizes", Electronics **56**(22), 157 (1983).

Wannier, G.H., "On the Motion of Gaseous Ions in a Strong Electric Field I.", Phys. Rev. **83**, 281 (1951).

Wannier, G.H., "Motion of Gaseous Ions in Strong Electric Fields", Bell System Tech. J. (January 1953), pp. 170.

Washida, N., M. Suto, S. Nagase, U. Nagashima, and K. Morokuma, "Emission Spectra of CF_3 Radicals IV. Excitation Spectra, Quantum Yields, and Potential Energy Surfaces of the CF_3 Fluorescences", J. Chem. Phys. **78**, 1025 (1983).

Watanabe, K., T. Nakayama, and J. Mottl, "Ionization Potentials of Some Molecules", J. Quant. Spectrosc. Radiat. Transfer **2**, 369 (1962).

Weast, R.C., ed., CRC Handbook of Chemistry and Physics, 56th edition, Chemical Rubber Co. Press, Cleveland (1975).

Weiss, A.D., "Endpoint Monitors", Semiconductor International **6**(9), 98 (1983a).

Weiss, A.D., "Etching Systems", Semiconductor International **6**(11), 114 (1983b).

Weiss, A.D., "Plasma Etching of Polysilicon: An Overview", Semiconductor International **7**(5), 214 (1984).

Winkler, U.W., "VLSI Polysilicon Etching: A Comparison of Different Techniques", Solid State Technol. **26**(4), 169 (1983).

Winters, H.F., "The Role of Chemisorption in Plasma Etching", J. Appl. Phys. **49**, 5165 (1978).

Winters, H.F., "Elementary Processes at Solid Surfaces Immersed in Low Pressure Plasmas", in Plasma Chemistry III (S. Veprek and M. Venugopalan, eds.), Topics in Current Chemistry **94**, 69 (1980), Springer-Verlag, New York.

Winters, H.F., "The Etching of Cu(100) with Cl₂", J. Vac. Sci. Technol. A **3**, 786 (1985).

Winters, H.F., J.W. Coburn, and T.J. Chuang, "Surface Processes in Plasma-Assisted Etching Environments", J. Vac. Sci. Technol. B **1**, 469 (1983).

Winters, H.F., J.W. Coburn, and E. Kay, "Plasma Etching - A 'Pseudo-Black-Box' Approach", J. Appl. Phys. **48**, 4973 (1977).

Winters, H.F., and M. Inokuti, "Total Dissociation Cross Section of CF₄ and other Fluoroalkanes for Electron Impact", Phys. Rev. A **25**, 1420 (1982).

Wormhoudt, J., A.C. Stanton, A.D. Richards, and H.H. Sawin, "Atomic Chlorine Concentration and Gas Temperature Measurements in a Plasma Etching Reactor", to be published (1986).

Wormhoudt, J., A.C. Stanton, and J. Silver, "Techniques for Characterization of Gas Phase Species in Plasma Etching and Vapor Deposition Processes", Proceedings of SPIE, Cambridge Symposium on Optical and Electro-Optical Engineering, Cambridge, MA (November 1983).

Yamaguchi, S., G. Sawa, and M. Ieda, "Effects of Plasma-Polymerized Film on the Current-Voltage Characteristics of Single Probe", in Plasma Polymerization (M. Shen and A.T. Bell, eds.), ACS Symposium Series 108, American Chemical Society, Washington, 1978, pp. 115.

Yokozeiki, A., unpublished results (1984).

Zarowin, C.B., "Relation between the RF Discharge Parameters and Plasma Etch Rates, Selectivity, and Anisotropy", J. Vac. Sci. Technol. A **2**, 1537 (1984).

Zarowin, C.B., and R.S. Horwath, "Control of Plasma Etch Profiles with Plasma Sheath Electric Field and RF Power Density", J. Electrochem. Soc. **129**, 2541 (1982).

This page intentionally left blank

APPENDIX A - NOMENCLATURE

Symbol	Meaning	Units
A	Electrode area	cm ²
[Ar]	Argon concentration	cm ⁻³
\bar{c}	Mean speed of neutrals	cm/second
C _b	Bulk plasma capacitance	picofarad
C _s	Sheath capacitance	picofarad
[CF ₃ Cl] ₀	CF ₃ Cl concentration	cm ⁻³
[Cl]	Atomic chlorine concentration	cm ⁻³
[Cl] _s	·Cl concentration at wafer surface	cm ⁻³
d	Interelectrode spacing	cm
d _s	Sheath thickness	cm
D	Diffusivity of ·Cl	cm ² /second
D ₀	Diffusivity of ·Cl at pressure P ₀	cm ² /second
[e ⁻]	Electron concentration	cm ⁻³
E	Dimensionless etching rate	
E _b	Bulk plasma electric field	volt/cm
E _s	Sheath electric field	volt/cm
E ₀	rf electric field	volt/cm
E ₁	Triangular IED approximation, constant	volt
E ₂	Triangular IED approximation, constant	volt
E*	Threshold energy	eV
E ₊	Ion energy	eV
\bar{E}_+	Mean ion energy	eV

$E_{+,max}$	Maximum ion bombardment energy	eV
f	rf excitation frequency	Hz
$f(\varepsilon)$	Electron energy distribution	eV^{-1}
$f(E_+)$	Ion energy distribution, measured	eV^{-1}
$F(E_+)$	Ion energy distribution, triangle model	eV^{-1}
F_1	Constant, triangle model	
$\tilde{F}(I /\omega P)$	Ion energy distribution, predicted	eV^{-1}
$g(E_+)$	Energy dependence of ion-assisted etch yield	
i_C	Current through sheath capacitor	amps
i_R	Current through sheath resistor	amps
$ I $	rms discharge current	amps
I_{Ar}	Intensity of optical emission from Ar	
I_{Br}	Intensity of optical emission from $\cdot Br$	
I_{Cl}	Intensity of optical emission from $\cdot Cl$	
j	Imaginary number index	
j_e	Electron current density	amps/cm ²
k	Boltzmann's constant	eV/molecule \cdot K
k_E	Etching rate constant	cm/second
k_F	Formation rate constant, $\cdot Cl$	cm ³ /second
$k_{F,D}$	Calculated k_F using Druyvestyn distribution	
$k_{F,M}$	Calculated k_F using Maxwellian distribution	
k_H	Homogeneous recombination rate constant	cm ³ /second
k_L	Total $\cdot Cl$ loss rate constant	
k_R	Surface recombination rate constant	cm ³ /second
k_{oi}	Chemical rate constant, model i	

k_{+i}	Ion-assisted rate constant, model i	
k'	Rate constant, lumped	
K_E	Constant	
L	Electron oscillation length	cm
m_e	Mass of electron	kg
m_i	Mass of ion	kg
m_0	Mass of neutral	kg
m_+	Mass of ion	kg
n	Exponent	
N	Neutral number density	cm^{-3}
N_{Cl}	$\cdot\text{Cl}$ flux to surface	$\text{cm}^{-2}\text{s}^{-1}$
N_0	Neutral number density at pressure p_0	cm^{-3}
P	Pressure	torr
P_0	Pressure, reference (1 torr)	torr
q	Electronic charge	coulombs
Q	Flow rate	sccm
R	Gas constant	$\text{cm}^3\cdot\text{torr}/\text{K}$
R_b	Bulk plasma resistance	ohms
R_s	Sheath resistance	ohms
$R_{o,i}$	Chemical etching rate, model i	$\text{\AA}/\text{minute}$
R_{+i}	Ion-assisted etching rate, model i	$\text{\AA}/\text{minute}$
S	Surface recombination probability	
t	Time	seconds
T	Plasma temperature	K
T_e	Electron temperature	K

U	Mask undercut	μm
V	Reactor volume	cm^3
$ V $	rms discharge voltage	volts
V_a	Applied voltage	volts
$ V _{\text{eff}}$	Effective applied voltage	volts
V_f	Floating potential	volts
V_p	Plasma potential	volts
$V_{p,\text{min}}$	Minimum plasma potential during rf cycle	volts
V_r	Retarding voltage on Faraday cup	volts
V_s	Time-averaged sheath potential	volts
W	Power input	watts
\dot{W}	Power density	watts/cm^2
x	Distance	cm
X_{Br}	·Br mole fraction	
X_{Cl}	·Cl mole fraction	
X_i	Generic process variable in RSM	
Y	Generic response in RSM	
Z_p	Plasma total impedance	ohms
α	Anisotropy coefficient	
α_i	Anisotropy coefficient prediction, model i	
α_0	Anisotropy coefficient at zero overetch	
β_i	Angle	
β_f	Angle	
ξ	Ratio, \bar{E}_+/E^* using measured \bar{E}_+	
$\tilde{\xi}$	Ratio, \bar{E}_+/E^* using predicted \bar{E}_+	

$\delta(E^*)$	Fraction of ions with $E_+ > E^*$	
ΔE	Energy loss of ion upon elastic collision	eV
$\Delta(E^*)$	Triangle model prediction of $\delta(E^*)$	
$\tilde{\Delta}(E^*)$	Triangle model prediction of $\delta(E^*)$	
ϵ_0	Permittivity of free space	farad/cm
$\langle \epsilon \rangle$	Mean electron energy	eV
ϕ	Temporal position in rf cycle	radians
γ	CF ₃ Cl mole fraction, mixtures with Ar	
Γ_+	Total positive ion flux	milliamp/cm ²
$\dot{\Gamma}_+$	Total positive ion flux, saturation	milliamp/cm ²
λ	Mean free path	cm
λ_E	Mean free path, field-directed	cm
λ_+	Mean free path, ion-neutral	cm
θ	Phase shift between voltage, current	degrees
θ	Dimensionless 'Cl concentration	
μ_e	Electron mobility	cm ² /V-s
η	Number of ion-neutral collisions in sheath	
ρ	Ratio, P/P ₀	
σ_D	CF ₃ Cl dissociation cross section	cm ²
σ_+	Ion-neutral collision cross section	cm ²
τ	Fractional overetch time	
ω	Angular excitation frequency	Hz

APPENDIX B - COMPUTER PROGRAM LISTINGS

```

PROGRAM ANALYZE

C
C THIS IS THE MAIN PROGRAM FOR THE CONVERSION OF THE PLASMA
C RUN DATA (SENT DOWN TO THE DATA GENERAL BY PROGRAM R_DATAKE
C ON THE LABTECH) INTO A MORE USEFUL FORMAT. THE PRIMARY
C PURPOSE OF THIS ROUTINE IS TO INPUT THE DATA AND CALL
C THE VARIOUS SUBROUTINES AS REQUESTED.
C K.D. ALLEN - AUGUST/SEPTEMBER 1984
C THE BLAME IS ALSO SHARED WITH A.D. RICHARDS AND B.E. THOMPSON
C FOR MANY CORRECTIONS, ADDITIONS, AND REVISIONS.
C
COMMON/IDENT/IDTRIAL(100),ALPHABET,ELDESCR(100),
& WDESCR(100)
COMMON/LABELS/PLABEL(10),ALABEL
COMMON/FLUX/PAREA,AVEFLUX
COMMON/SPECS/IDLEN(100),NUM_OF_TRIALS,ITRIAL_COUNTER,
& NUMFILE
COMMON/INFO/PRESSURE(100),ESPACE(100),MS_SCALE(100,10),
& FLOWRATE(100,4),MSC_ACT(100),OE_ACT(100),
& WF_ACT(100),ION_ACT(100),IF_SCALE(100),
& IE_ACT(100)
COMMON/IMPEDANCE/VARRU(100,3),CARRU(100,3),PARRU(100,3),
& VARRC(100,3),CARRC(100,3),PARRC(100,3),
& TPOW(100,3),DCB(100,3),FREQ(100,3)
COMMON/SWITCHES/IS_MSI,IS_MSP,IS_ACT,IS_OEP,IS_WFFA,IS_WFP,
& IS_WFH,IS_IFP,IS_IMPC,IS_IONC,IS_ICPLOT,
& IS_CODE,IS_SUM,IS_DES,IS_IE,IS_IEDP,IS_IEIP
COMMON/DESCRI/ ADDESCRI(100,3),DESCRI(100,3)

C
C
INTEGER OE_ACT,WF_ACT
CHARACTER*80 ADDESCRI
CHARACTER*40 DESCRI
CHARACTER*15 IDTRIAL,IDTEMP
CHARACTER*50 ELDESCR,WDESCR,ALABEL
CHARACTER*10 ALPHABET
CHARACTER*8 PLABEL

C
C
C READ THE RUN IDENTIFICATION NAMES
C
OPEN (20,FILE=':UDD:MEFL:ANALYSIS:INPUT:TRIAL_NAMES')
I=1
CONTINUE
READ (20,'(A)',END=10) IDTEMP
DO 3 II=1,15
IF (IDTEMP(II:II) .EQ. ' ' .OR.
& IDTEMP(II:II) .EQ. '<0>') GO TO 3
IPOSF=II
GO TO 4
3 CONTINUE
4 CONTINUE
C
DO 5 JJ=15,1,-1
IF (IDTEMP(JJ:JJ) .EQ. ' ' .OR.
& IDTEMP(JJ:JJ) .EQ. '<0>') GO TO 5
IPOSJ=JJ
GO TO 7
5 CONTINUE
7 CONTINUE
IDLEN(I)=IPOSJ-IPOSF+1
IDTRIAL(I)(1:IDLEN(I))=IDTEMP(IPOSF:IPOSJ)
I=I+1
GO TO 1
10 CONTINUE
C THE PREVIOUS TWO LOOPS ESTABLISH THE POSITIONS OF
C THE FIRST AND LAST SIGNIFICANT CHARACTERS IN THE
C FILE NAME. THIS IS USED LATER FOR REDUCTION OF
C THE TRIAL NAME SET.
C
NUM_OF_TRIALS=I-1 ! NUMBER OF RUNS ENTERED.

C
C SET THE SWITCHES FOR DESIRED FUNCTIONS
CALL SETSWITCH(MAXHARM)
CALL FILEOPEN ! OPENS ALL NECESSARY FILES

C
C

```

```

C      READ DATA SENT BY SUBROUTINE 'RUNINFO' ON OUTBOARD.
      CALL READINFO
C
C      PERFORM ELECTRICAL CALCULATIONS FOR EACH RUN
      IF (IS_WFFA .EQ. 0) GO TO 21
      DO 20 ITRIAL_COUNTER=1,NUM_OF_TRIALS
20     CALL WFM_CONVERT(MAXHARM)
21     CONTINUE
C
C      CORRECT ELECTRICAL MEASUREMENTS
      IF (IS_IMPC .EQ. 0) GO TO 91
      IF (IS_WFFA .EQ. 0) PRINT *,
&      'YOU MUST DO THE ELECTRICAL CALCULATIONS'
      IF (IS_WFFA .EQ. 0) PRINT *,
&      'IN ORDER TO DO THE IMPEDANCE CALCULATIONS.'
      IF (IS_WFFA .EQ. 0) STOP
      DO 90 ITRIAL_COUNTER=1,NUM_OF_TRIALS
90     CALL IMPED_CORR
91     CONTINUE
C
C      PERFORM IMPEDANCE CALCULATIONS FOR EACH RUN
      IF (IS_IMPC .EQ. 0) GO TO 31
      IF (IS_WFFA .EQ. 0) PRINT *,
&      'YOU MUST DO THE ELECTRICAL CALCULATIONS'
      IF (IS_WFFA .EQ. 0) PRINT *,
&      'IN ORDER TO DO THE IMPEDANCE CALCULATIONS.'
      IF (IS_WFFA .EQ. 0) STOP
      DO 30 ITRIAL_COUNTER=1,NUM_OF_TRIALS
30     CALL PLASMA_PAR
31     CONTINUE
C
C      PERFORM MASS SPEC ANALYSIS OF EACH RUN
      IF (IS_MSI .EQ. 0 .AND. IS_MSP .EQ. 0) GO TO 41
      DO 40 ITRIAL_COUNTER=1,NUM_OF_TRIALS
40     CALL MS_CONVERT
41     CONTINUE
C
C      PERFORM OPTICAL EMISSION ANALYSIS OF EACH RUN
      IF (IS_OEP .EQ. 0) GO TO 51
      DO 50 ITRIAL_COUNTER=1,NUM_OF_TRIALS
50     CALL OE_CONVERT
51     CONTINUE
C
C      PERFORM LASER INTERFEROMETRY CONVERSION FOR EACH RUN
      IF (IS_IFP .EQ. 0) GO TO 61
      DO 60 ITRIAL_COUNTER=1,NUM_OF_TRIALS
60     CALL IFR_CONVERT
61     CONTINUE
C
C      CALCULATE AND PLOT TOTAL ION FLUX
      IF (IS_IONC .EQ. 0) GO TO 56
      DO 55 ITRIAL_COUNTER=1,NUM_OF_TRIALS
55     CALL ION_FLUX
56     CONTINUE
C
      IF (IS_CODE .EQ. 0) GO TO 71
      CALL CODE_ICODING FOR PARAMETRIC FITTING
71     CONTINUE
C
C
C      EVALUATE ION ENERGIES
      IF (IS_IE .EQ. 0) GO TO 111
      DO 101 ITRIAL_COUNTER=1,NUM_OF_TRIALS
101    CALL IE_CONVERT
111    CONTINUE
C
C      COMPILER RUN SUMMARIES
      IF (IS_SUM.EQ.0) GO TO 81
      CALL SUMMARY
81     CONTINUE
C
      CALL FILECLOSE
      STOP
      END

```

```

SUBROUTINE CODE
C
C SUBROUTINE OF PROGRAM ANALYSIS - DATA ANALYSIS ROUTINE
C
C THIS SUBROUTINE DETERMINES THE CODED VALUES OF THE INDEPEN-
C   ENT VARIABLES FOR USE IN PARAMETRIC FITTING OF THE
C   EXPERIMENTAL DESIGN. THIS ROUTINE SHOULD ONLY BE CALLED
C   WHEN AN EXPERIMENTAL DESIGN WAS USED. THE DETAILS OF THE
C   CODING PROCEDURE CAN BE FOUND IN THE PAPER BY M.W. JENKINS,
C   ET AL., SOLID STATE TECHNOLOGY 29(4), 175 (1986).
C   THIS VERSION IS SET UP FOR A FOUR-VARIABLE DESIGN,
C   BUT IS NOT GENERALIZED FOR EVERY VARIABLE SET.
C   IT IS RECOMMENDED THAT IT NOT BE USED GENERALLY.
C
COMMON/SPECS/IDLEN(100),NUM_OF_TRIALS,ITRIAL_COUNTER,
&   NUMFILE
COMMON/IMPEDANCE/VARRU(100,3),CARRU(100,3),PARRU(100,3),
&   VARRC(100,3),CARRC(100,3),PARRC(100,3),
&   TPOW(100,3),DCB(100,3),FREQ(100,3)
COMMON/INFO/PRESSURE(100),ESPACE(100),MS_SCALE(100,10),
&   FLOWRATE(100,4),MSC_ACT(100),OE_ACT(100),
&   WF_ACT(100),ION_ACT(100),IF_SCALE(100),IE_ACT(100)
COMMON/IDENT/IDTRIAL(100),ALPHABET,ELDESCR(100),WDESCR(100)
COMMON/SWITCHES/IS_MSI,IS_MSP,IS_ACT,IS_OEP,IS_WFFA,IS_WFP,
&   IS_WFH,IS_IFP,IS_IMPC,IS_IONC,IS_ICPLOT,
&   IS_CODE,IS_SUM,IS_DES,IS_IE,IS_IEDP,IS_IEIP
C
C CHARACTER*50 ELDESCR,WDESCR
C CHARACTER*15 IDTRIAL
C CHARACTER*10 ALPHABET
C
C PARAMETER (PI=3.14159265)
C DIMENSION FRACT(100,4),TOTALFLOW(100),CODEDFLOW(100)
C DIMENSION CODEDPOW(100),CODEDPRE(100),CODEDARG(100)
C INTEGER OE_ACT,WF_ACT
C
C ASSUME THE ARGON FLOW RATE IS STORED IN THE FIRST
C COLUMN OF MATRIX 'FLOWRATE', FLOWRATES ARE IN SCCM.
C
C CALCULATE THE TOTAL GAS FLOWRATE. UP TO FOUR GASES
C ARE ALLOWED. THEN CALCULATE MOLE FRACTIONS OF EACH.
C DO 1 I=1,NUM_OF_TRIALS
TOTALFLOW(I)=FLOWRATE(I,1)+FLOWRATE(I,2)+
&   FLOWRATE(I,3)+FLOWRATE(I,4)
DO 20 J=1,4
FRACT(I,J)=FLOWRATE(I,J)/TOTALFLOW(I)
20 CONTINUE
C
C FIND THE AVERAGE VALUES OF THE VARIABLES.
C
SUMPOWER=0.
SUMPRESSURE=0.
SUMARGON=0.
SUMFLOW=0.
DO 2 I=1,NUM_OF_TRIALS
SUMPOWER=SUMPOWER+TPOW(I,1)
SUMPRESSURE=SUMPRESSURE+PRESSURE(I)
SUMFLOW=SUMFLOW+TOTALFLOW(I)
SUMARGON=SUMARGON+FRACT(I,1)
2 CONTINUE
AVGPOWER=SUMPOWER/NUM_OF_TRIALS
AVGPRESSURE=SUMPRESSURE/NUM_OF_TRIALS
AVGARGON=SUMARGON/NUM_OF_TRIALS
AVGFLOW=SUMFLOW/NUM_OF_TRIALS
C
C CALCULATE STANDARD DEVIATIONS OF THE VARIABLES.
C
SDPOWER=0.
SDPRESSURE=0.
SDARGON=0.
SDFLOW=0.

```

```

DO 3 I=1,NUM_OF_TRIALS
SDPOWER=SDPOWER+(TPOW(I,1)-AVGPOWER)**2.
SDPRESSURE=SDPRESSURE+(PRESSURE(I)-AVGPRESSURE)**2.
SDARGON=SDARGON+(FRACT(I,1)-AVGARGON)**2.
SDFLOW=SDFLOW+(TOTALFLOW(I)-AVGFLOW)**2.
3 CONTINUE
SDPOWER=SQRT(SDPOWER/(NUM_OF_TRIALS-1))
SDPRESSURE=SQRT(SDPRESSURE/(NUM_OF_TRIALS-1))
SDARGON=SQRT(SDARGON/(NUM_OF_TRIALS-1))
SDFLOW=SQRT(SDFLOW/(NUM_OF_TRIALS-1))
C
C NOW CODE THE VARIABLES USING THE MEAN AND S.D.
C
DO 10 I=1,NUM_OF_TRIALS
CODEDPOW(I)=(TPOW(I,1)-AVGPOWER)/SDPOWER
CODEDPRE(I)=(PRESSURE(I)-AVGPRESSURE)/SDPRESSURE
CODEDARG(I)=(FRACT(I,1)-AVGARGON)/SDARGON
CODEDFLOW(I)=(TOTALFLOW(I)-AVGFLOW)/SDFLOW
10 CONTINUE
C
C NOW PRINT OUT THE RESULTS IF REQUIRED.
C
1000 FORMAT (A15,F5.1,5X,F5.1,5X,F5.2,6X,F6.3,5X,F5.2,5X,4(F7.4,5X),F6.0)
1001 FORMAT (/,13X,"AVERAGES",8X,"STANDARD DEVIATIONS",/,"POWER",10X,F5.1,
& 15X,F5.1,/,"PRESSURE",8X,F4.2,16X,F4.2,/,"ARGON",10X,F5.3,15X,
& F5.3,/,"FLOW",11X,F5.2,15X,F5.2,/ )
WRITE (70,1001) AVGPOWER,SDPOWER,AVGPRESSURE,SDPRESSURE,
& AVGARGON,SDARGON,AVGFLOW,SDFLOW
RETURN
END

```

```

SUBROUTINE FILECLOSE
C
C SUBROUTINE OF PROGRAM ANALYSIS - DATA ANALYSIS ROUTINE
C THIS SUBROUTINE CLOSES ALL OPEN FILES,
C BOTH DATA FILES AND OUTPUT FILES.
C FILE NAMES ARE LISTED WITH CHANNEL NUMBERS
C IN SUBROUTINE FILEOPEN.
C

```

```

CLOSE (1)
CLOSE (13)
CLOSE (20)
CLOSE (22)
CLOSE (30)
CLOSE (51)
CLOSE (52)
CLOSE (70)
CLOSE (71)
CLOSE (82)
CLOSE (91)
RETURN
END

```

```

SUBROUTINE FILEOPEN
C
C SUBROUTINE OF PROGRAM ANALYSIS - DATA ANALYSIS ROUTINE
C THIS SUBROUTINE OPENS ALL FILES THAT ARE NECESSARY FOR
C PROGRAM EXECUTION AND PLACES THE HEADERS ON OUTPUT FILES.
C NOTE THAT INPUT FILES HAVE CHANNEL NUMBERS OF LESS THAN 50
C AND OUPUT FILES HAVE CHANNEL NUMBERS OF GREATER THAN 50.
C
C
COMMON/LABELS/PLABEL(10),ALABEL
COMMON/INTEGRATE/RDATA(4096),RMASS(4096),PEAKS(10,2),NPEAKS,
& IMASS(4096),MAXPP(10),PEAKCOMP,PHRAT(100,10,10)
COMMON/OECAL/CAL(3),CAL1(3),CAL2(3),R2(3),A11,A22,A33
COMMON/ACTINOM/P1L,P1H,P2L,P2H,BLL,BLH,RATIO(100,10)
COMMON/IMPDATA/MOBBPRES,STRAYC,CESPACE,L

```

```

COMMON/SWITCHES/IS_MSI,IS_MSP,IS_ACT,IS_OEP,IS_WFFA,IS_WFP,
& IS_WFH,IS_IFP,IS_IMPC,IS_IONC,IS_ICPLOT,
& IS_CODE,IS_SUM,IS_DES,IS_IE,IS_IEDP,IS_IEIP
C
C
CHARACTER*8 PLABEL
CHARACTER*50 ALABEL
REAL L,MOBPRES,MAXPP
INTEGER PEAKCOMP
C
C
OPEN INPUT FILES IN RESPONSE TO SWITCHES. NOTE TREE STRUCTURE.
IF (IS_MSI .EQ. 1)
& OPEN (13,FILE=':UDD:MEFL:ANALYSIS:INPUT:MS_RANGE')
IF (IS_EP .EQ. 1)
& OPEN (22,FILE=':UDD:MEFL:ANALYSIS:INPUT:CE_CAL')
IF (IS_ACT .EQ. 1)
& OPEN (12,FILE=':UDD:MEFL:ANALYSIS:INPUT:OEACT_RANGE')
OPEN (30,FILE=':UDD:MEFL:ANALYSIS:INPUT:IMPED_DATA')
C
C
OPEN OUTPUT FILES
IF (IS_WFFA .EQ. 1)
& OPEN (51,FILE=':UDD:MEFL:ANALYSIS:OUTPUT:IMP_OUT')
IF (IS_WFFA .EQ. 1)
& OPEN (52,FILE=':UDD:MEFL:ANALYSIS:OUTPUT:IMP_CALC')
IF (IS_CODE .EQ. 1)
& OPEN (70,FILE=':UDD:MEFL:ANALYSIS:OUTPUT:CODE_OUT')
IF (IS_WFH .EQ. 1)
& OPEN (82,FILE=':UDD:MEFL:ANALYSIS:OUTPUT:HARM_OUT')
C
C
CHANNEL NUMBERS AND INFORMATION THEREIN
C
C
1 DATAFILE FOR READINFO
12 DATAFILE FOR ACTINOMETRY PEAK RANGES
13 DATAFILE CONTAINING RANGES FOR M.S. PEAK HEIGHT COMPARISON
14 DATAFILE FOR MASS SPEC. FILES (TRANSIENT)
15 DATAFILE FOR OPT. EM. FILES (TRANSIENT)
20 DATAFILE CONTAINING TRIAL ID NAMES
22 DATAFILE CONTAINING OPTICAL EMISSION CALIBRATION VALUES
25 DATAFILE FOR LASER INT. FILES (TRANSIENT)
30 DATAFILE FOR IMPEDANCE CALCUATIONS
31 DATAFILE FOR WAVEFORM CURRENT (TRANSIENT)
32 DATAFILE FOR WAVEFORM VOLTAGE (TRANSIENT)
40 DATAFILE FOR ION_CURRENT (TRANSIENT)
45 DATAFILE FOR ION ENERGIES (TRANSIENT)
51 LISTFILE CONTAINING ELECTRICAL CALCULATIONS
52 LISTFILE CONTAINING IMPEDANCE CALCULATIONS
55 LISTFILE FOR M.S. PLOTS (TRANSIENT)
65 LISTFILE FOR O.E. PLOTS (TRANSIENT)
75 LISTFILE FOR LASER INT. PLOTS (TRANSIENT)
80 LISTFILE FOR EXPERIMENTAL DESIGN CODING
81 LISTFILE FOR WAVEFORM PLOTS (TRANSIENT)
82 LISTFILE FOR HARMONICS
86 LISTFILE FOR RUN SUMMARIES
90 LISTFILE FOR ION CURRENT PLOTS (TRANSIENT)
91 LISTFILE FOR MASS SPEC PEAK HEIGHTS
100 LISTFILE FOR ION ENERGY DISTRIBUTION PLOTS (TRANSIENT)
101 LISTFILE FOR ION ENERGY INTEGRAL PLOTS (TRANSIENT)
102 LISTFILE FOR ION ENERGY TABLES
C
C
NOW READ ALL VITAL INPUT DATA
C
C
IMPEDANCE CALCULATION CONSTANTS
READ (30,*) MOBPRES I (E- MOBILITY)X(PRESS) IN CM2/VOLT/S
READ (30,*) STRAYC I ELECTRODE STRAY CAPACITANCE, FARADS
READ (30,*) CESPAC I
READ (30,*) L I ELECTRODE LINE INDUCTANCE, HENRYS
C
C
READ THE CONSTANTS FOR THE OPTICAL EMISSION CALIBRATION.
THE CALIBRATION PROCEDURE IS GIVEN IN B.E. THOMPSON'S
THISIS OR LAB NOTEBOOKS.
C
C
IF (IS_OEP .EQ. 0) GO TO 20
READ (22,*) CAL
READ (22,*) CAL1
READ (22,*) CAL2

```



```

READ (22,*) R2
READ (22,*) A11,A22,A33
CONTINUE
20
C
C
C   READ OPTICAL EMISSION ACTINOMETRY PEAK RANGES.
C   THE INPUTS ARE HIGH/LOW RANGES FOR ANOTHER
C   SUBROUTINE WHICH DOES ACTINOMETRY. THE NUMBERS
C   SHOULD BE INPUT AS WAVELENGTHS, IN ANGSTROMS.
C
C   IF (IS_ACT .EQ. 0) GO TO 25
READ (12,*) BLL,BLH I ESTABLISH BASELINE FOR SCAN
READ (12,*) P1L,P1H I RANGE WHICH CONTAINS ACTINOMETER
READ (12,*) P2L,P2H I RANGE WHICH CONTAINS GAS
READ (12,*(A50)) ALABEL I COMMENT TO BE PRINTED IN SUMMARY
CONTINUE
25
C
C   READ IN THE MASS SPEC PEAK RANGES.
C
C   IF (IS_MSI .EQ. 0) GO TO 99
C   THE FILE PEAK_RANGES SHOULD BE ARRANGED AS FOLLOWS:
C   NPEAKS - THE NUMBER OF PEAKS TO BE COMPARED
C   PEAKCOMP - THE PEAK USED FOR NORMALIZATION
C   AND FOR EACH PEAK...
C   PEAKS(I,1),PEAKS(I,2) -- MIN AND MAX OF PEAK RANGES
C   PLABEL - LABEL FOR THE PEAK (8 CHARS.)
C
C   READ (13,*) NPEAKS
C   READ (13,*) PEAKCOMP
C   DO 100 I=1,NPEAKS
C   READ (13,*) PEAKS(I,1),PEAKS(I,2)
C   READ (13,*(A8)) PLABEL(I)
100 CONTINUE
C
C
C   NOW WRITE THE PEAK DATA TO THE HEADING OF THE
C   RESULTS OUTPUT FILE.
C
C   OPEN (91,FILE=':UDD:MEFL:ANALYSIS:OUTPUT:MS_PEAK')
C   WRITE (91,1010)
C   DO 200 I=1,NPEAKS
C   WRITE (91,1020) PLABEL(I)
200 CONTINUE
C   WRITE (91,1030)
C
C   CONTINUE
99
C
C   IF (IS_IE .EQ. 1)
C   & OPEN (102,FILE=':UDD:MEFL:ANALYSIS:OUTPUT:IE_TABLE')
C   IF (IS_IE .EQ. 1) WRITE (102,1050)
C
C   NOW WRITE HEADERS TO THE WAVEFORM ANALYSIS OUTPUT FILES.
C
C   IF (IS_WFFA .EQ. 1) WRITE (51,1001)
C   IF (IS_WFH .EQ. 1) WRITE (82,1040)
C   IF (IS_WFFA .EQ. 1) WRITE (52,1002)
C
C
C
C   FORMAT STATEMENTS
C1001 FORMAT ('TRIAL ID',7X,'ESPACE',4X,'PRESS',1X,'FREQUENCY',
C   & 3X,'VOLTS',3X,'AMPS',6X,'PHASE',2X,'DC BIAS',/,
C   & 16X,'(CM)',4X,'(TORR)',/,80('-'))
1002 FORMAT ('TRIAL ID',7X,'BULK RES',5X,'CAP',6X,'POWER',
C   & 7X,'E/P',7X,'VSHEATH',4X,'EDENSE',/,
C   & 16X,'(OHMS)',6X,'(PF)',4X,'(WATTS)',2X,'(V/CM/TORR)',3X,
C   & '(VOLT)',4X,'(xE+9/cc)',/,80('-'))
1010 FORMAT('RELATIVE PEAK HEIGHTS OF MASS SPECTRA',/,
C   & 'TRIAL ID', '$)
1020 FORMAT(A8,' ', '$)
1030 FORMAT(/)
1040 FORMAT(/, ' # VOLTAGE CURRENT ',
C   & 'VOLT_PHASE CURR_PHASE')
1050 FORMAT(/,1X,'TRIAL ID',4X,' ION FLUX ',4X,' ION FLUX (0)',4X,
C   & 'MEDIAN',2X,'REY. MED.',4X,'MEAN',4X,'MAX. E.',4X,
C   & ' 10 EV',4X,' 15 EV',4X,' 20 EV',3X,' 25 EV',/,
C   & 130('-')./)

```



```

IF (CUR(I) .LT. CURMID) ISIGN_NEW=-1
IF (CUR(I) .GE. CURMID) ISIGN_NEW=1
IF (ISIGN_NEW .NE. ISIGN_LAST) NSIGNC=NSIGNC+1
IF (NSIGNC .GE. 20) GO TO 10
IF (ISIGN_NEW .NE. ISIGN_LAST) ZEROS(NSIGNC,1)=1
IF (ISIGN_LAST .EQ. -1 .AND. ISIGN_NEW .EQ. 1) ZEROS(NSIGNC,2)=1
C NEGATIVE TO POSITIVE TRANSITION
C IF (ISIGN_LAST .EQ. 1 .AND. ISIGN_NEW .EQ. -1) ZEROS(NSIGNC,2)=-1
C POSITIVE TO NEGATIVE TRANSITION
ISIGN_LAST=ISIGN_NEW
10 CONTINUE
C
C FIND THE MAXIMUM NUMBER OF COMPLETE CYCLES AVAILABLE
C AND USE THE PERIOD TO FIND THE EXCITATION
C FREQUENCY. XINCR IS THE TIME INCREMENT PER POINT,
C AS SENT DOWN BY THE SCOPE.
C
NUM_CYCLES=0
DO 20 J=2,20
20 IF (ZEROS(J,2) .EQ. ZEROS(1,2)) NUM_CYCLES=NUM_CYCLES+1
NLOW=ZEROS(1,1)
NHIGH=ZEROS((2*NUM_CYCLES+1),1)
FREQ(ITRIAL_COUNTER,NUMWAVE)=FLOAT(NUM_CYCLES)/
& FLOAT((NHIGH-NLOW))/XINCR
C
C DETERMINE THE RANGE OF SAMPLING POINTS TO BE USED
C IN THE FOURIER ANALYSIS.
C START BY INITIALIZING PERTINENT VARIABLES.
C
DO 100 J=0,20
FHEVEN_V(J)=0.
FHODD_V(J)=0.
FHEVEN_C(J)=0.
FHODD_C(J)=0.
VOLT_A(J)=0.
THETA_V(J)=0.
CURR_A(J)=0.
THETA_C(J)=0.
100 CONTINUE
C
C THE FIRST 'MAXHARM' HARMONICS WILL BE EVALUATED,
C AS SPECIFIED BY THE OPERATOR IN THE MAIN DATA FILE.
C SCALE THE RANGE OF DISCRETE POINTS INTO [0,N]
C AND CALCULATE BOTH THE ODD AND EVEN HARMONICS.
C BOTH THE VOLTAGE AND CURRENT WAVEFORMS WILL
C BE EVALUATED HERE.
C
TIME_INT=FLOAT(NHIGH-NLOW+1)
DO 200 NHARM=0,MAXHARM
OMEGA=2.*PI*FLOAT(NUM_CYCLES)*FLOAT(NHARM)/
& (TIME_INT-1)
C
C OMEGA IS THE ANGULAR FREQUENCY.
C AS AN INTERMEDIATE STEP TO THE FOURIER COEFFICIENTS,
C CALCULATE THE ODD AND EVEN COMPONENTS THEREOF.
C
DO 300 IP=NLOW,NHIGH
FHEVEN_V(NHARM)=FHEVEN_V(NHARM)+
& COS((IP-NLOW)*OMEGA)*VOLT(IP)
& FHODD_V(NHARM)=FHODD_V(NHARM)+
& SIN((IP-NLOW)*OMEGA)*VOLT(IP)
FHEVEN_C(NHARM)=FHEVEN_C(NHARM)+
& COS((IP-NLOW)*OMEGA)*CUR(IP)
& FHODD_C(NHARM)=FHODD_C(NHARM)+
& SIN((IP-NLOW)*OMEGA)*CUR(IP)
300 CONTINUE
IF (NHARM .EQ. 0) GO TO 200
VOLT_A(NHARM)=2./TIME_INT*SQRT(FHEVEN_V(NHARM)*
& FHEVEN_V(NHARM)+
& FHODD_V(NHARM)*FHODD_V(NHARM))
& CURR_A(NHARM)=2./TIME_INT*SQRT(FHEVEN_C(NHARM)*
& FHEVEN_C(NHARM)+
& FHODD_C(NHARM)*FHODD_C(NHARM))
& THETA_V(NHARM)=ATAN(FHODD_V(NHARM)/FHEVEN_V(NHARM))*
& 180./PI+90.*(1-SIGN(1.,FHEVEN_V(NHARM)))
& THETA_C(NHARM)=ATAN(FHODD_C(NHARM)/FHEVEN_C(NHARM))*
& 180./PI+90.*(1-SIGN(1.,FHEVEN_C(NHARM)))

```

```

THETA(NHARM)=THETA_V(NHARM)-THETA_C(NHARM)
IF (THETA(NHARM) .LE. 0.) THETA(NHARM)=360.+THETA(NHARM)
200 CONTINUE
C
C THE PEAK CURRENT AND VOLTAGE ARE THE AMPLITUDES
C OF THE FIRST HARMONIC. THE PHASE SHIFT IS THE FIRST
C HARMONIC OF THE PHASE SHIFT DIFFERENCE
C BETWEEN CURRENT AND VOLTAGE.
C
VARRU(ITRIAL_COUNTER,NUMWAVE)=VOLT_A(1)
CARRU(ITRIAL_COUNTER,NUMWAVE)=CURR_A(1)
PARRU(ITRIAL_COUNTER,NUMWAVE)=THETA(1) IPHASE ANGLE IN DEG.
C
C CALCULATE THE DC BIAS, WHICH IS THE ZEROth ORDER
C HARMONIC OF THE VOLTAGE.
C
DCB(ITRIAL_COUNTER,NUMWAVE)=1./TIME_INT*FHEVEN_V(0)
DCB_CUR=1./TIME_INT*FHEVEN_C(0) DC BIAS ON THE CURRENT
C
C NOW CALCULATE THE TOTAL POWER INPUT TO THE PLASMA,
C WHICH IS THE PRODUCT OF THE CURRENT AND
C VOLTAGE WAVEFORMS, TIME-AVERAGED.
C
TPOWER=0.
TPOWERCB=0.
DO 500 I=NLOW,NHIGH
TPOWER=TPOWER+VOLT(I)*CUR(I)
TPOWERCB=TPOWERCB+VOLT(I)*(CUR(I)-DCB_CUR)
C CORRECTION FOR ANY OFFSET IN CURRENT.
500 CONTINUE
TPOW(ITRIAL_COUNTER,NUMWAVE)=TPOWERCB/TIME_INT
TP(ITRIAL_COUNTER,NUMWAVE)=TPOWER/TIME_INT
C
C NOW, WRITE THE RESULTS TO THE OUTPUT FILE
C FOR THE HARMONICS.
C
IF (IS_WFH .EQ. 0) GO TO 9999
RUNID=IDTRIAL(ITRIAL_COUNTER)(1:IDLEN(ITRIAL_COUNTER))//
& '_WF'//NUMBER(NUMWAVE:NUMWAVE)
C
C NOW RESTORE THE HARMONIC DATA FOR USE IN THE
C RUN SUMMARY SUBROUTINE.
C
DO 600 NH=1,MAXHARM
HARMDATA(ITRIAL_COUNTER,NUMWAVE,(5*NH-4))=NH
HARMDATA(ITRIAL_COUNTER,NUMWAVE,(5*NH-3))=VOLT_A(NH)
HARMDATA(ITRIAL_COUNTER,NUMWAVE,(5*NH-2))=CURR_A(NH)
HARMDATA(ITRIAL_COUNTER,NUMWAVE,(5*NH-1))=THETA_V(NH)
HARMDATA(ITRIAL_COUNTER,NUMWAVE,(5*NH))=THETA_C(NH)
600 WRITE (82,1001) NH,VOLT_A(NH),CURR_A(NH),THETA_V(NH),
& THETA_C(NH)
& WRITE (82,1002) RUNID,VARRU(ITRIAL_COUNTER,NUMWAVE),
& CARRU(ITRIAL_COUNTER,NUMWAVE),
& PARRU(ITRIAL_COUNTER,NUMWAVE),
& DCB(ITRIAL_COUNTER,NUMWAVE),DCB_CUR,
& TP(ITRIAL_COUNTER,NUMWAVE),
& TPOW(ITRIAL_COUNTER,NUMWAVE)
C
C
1001 FORMAT(I2,3X,4(E12.5,3X))
1002 FORMAT (/,A20,'/V/'=',F7.3,3X,'/I/'=',F7.5,3X,'PA=',
& F7.1,3X,'DCV=' ,F6.1,4X,'DCI=' ,F6.3,4X,
& 'POWER: ',F6.1,5X,F6.1,/,100('-' ),/)
C
9999 CONTINUE
RETURN
END

SUBROUTINE IE_CONVERT
C
C SUBROUTINE OF PROGRAM ANALYZE - DATA ANALYSIS ROUTINE
C
C SUBROUTINE TO CONVERT DATA FROM OUTBOARD FOR ION ENERGIES.

```

```

C      THE ELECTROMETER SCALE (MULTIPLIED BY 5) IS SENT DOWN IN
C      THE DATA FILE. THE DATA CONTAINS A DIGITAL OUTPUT VALUE
C      AND A DIGITAL INPUT VALUE. THIS SUBROUTINE READS THESE
C      DATA AND CONVERTS THEM TO ANALOG VOLTAGES IN AND OUT.
C      THE PROGRAM THEN CONVERTS THESE VOLTAGES
C      TO THE RETARDING VOLTAGE AND THE ION FLUX.
C
C      COMMON/IDENT/IDTRIAL(100),ALPHABET,ELDESCR(100),WDESCR(100)
C      COMMON/FLUX/PAREA,AVEFLUX
C      COMMON/SPECS/IDLEN(100),NUM_OF_TRIALS,ITRIAL_COUNTER,NUMFILE
C      COMMON/SWITCHES/IS_MSI,IS_MSP,IS_ACT,IS_OEP,IS_WFFA,IS_WFP,
&      IS_WFH,IS_IFP,IS_IMPC,IS_IONC,IS_ICPLOT,
&      IS_CODE,IS_SUM,IS_DES,IS_IE,IS_IEDP,IS_IEIP
C      COMMON/INFO/PRESSURE(100),ESPACE(100),MS_SCALE(100,10),
&      FLOWRATE(100,4),MSC_ACT(100),OE_ACT(100),WF_ACT(100),
&      ION_ACT(100),IF_SCALE(100),IE_ACT(100)
C
C      CHARACTER*50 ELDESCR,WDESCR,LINE,DES
C      CHARACTER*10 ALPHABET
C      CHARACTER*15 IDTRIAL,FNAME
C      CHARACTER*20 MINFO
C      INTEGER IDOUT(4096),IDIN(4096),ZEROPT,ENDPT,OPTION
C      DATA FNAME/' '
C      DIMENSION RETVOLT(4096),FLUX(4096),DFLUX(4096),
&      F(4096),DES(3)
C      REAL MEDENERGY
C
C      FIRST, OPEN THE DATA AND PLOT OUTPUT FILES
C
C      FNAME(1:IDLEN(ITRIAL_COUNTER))=IDTRIAL(ITRIAL_COUNTER)
&      (1:IDLEN(ITRIAL_COUNTER))
C      OPEN (45,
&      FILE='UDD:MEFL:DAAD:'//FNAME(1:IDLEN(ITRIAL_COUNTER))//'_DA1')
&      IF (IS_IEDP .EQ. 1) OPEN (100,FILE='UDD:MEFL:IEPLOT:'//
&      FNAME(1:IDLEN(ITRIAL_COUNTER))//'_DP')
&      IF (IS_IEIP .EQ. 1) OPEN (101,FILE='UDD:MEFL:IEPLOT:'//
&      FNAME(1:IDLEN(ITRIAL_COUNTER))//'_IP')
C
C      READ DATA FROM DATA FILE, RUN DESCRIPTION
C      FIRST, THEN DATA.
C
C      READ(45,1000) LINE
C      READ(45,1000) (DES(I),I=1,3)
1000  FORMAT(A)
C      READ(45,1000) MINFO
C      READ(45,*) ELSCALE
C      SCALE READING ON THE ELECTROMETER, SO THE
C      DIGITAL-VALUED DATA FROM THE A/D CONVERTER
C      CAN BE COVERTED BACK INTO A TRUE ION CURRENT.
C
C      NPT=0
100  READ(45,*,END=200) IDOUT(NPT+1),IDIN(NPT+1)
C      NPT=NPT+1
C      GOTO 100
C
C      200  VGAIN=20.
C      IF USING SURENDRA'S LANGMUIR PROBE BOX,
C      VOLTAGES ARE SENT TO THE OUTBOARD AFTER
C      BEING MULTIPLIED BY 0.05, SO THE GAIN
C      MUST BE REINSTATED TO GET CORRECT POTENTIALS.
C
C      CHANGE SIGN ON THE ION FLUXES IF NECESSARY
C
C      IF (IDIN(2) .GT. 0) GO TO 225
C      DO 220 K=1,NPT
C      IDNEG=-1*IDIN(K)
C      IDIN(K)=IDNEG
220  CONTINUE
225  CONTINUE
C
C      CALCULATE RETARDING VOLTAGES AND FLUXES
C      BY CONVERTING THE DIGITAL VALUES TO
C      ACTUAL VOLTAGES AND CURRENTS.
C
C      VMIN=0.

```

```

DO 250 I=(NPT-3),NPT
VMIN=VMIN+5.*REAL(IDIN(NPT))/32662./4.
DO 300 I=1,NPT
VOUT=5.*REAL(IDCUT(I))/2048.
VIN=5.*REAL(IDIN(I))/32662.
RETVOLT(I)=VOUT*VGAIN
300 FLUX(I)=.125*(VIN-VMIN)*ELSCALE/PAREA*1.E3
C
C   TO GET THE DISTRIBUTION, WE DIFFERENTIATE
C   THE CUMULATIVE DISTRIBUTION THAT IS MEASURED.
C   IN FINITE DIFFERENTIAL FORM, FIRST
C   EVALUATE D(FLUX)/D(VOLTAGE).
C   ALSO, CALCULATE THE VOLTAGES AT WHICH
C   THE MEDIAN AND ZERO ION FLUXES ARE REACHED.
C
ENDPT=NPT-1
HALFFLUX=FLUX(1)/2.
DO 400 I=1,NPT-1
DFLUX(I)=(FLUX(I)-FLUX(I+1))
IF(FLUX(I).GT.HALFFLUX) MEDENERGY=RETVOLT(I)
IF((FLUX(I).LT.0.).AND.(I.LT.ENDPT)) ENDPT=I
IF(RETVOLT(I).EQ.0.) ZEROPT=I
400 IF(RETVOLT(I).LT.0.) ZEROPT=I
C
C   CALCULATE THE SUMS REQUIRED FOR THE FIRST
C   MOMENT (MEAN) AND SECOND MOMENT (S.D.)
C   OF THE ION ENERGY DISTRIBUTION. ALSO,
C   CALCULATE A REVISED MEDIAN AFTER ALLOWING
C   FOR THE SMALL ERROR IN ION CURRENT NEAR
C   0 VOLTS (SEE B.E. THOMPSON ET AL.,
C   J. APPL. PHYS. 59, 1890 (1986).)
C
ESUM=0.
EESUM=0.
RFLUX=0.
REVHFLUX=FLUX(ZEROPT)/2.
DO 500 I=ZEROPT,ENDPT
IF(FLUX(I).GT.REVHFLUX) RMEDENERGY=RETVOLT(I)
500 RFLUX=RFLUX+DFLUX(I)
C
C   CALCULATE THE ION ENERGY DISTRIBUTION FUNCTION.
C   ALSO, DETERMINE MEAN AND S.D. OF DISTRIBUTION.
C
DO 505 I=1,(NPT-1)
F(I)=DFLUX(I)/(RETVOLT(I+1)-RETVOLT(I))/RFLUX
505 CONTINUE
C
DO 510 I=ZEROPT,ENDPT
ENERGY=(RETVOLT(I+1)+RETVOLT(I))/2.
ESUM=ESUM+F(I)*ENERGY*(RETVOLT(I+1)-RETVOLT(I))
510 EESUM=EESUM+ENERGY*ENERGY+F(I)*(RETVOLT(I+1)-RETVOLT(I))
C
AVEENERGY=ESUM
STDENERGY=-9.99
IF((EESUM-ESUM*ESUM).LT.0.) GOTO 520
STDENERGY=SQRT(EESUM-ESUM*ESUM)
520 CONTINUE
C
C   NOW, DETERMINE THE FRACTION OF IONS WITH
C   ENERGY ABOVE A SET OF GIVEN THRESHOLDS.
C   THE PROGRAM IS NOW SET UP FOR 10,15,20,
C   AND 25 VOLTS. IT SHOULD BE GENERALIZED
C   IN THE FUTURE SO THAT THE OPERATOR CAN
C   SPECIFY THE THRESHOLDS.
C
I10S=0
I15S=0
I20S=0
I25S=0
I10=ZEROPT
I15=ZEROPT
I20=ZEROPT
I25=ZEROPT
F10=0.
F15=0.
F20=0.
F25=0.

```

```

DO 800 I=ZEROPT,ENDPT
IF (RETVOLT(I) .GE. 10. .AND. I10S .EQ. 0) I10=I
IF (RETVOLT(I) .GE. 10.) I10S=1
IF (RETVOLT(I) .GE. 15. .AND. I15S .EQ. 0) I15=I
IF (RETVOLT(I) .GE. 15.) I15S=1
IF (RETVOLT(I) .GE. 20. .AND. I20S .EQ. 0) I20=I
IF (RETVOLT(I) .GE. 20.) I20S=1
IF (RETVOLT(I) .GE. 25. .AND. I25S .EQ. 0) I25=I
IF (RETVOLT(I) .GE. 25.) I25S=1
800 CONTINUE
IF (I10 .NE. ZEROPT) F10=FLUX(I10)/FLUX(ZEROPT)
IF (I15 .NE. ZEROPT) F15=FLUX(I15)/FLUX(ZEROPT)
IF (I20 .NE. ZEROPT) F20=FLUX(I20)/FLUX(ZEROPT)
IF (I25 .NE. ZEROPT) F25=FLUX(I25)/FLUX(ZEROPT)

C
C NOW CREATE THE INPUT FILES FOR SYSTEM ROUTINE
C EPLOT, THE PLOTTING ROUTINE. THE COMMAND SET
C FOR EPLOT CAN BE FOUND IN THE DEPARTMENTAL
C COMPUTER FACILITY.
C
IF (IS_IEDP .EQ. 0) GO TO 600

C
WRITE (100,1010) FNAME
OPTION=1+INT(NPT/500)
DO 550 I=1,(NPT-1),OPTION
FLDIST=0.
DO 560 J=I,I+OPTION-1
560 FLDIST=FLDIST+F(J)/OPTION
550 WRITE(100,1020) RETVOLT(I),FLDIST
C
600 CONTINUE
IF (IS_IEIP .EQ. 0) GO TO 700

C
WRITE (101,1030) FNAME
OPTION=1+INT(NPT/500)
DO 570 I=1,(NPT-1),OPTION
570 WRITE(101,1020) RETVOLT(I),FLUX(I)
700 CONTINUE
C
C
C
1001 FORMAT(1X,A15,5X,2(E10.3,5X),4(F5.1,5X),4(F5.3,5X))
WRITE (102,1001) IDTRIAL(ITRIAL_COUNTER),FLUX(I),FLUX(ZEROPT),
& MEDENERGY,RMEDENERGY,AVEENERGY,RETVOLT(ENDPT),
& F10,F15,F20,F25
1010 FORMAT('ION ENERGY DISTRIBUTION FOR',1X,A15,/, 'ENERGY',/,
& 'F(E)',/, 'SYMB 0.0',/, 'END')
1020 FORMAT(F7.2,',',,E12.3)
1030 FORMAT('ION FLUX VS. RETARDING VOLTAGE FOR',1X,A15,/,
& 'RETARDING VOLTAGE',/, 'FLUX',/, 'SYMB 0.0',/, 'END')
C
IF (IS_IEDP .EQ. 1) CLOSE (100)
IF (IS_IEIP .EQ. 1) CLOSE (101)
C
RETURN
END

SUBROUTINE IFR_CONVERT
C
C SUBROUTINE OF PROGRAM ANALYZE - DATA ANALYSIS ROUTINE
C
C THIS SUBROUTINE CONVERTS THE LASER INTERFEROMETRY
C DATA SENT DOWN FROM THE OUTBOARD COMPUTER TO
C EPLOT FILES. THE ETCHING RATE OF POLYSILICON
C IS ALSO CALCULATED.
C
COMMON/IDENT/IDTRIAL(100),ALPHABET,ELDESCR(100),
& WDESCR(100)
COMMON/SPECS/IDLEN(100),NUM_OF_TRIALS,
& ITRIAL_COUNTER,NUMFILE
COMMON/SWITCHES/IS_MSI,IS_MSP,IS_ACT,IS_OEP,IS_WFFA,IS_WFP,
& IS_WFH,IS_IFP,IS_IMPC,IS_IONC,IS_ICPLOT,
& IS_CODE,IS_SUM,IS_DES,IS_IE,IS_IEDP,IS_IEIP

```

```

COMMON/DESCRI/ ADDESCRI(100,3),DESCRI(100,3)
C
C
DIMENSION INTENS(5000),TIME(5000)
REAL INTENS
CHARACTER*80 ADDESCRI
CHARACTER*40 LABEL1,LABEL2,LABEL3,DESCRI
CHARACTER*12 FNAME
CHARACTER*50 ELDESCR,WDESCR,RUNID
CHARACTER*15 IDTRIAL
CHARACTER*10 ALPHABET
CHARACTER*20 PATHNAME
C
C
OPEN INTERFEROMETRY DATA FILE AND EPLOT
OUTPUT FILE.
C
PATHNAME=':UDD:MEFL:LASER_INT:'
RUNID=PATHNAME//IDTRIAL(ITRIAL_COUNTER)(1:IDLEN(ITRIAL_COUNTER))//'_IFR'
OPEN (25,FILE=RUNID)
PATHNAME=':UDD:MEFL:IFR:PLOT:'
RUNID=PATHNAME(1:18)//IDTRIAL(ITRIAL_COUNTER)(1:IDLEN(ITRIAL_COUNTER))
& //'_IFR'
OPEN (75,FILE=RUNID)
C
C
READ THE DATA FROM THE INPUT FILE.
FIRST, READ THE RUN INFORMATION.
C
READ (25,FMT='(A)') FNAME
READ (25,FMT='(A)') LABEL1
READ (25,FMT='(A)') LABEL2
READ (25,FMT='(A)') LABEL3
READ (25,*) NTIME
DESCRI(ITRIAL_COUNTER,1)=LABEL1
DESCRI(ITRIAL_COUNTER,2)=LABEL2
DESCRI(ITRIAL_COUNTER,3)=LABEL3
C
NOW READ THE DATA POINTS. THE DATA IS
ENTERED AS (1) TIME IN SECS, (2) TIME
IN MILLISECS, (3) INTENSITY.
C
IC=0
90 IF (NTIME .EQ. 1) GO TO 95
& READ (25,*,END=100) ITS1,ITMS1,INTENS(IC+1),
& ITS2,ITMS2,INTENS(IC+2),
& ITS3,ITMS3,INTENS(IC+3),
& ITS4,ITMS4,INTENS(IC+4)
C CONVERT TO REAL TIME, IN SECONDS.
TIME(IC+1)=ITS1+.25*ITMS1
TIME(IC+2)=ITS2+.25*ITMS2
TIME(IC+3)=ITS3+.25*ITMS3
TIME(IC+4)=ITS4+.25*ITMS4
IC=IC+4
GO TO 90
95 READ (25,*,END=100) ITS1,INTENS(IC+1),ITS2,INTENS(IC+2),
& ITS3,INTENS(IC+3),ITS4,INTENS(IC+4)
TIME(IC+1)=ITS1
TIME(IC+2)=ITS2
TIME(IC+3)=ITS3
TIME(IC+4)=ITS4
IC=IC+4
GO TO 90
100 CONTINUE
C
ESTABLISH THE MAX. AND MIN. OF THE
INTERFEROMETER SIGNAL.
C
YMIN=1000000
YMAX=-1000000
DO 110 I=1,IC
IF (INTENS(I) .LT. YMIN) YMIN=INTENS(I)
IF (INTENS(I) .GT. YMAX) YMAX=INTENS(I)
110 CONTINUE
C
NOW SCALE THE INTENSITIES FROM [-1,1]
AND CUT DOWN ON THE NUMBER OF POINTS.

```



```

C      SINCE EPLOTT CAN ONLY TAKE 512 POINTS.
C
RAVE=(YMAX+YMIN)/2.
ISTEP=INT(IC/500.)+1
DO 150 J=1,IC
INTENS(J)=(INTENS(J)-RAVE)*2./(YMAX-YMIN)
150 CONTINUE
C
C      NOW WRITE TO EPLOTT FILE
C
WRITE (75,1010) FNAME
WRITE (75,1020) LABEL1,LABEL2,LABEL3
WRITE (75,1030)
DO 30 I=1,IC,ISTEP
30 WRITE (75,1040) TIME(I),INTENS(I)
C
C      FORMAT STATEMENTS
C
1010 FORMAT ('LASER INTERFEROMETRY FOR ',A12,/, 'TIME IN SECS',/,
&          'RELATIVE INTENSITY',/, 'SYMB 99.0',/, 'YLEN 4.5',/,
&          'YMIN -1.5',/, 'YMAX 1.2',/, 'YTIC -1.0',/, '.40,1.0')
1020 FORMAT ('LABL -3.0',/, '0.25,0.65',/,A40,/, '0.25,0.5',/,A40,/,
&          '0.25,0.35',/,A40)
1030 FORMAT ('END')
1040 FORMAT (F7.2, ' ', F6.3)
CLOSE (25)
CLOSE (75)
RETURN
END

SUBROUTINE IMPED_CORR
C
C      SUBROUTINE OF PROGRAM ANALYZE - DATA ANALYSIS ROUTINE
C
C      THIS SUBROUTINE CORRECTS THE VOLTAGE, CURRENT,
C      AND PHASE DELAY FOR THE SERIES INDUCTANCE,
C      STRAY CAPACITANCE, AND ELECTRODE CAPACITANCE.
C      THE RESULTING WAVEFORMS ARE REPRESENTATIVE OF THOSE
C      AT THE POWERED ELECTRODE.
C
COMMON/INFO/PRESSURE(100),ESPACE(100),MS_SCALE(100,10),
&          FLOWRATE(100,4),MSC_ACT(100),OE_ACT(100),
&          WF_ACT(100),ION_ACT(100),IF_SCALE(100),
&          IE_ACT(100)
COMMON/IMPEDANCE/VARRU(100,3),CARRU(100,3),PARRU(100,3),
&          VARRC(100,3),CARRC(100,3),PARRC(100,3),
&          TPOW(100,3),DCB(100,3),FREQ(100,3)
COMMON/SPECS/IDLEN(100),NUM_OF_TRIALS,ITRIAL_COUNTER,
&          NUMFILE
COMMON/IMPDATA/MOBBPRES,STRAYC,CESPACE,L
COMMON/SWITCHES/IS_MSI,IS_MSP,IS_ACT,IS_OEP,IS_WFFA,IS_WFP,
&          IS_WFH,IS_IFP,IS_IMPC,IS_IONC,IS_ICPLOT,
&          IS_CODE,IS_SUM,IS_DES,IS_IE,IS_IEDP,IS_IEIP
COMMON/IMPSAVE/SAVEIMP(100,3,6)
C
C      INTEGER OE_ACT,WF_ACT,WFNUM
C      REAL MOBBPRES,MOBIL,L
C
PI=3.1415926
C
C      FOR EACH RUN, READ THE UNCORRECTED IMPEDANCE
C      PROPERTIES DETERMINED BY SUBROUTINE FOURIER.
C
DO 999 WFNUM=1,WF_ACT(ITRIAL_COUNTER)
VOLTS=VARRU(ITRIAL_COUNTER,WFNUM)
AMPSU=CARRU(ITRIAL_COUNTER,WFNUM)
PHASEU=PARRU(ITRIAL_COUNTER,WFNUM)/FREQ(ITRIAL_COUNTER,WFNUM)/360.
C
OMEGA=FREQ(ITRIAL_COUNTER,WFNUM)*2.*PI
C
C      CALCULATE PHASE SHIFT (THETA IN DEGREES, THETA1 IN RAD)

```

```

THETAU=PARRU(ITRIAL_COUNTER,WFNUM)
THETA1U=THETAU/180.*PI
C
C   CORRECT FOR STRAY CAPACITANCE. THE DETAILS
C   OF THIS PROCEDURE CAN BE FOUND IN
C   B.E. THOMPSON'S THESIS.

AMPSREAL=AMPSU*COS(THETA1U)
AMPSIM=AMPSU*SIN(THETA1U)-VOLTS*STRAYC*OMEGA
AMPS=SQRT(AMPSREAL*AMPSREAL+AMPSIM*AMPSIM)
THETA1=ASIN(AMPSIM/AMPS)
THETA=THETA1/PI*180.
PHASE=THETA/FREQ(ITRIAL_COUNTER,WFNUM)/360.
C
C   CORRECT FOR SERIES INDUCTANCE
C   BY A SIMILAR PROCEDURE.

VOLTSREAL=VOLTS*COS(THETA1)
VOLTSIM=VOLTS*SIN(THETA1)+AMPSU*L*OMEGA
VOLTS=SQRT(VOLTSIM*VOLTSIM+VOLTSREAL*VOLTSREAL)
THETA1=ASIN(VOLTSIM/VOLTS)
THETA=THETA1/PI*180.
PHASE=THETA/FREQ(ITRIAL_COUNTER,WFNUM)/360.
C
C   VARRC(ITRIAL_COUNTER,WFNUM)=VOLTS
C   CARRC(ITRIAL_COUNTER,WFNUM)=AMPS
C   PARRC(ITRIAL_COUNTER,WFNUM)=THETA
C   THESE ARE THE CORRECTED IMPEDANCE VALUES,
C   AND SHOULD REFLECT THE IMPEDANCE OF THE
C   DISCHARGE ONLY.
999  CONTINUE
      RETURN
      END

SUBROUTINE ION_FLUX
C
C   SUBROUTINE OF PROGRAM ANALYZE - DATA ANALYSIS ROUTINE
C
C   THIS SUBROUTINE CONVERTS THE ION CURRENT SIGNALS
C   INTO AN EPLOT DATA FILE. THE AVERAGE ION FLUX
C   IS ALSO CALCULATED.
C
COMMON/IDENT/IDTRIAL(100),ALPHABET,ELDESCR(100),
&   WDESCR(100)
COMMON/SPECS/IDLEN(100),NUM_OF_TRIALS,ITRIAL_COUNTER,
&   NUMFILE
COMMON/FLUX/PAREA,AVEFLUX
COMMON/SWITCHES/IS_MSI,IS_MSP,IS_ACT,IS_OEP,IS_WFFA,IS_WFP,
&   IS_WFH,IS_IFP,IS_IMPC,IS_IONC,IS_ICPLOT,
&   IS_CODE,IS_SUM,IS_DES,IS_IE,IS_IEDP,IS_IEIP
COMMON/INFO/PRESSURE(100),ESPACE(100),MS_SCALE(100,10),
&   FLOWRATE(100,4),MSC_ACT(100),OE_ACT(100),
&   WF_ACT(100),ION_ACT(100),IF_SCALE(100),
&   IE_ACT(100)
C
C   DIMENSION ITIME(1000),RTIME(1000),IDATA(1000),
&   TIFLUX(1000),TFSCALE(1000),RDATA(1000)
&   INTEGER OE_ACT,WF_ACT
&   CHARACTER*40 LABEL1,LABEL2,LABEL3
&   CHARACTER*50 ELDESCR,WDESCR,RUNID
&   CHARACTER*10 ALPHABET
&   CHARACTER*15 IDTRIAL
&   CHARACTER*20 PATHNAME
&   CHARACTER*12 FNAME
C
C   OPEN DATA AND EPLOT OUTPUT FILES.
C
PATHNAME=' :UDD:MEFL:ION_CUR:'
RUNID=PATHNAME(1:18)//IDTRIAL(ITRIAL_COUNTER)(1:IDLEN(ITRIAL_COUNTER))//
&   '_FLX'

```

```

OPEN (40,FILE=RUNID)
PATHNAME=':UDD:MEFL:ICPLOT:'
RUNID=PATHNAME(1:17)//IDTRIAL(ITRIAL_COUNTER)(1:IDLEN(ITRIAL_COUNTER))//
&
OPEN (90,FILE=RUNID)
READ (40,FMT='(A)') FNAME
READ (40,FMT='(A)') LABEL1
READ (40,FMT='(A)') LABEL2
READ (40,FMT='(A)') LABEL3
C
C NOW READ THE DATA POINTS
C
NLINE=1
10 READ (40,*,END=20) ITIME(4*NLINE-3),IDATA(4*NLINE-3),ITIME(4*NLINE-2),
& IDATA(4*NLINE-2),ITIME(4*NLINE-1),IDATA(4*NLINE-1),
& ITIME(4*NLINE),IDATA(4*NLINE)
NLINE=NLINE+1
GO TO 10
20 CONTINUE
NPOINT=4*(NLINE-1)
CLOSE (40)
C
C IDENTIFY THE END OF THE RUN BY THE DRAMATIC CHANGE IN THE ION CURRENT
C WHEN THE POWER IS TURNED OFF.
C
DO 100 I=1,NPOINT
RTIME(I)=REAL(ITIME(I))
100 RDATA(I)=-1.*REAL(IDATA(I))
C
IEND=1
DO 200 I=2,NPOINT
SLOPE=(RDATA(I)-RDATA(I-1))/(RTIME(I)-RTIME(I-1))
IF (SLOPE .LE. -20.) IEND=I
200 CONTINUE
IEND=IEND-1
C
C NOW SCALE THE DIGITAL RESULTS INTO AN ION CURRENT
C
FLUXMIN=10000.
FLUXMAX=-10000.
DO 250 I=1,NPOINT
IF (RDATA(I) .LE. FLUXMIN) FLUXMIN=RDATA(I)
IF (RDATA(I) .GE. FLUXMAX) FLUXMAX=RDATA(I)
250 CONTINUE
C
SCALE=10.**(-1.*REAL(IF_SCALE(ITRIAL_COUNTER)))
C
C THE GAIN ON THE CURRENT AMPLIFIER IS NOW
C USED TO GET AN ABSOLUTE ION CURRENT. THE
C FLUX IS CALCULATED, BASED ON THE
C PINHOLE APERATURE AREA.
C
DO 300 I=1,NPOINT
RDATA(I)=(RDATA(I)-FLUXMIN)/2048.*5.
TIFLUX(I)=RDATA(I)*SCALE/PAREA*1.E+3
FLUX IN MA/SQ. CM.
300 CONTINUE
C
C COMPUTE THE TIME-AVERAGED ION FLUX
C
SUMFLUX=0.
DO 400 I=2,IEND
SUMFLUX=SUMFLUX+(TIFLUX(I)+TIFLUX(I-1))*(RTIME(I)-RTIME(I-1))/2.
400 CONTINUE
AVEFLUX=SUMFLUX/(RTIME(IEND)-RTIME(1))
C
IF (IS_ICPLOT .EQ. 0) GO TO 999
C
1000 FORMAT('TOTAL ION CURRENT FOR ',A12,/, 'TIME IN SECS',/,
& 'ION FLUX IN MA/CM2',/, 'SYMB 0.0',/, 'YLEN 4.5',/, 'END')
1010 FORMAT(F6.1, ' ', F5.3)
WRITE (90,1000) FNAME
DO 600 I=1,NPOINT
WRITE (90,1010) RTIME(I),TIFLUX(I)
600 CONTINUE
C

```

999 CONTINUE
RETURN
END

SUBROUTINE MS_CONVERT

C
C
C
C
C
C
C

SUBROUTINE OF PROGRAM ANALYZE - DATA ANALYSIS ROUTINE

THIS SUBROUTINE CONVERTS THE MASS SPEC FILE SENT BY THE
OUTBOARD COMPUTER TO AN EPLT FILE ON THE DATA GENERAL
AND/OR INTEGRATES THE MASS SPEC PEAKS AS SPECIFIED.

COMMON/IDENT/IDTRIAL(100),ALPHABET,ELDESCR(100),
& WDESCR(100)
COMMON/LABELS/PLABEL(10),ALABEL
COMMON/SPECS/IDLEN(100),NUM_OF_TRIALS,ITRIAL_COUNTER,
& NUMFILE
COMMON/SWITCHES/IS_MSI,IS_MSP,IS_ACT,IS_OEP,IS_WFFA,IS_WFP,
& IS_WFH,IS_IFP,IS_IMPC,IS_IONC,IS_ICPLOT,
& IS_CODE,IS_SUM,IS_DES,IS_IE,IS_IEDP,IS_IEIP
COMMON/INTEGRATE/RDATA(4096),RMASS(4096),PEAKS(10,2),NPEAKS,
& IMASS(4096),MAXPP(10),PEAKCOMP,PHRAT(100,10,10)
COMMON/INFO/PRESSURE(100),ESPACE(100),MS_SCALE(100,10),
& FLOWRATE(100,4),MSC_ACT(100),OE_ACT(100),
& WF_ACT(100),ION_ACT(100),IF_SCALE(100),
& IE_ACT(100)

C
C

DIMENSION IDATA(4096),SCAN(20)
CHARACTER*40 LABEL1,LABEL2,LABEL3,PATHNAME
CHARACTER*50 ELDESCR,WDESCR,ALABEL
CHARACTER*20 SCANTIME,IDNAME
CHARACTER*1 SCAN
CHARACTER*15 FNAME,IDTRIAL
CHARACTER*8 PLABEL
CHARACTER*10 ALPHABET
REAL MAXPP
INTEGER OE_ACT,WF_ACT,PEAKCOMP
DATA ALPHABET/'ABCDEFGHIJ'/

C
C
C
C
C
C
C
C

DETERMINE WHICH MASS SPEC FILE IS TO BE WORKED ON.
EACH OF THE EXISTING FILES WILL BE CONVERTED.
UP TO 10 MASS SPEC FILES MAY BE INCLUDED
ON A GIVEN RUN.

READ THE RUN INFORMATION.

DO 9999 NUMFILE=1, MSC_ACT(ITRIAL_COUNTER)
PATHNAME=' :UDD:MEFL:M_SPEC: '//IDTRIAL(ITRIAL_COUNTER)
& (1:IDLEN(ITRIAL_COUNTER))//'_MS_//ALPHABET(NUMFILE:NUMFILE)
OPEN (14,FILE=PATHNAME)
READ (14,FMT='(A)') FNAME
READ (14,FMT='(A)') SCANTIME
READ (14,FMT='(A)') LABEL1
READ (14,FMT='(A)') LABEL2
READ (14,FMT='(A)') LABEL3

C
C
C

NOW READ THE DATA POINTS

DO 30 I=1,4096
RMASS(I)=0.
RDATA(I)=0.

30
C
C
C
C
C
C

THE MASS SPEC DATA IS ENTERED AS INTENSITIES,
IN GROUPS OF FOUR POINTS PER DATA LINE.
THE MASS (IN AMU) FOR A GIVEN POINT IS
CALCULATED LATER IN THE SUBROUTINE.

IC=0
90 IF (IC .GE. 4096) GO TO 100
READ (14,*,END=100) IMASS(IC+1),IDATA(IC+1),IMASS(IC+2),IDATA(IC+2),
& IMASS(IC+3),IDATA(IC+3),IMASS(IC+4),IDATA(IC+4)
IC=IC+4

```

GO TO 90
100 CONTINUE
C
C CONVERT TO REAL ARITHMETIC
DO 101 K=1, IC
RMASS(K)=FLOAT(IMASS(K))
101 RDATA(K)=FLOAT(IDATA(K))
C
C DETERMINE MAX. AND MIN. FOR BOTH MASS
AND INTENSITY.
IMAX=-5000
IMIN=5000
XMIN=RMASS(1)
XMAX=RMASS(IC)
DO 50 I=1, IC
IF (IDATA(I) .GT. IMAX) IMAX=IDATA(I)
IF (IDATA(I) .LT. IMIN) IMIN=IDATA(I)
50 CONTINUE
YMIN=FLOAT(IMIN)
YMAX=FLOAT(IMAX)
C MASS SPEC CALIBRATION - A/D CONVERTER
XMIN=0.962+0.050344*XMIN
XMAX=0.962+0.050344*XMAX
PMIN=INT(XMIN)-1
PMAX=INT(XMAX)+1
PTIC=20.*(1+INT(PMIN/20.))
C
C NOW MAP THE INTENSITIES INTO THE RANGE [0,1]
C WHERE 0 REPRESENTS BASELINE AND 1 REPRESENTS
C THE MAXIMUM ON THE RANGE.
C MAP THE MASSES INTO THE RANGE [1,200].
C
DO 20 J=1, IC
RD=RDATA(J)
RDATA(J)=(RD-YMIN)/(YMAX-YMIN)
RM=RMASS(J)
RMASS(J)=0.962+0.050344*RM
20 CONTINUE
C
C CALL THE MASS SPEC PEAK COMPARISON ROUTINE
C THIS SUBROUTINE INTEGRATES THE PEAK HEIGHTS
C OR MERELY SAMPLES PEAK HEIGHTS FROM SPECIFIED
C MASS RANGES.
C
IF (IS_MSI .EQ. 0) GO TO 201
CALL PEAKINT
201 IF (IS_MSP .EQ. 0) GO TO 9999
PATHNAME(11:17)='MSPLOT:'
OPEN (55, FILE=PATHNAME)
C
C FIND THE TIME OF THE SCAN DURING THE RUN
DO 105 K=1, 20
105 SCAN(K)=SCANTIME(K:K)
IS=1
IE=1
DO 102 L=1, 20
IF (SCAN(L) .EQ. '+') IS=L
IF (SCAN(L) .EQ. ' ' .AND. IS .NE. 1) IE=L
102 CONTINUE
C
C NOW WRITE TO EPLOTT FILE. THE RUN INFO
C IS INCLUDED IN THE PLOT FILE. RECALL
C THAT EPLOTT CAN ONLY ACCEPT 512 POINTS.
C
WRITE (55, 1010) FNAME, PMIN, PMAX, PTIC
WRITE (55, 1020) LABEL1, LABEL2, LABEL3, SCANTIME(1:IE), IMIN, IMAX
ISTEP=1
IF (IC .GT. 512) ISTEP=INT(IC-1)/512+1
WRITE (55, 1030)
DO 60 I=1, IC, ISTEP
DDMMAX=I
DO 62 II=I, I+ISTEP-1
62 IF (RDATA(II) .GT. RDATA(DDMMAX)) DDMMAX=II
60 WRITE (55, 1040) RMASS(DDMMAX), RDATA(DDMMAX)
C
C OPEN EPLOTT FILE

```

```

C      IDNAME=IDTRIAL(ITRIAL_COUNTER)(1:IDLEN(ITRIAL_COUNTER))
&      //'_MS'//ALPHABET(NUMFILE:NUMFILE)
WRITE (91,1050) IDNAME
DO 70 NNN=1,NPEAKS
WRITE (91,1060) PHRAT(ITRIAL_COUNTER,NUMFILE,NNN)
CONTINUE
70    WRITE (91,'( /)')

C
9999  CONTINUE
      WRITE (91,1070)
      CLOSE (55)
      CLOSE (14)

C
C      FORMAT STATEMENTS
C
1010  FORMAT ('MASS SPECTRUM OF ',A12,/, 'AMU' ,/,
&      'RELATIVE INTENSITY ',/, 'SYMB 99.0' ,/, 'YLEN 4.5' ,/,
&      'XMIN ',F5.1,/, 'XMAX ',F5.1,/, 'XTIC 0.0' ,/,F5.1,/, '0.0' ,/,
&      'YMIN -.25' ,/, 'YMAX 1.2' ,/, 'YTIC 0.0' ,/, '.2,1.0')
1020  FORMAT ('LABL -6.0' ,/, '.40,.60' ,/,A40,/, '.40,.45' ,/,A40,/,
&      '.40,.30' ,/,A40,/, '.40,.15' ,/,A20, ' SECONDS' ,/,
&      '0.25,4.2' ,/, 'MIN(0)= ',I4,/,
&      '2.7,4.2' ,/, 'MAX(1)= ',I4)
1030  FORMAT ('END')
1040  FORMAT (F5.1, ', ', F5.3)
1050  FORMAT ($,20A, ' ', '$)
1060  FORMAT ($,F5.3, ' ', '$)
1070  FORMAT (/ .125(' - '))
RETURN
END

```

SUBROUTINE OE_CONVERT

```

C
C      SUBROUTINE OF PROGRAM ANALYZE - DATA ANALYSIS ROUTINE
C
C      THIS SUBROUTINE CONVERTS THE OPTICAL EMISSION
C      INTENSITIES SENT DOWN BY THE OUTBOARD COMPUTER
C      TO AN EPLLOT FILE THAT CAN BE USED TO MAKE A
C      HARDCOPY PLOT. THIS VERSION CONVERTS THE DATA
C      TO WAVELENGTH AND INTENSITY. THE BACKGROUND
C      SCAN IS ALREADY SUBTRACTED OUT BEFORE THE DATA
C      IS SENT DOWNSTAIRS.
C
C
C      COMMON/IDENT/IDTRIAL(100),ALPHABET,ELDESCR(100),
&      WDESCR(100)
COMMON/LABELS/PLABEL(10),ALABEL
COMMON/SPECS/IDLEN(100),NUM_OF_TRIALS,ITRIAL_COUNTER,
&      NUMFILE
COMMON/SWITCHES/IS_MSI,IS_MSP,IS_ACT,IS_OEP,IS_WFFA,IS_WFP,
&      IS_WFH,IS_IFP,IS_IMPC,IS_IONC,IS_ICPLOT,
&      IS_CODE,IS_SUM,IS_DES,IS_IE,IS_IEDP,IS_IEIP
COMMON/INFO/PRESSURE(100),ESPACE(100),MS_SCALE(100,10),
&      FLOWRATE(100,4),MSC_ACT(100),OE_ACT(100),
&      WF_ACT(100),ION_ACT(100),IF_SCALE(100),
&      IE_ACT(100)
COMMON/OECAL/CAL(3),CAL1(3),CAL2(3),R2(3),A11,A22,A33
COMMON/ACTINOM/P1L,P1H,P2L,P2H,BLL,BLH,RATIO(100,10)
COMMON/ACTINOM2/OE_INFO

C
C      DIMENSION IDATA(1024),WAVEL(1024),RDATA(1024),SCAN(20)
REAL OE_INFO(100,10,3)
INTEGER HWAV,CNTR,GRTG,CNTR2,GRTG2
INTEGER OE_ACT,WF_ACT,OENUM
CHARACTER*40 LABEL1,LABEL2,LABEL3
CHARACTER*50 ELDESCR,WDESCR,RUNID,ALABEL
CHARACTER*15 IDTRIAL
CHARACTER*1 SCAN
CHARACTER*10 ALPHABET
CHARACTER*20 SCANTIME,PATHNAME
CHARACTER*8 PLABEL

```

```

CHARACTER*12 FNAME
C
C READ THE O.E. DATA FILE. RECALL THAT A RUN
C MAY CONTAIN UP TO 10 OPTICAL EMISSION SCANS
C
DO 999 OENUM=1,OE_ACT(ITRIAL_COUNTER)
PATHNAME=':UDD:MEFL:OP_EM:'
RUNID=PATHNAME(1:16)//IDTRIAL(ITRIAL_COUNTER)(1:IDLEN(ITRIAL_COUNTER))//
& '_OE'//ALPHABET(OENUM:OENUM)
OPEN (15,FILE=RUNID)
PATHNAME=':UDD:MEFL:OEPLT:'
& RUNID=PATHNAME(1:17)//IDTRIAL(ITRIAL_COUNTER)(1:IDLEN(ITRIAL_COUNTER))//
'_OE'//ALPHABET(OENUM:OENUM)
OPEN (65,FILE=RUNID)
READ (15,FMT='(A)') FNAME
READ (15,FMT='(A)') LABEL1
READ (15,FMT='(A)') LABEL2
READ (15,FMT='(A)') LABEL3
READ (15,FMT='(A)') SCANTIME
READ (15,*) CNTR,GRTG,ITIME
C
C NOW READ THE DATA POINTS
C THERE ARE EIGHT EMISSION INTENSITIES ON
C EACH DATA LINE. THE ASSOCIATED WAVELENGTHS
C ARE CALCULATED FROM THE CALIBRATION CURVE
C AND THE MONACHROMATOR SETTING.
C
IMIN=20000
IMAX=-20000
DO 100 I=1,128
100 & READ (15,*) IDATA(8*I-7),IDATA(8*I-6),IDATA(8*I-5),IDATA(8*I-4),
& IDATA(8*I-3),IDATA(8*I-2),IDATA(8*I-1),IDATA(8*I)
DO 101 K=1,1024
101 RDATA(K)=FLOAT(IDATA(K))
CLOSE (15)
DO 110 I=2,1022
110 IF (IDATA(I) .GT. IMAX) IMAX=IDATA(I)
IF (IDATA(I) .LT. IMIN) IMIN=IDATA(I)
YMIN=FLOAT(IMIN)
YMAX=FLOAT(IMAX)
C
C CONVERT TO WAVELENGTHS - FIRST, GET CALIBRATION.
C
R=R2(GRTG)
RCNTR=FLOAT(CNTR)
CL=CAL(GRTG)
CL1=CAL1(GRTG)
IF (GRTG .NE. 2) CL1=A11-A22*RCNTR-A33*RCNTR*RCNTR
CL2=CAL2(GRTG)
C
C NOW CALIBRATE THE POINTS
C
DO 10 I=1,1024
10 WAVEL(I)=(RCNTR+FLOAT(I-512)/1023.*CL1)*R-CL+(I-512)*(I-512)*CL2
C
C NOW MAP THE INTENSITIES INTO THE RANGE [0,1]
C WHERE 0 REPRESENTS BASELINE AND 1 REPRESENTS
C THE MAXIMUM ON THE RANGE.
C
DO 20 J=1,1024
20 RD=RDATA(J)
RDATA(J)=(RD-YMIN)/(YMAX-YMIN)
CONTINUE
C
C PERFORM ACTINOMETRIC CALCULATION IF REQUESTED.
C HERE, THE INTENSITIES OF TWO SPECIFIED
C PEAKS ARE COMPARED. ONE OF THE PEAKS SHOULD
C BE AN INERT GAS SUCH AS ARGON.
C THE CONSTANTS BLL, BLH, etc., ARE READ IN WHEN THE
C MAIN PROGRAM EXECUTES 'FILEOPEN'
C
IF (IS_ACT .EQ. 0) GO TO 301
C
C ESTABLISH BASELINE FOR THE OPTICAL EMISSION
C THE BASELINE IS NOT ALWAYS AT ZERO INTENSITY.
C THE WAVELENGTH RANGE FOR THE BASELINE
C IS INPUT BY THE OPERATOR AS [BLL,BLH].

```

```

C
SUMBASE=0.
IBLL=1
IBLH=1
DO 500 MB=1,1024
IF (WAVEL(MB) .LT. BLL) IBLL=MB
IF (WAVEL(MB) .LT. BLH) IBLH=MB
IF (WAVEL(MB) .LT. BLL .OR. WAVEL(MB) .GT. BLH) GO TO 500
SUMBASE=SUMBASE+RDATA(MB)
500 CONTINUE
NPBASE=IBLH-IBLL
BASELINE=SUMBASE/REAL(NPBASE)
C THIS IS THE MEAN INTENSITY IN THE
C BASELINE RANGE.
C NOW SUBTRACT OUT THE BASELINE.
C
RMAX1=-1.
RMAX2=-1.
DO 300 IP=1,1024
IF (WAVEL(IP) .GE. P1L .AND. WAVEL(IP) .LE. P1H)
& RMAX1=AMAX1(RMAX1,RDATA(IP))
IF (WAVEL(IP) .GE. P2L .AND. WAVEL(IP) .LE. P2H)
& RMAX2=AMAX1(RMAX2,RDATA(IP))
300 CONTINUE
RATIO(ITRIAL_COUNTER,OENUM)=(RMAX1-BASELINE)/(RMAX2-BASELINE)
OE_INFO(ITRIAL_COUNTER,OENUM,1) = RMAX1-BASELINE
OE_INFO(ITRIAL_COUNTER,OENUM,2) = RMAX2-BASELINE
OE_INFO(ITRIAL_COUNTER,OENUM,3) = REAL(ITIME)
301 CONTINUE
C
C FIND THE TIME OF THE SCAN DURING THE RUN.
C
DO 105 K=1,20
105 SCAN(K)=SCANTIME(K:K)
IS=1
IE=1
DO 102 L=1,20
IF (SCAN(L) .EQ. '+') IS=L
IF (SCAN(L) .EQ. ' ' .AND. IS .NE. 1) IE=L
102 CONTINUE
C
C NOW WRITE TO EPLOTT FILE
C
WRITE (65,1010) FNAME
WRITE (65,1020) LABEL1,LABEL2,LABEL1,SCANTIME(1:IE),IMIN,ITIME,
& IMAX
WRITE (65,1030)
DO 30 I=2,1020
I123=I
C IF(RDATA(I+1).GT.RDATA(I)) I123=I+1
30 WRITE (65,1040) WAVEL(I123),RDATA(I123)
C
C FORMAT STATEMENTS
C
1010 FORMAT ('SPECTRUM OF ',A12,/, 'WAVELENGTH IN NANOMETERS',/,
& 'RELATIVE INTENSITY',/, 'SYMB 99.0',/, 'YLEN 4.5',/, 'XTRA .1',
& /, 'YMIN -0.25',/, 'YMAX 1.1',/, 'YTIC 0.0',/, '.20,1.0')
1020 FORMAT ('LABL -6.0',/, '0.40,0.6',/, A40,/, '0.40,0.45',/, A40,/,
& '0.40,0.3',/, A40,/, '0.40,0.15',/, A18, ' SECONDS',/,
& '0.25,4.2',/, 'MIN(0)= ',I4, ' EXP = ',I4,/,
& '2.9,4.2',/, 'MAX(1)= ',I5)
1030 FORMAT ('END')
1040 FORMAT (F6.1, ' ', F5.3)
CLOSE (65)
999 CONTINUE
RETURN
END

```

SUBROUTINE PEAKINT

```

C
C SUBROUTINE OF PROGRAM ANALYZE - DATA ANALYSIS ROUTINE
C
C THIS SUBROUTINE COMPARES MASS SPEC PEAK HEIGHTS FOR UP

```



```

C      TO TEN SPECIFIED PEAKS.
C
C      COMMON/SPECS/IDLEN(100),NUM_OF_TRIALS,ITRIAL_COUNTER,
&      NUMFILE
COMMON/LABELS/PLABEL(10),ALABEL
COMMON/INTEGRATE/RDATA(4096),RMASS(4096),PEAKS(10,2),NPEAKS,
&      IMASS(4096),MAXPP(10),PEAKCOMP,PHRAT(100,10,10)
COMMON/SWITCHES/IS_MSI,IS_MSP,IS_ACT,IS_OEP,IS_WFFA,IS_WFP,
&      IS_WFH,IS_IFP,IS_IMPC,IS_IONC,IS_ICPLOT,
&      IS_CODE,IS_SUM,IS_DES,IS_IE,IS_IEDP,IS_IEIP
COMMON/INTDATA/PEAKDATA(20,10,20,4)
C
C      CHARACTER*8 PLABEL
CHARACTER*50 ALABEL
DIMENSION PHMAX(10)
REAL MAXPP
INTEGER PEAKCOMP
C
C      THE MASS SPEC PEAK DATA IS ALREADY
C      STORED IN THE ARRAYS RMASS, RDATA, ETC..
C      AS SENT THROUGH THE COMMON BLOCK.
C
C      THE PEAK RANGES OF INTEREST (UP TO 10)
C      ARE SPECIFIED BY THE OPERATOR, AND ARE
C      STORED IN ARRAY PEAKS.
C
C      GO THROUGH ONE PEAK RANGE AT A TIME AND
C      LOOK FOR THE HIGHEST PEAK WITHIN THAT RANGE.
C
C      MM=1
DO 200 IP=1,NPEAKS
MAXPP(IP)=0
PHMAX(IP)=0.
175  CONTINUE
IF (RMASS(MM) .LT. PEAKS(IP,1)) GO TO 180
IF (RMASS(MM) .GT. PEAKS(IP,2)) GO TO 200
IF (RDATA(MM) .LE. PHMAX(IP)) GO TO 180
PHMAX(IP)=RDATA(MM)
MAXPP(IP)=RMASS(MM)
180  MM=MM+1
GO TO 175
200  CONTINUE
C
C      NOW SCALE THE PEAK HEIGHTS TO THE MOST INTENSE
C      PEAK OBSERVED IN THE SET OF GIVEN RANGES.
C
C      DO 300 IL=1,NPEAKS
PHRAT(ITRIAL_COUNTER,NUMFILE,IL)=PHMAX(IL)/PHMAX(PEAKCOMP)
300  CONTINUE
C
C      RETURN
END

SUBROUTINE PLASMA_PAR
C
C      SUBROUTINE OF PROGRAM ANALYZE - DATA ANALYSIS ROUTINE
C
C      THIS SUBROUTINE PERFORMS THE IMPEDANCE CALCULATIONS
C      FOR THE PLASMA. INCLUDED ARE ELECTRIC FIELD/PRESSURE
C      RATIO, ELECTRON DENSITY, ETC.
C      DETAILS OF THE IMPEDANCE MODEL ARE PRESENTED IN
C      K.D. ALLEN ET AL., J. ELECTROCHEM. SOC. 1986
C
C      COMMON/IDENT/IDTRIAL(100),ALPHABET,ELDESCR(100),WDESCR(100)
COMMON/INFO/PRESSURE(100),ESPACE(100),MS_SCALE(100,10),
&      FLOWRATE(100,4),MSC_ACT(100),OE_ACT(100),
&      WF_ACT(100),ION_ACT(100),IF_SCALE(100),
&      IE_ACT(100)
COMMON/IMPEDANCE/VARRU(100,3),CARRU(100,3),PARRU(100,3),
&      VARRC(100,3),CARRC(100,3),PARRC(100,3),

```

```

&          TPOW(100,3),DCB(100,3),FREQ(100,3)
COMMON/SPECS/IDLEN(100),NUM_OF_TRIALS,ITRIAL_COUNTER,
&          NUMFILE
COMMON/IMPDATA/MOBPRES,STRAYC,CESPACE,L
COMMON/SWITCHES/IS_MSI,IS_MSP,IS_ACT,IS_OEP,IS_WFFA,IS_WFP,
&          IS_WFH,IS_IFP,IS_IMP,IS_IONG,IS_ICPLOT,
&          IS_CODE,IS_SUM,IS_DES,IS_IE,IS_IEDP,IS_IEIP
COMMON/IMPSAVE/SAVEIMP(100,3,6)

C
C
CHARACTER*15 IDTRIAL,WFIDAVG
CHARACTER*50 ELDESCR,WDESCR
CHARACTER*20 WFID
CHARACTER*3 NUMBER
CHARACTER*1 FREQ
CHARACTER*10 ALPHABET
INTEGER OE_ACT,WF_ACT,WFNUM
DATA WFIDAVG/'AVERAGE' '/'
DATA NUMBER,FREQ/'123','M'/'
REAL MOBPRES,MOBIL,L

C
C
SET PHYSICAL CONSTANTS AND ZERO VARIABLES.

PI=3.14159265
AREA=125.
ECHARGE=1.6E-19
SUMRES=0.
SUMCAP=0.
SUMPOW=0.
SUMEP=0.
SUMED=0.
SUMSV=0.
SUMFREQ=0.
SUMV=0.
SUMC=0.
SUMP=0.
SUMDCB=0.
NBADRUN=0

C
C
THE DATA IS OBTAINED THROUGH THE COMMON BLOCKS.

DO 999 WFNUM=1,WF_ACT(ITRIAL_COUNTER)
DCBIAS=DCB(ITRIAL_COUNTER,WFNUM)
PRES=PRESSURE(ITRIAL_COUNTER)
VOLTS=VARRC(ITRIAL_COUNTER,WFNUM)
AMPS=CARRC(ITRIAL_COUNTER,WFNUM)
THETA=PARRC(ITRIAL_COUNTER,WFNUM)
THETA1=THETA/180.*PI
OMEGA=FREQ(ITRIAL_COUNTER,WFNUM)*2.*PI

C
C
CALCULATE PLASMA PARAMETERS USING THE IMPEDANCE
MODEL AND THE CORRECTED IMPEDANCE PROPERTIES.

C
C
FIRST, CALCULATE POWER ASSUMING SINUSOIDAL
WAVEFORMS.

CPOWER=VOLTS*AMPS*COS(THETA1)/2.

C
C
CALCULATE BULK PLASMA RESISTANCE
AND SHEATH CAPACITANCE.

C
ZRE=VOLTS/AMPS*COS(THETA1)
ZIM=-VOLTS/AMPS*SIN(THETA1)
CE=CESPACE/ESPACE(ITRIAL_COUNTER)
OMEGACE=OMEGA*CE
TEMP=1.-4.*(ZRE*OMEGACE)*ZRE*OMEGACE
IF(TEMP.LT.0) GOTO 9999
RES=2.*ZRE/(1.+SQRT(TEMP))
CAP=2./OMEGA/(-ZIM-(OMEGACE/(1./(RES*RES)+OMEGACE*OMEGACE)))

C
C
CALCULATE OTHER PLASMA PROPERTIES
GIVEN RB AND CS.

C
SHTHV=AMPS/(OMEGA*CAP)
VRE=VOLTS*COS(THETA1)
VIM=VOLTS*SIN(THETA1)-2*SHTHV
RESVOLTS=SQRT(VRE*VRE+VIM*VIM)

```

```

EOVERP=RESVOLTS/ESPACE(ITRIAL_COUNTER)/1.414/PRES
MOBIL=MOBPRES/PRES
EDENSE=ESPACE(ITRIAL_COUNTER)/(AREA*ECHARGE*MOBIL*RES)
C
C PRINT OUT THE RESULTS. ALSO, STORE THE
C RESULTS FOR USE BY SUBROUTINE SUMMARY.
C
WFID=IDTRIAL(ITRIAL_COUNTER)(1:IDLEN(ITRIAL_COUNTER))
& //'_ '//NUMBER(WFNUM:WFNUM)
IF (FREQ(ITRIAL_COUNTER,WFNUM) .LT. 1.E+6) FREQCON=
& FREQ(ITRIAL_COUNTER,WFNUM)/1.E+3
IF (FREQ(ITRIAL_COUNTER,WFNUM) .LT. 1.E+6) FREQ='K'
IF (FREQ(ITRIAL_COUNTER,WFNUM) .GE. 1.E+6) FREQCON=
& FREQ(ITRIAL_COUNTER,WFNUM)/1.E+6
IF (FREQ(ITRIAL_COUNTER,WFNUM) .LE. 1.E+6) FREQ='M'
WRITE (51,1000) WFID,ESPACE(ITRIAL_COUNTER),
& PRESSURE(ITRIAL_COUNTER),FREQCON,FREQ,
& VARRC(ITRIAL_COUNTER,WFNUM),
& CARRC(ITRIAL_COUNTER,WFNUM),
& PARRC(ITRIAL_COUNTER,WFNUM),
& DCB(ITRIAL_COUNTER,WFNUM)
CAP_PF=1.E+12*CAP I CAP. IN PICO FARADS
ED_9=1.E-9*EDENSE
C MULTIPLY BY 10**9 TO GET ELECTRON DENSITY IN CC
C
SAVEIMP(ITRIAL_COUNTER,WFNUM,1)=RES
SAVEIMP(ITRIAL_COUNTER,WFNUM,2)=CAP_PF
SAVEIMP(ITRIAL_COUNTER,WFNUM,3)=CPOWER
SAVEIMP(ITRIAL_COUNTER,WFNUM,4)=EOVERP
SAVEIMP(ITRIAL_COUNTER,WFNUM,5)=SHTHV
SAVEIMP(ITRIAL_COUNTER,WFNUM,6)=ED_9
1000 WRITE (52,1001) WFID,RES,CAP_PF,CPOWER,EOVERP,SHTHV,ED_9
& FORMAT (A15,F5.2,2X,F6.1,2X,F6.2,1X,A1,'Hz',3X,F5.1,2X,F5.2,
& 6X,F4.1,2X,F6.1)
C
C SOMETIMES, BAD WAVEFORMS GET SENT DOWNSTAIRS.
C USUALLY, THESE WAVEFORMS HAVE VERY HIGH CALCULATED
C FREQUENCIES. IF F>20 MHZ, ASSUME THE RUN IS BAD.
C THE VARIABLE NBADRUN KEEPS TRACK OF THE NUMBER
C OF BAD WAVEFORMS ACQUIRED DURING EACH RUN.
C WHEN AVERAGEING THE IMPEDANCE PROPERTIES OVER A RUN,
C THESE BAD WAVEFORMS WILL BE DISCOUNTED.
C
IF (FREQ(ITRIAL_COUNTER,WFNUM) .GE. 2.0E+7) NBADRUN=NBADRUN+1
IF (FREQ(ITRIAL_COUNTER,WFNUM) .GE. 2.0E+7) GO TO 999
SUMRES=SUMRES+RES
SUMCAP=SUMCAP+CAP_PF
SUMPOW=SUMPOW+CPOWER
SUMEP=SUMEP+EOVERP
SUMED=SUMED+ED_9
SUMSV=SUMSV+SHTHV
SUMFREQ=SUMFREQ+FREQCON
SUMV=SUMV+VARRC(ITRIAL_COUNTER,WFNUM)
SUMC=SUMC+CARRC(ITRIAL_COUNTER,WFNUM)
SUMP=SUMP+PARRC(ITRIAL_COUNTER,WFNUM)
SUMDCB=SUMDCB+DCB(ITRIAL_COUNTER,WFNUM)
999 CONTINUE
IF (WF_ACT(ITRIAL_COUNTER)-REAL(NBADRUN).GT.0.0) GO TO 1234
AVGRES = 0.0
AVGCAP = 0.0
AVGPOW = 0.0
AVGEP = 0.0
AVGED = 0.0
AVGSV = 0.0
AVGFREQ = 0.0
AVGV = 0.0
AVGC = 0.0
AVGP = 0.0
AVGDCB = 0.0
GO TO 1235
1234 AVGRES=SUMRES/(WF_ACT(ITRIAL_COUNTER)-REAL(NBADRUN))
AVGCAP=SUMCAP/(WF_ACT(ITRIAL_COUNTER)-REAL(NBADRUN))
AVGPOW=SUMPOW/(WF_ACT(ITRIAL_COUNTER)-REAL(NBADRUN))
AVGEP=SUMEP/(WF_ACT(ITRIAL_COUNTER)-REAL(NBADRUN))
AVGED=SUMED/(WF_ACT(ITRIAL_COUNTER)-REAL(NBADRUN))
AVGSV=SUMSV/(WF_ACT(ITRIAL_COUNTER)-REAL(NBADRUN))
AVGFREQ=SUMFREQ/(WF_ACT(ITRIAL_COUNTER)-REAL(NBADRUN))

```

```

AVGV=SUMV/(WF_ACT(ITRIAL_COUNTER)-REAL(NBADRUN))
AVGC=SUMC/(WF_ACT(ITRIAL_COUNTER)-REAL(NBADRUN))
AVGP=SUMP/(WF_ACT(ITRIAL_COUNTER)-REAL(NBADRUN))
AVGDCB=SUMDCB/(WF_ACT(ITRIAL_COUNTER)-REAL(NBADRUN))
1235 CONTINUE
WRITE (51,1003)
WRITE (51,1000) WFIDAVG, ESPACE(ITRIAL_COUNTER),
& PRESSURE(ITRIAL_COUNTER),AVGFREQ,FREQL,
& AVGV,AVGC,AVGP,AVGDCB
WRITE (52,1003)
WRITE (52,1001) WFIDAVG,AVGRES,AVGCAP,AVGPOW,AVGEP,AVGSV,AVGED
WRITE (51,1002)
WRITE (52,1002)
1001 FORMAT (A15,F6.0,5X,F6.0,5X,F5.1,5X,F6.1,5X,F6.1,5X,F6.2)
1002 FORMAT(80('-'))
1003 FORMAT (/)
9999 CONTINUE
RETURN
END

```

```

SUBROUTINE READINFO
C
C SUBROUTINE OF PROGRAM ANALYZE - DATA ANALYSIS ROUTINE
C
C THIS SUBROUTINE READS IN ALL OF THE RUN INFORMATION
C DATA AS SENT FROM THE OUTBOARD. THIS DATA INCLUDES
C DESCRIPTORS, MASS SPEC SCALE SETTINGS, AND THE NUMBER
C OF O.E. AND M.S. SCANS TAKEN DURING THE RUN
C
COMMON/IDENT/IDTRIAL(100),ALPHABET,ELDESCR(100),
& WDESCR(100)
COMMON/SPECS/IDLEN(100),NUM_OF_TRIALS,ITRIAL_COUNTER,
& NUMFILE
COMMON/SWITCHES/IS_MSI,IS_MSP,IS_ACT,IS_OEP,IS_WFFA,IS_WFP,
& IS_WFH,IS_IFP,IS_IMPC,IS_IONC,IS_ICPLOT,
& IS_CODE,IS_SUM,IS_DES,IS_IE,IS_IEDP,IS_IEIP
COMMON/INFO/PRESSURE(100),ESPACE(100),MS_SCALE(100,10),
& FLOWRATE(100,4),MSC_ACT(100),OE_ACT(100),
& WF_ACT(100),ION_ACT(100),IF_SCALE(100),
& IE_ACT(100)
COMMON/GAS/GASTYPE(100,4)
COMMON/SCANTYPE/TYSCAN(100,10)
C
C DIMENSION GCONF(10),FMCAL(5),FMCONF(5),FMRANGE(5),FMZERO(5)
C INTEGER P,ES,GASN(4),GASR(4),GASMETER(4),OE_ACT,WF_ACT,WFAN
C CHARACTER*50 GASNAME,RUNID,ELDESCR,WDESCR
C CHARACTER*1 TYSCAN
C CHARACTER*10 ALPHABET
C CHARACTER*15 IDTRIAL
C CHARACTER*18 PATHNAME
C CHARACTER*5 GASTYPE
C DATA FMZERO/8,6,12,2,-1/
C DATA GCONF/1.45,0.86,0.26,0.42,0.38,0.35,0.33,0.37,0.24,0.24/
C DATA FMCAL/1.28,0.76,1.22,1.31,1.0/
C DATA FMCONF/0.42,1.0,0.42,1.454,0.86/
C DATA FMRANGE/10.,10.,50.,50.,10./
C DATA GASNAME/'ARGONCL2 SF6 F14 F13 F12 F11 F13B F116 F115'/
C GAS NAMES FOR GAS NUMBERS 1-10, IN ORDER
C
C THE FLOWRATES WILL BE CALCULATED BELOW. THE FOLLOWING
C VARIABLES ARE REQUIRED:
C GCONF- CONVERSION FACTORS FOR THE GASES (E.G., NITROGEN IS 1.0)
C FMZERO- ZERO OFFSET OF THE FLOWMETERS.
C FMCAL- CORRECTION FOR MISCALIBRATION OF THE FLOWMETERS.
C THIS NUMBER IS THE ACTUAL FLOW RATE DIVIDED BY THE
C FLOW RATE PREDICTED FROM THE METER READING.
C THE NUMBERS GIVEN WERE DETERMINED BY
C PRESSURE RISE FOR THE 15.4 LITER CHAMBER.
C FMCONF- CONVERSION FACTOR OF THE GAS
C FOR WHICH THE METER WAS CALIBRATED.
C FMRANGE- FLOWMETER MAX. RANGE, IN SCCM.
C

```

```

C      INITIALIZE VARIABLES
C
DO 1 L=1,100
OE_ACT(L)=0
MSC_ACT(L)=0
WF_ACT(L)=0
ION_ACT(L)=0
DO 1 M=1,4
1     FLOWRATE(L,M)=0.
C
C      READ IN THE DATA FOR EACH RUN TO BE ANALYZED
C      SEE THE DATA ACQUISITION ROUTINE
C      FOR THE FORMAT OF THE DATA,
C      IN B. E. THOMPSON'S THESIS.
C
PATHNAME=':UDD:MEFL:RUNINFO:'
DO 10 I=1,NUM_OF_TRIALS
RUNID='<0>' IRESET RUNID
RUNID=PATHNAME//IDTRIAL(I)(1:IDLEN(I))//'_INFO'
OPEN (1,FILE=RUNID)
PRINT *,'READING FILE .... ',RUNID
READ (1,*) P
PRESSURE(I)=FLOAT(P)/1000.
READ (1,FMT='(A)') ELDESCR(I)
READ (1,*) ES
ESPACE(I)=FLOAT(ES)/100.
READ (1,FMT='(A)') WDESCR(I)
C
C      CALCULATE THE FLOW RATES FROM THE METER READINGS,
C      IN SCCM. THE RATES OF INDIVIDUAL GASES ARE
C      CALCULATED, AS WELL AS THE TOTAL.
C
DO 24 KFLO=1,4
24    FLOWRATE(I,KFLO)=-100.
CONTINUE
C
DO 25 KK=1,4
GASTYPE(I,KK)='<0>'
READ (1,*) GASN(KK)
READ (1,*) GASR(KK)
READ (1,*) GASMETER(KK)
IF (GASN(KK) .EQ. 0) GO TO 25
IBEGIN=5*GASN(KK)-4
IEND=5*GASN(KK)
GASTYPE(I,KK)=GASNAME(IBEGIN:IEND)
FLOWRATE (I,KK)=(GASR(KK)-FMZERO(GASMETER(KK)))/1000.*
&      FMRANGE(GASMETER(KK))*FMCAL(GASMETER(KK))*
&      GCONF(GASN(KK))/FMCONF(GASMETER(KK))
25    CONTINUE
C
READ (1,*) OE_ACT(I),MSC_ACT(I),WFAN,ION_ACT(I)
C      THESE VARIABLES INDICATE THE NUMBER OF MASS SPEC
C      SCANS, ETC., ACQUIRED DURING A GIVEN RUN.
WF_ACT(I)=WFAN/2.
C
IF (IS_IE .EQ. 1) READ (1,*) IE_ACT(I)
IF (IS_IE .EQ. 1) GO TO 999
C
C      WAS THE MASS SPEC SCAN FOR IONS OR NEUTRALS?
C
DO 30 K=1,MSC_ACT(I)
READ (1,*) MS_SCALE(I,K), IONFLAG
TYSCAN(I,K)='N'
IF (IONFLAG.EQ.512) TYSCAN(I,K)='I'
30    CONTINUE
C
READ (1,*) IF_SCALE(I)
C
999    CONTINUE
CLOSE (1)
10    CONTINUE
RETURN
END

```

```

SUBROUTINE SETSWITCH(MAXHARM)
C
C SUBROUTINE OF PROGRAM ANALYZE - DATA ANALYSIS ROUTINE
C
C THIS SUBROUTINE SETS ALL THE SWITCHES THAT DETERMINE
C WHICH ANALYSIS SUBROUTINES ARE CALLED BY THE MAIN PROGRAM
C
COMMON/FLUX/PAREA,AVEFLUX
COMMON/SWITCHES/IS_MSI,IS_MSP,IS_ACT,IS_OEP,IS_WFFA,IS_WFP,
& IS_WFH,IS_IFP,IS_IMPC,IS_IONC,IS_ICPLOT,
& IS_CODE,IS_SUM,IS_DES,IS_IE,IS_IEDP,IS_IEIP
COMMON/DESCRI/ ADDESCRI(100,3),DESCRI(100,3)
CHARACTER*80 ADDESCRI
CHARACTER*40 DESCRI
CHARACTER*50 QUESTION(20)
CHARACTER*1 ANSWER(20)
C
C A SWITCH SET TO ZERO INDICATES THAT THE FUNCTION
C WILL NOT BE CALLED.
C
IS_MSI=0
IS_MSP=0
IS_ACT=0
IS_OEP=0
IS_WFFA=0
IS_WFP=0
IS_WFH=0
IS_IFP=0
IS_IMPC=0
IS_IONC=0
IS_ICPLOT=0
IS_CODE=0
IS_SUM=0
IS_DES=0
IS_IE=0
IS_IEDP=0
IS_IEIP=0
C
C OPEN THE DATA FILE. IN THIS FILE,
C THE RELEVANT QUESTIONS ARE ASKED. THE OPERATOR
C SIMPLY PROVIDES THE ANSWERS TO QUESTIONS SUCH AS
C 'DO YOU WANT A PLOT OF THE OPTICAL EMISSION
C RESULTS?'
C
OPEN (100,FILE=':UDD:MEFL:ANALYSIS:INPUT:RUN_OPTIONS')
C
READ (100,*) NQUESTIONS
DO 100 I=1,NQUESTIONS
READ (100,1000) QUESTION(I),ANSWER(I)
100 CONTINUE
1000 FORMAT(1X,A50,1X,A1)
C
IF (ANSWER(1)(1:1) .EQ. 'Y') IS_MSI=1
IF (ANSWER(2)(1:1) .EQ. 'Y') IS_MSP=1
IF (ANSWER(3)(1:1) .EQ. 'Y') IS_OEP=1
IF (ANSWER(4)(1:1) .EQ. 'Y') IS_ACT=1
IF (ANSWER(5)(1:1) .EQ. 'Y') IS_WFFA=1
IF (ANSWER(6)(1:1) .EQ. 'Y') IS_WFP=1
IF (ANSWER(7)(1:1) .EQ. 'Y') IS_WFH=1
C
IF (ANSWER(8)(1:1) .EQ. 'A') MAXHARM=1
IF (ANSWER(8)(1:1) .EQ. 'B') MAXHARM=2
IF (ANSWER(8)(1:1) .EQ. 'C') MAXHARM=3
IF (ANSWER(8)(1:1) .EQ. 'D') MAXHARM=5
IF (ANSWER(8)(1:1) .EQ. 'E') MAXHARM=10
IF (ANSWER(8)(1:1) .EQ. 'F') MAXHARM=20
C
IF (ANSWER(9)(1:1) .EQ. 'Y') IS_IFP=1
IF (ANSWER(10)(1:1) .EQ. 'Y') IS_IMPC=1
IF (ANSWER(11)(1:1) .EQ. 'Y') IS_IONC=1
C
IF (ANSWER(12)(1:1) .EQ. 'A') PDIAM=100.
IF (ANSWER(12)(1:1) .EQ. 'B') PDIAM=50.
IF (ANSWER(12)(1:1) .EQ. 'C') PDIAM=25.
IF (ANSWER(12)(1:1) .EQ. 'D') PDIAM=12.5
PAREA=3.14159/4.*(PDIAM*1.E-4)*(PDIAM*1.E-4)

```

```

C
IF (ANSWER(13))(1:1) .EQ. 'Y' IS_ICPLOT=1
IF (ANSWER(14))(1:1) .EQ. 'Y' IS_CODE=1
IF (ANSWER(15))(1:1) .EQ. 'Y' IS_SUM=1
IF (ANSWER(16))(1:1) .EQ. 'Y' IS_DES=1
IF (ANSWER(17))(1:1) .EQ. 'Y' IS_IE=1
IF (ANSWER(18))(1:1) .EQ. 'Y' IS_IEDP=1
IF (ANSWER(19))(1:1) .EQ. 'Y' IS_IEIP=1

C
C
C
C
C
NOW, THE OPERATOR CAN ADD SOME MORE INFORMATION
ABOUT THE RUN - FOR EXAMPLE, SETTINGS ON OTHER
DIAGNOSTIC EQUIPMENT, WAFER CLEARING PATTERNS, ETC.

IF (IS_DES .EQ. 0) GO TO 9999
OPEN (110,FILE='UDD:MEFL:ANALYSIS:INPUT:ADDESCR')
DO 200 I=1,NUM_OF_TRIALS
DO 300 J=1,3
READ (110,'(A80)') ADDESCR(I,J)
300 CONTINUE
200 CONTINUE
CLOSE (110)

C
9999 CONTINUE
CLOSE (100)
RETURN
END

```

SUBROUTINE SUMMARY

```

C
C
C
C
C
C
C
C
C
C
SUBROUTINE OF PROGRAM ANALYZE - DATA ANALYSIS ROUTINE

THIS SUBROUTINE CREATES A RUN SUMMARY FILE.
ALL OF THE PERTINENT RUN INFORMATION IS
LISTED IN THIS FILE, INCLUDING AVERAGES OVER
THE RUN.

COMMON/INFO/PRESSURE(100),ESPACE(100),MS_SCALE(100,10),
& FLOWRATE(100,4),MSC_ACT(100),OE_ACT(100),
& WF_ACT(100),ION_ACT(100),IF_SCALE(100),
& IE_ACT(100)
COMMON/IDENT/IDTRIAL(100),ALPHABET,ELDESCR(100),
& WDESCR(100)
COMMON/LABELS/PLABEL(10),ALABEL
COMMON/FLUX/PAREA,AVEFLUX
COMMON/SPECS/IDLEN(100),NUM_OF_TRIALS,ITRIAL_COUNTER,
& NUMFILE
COMMON/IMPEDANCE/VARRU(100,3),CARRU(100,3),PARRU(100,3),
& VARRC(100,3),CARRC(100,3),PARRC(100,3),
& TPOW(100,3),DCB(100,3),FREQ(100,3)
COMMON/HARMONI/HARMDATA(20,3,100),NUMWFM(20),TP(100,3),
& ZMAXHAR
COMMON/SWITCHES/IS_MSI,IS_MSP,IS_ACT,IS_OEP,IS_WFFA,IS_WFP,
& IS_WFH,IS_IFP,IS_IMPC,IS_IONC,IS_ICPLOT,
& IS_CODE,IS_SUM,IS_DES,IS_IE,IS_IEDP,IS_IEIP
COMMON/IMPSAVE/SAVEIMP(100,3,6)
COMMON/GAS/GASTYPE(100,4)
COMMON/ACTINOM/P1L,P1H,P2L,P2H,BLL,BLH,RATIO(100,10)
COMMON/ACTINOM2/ OE_INFO
COMMON/INTEGRATE/RDATA(4096),RMASS(4096),PEAKS(10,2),NPEAKS,
& IMASS(4096),MAXPP(10),PEAKCOMP,PHRAT(100,10,10)
COMMON/INTDATA/PEAKDATA(20,10,20,4)
COMMON/SCANTYPE/TYSCAN(100,10)
COMMON/DESCR1/ADDESCR(100,3),DESCR1(100,3)

C
C
DIMENSION XGAS(4)
INTEGER OE_ACT, WF_ACT,BL,ILOW(5)
REAL INTEN(1000),TIME(1000),ETCHRATE(4),AVGETCH
REAL MAXPP,OE_INFO(100,10,3)
CHARACTER*80 ADDESCR1
CHARACTER*40 DESCR1,RUNID,RUNIDF
CHARACTER*15 IDTRIAL

```

```

CHARACTER*50 ELDESCR,WDESCR,ALABEL
CHARACTER*10 ALPHABET
CHARACTER*8 PLABEL
CHARACTER*20 PATHNAME
CHARACTER*18 PATHNAMEQ
CHARACTER*15 WFID
CHARACTER*5 GASTYPE
CHARACTER*1 TYSCAN,FCHAR
DATA FCHAR/'M'/

C
DO 1000 IRUN=1,NUM_OF_TRIALS
C
C CREATE AND OPEN THE SUMMARY FILE
C
RUNIDF='<0>'
PATHNAME=':UDD:MEFL:SUMMARIES:'
RUNID=IDTRIAL(IRUN)(1:IDLEN(IRUN))
RUNIDF=PATHNAME//IDTRIAL(IRUN)(1:IDLEN(IRUN))//'_SUM'
OPEN (86,FILE=RUNIDF,CARRIAGECONTROL='FORTRAN')

C
C WRITE FILE HEADING
WRITE (86,11) RUNID
11 FORMAT (1X,/,1X,A40/)

C
C WRITE RUN DESCRIPTIONS
WRITE (86,14) (DESCRI(IRUN,K),K=1,3)
14 FORMAT (1X,A40,/,1X,A40,/,1X,A40,/)
IF (IS_DES.EQ.0) GO TO 17
WRITE (86,16) (ADDESCRI(IRUN,KK),KK=1,3)
16 FORMAT (1X,A80,/,1X,A80,/,1X,A80,/)
17 CONTINUE

C
C WRITE CALCULATED INFORMATION (GENERAL)
WRITE (86,12)
12 FORMAT (1X,'POWER      FREQ.      PRESSURE      SPACING')
WRITE (86,13)
13 FORMAT (1X,'(WATTS)   (HZ)      (TORR)      (CM)')

C
C CALCULATE AN AVERAGE POWER AND FREQUENCY
SUMI=0.0
SUMJ=0.0
COUNT=0.0
DO 100 I=1,NUMWFM(IRUN)
IF (FREQ(IRUN,I) .GE. 2.0E+7) GO TO 100
SUMI=SUMI+TPOW(IRUN,I)
SUMJ=SUMJ+FREQ(IRUN,I)
COUNT=COUNT+1.0
100 CONTINUE
IF (COUNT.GT.0.0) GO TO 118
AVGPOW = 0.0
AVGFREQ = 0.0
GO TO 119
118 AVGPOW=SUMI/COUNT
AVGFREQ=SUMJ/COUNT
119 CONTINUE
IF (AVGFREQ .LT. 1.E+6) AVF=AVGFREQ/1.E+3
IF (AVGFREQ .GE. 1.E+6) AVF=AVGFREQ/1.E+6
IF (AVGFREQ .LT. 1.E+6) FCHAR='K'
IF (AVGFREQ .GE. 1.E+6) FCHAR='M'
WRITE (86,8000) AVGPOW,AVF,FCHAR,PRESSURE(IRUN),ESPACE(IRUN)
8000 FORMAT(1X,F7.2,1X,F6.2,1X,1A,'Hz',2X,F5.3,6X,F6.3)

C
WRITE (86,47)
47 FORMAT (1X,/,1X,'FLOWRATES IN SCCM')
TOTFLOW=0.
DO 26 II=1,4
IF (FLOWRATE(IRUN,II) .GE. 0.) TOTFLOW=TOTFLOW+FLOWRATE(IRUN,II)
DO 27 JJ=1,4
IF (FLOWRATE(IRUN,JJ) .GE. 0.) XGAS(JJ)=FLOWRATE(IRUN,JJ)/TOTFLOW
DO 50 IGAS=1,4
IF (FLOWRATE(IRUN,IGAS).LT.-10.0) GO TO 60
WRITE (86,49) GASTYPE(IRUN,IGAS),FLOWRATE(IRUN,IGAS),XGAS(IGAS)
49 FORMAT (1X,A5,' = ',F7.2,3X,F6.3)
50 CONTINUE
60 CONTINUE
WRITE (86,55) TOTFLOW
55 FORMAT (/,1X,'TOTAL FLOW RATE OF ',F5.2,' SCCM')

```



```

C
  WRITE (86,62)
62  FORMAT (1X, '//1X, 'ETCH RATE DATA' //)
  WRITE (86,63)
63  FORMAT (1X, '      ETCH RATE BETWEEN PEAKS (MICRONS/MIN):
&    AVERAGE')
  WRITE (86,64)
64  FORMAT (1X, '      1-2      2-3      3-4      4-5
&    ETCH RATE')

C
C THIS SECTION TRIES TO CALCULATE THE ETCH RATE
C BETWEEN EACH OF THE FIVE INTERFEROMETRY PEAKS
C AND COMPUTES AN AVERAGE ETCH RATE
  DO 8100 II=1,1000
8100  INTEN(II)=999.0
      PATHNAMEQ=':UDD:MEFL:IFR:PLOT:'
      OPEN (87,FILE=PATHNAMEQ//IDTRIAL(IRUN)(1:IDLEN(IRUN))//'_IFR')
      READ (87,8151,END=8750)
8151  FORMAT (//////////)
      DO 8160 JK=1,1000
          READ (87,*,END=8170) TIME(JK),INTEN(JK)
8160  CONTINUE
8170  CONTINUE
      J=1
      IX=1
8200  IF (INTEN(IX).LT.-0.2) GO TO 8400
      IF (INTEN(IX).GT.990.0) GO TO 8800
      IX=IX+1
      GO TO 8200
8400  ILOW(J)=IX
      DO 8410 I=IX,IX+4
          IF (INTEN(I+1).LT.INTEN(I)) ILOW(J)=I+1
          IF (INTEN(I+1).GT.990.0) GO TO 8800
8410  CONTINUE
      IX=IX+5
8500  IF (INTEN(IX+1).LT.INTEN(IX)) ILOW(J)=IX+1
      IF (INTEN(IX+1).GT.-0.2) GO TO 8600
      IF (INTEN(IX+1).GT.(INTEN(ILOW(J))+0.05)) GO TO 8550
      IF (INTEN(IX+1).GT.990.0) GO TO 8800
      IX=IX+1
      GO TO 8500
8550  IF (INTEN(IX).GT.-0.2) GO TO 8600
      IF ((INTEN(IX).GT.990.0).AND.(J.EQ.5)) GO TO 8600
      IF (INTEN(IX).GT.990.0) GO TO 8800
      IX=IX+1
      GO TO 8550
8600  J=J+1
      IF (J.LT.6) GO TO 8200
      DO 8700 IJ=1,4
          IF (TIME(ILOW(IJ+1)) .EQ. TIME(ILOW(IJ))) GO TO 8700
          ETCHRATE(IJ)=60.0*0.0832/(TIME(ILOW(IJ+1))-TIME(ILOW(IJ)))
8700  CONTINUE
          AVGETCH=4.0*60.0*0.0832/(TIME(ILOW(5))-TIME(ILOW(1)))
          WRITE (86,8710) (ETCHRATE(IJ),IJ=1,4),AVGETCH
8710  FORMAT(1X,3X,4(F7.4,3X),4X,F7.4)
          GO TO 8900
8750  WRITE (86,8751)
8751  FORMAT(1X, 'INTERFEROMETRY DATA UNAVAILABLE')
          GO TO 8900
8800  WRITE (86,8801)
8801  FORMAT (1X, '
&    _____')
8900  CONTINUE
      WRITE (86,8901)
8901  FORMAT (1X, '//1X, 'IMPEDANCE DATA' //)
      WRITE (86,8902)
8902  FORMAT (1X, 'WFNUM RES CAP_PF CPOWER EOVERP
&    STHV ED_9')
          AVGRES = 0.0
          AVGCAP_PF = 0.0
          AVGCPOWER = 0.0
          AVGEOVERP = 0.0
          AVGSHTV = 0.0
          AVGED_9 = 0.0
      DO 9000 IIJ=1,NUMWFM(IRUN)
          WRITE (86,9010) IIJ,(SAVEIMP(IRUN,IIJ,IJK),IJK=1,6)
9010  FORMAT (1X,12,3X,F6.0,3X,F6.0,3X,F5.1,3X,F6.1,3X,F6.1,3X,F7.4)

```

```

    AVGRES = AVGRES + SAVEIMP(IRUN,IJJ,1)
    AVGCAP_PF = AVGCAP_PF + SAVEIMP(IRUN,IJJ,2)
    AVGCPOWER = AVGCPOWER + SAVEIMP(IRUN,IJJ,3)
    AVGEOVERP = AVGEOVERP + SAVEIMP(IRUN,IJJ,4)
    AVGSHTHV = AVGSHTHV + SAVEIMP(IRUN,IJJ,5)
    AVGED_9 = AVGED_9 + SAVEIMP(IRUN,IJJ,6)
    DIV = REAL(IJJ)
9000 CONTINUE
    AVGRES = AVGRES / DIV
    AVGCAP_PF = AVGCAP_PF / DIV
    AVGCPOWER = AVGCPOWER / DIV
    AVGEOVERP = AVGEOVERP / DIV
    AVGSHTHV = AVGSHTHV / DIV
    AVGED_9 = AVGED_9 / DIV
    WRITE (86,9011) AVGRES,AVGCAP_PF,AVGCPOWER,AVGEOVERP,
    & AVGSHTHV, AVGED_9
9011 FORMAT (/,1X,'AVGS',1X,F6.0,3X,F6.0,3X,F5.1,3X,F6.1,3X,F6.1,3X,F7.4)
C
C WRITE THE ION FLUX INFORMATION, IF TAKEN
C
    IF (IS_IONC .EQ. 0) GO TO 8955
8950 FORMAT (//,1X,'AVERAGE TOTAL ION FLUX = ',F4.2,' MILLIAM'S PER SQ. CM.',
    & /,1X,'DATA TAKEN USING A PINHOLE AREA OF ',E10.2,' SQ. CM.')
    WRITE (86,8950) AVEFLUX,PAREA
8955 CONTINUE
C
C WRITE THE ACTINOMETRIC INFORMATION, IF TAKEN
C
    IF (IS_ACT .EQ. 0) GO TO 8975
    WRITE (86,8960) ALABEL
8960 FORMAT (//,1X,'ACTINOMETRIC INFORMATION:',1X,A50,./)
    WRITE (86,8961)
8961 FORMAT(17X,'INTENSURE',2X,'INTENSURE',4X,'RATIO',4X,'EXPOSURE')
    WRITE (86,8962)
8962 FORMAT(17X,'OF PEAK 1',2X,'OF PEAK 2',4X,'P1/P2',4X,'TIME',/)
C
    AVGINT1 = 0.0
    AVGINT2 = 0.0
    AVGRATIO = 0.0
C
    DO 8970 NOE=1,OE_ACT(IRUN)
        AVGINT1 = AVGINT1 + OE_INFO(IRUN,NOE,1)
        AVGINT2 = AVGINT2 + OE_INFO(IRUN,NOE,2)
        AVGRATIO = AVGRATIO + RATIO(IRUN,NOE)
        WRITE (86,8963) NOE,(OE_INFO(IRUN,NOE,JJJ),JJJ=1,2),
    & RATIO(IRUN,NOE),OE_INFO(IRUN,NOE,3)
8963 FORMAT(1X,'O.E. SCAN ',I2,6X,F6.3,5X,F6.3,3X,F6.3,6X,F5.0)
8970 CONTINUE
C
    WRITE (86,8964)
8964 FORMAT(1X,' ')
    DIV = REAL(OE_ACT(IRUN))
    AVGINT1 = AVGINT1/DIV
    AVGINT2 = AVGINT2/DIV
    AVGRATIO = AVGRATIO/DIV
    WRITE (86,8965) AVGINT1, AVGINT2, AVGRATIO
8965 FORMAT(1X,'AVERAGES ',2X,6X,F6.3,5X,F6.3,3X,F6.3)
C
8975 CONTINUE
C
    IF (IS_MSI .EQ. 0) GO TO 9700
    PRINTINGTHE MASS SPEC PEAK HEIGHTS
C
9500 FORMAT (/,45X,'RELATIVE MASS SPEC PEAK HEIGHTS',/)
9501 FORMAT ('#',A8,' ')
9502 FORMAT (' ',I2,' ')
9503 FORMAT (' PEAK ')
9504 FORMAT ('#',F5.3,' ')
9505 FORMAT ('#',F5.1,' ')
9506 FORMAT (' ',/)
9507 FORMAT (' AMU ')
    WRITE (86,9500)
    WRITE (86,9503)
    DO 9600 NMSP=1,NPEAKS
    MOO=NMSP
    WRITE (86,9501) PLABEL(MOO)
9600 CONTINUE

```

```

WRITE (86,9507)
DO 9610 NMSP=1,NPEAKS
WRITE (86,9505) MAXPP(NMSP)
9610 CONTINUE
WRITE (86,9506)
III=IRUN
MSA=MSC_ACT(III)
DO 9620 NMS=1,MSA
MOO1=NMS
WRITE (86,9502) MOO1
DO 9630 NMSP=1,NPEAKS
MOO2=NMSP
WRITE (86,9504) PHRAT(III,MOO1,MOO2)
9630 CONTINUE
9620 CONTINUE
C
9700 IF (IS_WFH .EQ. 0) GO TO 9999
WRITE (86,9002) RUNID
9002 FORMAT ('1',//1X,'HARMONIC DATA FOR ',A40,/)
C
AVGVARRC = 0.0
AVGCARRC = 0.0
AVGPARRC = 0.0
AVGDCB = 0.0
AVGPOWCALC = 0.0
C
DO 9200 K=1,NUMWFM(IRUN)
POWCALC=VARRC(IRUN,K)*CARRC(IRUN,K)*
& COS(PARRC(IRUN,K)*3.14159/180.)/2.
WRITE (86,9320) K,VARRC(IRUN,K),CARRC(IRUN,K),
& PARRC(IRUN,K),DCB(IRUN,K),POWCALC
C
AVGVARRC = AVGVARRC + VARRC(IRUN,K)
AVGCARRC = AVGCARRC + CARRC(IRUN,K)
AVGPARRC = AVGPARRC + PARRC(IRUN,K)
AVGDCB = AVGDCB + DCB(IRUN,K)
AVGPOWCALC = AVGPOWCALC + POWCALC
C
9320 FORMAT (/,1X,'ELECTRICAL MEASUREMENTS CORRECTED FOR STRAY CAPACITANCE',
& ' AND LINE INDUCTANCE',/,1X,'WFM ',I2,2X,'/V/= ',F5.1,
& 3X,'/I/= ',F4.2,3X,
& 'PHASE= ',F4.1,3X,'DC BIAS = ',F6.1,4X,'POWER= ',F6.1,/)
C
C WRITE THE HARMONIC DATA
DO 9300 KK=1,ZMAXHAR
WRITE (86,9310) (HARMDATA(IRUN,K,(5*(KK-1)+KL)),KL=1,5)
9310 FORMAT (1X,F2.0,3X,4(E12.5,3X))
9300 CONTINUE
9200 CONTINUE
C
DIV = REAL(NUMWFM(IRUN))
AVGVARRC = AVGVARRC/DIV
AVGCARRC = AVGCARRC/DIV
AVGPARRC = AVGPARRC/DIV
AVGDCB = AVGDCB/DIV
AVGPOWCALC = AVGPOWCALC/DIV
WRITE (86,9220) AVGVARRC
WRITE (86,9221) AVGCARRC
WRITE (86,9222) AVGPARRC
WRITE (86,9223) AVGDCB
WRITE (86,9224) AVGPOWCALC
9220 FORMAT (/,/,1X,'AVERAGE /V/ = ',F5.1)
9221 FORMAT (1X,'AVERAGE /I/ = ',F4.2)
9222 FORMAT (1X,'AVERAGE PHASE = ',F4.1)
9223 FORMAT (1X,'AVERAGE DC BIAS = ',F6.1)
9224 FORMAT (1X,'AVERAGE CALC POWER = ',F6.1)
C
9999 CONTINUE
CLOSE (86)
CLOSE (87)
1000 CONTINUE
RETURN
END

```

```

SUBROUTINE WFMPLOT(RUNIDO,NPTS)
C
C SUBROUTINE OF PROGRAM ANALYZE - DATA ANALYSIS ROUTINE
C
C THIS SUBROUTINE CREATES AN EPLOT FILE FOR THE ELECTRICAL
C MEASUREMENTS: VOLTAGE,CURRENT, AND POWER.
C
COMMON/SCOPE/CUR(1024),VOLT(1024),XINCR
COMMON/SWITCHES/IS_MSI,IS_MSP,IS_ACT,IS_OEP,IS_WFFA,IS_WFP,
& IS_WFH,IS_IFP,IS_IMPC,IS_IONC,IS_ICPLOT,
& IS_CODE,IS_SUM,IS_DES,IS_IE,IS_IEDP,IS_IEIP
COMMON/IDENT/IDTRIAL(100),ALPHABET,ELDESCR(100),WDESCR(100)
COMMON/SPECS/IDLEN(100),NUM_OF_TRIALS,ITRIAL_COUNTER,NUMFILE
CHARACTER*15 IDTRIAL
CHARACTER*50 ELDESCR,WDESCR
CHARACTER*10 ALPHABET
CHARACTER*20 RUNIDO
DIMENSION SCCUR(300),SCVOL(300)
C
C FIRST, SCALE THE VOLTAGE AND CURRENT WAVEFORMS INTO
C THE RANGE [-1,1].
C
CURMAX=-1000.
CURMIN=1000.
VOLMAX=-1000.
VOLMIN=1000.
POWMAX=-1000.
POWMIN=1000.
DO 10 NI=1,NPTS
IF (CUR(NI) .GT. CURMAX) CURMAX=CUR(NI)
IF (CUR(NI) .LT. CURMIN) CURMIN=CUR(NI)
IF (VOLT(NI) .GT. VOLMAX) VOLMAX=VOLT(NI)
IF (VOLT(NI) .LT. VOLMIN) VOLMIN=VOLT(NI)
POW=CUR(NI)*VOLT(NI)
10 CONTINUE
CURMAG=(CURMAX-CURMIN)/2.
VOLMAG=(VOLMAX-VOLMIN)/2.
C
DO 15 J=1,300
SCCUR(J)=-1000.
SCVOL(J)=-1000.
15 CONTINUE
C
SCCUR AND SCVOL ARE THE SCALED VALUES
C
NSKIP=NPTS/200
DO 20 NI=1,300
NS=1+(NI-1)*NSKIP
IF (NS .GT. NPTS) GO TO 25
SCCUR(NI)=2.*(CUR(NS)-CURMIN)/(CURMAX-CURMIN)-1
SCVOL(NI)=2.*(VOLT(NS)-VOLMIN)/(VOLMAX-VOLMIN)-1
20 CONTINUE
25 CONTINUE
C
NOW WRITE TO THE EPLOT FILE
C
1010 FORMAT ('WAVEFORMS OF ',A20,/, 'TIME',/,
& 'SCALED UNITS ',/, 'SYMB 99.0',/, 'YLEN 4.5',/,
& 'XMIN 1.0',/, 'XMAX ',F5.1,/, 'XTIC 0.0',/, '200.-1.0',/,
& 'YMIN -1.2',/, 'YMAX 1.2',/, 'YTIC -1.0',/, '.4,1.0')
1020 FORMAT ('LABL -3.0',/, '.4,.4',/, 'CURRENT MAGNITUDE (PP) =',F4.2,
& ' AMPS',/, '.4,.25',/, 'VOLTAGE MAGNITUDE (PP) =',F7.1, ' VOLTS',
& ',.4,.1',/, 'TIME PER INCREMENT= ',E8.1, ' SECS.',/, 'END')
1040 FORMAT('1.E+32,-1.0')
1050 FORMAT('1.E+32,99.0')
C
XNP=FLOAT(NPTS)
WRITE (81,1010) RUNIDO,XNP
WRITE (81,1020) CURMAG,VOLMAG,XINCR
DO 50 I=1,300
IF (SCCUR(I) .EQ. -1000.) GO TO 60
NP=1+(I-1)*NSKIP
XNP=FLOAT(NP)
50 WRITE (81,FMT='(F6.1," ",F5.2)') XNP,SCCUR(I)
60 CONTINUE
WRITE (81,1040)

```

```

WRITE (81,FMT='(F6.1,"",F5.2)') 1.0,SCVOL(1)
WRITE (81,1050)
DO 70 I=1,300
IF (SCVOL(I) .EQ. -1000.) GO TO 80
NP=1+(I-1)*NSKIP
XNP=FLOAT(NP)
70 WRITE (81,FMT='(F6.1,"",F5.2)') XNP,SCVOL(I)
80 CONTINUE
100 CONTINUE
CLOSE (81)
RETURN
END

```

```

SUBROUTINE WFM_CONVERT(MAXHARM)
C
C SUBROUTINE OF PROGRAM ANALYZE - DATA ANALYSIS ROUTINE
C
C THIS SUBROUTINE CONVERTS THE WAVEFORMS
C SENT FROM THE TEKTRONIX 7D20 THROUGH
C THE OUTBOARD COMPUTER TO ACTUAL VALUES.
C A FOURIER TRANSFORM ANALYSIS ROUTINE IS CALLED
C THAT WILL CALCULATE CURRENT, VOLTAGE, AND PHASE DELAY.
C

```

```

COMMON/SCOPE/CUR(1024),VOLT(1024),XINCR
COMMON/IDENT/IDTRIAL(100),ALPHABET,ELDESCR(100),WDESCR(100)
COMMON/SPECS/IDLEN(100),NUM_OF_TRIALS,ITRIAL_COUNTER,NUMFILE
COMMON/SWITCHES/IS_MSI,IS_MSP,IS_ACT,IS_OEP,IS_WFFA,IS_WFP,
& IS_WFH,IS_IFP,IS_IMPC,IS_IONC,IS_ICPLOT,
& IS_CODE,IS_SUM,IS_DES,IS_IE,IS_IEDP,IS_IEIP
COMMON/INFO/PRESSURE(100),ESPACE(100),MS_SCALE(100,10),
& FLOWRATE(100,4),MSC_ACT(100),OE_ACT(100),
& WF_ACT(100),ION_ACT(100),IF_SCALE(100),
& IE_ACT(100)
C
C

```

```

DIMENSION DEC_NUM(10)
INTEGER OE_ACT,WF_ACT,PT_OFF,WFNUM,WFN
CHARACTER*40 DESCR1C,DESCR2C,DESCR3C
CHARACTER*40 DESCR1V,DESCR2V,DESCR3V
CHARACTER*50 ELDESCR,WDESCR
CHARACTER*72 LABELC,LABELV
CHARACTER*13 CHAR13
CHARACTER*14 CHAR14
CHARACTER*10 ALPHABET
CHARACTER*15 IDTRIAL
CHARACTER*20 PATHNAMEI,PATHNAMEO,RUNIDO
CHARACTER*18 JUNKC,JUNKV
CHARACTER*50 RUNID,RUNIDC,RUNIDV
CHARACTER*3 NUMBER
DATA NUMBER/'123'/
C
C

```

```

C
C READ DIGITAL DATA SENT DOWN BY THE SCOPE
C FROM THE INPUT FILES. OPEN OUTPUT FILES.
C

```

```

DO 999 WFNUM=1,WF_ACT(ITRIAL_COUNTER)
PATHNAMEI=':UDD:MEFL:IMP_WAVES:'
RUNIDC=PATHNAMEI//IDTRIAL(ITRIAL_COUNTER)(1:IDLEN(ITRIAL_COUNTER))//
& '_WFC'//NUMBER(WFNUM:WFNUM)
& RUNIDV=PATHNAMEI//IDTRIAL(ITRIAL_COUNTER)(1:IDLEN(ITRIAL_COUNTER))//
& '_WV'//NUMBER(WFNUM:WFNUM)
OPEN (31,FILE=RUNIDC)
OPEN (32,FILE=RUNIDV)
PATHNAMEO=':UDD:MEFL:WAVPLOT:'
RUNIDO=IDTRIAL(ITRIAL_COUNTER)(1:IDLEN(ITRIAL_COUNTER))
& //'_WF'//NUMBER(WFNUM:WFNUM)
& RUNID=PATHNAMEO(1:18)//RUNIDO
IF (IS_WFP .EQ. 1) OPEN (81,FILE=RUNID)

```

```

C
C READ THE LABELS, THE CHARACTERISTICS, AND THE DATA
C SEE THE 7D20 MANUAL FOR SPECIFICS OF
C THE DATA PRESENTATION.

```

```

C
READ (31,1001) LABELC,DESCR1C,DESCR2C,DESCR3C
READ (32,1001) LABELV,DESCR1V,DESCR2V,DESCR3V
READ (31,1002) CHAR13,NPTSC
READ (32,1002) CHAR13,NPTSV
READ (31,1003) CHAR13,XINCRC
READ (32,1003) CHAR13,XINCRV
READ (31,1004) CHAR14,PT_OFFC
READ (32,1004) CHAR14,PT_OFFV
READ (31,1003) CHAR13,YZEROC
READ (32,1003) CHAR13,YZEROV
READ (31,FMT='(A)') JUNKC
READ (32,FMT='(A)') JUNKV
IEXPC=0
IEXPV=0
DO 300 JJJ=14,25
IF (JUNKC(JJJ:JJJ) .EQ. 'E') IEXPC=1
300 IF (JUNKV(JJJ:JJJ) .EQ. 'E') IEXPV=1
BACKSPACE (31)
BACKSPACE (32)
IF (IEXPC .EQ. 0) READ (31,FMT='(A13,F4.2)') CHAR13,YMULTC
IF (IEXPV .EQ. 0) READ (32,FMT='(A13,F4.2)') CHAR13,YMULTV
IF (IEXPC .EQ. 1) READ (31,1003) CHAR13,YMULTC
IF (IEXPV .EQ. 1) READ (32,1003) CHAR13,YMULTV
C
FORMAT STATEMENTS FOR READS
C
1001 FORMAT(A72,/,3(A40,/))
1002 FORMAT (A13,I4)
1003 FORMAT (A13,E8.1)
1004 FORMAT (A14,E8.1)
IF (NPTSC .GT. NPTSV) NPTS=NPTSC
IF (NPTSV .GE. NPTSC) NPTS=NPTSV
PT_OFF=INT(PT_OFFC)
XINCR=XINCRC
C
C NOW READ THE DATA POINTS. THE DATA IS SENT
C EIGHT POINTS TO A DATA LINE.
C
ILOC=0
10 READ (31,*,END=12) CUR(8*ILOC+1),CUR(8*ILOC+2),CUR(8*ILOC+3),
& CUR(8*ILOC+4),CUR(8*ILOC+5),CUR(8*ILOC+6),
& CUR(8*ILOC+7),CUR(8*ILOC+8)
12 READ (32,*,END=20) VOLT(8*ILOC+1),VOLT(8*ILOC+2),VOLT(8*ILOC+3),
& VOLT(8*ILOC+4),VOLT(8*ILOC+5),VOLT(8*ILOC+6),
& VOLT(8*ILOC+7),VOLT(8*ILOC+8)
ILOC=ILOC+1
GO TO 10
20 CONTINUE
C
C CORRECT FOR THE OFFSET VOLTAGE ON THE
C SCOPE GROUND.
C
DO 200 J=1,NPTS
CUR(J)=CUR(J)*YMULTC-YZEROC
VOLT(J)=(VOLT(J)*YMULTV-YZEROV)*1. I 50 OHM LOAD
ON VOLTAGE PROBE
C
200 CONTINUE
C
IF (IS_WFP .EQ. 1) CALL WFMPLOT(RUNIDO,NPTS)
C
WFN=WFNUM
IF (IS_WFFA .EQ. 1) CALL FOURIER(NPTS,MAXHARM,WFN)
C
CLOSE (31)
CLOSE (32)
999 CONTINUE
CLOSE (81)
RETURN
END

```

```

PROGRAM RSM

C
C THIS PROGRAM PERFORMS THE CALCULATIONS FOR THE
C RESPONSE SURFACE METHODOLOGY STATISTICAL TECHNIQUE.
C THE TECHNIQUE IS DESCRIBED IN JENKINS ET AL.,
C SOLID STATE TECHNOLOGY 29(4), 175 (1986). THE RSM
C FIT IS SIMPLY A LINEAR REGRESSION OF THE DATA TO
C A CHOSEN POLYNOMIAL MODEL. THIS PROGRAM CAN HANDLE
C EITHER QUADRATIC OR CUBIC MODELS, AND UP TO 10
C RESPONSE SETS FOR EACH DATA LINE.
C
      IMPLICIT DOUBLE PRECISION (A-H,O-Z)
      DIMENSION XTX(100,100),XTY(100,10)
      DIMENSION FACTORS(100,3),TRFACTORS(100,3)
      DIMENSION GENMOD(20,3),GMOD2(10,3),GMOD3(20,3),
&      AVEF(3),SDF(3)
      DIMENSION X(100,20),Y(100,10),P(20,10)
      DIMENSION YHAT(100,10),RESID(100,10),RDSR(100,10)
      DIMENSION RESSSQ(10),REGSSQ(10),RESMSQ(10),
&      REGMSQ(10),ADJR2(10)
      DIMENSION TMSQ(10),RAVE(10),RSD(10)
      DATA GMOD2/0.,1.,0.,0.,1.,1.,0.,2.,0.,0.,
&      0.,0.,1.,0.,1.,0.,1.,0.,2.,0.,
&      0.,0.,0.,1.,0.,1.,1.,0.,0.,0.,2./
      DATA GMOD3/0.,1.,0.,0.,1.,1.,0.,2.,0.,0.,
&      2.,2.,1.,1.,0.,1.,0.,3.,0.,0.,
&      0.,0.,1.,0.,1.,0.,1.,0.,2.,0.,
&      1.,0.,1.,2.,2.,0.,1.,0.,3.,0.,
&      0.,0.,0.,1.,0.,1.,1.,0.,0.,2.,
&      0.,1.,1.,0.,1.,2.,2.,0.,0.,3./
      DATA X,Y,XTX,XTY,P/14200*0.0/
      DATA AVEF,SDF/6*0.0/
      DATA FACTORS,TRFACTORS/600*0.0/
      DATA YHAT,RESID,RDSR/3000*0.0/
      DATA RESSSQ,REGSSQ,RESMSQ,REGMSQ,
&      ADJR2,RAVE,RSD,TMSQ/80*0.0/

C
C THE PROGRAM CAN HANDLE UP TO 100 DATA POINTS,
C UP TO 10 RESPONSES (RIGHT-HAND SIDES),
C UP TO 20 PARAMETERS (CUBIC MODEL).
C
C
C OPEN ALL RELEVANT FILES.
C
      OPEN (1,FILE='RSM_DATA')
      OPEN (2,FILE='RSM_SPECS')
      OPEN (3,FILE='RSM_OUT')
      OPEN (4,FILE='CPGEN_DATA')

C
C READ THE NECESSARY DATA FOR THE REGRESSION.
C
      READ (2,*) NORDER IORDER OF MODEL (QUADRATIC OR CUBIC)
      READ (2,*) NDP INUMBER OF DATA POINTS
      READ (2,*) NRHS INUMBER OF RESPONSES
      READ (2,*) NFAC INUMBER OF FACTORS IN MODEL
      READ (2,*) NPARAMS INUMBER OF PARAMETERS IN MODEL

C
C NOW READ THE DATA SETS.
C
      DO 10 I=1,NDP
      READ (1,*) (FACTORS(I,K),K=1,NFAC),(Y(I,L),L=1,NRHS)
      CONTINUE
10
C
C CALCULATE THE MEAN AND STANDARD DEVIATIONS OF EACH OF THE
C FACTORS SO THAT THEY MAY BE TRANSFORMED.
C
      DO 5000 I=1,NPARAMS
      DO 5010 J=1,NFAC
      IF (NORDER .EQ. 2) GENMOD(I,J)=GMOD2(I,J)
      IF (NORDER .EQ. 3) GENMOD(I,J)=GMOD3(I,J)
5010 CONTINUE
5000 CONTINUE
C
C

```

```

DO 30 I=1,NFAC
AVEF(I)=0.
SDF(I)=0.
30 CONTINUE
C

DO 50 I=1,NDP
DO 60 J=1,NFAC
AVEF(J)=AVEF(J)+FACTORS(I,J)
60 CONTINUE
50 CONTINUE
C

DO 70 I=1,NFAC
AVEF(I)=AVEF(I)/REAL(NDP)
70 CONTINUE
C

DO 80 I=1,NDP
DO 90 J=1,NFAC
SDF(J)=SDF(J)+(AVEF(J)-FACTORS(I,J))*(AVEF(J)-FACTORS(I,J))
90 CONTINUE
80 CONTINUE
C

DO 100 I=1,NFAC
SDF(I)=SQRT(SDF(I)/REAL((NDP-1)))
100 CONTINUE
C
C THE FACTORS WILL NOW BE SCALED INTO THE TRANSFORMED UNITS
C FOR THE LINEAR REGRESSION.
C

DO 200 I=1,NDP
DO 210 J=1,NFAC
TRFACTORS(I,J)=(FACTORS(I,J)-AVEF(J))/SDF(J)
210 CONTINUE
200 CONTINUE
C

C THE ARRAY GENMOD CONTAINS THE INFORMATION NECESSARY FOR
C CONSTRUCTION OF THE QUADRATIC MODEL. THIS INFORMATION
C WILL BE USED TO CREATE THE ARRAY X, WHICH IS USED IN THE
C MATRIX EQUATION  $XX'B=X'Y$  TO GET THE PARAMETERS.
C

DO 300 I=1,NDP
DO 310 J=1,NPARAMS
Z=1.0
DO 320 K=1,NFAC
IG=INT(GENMOD(J,K))
DO 330 M=1,IG
Z=Z*TRFACTORS(I,K)
330 CONTINUE
320 CONTINUE
X(I,J)=Z
310 CONTINUE
300 CONTINUE
C

C NOW CALCULATE THE TRANSPOSE MATRIX OF X AND DO THE
C MULTIPLICATIONS NECESSARY.
C

DO 500 I=1,NPARAMS
DO 510 J=1,NPARAMS
SUM=0.
DO 520 K=1,NDP
SUM=SUM+X(K,I)*X(K,J)
520 CONTINUE
XTX(I,J)=SUM
510 CONTINUE
500 CONTINUE
C

DO 600 I=1,NPARAMS
DO 610 J=1,NRHS
SUM=0.
DO 620 K=1,NDP
SUM=SUM+X(K,I)*Y(K,J)
620 CONTINUE
XTY(I,J)=SUM
610 CONTINUE
600 CONTINUE
C

CALL MATINV(100,NPARAMS,XTX)
C

```



```

C      XTX IS NOW THE INVERSE OF THE OLD MATRIX XTX.
C      PREMULTIPLICATION OF XTX BY XTY WILL GIVE
C      THE SOLUTION VECTOR P. THE PARAMETERS IN
C      THE MODEL ARE CONTAINED IN P.
C
C      DO 700 I=1,NPARAMS
C      DO 710 J=1,NRHS
C      SUM=0.
C      DO 720 K=1,NPARAMS
720    SUM=SUM+XTX(I,K)*XTY(K,J)
C      CONTINUE
C      P(I,J)=SUM
710    CONTINUE
700    CONTINUE
C
C
C      NOW OUTPUT THE RESULTS OF THE FIT.
C      THE OUTPUT IS MODELLED AFTER THE DUPONT RSM PROGRAM,
C      ALTHOUGH THE FORMAT IS NOT AS NEAT.
C      THE ANALYSIS OF VARIANCE INFORMATION IS NOT INCLUDED.
C
C      WRITE (3,1004)
C      DO 2100 I=1,NFAC
C      WRITE (3,1005) I,AVEF(I),SDF(I)
C      WRITE (4,1100) AVEF(I),SDF(I)
2100    CONTINUE
C      WRITE (3,1003)
C      WRITE (3,1015)
C
C      NOW OUTPUT THE MODEL FIT STATISTICS
C      NOTE THAT THE R-SQUARED VALUE IS NOT
C      A TRUE ADJUSTED R-SQUARED.
C
C
C      DO 3000 J=1,NRHS
C      DO 3100 I=1,NDP
C      DO 3200 K=1,NPARAMS
3200    YHAT(I,J)=YHAT(I,J)+P(K,J)*X(I,K)
C      CONTINUE
C
C      RESID(I,J)=Y(I,J)-YHAT(I,J)
C      REGSSQ(J)=REGSSQ(J)+Y(I,J)*Y(I,J)
C      RESSQ(J)=RESSQ(J)+RESID(I,J)*RESID(I,J)
C      RAVE(J)=RAVE(J)+RESID(I,J)/NDP
3100    CONTINUE
3000    CONTINUE
C
C      DO 3400 I=1,NRHS
C      RESMSQ(I)=RESSQ(I)/(NDP-NPARAMS)
C      REGMSQ(I)=REGSSQ(I)/(NPARAMS-1)
C      TMSQ(I)=(RESSQ(I)+REGSSQ(I))/REAL(NDP-1)
C      ADJR2(I)=1.-RESMSQ(I)/TMSQ(I)
3400    CONTINUE
C
C      DO 3450 J=1,NRHS
C      DO 3460 I=1,NDP
C      RSD(J)=RSD(J)+(RESID(I,J)-RAVE(J))*2.
3460    CONTINUE
C      RSD(J)=SQRT(RSD(J)/(NDP-1))
3450    CONTINUE
C
C      DO 3500 I=1,NRHS
C      DO 3600 M=1,NDP
C      RDSR(M,I)=(RESID(M,I)-RAVE(I))/RSD(I)
3600    CONTINUE
3500    CONTINUE
C
C
C      PRINT OUT THE STATISTICS
C
C      DO 4000 I=1,NRHS
C      WRITE (3,1002) I
C      DO 2010 J=1,NPARAMS
C      WRITE (3,1001) J,P(J,I)
C      WRITE (4,1101) P(J,I)
2010    CONTINUE
C      WRITE (4,1102)

```

```

WRITE (3,1003)
C
WRITE (3,1010)
DO 4100 J=1,NDP
WRITE (3,1011) J,Y(J,I),YHAT(J,I),RESID(J,I),RDSR(J,I)
4100 CONTINUE
C
WRITE (3,1020) RESSQ(I),RESMSQ(I)
WRITE (3,1021) REGSSQ(I),REGMSQ(I)
WRITE (3,1022) TMSQ(I),ADJR2(I)
C
IF (I .LT. NRHS) WRITE (3,1012)
4000 CONTINUE
C
C
1001 FORMAT('PARAMETER ',I2,' =',F12.6)
1002 FORMAT('RIGHT HAND SIDE #',I2,/)
1003 FORMAT(35('-',)/)
1004 FORMAT(/,1X,'FACTOR          AVERAGE          S.D.')
```

		DATA	MODEL
1005	FORMAT(3X,I1,7X,F10.5,5X,F10.5)		
1010	FORMAT(/,1X,'NUMBER	RESIDUAL	STD. RESIDUAL',/)

```

&
&      116('-',)
1011 FORMAT(2X,I2,13X,F11.5,15X,F11.5,15X,F11.5,15X,F5.2)
1012 FORMAT('<FF>')
```

1015	FORMAT(/)		
1020	FORMAT(/,1X,'RESIDUAL SUM-OF-SQUARES=',E11.3,/,		
&	1X,'RESIDUAL MEAN SQUARE=',E11.3)		
1021	FORMAT(1X,'REGRESSION SUM-OF-SQUARES=',E11.3,/,		
&	1X,'REGRESSION MEAN SQUARE=',E11.3)		
1022	FORMAT(1X,'TOTAL MEAN SQUARE=',E11.3,/,		
&	1X,'ADJUSTED R-SQUARED=',F6.4)		
1100	FORMAT(F12.6,' ',F12.6)		
1101	FORMAT(F12.6)		
1102	FORMAT(/)		

```

END
```

SUBROUTINE MATINV(MAX,N,A)

```

C
C THIS SUBROUTINE WAS ADAPTED FROM AN IMSL
C LIBRARY ROUTINE.
C
C DESCRIPTION OF PARAMETERS:
C A - INPUT MATRIX, DESTROYED IN CALCULATION AND
C REPLACED BY RESULTANT INVERSE
C N - ORDER OF UPPER LEFT HAND SIDE OF MATRIX A INVERTING
C D - RESULTANT DETERMINANT
C L - WORK VECTOR OF LENGTH MAX
C M - WORK VECTOR OF LENGTH MAX
C MAX - ORDER OF MATRIX A
C REMARKS:
C MATRIX A MUST BE A GENERAL MATRIX
C METHOD:
C THE STANDARD GAUSS-JORDAN METHOD IS USED. THE
C DETERMINANT IS ALSO CALCULATED. A DETERMINANT OF
C ZERO INDICATES THAT THE MATRIX IS SINGULAR.
C
C IMPLICIT DOUBLE PRECISION (A-H,O-Z)
C DIMENSION A(MAX,MAX),L(100),M(100)
C DATA L,M/200*0/
C SEARCH FOR LARGEST ELEMENT
E = 1.
DO 80 K = 1,N
L(K) = K
M(K) = K
BIGA = A(K,K)
DO 20 J = K,N
DO 20 I = K,N
IF (ABS(BIGA) - ABS(A(I,J))) 15,20,20
15 BIGA = A(I,J)
L(K) = I
M(K) = J
20 CONTINUE
```

```

C
C INTERCHANGE ROWS
C
      J = L(K)
      IF (J - K) 35,35,25
25     DO 30 I = 1,N
          RHOLD = -A(K,I)
          A(K,I) = A(J,I)
30     A(J,I) = RHOLD
C
C INTERCHANGE COLUMNS
C
      I = M(K)
      IF (I - K) 45,45,38
38     DO 40 J = 1,N
          RHOLD = -A(J,K)
          A(J,K) = A(J,I)
40     A(J,I) = RHOLD
C
C DIVIDE COLUMN BY MINUS PIVOT
C VALUE OF PIVOT ELEMENT IS CONTAINED IN BIGA
C
      IF (BIGA) 48,46,48
45     D = 0.0
46     RETURN
48     DO 55 I = 1,N
          IF (I - K) 50,55,50
50     HOLD = A(I,K)/(-BIGA)
          A(I,K) = HOLD
55     CONTINUE
C
C REDUCE MATRIX
C
      DO 65 I = 1,N
          HOLD = A(I,K)
          DO 65 J = 1,N
              IF (I - K) 60,65,60
              IF (J - K) 62,65,62
              HOLD1 = HOLD*A(K,J)+A(I,J)
              A(I,J) = HOLD1
60
62
65     CONTINUE
C
C DIVIDE ROW BY PIVOT
C
      DO 75 J = 1,N
          IF (J - K) 70,75,70
70     HOLD = A(K,J)/BIGA
          A(K,J) = HOLD
75     CONTINUE
C
C PRODUCT OF PIVOTS
C
      E = E * BIGA
C
C REPLACE PIVOT BY RECIPROCAL
C
      HOLD = 1./BIGA
      A(K,K) = HOLD
80     CONTINUE
C
C FINAL ROW AND COLUMN INTERCHANGE
C
      K = N
100    K = K-1
      IF (K) 150,150,105
105    I = L(K)
      IF (I - K) 120,120,108
108    DO 110 J = 1,N
          RHOLD = A(J,K)
          A(J,K) = -A(J,I)
110    A(J,I) = RHOLD
120    J = M(K)
      IF (J - K) 100,100,125
125    DO 130 I = 1,N
          RHOLD = A(K,I)
          A(K,I) = -A(J,I)
130    A(J,I) = RHOLD

```

```
150 GO TO 100  
D = E  
RETURN  
END
```

```

PROGRAM UNIFORM
C
C THIS ROUTINE DETERMINES CHEMICAL ETCHING UNIFORMITY,
C USING ASSUMPTIONS DISCUSSED IN THE THESIS.
C SURFACE RECOMBINATION ON ALL SURFACES IS ACCOUNTED
C FOR, AS ARE FLOW LOSSES.
C IN THIS PROGRAM, HOMOGENEOUS RECOMBINATION IS NOT
C CONSIDERED.
C
C IMPLICIT DOUBLE PRECISION (A-H,O-Z)
C DIMENSION PHINEW(-1:101,-1:101),PHIOLD(-1:101,-1:101),
& EDENSE(-1:101,-1:101),C(-1:101,-1:101),MMZ(9)
C CHARACTER*6 STRING
C CHARACTER*3 EQUAL
C OPEN (1,FILE='PARAMETERS')
C OPEN (2,FILE='RESULTS')
C
C
C READ ALL INPUT DATA - RATE CONSTANTS, ETC.
C
C READ (1,1001) STRING,EQUAL,NZ INUMBER OF DIVISIONS IN Z
C READ (1,1001) STRING,EQUAL,NR INUMBER OF DIVISIONS IN R
C READ (1,1002) STRING,EQUAL,DIFF1 IDIFFUSIVITY AT 1 TORR, IN CM2/S
C READ (1,1002) STRING,EQUAL,ESPACE IELECTRODE SPACING IN CM
C READ (1,1002) STRING,EQUAL,FLOW IFLOW RATE IN SCCM
C READ (1,1002) STRING,EQUAL,PRESS IPRESSURE IN TORR
C READ (1,1002) STRING,EQUAL,EDIAM IELECTRODE DIAMETER IN CM
C READ (1,1002) STRING,EQUAL,WDIAM IWAFFER DIAMETER IN CM
C READ (1,1002) STRING,EQUAL,TDIAM ITEFLON DIAMETER IN CM
C READ (1,1002) STRING,EQUAL,RRELEC IREACTION RATE CONSTANT ON ELECTRODE
C READ (1,1002) STRING,EQUAL,RRWAF IREACTION RATE CONSTANT ON WAFER
C READ (1,1002) STRING,EQUAL,RRTEF IREACTION RATE CONSTANT ON TEFLON
C READ (1,1002) STRING,EQUAL,RRFORM IATOMIC CHLORINE RXN. RATE CONSTANT
C READ (1,1002) STRING,EQUAL,EDEN I AVERAGE ELECTRON DENSITY IN CM-3
1001 FORMAT (A6,A3,I3)
1002 FORMAT (A6,A3,E9.2)
C
C
C THE SOLUTION IS OBTAINED BY INTEGRATING OVER
C TIME UNTIL STEADY-STATE IS REACHED.
C
C SET ALL INITIAL PARAMETERS.
C
C
C PI=3.1415926535
C XNR=DBLE(NR)
C XNZ=DBLE(NZ)
C XR2=XNR*XNR
C XZ2=XNZ*XNZ
C DIFF=DIFF1/PRESS IDIFFUSIVITY AT REACTOR PRESSURE
C QFLOW=FLOW*760./PRESS/60. I CONVERTED TO CM3/S AT REACTOR PRESSURE
C IWAFFER=INT(XNR*WDIAM/TDIAM) I INDEX OF WAFER EDGE
C IELEC=INT(XNR*EDIAM/TDIAM) I INDEX OF ELECTRODE EDGE
C CONCA0=PRESS/760.*6.02E23/82.05/350. IGAS DENSITY IN CM-3
C RT=TDIAM/2.
C A=DIFF/RT/RT
C B=A-QFLOW/2./PI/RT/RT/ESPACE
C ITIME=0
C TIME=0.
C
C
C ALLOW FOR NONUNIFORMITY OF ELECTRON CONCENTRATION
C WITH AXIAL POSITION.
C
C
C CMAX=0.
C DO 100 KR=-1,NR
C DO 110 KZ=-1,NZ
C KSL=INT(0.1/ESPACE*XNZ)
C KSH=NZ-INT(0.1/ESPACE*XNZ)
C IF (KZ .LT. KSL .OR. KZ .GT. KSH .OR. KR .GT. IELEC) EDENSE(KR,KZ)=0.
C IF (KZ .GE. KSL .AND. KZ .LE. KSH .AND. KR .LE. IELEC)
& EDENSE(KR,KZ)=EDEN
C (KR,KZ)=RRFORM*EDENSE(KR,KZ)
C IF (KZ .EQ. 0 .OR. KZ .EQ. N) C(KR,KZ)=0.
C IF (C(KR,KZ) .GT. CMAX) CMAX=C(KR,KZ)
110 CONTINUE
100 CONTINUE
C DTMAX=1./(2.*A*(XZ2+XR2)+2.*CMAX)
C

```

```

C      SPECIFY TIME STEP, TOLERANCE ON SOLUTION.
C
      PRINT *, 'MAXIMUM STABLE TIME STEP IS: ',DTMAX
      PRINT *, 'ENTER TIME STEP TO BE USED: '
      READ *,DTIME
      PRINT *, 'TOLERANCE ON FINAL SOLUTION:'
      READ *,TOLERANCE
C
      DO 10 KR=-1,(NR+1)
      DO 20 KZ=0,(NZ+1)
      PHIOLD(KR,KZ)=0.0
20     CONTINUE
10     CONTINUE
C
      BEGIN THE CALCULATION LOOP
C
      CONTINUE
C
      DO 210 KZ=0,NZ
C      THE ZERO RADIUS CASE WILL BE TREATED AS A BOUNDARY CONDITION
      DO 220 KR=1,NR
      XKR=DBLE(KR)
      GROUP1=-2.*(A*(XZ2+XR2)+C(KR,KZ))*PHIOLD(KR,KZ)
      GROUP2=(A*XR2+B*XR/2./XKR)*PHIOLD((KR+1),KZ)
      GROUP3=(A*XR2-B*XR/2./XKR)*PHIOLD((KR-1),KZ)
      GROUP4=A*XZ2*(PHIOLD(KR,(KZ+1))+PHIOLD(KR,(KZ-1)))
      SUM=GROUP1+GROUP2+GROUP3+GROUP4+C(KR,KZ)
      PHINew(KR,KZ)=PHIOLD(KR,KZ)+DTIME*SUM
220    CONTINUE
210    CONTINUE
C
      NOW THE BOUNDARY CONDITIONS
C
      DO 30 JZ=1,(NZ-1)
      PHINew(-1,JZ)=PHINew(1,JZ) !CENTER RADIAL BOUNDARY CONDITION
      PHINew(0,JZ)=PHINew(1,JZ)
30     CONTINUE
C
      DO 40 JZ=1,(NZ-1)
      PHINew((NR+1),JZ)=PHINew((NR-1),JZ)
40     CONTINUE
C
      DO 50 JR=0,NR
      IF (JR .LE. IELEC) RR=RRELEC
      IF (JR .GT. IELEC) RR=RRTEF
      PHINew(JR,-1)=PHINew(JR,1)-2.*RR*ESPACE/XNZ/DIFF*PHINew(JR,0)
C      UPPER ELECTRODE AXIAL BOUNDARY CONDITION
50     CONTINUE
C
      DO 60 JR=0,NR
      IF (JR .LE. IWAFFER) RR=RRWAF
      IF (JR .GT. IWAFFER .AND. JR .LE. IELEC) RR=RRELEC
      IF (JR .GT. IELEC) RR=RRTEF
C      LOSS RATE ON LOWER ELECTRODE, WAFER, AND TEFLON
      PHINew(JR,(NZ+1))=PHINew(JR,(NZ-1))-2.*RR*ESPACE/XNZ/DIFF*PHINew(JR,0)
60     CONTINUE
      IF (PHINew(0,0) .EQ. 0.0) PHINew(0,0)=
&      (PHINew(0,1)+PHINew(0,-1)+PHINew(1,0)+PHINew(-1,0))/4.
      IF (PHINew(0,NZ) .EQ. 0.0) PHINew(0,NZ)=
&      (PHINew(0,(NZ+1))+PHINew(0,(NZ-1))+PHINew(-1,NZ)+PHINew(1,NZ))/4.
C
      BOUNDARY CONDITIONS ARE SET
C
      NOW CHECK FOR CONVERGENCE OF THE SCHEME. FIRST, CALCULATE THE
      FRACTIONAL CHANGE IN THE MATRIX UPON THE LAST ITERATION.
C
      SUM=0.0
      DO 500 LR=0,NR
      DO 510 LZ=0,NZ
      IF (PHINew(LR,LZ) .LE. 1.E-10) GO TO 510
      SUM=SUM+SQRT(((PHINew(LR,LZ)-PHIOLD(LR,LZ))/PHINew(LR,LZ))**2.)
510    CONTINUE
500    CONTINUE
      AVGERR=SUM/XNR/XNZ
      IF (AVGERR .LE. TOLERANCE) GO TO 2000
C
      NR1=NR+1

```

```

NZ1=NZ+1
DO 600 MR=-1,NR1
DO 610 MZ=-1,NZ1
PHIOLD(MR,MZ)=PHINew(MR,MZ)
610 CONTINUE
600 CONTINUE
C
C RETURN FOR NEXT ITERATION
C
ITIME=ITIME+1
TIME=TIME+DTIME
GO TO 1
C
2000 CONTINUE
C THE RESULTS WILL NOW BE WRITTEN TO THE OUTPUT FILE
C
C FIRST PRINT OUT THE PARAMETERS
C
WRITE (2,2001) FLOW,PRESS,DIFF,ESPACE,EDIAM,WDIAM,TDIAM,
& RRELEC,RRWAF,RRTEF,RRFORM
WRITE (2,2002) NR,NZ,ITIME,TIME,AVGERR
C
C NOW PRINT OUT THE CONCENTRATION PROFILES
C
DO 150 I=1,9
MMZ(I)=INT(DBLE(I-1)/8.*XNZ)
150 CONTINUE
WRITE (2,2003) ((MMZ(K)),K=1,9)
DO 160 IR=0,NR
RPOS=TDIAM*DBLE(IR)/XNR
WRITE (2,2003) RPOS,(PHINew(IR,MMZ(K)),K=1,9)
IF (IR .EQ. IWAFER) WRITE (2,2010)
IF (IR .EQ. IELEC) WRITE (2,2011)
160 CONTINUE
C
C ETCHING RATE UNIFORMITY, NORMALIZED TO EDGE OF WAFER
WRITE (2,2004)
DO 170 JR=0,IWAFER
POS=DBLE(JR)/XNR*TDIAM
ETCH=PHINew(JR,NZ)/PHINew(IWAFER,NZ)
170 WRITE (2,2005) POS,ETCH
CONTINUE
C
C NOW COMPUTE FRACTIONAL LOSSES OF ATOMIC CHLORINE BY VARIOUS MECHANISMS
C
SUMWAF=0.
SUMELEC=0.
SUMTEF=0.
SUMFLOW=0.
DO 250 JR=0,NR
ARING=PI*TDIAM*TDIAM/4./XR2*(2.*DBLE(JR)-1.)
IF (JR .LE. IWAFER) SUMWAF=SUMWAF+PHINew(JR,NZ)*ARING
IF (JR .GT. IWAFER .AND. JR .LE. IELEC)
& SUMELEC=SUMELEC+PHINew(JR,NZ)*ARING
IF (JR .LE. IELEC) SUMELEC=SUMELEC+PHINew(JR,0)*ARING
IF (JR .GT. IELEC) SUMTEF=SUMTEF+PHINew(JR,0)*ARING+PHINew(JR,NZ)*ARING
250 CONTINUE
DO 260 JZ=0,NZ
SUMFLOW=SUMFLOW+QFLOW/XNZ*PHINew(NR,JZ)
260 CONTINUE
TOTLOSS=SUMFLOW+SUMWAF+SUMELEC+SUMTEF
FFLOW=100.*SUMFLOW/TOTLOSS
FWAF=100.*SUMWAF/TOTLOSS
FELEC=100.*SUMELEC/TOTLOSS
FTEF=100.*SUMTEF/TOTLOSS
C
WRITE (2,2006) FWAF,FELEC,FTEF,FFLOW
C
C FORMAT STATEMENTS
2001 FORMAT('PARAMETERS USED IN CALCULATION:','/, 'FLOW RATE= ',F4.1, ' SCCM',
& /, 'PRESSURE= ',F5.3, ' TORR'./,
& 'DIFFUSIVITY OF ATOMIC CHLORINE =',F5.1, ' CM2/S'./,
& 'ELECTRODE SPACING=',F4.1, ' CM'./,
& 'ELECTRODE DIAMETER=',F5.2, ' CM'./, 'WAFER DIAMETER=',F5.2, ' CM',
& /, 'TEFLON DIAMETER=',F5.2, ' CM'./, 'REACTION RATES:','/,
& 'RECOMBINATION ON ELECTRODE=',E9.2, ' CM/S'./,
& 'ETCHING REACTION ON WAFER=',E9.2, ' CM/S'./,

```

```

&          'RECOMBINATION ON TEFLON=' ,E9.2, ' CM/S' ./,
&          'FORMATION IN BULK PLASMA=' ,E9.2, ' CM3/S')
2002  FORMAT(/, 'THE GRID SIZE IS ',I3, ' IN R BY ',I3, ' IN Z' ./,
&          'AFTER ',I5, ' ITERATIONS ('.E9.2, ' SECS.), AVGERR=' ,E9.2)
2003  FORMAT(2X,F5.2,3X,9(E10.3,2X))
2004  FORMAT(//, 'ETCH RATE UNIFORMITY WITH RADIAL DISTANCE')
2005  FORMAT('AT R=' ,F5.2, ' CM, RELATIVE RATE=' ,F5.2)
2006  FORMAT(//, 'FRACTIONAL LOSSES BY VARIOUS MECHANISMS' ./,
&          F5.2, '% BY ETCHING' ./, F5.2, '% BY RECOMBINATION AT ELECTRODES' ./,
&          F5.2, '% BY RECOMBINATION ON TEFLON' ./, F5.2, '% BY FLOW LOSSES')
2009  FORMAT(/.1X, 'RADIUS', 50X, 'POSITION IN Z' ./, 13X, 9('Z=' ,I3, 7X))
2010  FORMAT(50(' - '), ' EDGE OF WAFER ', 50(' - '))
2011  FORMAT(50(' - '), ' EDGE OF ELECTRODE ', 50(' - '))
      END

```



```

C      THIS PROGRAM CALCULATES ATOMIC CHLORINE CONCENTRATION
C      PROFILES, ASSUMING ELECTRON-IMPACT DISSOCIATION OF
C      CF3CL, GAS-PHASE RECOMBINATION, AND ELECTRODE SURFACE
C      RECOMBINATION. SEE CHAPTER 5 OF THESIS
C      FOR DETAILS.
C
C      IMPLICIT DOUBLE PRECISION (A-H,O-Z)
C      DIMENSION THETA(-1:100),THETAOLD(-1:100)
C      REAL*8 KFORM,KRSURF,KETCH,KRGAS
C
C      OPEN FILES.
C
C      OPEN (1,FILE='RECOMB_DATA')
C      OPEN (2,FILE='RECOMB_OUT')
C      OPEN (3,FILE='RECOMB_PLOT')
C
C      READ PARAMETERS FOR CALCULATION.
C
C      READ (1,*) NELEM
C      READ (1,*) PRESS
C      READ (1,*) EDEN
C      READ (1,*) ESP
C      READ (1,*) KFORM
C      READ (1,*) KRGAS
C      READ (1,*) EPROB
C      READ (1,*) KRSURF
C      READ (1,*) TOL
C
C      CALCULATE CONSTANTS SUCH AS DIFFUSIVITY.
C
C      DIFF0=2.0D2
C      DIFF=DIFF0/PRESS
C      DELTAE=1.D0/DBLE(NELEM)
C      CMEAN=5.D+4
C      KETCH=EPROB*CMEAN/4.D0
C
C      ASSUME GAS TEMP IS 500K.
C      CF3CL=1.8D16*PRESS
C
C      TIME=0.D0
C      DO 100 I=-1,100
C      THETA(I)=1.D-2
C      THETAOLD(I)=1.D-2
100  CONTINUE
C
C      THE SOLUTION IS OBTAINED BY INTEGRATING THE
C      PARTIAL DIFFERENTIAL EQUATION FOR CL OVER
C      TIME - THE TIME STEPS ARE NOW ASSIGNED.
C
C      PRINT *, 'TIME INCREMENT? '
C      READ *, DTIME
C      PRINT *, 'MAXIMUM INTEGRATION TIME? '
C      READ *, TMAX
C
C      ASSIGN CONSTANTS
C
C      ALPHA=DIFF/ESP/ESP/DELTAE/DELTAE
C      BETA=KRGAS*CF3CL
C      GAMMA=KFORM*EDEN
C      DELTA=2.D0*KRSURF*CF3CL*ESP*DELTAE/DIFF
C      NMID=NELEM/2
C
C      1000 CONTINUE
C
C      NOW INTEGRATE IN SPACE VIA FINITE DIFFERENCES,
C      STARTING AT THE LOWER ELECTRODE.
C      BOUNDARY CONDITION AT WAFER:
C
C      THETA(-1)=THETAOLD(1)-2.D0*ESP*KETCH*DELTAE/DIFF*THETAOLD(0)
C      Z1=2.D0*ALPHA*(1.D0-KETCH*ESP*DELTAE/DIFF)/BETA/DELTAE/DELTAE
C      Z2=ALPHA*(2.D0*THETA(-1)+GAMMA*DELTAE*DELTAE/ALPHA)/BETA/DELTAE/DELTAE
C      THETA(0)=(DSQRT(Z1*Z1+4.D0*Z2)-Z1)/2.D0
C
C      INTEGRATION SCHEME.
C
C      DO 200 I=1,(NELEM-1)

```

```

      THETA(I)=THETAOLD(I)+DTIME*
&      (ALPHA*(THETAOLD(I+1)-2.D0*THETAOLD(I)+THETAOLD(I-1))-
&      BETA*THETAOLD(I)+THETAOLD(I)+GAMMA)
      THETA(I)=DMAX1(THETA(I),0.D0)
200  CONTINUE
C
C      BOUNDARY CONDITION AT ELECTRODE
C
      Z3=2.D0*ALPHA/(BETA+ALPHA*DELTA)
      Z4=(2.D0*ALPHA*THETA(NELEM-1)+GAMMA)/
&      (BETA+ALPHA*DELTA)
      THETA(NELEM)=(DSQRT(Z3*Z3+4.D0*Z4)-Z3)/2.D0
      THETA(NELEM)=DMAX1(THETA(NELEM),0.D0)
      THETA(NELEM+1)=THETA(NELEM-1)-DELTA*THETA(NELEM)+THETA(NELEM)
      THETA(NELEM+1)=DMAX1(THETA(NELEM+1),0.D0)
C
C      CHECK FOR CONVERGENCE BY LOOKING AT D[CL]/DTIME.
C      WHEN THIS IS SUFFICIENTLY SMALL, ASSUME STEADY
C      STATE.
C
      IF (THETAOLD(NMID) .NE. 0.) RATIO=THETA(NMID)/THETAOLD(NMID)
      CHANGE=ABS(1.D0-RATIO)
C
      DO 300 K=0,NELEM
      THETAOLD(K)=THETA(K)
300  CONTINUE
C
      IF (CHANGE .LE. TOL .OR. TIME .GT. TMAX) GO TO 500
      TIME=TIME+DTIME
      GO TO 1000
C
500  CONTINUE
C      THE SOLUTION HAS BEEN OBTAINED.
C      WE HAVE ONLY TO PRINT IT OUT.
C
      WRITE (2,2001) PRESS,EDEN,ESP,KFORM,KRGAS,
&      KRSURF,EPROB,NELEM,TOL
      WRITE (2,2002)
      WRITE (3,2010)
C
      DO 750 I=0,NELEM
      CONCI=THETA(I)*CF3CL
      CONCI=CONCI/1.D+14
      DI=1.D0*DBLE(I)/DBLE(NELEM)*ESP
      WRITE (2,2003) DI,CONCI
      WRITE (3,2011) DI,CONCI
750  CONTINUE
C
C
C      IDENTIFY THE MAJOR SINKS IN THE DISCHARGE.
C      TOTAL UP ALL LOSS PROCESSES.
C
      SURFLOSS=KRSURF*THETA(NELEM)*THETA(NELEM)*CF3CL*CF3CL
      ETCHLOSS=KETCH*THETA(0)*CF3CL
      SUMCL=0.
      GASLOSS=0.
      DO 600 J=1,(NELEM-1)
      GASLOSS=GASLOSS+KRCAS*CF3CL*CF3CL*DELTA*ESP*
&      (THETA(J)+THETA(J+1))*(THETA(J)+THETA(J+1))/4.
      SUMCL=SUMCL+THETA(J)
600  CONTINUE
C
C      CALCULATE FRACTIONAL LOSS BY DIFFERENT MECHANISMS
C      AND COMPARE TOTAL WITH THE TOTAL FORMATION RATE.
C
      AVGCL=SUMCL*CF3CL/(NELEM-1)
      TLOSS=GASLOSS+SURFLOSS+ETCHLOSS
      TFORM=KFORM*ESP*EDEN*CF3CL
      FEL=ETCHLOSS/TLOSS
      FGL=GASLOSS/TLOSS
      FSL=SURFLOSS/TLOSS
      WRITE (2,2004) FGL,FSL,FEL,TFORM,TLOSS
C
C      CALCULATE CHEMICAL ETCHING RATE, ASSUMING SICL4
      ERATE=6.D1*KETCH*CF3CL*THETA(0)/4.D0/5.D22*1.D0
      WRITE (2,2005) ERATE,AVGCL
C

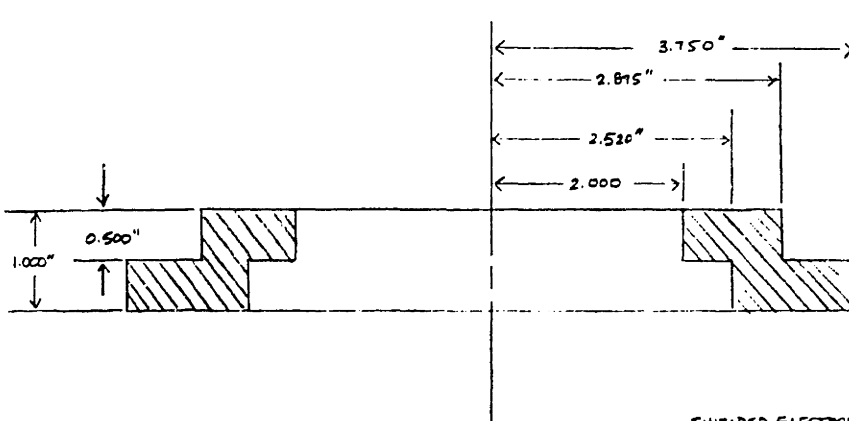
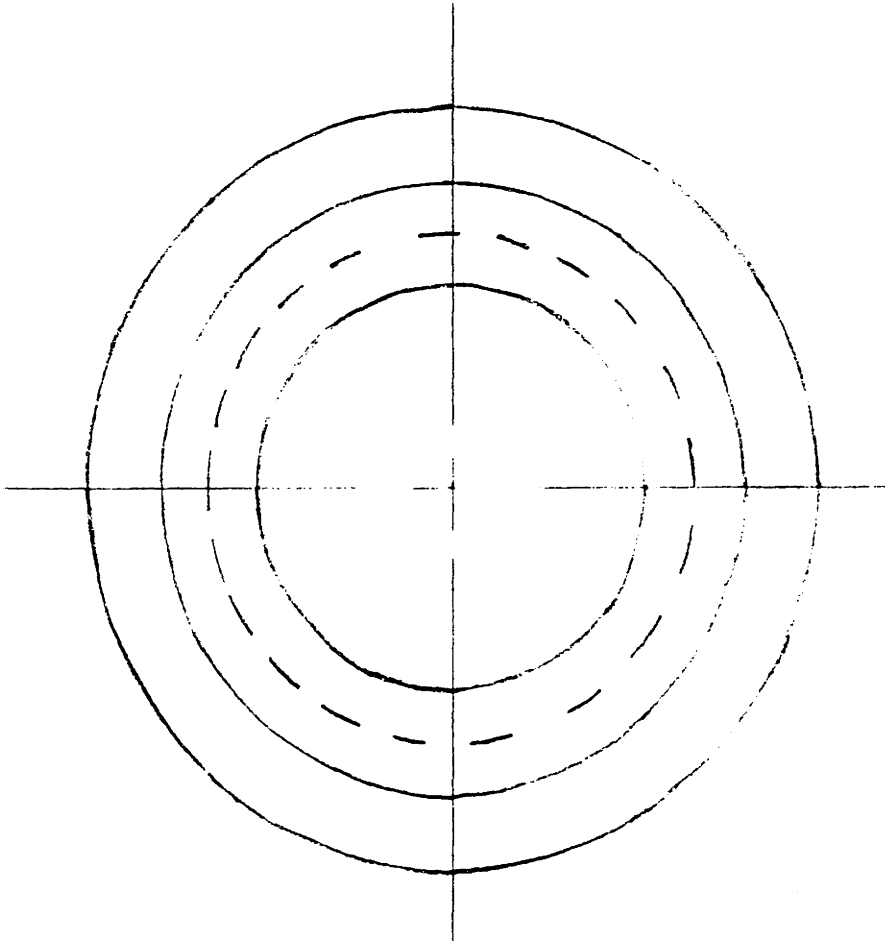
```

```

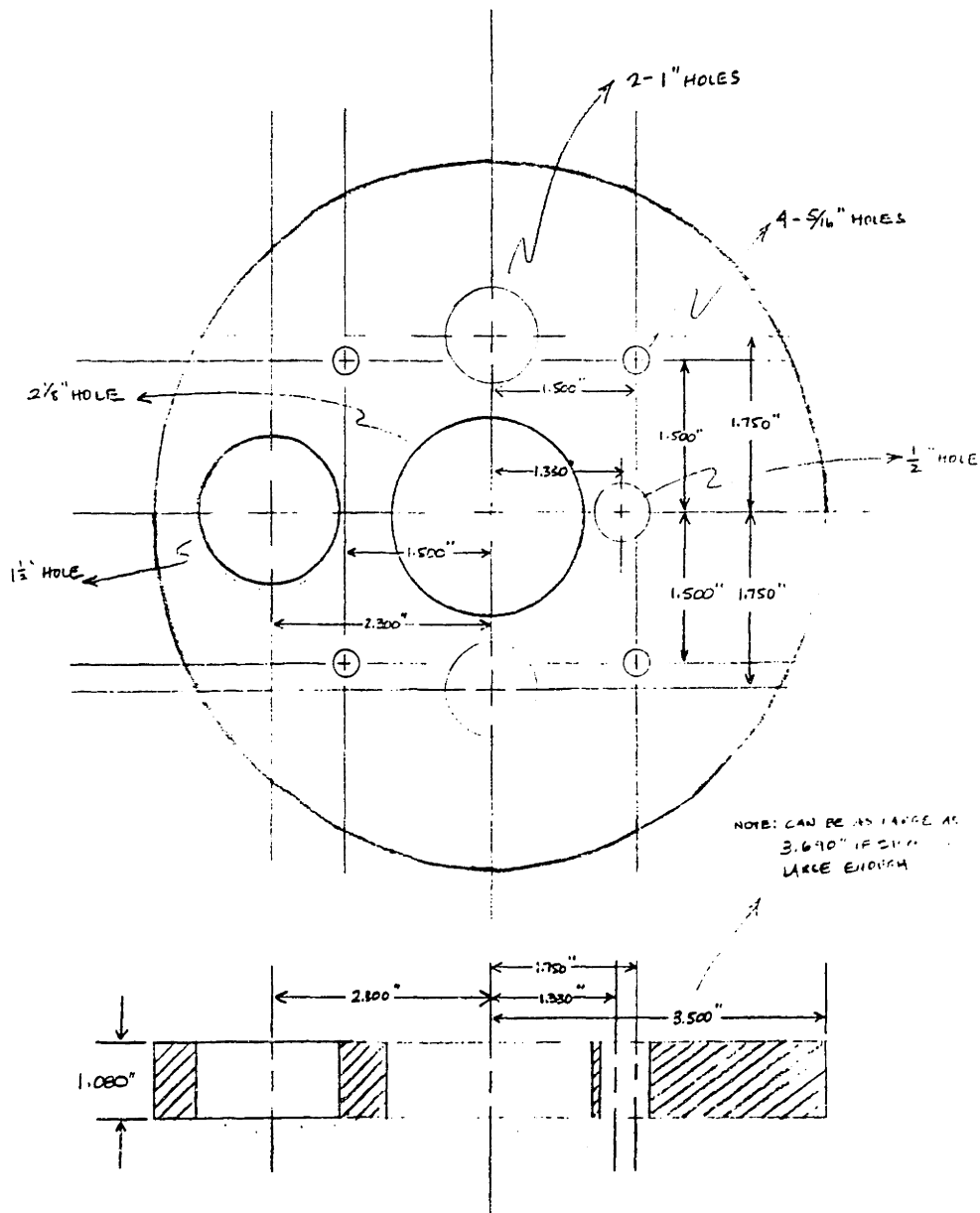
2001  FORMAT(1X,'P= ',F4.2,' TORR',/,1X,'ELECTRON DENSITY= ',E10.3,
&      /,1X,'ELECTRODE SPACING= ',F4.2,' CM',
&      /,1X,'KFORM= ',E10.3,/,1X,'KRGAS= ',E10.3,/,1X,
&      'KRSURF= ',E10.3,/,1X,'EPROB= ',E10.3,
&      /,1X,'NUMBER OF ELEMENTS: ',I3,/,1X,
&      'SPECIFIED ERROR TOLERANCE: ',E10.3)
2002  FORMAT(/,1X,'POSITION',4X,'CONC x1.E14',/,25('-'))
2003  FORMAT(1X,F5.3,5X,F7.3)
2004  FORMAT(/,1X,'FRACTION LOST BY GAS RECOMB.= ',F5.3,
&      /,1X,'FRACTION LOST BY SURFACE RECOMB.= ',F5.3,
&      /,1X,'FRACTION LOST BY ETCHING RXN= ',F5.3,
&      /,1X,'TOTAL FORMATION RATE= ',E10.3,
&      /,1X,'TOTAL LOSS RATE= ',E10.3)
2005  FORMAT(/,1X,'SILICON ETCHING RATE IN ANGSTROMS/MIN: ',E9.2,
&      /,1X,'AVERAGE CHLORINE CONCENTRATION = ',E9.2)
2010  FORMAT(1X,'OUTPUT FROM RECOMBINATION MODEL',/,
&      'DISTANCE FROM ELECTRODE, IN CM',/,
&      '[CL]x1.E-14, PER CC',/,
&      'SYMB 99.0',/, 'XMIN 0.0',/, 'YMIN 0.0',/, 'YMAX 2.5',/, 'END')
2011  FORMAT (F5.3,',',F7.3)
      END

```

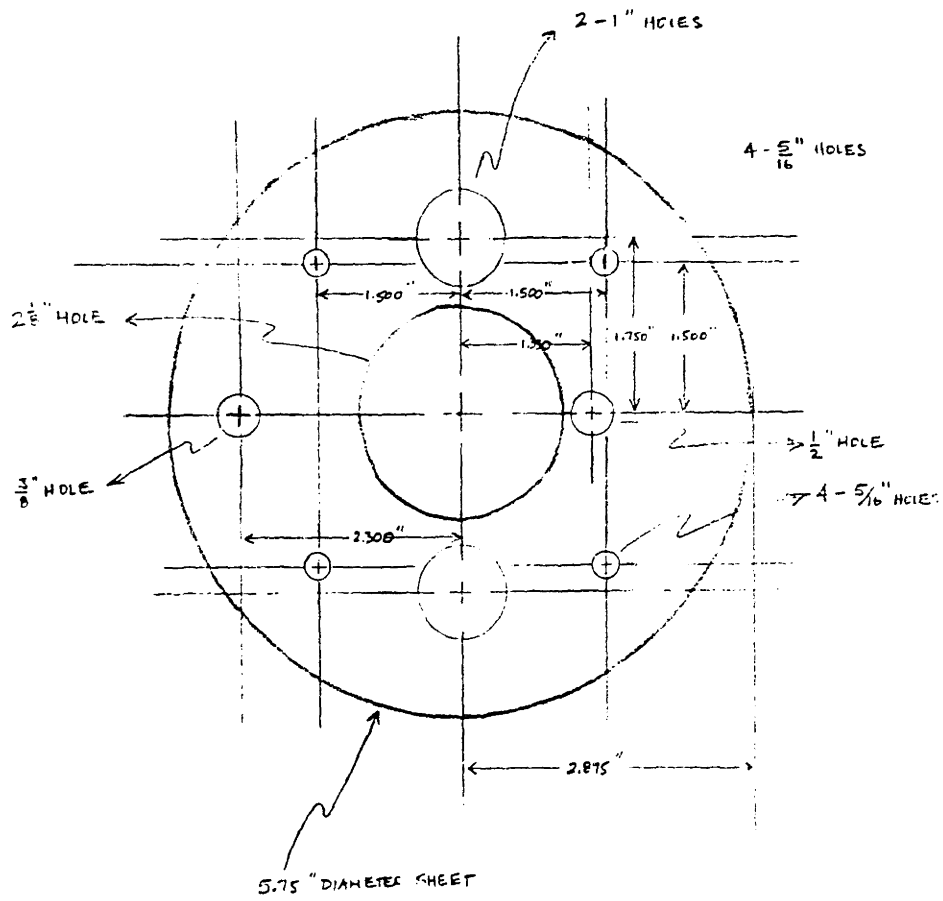
APPENDIX C - EQUIPMENT DRAWINGS



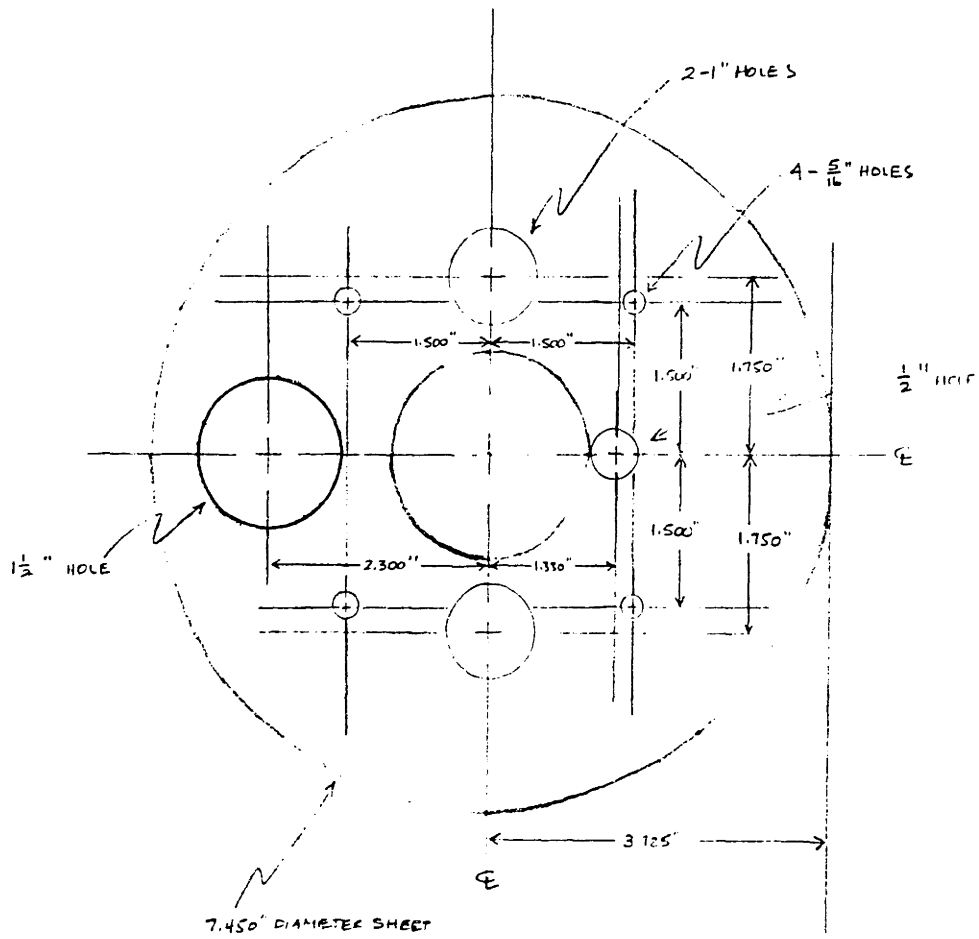
SHIELDED ELECTRODE ASSEMBLY
 DRAWING 1 OF
 MATERIAL: TEFCON
 K. ALLEN



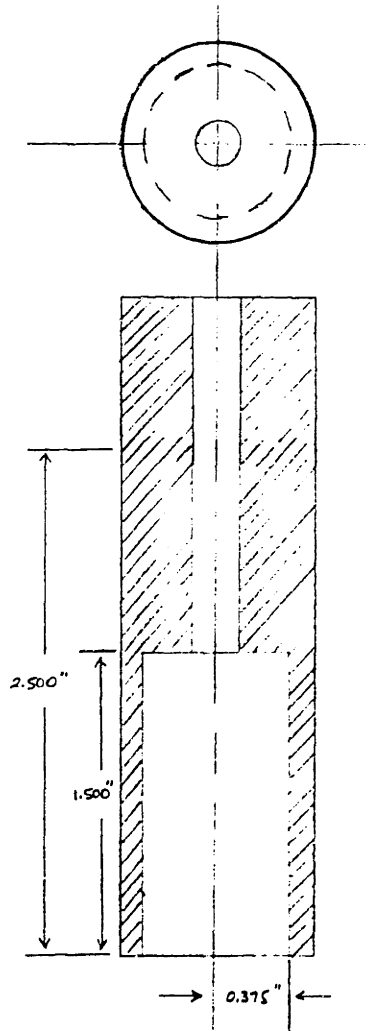
SHIELDED ELECTRODE ASSEMBLY
 DRAWING 2 OF
 MATERIAL: TEFLON
 K. ALLEN



SHIELDED ELECTRODE ASSEMBLY
 DRAWING 3 OF
 MATERIAL: $\frac{1}{16}$ " STAINLESS SHEET
 K. ALLEN
 (POWERED SHIELD)

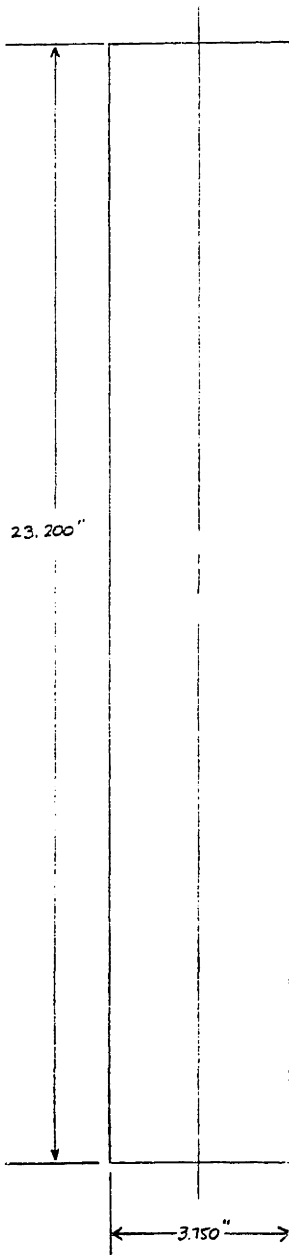


SHIELDED ELECTRODE ASSEMBLY
 DRAWING 4 OF
 MATERIAL: $\frac{1}{16}$ " STAINLESS SHEET
 K. ALLEN
 (GROUNDED SHIELD)

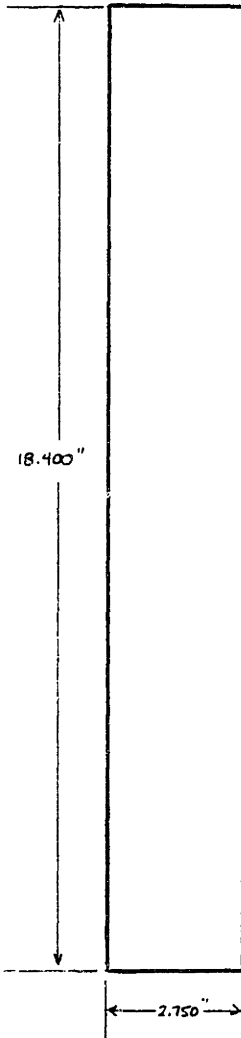


TWO (2) OF THIS PIECE
ARE REQUIRED

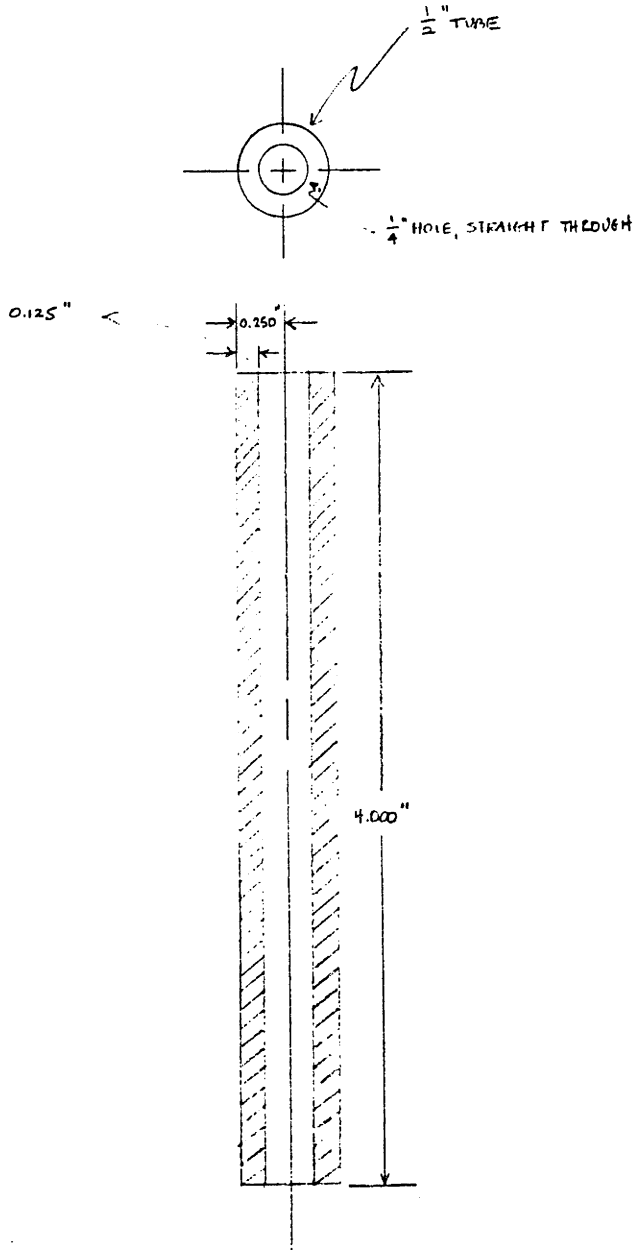
SHIELDED ELECTRODE ASSEMBLY
DRAWING 5 OF
MATERIAL: TEFLON
K. ALLEN



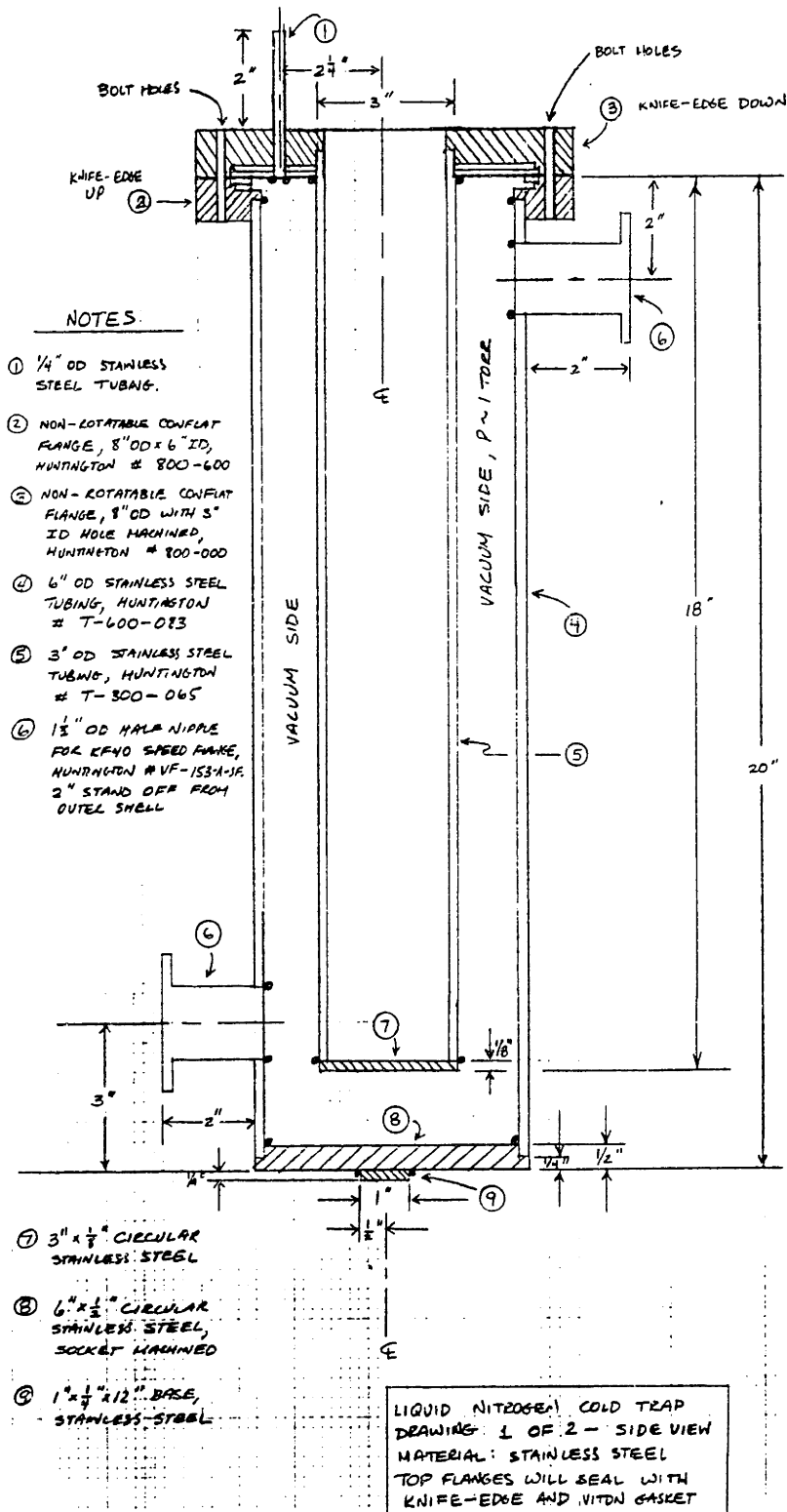
SHIELDED ELECTRODE ASSEMBLY
DRAWING 6 OF
MATERIAL: 1/32" STAINLESS STEEL
K. ALLEN



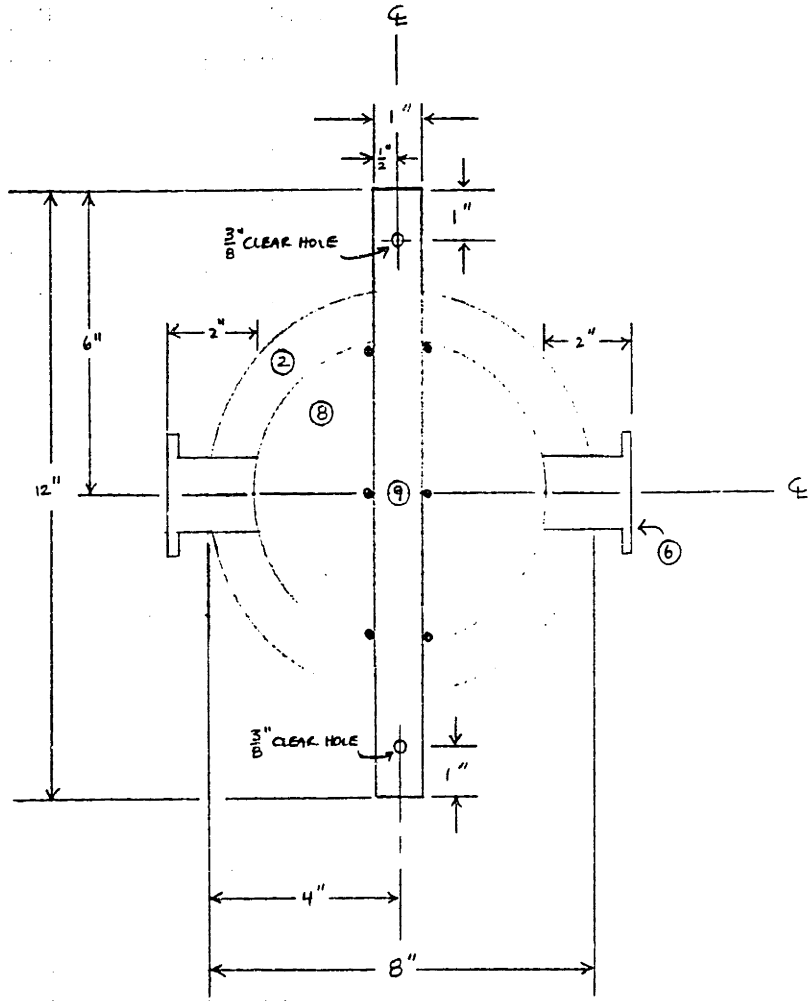
SHIELDED ELECTRODE ASSEMBLY
DRAWING 7 OF
MATERIAL: 1/2" STAINLESS STEEL
K. ALLEN



SHIELDED ELECTRODE ASSEMBLY
 DRAWING B OF
 MATERIAL: TEFLON
 K. ALLEN



R. D. AULEN
5/2/85



LIQUID NITROGEN COLD TRAP
 DRAWING 2 OF 2 - BOTTOM VIEW
 MATERIAL: STAINLESS STEEL
 CIRCLED NOTES REFER TO
 DRAWING 1

K.D. ALLEN
 5/3/15